

# **Study on Graphene-Metal Oxide Semiconductor Nanocomposite Based Sensors for Detection of Volatile Organic Compounds at Low Temperature**

**A thesis submitted for fulfillment of the degree of  
Doctor of Philosophy (Science)**

**To**



**Department of Chemistry  
Jadavpur University**

**By**

**Sovandeb Sen**

**Index no.: 38/20/Chem./27**

**Registration no.: SCHEM1503820**




**Functional Materials & Devices Division  
CSIR-Central Glass and Ceramic Research Institute  
196, Raja S. C. Mullick Road, Jadavpur  
Kolkata 700032, India**

**2024**



## CERTIFICATE FROM THE SUPERVISOR

This is to certify that the thesis entitled “Study on Graphene-Metal Oxide Semiconductor Nanocomposite Based Sensors for Detection of Volatile Organic Compounds at Low Temperature” being submitted by Sovandeb Sen (Registration No.: SCHEM1503820 and Index no.: 38/20/Chem./27) got his name registered on 14<sup>th</sup> October 2020 for the award of Doctor of Philosophy (Science), is the record of bonafide research work carried out by him under the supervision of Dr. Susmita Kundu, Principal Scientist, Functional Materials and Devices Division (FMDD), CSIR-Central Glass and Ceramic Research Institute (CGCRI), Kolkata 700032, West Bengal, India. To the best of my knowledge, the results presented in this thesis have not been submitted by him elsewhere before for the award of any other degree or diploma.

 **डॉ सुष्मिता कुंदु**  
**Dr. Susmita Kundu**  
प्रमुख वैज्ञानिक / Principal Scientist  
कार्यात्मक पदार्थ एवं उपकरण विभाग  
Functional Materials & Devices Division  
सीएसआईआर-केंद्रीय काँच एवं सिरामिक अनुसंधान संस्थान  
CSIR-Central Glass & Ceramic Research Institute  
१९६, राजा एस. सि. मल्लिक रोड, १९६, राजा एस. सी. मल्लिक रोड  
कोलकाता-७०० ०३२, भारत, Kolkata-700 032, India

*Susmita Kundu* 27/02/24

Dr. Susmita Kundu  
Principal Scientist  
FMDD, CSIR-CGRI  
Jadavpur, Kolkata 700032  
West Bengal, India

*Dedicated to...*

*Baba-Ma*





## **ACKNOWLEDGEMENTS**

*The Ph. D. journey of a researcher cannot be completed single-handedly. During my journey of research work, I have met many individuals who extended their motivation and continuously supported me with their knowledge and experience. At the stage of completion, I would like to grab the opportunity to thank those persons for their constant help, guidance, support, and prayer that encouraged me to enjoy this precise journey of work.*

*First and foremost, I would like to convey my heartfelt gratefulness to my guide and supervisor who introduced me to the world of research and development with great enthusiasm and patience. I would like to express my sincere gratitude to my mentor Dr. Susmita Kundu (Principal Scientist, Functional Materials and Devices Division, CSIR-Central Glass and Ceramic Research Institute) for her guidance and constant attention during the entire course of the Ph. D. program. My esteemed supervisor, Dr. Susmita Kundu, with her intellect has played a pivotal role in nurturing me as a researcher. I am deeply indebted to her for her critical wisdom and passionate involvement in the whole thesis work. Dr. Kundu's resourceful insights for an in-depth understanding of the subject introduced me to a new horizon of research and encouraged me to give my best. Without her excellent mentorship, this research work would not have taken such a comprehensive structure.*

*I feel honored for having come across brilliant academic personals throughout my whole research journey. I am highly obliged to Dr. K. Muraleedharan (former Director, CSIR-CGCRI) and Dr. Suman Kumari Mishra (present Director, CSIR-CGCRI) for allowing me to pursue my Ph. D. work in this esteemed Institute and they endorsed various requisite approvals to carry out my research work. I would like to express my genuine appreciation and profound gratitude to all of them. Dr. Mrinal Pal, Head of, the Functional Materials and Devices Division, CSIR-CGCRI, was very supportive, and always helped me whenever I needed it. I would like to acknowledge the help rendered by the technical faculties of FMDD, specially mentioned Dr. Sagnik Das, Md. Jalaluddin Mondal, and Mr. Raju Manna for their contribution to sensor module fabrication and sensing unit setup.*

*I am extremely thankful to the Head of, the Department of Chemistry, at Jadavpur University for allowing me to be registered in his department. I would also like to acknowledge all the faculty members of this department who introduced me to the different aspects of research-related topics during the coursework. I am immensely grateful to Dr. Sunirmal Jana (Chief Scientist, Specialty Glass Division, CSIR-CGCRI), the subject expert of my RAC of Jadavpur University for providing valuable suggestions and moral support in every aspect.*

*I acknowledge the Innovation in Science Pursuit for Inspired Research (INSPIRE) program of the Department of Science and Technology, Government of India, for the fellowship and contingency grant (IF180783) for carrying out my Ph. D. work.*

*I expand my thanks to the Central Material Characterization Section, especially, Mrs. Mousumi Baral Narjinari, for her consistent cooperation in characterization processes. I am very much thankful to Mr. Srikrishna Manna for Raman characterization. Also, all the members of the Electron Microscopy Section and X-Ray Characterization Section were extremely supportive every time I required any suggestions regarding characterization.*

*My appreciation would remain incomplete if I do not recognize the coordination and assistance received generously from scientists and staff of several divisions and laboratories along with those from the civil, electrical, stores, library, canteen, reception and security, and the administrative department of CSIR-CGCRI.*

*It's a great pleasure to thank my senior lab-mates Dr. Sugato Ghosh and Amit Nilabh, who were very much supportive in my early days of research. They introduced me to the pros and cons of research. I am deeply indebted to my seniors Dr. Puja Ghosh, Dr. Shewli Pratihar, Dr. Epsita Kar, Dr. Abhisek Sasmal, Dr. Subhankar Mishra, Tania Di, Saheli Di, for all the valuable discussions and suggestions. Also, my juniors namely Debojyoti, Zeeshan, Sourav, Pounomi, Animesh, Deepak, Subhojit, and Prosenjit helped me a lot whenever I needed their assistance throughout my Ph. D. journey.*

*I wish to express my sincere thanks to my school friends and presently researchers in different laboratories in India, Arnab Das, Soumya Biswas, and Soumen Ghosh for their motivation, constant support, and sharing opinions in different aspects. I would also like to give a heartfelt, special thanks to my dearest friend Shreyashi for her continuous inspiration and encouragement every now and then and I would not be able to convey her contribution in words.*

*Of course, this acknowledgment would not be completed without giving regard to my parents. Both of them have sacrificed a lot but become successful in conveying to me a good foundation to meet life. Without their unconditional love and support in my life, I could have never been able to complete this thesis. I owe everything to them. Their much-needed support, motivation, patience, understanding, love, and care helped me to overcome every difficulty I have faced.*

*I beg for pardon I had left out anyone who had in one way or another, helped me in the completion of this thesis. My memory is running short, but one thing you can be sure of – you are heartily appreciated and I express my sincere thanks to you.*

*Last but not least, I owe my reverence to the Almighty, by whose grace I have been able to strengthen, myself enough to complete my research work successfully.*

.....  
Sovandeb Sen

## **ABSTRACT**

Non-invasive diagnosis of different diseases via human exhaled breath analysis has been recognized as a promising technology. It's worth mentioning that in exhaled human breath several VOCs are present at ppm/ppb level concentration and some of them are identified as breath biomarkers; viz., ammonia for renal diseases, acetone for diabetes, toluene for lung cancer, etc. Though recently certain spectroscopic techniques are being used for non-invasive diagnosis of diseases; however, real-time application requires development of selective VOC sensors for precise detection of low concentration VOC.

In this purpose, among various types of sensors, chemiresistive metal oxide semiconductor (MOS) based sensors already proved their efficacy. Although MOS-based sensors are suitable for versatile gas sensing applications, but, in pristine form their potential applications are hindered due to their high operating temperature, low sensitivity, poor selectivity, etc. Different strategies are being adopted to get rid of the short-comings of MOS-based sensor, either engineering of heterojunction-based nanocomposites or metal ion doping in pristine lattice. Such functionalizations of pristine lattice facilitate the sorption of gas molecules via defect site generation and thereby boost the sensing response. Carbonaceous nanomaterials are regarded as highly promising composite materials due to their high charge carriers' mobility that facilitates the electronic interaction during gas sensing. Now, reduced graphene oxide (rGO) is one of the best carbonaceous materials which provide a large specific surface area with enhanced number of active sites for adsorption of gas molecules. Therefore, less activation energy is required for the interaction between gas molecules and the sensing materials which reduces the operating temperature of the sensor. The elimination of the heating element makes the fabrication of the sensor very simple and its durability also improves. Therefore, in the proposed Ph. D. dissertation work, the prime goal was to develop graphene-metal oxide semiconductor nanocomposite based sensors for selective detection of VOCs at a low operating temperature.

At first, ZnO-SnO<sub>2</sub> binary nanocomposites were synthesized and further decorated with rGO. The optimum rGO decorated ZnO-SnO<sub>2</sub> nanocomposite showed a significant decrease in optimum operating temperature from 300°C to 150°C. The sensors exhibited their high performance to detect very low concentration (~ 1 ppm) of acetone and ethanol in presence of many other interfering gases with quite good stability. The primary objective of this work was to

obtain the optimum operating temperature at ambient conditions, i.e., at room temperature. Therefore, in the next chapter, rGO decorated NiO-SnO<sub>2</sub> nanocomposite based sensors were fabricated and VOCs (acetone and ethanol) detection was achieved at room temperature. Nevertheless, the selectivity to a specific VOC was still remained as a challenge.

Among higher transition metal oxides, WO<sub>3</sub> is a prolific gas sensing material and so in the following work pristine WO<sub>3</sub> was doped with Fe<sup>3+</sup> and further nanocomposite was synthesized with rGO to obtain a promising VOC sensor. The as-prepared nanocomposite-based sensor exhibited an excellent selectivity towards acetone with rapid response/recovery time and long term stability; however, the operating temperature of the sensor was a little bit higher (~ 130°C). Low temperature operated selective acetone sensor was obtained, by changing the dopant ion from Fe<sup>3+</sup> to Cr<sup>3+</sup> in rGO decorated WO<sub>3</sub>. This induced crystalline phase change from monoclinic to hexagonal WO<sub>3</sub>, accounted for room temperature acetone sensing performance with better sensing response.

Among lower transition metal oxides, iron oxide is considered as conventional gas sensing material; so in the dissertation work, iron oxide was doped with Cr<sup>3+</sup> followed by decorated with rGO. This work revealed a temperature dependent transition of sensing response from n-type (at higher temperature) to p-type (at lower temperature). Even these sensors also demonstrated a selective acetone sensing performance at room temperature.

Some of the developed room temperature operated sensors also implemented for discrimination of exhaled breath of diabetic person from healthy person in terms of sensing response towards the acetone concentration present in those breath samples.

In a nutshell, in this thesis work, VOC sensing performance of different MOSs based sensors were delineated. Their sensing performance was improved in terms of working temperature reduction, enhancement of sensing response, and selective acetone sensing, either by formation of binary nanocomposite or by doping of metal ions and further introduction of rGO. The sensing mechanism of the sensors was elucidated by schematic band diagram modeling. This dissertation work unveiled the selective ppm-level acetone sensing performance at ambient condition and paved the way for non-invasive diabetes detection via exhaled human breath analysis.

## **TABLE OF CONTENTS**

<b>Particulars</b>	<b>Page No.</b>
<b>Acknowledgements</b>	<b>i-ii</b>
<b>Abstract</b>	<b>iii-iv</b>
<b>Table of Contents</b>	<b>v-x</b>
<b>Chapters</b>	<b>1-284</b>
<b>Chapter 1: Background Study and Literature Review</b>	<b>1-58</b>
1.1. Motivation of the present work	3
1.2. Introduction	4
1.3. Overview of sensors	5
1.4. Metal oxide semiconductor (MOS) based sensor	7
1.4.1. Brief history of MOS-based sensor	7
1.4.2. Working principle of MOS-based gas sensor	9
1.4.3. Essential parameters related to sensor	12
1.4.4. Advantages of MOS-based gas sensor	17
1.4.5. Disadvantages of MOS-based gas sensor	17
1.4.6. Major application areas of MOS-based sensors	17
1.4.7. Factors affecting sensing performance of MOS-based gas sensors	19
1.4.8. Plausible ways to enhance the performance of MOS-based gas sensor	21
1.4.8.1. Metal oxide nanocomposite formation	22
1.4.8.2. Metal ion doping	23
1.4.9. Low temperature operated MOS-based sensors	25
1.4.10. Functionalized graphene-MOS-based gas sensors	26
1.5. Breath biomarkers detection by gas sensing technology	32
1.6. Objective of the present work	36
References	38
<b>Chapter 2: Nanomaterial Synthesis and Characterization</b>	<b>59-92</b>
2.1. Introduction	61
2.2. Synthesis processes	62
2.2.1. Sol-gel synthesis	63

## **TABLE OF CONTENTS**

2.2.2. Advantages of sol-gel synthesis	63
2.3. Details of synthesis process used in present work	64
2.3.1. Synthesis of metal oxide nanomaterials	64
2.3.2. Synthesis of Graphene Oxide	64
2.3.3. Synthesis of Reduced Graphene Oxide	64
2.3.4. Synthesis of rGO-metal oxide nanocomposites	65
2.4. Characterization techniques of nanomaterials	65
2.4.1. Thermogravimetric Analysis (TGA)	65
2.4.2. Powder X-Ray Diffraction (XRD) Technique	66
2.4.3. Fourier Transforms Infrared Spectroscopy (FTIR)	68
2.4.4. Raman Analysis	69
2.4.5. Surface Area Analysis	71
2.4.6. Field Emission Scanning Electron Microscopy (FESEM)	74
2.4.7. Transmission Electron Microscopy (TEM)	75
2.4.8. X-Ray Photoelectron Spectroscopy (XPS)	77
2.4.9. UV-Visible Spectroscopy	78
2.4.10. Photoluminescence (PL) Spectroscopy	80
2.4.11. Impedance Spectroscopy	80
2.5. Details of sensor fabrication	83
2.5.1. Preparation of sensor substrate	83
2.5.2. Fabrication of sensor	83
2.5.3. Packaging of sensor module	84
2.6. Gas sensing measurement	85
References	89

### **Chapter 3.1: Reduced graphene oxide (rGO) decorated ZnO-SnO<sub>2</sub>: A ternary nanocomposite towards low concentration VOC sensing performance**

**93-128**

3.1.1. Introduction	95
3.1.2. Experimental	96
3.1.3. Results and discussions	98

## TABLE OF CONTENTS

3.1.3.1. Characterization of graphene materials	98
3.1.3.2. Characterization of nanocomposites	103
3.1.3.3. Gas sensing performance study	112
3.1.3.4. Gas sensing mechanism	120
3.1.4. Conclusion	123
References	124

### **Chapter 3.2: Reduced graphene oxide (rGO) decorated NiO-SnO<sub>2</sub> nanocomposite sensor towards room temperature VOC sensing performance**

**129-164**

3.2.1. Introduction	131
3.2.2. Experimental	131
3.2.3. Results and discussions	132
3.2.3.1. Characterization of nanocomposites	132
3.2.3.2. Gas sensing performance study	143
3.2.3.3. Gas sensing mechanism	153
3.2.3.3.1. Electron depletion model	153
3.2.3.3.2. Impedance spectroscopy	155
3.2.4. Conclusion	158
References	159

### **Chapter 4.1: Reduced graphene oxide (rGO) decorated Fe (III) doped WO<sub>3</sub> nanocomposite towards low temperature ppm level acetone detection**

**165-200**

4.1.1. Introduction	167
4.1.2. Experimental	167
4.1.3. Results and discussions	168
4.1.3.1. Characterization of nanocomposites	168
4.1.3.2. Gas sensing performance study	180
4.1.3.3. Gas sensing mechanism	189



## **TABLE OF CONTENTS**

4.2.3.3.1. Electron depletion model	189
4.2.3.3.2. Impedance spectroscopy	191
4.1.4. Conclusion	196
References	197

### **Chapter 4.2: Reduced graphene oxide (rGO)-Cr (III) doped hexagonal WO<sub>3</sub> nanocomposite towards room temperature ppm-level acetone**

<b>detection</b>	<b>201-236</b>
4.2.1. Introduction	203
4.2.2. Experimental	203
4.2.3. Results and discussions	204
4.2.3.1. Characterization of nanocomposites	204
4.2.3.2. Gas sensing performance study	213
4.2.3.3. Gas sensing mechanism	223
4.2.3.3.1. Electron depletion model	223
4.2.3.3.2. Impedance spectroscopy	225
4.2.4. Conclusion	229
References	230

### **Chapter 5: Reduced graphene oxide (rGO)-Cr (III) doped $\alpha$ -Fe<sub>2</sub>O<sub>3</sub> nanocomposite towards room temperature ppm-level acetone**

<b>detection</b>	<b>237-274</b>
5.1. Introduction	239
5.2. Experimental	239
5.3. Results and discussions	241
5.3.1. Characterization of nanocomposites	241
5.3.2. Gas sensing performance study	255
5.3.3. Gas sensing mechanism	263
5.4. Conclusion	268
References	269

## **TABLE OF CONTENTS**

<b>Chapter 6: Summary and Future Scope</b>	<b>275-284</b>
6.1. Summary and conclusions	277
6.2. Future perspectives	283
<b>Appendix</b>	<b>285-294</b>
Symbols and Abbreviations	285-290
Publications and Conferences	291-294
Publications offprint	

## TABLE OF CONTENTS

# CHAPTER 1

## Background Study and Literature Review



*Beyond the five sense organs of human beings, artificial sensors act as an important additional sensory assistance in our life. Gas sensor is an indispensable category of the sensors and chemiresistive sensor is one of the subgroups of gas sensors. This chapter represents the background study and available literature reviews on different metal oxide semiconductor based chemiresistive gas sensors, their novelty and working principles. It also highlighted the different promising application areas of these sensors and scope of sensing performance improvement. Finally, the motivation and objectives of this dissertation work have been outlined.*



### **1.1. Motivation of the present work:**

Human exhaled breath consists thousands of volatile organic compounds (VOCs) in ppm/ppb concentration and some of these VOCs, carrying the information regarding human metabolic processes, have been recognized as breath biomarkers. Recently, a new domain has been discovered for the early stage, comfortable non-invasive diagnosis of diseases by analyzing the concentration of these VOCs under certain pathological conditions, such as acetone for diabetes mellitus. Now, specific detection of VOC in trace concentration is utmost challenging and at present, different spectroscopic techniques are being adopted for this purpose. Despite prime accuracy, their complex, expensive, and tedious operational processes lead to the scope of development of gas sensor with good selectivity and low detection limit.

Chemiresistive metal oxide semiconductor (MOS) based sensors are quite effective as gas sensing material. However, in pristine form they suffer from inherent setbacks like high operating temperature, low sensitivity, poor selectivity etc. High operating temperature needs complex electronic design as well as it consumes a lot of energy for its operation which degrade the sensing material rapidly and thus shortens the lifetime of the sensor. Modulations of pristine material either by heterojunction formation or via doping of foreign metal ion in pristine lattice can perturb the inherent crystal structure or change the orientation. This alteration generates more defects and vacancies which facilitate sorption of gas molecules even at low temperature and thereby improve the sensing performance. As a compositing material, carbonaceous compounds are highly promising as they are also capable to reduce the working temperature by facilitating the charge mobility. Among different carbon-based materials, reduced graphene oxide (rGO) is highly appreciated due to several inherent advantages like planar network-like structure, large specific surface area, high electron mobility etc. Decoration of metal oxide with rGO facilitates charge transfer process during sensing experiments. As a result of this, operating temperature of the gas sensor reduces, which eventually improves the durability of the sensor. Therefore, motivated with the present state-of-art, the research work of this thesis is focused to the development of novel metal oxide (pristine/heterojunction/metal ion doped)-graphene based sensors through proper structural, morphological and electronic transfer mechanism analyses for selective detection of ppm-level VOC at ambient condition with prolonged stability. In long-term, these sensors will be very useful for non-invasive disease diagnosis through the fabrication of portable, patient-friendly, and inexpensive breath analyzer.

### 1.2. Introduction:

Human beings are by birth blessed with five cardinal sensory receptors like eyes, ears, nose, tongue, and skin. From the ancient ages, scientists have been interested in mimicking the sense organs of living beings and consistently with time their diligence resulted into some fruitful developments. The scientific revolution yielded different technology-based devices to imitate natural sensors of a person; such as, the images and beautiful scenarios observed by the eyes can be captured by camera lens, the voices and sounds heard by ears conceivably recorded by recording devices and different flexible electronic wearable gadgets are able to mimic the function of skin. Nevertheless, the purpose of noses and tongue can be served by chemical sensors. These sensors efficiently sense various gaseous analyte and provide vicenary details regarding the volatile analyte in the vicinity. Now-a-days, the environmental monitoring [1-3] and maintenance of safe ecosystem requires precise gas sensors working in both ambient as well as hazardous condition [4-6]. Such gas sensors are foremost to detect toxic gases like CO, CO<sub>2</sub>, SO<sub>2</sub>, Cl<sub>2</sub>, inflammable gases methane, LPG, H<sub>2</sub>, and motor-vehicle exhaust pollutants SO<sub>x</sub>, NO<sub>x</sub>, different hydrocarbons etc. In the same way, the sensors are well known for their versatility in application arena such as detection of explosives, fire and smoke, quality identification of food items, biomedical usage for non-invasive detection of different diseases and many more [7-10]. In past few decades, scientific evolution and technological advancements demand development of sensor technology as it is quintessential in multidisciplinary sectors starting from logistic applications to aerospace and automotive industries [11-14]. Sensors find its resourceful application in upgradation of daily lifestyle of civilians and are being prominently used in various indoor appliances like air conditioner, room-heater, refrigerator, toaster, fire and smoke detector etc. In outdoor sectors, sensors can be seen in automobile indicators, speed detectors on road, automatic door opening in different shopping complexes and departmental stores. Complex machineries like airplane, helicopters, aircrafts and other air-borne vehicles use high precision sensors in tandem for monitoring altitude, air pressure, wind speed, etc. In industries the processing unit requires sensors to ensure maximum efficiency with minimum wastages as well as for detection of toxic gases in minute concentration to take care of safety of workers. Therefore, to make the sensing device effective, it requires easy processing, facile fabrication technique, controllable physical and chemical properties, and long-term stability.

## 1.3. Overview of sensors:

The term ‘Sensor’ originates from a Latin word ‘Sentire’. In Latin, ‘Sentire’ means ‘to perceive’ [15]. From this perspective, sensor is a miniaturized device that can receive any signals in the form of physical, chemical or by any means, and convert it into an output signal like transducer, for analysis using any suitable technology. Briefly, these sensors detect alteration of different parameters in a confined environment and by analyzing the variation of the identity it renders the corresponding output. The input signal to a sensor can be delivered in the form of chemical, electrochemical, thermal, or mechanical, and the output signal obtained conventionally in the form of electrical signals.

A chemical sensor mainly composed of two fundamental units (Fig. 1.1):

- (a) Receptor: An identification system to accept incoming analyte and its primary function is to deliver a selective response to a specific analyte in presence of several other interfering analytes. The analyte concentration transforms into a chemical output signal with defined sensitivity.
- (b) Transducer: The transducer converts the incoming signal to a physiological output after analysis of the input.

In most of the chemical sensors the interaction between the receptor and analyte molecule triggers a change in physical properties in such a way that the transducer is able to read it and provide an electrical signal for further analysis.

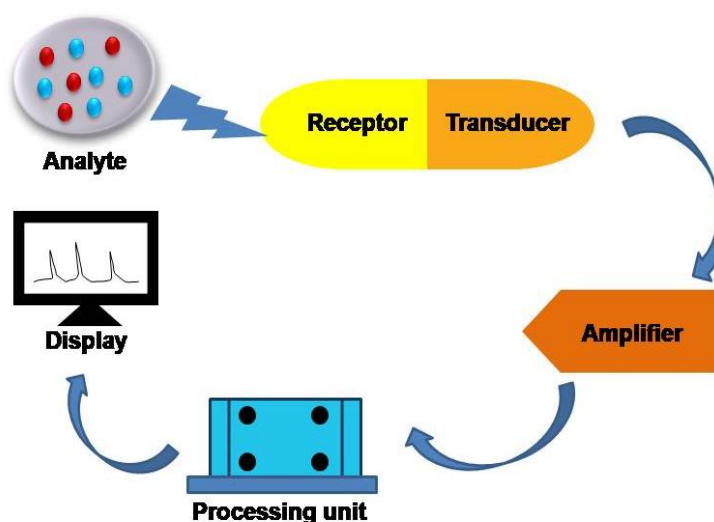


*Figure-1.1: Integral parts of a sensor*



Among several chemical sensors gas sensor is an imperative part of human daily life. A typical gas sensor interacts with the gas molecules in its near environment and generates an output signal after transducer mechanism. The obtained output signal in terms of sensing response symbolized the concentration of the gas detected.

As mentioned earlier, in technology-driven era of civilization, sensor (Fig. 1.1) holds a paramount state in terms of converting any physical or chemical input into analyzable output signal. Henceforth, in our society gas sensors are essential for multidimensional usage like households, automobiles, industries, safety and security purpose, in order to detect various colorless, odorless, harmful, and toxic gases. Gas sensors are primarily used in environmental pollution monitoring and detection of inflammable substances in different outdoor sectors.

The emission of colorless, odorless, inflammable gases in the environment can be risky and therefore to avoid the unforeseen danger, a gas sensor can be instrumental, as it can detect the minute concentration of those gases. Similarly, prolong exposure to volatile organic compounds (VOCs) is harmful for human beings as it accounted for several health hazards like allergy, nausea, headache, lung infections, cancer, etc [16-18]. On the other hand, there are various noxious gases such as  $\text{NH}_3$ ,  $\text{H}_2\text{S}$ ,  $\text{NO}_x$ ,  $\text{SO}_x$ , etc. are harmful and toxic for inhalation. Therefore gas sensors can be a handful tool to identify these unwanted gaseous species at a very low concentration and in an ambient environment.

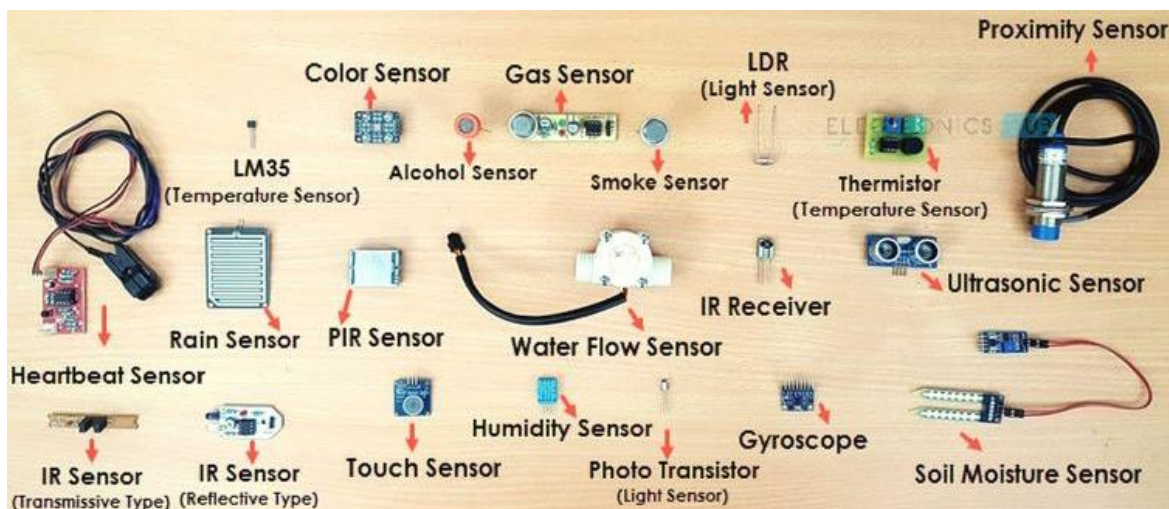


Figure-1.2: Different types of sensors [19]

Across the globe numerous researchers are devoted to develop a highly sensitive, robust, economically viable and durable gas sensing devices. At present there are a variety of gas sensors are available and they are operating on the basis of different working principals. However, their mode of operation is almost similar. The gas molecules comes in contact to the sensing materials and after their interaction there caused an imbalance of charge carriers, that modulation after transducer analysis expressed as sensing response. Now-a-days, with the revolution of gas sensing technology not only the sensors is capable to detect different gases but also exhibit distinguishable variation with the change in concentration of gas.

## **1.4. Metal oxide semiconductor (MOS) based gas sensor:**

### **1.4.1. Brief history of MOS-based sensor:**

It has been known for a long time that concentration of charge carriers of a metal oxide semiconductor (MOS) is very sensitive to the sorption of gas molecules over the surface and as a result charge carriers' concentration was modulated. In 1953, this effect was first demonstrated by Brattein and Bardeen for Ge [20] and for ZnO by Heiland at a later stage [21]. The pioneering work of Seiyama et al. in 1962 also supported the above facts [22]. N. Taguchi in early 1960s led to the fabrication of the first resistive type of gas sensor in alarm system by using semiconductor metal oxide [23]. Initially, the gas sensors devised and designed by Taguchi were commercially available in Japan and overseas for the gas leakage detection in households and industries in the name of 'Taguchi Gas Sensor' (TGS). In 1969, 'Figaro Engineering Inc.' was established by Taguchi in Japan for mass scale production and commercialization of versatile application based sensor. Till today, Figaro sensors are renowned globally and one of the major production house for utility gas sensors.

Basically, there are two different types of semiconductor metal oxides:

- a) n-type semiconductors: This type of semiconductor metal oxides use electrons as their charge carriers, e.g.  $\text{SnO}_2$ ,  $\text{ZnO}$ ,  $\text{WO}_3$ ,  $\text{Fe}_2\text{O}_3$ ,  $\text{TiO}_2$ , etc.
- b) p-type semiconductors: These semiconductor metal oxides have holes as their charge carriers, e.g.  $\text{NiO}$ ,  $\text{CuO}$ ,  $\text{Co}_2\text{O}_3$ ,  $\text{Cr}_2\text{O}_3$ , etc.

Nevertheless, in application domain, n-type semiconductors are highly preferred as compared to p-type semiconductors.

Briefly, the principle of operation of these MOS-based sensors is the alteration in base resistance upon the sorption of gaseous species on the surface of sensing material, i.e., this is a surface phenomena and it is regulated by the change in resistance. Henceforth, these types of sensors more often are known as ‘Chemiresistive sensor’ [24-26]. In fabricating these sensors, metal oxide based semiconducting materials such as SnO<sub>2</sub> [27, 28], TiO<sub>2</sub> [29, 30], ZnO [31, 32], NiO [33, 34], Fe<sub>2</sub>O<sub>3</sub> [35, 36], WO<sub>3</sub> [37, 38], In<sub>2</sub>O<sub>3</sub> [39, 40], Ga<sub>2</sub>O<sub>3</sub> [41, 42], MoO<sub>3</sub> [43, 44] etc. are considered as promising sensing materials for the detection of gases due to their prolific sensitivity and easy fabrication process in a miniaturized form. Till now several comprehensive reviews are available on MOS-based sensors [45-51] which present an overall idea regarding the potentiality as well as the contemporary scope of improvements of MOS-based sensors [52-56]. Semiconductor based gas sensors have already been established their potential superiority in the purpose of practical applications, such as gas leakage detection, environmental monitoring, industrial uses, public safety and human health monitoring etc. The nano-dimensional particles of MOSs allow gas sensors fabrication in miniaturized device form. They are also typically cost-effective and more suitable than a conventional instrument for similar use. Though a wide range of n-type and p-type semiconducting metal oxides have been studied for their gas sensing abilities for past several decades (Table 1.1), most successful investigations have been carried out on SnO<sub>2</sub> and ZnO. However, their progressive sensitivity is somehow counter-balanced by the limitation of selectivity.

Table-1.1: MOS-based sensors for detection of different VOCs:

<b>Sensing material</b>	<b>Analyte gas</b>	<b>Operating temp. (°C)</b>	<b>Conc. (ppm)</b>	<b>Resp. (R<sub>g</sub>/R<sub>a</sub>)</b>	<b>Res./rec. (s)</b>	<b>Ref.</b>
Rh-doped SnO <sub>2</sub> nanofibers	Acetone	200	50	60.6	2/64	[57]
Ag-doped SnO <sub>2</sub> hollow nanofibers	Acetone	160	200	117	6/10	[58]
La <sub>2</sub> O <sub>3</sub> -doped SnO <sub>2</sub> nanoparticulate	Acetone	350	400	3626	2.8/-	[59]
SnO <sub>2</sub> thick films	Acetone	180	10	7.27	38/90	[60]
PtO <sub>2</sub> catalysts-loaded SnO <sub>2</sub>	Acetone	400	5	194.5	12/-	[61]

nanofibers						
ZnO nanosheets	Acetone	300	50	36.4	19/14	[62]
ZnO nanostructure decorated with Pt and Nb	Acetone	400	1000	224	-/-	[63]
Ag doped ZnO nanoneedles	Acetone	370	200	30.233	10/21	[64]
Hollow ZnO/SnO <sub>2</sub> spheres	Ethanol	225	30	34.8	1/120	[65]
Sn doped NiO hollow nanofibers	TEA	180	100	16.6	40/11	[66]
NiO thin film	HCHO	200	0.5	16.8	110/120	[67]
NiO nanograins	HCHO	350	46	-	37/14	[68]
NiO nanostructure	HCHO	300	190	291.7	24/42	[69]
Pt-nanoparticle decorated WO <sub>3</sub>	NH <sub>3</sub>	250	1000	26.9	-/-	[70]
2D WO <sub>3</sub> nanosheet	H <sub>2</sub>	250	500	72	120/235	[71]
Ag/Pt/W <sub>18</sub> O <sub>49</sub> hybrid nanowire	TEA	240	5	56.5	15/35	[72]
Pt-loaded mesoporous WO <sub>3</sub>	NH <sub>3</sub>	125	200	13.61	43/272	[73]
Porous $\alpha$ -Fe <sub>2</sub> O <sub>3</sub> microflowers	Acetone	210	100	14.5	1/39	[74]
Au modified $\alpha$ -Fe <sub>2</sub> O <sub>3</sub> columnner superstructures	Acetone	150	100	42	13/16	[75]
Pt-loaded $\alpha$ -Fe <sub>2</sub> O <sub>3</sub> porous nanospheres	Acetone	220	100	27.2	1/46	[76]
Nanoporous TiO <sub>2</sub>	Acetone	370	500	25.97	13/8	[77]
Pt-functionalized nanoporous TiO <sub>2</sub>	Acetone	300	200	29.51	13/30	[78]
In <sub>2</sub> O <sub>3</sub> functionalized TiO <sub>2</sub> nanoparticles	Acetone	250	10	33.34	52/210	[79]
Soot template TiO <sub>2</sub> fractals	Acetone	325	12.5	97	12/174	[80]

## 1.4.2. Working principle of MOS-based gas sensor:

In principle, the change in resistivity of metal oxide semiconductor after sorption or reaction with gas molecules at the chemiresistive sensing material surface is an outcome of the chemical

state and electronic interaction of the adsorbed gas molecules. A metal oxide semiconductor when exposed to an open environment, atmospheric oxygen molecules are adsorbed on the oxide surface via chemical interactions, in the form of different oxygenated species ( $O^{2-}$ ,  $O^-$  or  $O_2^-$ ) according to different operating temperatures. The mobile electrons in the conduction band of the semiconductor material are abstracted by the adsorbed atmospheric oxygen to convert themselves into different oxygenated ions (Fig. 1.3). The following reactions depict the probable surface reaction upon oxygen adsorption [47-50]:

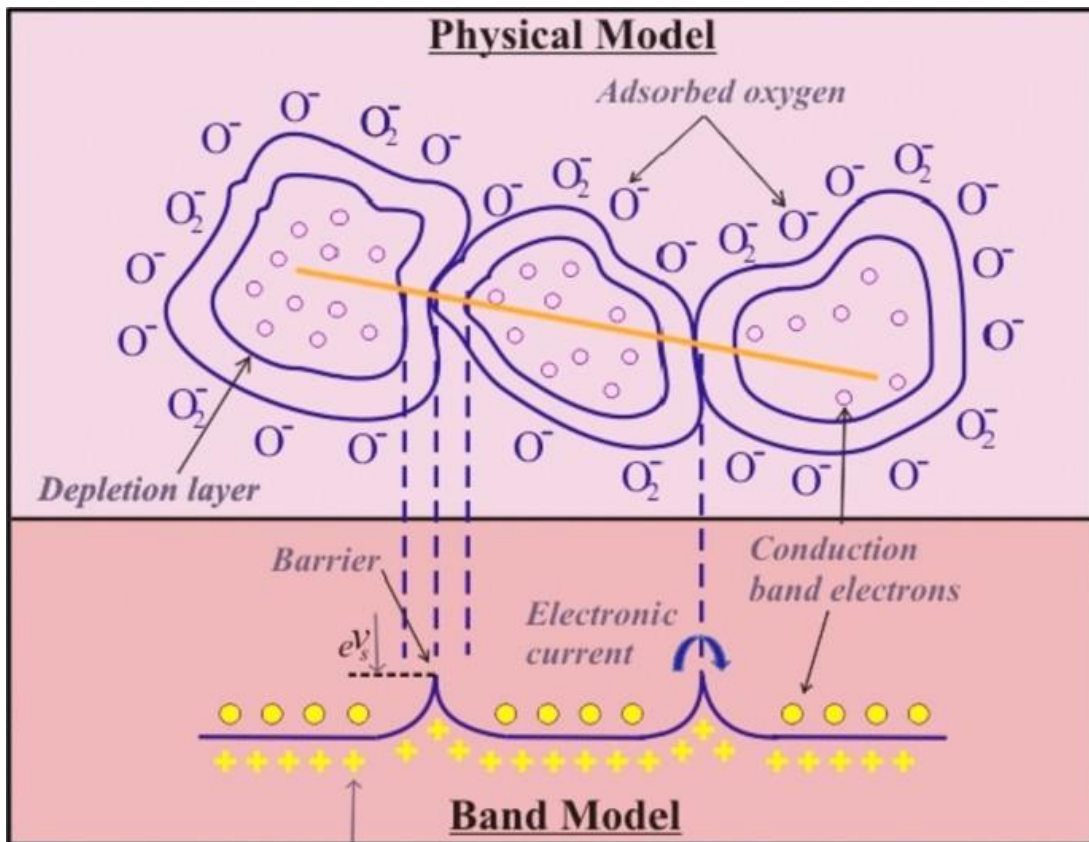


Figure-1.3: Energy band at grain boundary of polycrystalline metal oxide semiconductor [81]

The  $O^{2-}$  molecules dominate at temperature below  $150^{\circ}\text{C}$  and above that  $O^{\cdot-}$  species form. This resulted into a decrease of carrier concentration and leads to the increase of thickness of the depletion layer at the junction boundary. This certainly causes the increase of resistance.

The adsorbed oxygenated ions form potential energy barriers at grain boundaries, which restrict the free mobility of charge carriers across the polycrystalline sensing material (Fig. 1.4). This accounted for generation of an electrical resistance of the sensor. Upon exposure to trace amount of experimental gas such as acetone, ethanol,  $\text{NH}_3$ ,  $\text{H}_2$ ,  $\text{CO}$  etc. a counter reaction takes place, where the gas molecules react with the highly reactive oxygenated ions. Thereby, the surface-density of the negatively charged oxygen decreases. This release of electrons to the conduction band causes the decrease in height of the energy barrier at the grain boundary. This alteration of energy barrier height reflects in sensor resistance.

The magnitude of change in resistance is directly proportional to the concentration of the analyte gases. Therefore, the inter-granular energy barrier must play an important role in achieving high sensitivity of the sensors. The inter-granular contact of the nanomaterials that consist of space-charge layer is depleted of electrons and therefore it is usually more resistive as compared to bulk. The total resistance is then determined by the percolation path of the charge carriers across the low resistance bulk grains in series with the high resistance of inter-granular contacts. Electrons must overcome the inter-granular energy barrier to move across from one grain to another for conduction [82].

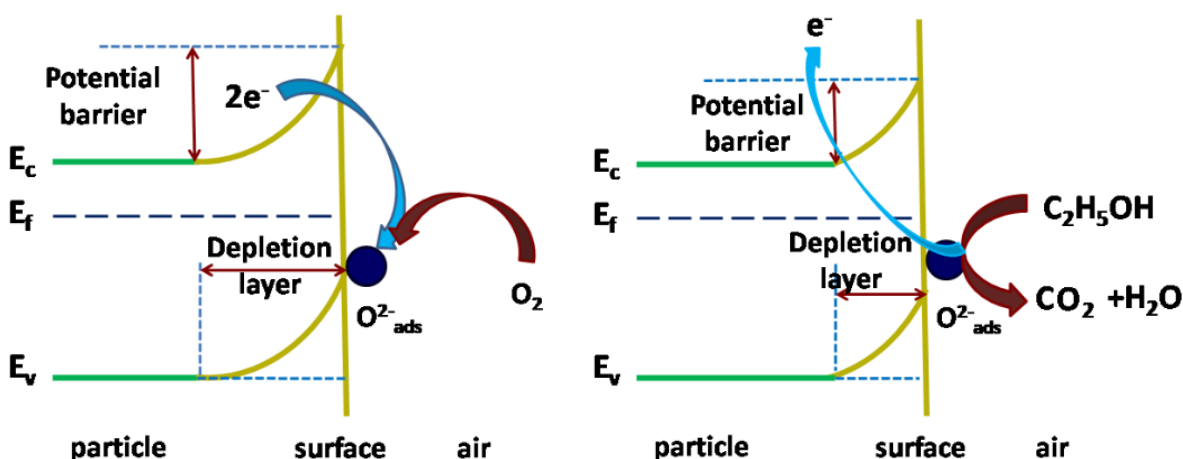


Figure-1.4: Energy band diagram of polycrystalline metal oxide semiconductor [83]

Accordingly, the sensor resistance (R) can be written as:

$$R = R_0 e^{(E_b/kT)} \quad \dots\dots\dots (1.5)$$

Where,  $R_0$  is a proportionality constant and  $E_b$  is the potential energy barrier height.

The energy of the potential energy barrier ( $E_b$ ) at the inter-grain junction is directly proportional to the square of the surface area coverage [82] and simultaneously the conductivity has a dependence on the exponential function of square of the area coverage by the gaseous species. A typical sketch of Taguchi type sensor is presented here (Fig. 1.5):

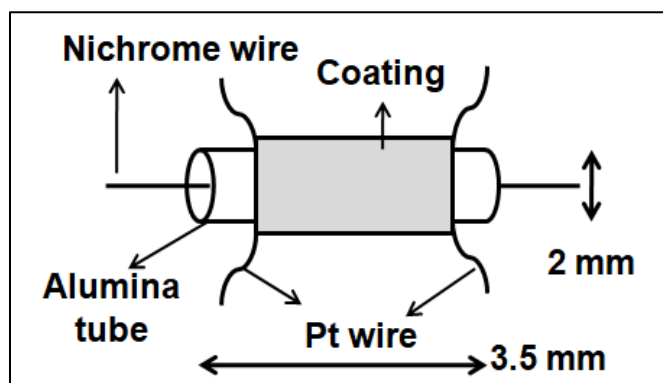


Figure-1.5: Schematic diagram of Taguchi type metal oxide semiconductor (MOS) sensor

### 1.4.3. Essential parameters related to sensor:

#### ➤ Sensing response:

Sensing response is the output expression to convincingly measure a given input. It is the ratio of enhancement of the output of a sensor with respect to a measured input. For a MOS-based gas sensor, it is expressed in terms of change in resistance after exposing the sensor to an analyte gas pulse. The sensing response (S) of a chemiresistive sensor (Fig. 1.6) can be calculated from either of the following relations [32, 84]:

$$S = R_a/R_g \quad \text{(For n-type sensing response)} \quad \dots\dots\dots (1.6)$$

$$S = R_g/R_a \quad \text{(For p-type sensing response)} \quad \dots\dots\dots (1.7)$$

Where, the resistance of the sensor in air is  $R_a$  and  $R_g$  is the resistance of the sensor in presence of experimental gas at a particular working temperature.



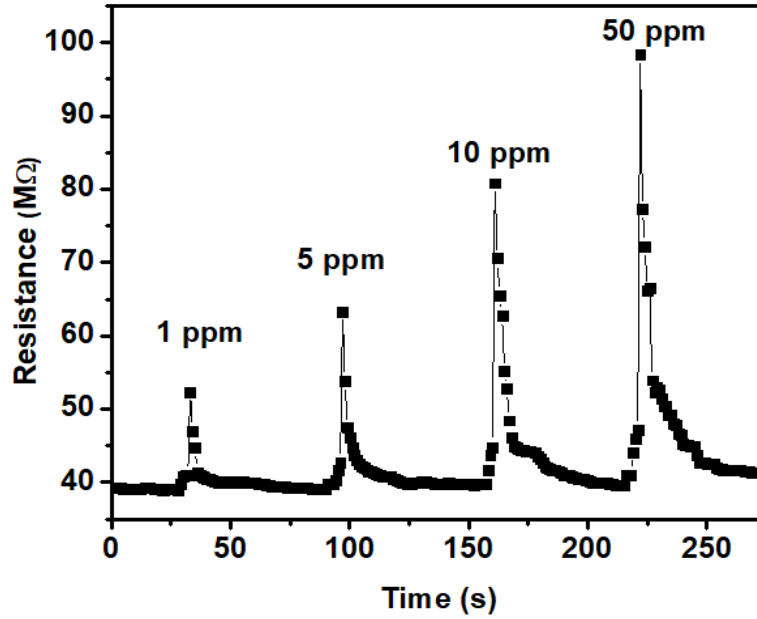


Figure 1.6: *p*-type sensing response of MOS-based sensor [84]

➤ **Lowest limit of detection (LOD):**

It is defined as the lowest concentration of a particular gas, a sensor can detect with considerable sensing response at an optimized experimental condition. The lower is the LOD of a sensor, better is its applicability in trace amount of gas detection purpose. In most of the cases, it is theoretically calculated on the basis of the gathered sensing data by following IUPAC recommended ‘Power Law of gas sensing’ [85]:

$$C_L = (k \times S_b)/S \quad \dots\dots\dots (1.8)$$

The limit of lowest detected concentration of the sensor is  $C_L$ , the standard deviation of base resistances at room temperature is  $S_b$ , average sensing response  $S$ , and according to IUPAC recommendation the value of constant  $k$  is 3.

➤ **Response and recovery time:**

Response time is the time required for a sensor to reach a stable value after exposing to a gas. It can be expressed as the time at which the output reaches ~ 90% of its maximum value. It can vary with sensing material as well as depends on optimized operating temperature. Recovery time is the time needed for the sensor signal to return to its ~ 90% of base value after switching of the input gas pulse [83, 84]. The recovery period introduces the desorption process of a sensor



at the identical experimental condition (Fig. 1.7). Rapid response and recovery time of a sensor are essential for detection of multiple pulses in a short span of time.

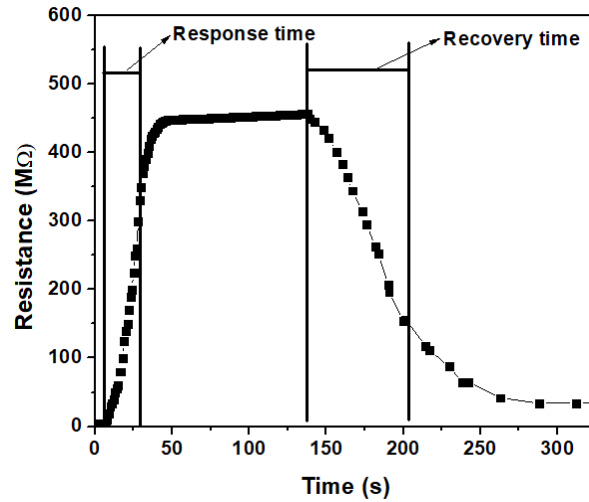


Figure-1.7: Response and recovery time of a sensor [84]

## ➤ **Reproducibility:**

Reproducibility is the sensor's capability to reproduce the response after alteration of some measurement conditions (Fig. 1.8). For example: a reproducible sensor will show the similarity in sensing response to the same measurement input, after closing and restarting the sensing system, as earlier.

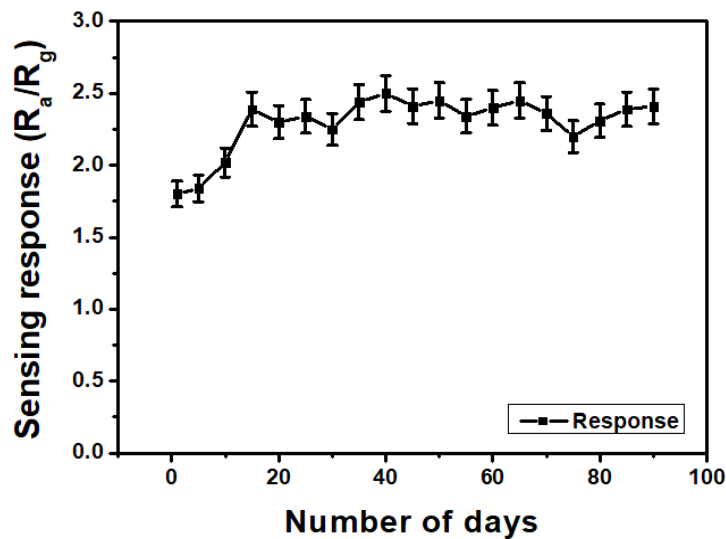
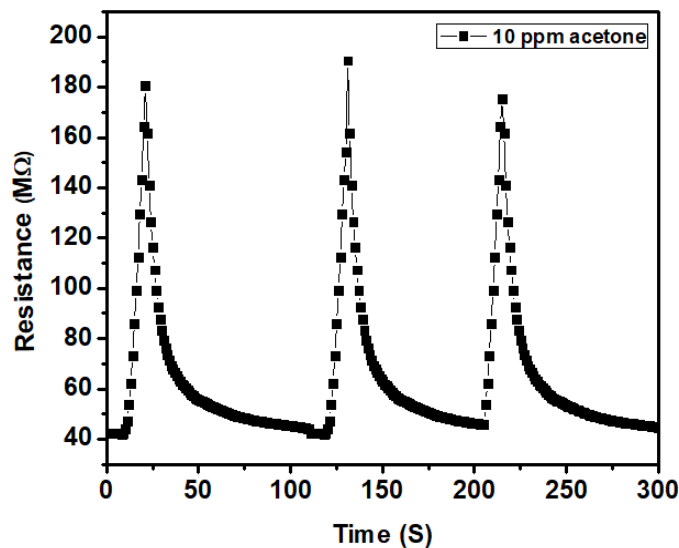


Figure-1.8: Reproducibility of a sensor towards a constant concentration of gas [84]

## ➤ **Repeatability:**

Repeatability is the sensors' ability to generate almost similar response for repetitive measurements (Fig. 1.9). Keeping all experimental parameters, like operating temperature and other environmental conditions unchanged, if the sensor is exposed to sequential gas pulses in a stipulated time period then it should produce nearly identical sensing responses to demonstrate repeatability.



*Figure-1.9: Repeatability of a sensor towards a constant concentration of gas [84]*

## ➤ **Resolution:**

Resolution signifies the smallest enhancement in the measurement that will yield a detectable change in the recorded output signal. Resolution is generally limited by any noise associated to the signal.

## ➤ **Selectivity:**

Selectivity is the most desired characteristics of a standard sensor. It is the ability of a sensor to detect a single component amidst of multi-component mixture under the influence of identical experimental condition (Fig. 1.10). The MOS-based sensing materials, by virtue of their inherent chemical characteristics and composition modification either by catalytic sensitization or by doping or composite formation, can be able to interact with a specific gas molecule more profusely over the others.

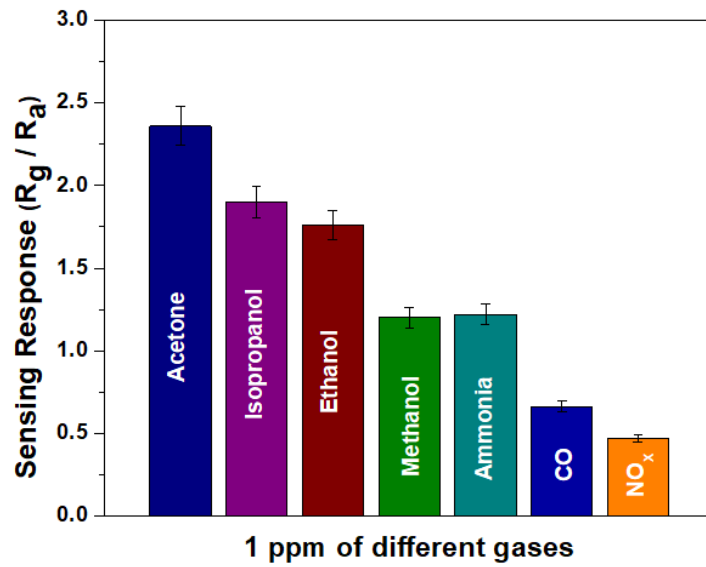


Figure-1.10: Selectivity of a sensor to different interfering gases [84]

## ➤ Stability:

Utility of a gas sensor device for real life applications demands good sensing response as well as long term durability. A sensor should demonstrate negligible deviation in base resistance as well as sensing response (Fig. 1.11). This actually eliminate the complicity of frequent changing of sensor as well reduce the cost of sensing appliances.

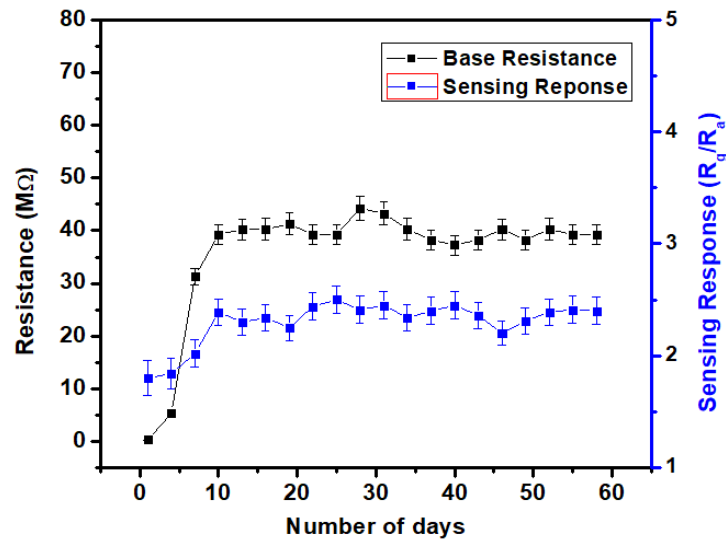


Figure-1.11: Stability of metal oxide semiconductor (MOS) sensor [84]

## **1.4.4. Advantages of MOS-based gas sensor:**

Advantages of MOS-based gas sensor can be shortly summarized as follows:

- Facile synthesis of nanomaterials
- Easy sensor fabrication techniques (e.g. Taguchi-type sensor)
- Miniaturized and compact sensor modules
- Good sensing response
- High surface area
- Porous architectures to facilitate gas sorption
- Cost effective sensor devices

## **1.4.5. Disadvantages of MOS-based gas sensor:**

There also have concerns regarding the MOS-based gas sensor about their some inherent disadvantages. Those drawbacks are pointed out below:

- Elevated operating temperature
- Sluggish response and delayed recovery
- Inconvenient reproducibility
- Poor selectivity
- Sensitive to humid environment
- Long term signal drift

## **1.4.6. Major application areas of MOS-based sensors:**

Recently, the need of gas sensors in environmental monitoring and safety control has been immensely expanded. Among different sensing methodologies: IR detection, UV-visible Spectroscopy, Mass Spectrometry or Gas Chromatography is very reliable and conclusive methods for detection of low concentration of gases at a high precision. However, procurement cost, physical sizes, and operational complicity, prevent them from daily usages and mass-commercialization. In contrast, gas sensors are a good alternative for swift applications, cost-effective, user-friendliness and portability. There is an urge to detect the minute concentration of toxic gases which are seldom encountered in our everyday life. Therefore, the gas sensors are important frontline monitors and find applications (Fig. 1.12) in diverse areas [86-88].

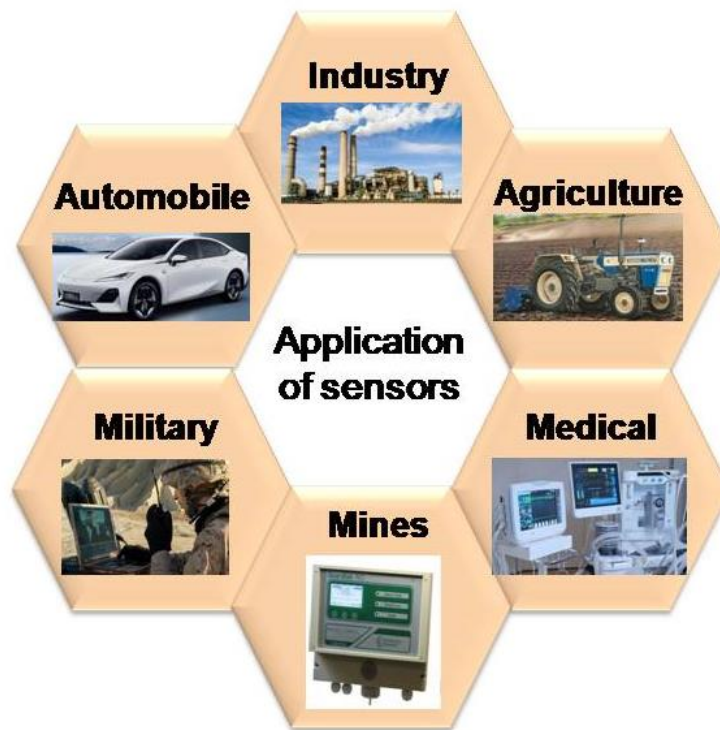


*Figure-1.12: Major application areas of sensors*

❖ **Automobile:**

- Car ventilation
- Air filter control
- Detection of different vapour (e.g. Gasoline)

❖ **Safety in industrial sectors:**

- Flammable gases like LPG, CNG, methane, hydrogen etc.
- Toxic gases like CO, CO<sub>2</sub>, NH<sub>3</sub>, H<sub>2</sub>S, NO<sub>x</sub>, SO<sub>x</sub> etc.
- Fire, smoke, explosive
- Nerve gas, poisons like sulfur mustard
- Boiler control

❖ **Military:**

- Military aircraft and battlefield surveillance
- Security systems for detection of explosives

## ❖ Mine:

- Detection of harmful gases in mines (e.g. methane)
- Smoke detector sensor to ensure the safety of the workers

## ❖ Agriculture:

- Food quality control (freshness of fruits and fishes etc.)
- Process and packaging control
- Odor detection (sulphide and amines)

## ❖ Medical applications:

- Non-invasive diseases detection by breath biomarker VOCs analysis: diabetes (acetone), renal diseases (ammonia), asthma ( $\text{NO}_x$ ) etc.

### 1.4.7. Factors affecting sensing performance of MOS-based gas sensors:

Worldwide researchers are working on different aspects to tailor the sensing materials' properties (Fig. 1.13) and thereby to accomplish an enhanced sensing performance. The sensing material in the pristine form can barely sense the gas molecules, however, they hardly able to exhibit any selectivity and also require a high operating temperature. From the application-oriented point-of-view, precise sensing device with an ability to detect a definite gas at trace concentration and also operating at low temperature is quintessential. Henceforth, several possibilities have been successfully explored in this purpose. The modulation of crystal structure of the sensing material is one of the primitive methods to achieve this. Again, surface modification can be achieved either by doping or compositing with transition metal ions/oxides or by addition of noble metal catalysts (viz. Pt, Pd, Au, Ag, etc.) in pristine MOS lattice [27, 29, 30, 31, 83, 84]. Also, tuning of sensing material morphologies (e.g.: nanowires, nanorods, nanosheets, urchin like structure, etc.), proved to be beneficial from gas sensing perspectives in many cases.

In general, the MOS-based materials prefer a high operating temperature for sensing. However, at an elevated temperature, the inclusion of heater element with the sensor system degrades the sensing performance as well as shortens the lifetime of the sensor. Therefore, the fabrication of low/room temperature sensor is the prime agenda of the modern research community.

On the other hand, sensing film thickness can be instrumental to determine the sensitivity of a sensor. In most of the cases, thin film sensors are preferred over thick film sensors. A thin film sensor with sensing layer thickness in nanometer range allows almost uniform current flow. As the standard deviation of acquired data points is very less, hence it is suitable mainly for high frequency measurements. On the contrary, thick film sensors are useful for robust application purpose.

- Gas sensing is a surface phenomenon that considers the electronic interactions between experimental gas molecules and sensing material.
- Different metal oxide semiconductors require different amount of activation energy to trigger the reaction between the gas molecules and sensing material surface.
- Pristine MOSs exhibit poor sensitivity and selectivity as compared to multi-component nanocomposite.
- Impregnation with catalyst can improve the sensing performances.
- Increase in aspect ratio of the nanomaterials, i.e., surface properties tailoring also facilitates the gas sensing performance.
- Enhancement of surface area of sensing material, allows the adsorption of greater number of gas molecules.
- As well, porosity of the nanomaterials plays a pivotal role in the sorption of gas molecules on the sensing material surface that in turn alter the sensing performance.
- Molecular level distribution (thin film) of the particles in the sensing film can provide an extended chain of electronic transportation to influence the sensitivity.
- Several other physical properties of MOS; like crystallite size, grain boundary, band gap, work function, etc. can govern the sensing parameters of a sensor.
- High working temperature of sensor actually detrimental for its endurance as it induces grain coalescence and grain boundary damage.
- The response/recovery time of a sensor can be attuned by changing the working temperature of the sensor as the sorption process of gas molecules controlled by the working temperature of the sensor.
- Humidity (%RH) in the experimental environment imparts an adverse effect on the sensing performance.

- Selectivity is another aspect needed to be taken care of for precise detection of a particular gas without any interference from other gaseous species.

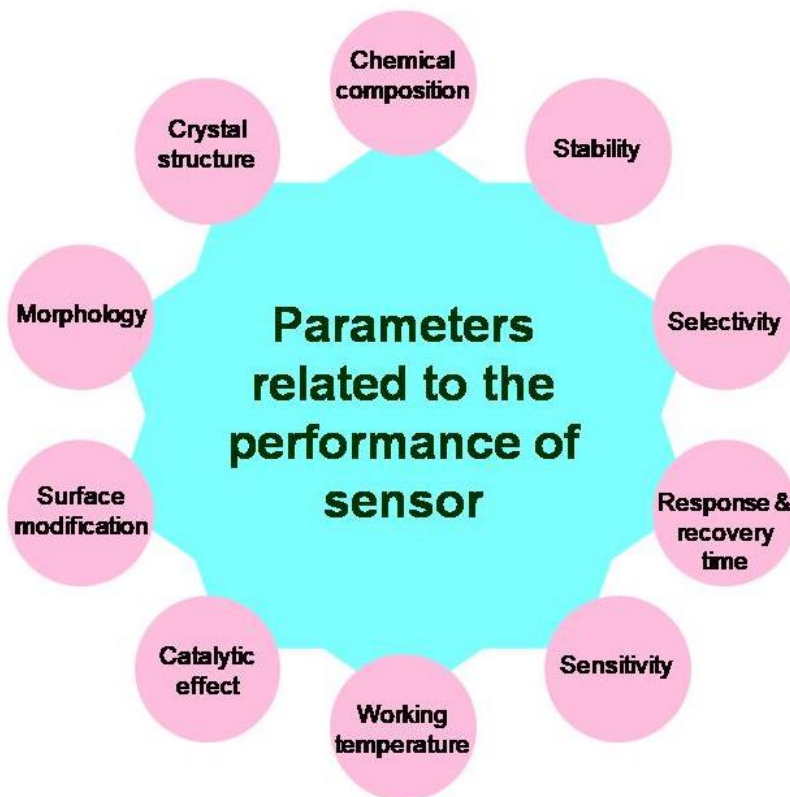


*Figure-1.13: Sensing performance influencing parameters*

### 1.4.8. Plausible ways to enhance the performance of MOS-based gas sensor:

Among different sensing materials MOS-based nanomaterials are mostly appreciated as a prolific gas sensing material. From the very beginning of MOS-based gas sensors, they were basically used in pristine form. However, with the growing interest in gas sensors, their applications require greater efficiency in sensitivity and selectivity in addition to detection of gases at trace concentration with profound accuracy and precision. In spite of several advantages, some major setbacks restrict the frequent uses of these MOS-based gas sensors in pristine form. Hence, much technological efforts have still been employed in order to improve their sensing performances. A few of them have been highlighted in followings:



- Crystal structure modification to develop new phase of the nanomaterials
- Tuning of crystallite size to induce the grain size effect
- Optimization of calcination or sintering temperature of the nanomaterials
- Sensitization by addition of noble metal catalysts (viz. Pt, Pd, Ag, Au, etc.)
- Doping with transition metal ions to introduce defects and oxygen vacancies in lattice
- Formation of composite between different metal oxides in the form of heterojunction
- Modulation of morphological aspects of the nanomaterials
- Enhancement of surface-to-volume ratio of sensing materials
- Controlling the thickness of the sensing layer

Among several plausible ways to boost up the sensitivity of a sensor, the most effective techniques are: (a) Nanocomposite formation, (b) Metal ion doping.

### 1.4.8.1. Metal oxide nanocomposite formation:

In the history of material science, scientists and researchers vividly explored numerous number of metal oxide semiconductors as a reliable sensing material. In spite of that, pristine MOSs suffering from their integral inherent drawbacks like low sensitivity, poor selectivity, delayed response/recovery time, high operating temperature, etc. Therefore, to overcome these drawbacks, researchers are inclined towards the development of heterojunctions by combining two dissimilar MOS. The interfacial contact established between two different MOS can comprehensively attune the electronic transportation across the heterojunction boundary to attain the Fermi-level equilibrium. As a result of this, at the junction boundary a depletion (or accumulation) layer is formed that can regulate the charge carriers' concentration and thereby modulate the sensing performance. This heterojunction can be of two types: p-n or n-p type and n-n and p-p type. In p-n or n-p type of heterojunction, the charge carrier of n-type semiconductor (electron) and that of p-type semiconductor (hole) migrate into the opposite direction; this induces a change in charge carriers' concentration. On the other hand, combining two similar types of MOS (either n-type or p-type), give rise to alteration in potential barrier height at the junction, this can regulate the electron transportation across the heterojunction. This synergistic effect proves to be beneficial for better sorption of gas on sensor surface and rapid interaction between analyte gas and sensing material, overall improves the sensing performance. Nakate et al. [89] explored the selective CO sensing performance of p-CuO/n-TiO<sub>2</sub> heterojunction device.

Wang et al. [90] showed ethanol sensing by hierarchical  $\text{CoO}_3/\text{SnO}_2$  heterostructure synthesized by hydrothermal method. On the other hand, Maziarz et al. [91] demonstrated low concentration  $\text{NO}_2$  sensing properties of two different types of nano-heterostructure  $\text{TiO}_2/\text{SnO}_2$  and  $\text{TiO}_2/\text{CuO}$ , however the sensitivity of n-p heterostructure was comparatively lesser than n-n type heterostructure. Jia et al. [92] reported an anatase/rutile  $\text{TiO}_2/\text{SnO}_2$  hollow heterostructure for low concentration TEA detection. Sharma et al. [93] synthesized  $\text{SnO}_2/\text{ZnO}$  heterostructure by sputtering and studied low temperature  $\text{NO}_2$  sensing properties with quicker response and recovery time. Peng et al. [94] developed a gas sensor array based on sol-gel prepared  $\text{ZnO}/\text{SnO}_2$  nanocomposite for accurately predicting the presence of different toxic gases.

## 1.4.8.2. Metal ion doping:

Introduction of dopant ions in pristine lattice can introduce foreign electronic levels somewhere between valence band and conduction band of the pure MOS. This results into the passage of electrons via the newly generated electronic level which reduces the required energy for electronic transportation and creates a conduction channel for electron transfer. Doping in a pristine metal oxide lattice induces distortion in ordered atomic array and thereby generates defect sites in the periodic atomic arrangement [57-59]. Also, it can be able to create oxygen vacancies to facilitate the sorption of gas molecules on sensing materials surface. Doping can also attunes the crystallite size and grain dimension (Fig. 1.14a) to influence the sensing performance of MOS-based sensors. Tuning of these properties can regulate the adsorption of gas molecules and in turn govern the sensitivity of a gas sensor. One of the most efficacious strategies is the reduction of grain dimensions to nanoscale level. The inter-relation between depletion layer thickness (L) and crystallite size (D) can be reviewed in three possible ways; namely boundary control, neck control, and grain control. Nanomaterials consist of larger grain size with small surface-to-volume ratio resulted into the depletion layer thickness appreciably smaller than the crystallite size ( $D \gg 2L$ ). In this case, the existing grains are hardly affected by the surface interaction of the gas molecules. This is known as boundary controlled process, where, the wide conducting channel making the gas sensing monitored by the grain boundary only and remains independent of grain size.

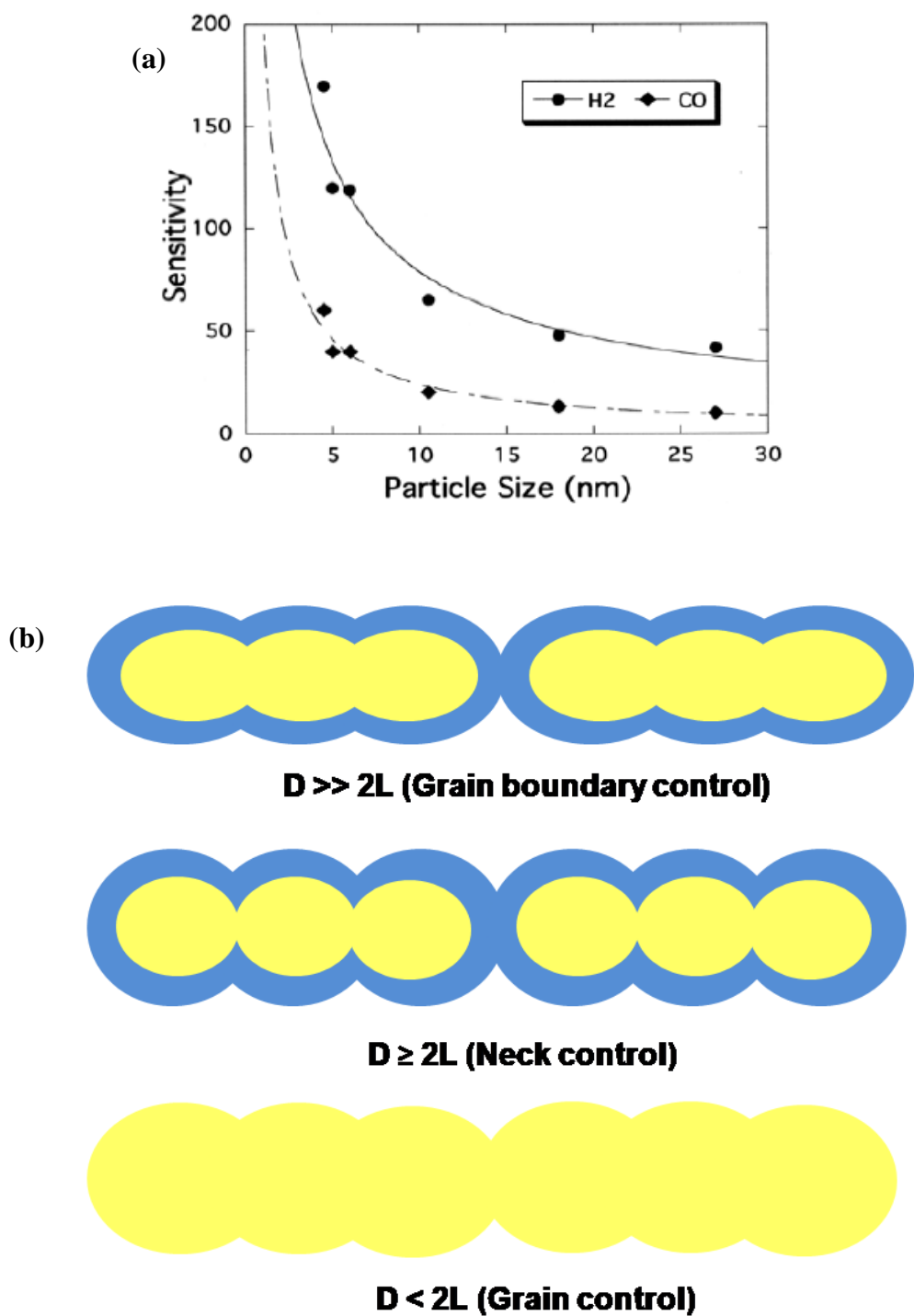


Figure-1.14: (a) Change of sensitivity with particle size [95], (b) Schematic representation of interdependence of crystallite size and sensitivity

On the other hand, higher surface-to-volume ratio of nanomaterial produces grain size almost equal to the depletion layer thickness ( $D \geq 2L$ ). This allows the formation of neck around the individual crystallites and the coordination between the grain boundary barrier and cross-sectional area of this neck regulates the electrical performance of the sensing material as well as the sensing properties. In another scenario, extensive reduction of grain size results into larger depletion layer thickness around the crystallites as compared to grain size ( $D < 2L$ ) [95, 96]. This results into extended existence of depletion layer almost through the whole grain and in this grain control process the resistivity of the sensor majorly guides by the grain size. As the grain size decreases and the depletion layer thickness increases, the potential energy barrier becomes flattened and as a consequence there observe a surge in the resistance of the sensing material and simultaneously a lesser amount of energy is required for sensing. Thus, the alteration of  $D/L$  ratio can effectively attune the sensing performance of nanomaterial based sensors (Fig. 1.14b).

## 1.4.9. Low temperature operated MOS-based sensors:

As earlier mentioned, most of the MOS-based gas sensors operated at an elevated temperature, as they require activation energy to initiate the interaction with the experimental gas molecules. However, at high operating temperature, there observes some internal damages of sensing materials (such as grain boundary damage, agglomeration of particles etc.) which in turn shortens the lifetime of the sensor. Therefore, in order to improve the lifespan of the sensor, from the past few decades, researchers are in search for suitable material that can demonstrate sensing at a comparatively low temperature or room temperature [97-99]. The low temperature sensor also reduces the consumption of energy. The room temperature operated sensor allows the easy fabrication of sensor modules by eliminating the heating element. All these reasons motivate to functionalize the sensing material in such a way that the electronic transportation requires less energy and even the interaction between gas molecules and sensing material becomes pronounce in that low operating temperature. In this purpose, several 2-D nanomaterials, like transition metal chalcogenides, graphene, MXene, etc., emerges as efficient candidate to detect gases at low operating temperature. By virtue of their high specific surface area and chemically functionalized surface properties, the 2-D materials can be considered to have an important role for low temperature gas sensing applications. Charge carriers' density modulation influences the sensing performance due to variation in mobile electrons (or holes) in the nanocomposite matrix.

In 2-D structure one atom thick dimension allows to and fro movement of charge carriers across the lattice as well as porous and defect rich surface property comprehensively enhances the sensing response by many folds. Moreover, the 2-D architecture also provides a layer like structure for the decoration of MOS nanoparticles on it. As a result of this, the extended surface area facilitates the adsorption of greater number of gas molecules. Beside this the one atom thick layer like architecture also prevents the spilling of gas molecules to the inner grains and this allows the sensing materials to exhibit a quick response and recovery time.

### **1.4.10. Functionalized graphene-MOS-based gas sensors:**

2-D carbonaceous materials have fascinated researchers owing to their unique physical and chemical properties over other planar nanomaterials. Basically, graphite, a hexagonal planar crystalline structure of elemental carbons, existed in nature as a major allotrope of carbon. The individual layers of graphite are stacked together by means of Van der Waals force. Every layer of graphite is consisting of  $sp^2$  carbon atoms bonded together in a honeycomb like pattern [100, 101]. Graphene is a 2-D array of single layer carbon atoms arranged in a densely packed hexagonal lattice (Fig. 1.15). This is actually the exfoliated graphite. So, graphite can be described as multilayer graphene. In graphene, each atom contains four bonds: one  $\sigma$  bond with each of its three neighbors and one  $\pi$ -bond that is oriented out of plane. The atoms are about 1.42 Å apart. Graphene has a closely packed carbon skeleton where the carbon atoms are bonded through  $sp^2$  hybridization (a combination of orbitals s,  $p_x$  and  $p_y$  that constitute the  $\sigma$ -bonds) and such unique association of atoms in a tightly packed assembly accounts for its higher stability. It can be considered as an indefinitely large chain of carbons.

- It is one of the strongest material (high mechanical strength) ever tested.
- It conducts heat and electricity efficiently (low electrical resistivity).
- Graphene possess zero or quasi-zero band gap energy.
- Graphene by virtue of its 2D structural property can provide a large specific surface area.
- Graphene is extensively sensitive to the changes in different environmental parameters such as temperature, moisture, residual charge build-up, or any kind of contaminations.
- The thermal energy of graphene at room temperature is typically too low to overcome the activation energy needed for molecular desorption for gases.

- Graphene is highly sensitive to the chemical environment and thus it is easily affected by different gaseous species and other chemicals.

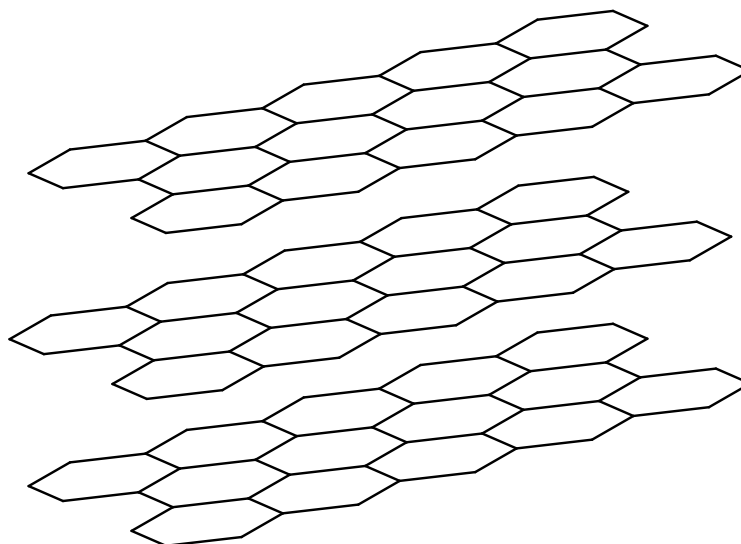


*Figure-1.15: Layered structure of graphite*

In spite of all these extraordinary physical and chemical properties, neither graphene itself nor MOS-graphene nanocomposite can act as a good sensing material, due to absence of any functional group on its surface which restricts the chemical reactivity of graphene as well as its interaction with other MOS. However, high surface areas, good electrical conductivity, efficient charge carriers' mobility etc. made graphene as promising addition in the world of MOS-based gas sensing. Henceforth, functionalization of graphene is necessary for the best interest of its utility as a promising sensing material for low temperature usage.

Graphene oxide (GO), a functionalized form of graphene, is synthesized via the oxidation of graphene by using a suitable oxidizing agent or by exfoliation process [102, 103]. Several oxygen containing groups like epoxy, carboxy, hydroxyl, peroxy, etc. and defect sites are decorated at the surface when graphene is chemically oxidized (Fig. 1.16). These oxidizing groups on the surface of graphene oxide activate graphene and improve its solubility in the reaction medium. GO possess remarkably high surface area, high surface-to-volume ratio, mechanical stability, tuneable electric and optical property, surface permeability, and better solubility in polar solvents. These variations modulate the electronic structure of graphene, and thereby convert it to a semiconductor although it is an insulator due to the large portion of  $sp^3$

hybridized carbon atoms bonded with several oxygen containing functional groups. The sensing performance of the sensors depends on the number of oxygen-containing functional groups present on the GO surface.

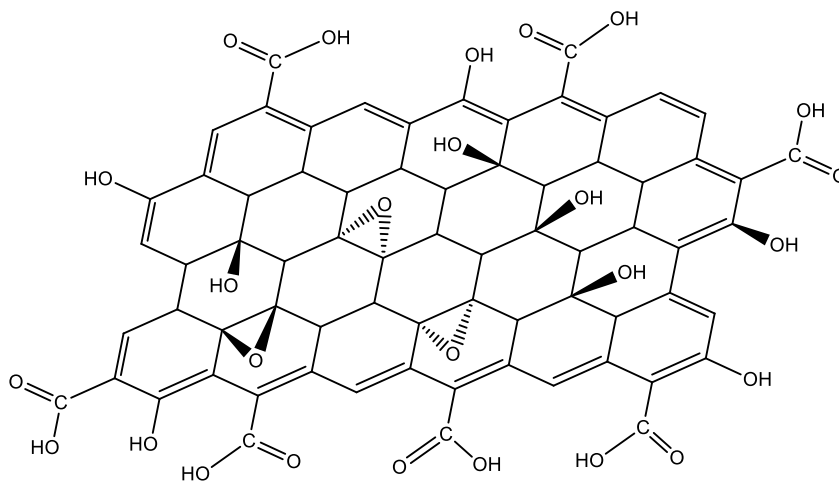


Figure-1.16: Structural pattern of graphene oxide (GO)

Due to uncontrolled oxidation of graphene, there are numerous number of surface decorated functional groups in GO. The existence of these functional groups makes GO electrically insulating material as well as it deviates from the graphene like structure due to the conversion of  $sp^2$ -C to  $sp^3$ -C.

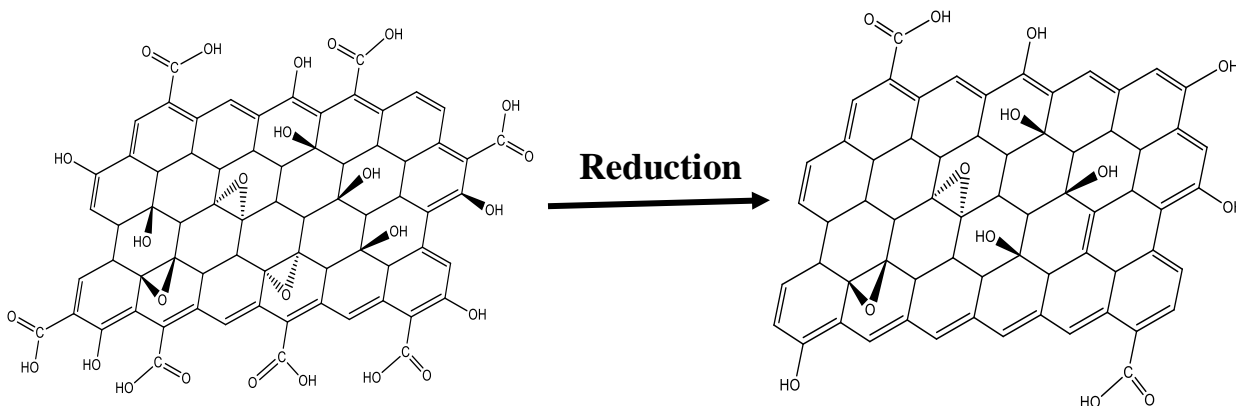


Figure-1.17: Conversion of graphene oxide (GO) to reduced graphene oxide (rGO)

To address this problem, some functional groups from the GO surface are omitted by reduction and the product obtained after reduction (Fig. 1.17) is known as reduced graphene oxide (rGO). The reduction can be carried out by three different processes [103-105], such as:

- (i) Chemical reduction
- (ii) Thermal reduction
- (iii) Electrochemical reduction

After the reduction, removal of some oxygen-containing functional groups from GO surface restores the unsaturation in those parts, also some defect sites and vacancies are created, which might be influential for the gas adsorption. The functionalized defect rich surface of rGO provides the active sites for the gas molecules adsorption. The oxygen-containing functional groups on the rGO surface lead to an electronic transfer from rGO to attached oxygenated functional groups, and thus holes become the main charge carriers, therefore rGO is considered as a p-type semiconductor. Due to high mechanical stability, low resistivity, and high conductivity these materials are used as a good sensing materials. Combining with MOS nanomaterials, the rGO furnishes the electronic channel for facile interaction between analyte gas molecules and the sensing material, without requiring much energy. Thus, the rGO decorated MOS nanocomposite appears as a prosperous successor of pristine MOS-based sensing material with a lot of potential of low temperature sensing. Henceforth, several researches are going on rGO-based low temperature sensing materials and some of them are enlisted here (Table 1.2).

Table – 1.2: Different MOS-rGO nanocomposite sensors for detection of VOCs:

<b>Sensing material</b>	<b>Analyte Gas</b>	<b>Operating temp. (°C)</b>	<b>Conc. (ppm)</b>	<b>Resp. (<math>R_g/R_a</math>)</b>	<b>Res./rec. (s)</b>	<b>Ref.</b>
WO <sub>3</sub> nanolamellae/ reduced graphene oxide nanocomposites	Acetone	200	20	8.1	1.76/8	[106]
WO <sub>3</sub> /Pt –decorated rGO nanosheets	Acetone	200	10	18	14.1/16.8	[107]
Gd doped WO <sub>3</sub> /reduced graphene oxide	Acetone	200	50	54	-/-	[108]



nanocomposite						
WO <sub>3</sub> @graphene aerogel	Acetone	150	50	16	13/120	[109]
nanocomposites						
Pd doped WO <sub>3</sub> /reduced graphene oxide	Acetone	250	50	56	-/-	[110]
nanocomposite						
rGO decorated WO <sub>3</sub> -ZnFe <sub>2</sub> O <sub>4</sub> heterojunction	TEA	130	10	26.92	51/144	[111]
MXene/rGO/CuO hybrid aerogels	Acetone	RT	100	52.09%	6.5/7.5	[112]
Sn-TiO <sub>2</sub> @rGO/CNT	NH <sub>3</sub>	RT	250	85.9%	99/66	[113]
nanocomposite						
ZnO nanowires- reduced graphene oxide	NH <sub>3</sub>	RT	50	19.2%	50/250	[114]
nanocomposite						
Au-decorated $\alpha$ -Fe <sub>2</sub> O <sub>3</sub> /rGO	TEA	320	100	43.6	5/7	[115]
ternary nanocomposite						
Ag/SnO <sub>2</sub> /rGO	TEA	220	100	82.47	11/-	[116]
nanocomposites						
$\alpha$ -Fe <sub>2</sub> O <sub>3</sub> @GO	Ethanol	260	100	14.82	7/6	[117]
nanocomposite						
CNTs/Co <sub>3</sub> O <sub>4</sub> @rGO	Ethanol	RT	50	136	-/-	[118]
Mesoporous Nanocomposite						
NiCo <sub>2</sub> O <sub>4</sub> functionalized with rGO catalyst	NH <sub>3</sub>	RT	100	1.068	57/185	[119]
rGO/CoTiO <sub>3</sub> nanocomposite	Ethanol	195	10	5.5	2/4	[120]
Bi doped rGO/Co <sub>3</sub> O <sub>4</sub>	Ethanol	120	100	150	5/-	[121]
nanohybrids						
Au@ZnO/rGO	NO <sub>2</sub>	60	1	67.38	248/170	[122]
nanocomposite						
ZnO/rGO heterojunction	NO <sub>2</sub>	110	2.5	33.11	182/234	[123]

Porous ZnO/rGO nanosheets	NO <sub>2</sub>	RT	2	13.46	26/164	[124]
Sm <sub>2</sub> O <sub>3</sub> /rGO hybrid nanocomposite	LPG	RT	700	116	28/25	[125]
Gold decorated rGO/ZnO heterostructured nanocomposite	H <sub>2</sub>	RT	500	96	8/612	[126]
Cu-doped ZnO/RGO nanocomposite	H <sub>2</sub> S	RT	150	0.93%	12/13	[127]
rGO-loaded Ni-doped ZnO nanostructures	H <sub>2</sub>	150	100	63.8%	28/-	[128]
Ternary rGO/ZnO/Pt system	H <sub>2</sub>	100	400	99%	12/412	[129]
Hierarchically porous Co <sub>3</sub> O <sub>4</sub> /rGO nanocomposite	Acetone	160	100	7.9	52/69	[130]
rGO/Co <sub>3</sub> O <sub>4</sub> nanocomposites	NH <sub>3</sub>	RT	100	3.50	351/1199	[131]
ZnFe <sub>2</sub> O <sub>4</sub> -Pd decorated rGO nanocomposite	H <sub>2</sub>	RT	200	11.43	18/39	[132]
NiO@rGO nanocomposite	H <sub>2</sub>	50	1%	0.64	28/142	[133]
rGO-loaded SnO <sub>2</sub> nanocomposite	C <sub>2</sub> H <sub>2</sub>	180	50	12.4	54/23	[134]
rGO decorated NiO-BiVO <sub>4</sub> heterojunction	NO <sub>2</sub>	60	2	8.1	57.8/126	[135]
rGO decorated CdS/CdO composite	NO <sub>2</sub>	125	2	27.5	76/82	[136]
rGO decorated ZnO/BiVO <sub>4</sub> heterojunction	NO <sub>2</sub>	95	2	126.6	40/27	[137]
BiVO <sub>4</sub> /Cu <sub>2</sub> O decorated with rGO	NO <sub>2</sub>	60	1	8.1	51.3/87.8	[138]
ZnO/SnO <sub>2</sub> heterostructure on reduced graphene oxide	NO <sub>2</sub>	RT	5	141	33/92	[139]

### **1.5. Breath biomarkers detection by gas sensors:**

In bio-medical domain, gas sensors have manifested another remarkable application through breath biomarker identification. It's worth mentioning that, the practice of breath analysis for detection of sickness was initiated from the ages of Hippocrates. In recent past, the non-invasive disease detection has been considered as futuristic promising handful tool for early stage diagnosis of diseases, under certain pathological condition. The exhaled human breath consists of more than thousands gases including several VOCs in very minute concentration (ppm/ppb level). Some of them can be corresponded to specific diseases and identified as breath biomarkers. The presence of a certain compound in the exhale breath at a concentration beyond pre-determined threshold limit (according to WHO guidelines) indicates toward a condition where the patient is suffering from that specified disease. The gas sensors have a task to identify a particular gaseous compound in such a minute concentration, amidst of several other interfering ones [140, 141].

From the ancient ages, the pathological detection of diseases by non-invasive pathways followed different types of spectroscopic methods, such as gas chromatography (GC), mass spectrometry (MS), cavity ring down spectroscopy, selected ion flow tube mass spectroscopy, and so on. Also, as a result of modern pathological improvements, various non-invasive detection instruments like X-Ray, MRI, CT-scan, ECG, eye-testing and many more have been developed. However, all these invasive methods are expensive, painful, and complicated. In this perspective, the non-invasive breath biomarker detection for diagnosis of diseases is highly appreciated [142-145]. Nevertheless, portable gas sensor based sensing devices are ground-breaking discovery in terms of its versatility and applicability. They are capable of identifying different gases and simultaneously state the patient's condition by analyzing the concentration of the gas. Such non-invasive exhaled breath analysis technique is simple, inexpensive, painless, and instantaneous.

Among different diseases, diabetes is a chronic disease which leads to several other health problems and in some cases proved to be fatal also. In our daily life, main ingredient of food is carbohydrate, mostly in the form of glucose. In metabolic process this glucose decomposes to produce energy. There are several other food ingredients like fatty acids and lipids; they are metabolizes to glucose by a process known as ketogenesis. This ketogenesis is the only pathway to produce ketone in human body. On the other hand, the glucose level in human blood is controlled by a hormone, named insulin, secreted from pancreas. In some cases due to metabolic

disorder, the regulatory function of insulin in human body gets hampered in such a way that either their secretion stopped or they cannot absorb glucose from blood. The disease caused by inadequate insulin in human body is called type-I diabetes, whereas, if insulin is unable to absorb glucose, then it is termed as type-II diabetes or diabetes mellitus [146-149]. In diabetes mellitus, the production of ketone bodies increased due to uncontrolled ketogenesis process. Among different ketones produced in metabolism, acetone is the primary one and basically the fundamental ketone produced in human body. The most popular standard diabetes detection techniques used now-a-days are fasting plasma glucose post prandial (FPG-PP), oral glucose tolerance test (OGTT), etc. Although being standard, these invasive processes dealt with too much complicacy. Firstly, the tests require a trained pathologist with proper pathological laboratory setup and they also need a long time to produce the results. From these points of interest, commercially available hand-held glucometer gained the recognition as the results are almost accurate and instantaneous. Moreover, it does not require any trained personal and even the test can be performed at home only. However, the only demerit of this process is that, the patient need to bear painful piercing of needle on a regular basis. Henceforth, the non-invasive breath analysis is mostly favoured for its straightforward, economically viable, and facile operational technique. From the pathological perspectives, the breath biomarker for non-invasive detection of diabetes is acetone and its concentration in human exhaled breath has a direct correlation with the non-invasive detection of diabetes. As per WHO guidelines, the concentration of acetone in healthy person's exhaled breath is below 0.9 ppm, whereas this acetone concentration goes beyond ~ 1.8 ppm for a diabetic-prone person.

In twenty first century, diabetes is a severe health challenge which is galloping with passing years. According to statistics in past two decades, the number of worldwide diabetic patients increased almost three times. Overall, it's very convenient that, the global status of diabetes is very frightening and it is deteriorating with time. Therefore, proper monitoring and timely diagnosis of diabetes is crucial. It is the high time to embrace non-invasive breath analyzing diabetic sensors as a potential alternative of pathological diagnosis. Different VOC breath biomarkers, their tolerable concentration and corresponding diseases are presented in tabulated form (Table 1.3).

Table - 1.3: Different VOCs as biomarker of some specific diseases and their tolerance limit:

Gas	Biomarker	Maximum permissible limit	Reference
Acetone	Diabetes	0.9 ppm	[146-149]
Ammonia	Renal dysfunction	250 ppb	[150, 151]
Ethanol	Blood alcohol level	130 ppm	[152, 153]
Nitric oxide	Asthma	30 ppb	[154, 155]
Hydrogen sulphide	Halitosis	16 ppb	[156, 157]
Isoprene	Diabetes	105 ppb	[158, 159]
Toluene	Lung cancer	100 ppb	[160, 161]

It has already been discussed that, due to ketogenesis the acetone concentration in human blood increases and this disorder related to diabetes. Even, acetone can be produced in human body due to different food habit, physical exercise, or any other metabolic process that convert fatty acid to ketone bodies. This acetone concentration in exhaled human breath has a direct correlation with non-invasive diabetes detection if other pathological conditions are kept under control. Therefore, by analyzing the exhaled human breath the metabolic disorder or identification of a specific sickness is possible. In presence of thousands of volatile components, detection of a particular gas in ppm concentration is challenging. However, revolution of technology-driven sensor systems makes it easier by fabricating MOS-based sensing devices suitable for trace concentration gas detection at an ambient condition in a hand-held compatible mode. Such innovation makes the disease detection accurate, painless, instantaneous, and inexpensive. Till today, researches are going on for development of low concentration (1 to 50 ppm) acetone sensor where selectivity and operating conditions are also very crucial. However, for practical perspectives there are still some challenges to accomplish the prominent acetone detector as a futuristic tool for non-invasive diabetes detection (Table 1.4).

Table – 1.4: MOS-based sensors for diabetic breath biomarker (acetone) detection:

Sensing material	Operating temp. (°C)	Conc. (ppm)	Resp. ( $R_g/R_a$ )	Res./rec. (s)	Ref.
WO <sub>3</sub> nanosheets modified by g-C <sub>3</sub> N <sub>4</sub>	340	100	35	9/3.8	[162]
Co <sub>0.5</sub> Zn <sub>0.5</sub> Fe <sub>2</sub> O <sub>4</sub> nanomaterial	650	100	132	10/-	[163]

WO <sub>3</sub> /Pt-decorated rGO nanosheets	200	10	12.2	14.1/16.8	[164]
Fe and C codoped WO <sub>3</sub>	300	2	10.3	-/-	[165]
Triple-shelled ZnO/ZnFe <sub>2</sub> O <sub>4</sub> hollow microspheres	140	200	23.5	5.2/12.8	[166]
LaFeO <sub>3</sub> microspheres	225	100	25.5	5/25	[167]
Pt-loaded WO <sub>3</sub> nanofiber scaffold	350	5	88.04	-/-	[168]
Ru-loaded WO <sub>3</sub> nanoparticles	300	5	32	-/-	[169]
ZnFe <sub>2</sub> O <sub>4</sub> double-shell microspheres	206	20	13.6	6/10	[170]
Sb-doped In <sub>2</sub> O <sub>3</sub> microstructures	240	50	64.3	8/27	[171]
ZnFe <sub>2</sub> O <sub>4</sub> hollow octahedral nanocages	120	200	64.4	-/-	[172]
Bimodal porous $\alpha$ -Fe <sub>2</sub> O <sub>3</sub>	300	100	26.3	6/-	[173]
BiFeO <sub>3</sub> nanoparticles	350	10	12	25/17	[174]
Mesoporous WO <sub>3</sub> nanofibers	350	50	22.1	24/27	[175]
GO-SnO <sub>2</sub> -TiO <sub>2</sub> ternary nanocomposite	200	5	59.7	10/12	[176]
Pt-functionalized SnO <sub>2</sub> hemipill network	300	0.2	1.4	225/256	[177]
ZnO coated SnO <sub>2</sub> nanofibers	350	5	3.08	12/27	[178]
Au-doped SnO <sub>2</sub> nanofibers	250	10	4	7/40	[179]
Microsheet-assembled hierarchical Fe <sub>2</sub> O <sub>3</sub>	220	100	52	8/19	[180]
Ni doped ZnO nanostructures	450	100	90	50/90	[181]
Eu doped SnO <sub>2</sub> nanobelt	210	100	8.56	8/9	[182]
Pt@In <sub>2</sub> O <sub>3</sub> nanowires	320	5	14	11/13	[183]
LaFeO <sub>3</sub> nanocrystal	180	10	14.1	21/6	[184]
Au:SmFe <sub>0.9</sub> Zn <sub>0.1</sub> O <sub>3</sub>	200	1	14.76	23/7	[185]
NiFe <sub>2</sub> O <sub>4</sub> nanocubes	160	1	1.9	8/40	[186]
Bamboo raft-like Co <sub>3</sub> O <sub>4</sub>	180	200	10.5	32/35	[187]
Cuboid WO <sub>3</sub> nanosheets	300	100	49.1	7/19	[188]

## 1.6. Objective of the present work:

In the proposed Ph. D. dissertation work, the prime goal is to develop graphene-metal oxide semiconductor nanocomposite-based sensors for selective detection of VOCs (ppm level) at low operating temperature. These sensors are mainly useful for noninvasive diagnosis of diseases by exhaled breath analysis. The thesis work emphasizes on the synthesis of pristine nanomaterial, binary nanocomposite (n-n/p-n type), doped nanomaterial, and their composites with rGO. It is followed by their detailed characterizations to understand the modulation effect of crystalline phase, surface phenomena, and electronic properties as well as their correlation with the VOC sensing performances. The prime objective of the thesis work is to fabricate the sensors from the synthesized novel rGO-MOS nanocomposites to achieve:

- Low concentration VOC response (~ 1-10 ppm)
- Reduction of operating temperature (near about room temperature)
- Rapid response/recovery time
- Good selectivity
- Prolonged stability

To achieve aforementioned objectives, the outline of working methodology is as follows:

- Synthesis of the nanomaterials using an environment-friendly sol-gel process.
- Characterization of the as-synthesized nanomaterials by different structural (XRD, FTIR spectroscopy, Raman spectroscopy, BET surface area and BJH pore size analysis, XPS), morphological (FESEM, TEM), optical (UV-visible, Photoluminescence), and electrical methods (Impedance spectroscopy).
- Fabrication of the Taguchi-type sensing modules using as-prepared nanomaterials.
- Analysis of different aspects of sensing performance: like sensing response, lowest limit of detection, response and recovery time, repeatability and reproducibility, selectivity, and stability.
- Impedance spectroscopic analysis to rationalize the charge carriers' migration and electrical properties of the sensors.
- Elucidation of the sensing mechanism of the sensors using band-diagram model.
- Finally, implementation of the sensors for non-invasive disease detection by human exhaled breath analysis.

On the basis of the disserted work, thesis is arranged into the following chapters:

**Chapter 1:** Background study and literature survey of metal oxide semiconductor (MOS) gas sensors, advantage of graphene and utility of graphene-metal oxide semiconductor nanocomposites as gas sensing material.

**Chapter 2:** Sol-gel synthesis of pristine metal oxides, reduced graphene oxide, and rGO-MOS nanocomposites, a brief description of different characterization techniques with working principle, Taguchi-type sensor fabrication and VOC sensing measurement.

**Chapter 3.1:** Synthesis of rGO incorporated binary n-n type ZnO-SnO<sub>2</sub> heterojunction based nanocomposites and their VOC sensing performance study.

**Chapter 3.2:** Synthesis of rGO decorated p-n heterojunction based NiO-SnO<sub>2</sub> nanocomposites and their VOC sensing at low temperature.

**Chapter 4.1:** Synthesis of rGO decorated Fe<sup>3+</sup> doped WO<sub>3</sub> nanocomposites and their selective acetone sensing performance.

**Chapter 4.2:** Synthesis of rGO decorated Cr<sup>3+</sup> doped WO<sub>3</sub> nanocomposites and their selective acetone sensing performance at lower operating temperature.

**Chapter 5:** Synthesis of Cr<sup>3+</sup> doped Fe<sub>2</sub>O<sub>3</sub>-rGO nanocomposite and the selective acetone sensing performance to ppm level concentration with reduction of operating temperature.

**Chapter 6:** Summarization of the results of the above-mentioned dissertation work and outline of the future scope of the research work.

.



**References:**

- [1] B. Pejčic, P. Eadington, A. Ross, Environmental Monitoring of Hydrocarbons: A Chemical Sensor Perspective, *Environ. Sci. Technol.* 41 (2007) 6333-6342. <http://dx.doi.org/10.1021/es0704535>.
- [2] C. K. Ho, A. Robinson, D. R. Miller, M. J. Davis, Overview of Sensors and Needs for Environmental Monitoring, *Sensors* 5 (2005) 4-37. <http://dx.doi.org/10.3390/s5010004>.
- [3] A. Kumar, H. Kim, G. P. Hancke, Environmental Monitoring Systems: A Review, *IEEE Sens. J.* 13 (2013) 1329-1339. <http://dx.doi.org/10.1109/JSEN.2012.2233469>.
- [4] S. Pamukcu, L. Cheng, *Underground Sensing: Monitoring and Hazard Detection for Environment and Infrastructure*, Academic Press, Elsevier (2018).
- [5] T. Liu, Y. Wei, G. Song, B. Hu, L. Li, G. Jin, J. Wang, Y. Li, C. Song, Z. Shi, L. Zhao, J. Hu, W. Zhao, M. Hou, R. Li, J. Wang, Fibre optic sensors for coal mine hazard detection, *Measur.* 124 (2018) 211-223. <http://dx.doi.org/10.1016/j.measurement.2018.03.046>.
- [6] A. Schütze, Integrated sensor systems for indoor applications: ubiquitous monitoring for improved health, comfort and safety, *Procedia Eng.* 120 (2015) 492-495. <http://dx.doi.org/10.1016/j.proeng.2015.08.681>.
- [7] A. Mastropietro, M. W. Rivolta, A. Scano, Biomedical Sensors for Functional Mapping: Techniques, Methods, Experimental and Medical Applications, *Sensors* 23 (2023) 7063. <http://dx.doi.org/10.3390/s23167063>.
- [8] G. Harsányi, *Sensors in Biomedical Applications: Fundamentals, Technology and Applications*, CRC Press, Taylor & Francis Group, New York (2000).
- [9] A. Chen, S. Chatterjee, Nanomaterials based electrochemical sensors for biomedical applications, *Chem. Soc. Rev.* 42 (2013) 5425. <http://dx.doi.org/10.1039/c3cs35518g>.
- [10] T. Han, S. Kundu, A. Nag, Y. Xu, 3D Printed Sensors for Biomedical Applications: A Review, *Sensors* 19 (2019) 1706. <http://dx.doi.org/10.3390/s19071706>.
- [11] W. J. Fleming, Overview of Automotive Sensors, *IEEE Sens. J.* 1 (2001) 296-308. <http://dx.doi.org/10.1109/7361.983469>.
- [12] S. Bhattacharya, A. K. Agarwal, O. Prakash, S. Singh, (Eds.), *Sensors for Automotive and Aerospace Applications*, Springer Nature, Singapore (2019).

- [13] M. Kraft, N. M. White, (Eds.), MEMS for Automotive and Aerospace Applications, Woodhead Publishing, Philadelphia (2013).
- [14] S. J. Prosser, Advances in sensors for aerospace applications, Sens. Actuators A Phys. 37 (1993) 128-134. [http://dx.doi.org/10.1016/0924-4247\(93\)80024-B](http://dx.doi.org/10.1016/0924-4247(93)80024-B).
- [15] M. J. Usher, D. A. Keating, Sensors and Transducers: Characteristics, Applications, Instrumentation, Interfacing, (2<sup>nd</sup> Edition), Palgrave Macmillan, London UK (1996).
- [16] T. Saidi, K. Tahri, N. El Bari, R. Ionescu, B. Bouchikhi, Detection of Seasonal Allergic Rhinitis from Exhaled Breath VOCs Using an Electronic Nose Based on an Array of Chemical Sensors, IEEE Sens. (2015). <http://dx.doi.org/10.1109/ICSENS.2015.7370579>.
- [17] N. Queralto, A. N. Berliner, B. Goldsmith, R. Martino, P. Rhodes, S. H. Lim, Detecting cancer by breath volatile organic compound analysis: a review of array-based sensors, J. Breath Res. 8 (2014) 027112. <http://dx.doi.org/10.1088/1752-7155/8/2/027112>.
- [18] J. Chang, D. Lee, S. Ban, J. Oh, M. Y. Jung, S. Kim, S. Park, K. Persaud, S. Jheon, Analysis of volatile organic compounds in exhaled breath for lung cancer diagnosis using a sensor system, Sens. Actuators B Chem. 255 (2018) 800-807. <http://dx.doi.org/10.1016/j.snb.2017.08.057>.
- [19] <https://www.electronicshub.org/different-types-sensors/>
- [20] W. H. Brattain, J. Bardeen, Surface Properties of Germanium, Bell Syst. Tech. J. 32 (1953) 1-41. <http://dx.doi.org/10.1002/j.1538-7305.1953.tb01420.x>.
- [21] G. Heiland, E. Mollwo, F. Stockman, Solid State Physics, Academic Press, Inc., , New York (1959).
- [22] T. Seiyama, A. Kato, K. Fujiishi, M. Nagatani, A New Detector for Gaseous Components Using Semiconductive Thin Films, Anal. Chem. 34 (1962) 1502-1503. <http://dx.doi.org/10.1021/ac60191a001>.
- [23] N. Taguchi, Gas detecting device, US Patent No. 3631436 (1970).
- [24] S. M. Majhi, A. Mirzaei, H. W. Kim, S. S. Kim, T. W. Kim, Recent advances in energy-saving chemiresistive gas sensors: A review, Nano Energy 79 (2021) 105369. <http://dx.doi.org/10.1016/j.nanoen.2020.105369>.
- [25] D. K. Aswal, S. K. Gupta, (Eds.), Science and Technology of Chemiresistive Gas Sensors, Nova Science Publishers, Inc., New York (2007).

- [26] Y. Jian, W. Hu, Z. Zhao, P. Cheng, H. Haick, M. Yao, W. Wu, Gas Sensors Based on Chemi-Resistive Hybrid Functional Nanomaterials, *Nano-Micro Lett.* 12 (2020) 71. <http://dx.doi.org/10.1007/s40820-020-0407-5>.
- [27] Z. Jiang, R. Zhao, B. Sun, G. Nie, H. Ji, J. Lei, C. Wang, Highly sensitive acetone sensor based on Eu-doped SnO<sub>2</sub> electrospun nanofibers, *Ceram. Int.* 42 (2016) 15881-15888. <http://dx.doi.org/10.1016/j.ceramint.2016.07.060>.
- [28] W. Tan, X. Ruan, Q. Yu, Z. Yu, X. Huang, Fabrication of a SnO<sub>2</sub>-Based Acetone Gas Sensor Enhanced by Molecular Imprinting, *Sensors* 15 (2015) 352-364. <http://dx.doi.org/10.3390/s150100352>.
- [29] S. Phanichphant, C. Liewhiran, K. Wetchakun, A. Wisitsoraat, A. Tuantranout, Flame-Made Nb-Doped TiO<sub>2</sub> Ethanol and Acetone Sensors, *Sensors* 11 (2011) 472-484. <http://dx.doi.org/10.3390/s110100472>.
- [30] G. Sun, H. Kheel, S. Park, S. Lee, S. E. Park, C. Lee, Synthesis of TiO<sub>2</sub> nanorods decorated with NiO nanoparticles and their acetone sensing properties, *Ceram. Int.* 42 (2016) 1063-1069. <http://dx.doi.org/10.1016/j.ceramint.2015.09.031>.
- [31] X. L. Xu, Y. Chen, S. Y. Ma, W. Q. Li, Y. Z. Mao, Excellent acetone sensor of La-doped ZnO nanofibers with unique bead-like structures, *Sens. Actuators B Chem.* 213 (2015) 222-233. <http://dx.doi.org/10.1016/j.snb.2015.02.073>.
- [32] K. Muthukrishnan, M. Vanaraja, S. Boomadevi, R. K. Karn, V. Singh, P. K. Singh, K. Pandiyan, Studies on acetone sensing characteristics of ZnO thin film prepared by sol-gel dip coating, *J. Alloys Compd.* 673 (2016) 138-143. <http://dx.doi.org/10.1016/j.jallcom.2016.02.222>.
- [33] H. T. Hien, D. T. A. Thu, P. Q. Ngan, G. H. Thai, D. T. Trung, T. Trung, M. M. Tan, H. T. Giang, High NH<sub>3</sub> sensing performance of NiO/PPy hybrid nanostructures, *Sens. Actuators B Chem.* 340 (2021) 129986. <http://dx.doi.org/10.1016/j.snb.2021.129986>.
- [34] S. S. Niavol, M. Budde, A. Papadogianni, M. Heilmann, H. M. Moghaddam, C. M. Aldao, G. Ligorio, E. J. W. List-Kratochvil, J. M. J. Lopes, N. Barsan, O. Bierwagen, F. Schipani, Conduction mechanisms in epitaxial NiO/Graphene gas sensors, *Sens. Actuators B Chem.* 325 (2020) 128797. <http://dx.doi.org/10.1016/j.snb.2020.128797>.

- [35] S. Liang, J. Li, F. Wang, J. Qin, X. Lai, X. Jiang, Highly sensitive acetone gas sensor based on ultrafine  $\alpha$ -Fe<sub>2</sub>O<sub>3</sub> nanoparticles, *Sens. Actuators B Chem.* 238 (2017) 923-927. <http://dx.doi.org/10.1016/j.snb.2016.06.144>.
- [36] Z. Qiang, S. Y. Ma, H. Y. Jiao, W. X. Jin, T. T. Wang, X. H. Jiang, Z. Y. Zhang, Solvothermal synthesis of 3D leaf-like  $\alpha$ -Fe<sub>2</sub>O<sub>3</sub> and its gas-sensing properties research, *Mater. Lett.* 181 (2016) 29-33. <http://dx.doi.org/10.1016/j.matlet.2016.06.004>.
- [37] C. M. Hung, D. Q. Dat, N. V. Duy, V. V. Quang, N. V. Toan, N. V. Hieu, N. D. Hoa, Facile synthesis of ultrafine rGO/WO<sub>3</sub> nanowire nanocomposites for highly sensitive toxic NH<sub>3</sub> gas sensors, *Mater. Res. Bull.* 125 (2020) 110810. <http://dx.doi.org/10.1016/j.materresbull.2020.110810>.
- [38] S. Wei, J. Zhao, B. Hu, K. Wu, W. Du, M. Zhou, Hydrothermal synthesis and gas sensing properties of hexagonal and orthorhombic WO<sub>3</sub> nanostructures, *Ceram. Int.* 43 (2017) 2579-2585. <http://dx.doi.org/10.1016/j.ceramint.2016.11.064>.
- [39] V. Kumar, S. M. Majhi, K. Kim, H. W. Kim, E. E. Kwon, Advances in In<sub>2</sub>O<sub>3</sub>-based materials for the development of hydrogen sulfide sensors, *Chem. Eng. J.* 404 (2021) 126472. <http://dx.doi.org/10.1016/j.cej.2020.126472>.
- [40] J. Wang, Z. Zheng, D. An, X. Tong, Q. Zhou, Highly selective n-butanol gas sensor based on porous In<sub>2</sub>O<sub>3</sub> nanoparticles prepared by solvothermal treatment, *Mater. Sci. Semicond. Process.* 83 (2018) 139-143. <http://dx.doi.org/10.1016/j.mssp.2018.04.014>.
- [41] H. Zhai, Z. Wu, Z. Fang, Recent progress of Ga<sub>2</sub>O<sub>3</sub>-based gas sensors, *Ceram. Int.* 48 (2022) 24213-24233. <http://dx.doi.org/10.1016/j.ceramint.2022.06.066>.
- [42] A. Afzal,  $\beta$ -Ga<sub>2</sub>O<sub>3</sub> nanowires and thin films for metal oxide semiconductor gas sensors: Sensing mechanisms and performance enhancement strategies, *J. Mater.* 5 (2019) 542-557. <http://dx.doi.org/10.1016/j.jmat.2019.08.003>.
- [43] A. A. Mane, A. V. Moholkar, Orthorhombic MoO<sub>3</sub> nanobelts based NO<sub>2</sub> gas sensor, *Appl. Surf. Sci.* 405 (2017) 427-440. <http://dx.doi.org/10.1016/j.apsusc.2017.02.055>.
- [44] S. Yang, Y. Liu, W. Chen, W. Jin, J. Zhou, H. Zhang, G. S. Zakharova, High sensitivity and good selectivity of ultralong MoO<sub>3</sub> nanobelts for triethylamine gas, *Sens. Actuators B Chem.* 226 (2016) 478-485. <http://dx.doi.org/10.1016/j.snb.2015.12.005>.
- [45] H. Ji, W. Zeng, Y. Li, Gas sensing mechanisms of metal oxide semiconductors: a focus review, *Nanoscale* 11 (2019) 22664. <https://doi.org/10.1039/c9nr07699a>.

- [46] C. Zhang, G. Liu, X. Geng, K. Wu, M. Debligny, Metal oxide semiconductors with highly concentrated oxygen vacancies for gas sensing materials: A review, *Sens. Actuators A Phys.* 309 (2020) 112026. <https://doi.org/10.1016/j.sna.2020.112026>.
- [47] V. S. Bhati, M. Kumar, R. Banerjee, Gas sensing performance of 2D nanomaterials/metal oxide nanocomposites: a review, *J. Mater. Chem. C* 9 (2021) 8776. <https://doi.org/10.1039/d1tc01857d>.
- [48] S. Yang, G. Lei, H. Xu, Z. Lan, Z. Wang, H. Gu, Metal Oxide Based Heterojunctions for Gas Sensors: A Review, *Nanomaterials* 11 (2021) 1026. <https://doi.org/10.3390/nano11041026>.
- [49] V. Amiri, H. Roshan, A. Mirzaei, G. Neri, A. I. Ayeshe, Nanostructured Metal Oxide-Based Acetone Gas Sensors: A Review, *Sensors* 20 (2020) 3096. <https://doi.org/10.3390/s20113096>.
- [50] B. Saruhan, R. L. Fomekong, S. Nahirniak, Review: Influence of Semiconductor Metal Oxide Properties on Gas Sensing Characteristics, *Front. Sens.* 2 (2021) 657931. <https://doi.org/10.3389/fsens.2021.657931>.
- [51] T. Lin, X. Lv, Z. Hu, A. Xu, C. Feng, Semiconductor Metal Oxide as Chemoresistive Sensors for Detecting Volatile Organic Compounds, *Sensors* 19 (2019) 233. <https://doi.org/10.3390/s19020233>.
- [52] Z. Li, H. Li, Z. Wu, M. Wang, J. Luo, H. Torun, P. Hu, C. Yang, M. Grundmann, X. Liu, Y. Q. Fu, Advances in designs and mechanisms of semiconducting metal oxide nanostructures for high-precision gas sensors operated at room temperature, *Mater. Horiz.* 6 (2019) 470. <https://doi.org/10.1039/c8mh01365a>.
- [53] M. Masikini, M. Chowdhury, O. Nemraoui, Review-Metal Oxides: Application in Exhaled Breath Acetone Chemiresistive Sensors, *J. Electrochem. Soc.* 167 (2020) 037537. <https://doi.org/10.1149/1945-7111/ab64bc>.
- [54] Y. Xia, R. Li, R. Chen, J. Wang, L. Xiang, 3D Architected Graphene/Metal Oxide Hybrids for Gas Sensors: A Review, *Sensors* 18 (2018) 1456. <https://doi.org/10.3390/s18051456>.
- [55] A. Dey, Semiconductor metal oxide gas sensors: A review, *Mater. Sci. Eng. B* 229 (2018) 206-217. <https://doi.org/10.1016/j.mseb.2017.12.036>.

- [56] B. Sowmya, J. Athira, P. K. Panda, A review on metal-oxide based p-n and n-n heterostructured nano-materials for gas sensing applications, *Sens. Intl.* 2 (2021) 100085. <https://doi.org/10.1016/j.sintl.2021.00085>.
- [57] X. Kou, N. Xie, F. Chen, T. Wang, L. Guio, C. Wang, Q. Wang, J. Ma, Y. Sun, H. Zhang, G. Lu, Superior acetone gas sensor based on electrospun SnO<sub>2</sub> nanofibers by Rh doping, *Sens. Actuators B Chem.* 256 (2018) 861-869. <http://dx.doi.org/10.1016/j.snb.2017.10.011>.
- [58] X. Xu, Y. Chen, G. Zhang, S. Ma, Y. Lu, H. Bian, Q. Chen, Highly sensitive VOCs-acetone sensor based on Ag-decorated SnO<sub>2</sub> hollow nanofibers, *J. Alloys Compd.* 703 (2017) 572-579. <http://dx.doi.org/10.1016/j.jallcom.2017.01.348>.
- [59] N. Tammanoon, A. Wisitsoraat, D. Phokharatkul, A. Tuantranont, S. Phanichphant, V. Yordsri, C. Liewhiran, Highly sensitive acetone sensors based on flame-spray-made La<sub>2</sub>O<sub>3</sub>-doped SnO<sub>2</sub> nanoparticulate thick films, *Sens. Actuators B Chem.* 262 (2018) 245-262. <http://dx.doi.org/10.1016/j.snb.2018.01.238>.
- [60] Y. Chen, H. Qin, Y. Cao, H. Zhang, J. Hu, Acetone Sensing Properties and Mechanism of SnO<sub>2</sub> Thick-Films, *Sensors* 18 (2018) 3425. <http://dx.doi.org/10.3390/s18103425>.
- [61] Y. J. Jeong, W. Koo, J. Jang, D. Kim, M. Kim, I. Kim, Nanoscale PtO<sub>2</sub> Catalysts-Loaded SnO<sub>2</sub> Multichannel Nanofibers toward Highly Sensitive Acetone Sensor, *ACS Appl. Mater. Interfaces* 10 (2018) 2016-2025. <http://dx.doi.org/10.1021/acsami.7b16258>.
- [62] S. Li, L. Zhang, M. Zhu, G. Ji, L. Zhao, J. Yin, L. Bie, Acetone sensing of ZnO nanosheets synthesized using room-temperature precipitation, *Sens. Actuators B Chem.* 249 (2017) 611-623. <http://dx.doi.org/10.1016/j.snb.2017.04.007>.
- [63] E. Wongrat, N. Chanlek, C. Chueaiarrom, W. Thupthimchun, B. Samransuksamer, S. Choopun, Acetone gas sensors based on ZnO nanostructures decorated with Pt and Nb, *Ceram. Int.* 43 (2017) S557-S566. <http://dx.doi.org/10.1016/j.ceramint.2017.05.296>.
- [64] Y. Al-Hadeethi, A. Umar, A. A. Ibrahim, S. H. Al-Heniti, R. Kumar, S. Baskoutas, B. M. Raffah, Synthesis, characterization and acetone gas sensing applications of Ag-doped ZnO nanoneedles, *Ceram. Int.* 43 (2017) 6765-6770. <http://dx.doi.org/10.1016/j.ceramint.2017.02.088>.
- [65] J. Liu, T. Wang, B. Wang, P. Sun, Q. Yang, X. Liang, H. Song, G. Lu, Highly sensitive and low detection limit of ethanol gas sensor based on hollow ZnO/SnO<sub>2</sub> spheres

- composite material, *Sens. Actuators B Chem.* 245 (2017) 551-559. <http://dx.doi.org/10.1016/j.snb.2017.01.148>.
- [66] J. Yang, W. Han, J. Ma, C. Wang, K. Shimanoe, S. Zhang, Y. Sun, P. Cheng, Y. Wang, H. Zhang, G. Lu, Sn doping effect on NiO hollow nanofibers based gas sensors about the humidity dependence for triethylamine detection, *Sens. Actuators B Chem.* 340 (2021) 129971. <http://dx.doi.org/10.1016/j.snb.2021.129971>.
- [67] R. Prajesh, V. Goyal, M. Nahid, V. Saini, A. K. Singh, A. K. Sharma, J. Bhargava, A. Agarwal, Nickel oxide (NiO) thin film optimization by reactive sputtering for highly sensitive formaldehyde sensing, *Sens. Actuators B Chem.* 318 (2020) 128166. <http://dx.doi.org/10.1016/j.snb.2020.128166>.
- [68] R. K. Kampara, T. Sonia, D. Balamurugan, B. G. Jeyapraksh, Formaldehyde vapour, sensing property of electrospun NiO nanograins, *Front. Mater. Sci.* 15 (2021) 416-430. <http://dx.doi.org/10.1007/s11706-021-0559-3>.
- [69] S. Dey, S. Santra, S. Sen, D. Burman, S. K. Ray, P. K. Guha, Photon assisted ultra-selective Formaldehyde sensing by defect induced NiO nanostructured sensing layer, *IEEE Sensors* 2017. <http://dx.doi.org/10.1109/ICSENS.2017.8234446>.
- [70] I. Liu, C. Chang, T. C. Chou, K. Lin, Ammonia sensing performance of a platinum nanoparticle-decorated tungsten trioxide gas sensor, *Sens. Actuators B Chem.* 291 (2019) 148-154. <http://dx.doi.org/10.1016/j.snb.2019.04.046>.
- [71] M. B. Rahmani, M. H. Yaacob, Y. M. Sabri, Hydrogen sensors based on 2D WO<sub>3</sub> nanosheets prepared by anodization, *Sens. Actuators B Chem.* 251 (2017) 57-64. <http://dx.doi.org/10.1016/j.snb.2017.05.029>.
- [72] Y. Xu, T. Ma, Y. Zhao, L. Zheng, X. Liu, J. Zhang, Multi-metal functionalized tungsten oxide nanowires enabling ultra-sensitive detection of triethylamine, *Sens. Actuators B Chem.* 300 (2019) 127042. <http://dx.doi.org/10.1016/j.snb.2019.127042>.
- [73] Y. Wang, J. Liu, X. Cui, Y. Gao, J. Ma, Y. Sun, P. Sun, F. Liu, X. Liang, T. Zhang, G. Lu, NH<sub>3</sub> gas sensing performance enhanced by Pt-loaded on mesoporous WO<sub>3</sub>, *Sens. Actuators B Chem.* 238 (2017) 473-481. <http://dx.doi.org/10.1016/j.snb.2016.07.085>.
- [74] C. Liu, Y. Wang, P. Zhao, W. Li, Q. Wang, P. Sun, X. Chuai, G. Lu, Porous  $\alpha$ -Fe<sub>2</sub>O<sub>3</sub> microflowers: Synthesis, structure, and enhanced acetone sensing performances, *J.*



- Colloid Interface Sci. 505 (2017) 1039-1046.  
<http://dx.doi.org/10.1016/j.jcis.2017.07.007>.
- [75] J. Li, L. Wang, Z. Liu, Y. Wang, S. Wang, Au-modified  $\alpha$ -Fe<sub>2</sub>O<sub>3</sub> columnar superstructures assembled with nanoplates and their highly improved acetone sensing properties, J. Alloys Compd. 728 (2017) 944-951.  
<http://dx.doi.org/10.1016/j.jallcom.2017.09.039>.
- [76] C. Liu, H. Gao, L. Wang, T. Wang, X. Yang, P. Sun, Y. Gao, X. Liang, F. Liu, H. Song, G. Lu, Facile synthesis and the enhanced sensing properties of Pt-loaded  $\alpha$ -Fe<sub>2</sub>O<sub>3</sub> porous nanospheres, Sens. Actuators B Chem. 252 (2017) 1153-1162.  
<http://dx.doi.org/10.1016/j.snb.2017.06.012>.
- [77] N. Chen, Y. Li, D. Deng, X. Liu, X. Xing, X. Xiao, Y. Wang, Acetone sensing performance based on nanoporous TiO<sub>2</sub> synthesized by a facile hydrothermal method, Sens. Actuators B Chem. 238 (2017) 491-500.  
<http://dx.doi.org/10.1016/j.snb.2016.07.094>.
- [78] X. Xing, N. Chen, Y. Yang, R. Zhao, Z. Wang, Z. Wang, T. Zou, Y. Wang, Pt-Functionalized Nanoporous TiO<sub>2</sub> Nanoparticles With Enhanced Gas Sensing Performances Toward Acetone, Phys. Status Solidi A 215 (2018) 1800100.  
<http://dx.doi.org/10.1002/pssa.201800100>.
- [79] S. Park, Acetone gas detection using TiO<sub>2</sub> nanoparticles functionalized In<sub>2</sub>O<sub>3</sub> nanowires for diagnosis of diabetes, J. Alloys Compd. 696 (2017) 655-662.  
<http://dx.doi.org/10.1016/j.jallcom.2016.11.298>.
- [80] Y. M. Sabri, A. E. Kandjani, S. S. A. A. H. Rashid, C. J. Harrison, S. J. Ippolito, S. K. Bhargava, Soot template TiO<sub>2</sub> fractals as a photoactive gas sensor for acetone detection, Sens. Actuators B Chem. 275 (2018) 215-222.  
<http://dx.doi.org/10.1016/j.snb.2018.08.059>.
- [81] D. Y. Nadargi, A. Umar, J. D. Nadargi, S. A. Lokare, S. Akbar, I. S. Mulla, S. S. Suryavanshi, N. L. Bhandari, M. G. Chaskar, Gas sensors and factors influencing sensing mechanism with a special focus on MOS sensors, J. Mater. Sci. 58 (2023) 559-582.  
<http://dx.doi.org/10.1007/s10853-022-08072-0>.
- [82] M. J. Madou, S.R. Morrison, Chemical Sensing with Solid State Devices, Academic Press, Inc., New York (1989).



- [83] A. Nilabh, S. Sen, M. Narjinary, S. Kundu A novel ppm level ethanol sensor based on La loaded ITO impregnated with Pd and Sb additives, *Microchem. J.* 158 (2020) 105146. <http://dx.doi.org/10.1016/j.microc.2020.105146>.
- [84] S. Sen, A. Nilabh, S. Kundu, Room temperature acetone sensing performance of Pt/Sb<sub>2</sub>O<sub>3</sub> impregnated Fe<sub>2</sub>O<sub>3</sub> thin film: Noninvasive diabetes detection, *Microchem. J.* 165 (2021) 106111. <http://dx.doi.org/10.1016/j.microc.2021.106111>.
- [85] Analytical Methods Committee, Recommendations for the definition, estimation and use of the detection limit, *Analyst* 112 (1987) 199-204. <http://doi.org/10.1039/AN9871200199>.
- [86] Z. Xiao, L. B. Kong, S. Ruan, X. Li, S. Yu, X. Li, Y. Jiang, Z. Yao, S. Ye, C. Wang, T. Zhang, K. Zhou, S. Li, Recent development in nanocarbon materials for gas sensor applications, *Sens. Actuators B Chem.* 274 (2018) 235-267. <http://dx.doi.org/10.1016/j.snb.2018.07.040>.
- [87] L. Ge, X. Mu, G. Tian, Q. Huang, J. Ahmed, Z. Hu, Current Applications of Gas Sensor Based on 2-D Nanomaterial: A Mini Review, *Front. Chem.* 7 (2019) 839. <http://dx.doi.org/10.3389/fchem.2019.00839>.
- [88] H. Nazemi, A. Joseph, J. Park, A. Emadi, Advanced Micro- and Nano-Gas Sensor Technology: A Review, *Sensors* 19 (2019) 1285. <http://dx.doi.org/10.3390/s19061285>.
- [89] U. T. Nakate, P. Patil, S. Na, Y. T. Yu, E. Suh, Y. Hahn, Fabrication and enhanced carbon monoxide gas sensing performance of p-CuO/n-TiO<sub>2</sub> heterojunction device, *Colloids Surf. A Physicochem. Eng. Asp.* 612 (2021) 125962. <https://doi.org/10.1016/j.colsurfa.2020.125962>.
- [90] Q. Wang, X. Kou, C. Liu, L. Zhao, T. Lin, F. Liu, X. Yang, J. Lin, G. Lu, Hydrothermal synthesis of hierarchical CoO/SnO<sub>2</sub> nanostructures for ethanol gas sensor, *J. Colloid Interface Sci.* 513 (2018) 760-766. <https://doi.org/10.1016/j.jcis.2017.11.073>.
- [91] W. Maziarz, TiO<sub>2</sub>/SnO<sub>2</sub> and TiO<sub>2</sub>/CuO thin film nano-heterostructures as gas sensors, *Appl. Surf. Sci.* 480 (2019) 361-370. <https://doi.org/10.1016/j.apsusc.2019.02.139>.
- [92] C. Jia, T. Dong, M. Li, P. Wang, P. Yang, Preparation of anatase/rutile TiO<sub>2</sub>/SnO<sub>2</sub> hollow heterostructures for gas sensor, *J. Alloys Compd.* 769 (2018) 521-531. <https://doi.org/10.1016/j.jallcom.2018.08.035>.

- [93] B. Sharma, A. Sharma, M. Joshi, J. Myung, Sputtered SnO<sub>2</sub>/ZnO Heterostructures for Improved NO<sub>2</sub> Gas Sensing Properties, *Chemosensors* 8 (2020) 67. <https://doi.org/10.3390/chemosensors8030067>.
- [94] M. Peng, D. Lv, D. Xiong, W. Shen, W. Song, R. Tan, Facile Preparation of a ZnO/SnO<sub>2</sub>-Based Gas Sensor Array by Inkjet Printing for Gas Analysis with BPNN, *J. Electron. Mater.* 48 (2019) 2373-2381. <https://doi.org/10.1007/s11664-019-06938-9>.
- [95] G. Neri, First Fifty Years of Chemoresistive Gas Sensors, *Chemosensors* 3 (2015) 1-20. <https://doi.org/10.3390/chemosensors3010001>.
- [96] S. Sharma, M. Madou, A new approach to gas sensing with nanotechnology, *Phil. Trans. R. Soc. A* 370 (2011) 2448-2473. <https://doi.org/10.1098/rsta.2011.0506>.
- [97] Y. Zhao, J. Song, G. H. Ryu, K. Y. Ko, W. J. Woo, Y. Kim, D. Kim, J. H. Lim, S. Lee, Z. Lee, J. Park, H. Kim, Low-temperature synthesis of 2D MoS<sub>2</sub> on a plastic substrate for a flexible gas sensor, *Nanoscale* 10 (2018) 9338-9345. <http://dx.doi.org/10.1039/c8nr00108a>.
- [98] Z. Yuan, Y. Liu, J. Zhang, F. Meng, H. Zhang, Rose-Like MoO<sub>3</sub>/MoS<sub>2</sub>/rGO Low-Temperature Ammonia Sensors Based on Multigas Detection Methods, *IEEE Trans. Instrum. Meas.* 70 (2021) 9506109. <http://dx.doi.org/10.1109/TIM.2021.3060566>.
- [99] J. Xuan, G. Zhao, M. Sun, F. Jia, X. Wang, T. Zhou, G. Yin, B. Liu, Low-temperature operating ZnO-based NO<sub>2</sub> sensors: a review, *RSC Adv.* 10 (2020) 39786. <http://dx.doi.org/10.1039/d0ra07328h>.
- [100] F. Li, X. Jiang, J. Zhao, S. Zhang, Graphene oxide: A promising nanomaterial for energy and environmental applications, *Nano Energy* 16 (2015) 488-515. <http://dx.doi.org/10.1016/j.nanoen.2015.07.014>.
- [101] M. Donarelli, L. Ottaviano, 2D Materials for Gas Sensing Applications: A Review on Graphene Oxide, MoS<sub>2</sub>, WS<sub>2</sub> and Phosphorene, *Sensor* 18 (2018) 3638. <http://dx.doi.org/10.3390/s18113638>.
- [102] E. J. Frankberg, L. George, A. Efimov, M. Honkanen, J. Pessi, E. Levänen, Measuring Synthesis Yield in Graphene Oxide Synthesis by Modified Hummers Method, *Fuller. Nanotub. Carbon Nanostructures* 23 (2015) 755-759. <http://dx.doi.org/10.1080/1536383X.2014.993754>.

- [103] S. N. Alam, N. Sharma, L. Kumar, Synthesis of Graphene Oxide (GO) by Modified Hummers Method and Its Thermal Reduction to Obtain Reduced Graphene Oxide (rGO), Graphene 6 (2017) 1-18. <http://dx.doi.org/10.4236/graphene.2017.61001>.
- [104] A. Romero, M. P. Lopez, L. Silva, J. L. Valverde, A. Carrero, Comparative study of different scalable routes to synthesize graphene oxide and reduced graphene oxide, Mater. Chem. Phys. 203 (2018) 284-292. <http://dx.doi.org/10.1016/j.matchemphys.2017.10.013>.
- [105] A. Zhou, J. Bai, W. Hong, H. Bai, Electrochemically reduced graphene oxide: Preparation, composites, and applications, Carbon 191 (2022) 301-332. <http://dx.doi.org/10.1016/j.carbon.2022.01.056>.
- [106] J. Kaur, K. Anand, K. Anand, R. C. Singh, WO<sub>3</sub> nanolamellae/reduced graphene oxide nanocomposites for highly sensitive and selective acetone sensing, J. Mater. Sci. 53 (2018) 12894-12907. <https://doi.org/10.1007/s10853-018-2558-z>.
- [107] L. Chen, L. Huang, Y. Lin, L. Sai. Q. Chang, W. Shi, Q. Chen, Fully gravure-printed WO<sub>3</sub>/Pt-decorated rGO nanosheets composite film for detection of acetone, Sens. Actuators B Chem. 255 (2018) 1482-1490. <https://doi.org/10.1016/j.snb.2017.08.158>.
- [108] J. Kaur, K. Anand, A. Kaur, R. C. Singh, Sensitive and selective acetone sensor based on Gd doped WO<sub>3</sub>/reduced graphene oxide nanocomposite, Sens. Actuators B Chem. 258 (2018) 1022-1035. <https://doi.org/10.1016/j.snb.2017.11.159>.
- [109] T. Zhao, Y. Ren, G. Jia, Y. Zhao, Y. Fan, J. Yang, X. Zhang, W. Jiang, L. Wang, W. Luo, Facile synthesis of mesoporous WO<sub>3</sub>@graphene aerogel nanocomposites for low temperature acetone sensing, Chin. Chem. Lett. 30 (2019) 2032-2038. <https://doi.org/10.1016/j.cclet.2019.05.006>.
- [110] J. Kaur, K. Anand, N. Kohli, A. Kaur, R. C. Singh, Temperature dependent selective detection of hydrogen and acetone using Pd doped WO<sub>3</sub>/reduced graphene oxide nanocomposite, Chem. Phys. Lett. 701 (2018) 115-125. <https://doi.org/10.1016/j.cplett.2018.04.049>.
- [111] S. Bai, Y. Zuo, K. Zhang, Y. Zhao, R. Luo, D. Li, A. Chen, WO<sub>3</sub>-ZnFe<sub>2</sub>O<sub>4</sub> heterojunction and rGO decoration synergistically improve the sensing performance of triethylamine, Sens. Actuators B Chem. 347 (2021) 130619. <https://doi.org/10.1016/j.snb.2021.130619>.

- [112] M. Liu, Z. Wang, P. Song, Z. Yang, Q. Wang, Flexible MXene/rGO/CuO hybrid aerogel for high performance acetone sensing at room temperature, *Sens. Actuators B Chem.* 340 (2021) 129946. <https://doi.org/10.1016/j.snb.2021.129946>.
- [113] Y. Seekaew, W. Pon-on, C. Wongchoosuk, Ultrahigh Selective Room-Temperature Ammonia Gas Sensor Based on Tin-Titanium Dioxide/reduced Graphene/Carbon Nanotube Nanocomposites by the Solvothermal Method, *ACS Omega* 4 (2019) 16916-16924. <https://doi.org/10.1021/acsomega.9b02185>.
- [114] T. Wang, Z. Sun, D. Huang, Z. Yang, Q. Ji, N. Hu, G. Yin, D. He, H. Wei, Y. Zhang, Studies on NH<sub>3</sub> gas sensing by zinc oxide nanowires-reduced graphene oxide nanocomposites, *Sens. Actuators B Chem.* 252 (2017) 284-294. <https://doi.org/10.1016/j.snb.2017.05.162>.
- [115] M. Liu, P. Song, X. Zhong, Z. Yang, Q. Wang, Facile synthesis of Au-decorated  $\alpha$ -Fe<sub>2</sub>O<sub>3</sub>/rGO ternary hybrid structure nanocomposites for enhanced triethylamine gas sensing properties, *J. Mater. Sci. Mater. Electron.* 31 (2020) 22713-22726. <https://doi.org/10.1007/s10854-020-04796-4>.
- [116] S. Zhang, B. Zhang, G. Sun, Y. Li, B. Zhang, Y. Wang, J. Cao, Z. Zhang, One-step synthesis of Ag/SnO<sub>2</sub>/rGO nanocomposites and their trimethylamine sensing properties, *Mater. Res. Bull.* 114 (2019) 61-67. <https://doi.org/10.1016/j.materresbull.2019.02.019>.
- [117] X. Jia, D. Lian, B. Shi, R. Dai, C. Li, X. Wu, Facile synthesis of  $\alpha$ -Fe<sub>2</sub>O<sub>3</sub>@graphene oxide nanocomposites for enhanced gas-sensing performance to ethanol, *J. Mater. Sci. Mater. Electron.* 28 (2017) 12070-12079. <https://doi.org/10.1007/s10854-017-7019-y>.
- [118] M. Morsy, I. S. Yahia, H. Y. Zahran, M. Ibrahim, Hydrothermal Synthesis of CNTs/Co<sub>3</sub>O<sub>4</sub>@rGO Mesoporous Nanocomposite as a Room Temperature Gas Sensor for VOCs, *J. Inorg. Organomet. Polym. Mater.* 29 (2019) 416-422. <https://doi.org/10.1007/s10904-018-1011-8>.
- [119] G. Marimuthu, G. Palanisamy, T. Pazhanivel, G. Bharathi, K. P. Tiruppathi, D.Nataraj, NiCo<sub>2</sub>O<sub>4</sub> functionalized with rGO catalyst as an active layer for ammonia sensing, *Ionics* 26 (2020) 5233-5240. <https://doi.org/10.1007/s11581-020-03598-2>.
- [120] J. Lu, N. Jia, L. Cheng, K. Liang, J. Huang, J. Li, rGO/CoTiO<sub>3</sub> nanocomposite with enhanced gas sensing performance at low working temperature, *J. Alloys Compd.* 739 (2018) 227-234. <https://doi.org/10.1016/j.jallcom.2017.12.129>.

- [121] S. Cai, X. Song, Z. Chi, Y. Fu, Z. Fang, S. Geng, Y. Kang, X. Yang, J. Qin, W. Xie, Rational design of Bi-doped rGO/Co<sub>3</sub>O<sub>4</sub> nanohybrids for ethanol sensing, *Sens. Actuators B Chem.* 343 (2021) 130118. <https://doi.org/10.1016/j.snb.2021.130118>.
- [122] P. J. Cao, Y. Z. Cai, D. Pawar, S. Han, W. Y. Xu, M. Fang, X. K. Liu, Y. X. Zeng, W. J. Liu, Y. M. Lu, D. L. Zhu, Au@ ZnO/rGO nanocomposite-based ultra-low detection limit highly sensitive and selective NO<sub>2</sub> gas sensor, *J. Mater. Chem. C* 10 (2022) 4295-4305. <https://doi.org/10.1039/d1tc05835e>.
- [123] P. J. Cao, Y. Z. Cai, D. Pawar, S. T. Navale, C. N. Rao, S. Han, W. Y. Xu, M. Fang, X. K. Liu, Y. X. Zeng, W. J. Liu, Y. M. Lu, D. L. Zhu, Y. M. Lu, Down to ppb level NO<sub>2</sub> detection by ZnO/rGO heterojunction based chemiresistive sensors, *Chem. Eng. J.* 401 (2020) 125491. <https://doi.org/10.1016/j.cej.2020.125491>.
- [124] Z. Chen, H. Guo, F. Zhang, X. Li, J. Yu, X. Chen, Porous ZnO/rGO Nanosheet-Based NO<sub>2</sub> Gas Sensor with High Sensitivity and ppb-level Detection Limit at Room Temperature, *Adv. Mater. Interfaces* 8 (2021) 2101511-2101521. <https://doi.org/10.1002/admi.202101511>.
- [125] M. S. B. Reddy, B. G. Rani, S. Kailasa, N. Jayarambabu, P. Munindra, N. Kundana, K. V. Rao, Sm<sub>2</sub>O<sub>3</sub> rice-like nanorods decorated on rGO flexible resistive sensor for room temperature LPG detection, *Mater. Sci. Eng. B* 262 (2020) 114757. <https://doi.org/10.1016/j.mseb.2020.114757>.
- [126] Q. A. Drmash, A. H. Hendi, M. K. Hossain, Z. H. Yamani, R. A. Moqbel, A. Hezam, M. A. Gondal, UV-activated gold decorated rGO/ZnO heterostructured nanocomposite sensor for efficient room temperature H<sub>2</sub> detection, *Sens. Actuators B Chem.* 290 (2019) 666-675. <https://doi.org/10.1016/j.snb.2019.03.077>.
- [127] P. S. Shewale, K. Yun, Synthesis and characterization of Cu-doped ZnO/rGO nanocomposites for room-temperature H<sub>2</sub>S gas sensor, *J. Alloys Compd.* 837 (2020) 155527. <https://doi.org/10.1016/j.jallcom.2020.155527>.
- [128] V. S. Bhati, S. Ranwa, S. Rajamani, K. Kumari, R. Raliya, P. Biswas, M. Kumar, Improved Sensitivity with Low Limit of Detection of a Hydrogen Gas Sensor Based on rGO-Loaded Ni-Doped ZnO Nanostructures, *ACS Appl. Mater. Interfaces*, 10 (2018) 11116-11124. <https://doi.org/10.1021/acsami.7b17877>.

- [129] Q. A. Drmash, Z. H. Yamani, A. H. Hendi, M. A. Gondal, R. A. Moqbel, T. A. Saleh, M. Y. Khan, A novel approach to fabricating a ternary rGO/ZnO/Pt system for high-performance hydrogen sensor at low operating temperature, *Appl. Surf. Sci.* 464 (2019) 616-626. <https://doi.org/10.1016/j.apsusc.2018.09.128>.
- [130] Y. Gao, D. Chen, X. Hou, Y. Zhang, S. Yi, H. Ji, Y. Wang, L. Yin, J. Sun, Microwave-assisted synthesis of hierarchically porous Co<sub>3</sub>O<sub>4</sub>/rGO nanocomposite for low-temperature acetone detection, *J. Colloid interface Sci.* 594 (2021) 690-701. <https://doi.org/10.1016/j.jcis.2021.03.041>.
- [131] S. Srirattanapibul, P. Nakarungsee, C. Issro, I. Tang, S. Thongmee, Enhanced room temperature NH<sub>3</sub> sensing of rGO/Co<sub>3</sub>O<sub>4</sub> nanocomposites, *Mater. Chem. Phys.* 272 (2021) 125033. <https://doi.org/10.1016/j.matchemphys.2021.125033>.
- [132] L. Satish, K. Achary, B. Maji, A. Kumar, S. P. Ghosh, J. P. Kar, P. Dash, Efficient room temperature detection of H<sub>2</sub> gas by novel ZnFe<sub>2</sub>O<sub>4</sub>-Pd decorated rGO nanocomposite, *Int. J. Hydrog. Energy* 45 (2020) 5073-5085. <https://doi.org/10.1016/j.ijhydene.2019.12.048>.
- [133] H. Ren, C. Gu, S. W. Joo, J. Zhao, Y. Sun, J. Huang, Effective hydrogen gas sensor based on NiO@rGO nanocomposite, *Sens. Actuators B Chem.* 266 (2018) 506-513. <https://doi.org/10.1016/j.snb.2018.03.130>.
- [134] L. Jin, W. Chen, H. Zhang, G. Xiao, C. Yu, Q. Zhou, Characterization of Reduced Graphene Oxide (rGO)-Loaded SnO<sub>2</sub> Nanocomposite and Applications in C<sub>2</sub>H<sub>2</sub> Gas Detection, *Appl. Sci.* 7 (2017) 19. <https://doi.org/10.3390/app7010019>.
- [135] S. Bai, K. Zhang, Y. Y. Zhao, Q. Li, R. Luo, D. Li, A. Chen, rGO decorated NiO-BiVO<sub>4</sub> heterojunction for detection of NO<sub>2</sub> at low-temperature, *Sens. Actuators B Chem.* 329 (2021) 128912. <https://doi.org/10.1016/j.snb.2020.128912>.
- [136] J. Sun, L. Sun, N. Han, H. Chu, S. Bai, X. Shu, R. Luo, A. Chen, rGO decorated CdS/CdO composite for detection of low concentration NO<sub>2</sub>, *Sens. Actuators B Chem.* 299 (2019) 126832. <https://doi.org/10.1016/j.snb.2019.126832>.
- [137] S. BAi, K. Tian, N. Han, J. Guo, R. Luo, D. Li, A. Chen, Novel rGO decorated ZnO/BiVO<sub>4</sub> heterojunction for enhancement of NO<sub>2</sub> sensing properties, *Inorg. Chem. Front.* (2020). <https://doi.org/10.1039/C9QI01608B>.

- [138] Q. Li, N. Han, K. Zhang, S. Bai, J. Guo, R. Luo, D. Li, A. Chen, Novel p-n heterojunction of BiVO<sub>4</sub>/Cu<sub>2</sub>O decorated with rGO for low concentration of NO<sub>2</sub> detection, *Sens. Actuators B Chem.* 320 (2020) 128284. <https://doi.org/10.1016/j.snb.2020.128284>.
- [139] Z. Wang, S. Gao, T. Fei, S. Liu, T. Zhang, Construction of ZnO/SnO<sub>2</sub> Heterostructure on Reduced Graphene Oxide for Enhanced Nitrogen Dioxide Sensitive Performance at Room Temperature, *ACS Sens.* 4 (2019) 2048-2057. <https://doi.org/10.1021/acssensors.9b00648>.
- [140] M. D. Davis, S. J. Fowler, A. J. Montpetit, Exhaled Breath Testing- A Tool for the Clinical and Researchers, *Paediatr. Respir. Rev.* 29 (2019) 37-41. <http://doi.org/10.1016/j.prrv.2018.05.002>.
- [141] O. Lawal, W. M. Ahmed, T. M. E. Nijsen, R. Goodacre, S. J. Fowler, Exhaled breath analysis: a review of ‘breath-taking’ methods for off-line analysis, *Metabolomics* 13 (2017) 110-125. <https://doi.org/10.1007/s11306-017-1241-8>.
- [142] Z. Feng, H. Fan, L. Cheng, H. Zhang, H. Fan, J. Liu, Advanced Biomimetic Nanomaterials for Non-invasive Disease Diagnosis, *Front. Mater.* 8 (2021) 664795. <https://doi.org/10.3389/fmats.2021.664795>.
- [143] K. M. Tripathi, T. Kim, D. Losic, T. T. Tung, Recent advances in engineered graphene and composites for detection of volatile organic compounds (VOCs) and non-invasive disease diagnosis, *Carbon* 110 (2016) 97-129. <https://doi.org/10.1016/j.carbon.2016.08.040>.
- [144] J. Pereira, P. Porto-Figueira, C. Cavaco, K. Taunk, S. Rapole, R. Dhakne, H. Nagarajaram, J. S. Câmara, Breath Analysis as a Potential and Non-invasive Frontier in Disease Diagnosis: An Overview, *Metabolites* 5 (2014) 3-55. <https://doi.org/10.3390/metabo5010003>.
- [145] R. Kalidoss, R. Kothalam, A. Manikandan, S. K. Jaganathan, A. Khan, A. M. Asiri, Socio-economic demands and challenges for non-invasive disease diagnosis through a portable breathalyzer by the incorporation of 2D nanosheets and SMO nanocomposite, *RSC Adv.* 11 (2021) 21216. <https://doi.org/10.1039/d1ra02554f>.
- [146] X. Chang, X. Qiao, K. Li, P. Wang, Y. Xiong, X. Li, F. Xia, Q. Xue, UV assisted ppb-level acetone detection based on hollow ZnO/MoS<sub>2</sub> nanosheets core/shell



- heterostructures at low temperature, *Sens. Actuators B: Chem.* 317 (2020) 128208. <https://doi.org/10.1016/j.snb.2020.128208>.
- [147] S. P. M. Hosking, R. Bhatia, P. A. Crock, I. Wright, M. L. Squance, G. Reeves, Non-invasive detection of microvascular changes in a paediatric and adolescent population with type 1 diabetes: a pilot cross-sectional study, *BMC Endocr. Disord.* 13 (2013) 41-49. <https://doi.org/10.1186/1472-6823-13-41>.
- [148] V. Saasa, M. Beukes, Y. Lemmer, B. Mwakikunga, Blood Ketone Bodies and Breath Acetone Analysis and Their Correlations in Type 2 Diabetes Mellitus, *Diagnostics* 9 (2019) 224. <https://doi.org/10.3390/diagnostics9040224>.
- [149] V. Ruzsányi, M. P. Kalapos, Breath acetone as a potential marker in clinical practice, *J. Breath Res.* 11 (2017) 024002. <https://doi.org/10.1088/1752-7163/aa66d3>.
- [150] D. Zhang, C. Jiang, P. Li, Y. Sun, Layer-by-Layer Self-assembly of Co<sub>3</sub>O<sub>4</sub> Nanorod-Decorated MoS<sub>2</sub> Nanosheet-based Nanocomposite toward High-performance Ammonia Detection, *ACS Appl. Mater. Interfaces* 9 (2017) 6462-6471. <https://doi.org/10.1021/acsami.6b15669>.
- [151] C. Chen, J. Hsieh, C. Chao, W. Yang, H. Cheng, C. Chan, C. Lu, H. Meng, H. Zan, Correlation between Breath Ammonia and Blood Urea Nitrogen Levels in Chronic Kidney Disease and Dialysis Patients, *J. Breath Res.* 14 (2020) 036002. <https://doi.org/10.1088/1752-7163/ab728b>.
- [152] T. Arakawa, T. Suzuki, M. Tsujii, P. Chien, M. Ye, K. Toma, Y. Iwasaki, K. Mitsubayashi, Real-time monitoring of skin ethanol gas by a high-sensitivity gas phase biosensor (bio-sniffer) for the non-invasive evaluation of volatile blood compounds, *Biosens. Bioelectron.* 129 (2019) 245-253. <https://doi.org/10.1016/j.bios.2018.09.070>.
- [153] P. X. Zhao, Y. Tang, J. Mao, Y. X. Chen, H. Song, J. W. Wang, Y. Song, Y. Q. Liang, X. M. Zhang, One-Dimensional MoS<sub>2</sub>-Decorated TiO<sub>2</sub> nanotube gas sensors for efficient alcohol sensing, *J. Alloys Compd.* 674 (2016) 252-258. <https://doi.org/10.1016/j.jallcom.2016.03.029>.
- [154] D. Han, L. Zhai, F. Gu, Z. Wang, Highly sensitive NO<sub>2</sub> gas sensor of ppb-level detection based on In<sub>2</sub>O<sub>3</sub>nanobricks at low temperature, *Sens. Actuators B: Chem.* 262 (2018) 655-663. <https://doi.org/10.1016/j.snb.2018.02.052>.



- [155] T. Xu, Y. Liu, Y. Pei, Y. Chen, Z. Jiang, Z. Shi, J. Xu, D. Wu, Y. Tian, X. Li, The ultra-high NO<sub>2</sub> response of ultra-thin WS<sub>2</sub> nanosheets synthesized by hydrothermal and calcination processes, *Sens. Actuators B: Chem.* 259 (2018) 789-796. <https://doi.org/10.1016/j.snb.2017.12.070>.
- [156] D. Feng, L. Du, X. Xing, C. Wang, J. Chen, Z. Zhu, Y. Tian, D. Yang, Highly Sensitive and Selective NiO/WO<sub>3</sub> Composite Nanoparticles in Detecting H<sub>2</sub>S Biomarker of Halitosis, *ACS Sens.* 6 (2021) 733-741. <https://doi.org/10.1021/acssensors.0c01280>.
- [157] S. Singh, N. Dogra, S. Sharma, A sensitive H<sub>2</sub>S sensor using MoS<sub>2</sub>/WO<sub>3</sub> composite, *Mater. Today: Proc.* 28 (2020) 8-10. <https://doi.org/10.1016/j.matpr.2019.12.104>.
- [158] J. V. D. Broek, A. T. Güntner, S. E. Pratsinis, Highly Selective and Rapid Breath Isoprene Sensing Enabled by Activated Alumina Filter, *ACS Sens.* 3 (2018) 677-683. <https://doi.org/10.1021/acssensors.7b00976>.
- [159] Y. Park, R. Yoo, S. R. Park, J. H. Lee, H. Jung, H. Lee, W. Lee, Highly sensitive and selective isoprene sensing performance of ZnO quantum dots for a breath analyzer, *Sens. Actuators B Chem.* 290 (2019) 258-266. <https://doi.org/10.1016/j.snb.2019.03.118>.
- [160] L. André, N. Desbois, C. P. Gros, S. Brandès, Porous materials applied to biomarker sensing in exhaled breath for monitoring and detecting non-invasive pathologies, *Dalton Trans.* 49 (2020) 15161. <https://doi.org/10.1039/d0dt02511a>.
- [161] H. Wang, X. Shi, F. Liu, T. Duan, B. Sun, Non-Invasive Rapid Detection of Lung Cancer Biomarker Toluene with a Cataluminescence Sensor Based on the Two-Dimensional Nanocomposite Pt/Ti<sub>3</sub>C<sub>2</sub>T<sub>x</sub>-CNT, *Chemosensors* 10 (2022) 333. <https://doi.org/10.3390/chemosensors10080333>.
- [162] D. Wang, S. Huang, H. Li, A. Chen, P. Yang, X. Wang, J. Yang, Ultrathin WO<sub>3</sub> nanosheets modified by g-C<sub>3</sub>N<sub>4</sub> for highly efficient acetone vapor detection, *Sens. Actuators B Chem.* 282 (2019) 961-971. <http://dx.doi.org/10.1016/j.snb.2018.11.138>.
- [163] X. Hao, B. Wang, C. Ma, F. Liu, X. Yang, T. Liu, X. Liang, C. Yang, H. Zhu, G. Lu, Mixed potential type sensor based on stabilized zirconia and Co<sub>1-x</sub>Zn<sub>x</sub>Fe<sub>2</sub>O<sub>4</sub> sensing electrode for detection of acetone, *Sens. Actuators B Chem.* 255 (2018) 1173-1181. <http://dx.doi.org/10.1016/j.snb.2017.06.002>.

- [164] L. Chen, L. Huang, Y. Lin, L. Sai, Q. Chang, W. Shi, Q. Chen, Fully gravure-printed WO<sub>3</sub>/Pt-decorated rGO nanosheets composite film for detection of acetone, *Sens. Actuators B Chem.* 255 (2018) 1482-149. <http://dx.doi.org/10.1016/j.snb.2017.08.158>.
- [165] J. Shen, M. Wang, Y. Wang, J. Hu, Y. Zhu, Y. Zhang, Z. Li, H. Yao, Iron and carbon codoped WO<sub>3</sub> with hierarchical walnut-like microstructure for highly sensitive and selective acetone sensor, *Sens. Actuators B Chem.* 256 (2018) 27-37. <http://dx.doi.org/10.1016/j.snb.2017.10.073>.
- [166] X. Song, L. Qiao, K. Sun, Z. Tan, W. Ma, X. Kang, F. Sun, T. Huang, X. Wang, Triple-shelled ZnO/ZnFe<sub>2</sub>O<sub>4</sub> heterojunctional hollow microspheres derived from Prussian Blue analogue as high-performance acetone sensors, *Sens. Actuators B Chem.* 256 (2018) 374-382. <http://dx.doi.org/10.1016/j.snb.2017.10.081>.
- [167] B. Wang, Q. Yu, S. Zhang, T. Wang, P. Sun, X. Chuai, G. Lu, Gas sensing with yolk-shell LaFeO<sub>3</sub> microspheres prepared by facile hydrothermal synthesis, *Sens. Actuators B Chem.* 258 (2018) 1215-1222. <http://dx.doi.org/10.1016/j.snb.2017.12.018>.
- [168] D. Kim, J. Jang, W. Koo, S. Choi, S. Kim, I. Kim, Hierarchically interconnected porosity control of catalyst-loaded WO<sub>3</sub> nanofiber scaffold: Superior acetone sensing layers for exhaled breath analysis, *Sens. Actuators B Chem.* 259 (2018) 616-625. <http://dx.doi.org/10.1016/j.snb.2017.12.051>.
- [169] Y. Li, Z. Hua, Y. Wu, Y. Zheng, Z. Qiu, X. Tian, M. Wang, E. Li, Modified impregnation synthesis of Ru-loaded WO<sub>3</sub> nanoparticles for acetone sensing, *Sens. Actuators B Chem.* 265 (2018) 249-256. <http://dx.doi.org/10.1016/j.snb.2018.03.037>.
- [170] F. Qu, W. Shang, T. Thomas, S. Ruan, M. Yang, Self-template derived ZnFe<sub>2</sub>O<sub>4</sub> double-shell microspheres for chemiresistive gas sensing, *Sens. Actuators B Chem.* 265 (2018) 625-631. <http://dx.doi.org/10.1016/j.snb.2018.03.108>.
- [171] X. Liu, X. Tian, X. Jiang, L. Jiang, P. Hou, S. Zhang, X. Sun, H. Yang, R. Cao, X. Xu, Facile preparation of hierarchical Sb-doped In<sub>2</sub>O<sub>3</sub> microstructures for acetone detection, *Sens. Actuators B Chem.* 270 (2018) 304-311. <http://dx.doi.org/10.1016/j.snb.2018.05.046>.
- [172] X. Song, Y. Meng, Z. Tan, L. Qiao, T. Huang, X. Wang, Concave ZnFe<sub>2</sub>O<sub>4</sub> Hollow Octahedral Nanocages Derived from Fe-Doped MOF-5 for High-Performance

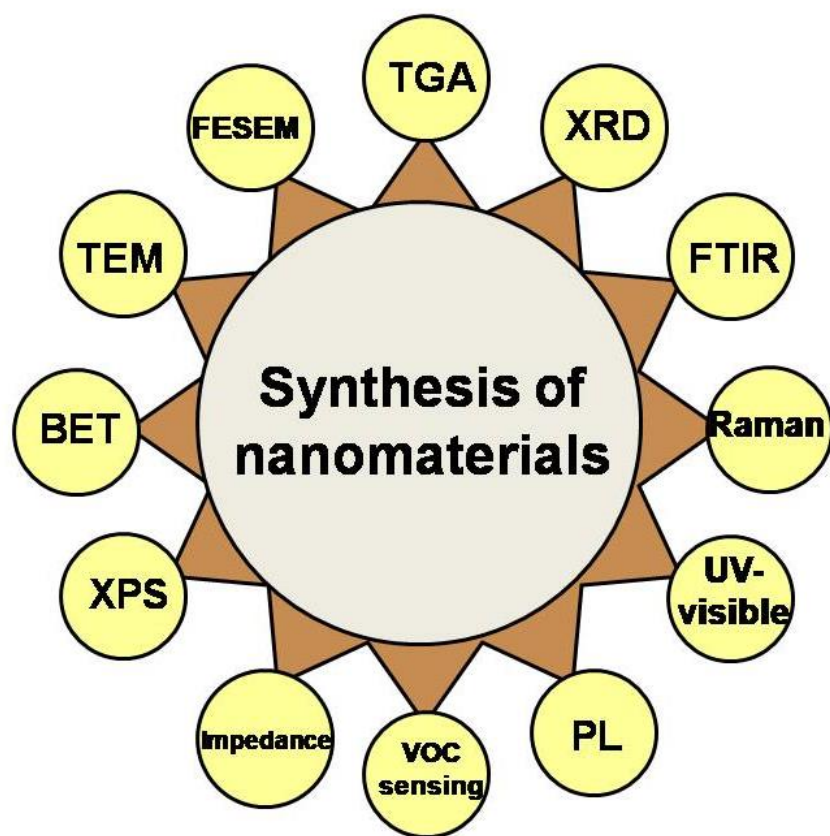
- Acetone Sensing at Low-Energy Consumption, *Inorg. Chem.* 56 (2017) 13646-13650. <http://dx.doi.org/10.1021/acs.inorgchem.7b02425>.
- [173] W. Geng, S. Ge, X. He, S. Zhang, J. Gu, X. Lai, H. Wang, Q. Zhang, Volatile Organic Compound Gas-Sensing Properties of Bimodal Porous  $\alpha$ -Fe<sub>2</sub>O<sub>3</sub> with Ultrahigh Sensitivity and Fast Response, *ACS Appl. Mater. Interfaces* 10 (2018) 13702-13711. <http://dx.doi.org/10.1021/acsami.8b02435>.
- [174] S. Chakraborty, M. Pal, Highly selective and stable acetone sensor based on chemically prepared bismuth ferrite nanoparticles, *J. Alloys Compd.* 787 (2019) 1204-1211. <http://dx.doi.org/10.1016/j.jallcom.2019.02.153>.
- [175] H. Xu, J. Gao, M. Li, Y. Zhao, M. Zhang, T. Zhao, L. Wang, W. Jiang, G. Zhu, X. Qian, Y. Fan, J. Yang, W. Luo, Mesoporous WO<sub>3</sub> Nanofibers With Crystalline Framework for High-Performance Acetone Sensing, *Front. Chem.* 7 (2019) 1-11. <http://dx.doi.org/10.3389/fchem.2019.00266>.
- [176] R. Kalidoss, S. Umashathy, Y. Sivalingam, An investigation of GO-SnO<sub>2</sub>-TiO<sub>2</sub> ternary nanocomposite for the detection of acetone in diabetes mellitus patient's breath, *Appl. Surf. Sci.* 449 (2018) 677-684. <http://dx.doi.org/10.1016/j.apsusc.2017.12.090>.
- [177] H. G. Moon, Y. Jung, D. Jun, J. H. Park, Y. W. Chang, H. Park, C. Kang, C. Kim, R. B. Kaner, Hollow Pt-Functionalized SnO<sub>2</sub> Hemipill Network Formation Using a Bacterial Skeleton for the Non-Invasive Diagnosis of Diabetes, *ACS Sens.* 3 (2018) 661-669. <http://dx.doi.org/10.1021/acssensors.7b00955>.
- [178] H. Du, X. Li, P. Yao, J. Wang, Y. Sun, L. Dong, Zinc Oxide Coated Tin Oxide Nanofibers for Improved Selective Acetone Sensing, *Nanomaterials* 8 (2018) 509-524. <http://dx.doi.org/10.3390/nano8070509>.
- [179] M. J. Priya, P. M. Aswathy, M. K. Kavitha, M. K. Jayaraj, K. R. Kumar, Improved acetone sensing properties of electrospun Au-doped SnO<sub>2</sub> nanofibers, *AIP Conf. Proc.* 2082 (2019) 030026. <http://dx.doi.org/10.1063/1.5093825>.
- [180] H. Wang, L. Yan, S. Li, Y. Li, L. Liu, L. Du, H. Duan, Y. Cheng, Acetone sensors based on microsheet-assembled hierarchical Fe<sub>2</sub>O<sub>3</sub> with different Fe<sup>3+</sup> concentrations, *Appl. Phys. A* 124 (2018) 212-220. <http://dx.doi.org/10.1007/s00339-018-1625-2>.

- [181] Z. E. Khalidi, B. Hartiti, M. Siadat, E. Comini, H. M. M. M. Arachchige, S. Fadili, P. Thevenin, Acetone sensor based on Ni doped ZnO nanostructures: growth and sensing capability, *J. Mater. Sci. Mater. Electron.* 30 (2019) 7681-7690. <http://dx.doi.org/10.1007/s10854-019-01083-9>.
- [182] W. Chen, Z. Qin, Y. Liu, Y. Zhang, Y. Li, S. Shen, Z. M. Wang, H. Song, Promotion on Acetone Sensing of Single SnO<sub>2</sub> Nanobelt by Eu Doping, *Nanoscale Res. Lett.* 12 (2017) 405. <http://dx.doi.org/10.1186/s11671-017-2177-7>.
- [183] W. Liu, L. Xu, K. Sheng, X. Zhou, B. Dong, G. Lu, H. Song, A highly sensitive and moisture-resistant gas sensor for diabetes diagnosis with Pt@In<sub>2</sub>O<sub>3</sub> nanowires and a molecular sieve for protection, *NPG Asia Mater.* 10 (2018) 293-308. <http://dx.doi.org/10.1038/s41427-018-0029-2>.
- [184] H. Zhang, H. Qin, C. Gao, G. Zhou, Y. Chen, J. Hu, UV Light Illumination Can Improve the Sensing Properties of LaFeO<sub>3</sub> to Acetone Vapor, *Sensors* 18 (2018) 1990. <http://dx.doi.org/10.3390/s18071990>.
- [185] H. Zhang, H. Qin, C. Gao, J. Hu, An Ultrahigh Sensitivity Acetone Sensor Enhanced by Light Illumination, *Sensors* 18 (2018) 2318. <http://dx.doi.org/10.3390/s18072318>.
- [186] X. Wang, W. Ma, F. Jiang, E. Cao, K. Sun, L. Cheng, X. Song, Prussian Blue analogue derived porous NiFe<sub>2</sub>O<sub>4</sub> nanocubes for low-concentration acetone sensing at low working temperature, *Chem. Eng. J.* 338 (2018) 504-512. <http://dx.doi.org/10.1016/j.cej.2018.01.072>.
- [187] S. Wang, J. Cao, W. Cui, L. Fan, X. Li, D. Li, Facile synthesis of bamboo raft-like Co<sub>3</sub>O<sub>4</sub> with enhanced acetone gas sensing performances, *J. Alloys Compd.* 758 (2018) 45-53. <http://dx.doi.org/10.1016/j.jallcom.2018.05.139>.
- [188] M. Yin, L. Yu, S. Liu, Synthesis of thickness-controlled cuboid WO<sub>3</sub> nanosheets and their exposed facets-dependent acetone sensing properties, *J. Alloys Compd.* 696 (2017) 490-497. <http://dx.doi.org/10.1016/j.jallcom.2016.11.149>.



# CHAPTER 2

## Nanomaterials Synthesis and Characterization



*This chapter elaborates the synthesis process of metal oxide nanomaterials, reduced graphene oxide and their nanocomposites. The detailed procedures and working principles of different structural, morphological and optical characterization techniques have also been thoroughly discussed. Taguchi-type sensor fabrication technique using as-synthesized nanomaterials and their sensing performance measurement strategy have been vividly described.*



## 2.1. Introduction:

Technological dependency in our day-to-day lifestyle has been introduced nano-science and technology as one of the trending topic in research and development (R & D) field far and wide. The invention of nanomaterials, opens up different horizons of application; starting from electronics to energy materials (including materials chemistry and catalysis) even in materials for bioscience arena. These nanomaterials differ from conventional bulk materials mainly in their dimensions; the materials with particle size in the range  $\sim 1$  nm to  $\sim 100$  nm generally categorized as nanomaterials. The nanomaterials can provide diversity of properties depending on shape, size, and morphologies (0D, 1D, 2D, and 3D). These dimensional properties can be controlled by varying their synthesis route. Henceforth, selection of proper synthesis method is consequential for tuning the physical and chemical properties of nanomaterials. Generally, two different techniques [1-6] are adopted in this synthesis purpose (Fig. 2.1), such as:

### (a) Top down method:

Top-down approach of nanomaterials preparation involves scalable reduction of precursor bulk material. From a small amount of precursor, a large amount of desired nanomaterials can be obtained. However, the fine tuning of particle dimension is somehow compromised in this method. Example: Ball-milling, RF Sputtering, thermal decomposition, lithography etc.

### (b) Bottom up method:

In bottom up method, as a starting material atoms or molecules or even clusters has been chosen. The inter-particle short-range attraction forces bring the precursor particles close together to form an assembly. This provides an opportunity of scalable synthesis of nanomaterials with almost uniform dimension and nearly homogeneous distribution of particles. Bottom up approach is a constructive way of nanomaterials synthesis and more favoured in laboratory as well as in industrial purpose. Example: Sol-gel, CVD, PVD, wet chemical synthesis, etc.

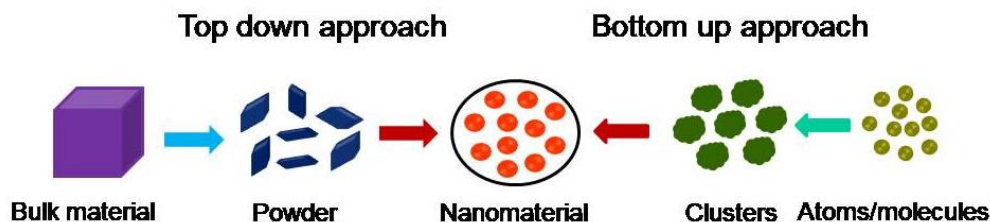
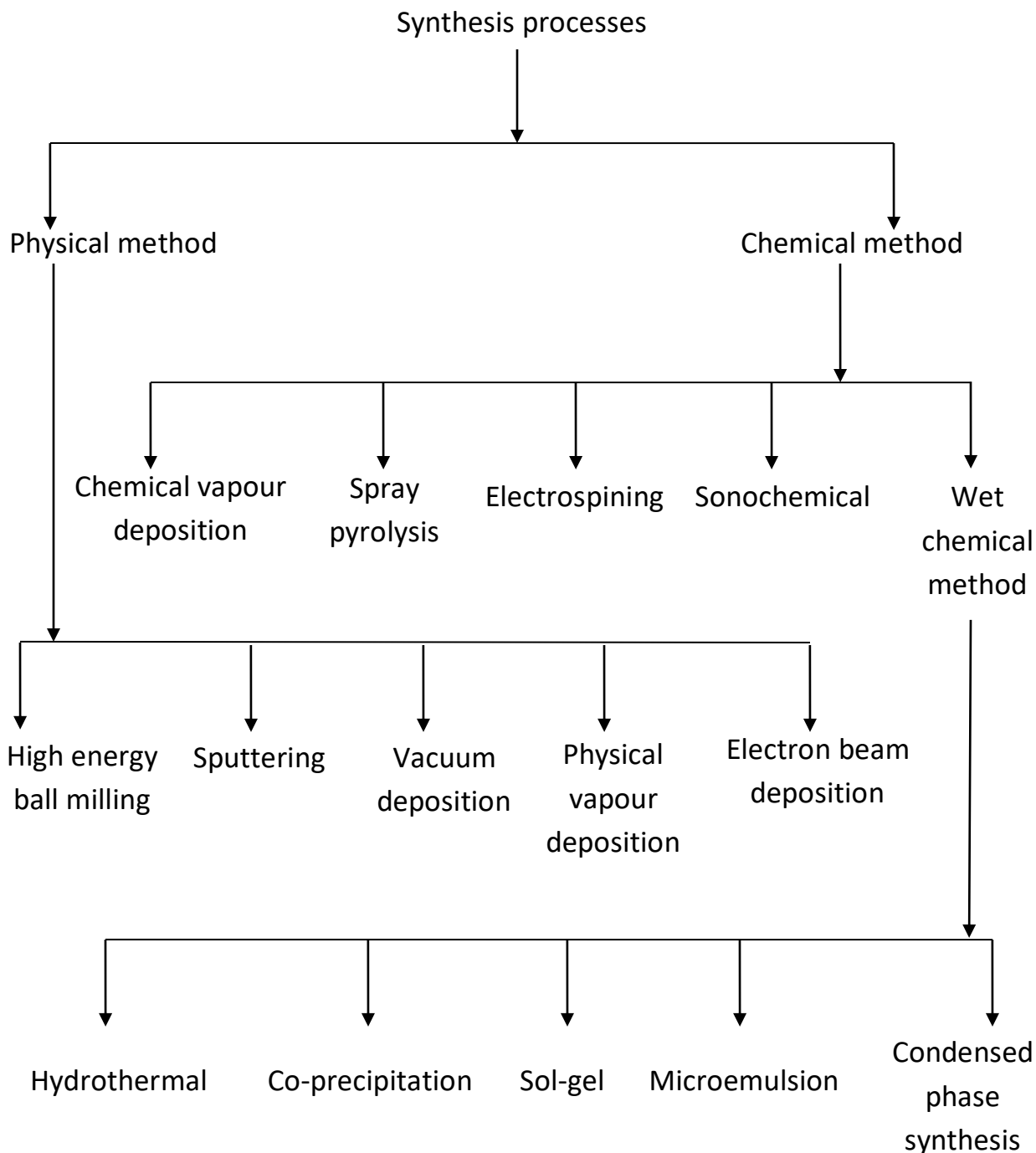


Figure-2.1: Schematic representation of nanomaterials synthesis



**2.2. Synthesis processes:**

Generally, the metal oxide semiconductors used in sensing purpose are synthesized in the dimensions of nano meter ranges. There are several procedures to synthesize the nanomaterials as depicted in the following flowchart (Fig. 2.2).



*Figure-2.2: Flowchart of different synthesis processes*

### **2.2.1. Sol-gel synthesis:**

Among different bottom up approach for nanomaterial synthesis sol-gel process is the most common one [7-12]. This is a cost-effective and simplest synthesis technique that provides molecular level mixing of chemicals. The process involves conversion of small precursor monomer molecules into a colloidal solution called sol that eventually converts to an integrated network like structure known as gel. In a typical sol-gel process, a sol is formed from the hydrolysis and polymerisation reactions of the precursors, which are usually inorganic metal salts or metal organic compounds such as metal alkoxides that dissolves in an aqueous or organic medium. The colloidal solution (sol) slowly transforms into a biphasic system (gel) containing solid assemblies in liquid dispersion phase. Increasing bulk concentration of the dispersed phase or other changes in external conditions leads to the intense formation of contacts between particles and formation of gel in which solvent molecules are enclosed in a flexible but fairly stable three-dimensional grid form by particles of alkoxides. The dispersed phase of the gel system is removed by heating at a low temperature, results into the compression of the biphasic system. Finally, calcination at a higher temperature yields the desired nanocomposite. This heating rate controls the morphology and porosity of the solid nanoparticles.

### **2.2.2. Advantages of sol-gel synthesis:**

- 1. Versatile:** Better control of the structure, including porosity and particle size; possibility of incorporating nanoparticles and organic materials into sol-gel derived oxides.
- 2. Extended composition ranges:** It allows the fabrication of any oxide composition, but also some non-oxides, as well as the production of new hybrid organic-inorganic materials, which do not exist naturally.
- 3. Better homogeneity:** Due to mixing at the molecular level; high purity nanomaterials obtain.
- 4. Less energy consumption:** There is no need to reach the melting temperature, since the network structure can be achieved at relatively low temperatures.
- 5. Coatings and thin films, monoliths, composites, porous membranes, powders and fibers.**
- 6. No need for special or expensive equipment.**

### **2.3. Details of synthesis process used in present work:**

#### **2.3.1. Synthesis of metal oxide nanomaterials:**

In this thesis work, for the synthesis of nanomaterials sol-gel technique was adopted. In a typical sol-gel synthesis process, requisite amount of precursor inorganic salts were mixed in suitable aqueous organic solvent and stirred to obtain a homogeneous sol. Then the sol was kept for ageing for ~ 72 hours. After ageing, the sol was converted to gel by heating it at ~ 60°C. Then the gel was calcined in a muffle furnace at a suitable temperature (determined from the TGA curve) for ~ 2 hours to obtain the desired nanomaterial.

#### **2.3.2. Synthesis of Graphene Oxide (GO):**

Graphene oxide was synthesized by employing modified Hummer's method [13-17]. Initially, graphite was grounded to fine powders. ~ 1.0 g fine graphite powder was added in ~ 25 ml concentrated  $\text{H}_2\text{SO}_4$  (~ 98%), followed by ~ 1.25 g  $\text{NaNO}_3$  addition. The mixture was vigorously stirred for ~ 1 hour in an ice bath, maintaining the temperature below 5°C. After that, ~ 3.0 g  $\text{KMnO}_4$  powder was slowly added to the reaction mixture under continuously stirring condition for ~ 2 hours. The temperature of this reaction was kept below 20°C. Thereafter, the mixture was allowed to stir for another ~ 2 hours at ~ 35°C. Then, ~ 50 ml water was added to the reaction mixture and heated at ~ 95°C under stirring condition for ~ 30 minutes. Finally, the reaction was quenched with the addition of ~ 150 ml water and ~ 10 ml 30%  $\text{H}_2\text{O}_2$  in it. The obtained solution was kept for settle down and then centrifuged followed by washing with ~ 5% aqueous HCl. The obtained precipitate was dried at ~ 50°C in a vacuum oven for ~ 24 hours.

#### **2.3.3. Synthesis of Reduced Graphene Oxide (rGO):**

Graphene oxide was chemically reduced [18-21] to obtain reduced graphene oxide. ~ 0.05 g as-synthesized GO powder was dispersed in ~50 ml de-ionized water by sonication for ~ 1 hour. Then, ~ 0.5 ml hydrazine hydrate ( $\text{NH}_2\text{NH}_2 \cdot 2\text{H}_2\text{O}$ ) was added to it under ammoniacal medium. The mixture was stirred for ~ 15 minutes. After that, the solution was heated at ~ 95°C under stirring condition for ~ 2 hours. The mixture was allowed to settle for ~ 6 hours. Then the solution was centrifuged and washed with ~ 5% aqueous HCl. The precipitate was dried at ~ 50°C under vacuum for ~ 24 hours to obtain reduced graphene oxide.

### **2.3.4. Synthesis of rGO-metal oxide nanocomposites:**

To synthesis rGO-metal oxide nanocomposite, as-prepared nanomaterial was dispersed in suitable aqueous organic solvent. After that, required amount of rGO was dispersed in the previous solution by ultrasonication. As a binder CTAB was used. Then, the obtained mixture was stirred for ~ 2 hours for homogeneous dispersion. Thereafter, the sol was kept aside for ageing. After ageing for ~ 72 hours, the sol was heated at ~ 70°C to form gel. The gel was calcined in a muffle furnace for ~ 1 hour to obtain rGO-metal oxide nanocomposite powder.

## **2.4. Characterization techniques of nanomaterials:**

### **2.4.1. Thermogravimetric Analysis (TGA):**

Thermo-gravimetric analysis (TGA) is a physico-chemical characterization technique that measures the change in weight with respect to temperature (Fig. 2.3). To obtain different morphology, phase transformation, proper grain growth, porosity and sintering, and for removal of solvent and binder surfactant molecules, calcination of nanomaterials is inevitable [22]. Therefore, it is very essential to get a better idea about the ideal calcination temperature of metal oxide semiconductors. A derivative weight loss curve can identify the point where weight loss is most apparent. Again interpretation is limited without further modification and therefore, deconvolution of overlapping peaks may be required. To determine composition and purity one must calculate the mass of the substance in the mixture by using thermo-gravimetric analysis. This is the act of heating a mixture to a high enough temperature (generally ~ 1000°C) so that one of the components decomposes into a gas, which dissociates into the air. The measurement is carried out in an ambient or inert condition. The nanomaterial powder is generally taken in a pan made of porcelain or alumina or platinum and hanged from a high precision microbalance. The thermocouple remains suspended close to the sample containing pan but not in contact. The weight loss with temperature does not hamper the stability of the pan. It is a process that utilizes heat and stoichiometric ratios to determine the percentage of mass. If the compounds in a mixture remain unknown, then the percentage by mass can be determined by taking the weight of what is left in the mixture and dividing it by the initial mass. Knowing the mass of the original mixture and total mass of impurities liberating upon heating, the stoichiometric ratio can be used to calculate the percentage mass of the substance in a sample. TGA is commonly employed to

determine degradation temperature, adsorbed moisture content of materials, the level of inorganic and organic components in a material and solvent residue. The thermal analysis of the synthesized nanomaterials was done by thermogravimetric analysis (TG) using a Perkin-Elmer thermal analyzer (TGA4000) at a heating rate of 10°C/minute in the temperature range of 50°C to 950°C.



*Figure-2.3: Thermogravimetric analyzer (CSIR-CGCRI)*

### **2.4.2. Powder X-Ray Diffraction (XRD) Technique:**

The structure of crystals remained as a mystery to us for many years. The assumption about the crystal was that it is a periodic arrangement of symmetric units but without experimental proof it was inconclusive. Therefore, to establish the structure experimentally we need to develop a system to collect the information regarding the crystal structure of a solid. X-Ray diffraction is a versatile, non-destructive analytical method for identification and quantitative determination of various crystalline forms, known as ‘phases’ of compounds present in powder and solid samples [23]. X-Rays are electromagnetic radiation with the wavelength of the order  $10^{-10}$  m was first discovered by Wilhelm Conrad Roentgen in 1895. They are typically generating by bombarding a metal with high-frequency electrons. These electrons must penetrate through the outer electron shell and interact with the inner shell electrons. If more than threshold energy is transferred to an

inner shell electron, that electron will escape the nuclear attraction force and will be ejected. This creates a hole in the inner shell and generates ionized atom. The ionized atom returns to the lowest energy level by filling in the missing electron with one from the outer shell. It is this transition which is accompanied either by the emission of an X-Ray or an Auger electron.

X-Ray diffraction is a method of determining the arrangement of atoms in a crystal. In principle, any wave impinging on a regular array of scatterers produces diffraction, as predicted first by Francesco Maria Grimaldi in 1665. X-Rays are used to produce the diffraction pattern because their wavelength ( $\lambda$ ) is typically in the same order of magnitude (1-100 Å) as the spacing ( $d$ ) between the planes in a crystal. When X-Ray strikes a crystal, which is a periodic array of atoms, they scatter X-Ray waves, primarily through the atoms' electrons. An X-Ray striking an electron produces secondary spherical waves emanating from the electron. This phenomenon is known as elastic scattering and the electron is called scatterer.

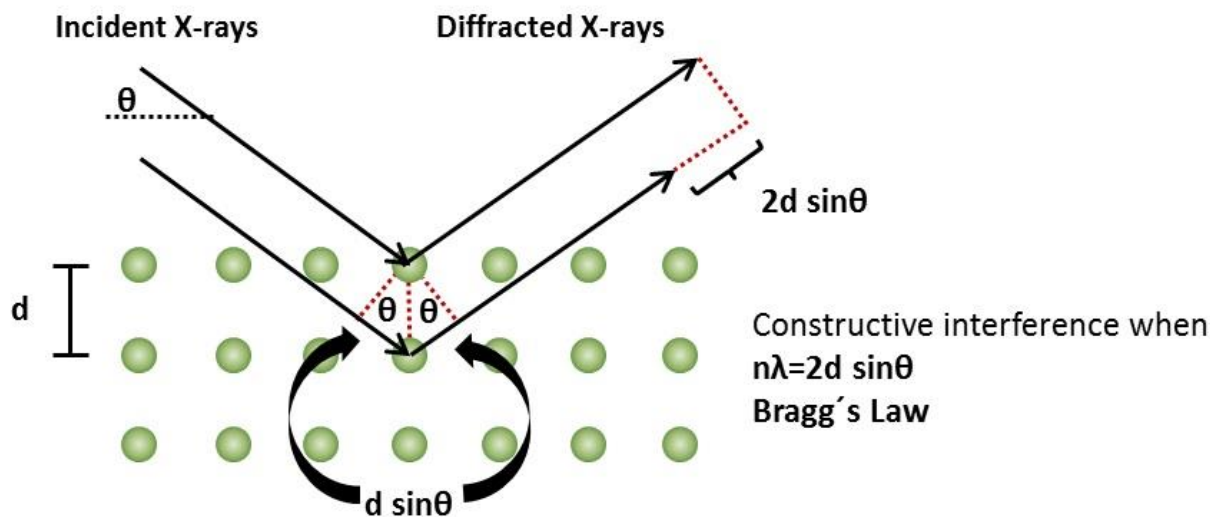


Figure-2.4: Bragg's diffraction in a periodic crystal [24]

A regular array of scatterers produces an arranged array of spherical waves. Although these waves cancel each other in most directions through destructive interference, they add constructively in a few specific directions (Fig. 2.4), following the equation:

$$2d \sin \theta = n\lambda \quad \dots\dots\dots (2.1)$$

Where,  $d$ = spacing between diffraction planes

$\theta$ = incident angle of X-Ray

$n$ = order of diffraction

$\lambda$ = wavelength of X-Ray beam

This equation is known as **Bragg's law** [23].

These specific directions appear as spots on the diffraction pattern. From the angle and intensities of these diffracted beams, a crystallographer can produce a 3-D picture of the density of electrons within the crystal. From this electron density, the mean position of the atoms in a crystal can be determined, as well as their chemical bonds, disorder and various other information. The crystal structure and phases of the nanocomposites were characterized by an X-ray diffractometer (Philips PW 1730), operating with a Cu  $K\alpha$  ( $\lambda = 1.54 \text{ \AA}$ ) filter and data collected with an incident angle ( $2\theta$ ) range of  $20^\circ$  to  $80^\circ$  with a step size  $0.02^\circ$ .

The distance between two planes of a crystal with different crystal arrangements is calculated from the lattice index ( $h, k, l$ ) and lattice parameter ( $a, b, c$ ) values. The formulas used to calculate the interplanar distance of some important Bravais lattices are as follows:

$$\text{a) Cubic system: } (1/d) = [(h^2+k^2+l^2)/a^2]^{1/2} \dots\dots\dots (2.2)$$

$$\text{b) Tetragonal system: } (1/d) = [\{(h^2+k^2)/a^2\} + (l^2/c^2)]^{1/2} \dots\dots\dots (2.3)$$

$$\text{c) Orthorhombic system: } (1/d) = [(h^2/a^2) + (k^2/b^2) + (l^2/c^2)]^{1/2} \dots\dots\dots (2.4)$$

$$\text{d) Hexagonal system: } (1/d) = [\{(4/3)(h^2+hk+k^2)/a^2\} + (l^2/c^2)]^{1/2} \dots\dots\dots (2.5)$$

Notably, metal oxide semiconductors are generally obtained after prolong calcination of reaction mixture at different temperatures. This calcination process can easily modulate the particle size of the crystals. The particle size was determined from the XRD pattern by the using Scherer's formula [25]:

$$D = k\lambda/\beta\cos\theta \dots\dots\dots (2.6)$$

Where,  $D$  is the particle size,  $k$  is the shape factor generally valued 0.9 and a dimensionless identity,  $\lambda$  is the wavelength of the X-Ray,  $\beta$  is the full width at half maxima (FWHM), and  $\theta$  is the peak position.

### 2.4.3. Fourier Transforms Infrared Spectroscopy (FTIR):

Fourier transform infrared spectroscopy (FTIR) is a spectroscopic technique to gather information about the functional groups present in the specimen by collecting spectral data using the infrared electromagnetic wave (Fig. 2.5). The absorption or transmission peaks obtained in the spectra are analogous to the bonds present in the sample [26]. Each and every bond has a



specific vibration frequency, that distinctive molecular fingerprint can be used to screen and scan samples for many different components. The infrared spectrum is divided into three parts depending on the harmonic vibration, fundamental vibration and rotational mode of vibration of the molecules; near infra red ( $14000 - 4000 \text{ cm}^{-1}$ ), mid infra red ( $4000 - 200 \text{ cm}^{-1}$ ), and near infra red ( $1000 - 50 \text{ cm}^{-1}$ ). FTIR spectrometers operate and detect bonds with the vibrational frequencies in the mid and near IR zone. Fourier Transformed Infrared spectroscopy (FTIR) measurement was done by IR spectrometer (Nicolet 5700, Thermo Electron Corporation).

The IR-active molecules must possess a finite dipole moment, i.e., the molecule should be of polar nature. The incident infrared light is passing through a beam splitter that directs the beams to two mutually perpendicular directions [27]. One goes to the stationary mirror and the other strikes the moving mirror. Again these two beams meet at the beam splitter to produce constructive and destructive interferences. The variation of energy caused by the interference at all the wavelengths detected by the detector and further Fourier transformation of the raw data gives the FTIR spectrum.



*Figure-2.5: FTIR instrument [28]*

#### **2.4.4. Raman Analysis:**

Raman scattering, most commonly known as Raman Effect was first discovered in 1928 by C. V. Raman and was awarded Nobel Prize for his pioneering work. In Chemistry related work Raman spectroscopy helps to identify molecules by providing information regarding unique structural features. A molecule or crystal when irradiated with monochromatic light, most of the photons



undergo elastic scattering, only a few of them encounter inelastic scattering (Fig. 2.6). This elastic scattering is called Rayleigh scattering and the inelastic one is known as Raman scattering [29, 30]. The extent of Raman Effect is proportional with the polarizability of electrons in a molecule. If a molecule illuminate with a beam of photons then the molecule reaches to a virtual energy state differs from the actual vibrational level. Inelastic scattering, measured at the right angle to the incident radiation, causes emission of photons of higher and lower energy compared to incident photon energy. Upon irradiated with a monochromatic light, the spectrum of the scattered light consist of lines with the frequency less than the incident frequency are Stokes line and the other lines with frequency greater than the incident frequency are called anti-Stokes line. Stokes line involves the transition from a lower energy level to higher energy vibration level, whereas anti-Stokes line generates from transition from higher energy to lower energy level. Therefore, Stokes lines are intense and anti-Stokes lines are weaker.



*Figure-2.6: Raman spectrometer [31]*

Raman shift is generally calculated in terms of wave number, however, in order to convert it between spectral wavelength and wave number of Raman shift the following formula is used:

$$\Delta\tilde{\nu} = [(1/\lambda_0) - (1/\lambda_1)] \dots\dots\dots (2.7)$$

Where,  $\Delta\tilde{\nu}$  is the Raman shift,  $\lambda_0$  is the excitation wavelength and  $\lambda_1$  is the spectral wavelength.

In a typical Raman spectrometer, a laser beam (monochromatic and coherent) is passed through the sample containing cell (glass or quartz tube) and the light scattered sideways collected by

lens and directed towards a monochromator. Raman spectra were recorded using Jobin Yvon Horiba Raman spectrometer (France, excitation source Ar-Kr mixed ion gas laser, Model 2018 RM) with a  $\sim 532$  nm laser filter.

#### **2.4.5. Surface Area Analysis:**

The adsorption interaction between gas molecules and solid surface can be interpreted from BET isotherm, proposed by Stephen Brunauer, Paul Hugh Emmett and Edward Teller in 1938 [32, 33]. It can directly measure the surface area and pore size distribution of the synthesized nanocomposites. In fact, BET isotherm is a logical extension of Langmuir isotherm model where kinetic behaviour of the adsorption process is studied. The basic condition of this adsorption is that the rate of adsorption is equal to the rate of desorption. Further in this theory it is assumed that:

- All the surface sites are equivalent and have same energy of adsorption
- Adsorbate molecules cannot interact laterally and they are immobile
- There is equilibrium between the uppermost layer and vapour phase
- Adsorption can be mono-layered or multi-layered

Adsorption is a process involving attachment of the gas molecules on the solid surface whereas, desorption is the removal of those molecules from the solid surface. Increasing of pressure facilitates the adsorption process but desorption increases at decreased pressure. In physisorption the interactions between the solid surface and adsorbate molecules are relatively weak Van der Waal's interaction and predominantly monolayer and completely reversible in nature. Chemisorption is associated with a strong electrostatic interaction between the adsorbate and solid surface. Therefore, the adsorbate molecules need some activation energy to be attached on the adsorbate surface. Hence, this type of adsorption is often irreversible and multi-layered.

In these experiments, solid samples are purified from any moisture or organic solvents either by heating under a vacuum or by degassing under a flow of dry inert gas. The contaminant free sample is exposed to a small amount of adsorbate gas molecules. The molecules adsorbed to the solid surface and from the amount of monolayer adsorbed gas the surface area calculated, whereas the pore size calculated from the pore filling pressure. It simply records different pressures of gas in the sample cell during adsorption and desorption processes. Then the amount

of gas adsorbed or desorbed is calculated by the instrument and corresponding surface area, pore size are calculated by software.

The conventional BET equation is as follows:

$$[1/W ((P_0/P) - 1)] = (1/W_m C) + [(C - 1)/W_m C](P/P_0) \quad \dots\dots\dots (2.8)$$

Where, W is the weight of gas adsorbed, W<sub>m</sub> is the weight of adsorbate, (P/P<sub>0</sub>) is the relative pressure and C is the BET constant.

To determine the surface area and pore size of the adsorbate, BET equation requires a linear plot of  $[1/W ((P_0/P) - 1)]$  against P/P<sub>0</sub>. The slope (S) and intercept (i) of the plot are given by:

$$S = [(C - 1)/W_m C] \quad \dots\dots\dots (2.9)$$

$$i = (1/W_m C) \quad \dots\dots\dots (2.10)$$

The specific surface area of the nanocomposites is calculated from the linear fitted multi-point BET plot using the equation as follows:

$$S_{BET} = [(N_A \times s) \div \{M \times (A + I)\}] \quad \dots\dots\dots (2.11)$$

Where, N<sub>A</sub> is the Avogadro's number ( $6.023 \times 10^{23}$ ), s represents adsorbing species' adsorption cross-section, M is the molar mass of the gas (N<sub>2</sub>, 28.0134 g/mol), A and I denote slope and intercept of the linear fit.

BET data recording can be two types:

- (a) Single point BET: determines specific surface area using a single point on the isotherm
- (b) Multi point BET: specific surface area determination based on minimum of three data points

Using desorption data of liquid nitrogen at 77K BJH pore size distribution is determined. From the adsorption-desorption isotherm the pore size, pore volume, and pore distribution can be calculated. Three scientists namely Barrett, Joyner, and Halenda classified the isotherms in six categories (Fig. 2.7) and documented in IUPAC [34, 35].

- i. **Type I:** This type of isotherm is concave in nature and approaches a limiting value as relative pressure approaches to unity. It mainly characterize microporous surface leaving hardly any external surface for further adsorption.
- ii. **Type II:** Most frequently encountered type II isotherm generally obtains for nonporous or for sample exceeding the diameter of micropores. At the initial part of the isotherm, the rounded knee indicates the approx location of monolayer formation, followed by almost linear low slope zone hinted the completion of monolayer and

starting of multilayer formation. The absence of hysteresis loop infers the non-porous nature and abundant monolayer-multilayer formation.

- iii. **Type III:** This isotherm indicates adsorbate heat of liquefaction is more than heat of adsorption. Here the convex nature of the isotherm hints weak adsorbate-adsorbent interaction due to greater interaction between adsorbate and adsorbed layer.
- iv. **Type IV:** Generally mesoporous solid surface exhibits this type of isotherm which is very common in conventional metal oxides and ceramic materials. At higher pressure increased uptake of adsorbate observes and the inflection point arises near the completion of monolayer. The notable feature of the hysteresis loop is the capillary condensation at the mesopores and limiting uptake over the range of high relative pressure.

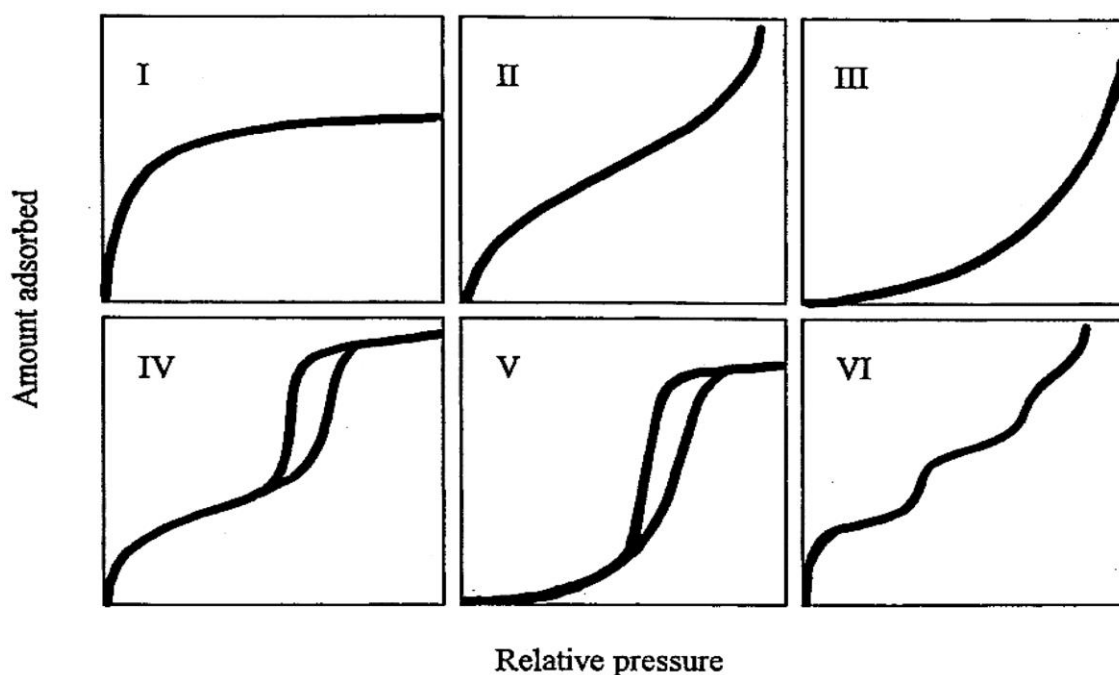


*Figure-2.7: Different BET adsorption curves [36]*

- v. **Type V:** This isotherm is similar kind as that of type III, except the fact that the solid material is mesoporous in nature. This is a very rare nature of isotherm.

- vi. **Type VI:** This isotherm obtained from uniform non-porous surface with stepwise multilayer adsorption. Homogeneous nature of the solid material can be inferred from the almost constant step height of the individual monolayer upto 3-4 layers.

According to the IUPAC convention, the solid surfaces can be categorised in three classes as follows:

- a) Macroporous: Pore size is greater than 50 nm
- b) Mesoporous: Pore size in the range 2 to 50 nm
- c) Microporous: Pore size lesser than 2 nm

The BET Surface area measurements and corresponding BJH pore dimension analyses were done in Anton Paar, USA's iSorp HP1-100 gas adsorption analyzer, and the temperature was maintained at  $\sim 77$  K throughout the measurement.

#### **2.4.6. Field Emission Scanning Electron Microscopy (FESEM):**

The first concept of Scanning Electron Microscopy (SEM) image was developed by Max Knoll in 1935, with an image of silicon steel showing electron channeling contrast. Further progress on the physical principles of the SEM and beam specimen interactions was pioneered by Manfred von Ardenne in 1937 who produced a British patent. The SEM was further evolved by Professor Sir Charles Oatley and his postgraduate student Gary Stewart and first marketed in 1965 by Cambridge Scientific Instrument Company as the 'Stereoscan'. The first instrument was delivered to DuPont.

SEM is a type of electron microscope that produces a largely magnified image of a sample by scanning it with a high energy beam of electrons in a raster scan pattern instead of light (Fig. 2.8). The electrons interact with the atoms that contain information about the sample's surface topography, composition and other properties such as electrical conductivity [37, 38].

In presence of an applied electrostatic field under vacuum condition electron from a metal or semiconductor emits and this phenomenon is known as 'field emission'. A microscope was designed on the concept of field emission based on the difference in work function of surface oriented crystal planes. As the intensity of the applied electrical field is dependent of the diameter of the electron emitting tip, so the tip used for the generation of an intense electrical field is of nanometer order. It is made of metal having high melting point. A beam of electrons is produced at the top of the microscope by an electron gun. The electron beam which typically has

an energy ranging from 0.5 keV to 40 keV follows a vertical path through the microscope within a vacuum. The beam travels through electromagnetic fields and lenses, which focused towards the sample. Once the beam hits the sample, electrons and X-Rays are ejected from the sample and generate an impression on the fluorescent screen. Detectors collect these X-Rays, backscattered electrons and secondary electrons and convert them into a signal by comparing the intensity of these scattered electrons to the primary electron beam and that is sent to a screen similar to a television screen to produce the final image. The Energy-Dispersive Spectroscopy (EDS) system coupled with it detects emitted X-rays from the sample as the high-energy electron beam interaction with the sample. This yields quantitative elemental information about the sample. FESEM can provide better information regarding the surface morphological properties and topographical characteristics of the nanomaterial (either in the form of thin film or powder sample), coating thickness of nanomaterial films as compared to conventional SEM. Field Emission Scanning Electron Microscopy (FESEM, Carl Zeiss Supra 35 VP microscope) was used for surface morphological study.



*Figure-2.8: FESEM measurement unit [39]*

### **2.4.7. Transmission Electron Microscopy (TEM):**

Transmission Electron Microscopy (TEM) is a microscopic technique that uses a beam of electrons transmitted through an ultra thin specimen. The interaction between the incident

electron beam and the specimen produces an image which is magnified and focused onto an imaging device, such as a fluorescent screen, on a layer of photographic film, or to be detected by a sensor such as a CCD camera. In TEM, the interaction between the electron beam and sample takes place in vacuum, maintained by pumping the air out of the chamber. Transmission electron microscope is also following the principle of a common microscope except instead of light source a projected electron beam is used to illuminate the sample [40, 41]. The TEM samples should have two essential characteristics; the sample should withstand the vacuum of the chamber and it need to be electron transparent.

In TEM the images are obtained in the form of either bright field or dark field, along with high resolution images to understand the inner architecture of the nanomaterials (Fig. 2.9). By varying the voltage of electron gun, the speed of the emitted electrons can be controlled. The speed of the electrons is inversely proportional to the electromagnetic wavelength. The faster moving electrons with shorter wavelength can produce high quality images. The lighter area in the image contains lesser number of molecules and hence greater number of electrons passed through it and vice versa. This difference in light intensities in the images gives an idea regarding the structure, size, shape, and texture of the nanomaterials.

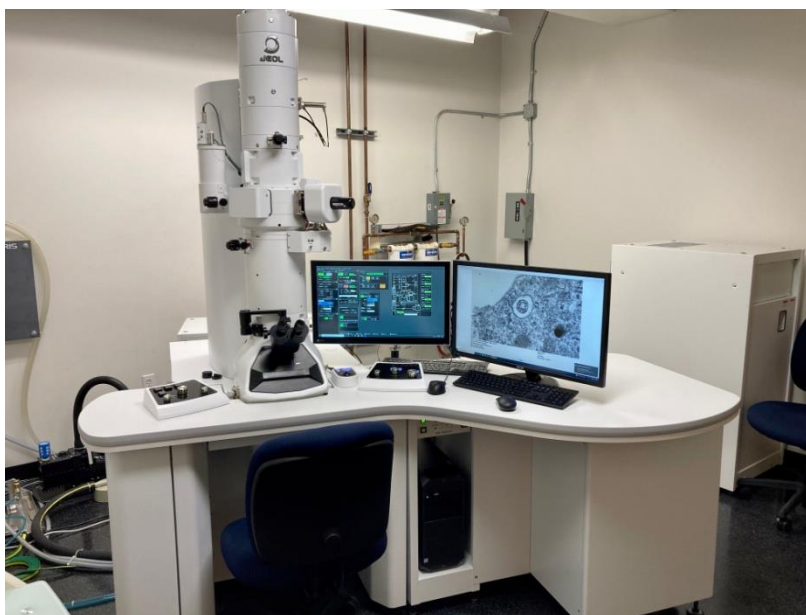


*Figure-2.9: TEM instrument [42]*



The high resolution TEM image shows the lattice fringes correspond to interplanar distance of diffraction planes analogous to XRD pattern. As well as the stacking fault, grain boundary regions even the stacking of particles in the nanomaterials also can be identified. The angular distribution of diffraction pattern, obtained from selected area electron diffraction (SAED) delivers important information crystal orientations and structural properties. Energy dispersive analysis using X-rays (EDAX) determines the chemical composition and their stoichiometric properties in the nanomaterials. An Electron Microscopy instrument (Model- JEM 2100F, JEOL) with an ultra-high-resolution field emission gun (UHR-FEG) was deployed for Transmission Electron Microscope (TEM) images collection and Selected Area Electron Diffraction (SAED) pattern of the nanocomposite.

### 2.4.8. X-Ray Photoelectron Spectroscopy (XPS):

In conventional absorption spectroscopy we are dealing with photon energy whereas in photoelectron spectroscopy we detect electrons to study the electronic structures of a material. A sample is bombarded with a focused beam of X-rays (photons) and by absorbing the energy electron will be ejected from the sample with a certain amount of kinetic energy. Those ejected electrons will be detected by a detector and a plot of the relative energy against relative number of electrons will be obtained. Electrons with different energies will follow different paths to the detector and it will be reflected in the obtained survey spectrum (Fig. 2.10). This process can be expressed in the following way [43]:

$$A + h\nu \rightarrow A^+ + e^- \quad \dots\dots\dots (2.12)$$

For conservation of energy:

$$E(A) + h\nu \rightarrow E(A^+) + K.E. \quad \dots\dots\dots (2.13)$$

$$\text{Therefore, } K.E. = h\nu - B.E. \quad \dots\dots\dots (2.14)$$

This is the basic equation of photoelectron spectroscopy. For the removal of electron from the core level of an atom higher energy of photon (soft X-ray) is required as compared to lower energy photons (hard X-ray) will be needed to remove an electron from the valence shell. In X-ray photoelectron spectroscopy (XPS) the electrons will be removed from the core level, so that higher energy X-ray is require for ionisation. From the fundamental equation, binding energy (B.E.) of the electrons can be calculated after knowing the kinetic energy of the ejected electrons and the energy of the incident photons. Electrons ejected from the different orbitals (s, p, d, f)



having different energies and will be differentiated from each other and consequent chemical composition of the material can be determined. The greater the binding energy greater will be the attraction of nucleus to that electron and higher will be the peak intensity. XPS is capable of distinguish between different chemical states of an element as well as able to identify oxidation states of the elements. The X-ray Photoelectron Spectra (XPS) were conducted with PHI 5000 Versa Probe III Scanning XPS microprobe surface analysis system using Al X-rays source having focused beam ( $< 10\ \mu\text{m}$  to  $300\ \mu\text{m}$ ).

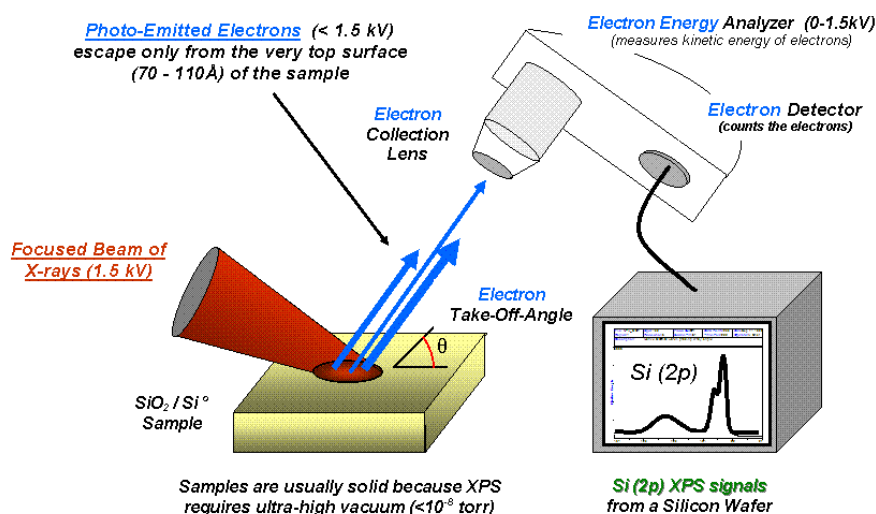


Figure-2.10: Schematics of XPS measurement [44]

Actually, XPS has a greater range of applications and some of its crucial applications are mentioned here:

- ◆ Determination of ionisation energies of valence electrons and core electrons.
- ◆ Predict the electronic structure of the atoms and molecules.
- ◆ Analyse the surface chemical compositions of the sample.

## 2.4.9. UV-Visible Spectroscopy:

UV-visible spectroscopy is a type of absorption spectroscopy in which light of ultra-violet and visible region (200-800 nm) is absorbed by the molecule (Fig. 2.11). Absorption of the ultra-violet radiations results in the excitation of the electrons from the ground state to higher energy

state. The energy of the ultra-violet radiation that are absorbed is equal to the energy difference between the ground state and higher energy states ( $\Delta E = h\nu$ ) [45].

Generally, the most favored transition is from the highest occupied molecular orbital (HOMO) to lowest occupied molecular orbital (LUMO). For most of the molecules, the LUMO are s orbital, which correspond to  $\delta$ -bonds. The p-orbitals are at somewhere higher energy levels, the orbitals (nonbonding orbitals) with unshared pair of electrons lie at higher energy levels. The unoccupied and anti-bonding orbitals ( $\pi^*$  and  $\delta^*$ ) are the HOMO. UV-Visible absorption study was performed using Shimadzu UV-3600 UV-visible spectrometer.



*Figure-2.11: UV-Visible spectrometer [46]*

The prime objective of UV-visible spectroscopy is to calculate the energy band gap between conduction band and valence band of the synthesized nanomaterial. The band gap is the difference in energy between the conduction band and valence band of the semiconductor material. The relation between the absorption coefficient ( $\alpha$ ) and incident photon energy ( $h\nu$ ) is presented in the following equation:

$$(\alpha h\nu)^2 = A(h\nu - E_g) \quad \dots\dots\dots (2.15)$$

This equation is well known as Tauc equation, where,  $h$  is Planck's constant,  $\nu$  is the frequency of the photon,  $A$  is a constant that depends on spectral properties and  $E_g$  is the calculated band gap. Plotting of  $(\alpha h\nu)^2$  against incident photon energy generates the Tauc plot corresponded to the UV-visible absorption spectrum. The X-intercepts of the linear extrapolation of Tauc plot gives the experimental band gap.

**2.4.10. Photoluminescence (PL) Spectroscopy:**

Photoluminescence is a spectroscopic technique that reciprocates absorption spectroscopy. In absorption spectroscopy energy is required for transition of electron from the ground state to higher excited state, whereas in luminescence spectroscopy energy is emitted for returning of electrons from any of the higher excited state to ground state (Fig. 2.12). The luminescence spectrum gives an indication of presence of impurity in phase-pure nanomaterial, presence of defect sites in the lattice, the recombination and relaxation process in electronic level, as well as band gap energy can also be calculated.



*Figure-2.12: Photoluminescence spectroscopy instrument [47]*

In luminescence spectroscopy an incident beam of light is focused onto the sample and the sample absorbs a certain amount of energy for electronic excitation. The excess energy impart in the sample for photo-excitation. Upon this photo-excitation the excess energy dissipates from the sample to generate photoluminescence spectrum. As the electrons return from the excited state to the ground state equilibrium, the absorbed energy is released through radiative or non-radiative process. The energy of the radiated light is related to the energy required for crossing the energy gap between valence and conduction band of the semiconductor [45]. In electronic level the recombination of electron-hole pair releases a photon with a characteristic wavelength analogous to a particular radiative process. Room temperature photoluminescence (PL) spectra were recorded in Horiba FluroMax 4 spectrometer.

**2.4.11. Impedance Spectroscopy:**

Impedance spectroscopy is a technique to rationalize the perturbation to the response of current to a varying frequency of voltage applied over a wide range and the impedance can be expressed

as a combination of real and imaginary components. Impedance is an inherent property of semiconductor material that opposes the alternating current to pass through it. Generally, impedance spectroscopy reveals the electrical behavior of different integral components (grain, grain boundary and electrode interface) of a polycrystalline sensing material and effectively differentiate their contribution towards overall electrical properties.

Impedance is actually an extension of resistance in AC circuit and unlike resistance impedance possesses both phase and magnitude. In AC circuit the induction of voltage in conductor by magnetic field is called inductance and induction of electrostatic charge storage by voltage in between conductors is known as capacitance. The impedance caused by the combined effect of inductance and capacitance is referred as reactance. The impedance of two-terminal AC circuit can be expressed as a summation of real part (resistance) and an imaginary complex part (reactance). Thus the impedance can be defined as [48]:

$$Z = R + jX \quad \dots\dots\dots (2.16)$$

Where,  $Z$  is the complex identity known as impedance,  $R$  is the real part and  $X$  is the imaginary part of the impedance,  $j$  is the imaginary number valued ( $\sqrt{-1}$ ). Further, the real and imaginary part of impedance can be written as:

$$R = |Z| \cos\theta \quad \dots\dots\dots (2.17)$$

$$X = |Z| \sin\theta \quad \dots\dots\dots (2.18)$$

Where,  $|Z|$  is the magnitude of impedance and  $\theta$  is the phase angle of the sinusoidal wave analogous to the impedance. Comprehensive analysis of the real and imaginary components of complex impedance ( $Z$ ) at varying frequency and temperature gives an idea about electrical characteristic of the material (Fig. 2.13). Nyquist plot, a plot of resistive component ( $Z'$ ) against reactive component ( $Z''$ ) of impedance clarifies the contributions of different electrical components depending on the number of semicircles produce. A single semicircle indicates the grain contribution, whereas grain boundary contribution describes by second semicircle and the presence of a third semicircle specifies the contribution from electrode interface.

In most of the metal oxide semiconductor based sensing materials the circuit diagram can be modeled by using a resistance and parallely connected constant phase element (CPE) analogous to marginally deformed semicircles, with the centre of the arc below  $Z'$  axis. This kind of semicircle results from non-ideal Debye type of relaxation caused due to presence of inhomogeneous surface phenomena of the materials. Another noticeable fact is that there

observes a gradual decrease in resistance of the sensors in presence of experimental gas as well as with raise in temperature. The change in resistance with temperature certifies the typical semiconducting nature. The variation of  $Z'$  with frequency at low frequency region exhibits dispersed nature accompanying a decrease in resistive impedance ( $Z'$ ) with temperature. This accounts for negative temperature coefficient of resistance (NTCR) which is a characteristic of semiconductor. Nonetheless, at high frequency zone, the individual dispersed plots are converge to a single line. Impedance spectroscopy was recorded using Wayne Kerr India (SH-1000) instrument.

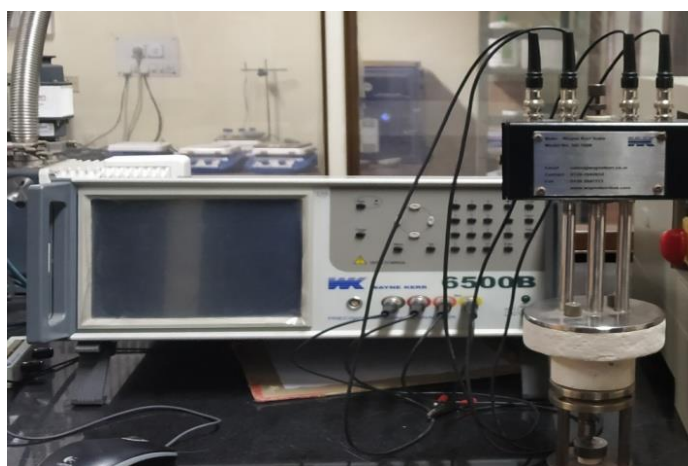


*Figure-2.13: Impedance spectrometer (CSIR-CGCRI)*

The plot of reactive component of impedance ( $Z''$ ) with frequency displays maxima corresponding to different temperatures, known as relaxation frequency ( $f_{\max}$ ). The activation energy of this relaxation process can be calculated by using the Arrhenius type relation:

$$f_{\max} = f_0 e^{(-E_{\text{rel}}/kT)} \quad \dots\dots\dots (2.19)$$

Where,  $E_{\text{rel}}$  is the activation energy of the relaxation process,  $f_{\max}$  is the frequency maxima,  $f_0$  is the initial frequency,  $k$  is the Boltzmann constant and  $T$  is the temperature in Kelvin unit. It is well known that in a semiconductor lattice the majority of conducting species are charged oxygenated ions. The hopping of these ions modulates the oxygen vacancies in sensing material. In absence and presence of analyte gas molecules there develops a potential energy barrier via the variation of charge carrier concentration. The activation energy close to 1eV indicates doubly ionized oxygen vacancies and for singly ionized oxygen vacancies it is ~0.3-0.5 eV.

## **2.5. Details of sensor fabrication:**

### **2.5.1. Preparation of sensor substrate:**

Taguchi type sensor substrates (Fig. 2.14), used for chemiresistive gas sensing application, were made of ceramic alumina and had fixed dimensions. These tubular alumina substrates were originally hollow cylindrical tube with  $\sim 12$  mm length and outer diameter  $\sim 2$  mm with thickness of the  $\sim 0.5$  mm. For preparation of sensor substrates these tubes were cut at a length of  $\sim 3$  mm, polished at the both ends and properly cleaned with dilute HCl and ethanol successively. Finally, the tubes were sonicated in distilled water and dried at  $100^\circ\text{C}$  for one hour. Then, the tubes were electroded with the help of gold paste (Gwent Electronic Materials Limited, United Kingdom, Product code: C2070117D2) and dried in a vacuum oven for  $\sim 30$  minutes.

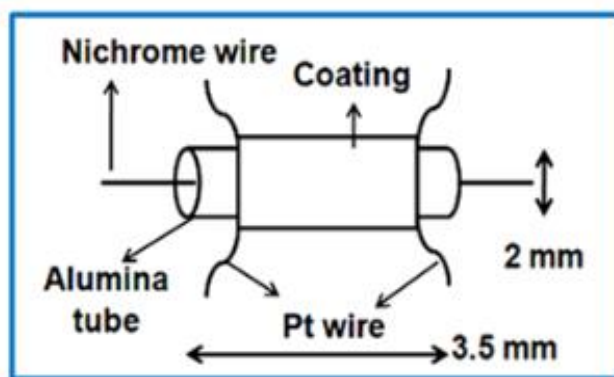


*Figure-2.14: Schematics of sensor unit*

After that, platinum wire electrodes were attached at the both ends of the tube with the help of gold paste coating. The separation between the two electrodes was  $\sim 2$  mm. The electrode-attached substrates were cured at  $\sim 950^\circ\text{C}$  for  $\sim 1$  hour in a tube furnace to remove the thinner solvent used for gold paste preparation. The uncoated part in between the two electrodes on the alumina tube was used for sensing material coating.

### **2.5.2. Fabrication of sensor:**

In every case, a small amount of synthesized nanopowder was taken in an agate mortar and grinded with a pestle to prepare a homogeneous paste using isopropanol. The paste applied as uniform coating on the tubular substrate (Fig. 2.15). The coating cycle repeated to maintain an

approximate thickness of 700-900 nm. The coated sensor substrate was then cured in a tube furnace at a temperature  $\sim 150^{\circ}\text{C}$  for  $\sim 2$  hours. This final curing after coating of sensing material allowed the binding between the nanoparticles in the thin film layer as well as it removed the solvent molecules used for paste formation.

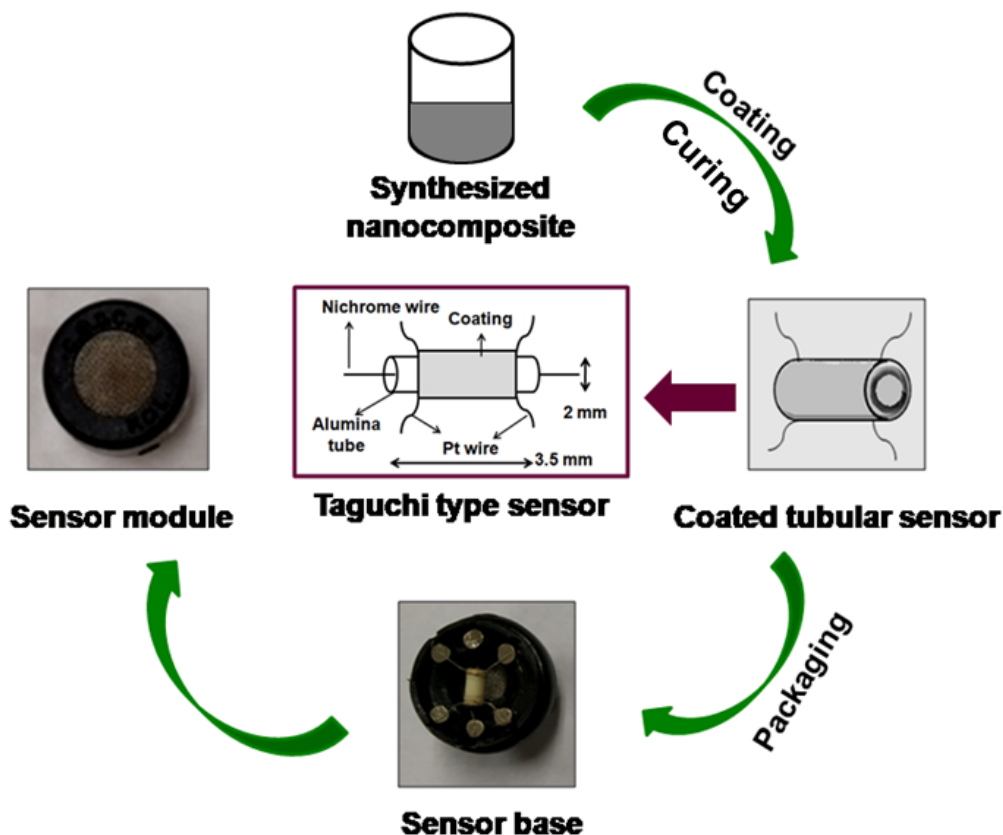


Figure-2.15: Flowchart of sensor fabrication

### 2.5.3. Packaging of sensor module:

The miniaturized sensor substrate mounted in a customized polyamide made sensor socket with six nickel pin arrangement and a cap with double mesh (200 meshes each) push-fitted to the socket. The coated sensor substrate was attached to this customized socket by spot-welding the platinum wire electrode to the 1, 3 and 4, 6 pins. Then a coiled nichrome wire (Ni-Cr based alloy; 80% Ni and 20% Cr by mass, melting point  $\sim 1400^{\circ}\text{C}$ , resistance  $\sim 24 \mu\Omega$ ) inserted through the hollow cylindrical tube and used as a heating coil for indirect heating of the sensor during sensing experiments. The heater wire welded to the central 2 and 5 pins opposite to each other (Fig. 2.16). These fabricated sensor modules were used for the further gas sensing



measurement. For every synthesized nanomaterial five numbers of sensors were fabricated and used for further gas sensing experiments.

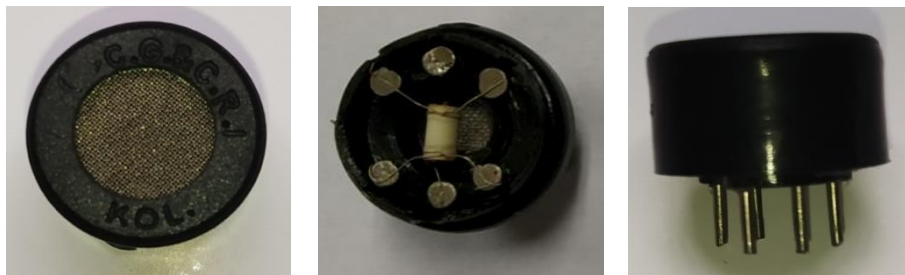


*Figure-2.16: Fabricated customized sensor modules*

### 2.6. Gas sensing measurement:

During gas sensing measurement study, the fabricated sensors were attached to a sensor base socket (containing six holes to fit to the six pins of the sensor module). This sensor base connected the heating coil to a DC power source (220V-5A constant voltage/current source; GWINSTEK made Dual range power supply: model no. SPD-3606) and the electrodes to a digital multimeter (Keysight made, model no. 34470A, maximum resistance limit 500MΩ) for measuring the change in resistance of the sensing material. The applied DC voltage across the heating coil was regulated to vary the heating temperature. The operating temperature also tuned for a sensor from that power source by optimizing the stability of base resistance shown by the digital multimeter.

The circuit diagram of this sensor module could be elucidated to explain the electrical properties of the fabricated sensor. In the proposed circuit diagram  $R_S$  was the sensor resistance,  $R_L$  was load resistance,  $V_H$  was source voltage, and  $V_S$  was the voltage drop against the load (Fig. 2.17). Thus the sensor resistance could be calculated by using the formula as follows:

$$R_S = [(V_H / V_S) - 1] \times R_L \quad \dots\dots\dots (2.20)$$

By using the above mentioned constant voltage/current source meter the voltage could be regulated from 1.5 V to 6.0 V and corresponding temperature varied in a wide range from 70°C to 450°C (Table. 2.1).



Table-2.1: Calibration table of current, voltage, and temperature:

<b>Voltage (V)</b>	<b>Current (I)</b>	<b>Power (V × I)</b>	<b>Temperature (°C)</b>
1.5	0.06	0.090	70
1.7	0.07	0.119	82
2.0	0.08	0.160	100
2.2	0.09	0.198	116
2.4	0.10	0.240	126
2.6	0.11	0.285	138
2.7	0.11	0.297	148
2.9	0.12	0.348	162
3.1	0.13	0.403	178
3.3	0.13	0.429	190
3.5	0.14	0.490	204
3.7	0.15	0.555	224
3.9	0.16	0.624	252
4.1	0.17	0.697	270
4.3	0.18	0.774	288
4.5	0.18	0.810	308
4.7	0.19	0.893	328
4.8	0.20	0.960	336
4.9	0.20	0.980	342
5.0	0.20	1.000	352
5.2	0.21	1.092	370
5.4	0.22	1.188	390
5.6	0.23	1.288	408
5.8	0.24	1.392	430
6.0	0.24	1.440	454

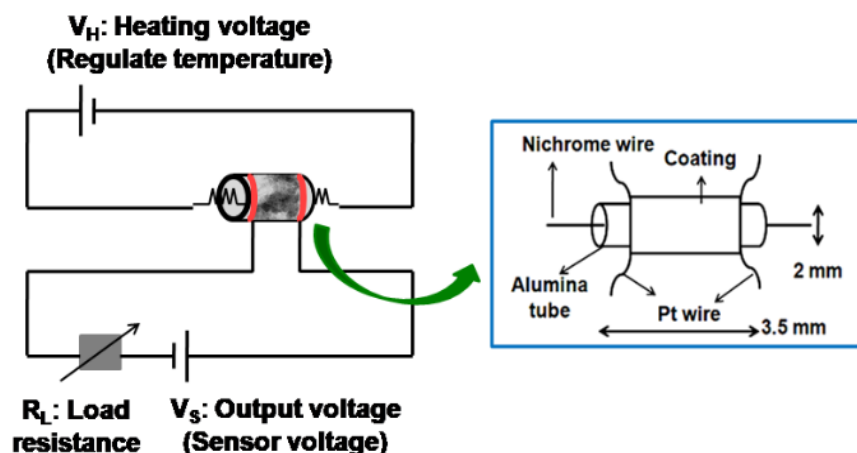


Figure-2.17: Electrical circuit diagram of Taguchi type sensor

The chemiresistive sensing performance of the metal oxide semiconductor based gas sensor was analysed by DC (direct current) measurement. The fabricated sensor was placed inside an in-house (CSIR-CGCRI) customized sensing experimental setup under the ambient environment and gas purging facilities (Fig. 2.18). The sensor was activated by indirect heating through the heating coil inserted into the hollow alumina based sensor substrate using a source meter. The sensor under the course of experiment was exposed to a flow rate of 50 sccm (standard cubic centimetre per minute) under normal atmospheric pressure. The analyte gas with a fixed flow rate passed through a MFC (mass flow controller, MKS Instruments, model no. PR4000) to monitor the concentration of experimental gas, even the flow rate could be regulated to alter the concentration of gas. The analyte gases (acetone, ethanol, ammonia, formaldehyde, hydrogen sulphide, methane, carbon monoxide) of different concentrations (1-100 ppm,  $N_2$  balance, with a certified accuracy of  $\pm 2\%$ ) were procured from M/S CHEMIX Speciality Gases & Equipment, Bangalore, India. At different operating temperature the sensor was exposed to a specific gas pulse until it reached a saturation limit and from this saturated response curve the response and recovery time of the sensor was calculated. For each fabricated sensors the dynamic response was recorded for different VOCs at their optimized operating temperatures.

In presence of gas pulse the resistance of the sensor changes from its base resistance. This resistance of the sensor at optimum working temperature (base resistance) denoted by  $R_a$  and the resistance of the sensor in presence of analyte gas for a stipulated time marked as  $R_g$ . The

alteration of the resistances of the sensor is recorded in a Lab View-based control and data acquisition software using a graphical user interface (GUI) by interface cable with “IR to USB” connector facility. By measuring the change in resistance upon the exposure of the sensor to a gas, the sensing response can be calculated by using the formulas as follows:

For n-type sensing response:

$$S = (R_a - R_g)/R_a \times 100\% \quad \dots\dots\dots (2.21)$$

$$S = R_a/R_g \quad \dots\dots\dots (2.22)$$

For p-type sensing response:

$$S = R_g/R_a \quad \dots\dots\dots (2.23)$$

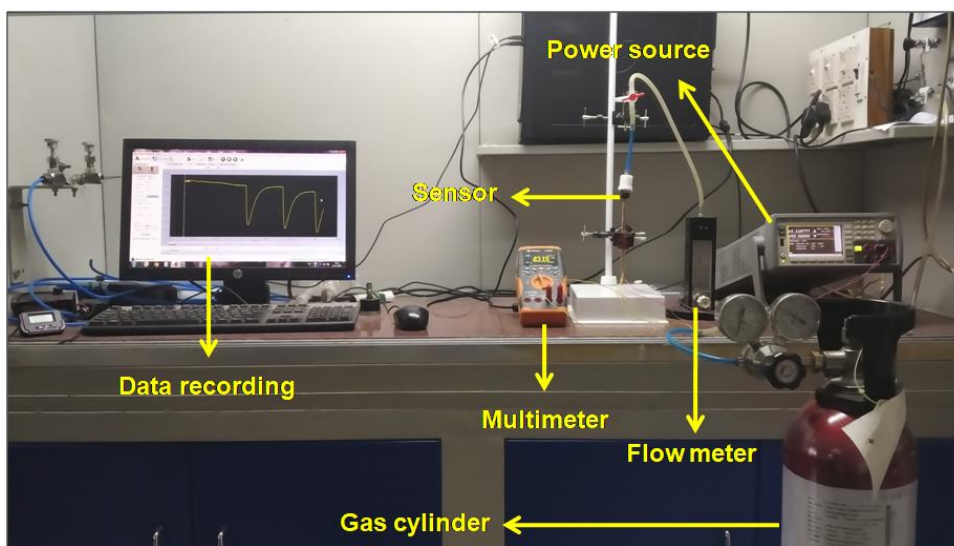


*Figure-2.18: In-house customized gas sensing set up (CSIR-CGCRI)*

The sensing responses were recorded at a certain interval of days for a period of 90 to 150 days and in that time period the sensors exhibited reproducibility of sensing performances with almost consistent base resistance and sensing response.

**References:**

- [1] L. A. Kolahalam, I. V. K. Viswanath, B. S. Diwakar, B. Govindh, V. Reddy, Y. L. N. Murthy, Review on nanomaterials: Synthesis and applications, Mater. Today: Proc. 18 (2019) 2182-2190. <https://doi.org/10.1016/j.matpr.2019.07.371>.
- [2] N. Baig, I. Kammakakam, W. Falath, Nanomaterials: a review of synthesis methods, properties, recent progress, and challenges, Mater. Adv. 2 (2021) 1821. <https://doi.org/10.1039/d0m00807a>.
- [3] C. N. R. Rao, A. Müller, A. K. Cheetham, (Eds.) The Chemistry of Nanomaterials Synthesis, Properties and Applications, Wiley-VCH Verlag GmbH & Co., KGaA (2004).
- [4] G. Gao, Nanostructures & Nanomaterials: Synthesis, Properties, and Applications, Imperial College Press (2004).
- [5] A. S. Edelstein, R. C. Cammarata, (Eds.) Nanomaterials: Synthesis, Properties and Applications, 2<sup>nd</sup> Edition, Taylor & Francis, New York (1996).
- [6] Y. Chen, Z. Fan, Z. Zhang, W. Niu, C. Li, N. Yang, B. Chen, H. Zhang, Two-Dimensional Metal Nanomaterials: Synthesis, Properties, and Applications, Chem. Rev. 118 (2018) 6409-6455. <https://doi.org/10.1021/acs.chemrev.7b00727>.
- [7] D. Bokov, A. T. Jalil, S. Chupradit, W. Suksatan, M. J. Ansari, I. H. Shewael, G. H. Valiev, E. Kianfar, Nanomaterial by Sol-Gel Method: Synthesis and Application, Adv. Mater. Sci. Eng. (2021) 5102014. <https://doi.org/10.1155/2021/5102014>.
- [8] L. L. Hench, J. K. West, The Sol-Gel Process, Chem. Rev. 90 (1990) 33-72. <https://doi.org/10.1021/cr00099a003>.
- [9] S. Sakka, Handbook of Sol-Gel Science and Technology Processing, Characterization and Applications, Volume II, Kluwer Academic Publishers (2005).
- [10] M. Parashar, V. K. Shukla, R. Singh, Metal oxides nanoparticles via sol-gel method: a review on synthesis, characterization and applications, J. Mater. Sci. Mater. Electron. 31 (2020) 3729-3749. <https://doi.org/10.1007/s10854-020-02994-8>.
- [11] A. E. Danks, S. R. Hall, Z. Schnepf, The evolution of ‘sol-gel’ chemistry as a technique for material synthesis, Mater. Horiz. 3 (2016) 91. <https://doi.org/10.1039/c5mh00260e>.
- [12] C. J. Brinker, G. W. Scherer, Sol-Gel Science: The Physics and Chemistry of Sol-Gel Processing, Academic Press Inc., (1990).

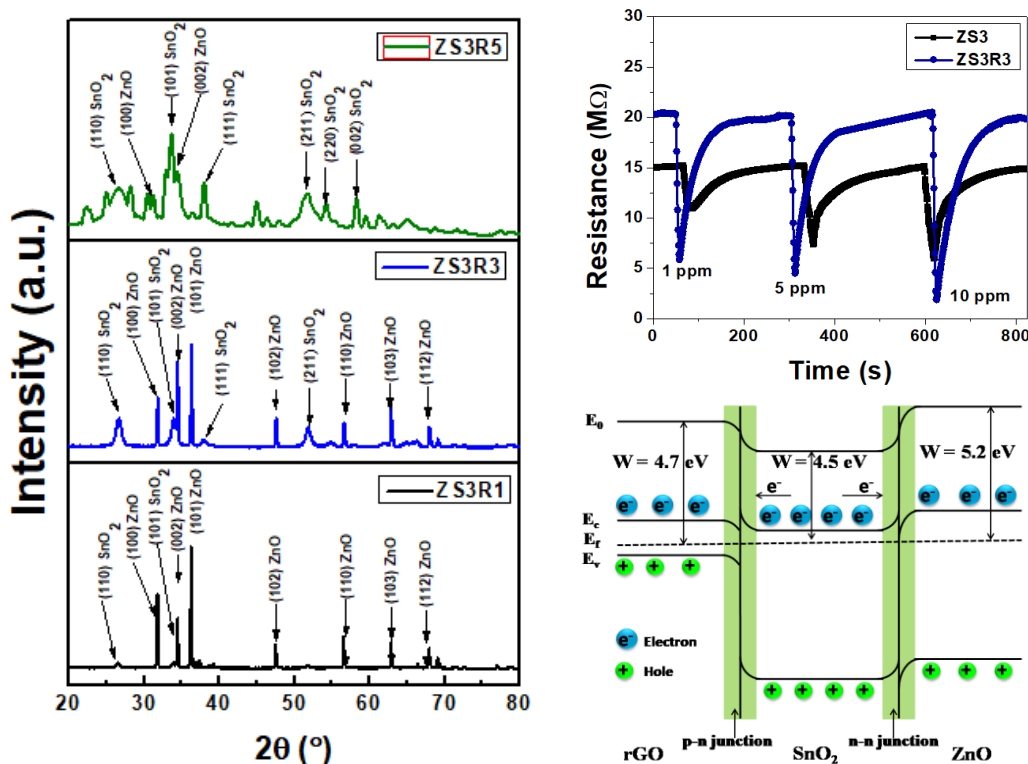
- [13] D. C. Marcano, D. V. Kosynkin, J. M. Berlin, A. Sinitskii, Z. Sun, A. Slesarev, L. B. Alemany, W. Lu, J. M. Tour, Improved Synthesis of Graphene Oxide, *ACS Nano* 4 (2010) 4806-4814. <https://doi.org/10.1021/nm1006368>.
- [14] J. Chen, B. Yao, C. Li, G. Shi, An improved Hummers method for eco-friendly synthesis of graphene oxide, *Carbon*, 64 (2013) 225-229. <https://doi.org/10.1016/j.carbon.2013.07.055>.
- [15] H. Yu, B. Zhang, C. Bulin, R. Li, R. Xing, High-efficient Synthesis of Graphene Oxide Based on Improved Hummers Method, *Sci. Rep.* 6 (2016) 36143. <https://doi.org/10.1038/srep36143>.
- [16] B. Paulchamy, G. Arthi, B. D. Lignesh, A Simple Approach to Stepwise Synthesis of Graphene Oxide Nanomaterial, *J. Nanomed. Nanotechnol.* 6 (2015) 1000253. <https://doi.org/10.4172/2157-7439.1000253>.
- [17] A. Jiříčková, O. Jankovský, Z. Sofer, D. Sedmidubský, Synthesis and Applications of Graphene Oxide, *Materials* 15 (2022) 920. <https://doi.org/10.3390/ma15030920>.
- [18] S. Abdolhosseinzadeh, H. Asgharzadeh, H. S. Kim, Fast and fully-scalable synthesis of reduced graphene oxide, *Sci. Rep.* 5 (2015) 10160. <https://doi.org/10.1038/srep10160>.
- [19] M. P. Lavin-Lopez, A. Paton-Carrero, L. Sanchez-Silva, J. L. Valverde, A. Rmero, Influence of the reduction strategy in the synthesis of reduced graphene oxide, *Adv. Powder Technol.* 28 (2017) 3195-3203. <https://doi.org/10.1016/j.apr.2017.09.032>.
- [20] J. Shen, Y. Hu, M. Shi, X. Lu, C. Qin, C. Li, M. Ye, Fast and Facile Preparation of Graphene Oxide and Reduced Graphene Oxide Nanoplatelets, *Chem. Mater.* 21 (2009) 3514-3520. <https://doi.org/10.1021/cm901247t>.
- [21] Y. Wang, Z. Shi, J. Yin, Facile Synthesis of Soluble Graphene via a Green Reduction of Graphene Oxide in Tea Solution and Its Biocomposites, *ACS Appl. Mater. Interfaces* 3 (2011) 1127-1133. <https://doi.org/10.1021/am1012613>.
- [22] G. H. Jeffery, J. Bassett, J. Mendham, R. C. Denney, *VOGEL's Text Book of Quantitative Chemical Analysis*, 5<sup>th</sup> Edition, Longman Scientific & Technical, John Wiley and Sons Inc., New York (1989).
- [23] B. D. Cullity, S. R. Stock, *Elements of X-Ray Diffraction*, 3<sup>rd</sup> Edition, Pearson New International Edition (2014).
- [24] <https://wiki.anton-paar.com/en/x-ray-diffraction-xrd/>

- [25] W. H. Zachariasen, Theory of X-Ray Diffraction in Crystals, Courier Dover Publications, New York (2004).
- [26] C. N. Banwell, Fundamentals of Molecular Spectroscopy, 3<sup>rd</sup> Edition, McGraw-Hill Book Company, (1972).
- [27] K. Nakamoto, Infrared and Raman Spectra of Inorganic and Coordination Compounds, Part A, Theory and Applications in Inorganic Chemistry, John Wiley and Sons Inc., New York (1997).
- [28] [https://www.lpdlabservices.co.uk/analytical\\_techniques/chemical\\_analysis/ftir\\_instrument.php](https://www.lpdlabservices.co.uk/analytical_techniques/chemical_analysis/ftir_instrument.php)
- [29] D. J. Gardiner, P. R. Graves, (Eds.) Practical Raman Spectroscopy, Springer-Verlag, Berlin, Heidelberg, New York (1989).
- [30] L. A. Lyon, C. D. Keating, A. P. Fox, B. E. Baker, L. He, S. R. Nicewamer, S. P. Mulvaney, M. J. Natan, Raman Spectroscopy, Anal. Chem. 70 (1998) 341R-361R. <https://doi.org/10.1021/a1980021p>.
- [31] <https://www.uakron.edu/soa/instruments/raman/>
- [32] S. Brunauer, P. H. Emmett, E. Teller, Adsorption of Gases in Multimolecular Layers, J. Am. Chem. Soc. 60 (1938) 309-319. <https://doi.org/10.1021/ja01269a023>.
- [33] K. S. W. Sing, D. H. Everett, R. A. W. Haul, L. Moscou, R. A. Pierotti, J. Rouquérol, T. Siemieniewska, Reporting physisorption data for gas/solid systems with special reference to the determination of surface area and porosity, Pure Appl. Chem. 57 (1985) 603-619. <https://doi.org/10.1351/pac198557040603>.
- [34] E. P. Barrett, L. G. Joyner, P. P. Halenda, The determination of pore volume and area distribution in porous substances. I. computations from nitrogen isotherms, J. Am. Chem. Soc. 73 (1951) 373-380. <https://doi.org/10.1021/ja01145a126>.
- [35] F. Rouquerol, J. Rouquerol, K. Sing, Adsorption by Powder & Porous Solid, Academic Press, London (1999).
- [36] <https://journals.sagepub.com/doi/10.1177/0144598720934004?icid=int.sj-full-text.similar-articles.3>
- [37] J. Goldstein, D. E. Newbury, D. P. Echlin, D. C. Joy, C. Fiori, E. Lifshin, L. C. Sawyer, J. R. Michael, Scanning Electron Microscopy and X-Ray Microanalysis, Plenum Press, New York (2003).

- [38] P. J. Goodhew, J. Humphreys, R. Beanland, Electron Microscopy and Analysis, CRC Press, Taylor & Francis Inc., New York, USA and Canada (2001).
- [39] <https://speciation.net/Database/Instruments/Carl-Zeiss-AG/SUPRA-55VP-;i669>
- [40] D. B. Williams, C. B. Carter, Transmission Electron Microscopy: A Textbook for Materials Science, Plenum Press, New York and London (1996).
- [41] N. Yao, Z. L. Wang, (Eds.) Handbook of Microscopy for Nanotechnology, Springer, New York (2005).
- [42] <https://research.rice.edu/sea/instruments/microscopes/microscope-jeol-jem-1400flash-transmission-electron-microscope>
- [43] D. W. Turner, Molecular photoelectron spectroscopy, Phil. Trans. Roy. Soc. Lond. A. 268 (1970) 7-31. <https://doi.org/10.1098/rsta.1970.0059>.
- [44] [https://en.wikipedia.org/wiki/X-ray\\_photoelectron\\_spectroscopy](https://en.wikipedia.org/wiki/X-ray_photoelectron_spectroscopy)
- [45] D. A. Skoog, D. M. West, F. J. Holler, S. R. Crouch, Fundamentals of Analytical Chemistry, 9<sup>th</sup> Edition, Brooks/Cole Cengage Learning, (2014).
- [46] <https://www.labwrench.com/equipment/32510/cecil-instruments-cecil-7400-double-beam-uv-vis-spectrophotometer>
- [47] <https://www.horiba.com/deu/scientific/products/detail/action/show/Product/deltaflex-1583/>
- [48] E. Barsoukov, J. R. Macdonald, Impedance Spectroscopy Theory, Experiment, and Applications, 3<sup>rd</sup> Edition, John Wiley & Sons, Inc., (2018).

# CHAPTER 3.1

## Reduced graphene oxide (rGO) decorated ZnO-SnO<sub>2</sub>: A ternary nanocomposite towards low concentration VOC sensing performance



*Ternary p-n-n heterojunction based nanocomposites were prepared by introducing reduced graphene oxide (rGO) in the ZnO-SnO<sub>2</sub> matrix, and their ppm level volatile organic compounds (VOCs) sensing properties were explored. The sensing study revealed that the optimum ternary nanocomposite sensor delineated ~ 91% n-type sensing response towards ~ 10 ppm acetone gas at an optimum working temperature of ~ 150°C with rapid response (~ 10 s) and recovery time (~ 100 s) suitable for detecting multiple pulses in short time duration. It also exhibited a considerable ~ 65% sensing response towards ~ 10 ppm ethanol at ~ 150°C. The sensor was also able to detect ~ 1 ppm acetone with an appreciable sensing response of ~ 71%. This superior sensing performance of rGO decorated ZnO-SnO<sub>2</sub> was illustrated with band structure modification.*





**3.1.1. Introduction:**

As mentioned earlier in Chapter 1, that from the past few decades, the study of metal oxide semiconductors (MOs) has been evaluated as the most discussed topic due to their growing impact in versatile applications. Among all the MOSs, tin oxide ( $\text{SnO}_2$ ), a typical n-type material with considerable band gap energy (3.6 eV) at 300K [1, 2], is the extensively used material in numerous applications, viz., Li-ion batteries, sensitized solar cells, gas sensors etc. But, its practical applications as an efficient gas sensor are limited due to poor selectivity, extended response and recovery time, low sensing response, and high temperature operation. On the other hand, ZnO is another well-known wide band gap (3.4 eV) n-type semiconductor [3, 4]. It is considered as an exciting sensing material for its non-toxicity, high electrochemical stability, good response to several oxidizing and reducing gases, and suitability of doping. Despite these inherent advantageous characteristics, ZnO-based sensors have several unsolved drawbacks like, limited physical and chemical properties of the material, and short lifetime, which restrict their potential applications. As we know, electron migration and transportation is the key to sensing, but MOSs still needs to improve in this perspective. So, modern researchers have been inclined to introduce different carbonaceous materials. Considering all carbon-based hybrid nanostructures, graphene-related materials emerge as the most promising candidate. Among all graphene-based systems, rGO, a unique 2D honeycomb lattice of  $\text{sp}^2$ -C atoms with a surface decorated with several oxygenated functional groups and defect sites [5-10], is suitable for gas sensing. By virtue of its structural properties, rGO has tunable band gap energy (0-2.5eV) and this makes it suitable for composite functionality. It also possesses high charge carrier mobility, large specific surface area favorable for gas molecules adsorption, mechanical robustness, high thermal stability, and low electrical noise and hence highly sensitive to electrical perturbation in order to monitor faint signals in presence of experimental gas. But, extensive use of pristine rGO as gas sensor prevented due to their poor selectivity, relatively large response and recovery time, and inability to sustain under complicated and harsh conditions. Henceforth, rGO incorporated metal oxide-based sensors are being explored for improvement of sensing, e.g., Zhu et al. [11] synthesized rGO/ $\text{SnO}_2$  nanocomposite film for improved  $\text{NO}_2$  sensing properties. Toloman et al. [12] synthesized rGO decorated Fe doped  $\text{SnO}_2$  nanoparticles as an efficient humidity sensor. Meti et al. [13] showed excellent photo-catalytic properties of rGO-ZnO. Wang et al. [14] used

ZnO nanosheet/graphene nanocomposite for acetone sensing, but the optimum concentration was 100 ppm.

Besides these, as a promising technique to enhance the sensing performance of MOS-based sensors, as discussed before, several research groups are interested in developing heterojunction-based sensing materials by combining different metal oxides. The heterojunction could tune the charge carrier concentration, modify the depletion layer, change in potential energy barrier's height, and thereby band bending to achieve Fermi-level equilibrium. For example, Bai et al. [15] reported ZnO-SnO<sub>2</sub> hollow nanofibers heterojunction for enhanced NO<sub>2</sub> sensing. Wang et al. [16] demonstrated a 1D SnO<sub>2</sub>-coated ZnO nanowire, which can improve n-butyl amine sensing at 240°C, but the gas concentration was 10 ppm. Thus, the literature survey revealed enough scopes to improve gas sensing involving these materials.

Recently, some researchers have been focusing on enhancing sensing performance via the formation of the ternary composite. Wang et al. [17] developed a hybrid material containing Zn<sub>2</sub>SnO<sub>4</sub> nanoparticles and rGO to detect oxidizing gases at the ppb level. Zhang et al. [18] prepared NiO-SnO<sub>2</sub>-rGO nanocomposite to see NO<sub>2</sub> gas where the gas concentration was 60 ppm. Wang et al. [19] constructed ZnO/SnO<sub>2</sub> heterostructure on rGO for NO<sub>2</sub> sensing study at room temperature, and the concentration of the gas detected was 5 ppm. However, to the best of our knowledge, no work has been reported for VOC sensing performance by any ternary nanocomposite. However, as already stated in Chapter 1 (Section: 1.5) VOC detection in ppm level is crucial to apply the sensors as non-invasive clinical diagnostic tool for breath analysis, e.g., acetone detection (~ 1 ppm) for diabetes diagnosis. Recently, ZnO-SnO<sub>2</sub> nanocomposites have been used to detect several VOCs, but concentration levels and working temperatures were unsuitable for aforesaid practical application [20-28]. So, in this work, it was planned to modify the ZnO-SnO<sub>2</sub> nanocomposite by introducing rGO and preparing a ternary composite followed by their ppm level VOC sensing performances study at comparatively low temperatures.

### **3.1.2. Experimental:**

The pristine ZnO, SnO<sub>2</sub> and other desired nanocomposites were synthesized in laboratory scale by applying sol-gel technique. Different ZnO-SnO<sub>2</sub> nanocomposite powders were prepared (Fig. 3.1.1a) by varying wt% of ZnO (5, 10, 15, and 20) in SnO<sub>2</sub> matrix and the samples were marked as ZS1, ZS2, ZS3, and ZS4, respectively. Zinc nitrate hexahydrate (Zn(NO<sub>3</sub>)<sub>2</sub>·6H<sub>2</sub>O) and tin

tetrachloride pentahydrate ( $\text{SnCl}_4 \cdot 5\text{H}_2\text{O}$ ) were taken as the precursor salts. The details of process already discussed in Chapter-2 (Section: 2.3.1).

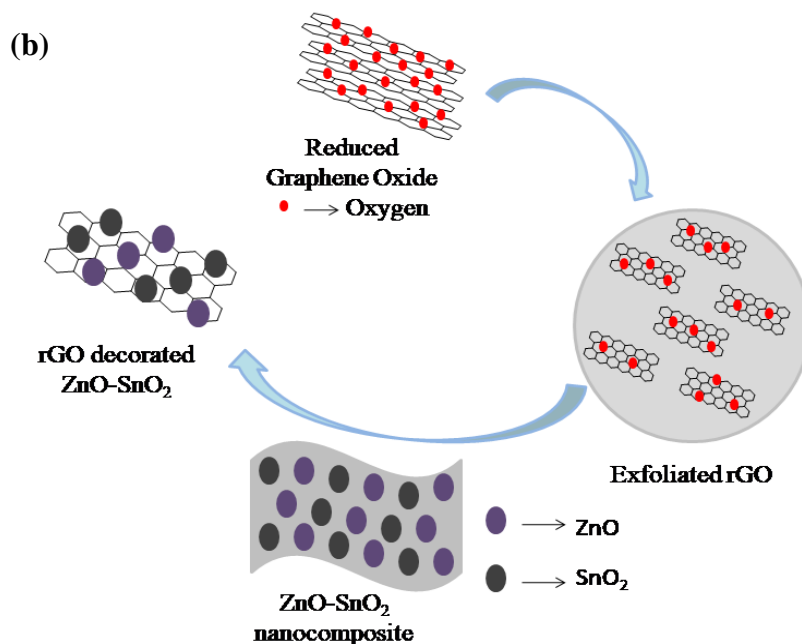
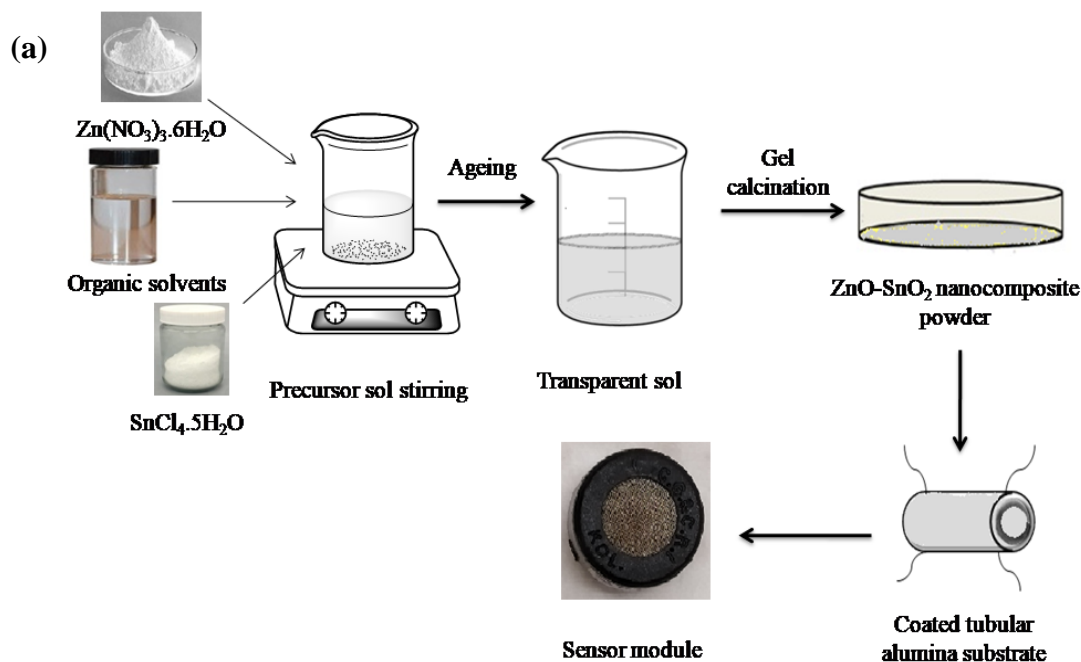


Figure-3.1.1: Graphical representation of synthesis (a)  $\text{ZnO-SnO}_2$  nanocomposites, (b) rGO decorated  $\text{ZnO-SnO}_2$  nanocomposites

Reduced graphene oxide (rGO) was prepared from graphene oxide (modified Hammers method, details given in 2.3.2 and 2.3.3). Afterwards rGO decorated ZnO-SnO<sub>2</sub> nanocomposites were synthesized with 1, 3, and 5 wt% concentration of rGO in ZS3 sol using same procedure. They were labeled as ZS3R1, ZS3R3, and ZS3R5 accordingly as per rGO concentration (Fig. 3.1.1b).

## 3.1.3. Results and discussions:

### 3.1.3.1. Characterization of graphene materials:

The XRD pattern (Fig. 3.1.2) of graphite showed one high intense peak at a diffraction angle ( $2\theta$ ) 26.43 corresponded to lattice plane (002) according to JCPDS no.: 41-1487. The high intensity peak signified the existence of uniform nano-dimensional layered structure of graphite [29].

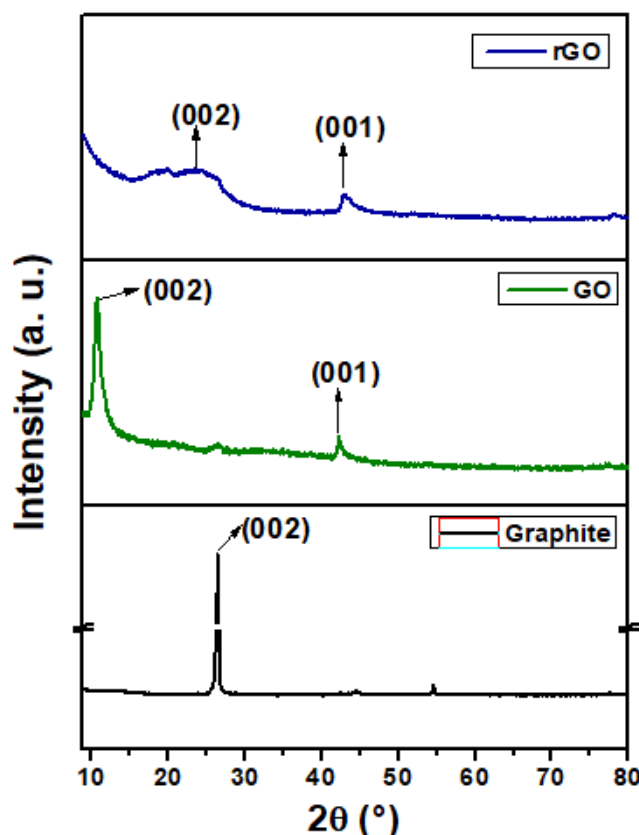


Figure-3.1.2: X-ray diffraction spectra of graphite, GO, and rGO

After oxidation of graphite powder to graphene oxide by modified Hummer's method, this diffraction peak shifted to lower  $2\theta$  value and a strong peak at 10.61, indexed as (002) plane was

observed. Another very weak peak was noticed at  $2\theta$  value 42.12 for (001) plane. Oxidation of graphite resulted into the introduction of different oxygenated functional groups into the layered structure of graphite bonded to the  $sp^2$ -C atoms. Such modulation of lattice structure resulted into the shifting of peak. Further reduction of graphene oxide via chemical route yielded reduced graphene oxide which showed a low intensity peak at diffraction angle 43.28 for (001) plane and along with that a broad shoulder was observed in the  $2\theta$  range 15.73 to 28.26. This alteration of peak position ensured the successful conversion of graphite to graphene oxide to reduced graphene oxide.

The FTIR spectra (Fig. 3.1.3) of graphite, GO and rGO provided information regarding the different bonds present in the samples [29]. In graphite, one broad peak for stretching vibration of -OH group was observed after  $3400\text{ cm}^{-1}$ , might be due to the presence of abundant moisture from the environment, and the corresponding -OH group bending vibration peak was noticed at  $1410\text{ cm}^{-1}$ . Due to the presence of  $sp^2$ -C skeleton only, two -C=C- stretching vibration signal was obtained; one at  $1635\text{ cm}^{-1}$  for alkene-type stretching vibration and the other one at  $1557\text{ cm}^{-1}$  owing to graphitic ring stretching vibration.

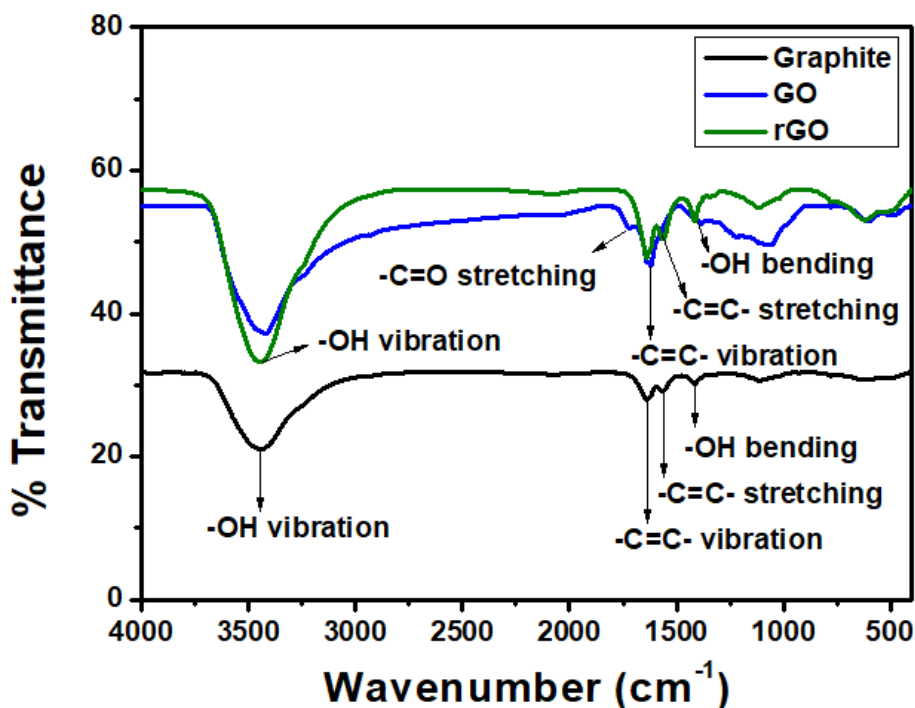


Figure-3.1.3: FTIR spectra of graphite, GO, and rGO

In both GO and rGO, the signals (stretching and bending) obtained from –OH group vibration was present, however, the intensity of the signals were increased. As well as, the peak corresponded to –C=C- stretching was also present. The signal originated from graphitic ring was absent in GO due to abolishment of hexagonal graphitic rings after oxidation, however, that signal was present in rGO perhaps due to restoration of some of the graphitic moieties. Besides these, one peak analogous to carbonyl group (–C=O) was observed at  $1718\text{ cm}^{-1}$  only in GO but absent in rGO. One peak for –OH group deformation of –C–OH functionality was observed at  $1378\text{ cm}^{-1}$  in GO. Another peak related to –C–O–C- stretching vibration was present at  $1053\text{ cm}^{-1}$  for GO and at  $1117\text{ cm}^{-1}$  for rGO.

Raman spectroscopy revealed the presence of two characteristic peaks in carbonaceous samples [29, 30]. The peak at lower wavenumber is called D-band and the other one at higher wavenumber is known as G-band (Fig. 3.1.4).

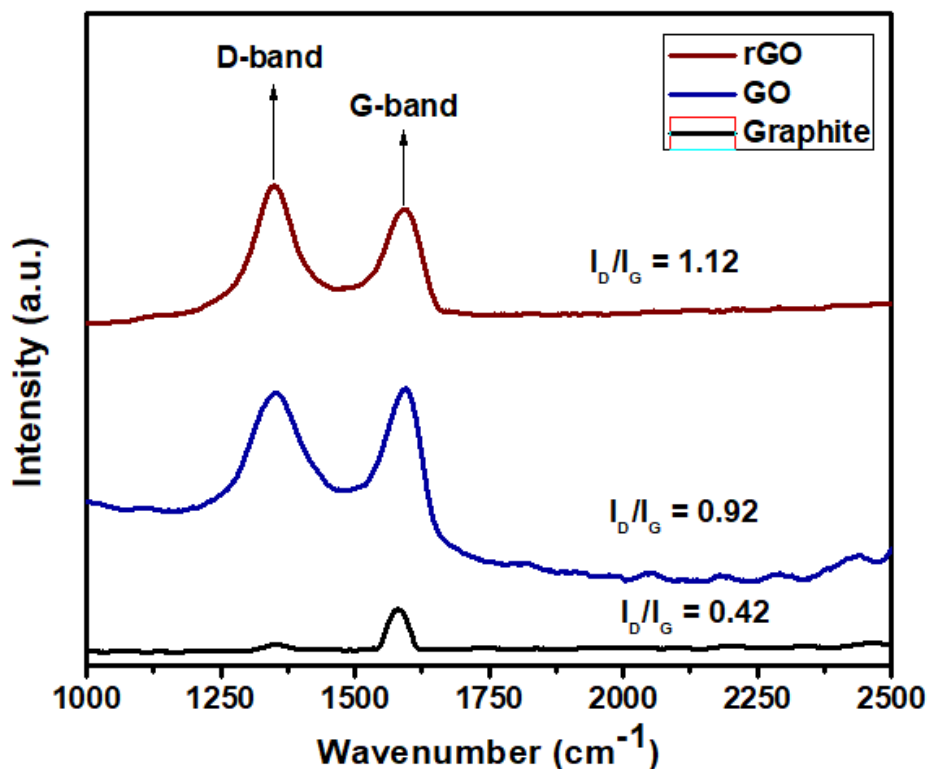
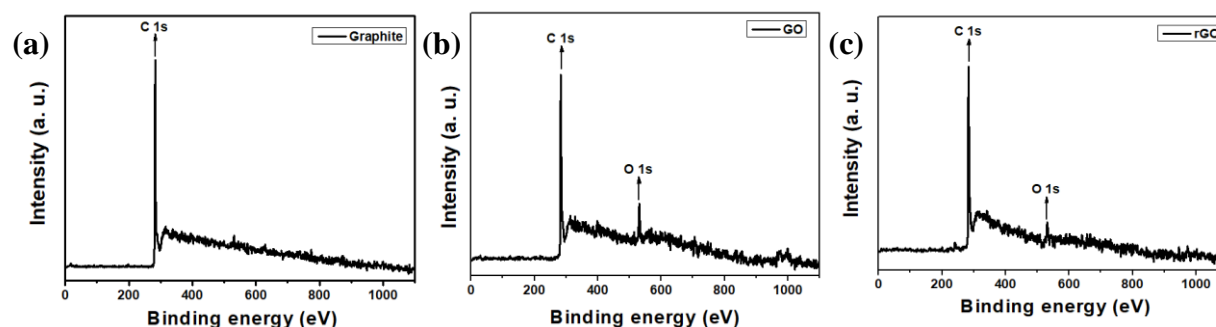


Figure-3.1.4.: Raman spectra of graphite, GO, and rGO

In graphite, D-band peak obtained at  $1348\text{ cm}^{-1}$  and the G-band peak at  $1581\text{ cm}^{-1}$ . In graphene oxide both the peaks were marginally shifted to higher wavenumber;  $1350\text{ cm}^{-1}$  and  $1594\text{ cm}^{-1}$

respectively. Similarly in rGO, the D-band peak was at  $1348\text{ cm}^{-1}$  and the G-band peak at  $1594\text{ cm}^{-1}$ . The D-band signified the defects in the graphitic moiety due to out-of-plane vibrations having  $A_{1g}$  symmetry and the G-band originated from the scattering of  $E_{2g}$  phonons by in-plane  $sp^2$ -C atoms. Henceforth, very low signal of D-band in graphite signified hardly any functional group was present in it, and subsequent increase in D-band signal indicated the introduction of functional groups in graphitic moiety. The intensity ratio ( $I_D/I_G$ ) of this two peaks were  $\sim 0.92$  for GO, which was increased to  $\sim 1.12$  in rGO. Higher intensity D-band in rGO signified the presence of greater number of isolated graphene domain due to removal of some of the functional groups and restoration of  $sp^2$ -C moieties after reduction.

XPS full survey spectra showed the presence of C signal in all three samples and O peak in GO and rGO sample (Fig. 3.1.5 a, b, c). However, core level elemental scanning revealed the characteristic of individual peaks [30]. Deconvolution of C1s spectra of graphite (Fig. 3.1.5d) showed only one peak for  $-C=C-$  binding and the O1s showed spectrum (Fig. 3.1.5g) similar to that of noise without any distinct binding energy peak. In GO, along with  $-C=C-$  peak another peak corresponded to  $-C=O$  was also deconvoluted (Fig. 3.1.5e). In O1s peak (Fig. 3.1.5h) deconvolution showed the existence of only one peak for lattice oxygen. Similar results were obtained for C1s (Fig. 3.1.5f) and O1s (Fig. 3.1.5i) peak of rGO. However, intensity and area under the curve of the O1s peak in GO sample was more than the rGO. This implied that the number of oxygen containing functional groups in GO was reduced in rGO after chemical reduction. Moreover, the C/O ratio could also provide an idea regarding the functionalization. In GO, the C/O ratio was  $\sim 3.22$ , which was increased in rGO to  $\sim 5.99$ . This might be considered as an indication that, in GO due to presence of large number of oxygen-containing functional groups, the C/O ratio was lesser than rGO, where the reduction restored some of the graphitic  $sp^2$ -C skeleton by omitting the O-containing functional groups.





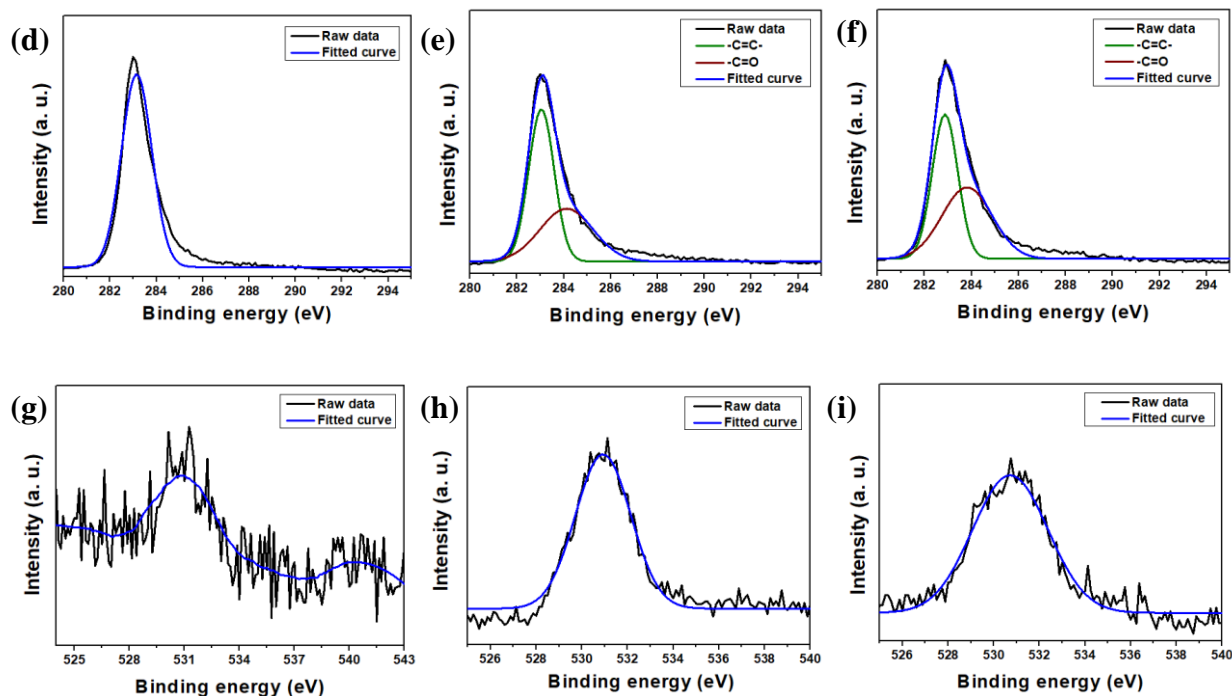
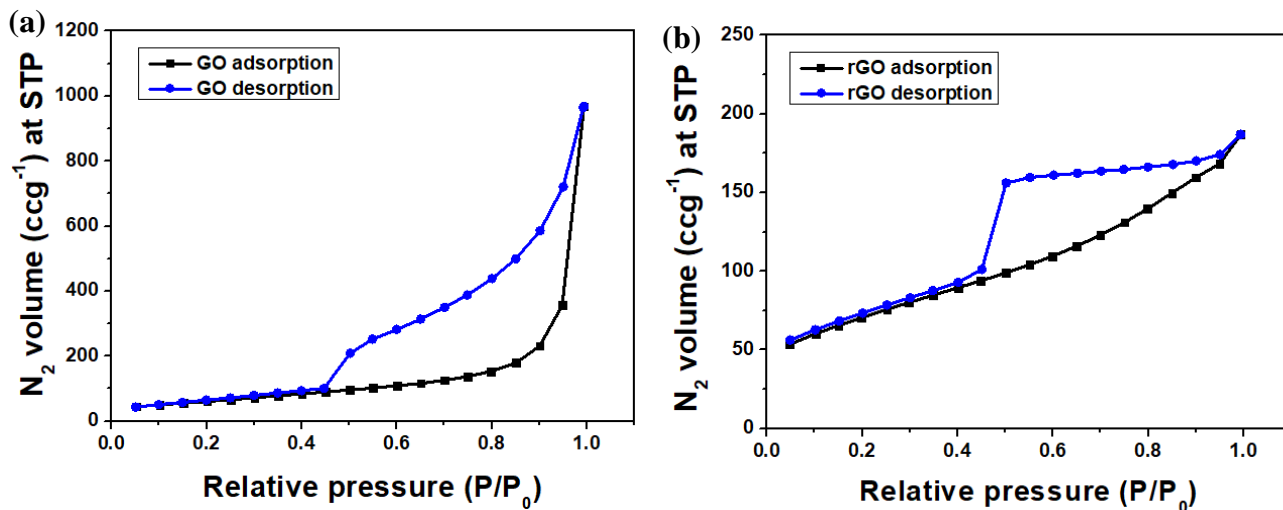


Figure-3.1.5: XPS full survey spectrum (a) graphite, (b) GO, and (c) rGO, core-level spectra of C1s (d) graphite, (e) GO, and (f) rGO, O1s (g) graphite, (h) GO, and (i) rGO

The N<sub>2</sub> sorption isotherms of GO (Fig. 3.1.6a) exhibited steady capillary uptake at low P/P<sub>0</sub>, followed by a significant and sharp increase in N<sub>2</sub> uptake at a higher P/P<sub>0</sub> region with increase in sorption area. Further, at higher pressure, there was a steep hysteresis. In case of rGO, there was a continuous and steady increase in N<sub>2</sub> uptake throughout the pressure range (Fig. 3.1.6b).



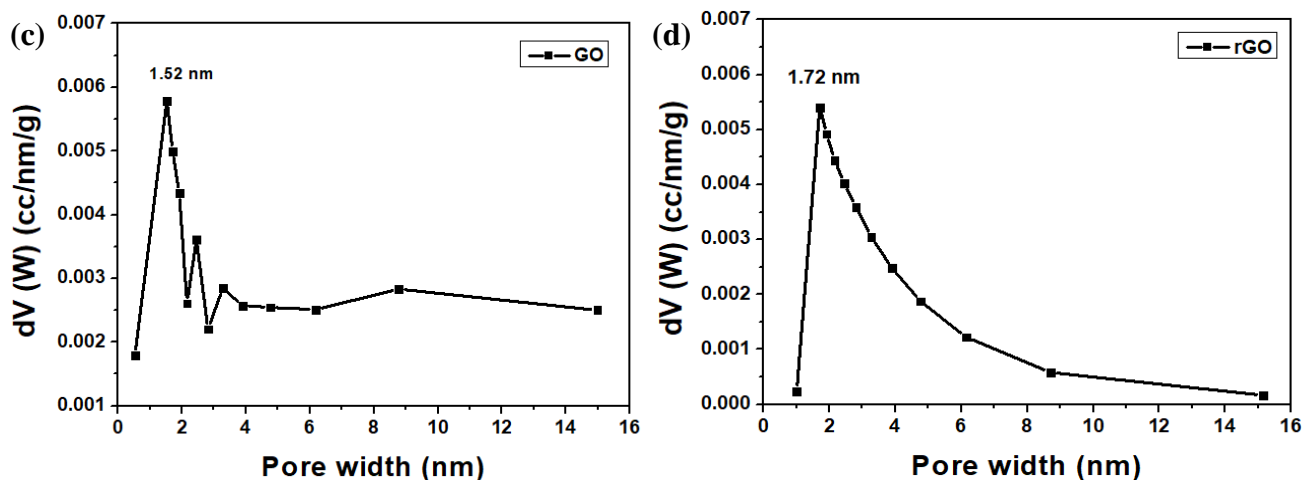


Figure-3.1.6: BET adsorption-desorption isotherm (a) GO and (b) rGO, pore size distribution (c) GO and (d) rGO

The isotherms for both the samples presented a type IV isotherm (according to the IUPAC). Pronounced hysteresis, along with a steady increase in  $N_2$  uptake, could be the reason of the presence of mesopores. The Brunauer-Emmett-Teller (BET) surface area of GO was  $\sim 225.37 \text{ m}^2/\text{g}$  and for rGO it was increased to  $\sim 249.68 \text{ m}^2/\text{g}$ . Besides these, pore size distribution plot showed the average pore size of GO  $\sim 1.52 \text{ nm}$  (Fig. 3.1.6c), which was increased to  $\sim 1.72 \text{ nm}$  in rGO (Fig. 3.1.6d).

### 3.1.3.2. Characterization of nanocomposites:

The XRD patterns of as-synthesized pristine ZnO,  $\text{SnO}_2$  and ZnO- $\text{SnO}_2$  nanocomposite powders were demonstrated in Fig. 3.1.7a. The diffraction peaks of pristine tin oxide and zinc oxide were marked according to tetragonal rutile phase (JCPDs card no.: 72-1147) and hexagonal structure (JCPDs card no.: 80-0075) respectively. All the ZnO- $\text{SnO}_2$  nanocomposite samples exhibited well-assigned peaks of characteristic planes of both tetragonal  $\text{SnO}_2$  and hexagonal ZnO as well. No distinct peak shift or trace of impurity peaks such as  $\text{Zn}_x\text{SnO}_y$  was observed, implied the coexistence of separate phases of ZnO and  $\text{SnO}_2$ . The diffraction peaks at  $2\theta$  values 26.48, 33.73, 37.97, and 51.71 represented (110), (101), (111), and (211) planes of  $\text{SnO}_2$  [27] and that of 31.77, 34.54, 36.27, 47.54, 56.55 and 62.81 corresponded to (100), (002), (101), (102), (110), and (103) planes of ZnO [31] respectively. It was observed that in different samples the intensities of the peaks changed proportionately according to ratio of ZnO and  $\text{SnO}_2$ .

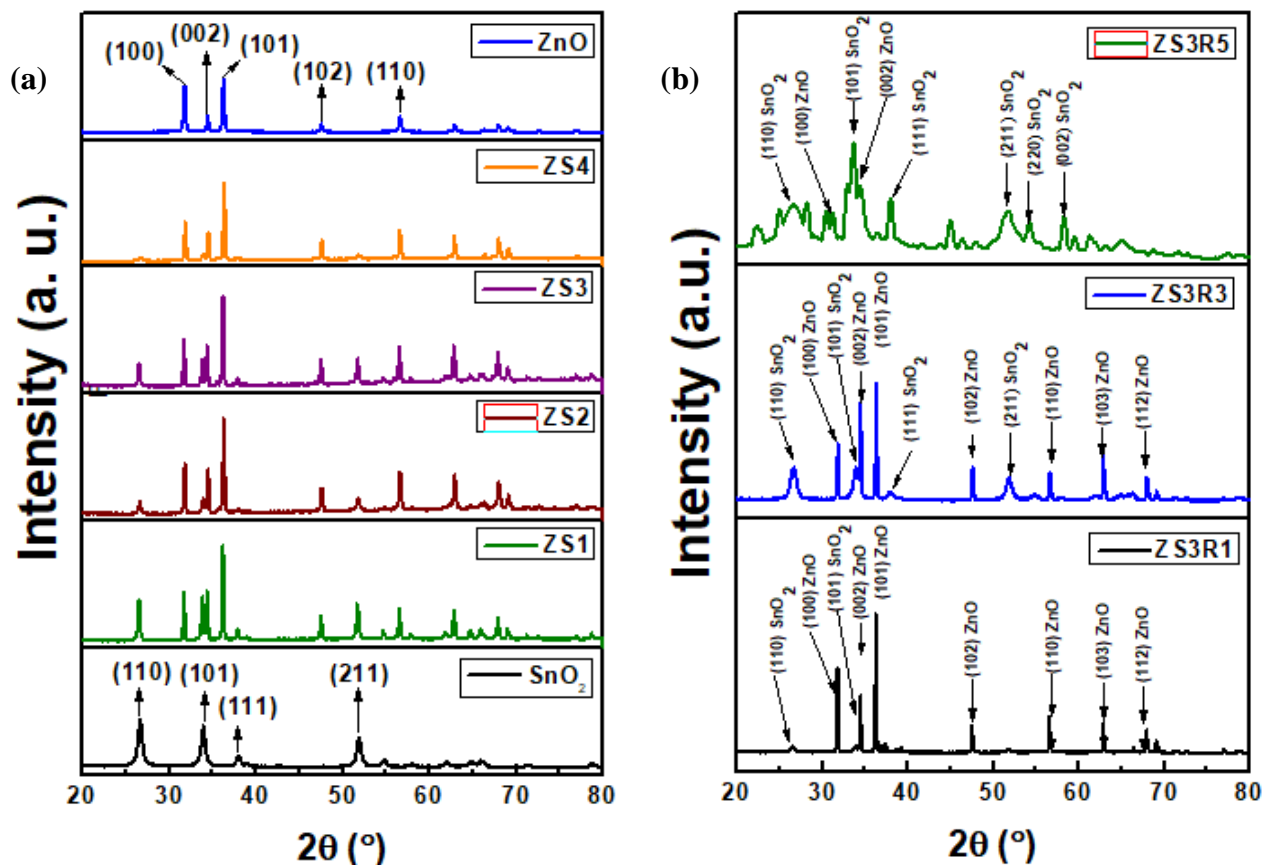


Figure-3.1.7: X-ray diffraction spectra of (a) ZnO-SnO<sub>2</sub> nanocomposites, (b) rGO decorated ZnO-SnO<sub>2</sub> nanocomposites

The XRD pattern of rGO decorated ZnO-SnO<sub>2</sub> nanocomposites, shown in Fig. 3.1.7b, revealed no additional peak or shifting of any peak position for incorporation of rGO. This might be due to good exfoliation of a small amount of rGO [32]. This also ensured no change in the crystalline phase of ZnO-SnO<sub>2</sub> powder. The sharp and intense peaks obtained in XRD spectra showed that all the calcined samples were of high crystallinity.

The FTIR patterns of a typical ZnO-SnO<sub>2</sub> (ZS3) and rGO decorated ZnO-SnO<sub>2</sub> (ZS3R3) nanocomposites were shown in Fig. 3.1.8. Both spectrum contain a broad peak at ~ 3128 cm<sup>-1</sup> attributed to -O-H stretching vibrations, whereas the peak at ~ 1643 cm<sup>-1</sup> was due to -C=C stretching vibration. The absorption band at ~ 1405 cm<sup>-1</sup> represented -O-H bending vibration. In case of ZnO-SnO<sub>2</sub> sample, these peaks were generated from residual solvents. All other peaks below 1000 cm<sup>-1</sup> were associated with metal oxide bond stretching vibration. The peak at 625 cm<sup>-1</sup> and 515 cm<sup>-1</sup> were related to Sn-O and O-Sn-O stretching vibrations respectively whereas the peak at 527 cm<sup>-1</sup> was for Zn-O stretching [33]. No additional peak for rGO was observed.

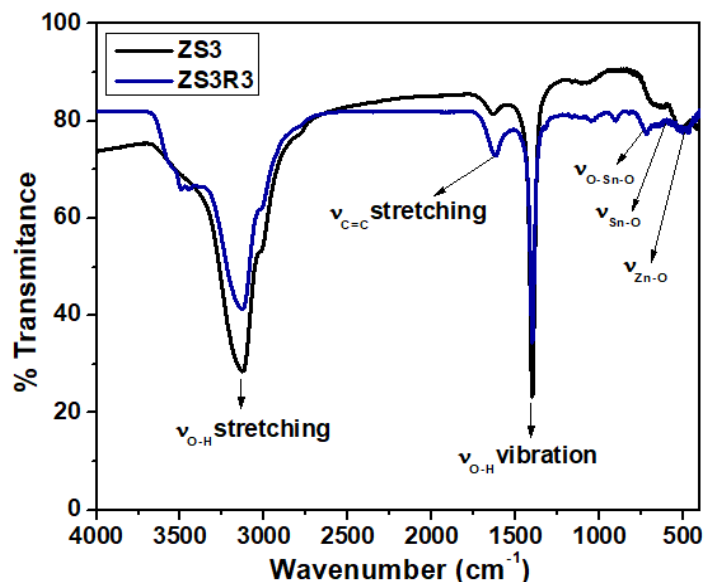


Figure-3.1.8: FTIR spectra of ZS3 and ZS3R3 nanocomposites

Figure 3.1.9 exhibited the Raman spectra of ZS3 and ZS3R3 nanocomposites. The spectrum for ZS3 showed three characteristic bands at 329, 436, and 1129  $\text{cm}^{-1}$  for ZnO and a scattering band at 569  $\text{cm}^{-1}$  for  $\text{SnO}_2$ . All the bands shifted to lower wave numbers than reported wave number values for ZnO and  $\text{SnO}_2$  [34, 35]. The Raman shift at 436  $\text{cm}^{-1}$  for ZnO corresponded to  $E_2$  high-frequency mode. The other peaks of ZnO at 329 and 1129  $\text{cm}^{-1}$  were due to the multiple-phonon scattering process. The  $B_2$  vibration mode of  $\text{SnO}_2$  at 569  $\text{cm}^{-1}$  corresponded to the surface-sensitive mode. During nanocomposite synthesis, the perturbation in a long-range ordered arrangement of pure  $\text{SnO}_2$  crystal led to the formation of small-sized particles with highly defective surface layers. It thereby accounted for the appearance of symmetry forbidden oscillation mode ( $B_2$ ). These surface defects and in-plane oxygen vacancies improved the sensing performances by facilitating gas molecule adsorption and desorption. In the Raman spectrum of ZS3R3 nanocomposite, we observed all the above peaks at the same wave number and two new prominent peaks for rGO. One was the D-band, centered at 1349  $\text{cm}^{-1}$ , corresponding to the defects originated in graphene structure during rGO conversion — another intense peak at 1593  $\text{cm}^{-1}$  named as G-band for the scattering of  $\text{sp}^2$ -carbon atoms in graphene lattice. The ratio of  $I_D/I_G$  was 1.058 [36], which strongly suggested the chemical conversion of GO to rGO. These peaks for rGO confirmed the successful incorporation of rGO in the nanocomposite.

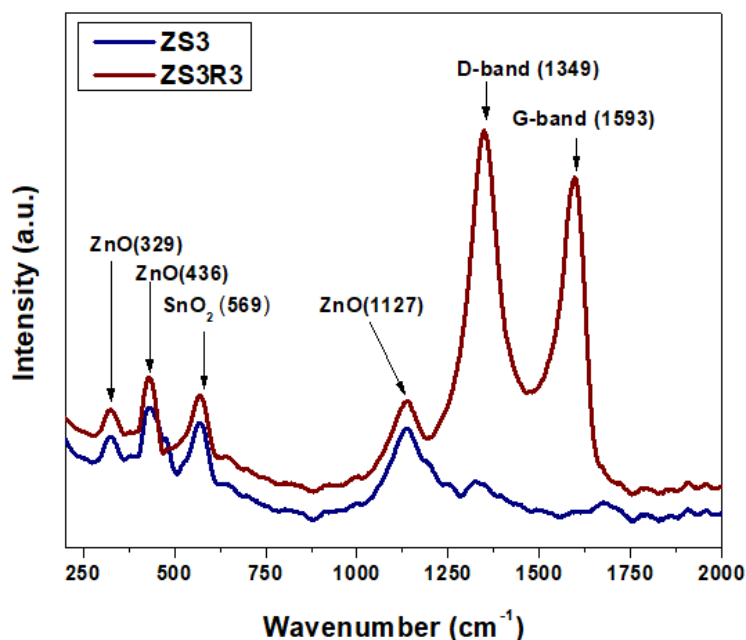


Figure -3.1.9: Raman spectra of ZS3 and ZS3R3 nanocomposites

The specific surface areas of the synthesized nanocomposites were calculated from the linear fitted multi-point BET plot (Fig. 3.1.10) using the equation as follows:

$$S_{\text{BET}} = [(N_A \times s) \div \{M \times (A + I)\}] \quad \dots\dots\dots (3.1.1)$$

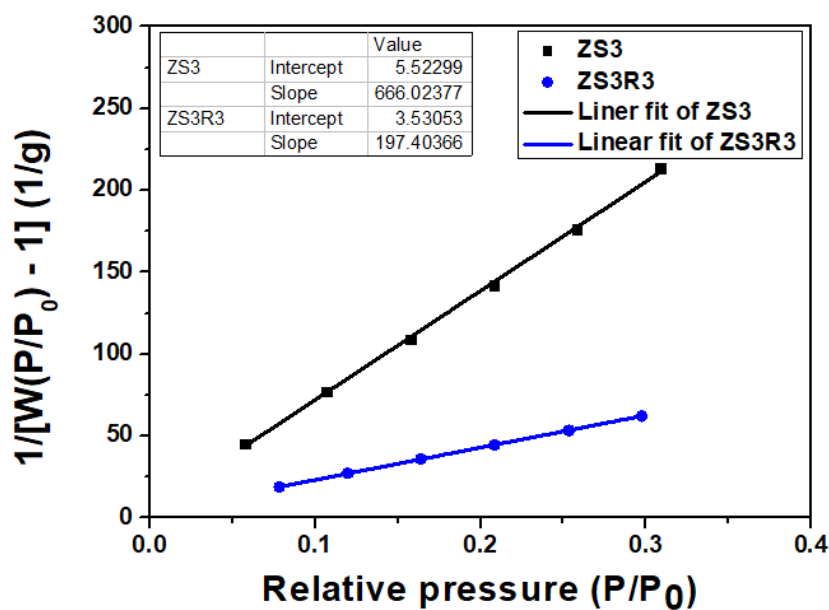
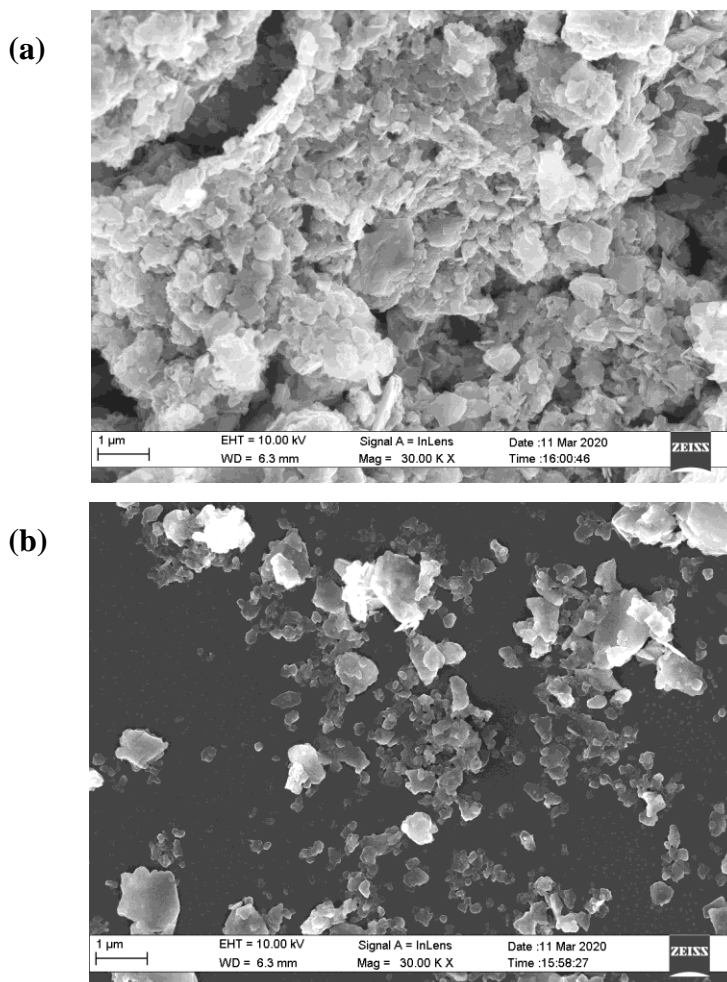


Figure -3.1.10: Specific surface area of ZS3 and ZS3R3 nanocomposites

Where,  $N_A$  is the Avogadro's number ( $6.023 \times 10^{23}$ ),  $s$  represents adsorbing species' adsorption cross-section,  $M$  is the molar mass of the carrier gas ( $N_2$ , 28.0134 g/mol),  $A$  and  $I$  denote slope and intercept of the linear fit. The straight lines were effectively fitted with prominent accuracy (Adjacent  $R^2 \sim 0.99$  in both the cases). The calculated specific surface area of ZS3 nanocomposite was  $\sim 5.18 \text{ m}^2/\text{g}$ , which was enhanced to  $\sim 17.33 \text{ m}^2/\text{g}$ , after rGO incorporation in ZS3 nanocomposite. This enhanced surface area of the ZS3R3 nanocomposite actually proved to be beneficial for gas sensing purpose.

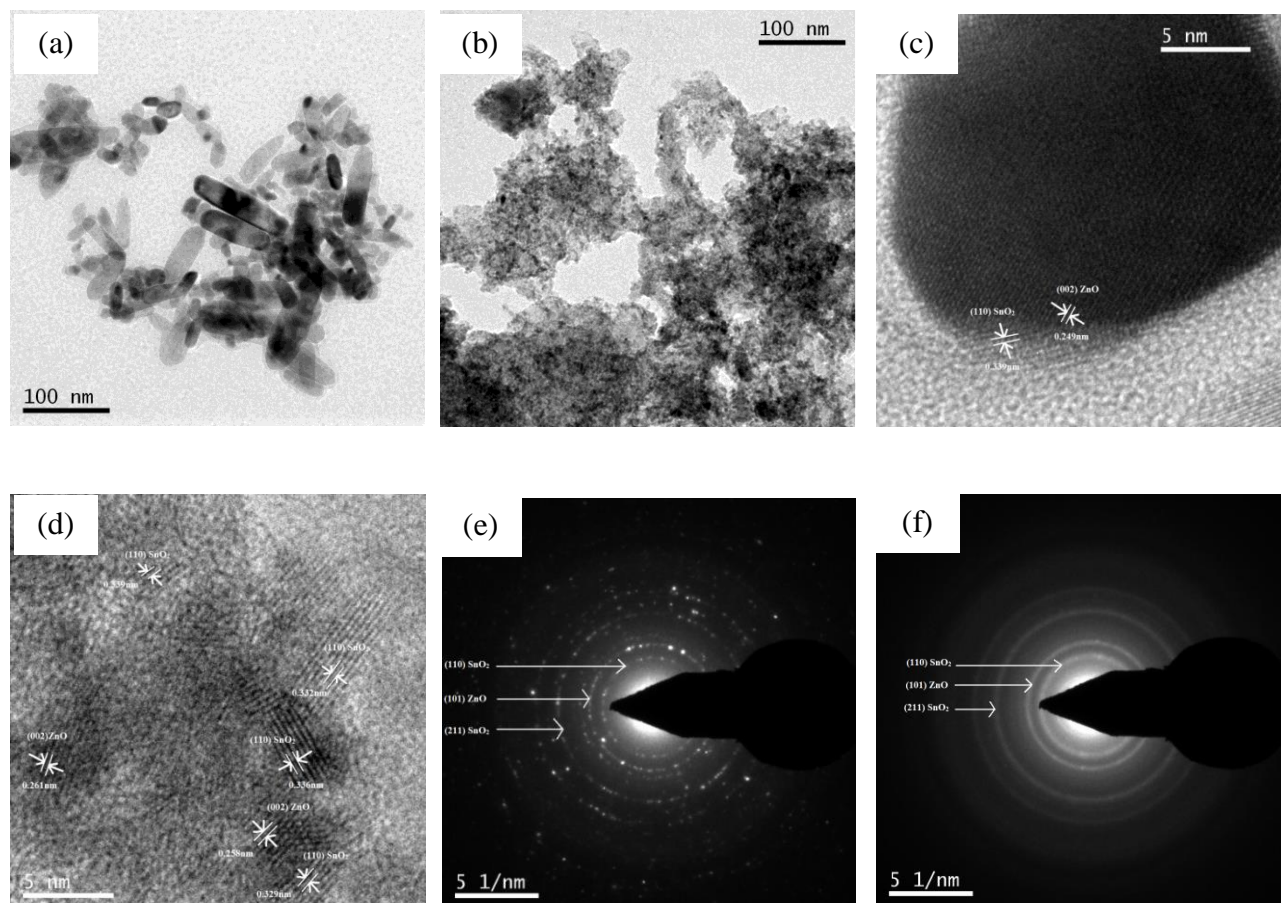
FESEM micrographs (Fig. 3.1.11a, b) were analyzed to determine the morphology and microstructure of ZS3 and ZS3R3 nanocomposites. A scattered distribution of irregularly shaped particles was observed, however, due to high agglomeration, accurate particle size and morphology determination was tricky to obtain specific insights of the nanomaterials.



*Figure-3.1.11: FESEM images of (a) ZS3, (b) ZS3R3*



In a typical bright field TEM (BFTEM) image of ZS3 nanocomposite (Fig. 3.1.12a), we observed nanorods and ovoid-shaped particles. For ZS3R3, the BFTEM image (Fig. 3.1.12b) exhibited well-dispersed particles on ultrathin rGO layers [17, 37], strongly bonded together by Van der Waal's force. This ensured the successful formation of rGO decorated ZnO-SnO<sub>2</sub> nanocomposite. These results were well coordinated with FESEM micrographs. In HRTEM images of both the nanocomposites, lattice fringes corresponded to some parallel sets of crystalline planes were observed. For ZS3, the interplanar distance calculations revealed the (110) plane of SnO<sub>2</sub> and (002) plane of ZnO (Fig. 3.1.12c). For ZS3R3 in HRTEM, the lattice planes were distinguished as (110) plane of SnO<sub>2</sub>, and (002) planes of ZnO (Fig. 3.1.12d). The selected area energy diffraction (SAED) pattern of ZS3 (Fig. 3.1.12e) showed the existence of (110) and (211) SnO<sub>2</sub> plane and (101) plane of ZnO. Identical results were also observed in the SAED pattern of ZS3R3 (Fig. 3.1.12f). All the crystal planes followed the XRD patterns of the nanocomposites. These results signified the growth of well-crystalline samples by the sol-gel process.



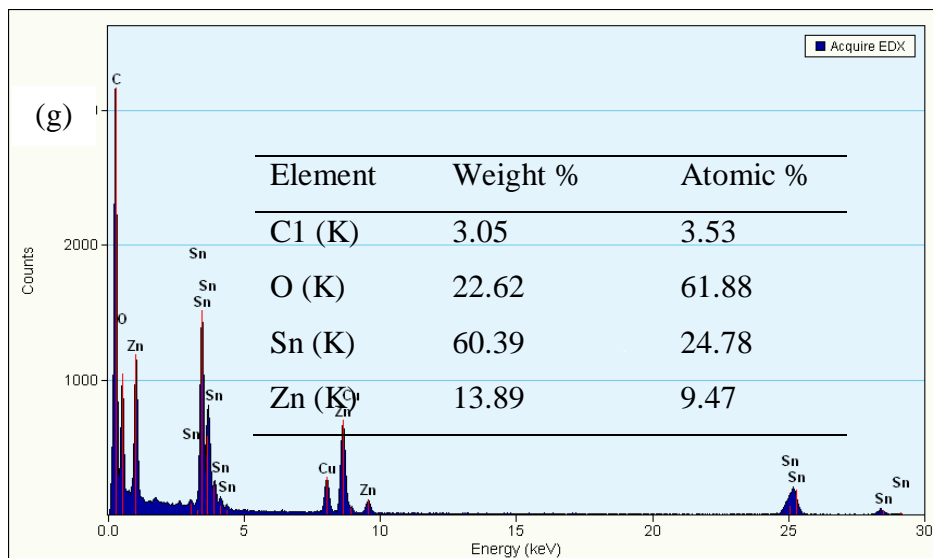


Figure-3.1.12: Bright field TEM images: (a) ZS3 and (b) ZS3R3, HRTEM images: (c) ZS3 and (d) ZS3R3, SAED pattern: (e) ZS3 and (f) ZS3R3, and (g) EDX spectrum of ZS3R3 nanocomposite

The EDX analysis of the ZS3R3 nanocomposite (Fig. 3.1.12g) clearly showed the signatures for Zn, Sn, O, and C, and the peaks of Cu and Cl were generated from the copper grid. This quantitative analysis (inset of Fig. 3.1.12g) supported nanocomposite powders' high-purity molecular-level synthesis.

The surface elemental compositions and their corresponding chemical binding states of rGO decorated ZnO-SnO<sub>2</sub> nanocomposite (ZS3R3) were investigated by using X-ray photoelectron spectra (XPS). The XPS full survey spectrum of ZSR nanocomposite (Fig. 3.1.13a) contained peaks for three significant elements, Zn, Sn, and O, along with a small signature for carbon. However, no significant peaks for impurities were present. The Zn 2p, Sn 3d, and O 1s core level spectra were shown in Fig. 3.1.13 (b-e). Sn 3d existed as a doublet with binding energies of 486.28 eV and 494.67 eV (Fig. 3.1.13b) representing Sn 3d<sub>5/2</sub> and Sn 3d<sub>3/2</sub> respectively [38]. In Fig. 3.1.13c, two peaks centered at 1021.54 eV and 1044.59 eV demonstrated Zn 2p<sub>3/2</sub> and Zn 2p<sub>1/2</sub> binding energies respectively [16]. These results indicated that Sn was present in the +4 valence state in the nanocomposite, whereas Zn was in the +2 oxidation state. The broad curve of the O 1s spectrum in Fig. 3.1.13d deconvoluted into two peaks with binding energies 530.10 eV and 531.07 eV respectively suggested the presence of two different types of oxygen species [16].



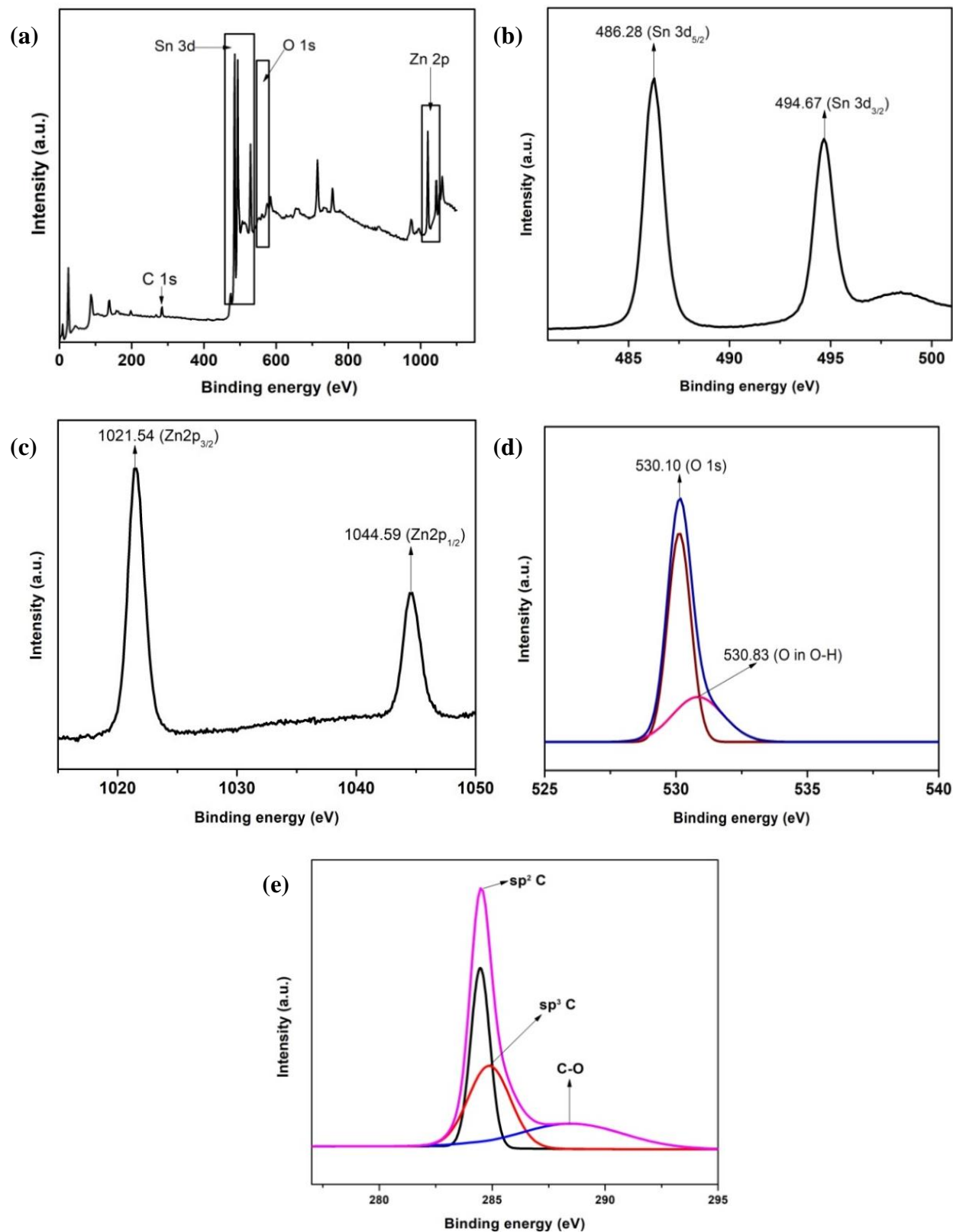
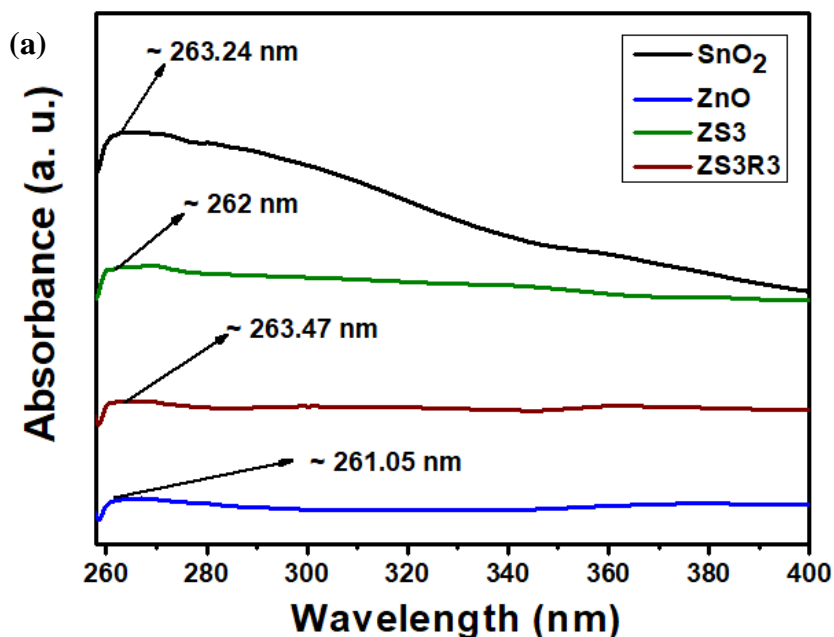


Figure-3.1.13: XPS survey spectra (a) full scan spectrum of ZS3R3, core level analysis: (b) Sn 3d, (c) Zn 2p, (d) O 1s, and (e) C 1s

The peak at 530.10 eV indicating lattice oxygen atoms ( $O^{2-}$ ) involved in several metal oxide bonds in the nanocomposite. The other peak at 531.07 eV referred to the chemically adsorbed oxygenated species  $O^{\delta-}$  ( $O^{2-}$ ,  $O^-$  etc.). These chemisorbed oxygen species on the semiconductor sensing material surface could improve the gas sensing performance by interacting with experimental gas molecules. The carbon peak deconvoluted in Fig. 3.1.13e ensured the presence of both  $sp^2$  and  $sp^3$ -C and C-O bonds [38].

The optical characterization of the as-synthesized samples was carried out by UV-visible spectroscopy (Fig. 3.1.14a). The pristine  $SnO_2$  showed a small absorption peak at  $\sim 263.24$  nm, whereas, pristine  $ZnO$  showed a low intensity peak at  $\sim 261.05$  nm. In ZS3 nanocomposite the peak at  $\sim 262$  nm was in between the absorption peaks of pristine oxides. After rGO addition, absorption peak in ZS3R3 nanocomposite exhibited red shifting to  $\sim 263.47$  nm. The band gap values of the synthesized nanomaterials were calculated from the absorption spectra by using Tauc equation. The band gap value for pristine  $SnO_2$  and  $ZnO$  were 2.41 eV (Fig. 3.1.14b) and 2.47 eV (Fig. 3.1.14c), respectively. The band gap value of ZS3 nanocomposite  $\sim 2.46$  eV (Fig. 3.1.14d) was near to that of pristine  $ZnO$ , whereas the least band gap value was calculated for ZS3R3 nanocomposite at  $\sim 2.38$  eV (Fig. 3.1.14e). Such reduction of band gap in ZS3R3 facilitated the electronic transition during gas sensing.



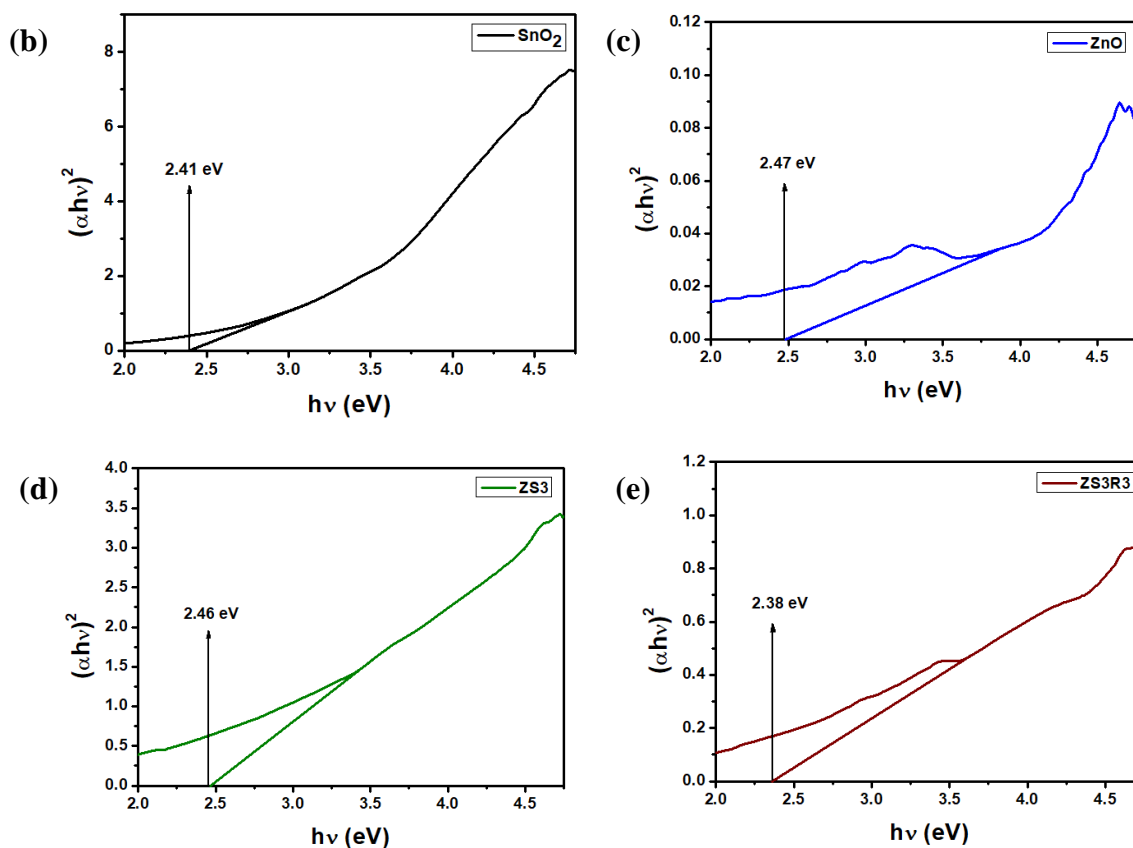


Figure-3.1.14: (a) UV-visible absorption spectra, Tauc plots of (b) pristine  $\text{SnO}_2$ , (c) pristine  $\text{ZnO}$ , (d) ZS3, and (e) ZS3R3

### 3.1.3.3. Gas sensing performance study:

The gas sensing performance of the fabricated sensors was studied by exposing them to different experimental gas pulses. One of the most critical parameters for a sensor is its operating temperature. In order to optimize the working temperature initially, the change in base resistance (i.e., resistance in air atmosphere) of the  $\text{ZnO-SnO}_2$  nanocomposite sensors was measured over a temperature range of  $200^\circ\text{C}$  -  $350^\circ\text{C}$ , followed by measurement of sensing performances. The result exhibited (Fig.3.1.15a) that the resistance gradually decreased with an increase in temperature, satisfying the semiconductor nature of the nanocomposites. It was also clearly seen that increased  $\text{ZnO}$  content in the  $\text{SnO}_2$  matrix decreased resistance at any particular temperature. This might be because of slightly higher electrical conductivity of  $\text{ZnO}$  than  $\text{SnO}_2$ .

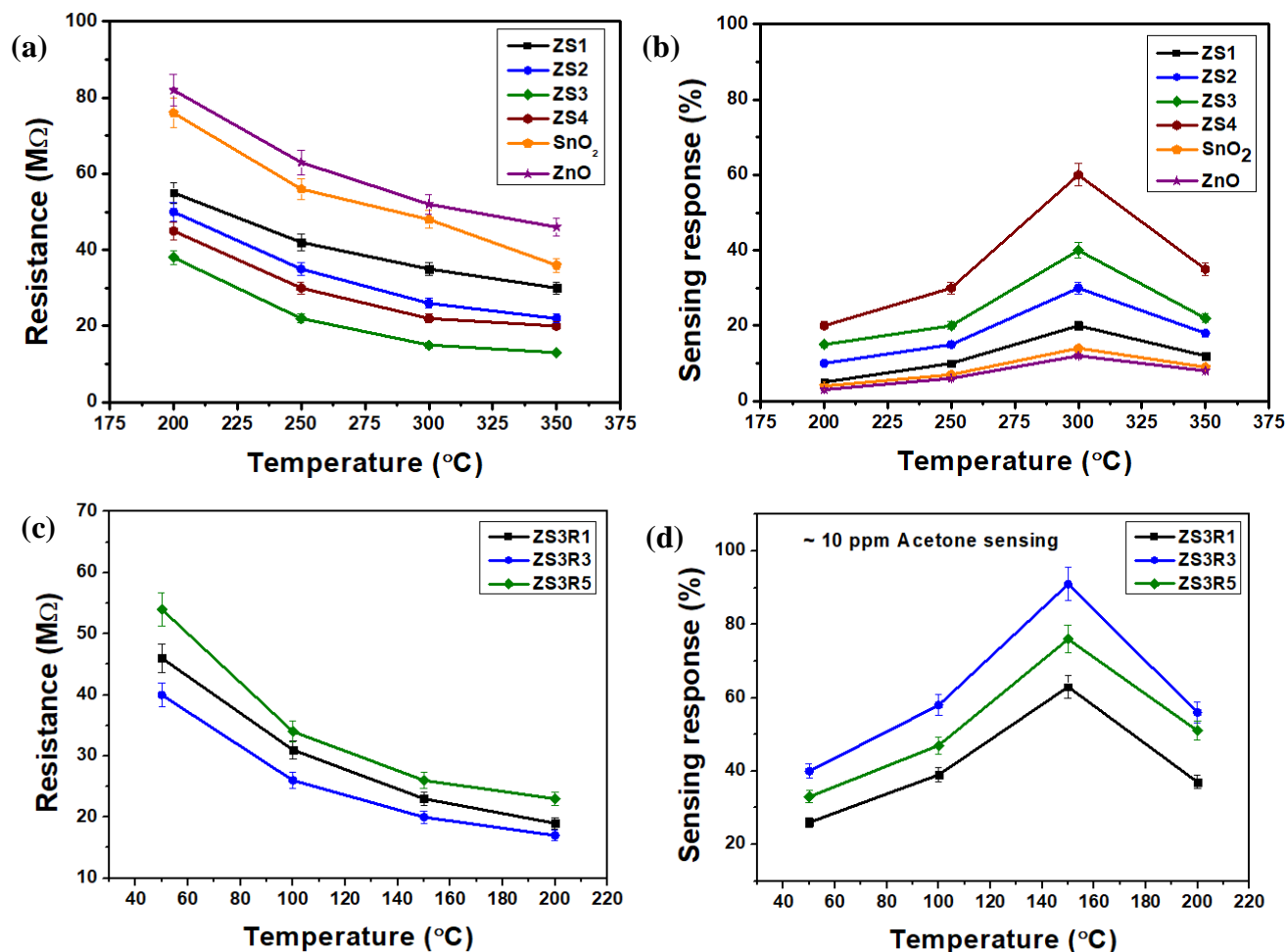
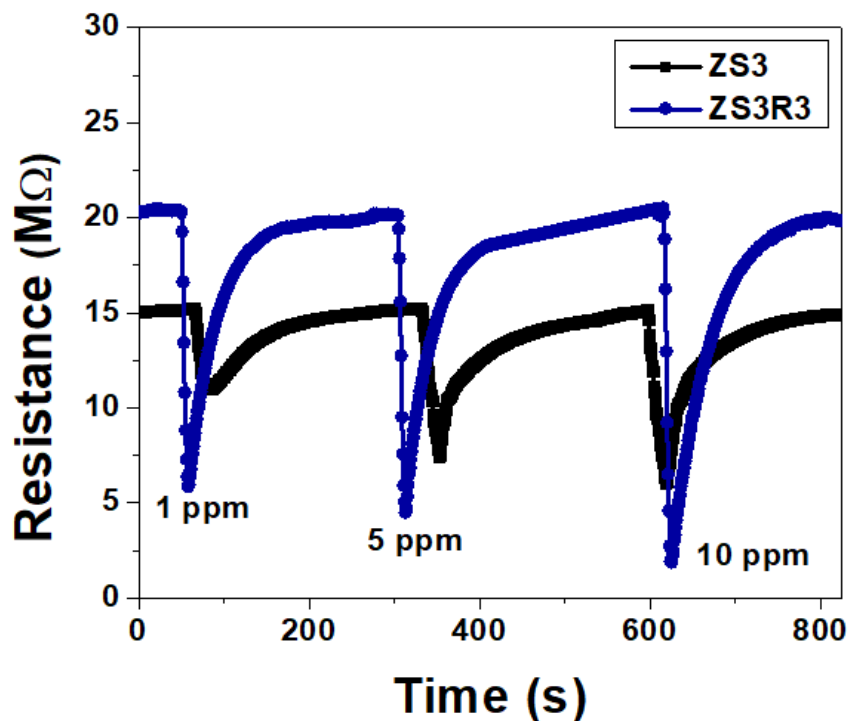


Figure-3.1.15: ZnO-SnO<sub>2</sub> nanocomposites: (a) Change in resistance, (b) change in acetone sensing responses at different working temperatures, rGO decorated ZS3 nanocomposite: (c) change in resistance and (d) change in acetone sensing responses with operating temperature

The sensing response (Fig. 3.1.15b) of all the ZnO-SnO<sub>2</sub> sensors changed with temperatures and ZnO concentrations on exposure to ~ 10 ppm acetone. In all cases, the maximum sensing response was obtained at ~ 300 $^{\circ}C$ . The response was observed to be increased with an increase in the amount of ZnO addition up to 15 wt%, and the maximum response was given by the ZS3-made sensor, followed by a decrease of sensing response in the ZS4 sensor. It was probably due to agglomeration of nanoparticles which inhibit the proper interaction with the gas molecules. The rGO decorated ZnO-SnO<sub>2</sub> sensor (ZS3 was chosen for rGO incorporation for having maximum sensing response) demonstrated a measurable resistance at comparably low operating temperature due to the interaction of p-type rGO with n-n type ZnO-SnO<sub>2</sub> heterojunction. The

resistance of this ternary nanocomposite sensor (ZS3R3) also decreased with the increased operating temperature (Fig. 3.1.15c), as usual, showing its semiconducting behavior. At any particular operating temperature, the resistance of the ZS3R3 sensor was appreciably higher than the corresponding sensor, most probably for the introduction of p-type rGO, which increased the hole concentration at the cost of charge carrier, and, thereby, increased resistivity of the sensing material. The sensing response curve of the ZS3R3 sensor as a function of temperature displayed the optimum sensing response (Fig. 3.1.15d) at an operating temperature of  $\sim 150^{\circ}\text{C}$ , which was much lower than that of the ZS3 sensor. At the same time, the response value was also enhanced. These sensors (ZS3 and ZS3R3) were also exposed to different concentrations of acetone gases in the range of  $\sim 1$  ppm to  $\sim 10$  ppm at their optimum working temperature and the dynamic response curves were shown in Fig. 3.1.16.



*Figure-3.1.16: Sensing response of ZS3 and ZS3R3 sensor in presence of  $\sim 10$  ppm acetone*

In the presence of  $\sim 10$  ppm acetone gas, the ZS3-made sensor showed  $\sim 60\%$  response, which reached  $\sim 91\%$  for the ZS3R3 sensor. The ZS3R3 sensor also provided an excellent  $\sim 71\%$  response to  $\sim 1$  ppm acetone compared to the  $\sim 28\%$  response of the other sensor at the same experimental condition. Similarly, for the ZS3 sensor, a considerable  $\sim 51\%$  response and for the

ZS3R3 sensor, ~ 77% response were obtained respectively in ~ 5 ppm acetone. So, it was evident that both the sensors exhibited well behaved gradual increase in sensing response with an increase in acetone concentration. The introduction of rGO greatly influenced the acetone sensing response of ZnO-SnO<sub>2</sub> nanocomposite by improvising the electronic behavior of the metal oxide composite. Hence, rGO decorated ZnO-SnO<sub>2</sub> sensor could effectively detect trace amounts of acetone.

Chemiresistive gas sensing relies on the adsorption interaction between analyte gas molecules and sensing materials at the surface and the consequent change in base resistance of the sensor. Therefore, physisorption is more favored than chemisorption for fast response/recovery time. We can easily determine the nature of existing adsorption interaction by applying the Freundlich adsorption isotherm and corresponding empirical formulas (equation: 3.1.2 and 3.1.3) [39].

$$S = \alpha C^\beta \quad \dots\dots\dots (3.1.2)$$

$$\log S = \log \alpha + \beta \log C \quad \dots\dots\dots (3.1.3)$$

Where S is the sensing response,  $\alpha$  is the proportionality constant, C is the concentration of the experimental gas, and  $\beta$  is the exponential term [40].

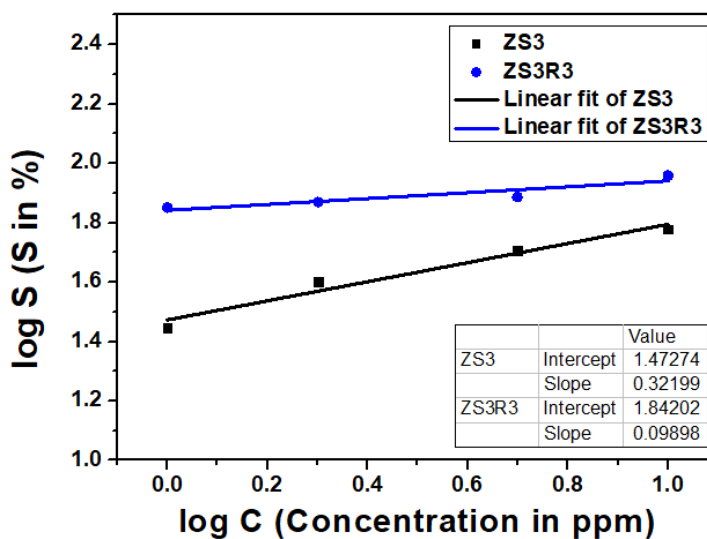


Figure-3.1.17: log S vs. log C plot

The  $\beta$  value lower than 1, indicates feeble interactions, i.e., physisorption between adsorbent and adsorbed species [41] and greater value corresponded to chemisorptions. In the present work, the  $\beta$  value obtained from the slope of the log S vs. log C plot (Fig. 3.1.17) justified the interaction as physisorption.

Now, the physisorption of gas molecules on the sensing material surface relates to a fast recovery time which is defined as the time required regaining ~ 90% of the base resistance after switching off the gas flow [42]. Here, Fig. 3.1.18 demonstrated the response and recovery time of the sensors at their optimum operating temperatures. The response and recovery times of ZS3 sensor were ~ 20 s and ~ 135 s respectively. On the other hand, the ZS3R3 sensor showed faster response and recovery time. The sensor response time was ~ 10 s and the recovery time was ~ 100 s for ZS3R3 sensor. These quick response and recovery times of the ZS3R3 sensors also ensured physisorbed interaction between sensing material and gas molecules. Therefore, from this point of view, it was understood that rGO decorated ZnO-SnO<sub>2</sub> sensor could be more suitable for fast and accurate detection of VOCs.

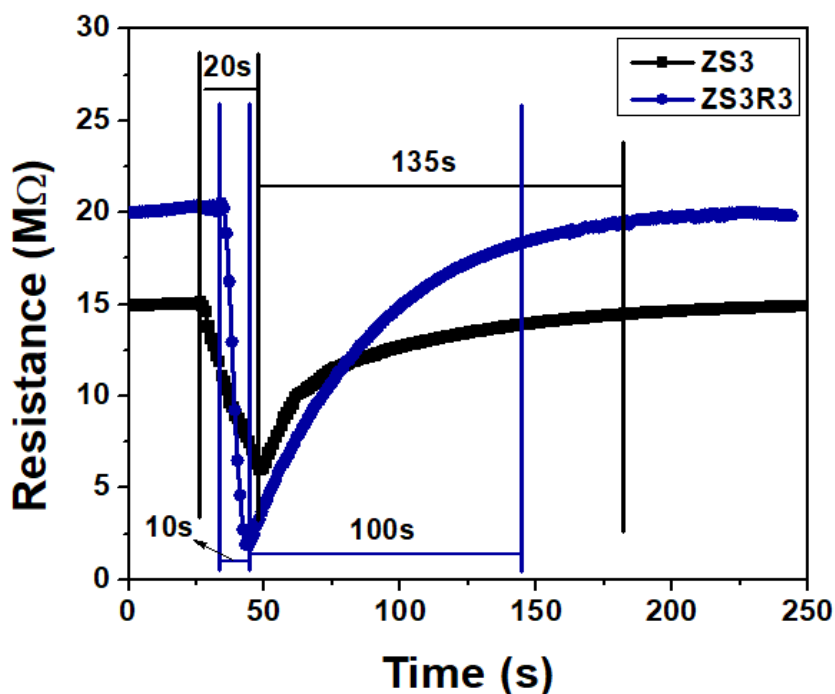


Figure-3.1.18: Response and recovery time of ZS3 and ZS3R3 sensor against ~ 10 ppm of acetone vapour

The lowest Limit of Detection (LOD) is an important characteristic of a good sensor. For ZS3R3 sensor, the calculated sensing responses at ~ 150°C against acetone concentrations, giving a good linear fitting of data with an R<sup>2</sup> value of 0.97. Besides this, the theoretically calculated LOD by using the standard IUPAC equation as follows [43]:

$$C_L = (k \times S_b)/S \quad \dots\dots\dots (3.1.4)$$

Where 'k' is a numerical constant whose value is 3, strongly recommended by IUPAC,  $S_b$  is the standard deviation of the base resistances, and  $S$  is the sensing response. Thereby, the value obtained by calculation was 0.675 ppm for ZS3R3 sensor.

The sensing response of the ZS3R3 sensor was also measured for higher concentrations of 25, 50, and 100 ppm acetone vapour. The diagram (Fig. 3.1.19) displayed that response increased proportionately with the concentration of gas and  $\sim 10$  ppm afterward; there was a slow increase up to  $\sim 25$  ppm. However, beyond that, there was literally no change in sensing response with increased gas concentration. This might be due to the complete occupation of the active sites on the sensor surface by the experimental gas molecules near  $\sim 25$  ppm concentration.

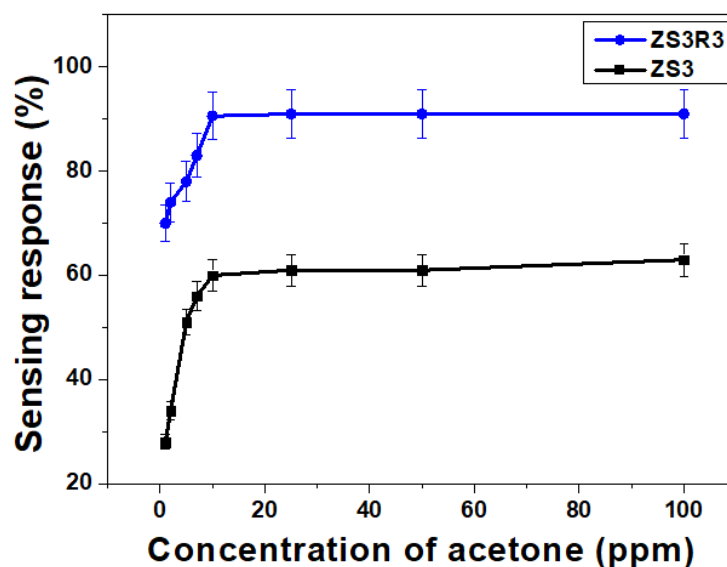


*Figure-3.1.19: Saturation of sensing response in presence of acetone*

It was observed that ZS3 (Fig. 3.1.20a) and ZS3R3 (Fig. 3.1.20b) both the sensors were showed similar trends of sensing responses in the presence of ethanol. The ZS3 sensor revealed  $\sim 44\%$  sensing response in  $\sim 10$  ppm ethanol gas at an operating temperature of  $\sim 300^\circ\text{C}$ , which reached  $\sim 65\%$  for ZS3R3 sensor at  $\sim 150^\circ\text{C}$  (Fig. 3.1.20c). This drop in ethanol sensing performance compared to acetone could be explained by the fact that, high energy value required for dissociating H-O-C<sub>2</sub>H<sub>5</sub> bond ( $\sim 436.8$  kJ/mol) in ethanol as compared to H-CH<sub>2</sub>COCH<sub>3</sub> bond ( $\sim 393.0$  kJ/mol) in acetone. Nevertheless, both sensors showcased their superiority in VOC sensing. The dynamic response curves ensured good reproducibility and reversibility of the sensors with the change in experimental gas pulse.



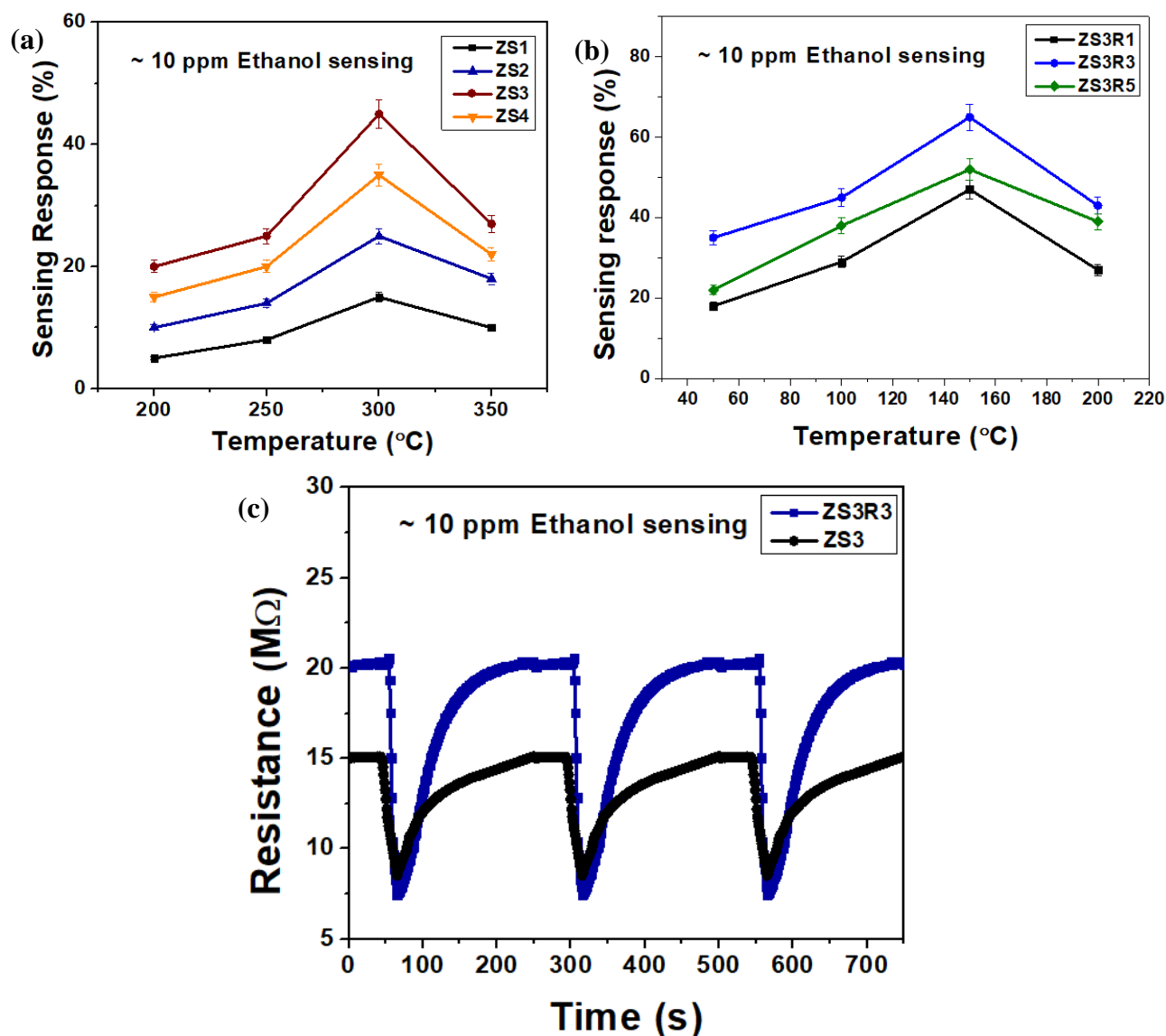


Figure-3.1.20: Change in sensing responses in presence of ~10 ppm ethanol at different working temperature: (a) ZnO-SnO<sub>2</sub> nanocomposite-based sensors, (b) rGO decorated ZS3 based sensors, (c) Dynamic Sensing response graphs of ZS3 and ZS3R3 sensor to ~ 10 ppm of ethanol

In order to study the sensing performance of a sensor, it is necessary to measure its selectivity in the presence of different interfering gases. To study the cross-selectivity of the ZS3 and ZS3R3 sensors, we measured its response in a mixture of gas containing ~ 10 ppm concentration of each, ammonia (NH<sub>3</sub>), methane (CH<sub>4</sub>), and carbon monoxide (CO) along with two analyte gases acetone (CH<sub>3</sub>COCH<sub>3</sub>) and ethanol (C<sub>2</sub>H<sub>5</sub>OH). It was noticed that with respect to two gases (acetone and ethanol), others gave almost negligible responses at ~ 150°C operating temperature (Fig. 3.1.21). So, it could be inferred that this sensor offered excellent selectivity to VOCs.

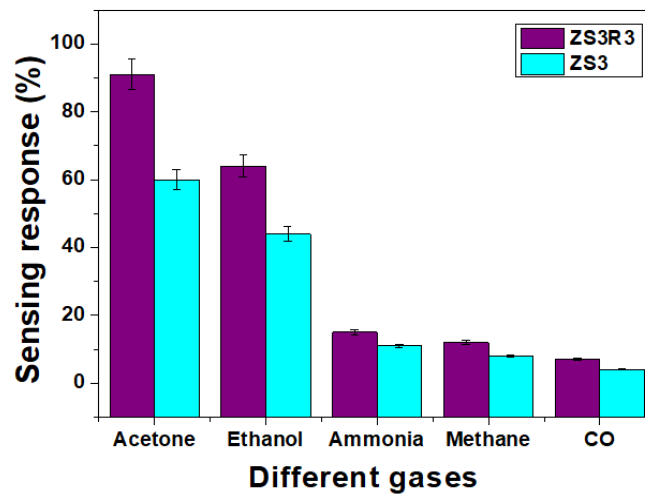


Figure-3.1.21: Selectivity curve against ~ 10 ppm of different gases

For any sensor, its durability is the prime objective from the viewpoint of practical applications in commercial fields because it eliminates the probability of rapid degradation and frequent recalibration of the sensors. To satisfy that, the stability and sensing response value of the ZS3 and ZS3R3 sensors at their optimal working temperatures were checked at 15 days intervals over 90 days span. The result (Fig. 3.1.22 a, b) suggested that the sensor maintained almost constant sensing response and base resistance values at that temperature with minimal variation. Thereby, the sensor satisfied its long-term stability issue.

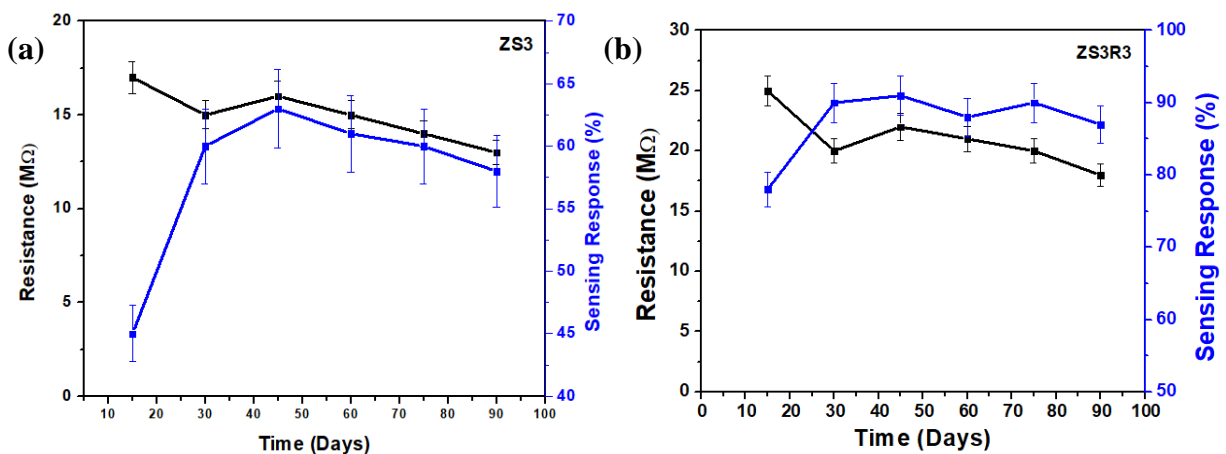


Figure-3.1.22: Stability curves of (a) ZS3 and (b) ZS3R3 nanocomposite sensors

### 3.1.3.4. Gas sensing mechanism:

To understand the gas sensing behavior of the sensors, the plausible sensing mechanism has been proposed. Enhanced gas sensing performance of rGO decorated ZnO-SnO<sub>2</sub> nanocomposite was likely to be explained with the help of surface reaction properties of semiconductor metal oxide and band diagram elucidation (Fig. 3.1.23) [44, 45]. The surface chemical reactions between experimental gas and the adsorbed oxygen species depended on the acid-base nature of the sensor material surface [3]. ZnO being a basic oxide, its addition to the SnO<sub>2</sub> matrix enhanced the basicity of the ZnO/SnO<sub>2</sub> nanocomposite. This increase in basicity was actually beneficial for the oxidation of reducing gas [16]. In the nanocomposite ZnO and SnO<sub>2</sub> both metal oxides were involved in formation of n-n heterojunction. As we know, ZnO has a greater work function value ( $W = 5.2$  eV) as compared to SnO<sub>2</sub> ( $W = 4.5$  eV), it was obvious that, SnO<sub>2</sub> would transfer electrons to the conduction band of ZnO until Fermi level equilibrium reached. In the mean time, due to high affinity towards electrons, aerial oxygen molecules spontaneously adsorbed on the metal oxide semiconductor (MOS) surface. These chemisorbed oxygen molecules extracted electrons from the conduction band of nanocomposite, and thereby converted to different oxygenated ions depending on working temperature as follows [46, 47]:



As a result, a depletion layer developed across the n-n junction and corresponding potential energy barrier increased. The generation of these oxygenated species decreased the carrier (electrons) concentration; consequently, a high base resistance of the sensor in air was observed. Now, during gas sensing, when the sensor was exposed to reducing gases like acetone, a reaction between gas molecules and adsorbed oxygenated ions occurred. This mutual interaction resulted into oxidation of experimental gas and thus released adsorbed oxygen ions from the surface. Due to this phenomenon, the trapped electrons were returned to conduction band of the nanocomposite which increased the carrier concentration and decreased the depletion layer as well as effective potential barrier. Therefore, a decrease in resistance (n-type response) in presence of reducing gases was obtained. The ZS3 sensor showed the maximum response most

possibly due to the optimized n-n interaction between its components in presence of ~ 15 wt% ZnO in SnO<sub>2</sub> matrix.

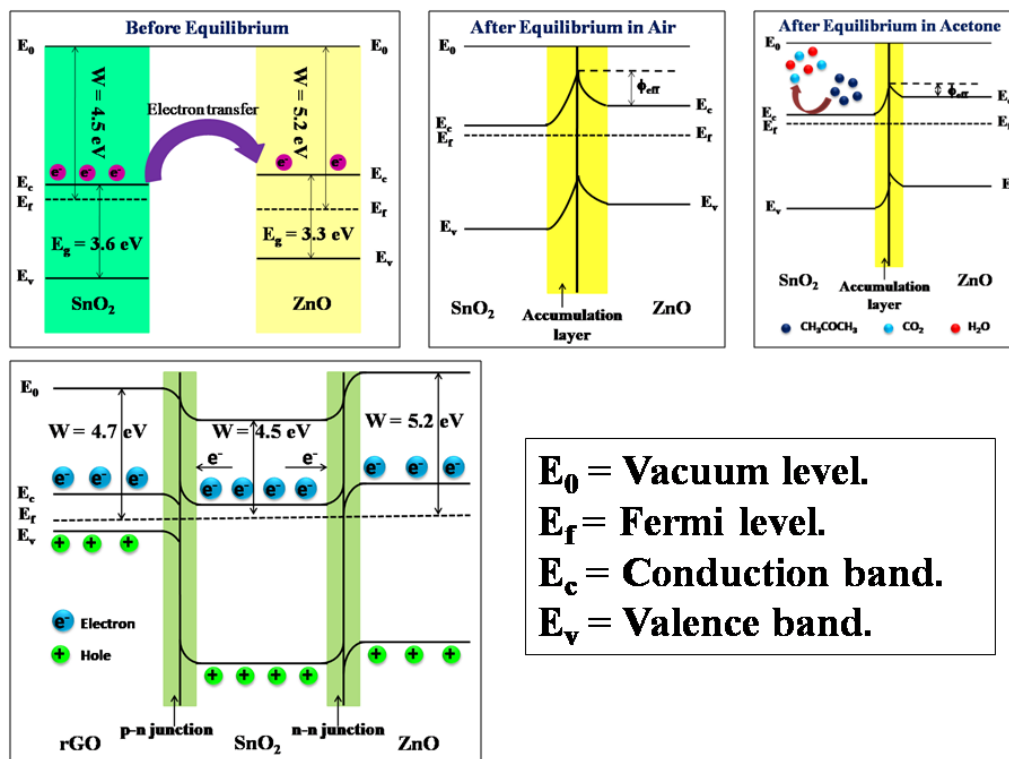


Figure-3.1.23: Band diagram elucidation for acetone sensing of the nanocomposite systems

In case of rGO decorated sensing material, a p-n-n heterojunction was formed by adding n-type rGO in n-n ZnO-SnO<sub>2</sub> heterojunction. This introduction of rGO actually developed an accumulation layer across the p-n junction in addition to the depletion region across n-n junction in presence of oxygenated ions. Simultaneously, rGO increased the number of active sites, owing to its high specific surface area and defect sites (inherent property) which eventually increased the adsorption of gas molecules. Now, the gas molecules reacted with the oxygenated ions and the trapped electrons reverted back to the conduction band of the nanomaterials, as a result, both accumulation layer and depletion layer became thinner. As more number of gas molecules adsorbed, the reaction probability between gas molecules and oxygenated species increased, accounting for further decrease in resistance. Hence, the sensing response of this ternary sensing

system improved. The comparative sensing performance of some literature works with the developed rGO decorated ZnO-SnO<sub>2</sub> nanocomposite sensor was tabulated here (Table 3.1.1).

Table – 3.1.1: Comparison of different VOC sensors based on ZnO-SnO<sub>2</sub> nanocomposites:

Sensing material	Synthesis technique	Sensing gas	Working temp.(°C)	Detection conc. (ppm)	Response (R <sub>g</sub> /R <sub>a</sub> )	Res./ Rec. time (s)	Ref.
SnO <sub>2</sub> -ZnO nanofibers	Electrospining	Acetone	300	20	17	19/9	[20]
ZnO/SnO <sub>2</sub> nanocomposite	Hydrothermal	Acetone	110	100	54.5%	12.6/-	[21]
SnO <sub>2</sub> /ZnO nanorod	Hydrothermal	Ethanol	275	100	18.1	3/38	[22]
ZnO-SnO <sub>2</sub> nanosheet	Co-precipitation	Ethanol	240	50	80	7/42	[23]
ZnO nanorod on SnO <sub>2</sub> thin film	Spray pyrolysis	Ethanol	400	25	50	-	[24]
ZnO/SnO <sub>2</sub> thick films	Sol-gel	Acetone	180	5	13.83	57/63	[25]
ZnO/SnO <sub>2</sub> spheres composite	Hydrothermal	Ethanol	225	30	34.8	1/50	[26]
ZnO-SnO <sub>2</sub> core-shell nanofibers	Hydrothermal	Ethanol	200	100	392.29	75/12	[27]
Octahedral porous ZnO/SnO <sub>2</sub> composite	Hydrothermal	Ethanol	35	100	17.8	1/12	[28]

rGO decorated ZnO-SnO <sub>2</sub>	Sol-gel	VOC	150	10	91%	10/100	This Work
------------------------------------------	---------	-----	-----	----	-----	--------	--------------

## 3.1.4. Conclusion:

Here, a facile sol-gel process was used to prepare ZnO-SnO<sub>2</sub> nanocomposites of different compositions (5, 10, 15, and 20 wt% ZnO) for VOCs sensing performance study. Afterwards, rGO (1, 3, and 5 wt%) were introduced in the optimized ZnO-SnO<sub>2</sub> nanocomposites (ZS3) to generate a heterojunction-based hybrid ternary nanocomposite. A multi-folds enhancement in sensing performances was achieved with ~ 3 wt% rGO incorporated ZnO-SnO<sub>2</sub> nanocomposite based sensor. The rGO based sensor showed repeatable and reproducible n-type sensing with ~ 91% response in the presence of ~ 10 ppm acetone vapor as well as ~ 65% response to ~ 10 ppm ethanol gas at an operating temperature of ~ 150°C. The fabricated sensor was also able to detect VOCs at a concentration as low as ~ 1 ppm. The developed sensor exhibited a considerably fast response (~ 10 s) and recovery time (~ 100 s) with almost negligible cross-sensitivities towards other significant components of VOCs. The sensor also established prolific long-term stability in terms of base resistance and sensing performances. Here, the optimized ternary nanocomposite authenticated its superiority as a low ppm VOC sensor with outstanding sensing response and selectivity compared to already available other VOC sensors.

### References:

- [1] N. Rajesh, J. C. Kannan, T. Krishnakumar, S.G. Leonardi, G. Neri, Sensing behavior to ethanol of tin oxide nanoparticles prepared by microwave synthesis with different irradiation time, *Sensors and Actuators B* 194 (2014) 96–104. <https://doi.org/10.1016/j.snb.2013.12.060>.
- [2] H. Wang, A. L. Rogach, Hierarchical SnO<sub>2</sub> Nanostructures: Recent Advances in Design, Synthesis, and Applications, *Chem. Mater.* (2013). <https://doi.org/10.1021/cm4018248>.
- [3] Y. Xia, J. Wang, X. Li, D. Xie, D. Zhou, L. Xiang, S. Komarneni, Nanoseed-assisted rapid formation of ultrathin ZnO nanorods for efficient roomtemperatureNO<sub>2</sub> detection, *Ceramics International* 42(2016)15876–15880. <https://doi.org/10.1016/j.ceramint.2016.07.058>.
- [4] L. Wang, Y. Kang, X. Liu, S. Zhang, W. Huang, S. Wang, ZnO nanorod gas sensor for ethanol detection, *Sens. Actuators B: Chem.* 162 (2012) 237-243. <https://doi.org/10.1016/j.snb.2011.12.073>.
- [5] O. C. Compton, S. T. Nguyen, Graphene Oxide, Highly Reduced Graphene Oxide, and Graphene: Versatile Building Blocks for Carbon-Based Materials, *Small* 6 (2010) 711–723. <https://doi.org/10.1002/sml.200901934>.
- [6] Y. Zhu, S. Murali, W. Cai, X. Li, J. W. Suk, J. R. Potts, R. S. Ruoff, Graphene and Graphene Oxide: Synthesis, Properties, and Applications, *Adv. Mater.* 22 (2010) 3906–3924. <https://doi.org/10.1002/adma.201001068>.
- [7] S. Park, R. S. Ruoff, Chemical methods for the production of graphene, *Nature Nanotechnol.* 2009. <https://doi.org/10.1038/nnano.2009.58>.
- [8] F. Rigoni, R. Maiti, C. Baratto, M. Donarelli, J. MacLeod, B. Gupta, M. Lyu, A. Ponzoni, G. Sberveglieri, N. Motta, G. Faglia, Transfer of CVD-grown graphene for room temperature gas sensors, *IOP Science* 2017. <https://doi.org/10.1088/1361-6528/aa8611>.
- [9] W. Yuan, G. Shi, Graphene-based gas sensors, *J. Mater. Chem. A* 1 (2013) 10078–10091. <https://doi.org/10.1039/c3ta11774j>.
- [10] S. Gupta Chatterjee, S. Chatterjee, A. K. Ray, A. K. Chakraborty, Graphene–metal oxide nanohybrids for toxic gas sensor, *Sens. Actuators B: Chem.* (2015). <https://doi.org/10.1016/j.snb.2015.07.070>.

- [11] X. Zhu, Y. Guo, H. Ren, C. Gao, Y. Zhou, Enhancing the NO<sub>2</sub> gas sensing properties of rGO/SnO<sub>2</sub> nanocomposite films by using microporous substrates, *Sens. Actuators B: Chem.* (2017). <https://doi.org/10.1016/j.snb.2017.04.030>.
- [12] D. Toloman, A. Popa, M. Stan, C. Socaci, A.R. Biris, G. Katona, F. Tudorache, I. Petrila, F. Iacomì, Reduced graphene oxide decorated with Fe doped SnO<sub>2</sub> nanoparticles for humidity sensor, *Appl. Surf. Sci.* 402 (2017) 410–417. <https://doi.org/10.1016/j.apsusc.2017.01.064>.
- [13] S. Meti, M. R. Rahman, Md. I. Ahmad, K. U. Bhat, Chemical free synthesis of graphene oxide in the preparation of reduced graphene oxide-zinc oxide nanocomposite with improved photocatalytic properties, *Appl. Surf. Sci.* 451 (2018) 67–75. <https://doi.org/10.1016/j.apsusc.2018.04.138>.
- [14] P. Wang, D. Wang, M. Zhang, Y. Zhu, Y. Xu, X. Ma, X. Wang, ZnO nanosheets/graphene oxide nanocomposites for highly effective acetone vapor detection, *Sens. Actuators B: Chem.* 230 (2016) 477–484. <https://doi.org/10.1016/j.snb.2016.02.056>.
- [15] S. Bai, H. Fu, Y. Zhao, K. Tian, R. Luo, D. Li, A. Chen, On the construction of hollow nanofibers of ZnO/SnO<sub>2</sub> heterojunctions to enhance the NO<sub>2</sub> sensing properties, *Sens. Actuators B: Chem.* (2018). <https://doi.org/10.1016/j.snb.2018.03.055>.
- [16] L. Wang, J. Li, Y. Wang, K. Yu, X. Tang, Y. Zhang, S. Wang, C. Wei, Construction of 1D SnO<sub>2</sub>-coated ZnO nanowire heterojunction for their improved n-butylamine sensing performances, *Nature Scientific Reports* 6 (2016) 35079–35090. <https://doi.org/10.1038/srep3507>.
- [17] Z. Wang, A. Sackmann, S. Gao, U. Weimar, G. Lu, S. Liu, T. Zhang, N. Barsan, Study on highly selective sensing behavior of ppb-level oxidizing gas sensors based on Zn<sub>2</sub>SnO<sub>4</sub> nanoparticles immobilized on reduced graphene oxide under humidity conditions, *Sens. Actuators: B. Chem.* 285 (2019) 590–600. <https://doi.org/10.1016/j.snb.2019.01.109>.
- [18] J. Zhang, J. Wu, X. Wang, D. Zeng, C. Xie, Enhancing room-temperature NO<sub>2</sub> sensing properties via forming heterojunction for NiO-rGO composited with SnO<sub>2</sub> nanoplates, *Sens. Actuators B: Chem.* (2016). <https://doi.org/10.1016/j.snb.2016.12.062>.
- [19] Z. Wang, S. Gao, T. Fei, S. Liu, T. Zhang, Construction of ZnO/SnO<sub>2</sub> Heterostructure on Reduced Graphene Oxide for Enhanced Nitrogen Dioxide Sensitive Performances at Room Temperature, *ACS Sens.* 4 (2019) 2048–2057. <https://doi.org/10.1021/acssensors.9b00648>.



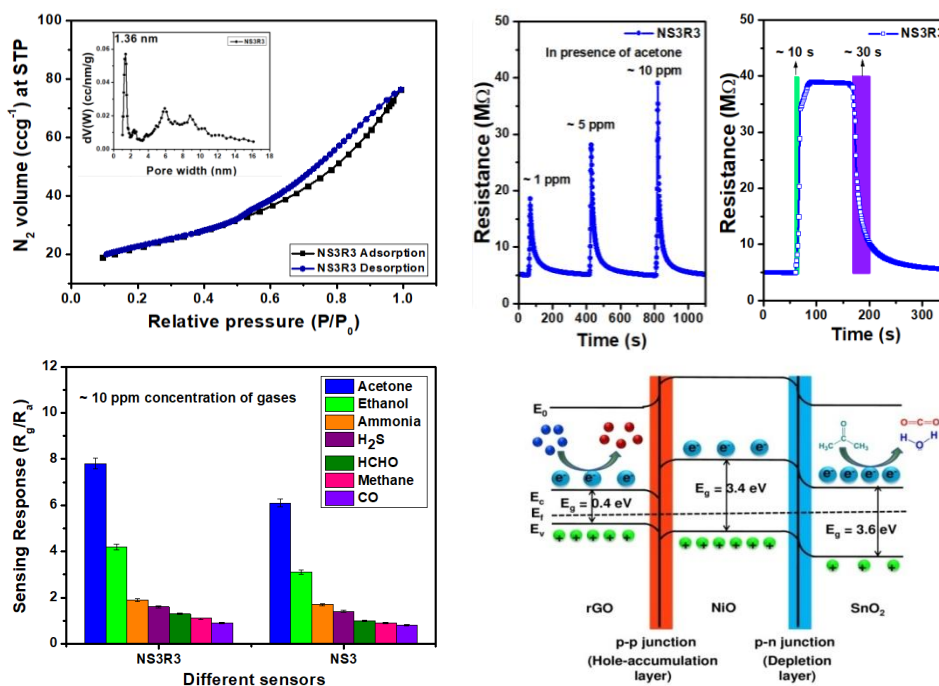
- [20] S.H. Yan, S.Y. Ma, X.L. Xu, W.Q. Li, J. Luo, W.X. Jin, T.T. Wang, X.H. Jiang, Y. Lu, H.S. Song, Preparation of SnO<sub>2</sub>-ZnO hetero-nanofibers and their application in acetone sensing performance, *Mater. Lett.* 159 (2015) 447–450. <https://doi.org/10.1016/j.matlet.2015.07.051>.
- [21] M. Asal, S. Nasirian, Acetone gas sensing features of zinc oxide/Tin dioxide nanocomposite for diagnosis of diabetes, *Mater. Res. Exp.* (2019). <https://doi.org/10.1088/2053-1591/ab332c>.
- [22] X. Yang, S. Zhang, Q.yu, L. Zhao, P. Sun, T. Wang, F. Liu, X. Yan, Y. Gao, X. Liang, S. Zhang, G. Lu, One step synthesis of branched SnO<sub>2</sub>/ZnO heterostructures and their enhanced gas-sensing properties, *Sens. Actuators: B. Chem.* 281 (2019) 415–423. <https://doi.org/10.1016/j.snb.2018.10.138>.
- [23] S. Qin, P. Tang, Y. Feng, D. Li, Novel ultrathin mesoporous ZnO-SnO<sub>2</sub> n-n heterojunction nanosheets with high sensitivity to ethanol, *Sens. Actuators: B. Chem.* 309 (2020) 127801. <https://doi.org/10.1016/j.snb.2020.127801>.
- [24] T. Tharsika, M. Thanihaichelvan, A. S. M. A. Haseeb, S. A. Akbar, Highly Sensitive and Selective Ethanol Sensor Based on ZnO Nanorod on SnO<sub>2</sub> Thin Film Fabricated by Spray Pyrolysis, *Front. Mater.* 6 (2019). <https://doi.org/10.3389/fmats.2019.00122>.
- [25] Y. Chen, Y. Cao, Ultrasensitive and low detection limit of acetone gas sensor based on ZnO/SnO<sub>2</sub> thick films, *RSC Adv.* 10 (2020) 35958–35965. <https://doi.org/10.1039/d0ra06406h>.
- [26] J. Liu, T. Wang, B. Wang, P. Sun, Q. Yang, X. Liang, H. Song, G. Lu, Highly sensitive and low detection limit of ethanol gas sensor based on hollow ZnO/SnO<sub>2</sub> spheres composite material, *Sens. Actuators: B. Chem.* 245 (2017) 551–559. <https://doi.org/10.1016/j.snb.2017.01.148>.
- [27] W. Li, S. Ma, Y. Li, G. Yang, Y. Mao, J. Luo, D. Gengzang, X. Xu, S. Yan, Enhanced ethanol sensing performance of hollow ZnO-SnO<sub>2</sub> core-shell nanofibers, *Sens. Actuators: B. Chem.* 211 (2015) 392–402. <https://doi.org/10.1016/j.snb.2015.01.090>.
- [28] J. Yu, M. Sun, M. Yu, M. Yang, H. Yu, Y. Yang, X. Dong, Preparation of near room temperature gas sensor based on regular octahedral porous ZnO/SnO<sub>2</sub> composite, *J. Alloys Comp.* 920 (2022) 165884. <https://doi.org/10.1016/j.jallcom.2022.165884>.

- [29] N. M. S. Hidayah, W. Liu, C. Lai, N. Z. Noriman, C. Khe, U. Hashim, H. C. Lee, Comparison on Graphite, Graphene Oxide and Reduced Graphene Oxide: Synthesis and Characterization, AIP Conf. Proc. <https://doi.org/10.1063/1.5005764>.
- [30] O. Akhavan, K. Bijanzad, A. Mirsepah, Synthesis of graphene from natural and industrial carbonaceous wastes, RSC Adv. 4 (2014) 20441-20448. <https://doi.org/10.1039/c4ra01550a>.
- [31] N. Kumar, A. K. Srivastava, H. S. Patel, B. K. Gupta, G. Das Varma, Facile Synthesis of ZnO–Reduced Graphene Oxide Nanocomposites for NO<sub>2</sub> Gas Sensing Applications, Eur. J. Inorg. Chem. (2014). <https://doi.org/10.1002/ejic.201403172>.
- [32] J. Liu, S. Li, B. Zhang, Y. Xiao, Y. Gao, Q. Yang, Y. Wang, G. Lu, Ultrasensitive and low detection limit of nitrogen dioxide gas sensor based on flower-like ZnO hierarchical nanostructure modified by reduced graphene oxide, Sens. Actuators B: Chem. 249 (2017) 715–724. <https://doi.org/10.1016/j.snb.2017.04.190>.
- [33] A. Ghaderi, S. Abbasi, F. Farahbod, Synthesis, characterization and photocatalytic performance of modified ZnO nanoparticles with SnO<sub>2</sub> nanoparticles, Mater. Res. Express (2018). <https://doi.org/10.1088/2053-1591/aacd40>.
- [34] E.M. Seftel, E. Popovici, M. Mertens, E.A. Stefaniak, R. Van Grieken, P. Cool, E.F. Vansant, Sn<sup>IV</sup>-containing layered double hydroxides as precursors for nano-sized ZnO/SnO<sub>2</sub> photocatalysts, Applied Catalysis B: Environmental 84 (2008) 699–705. <https://doi.org/10.1016/j.apcatb.2008.06.006>.
- [35] A. Nasriddinov, M. Rumyantseva, A. Marikutsa, A. Gaskov, J. Lee, J. Kim, J. Kim, S. S. Kim, H. W. Kim, Sub-ppm Formaldehyde Detection by n-n TiO<sub>2</sub>@SnO<sub>2</sub> Nanocomposites, Sensors 19 (2019) 3182. <https://doi.org/10.3390/s19143182>.
- [36] X. Li, J. Wang, D. Xie, J. Xu, R. Dai, L. Xiang, H. Zhu, Y. Jiang, Reduced graphene oxide/hierarchical flower-like zinc oxide hybrid films for room temperature formaldehyde detection, Sens. Actuators B: Chem. 221 (2015) 1290–1298. <https://doi.org/10.1016/j.snb.2015.07.102>.
- [37] C. A. Zito, T. M. Perfecto, D. P. Volanti, Impact of reduced graphene oxide on the ethanol sensing performance of hollow SnO<sub>2</sub> nanoparticles under humid atmosphere, Sens. Actuators B Chemical 244 (2017) 466–474. <https://doi.org/10.1016/j.snb.2017.01.015>.

- 
- [38] L. Li, S. He, M.Liu, C.Zhang, W. Chen, Three-Dimensional Mesoporous Graphene Aerogel-Supported SnO<sub>2</sub> Nanocrystals for High-Performance NO<sub>2</sub> Gas Sensing at Low Temperature, *Anal. Chem.* 87 (2015) 1638–1645. <https://doi.org/10.1021/ac503234e>.
- [39] S. Chakraborty, M. Pal, Highly selective and stable acetone sensor based on chemically prepared bismuth ferrite nanoparticles, *J. Alloys Comp.* 787 (2019) 1204–1211. <https://doi.org/10.1016/j.jallcom.2019.02.153>.
- [40] M. Sinha, R. Mahapatra, B. Mondal, T. Maruyama, R. Ghosh, Ultra-fast and Reversible Gas Sensing Properties Of ZnO Nanowire Arrays Grown By Hydrothermal Technique, *J. Phys. Chem. C* (2016). <https://doi.org/10.1021/acs.jpcc.5b11012>.
- [41] S. M. Ahmed, M. R. Taha, O. M. E. Taha, Kinetics and isotherms of dichlorodiphenyltrichloroethane (DDT) adsorption using soil–zeolite mixture, *Nanotechnol. Environ. Eng.* 3 (2018). <https://doi.org/10.1007/s41204-017-0033-8>.
- [42] T. Kida, T. Kuroiwa, M. Yuasa, K. Shimano, N. Yamazoe, Study on the response and recovery properties of semiconductor gas sensors using a high-speed gas-switching system, *Sens. Actuators B: Chem.* 134 (2008) 928–933. <https://doi.org/10.1016/j.snb.2008.06.044>.
- [43] Analytical Methods Committee, Recommendations for the Definition, Estimation and Use of the Detection Limit, *ANALYST* 112 (1987) 199–204. <https://doi.org/10.1039/AN9871200199>.
- [44] S. Park, S. An, Y. Mun, C. Lee, UV-Enhanced NO<sub>2</sub> Gas Sensing Properties of SnO<sub>2</sub>-Core/ZnO-Shell Nanowires at Room Temperature, *ACS Appl. Mater. Interfaces* (2016). <https://doi.org/10.1021/am400500a>.
- [45] Y. Chen, H. Li, Q. Ma, Q. Che, J. Wang, G. Wang, P. Yang, Morphology-controlled porous α-Fe<sub>2</sub>O<sub>3</sub>/SnO<sub>2</sub> nanorods with uniform surface heterostructures and their enhanced acetone gas-sensing properties, *Mater. Lett.* 211 (2018) 212–215. <https://doi.org/10.1016/j.matlet.2017.10.012>.
- [46] N. Song, H. Fan, H. Tian, PVP assisted in situ synthesis of functionalized graphene/ZnO (FGZnO) nanohybrids with enhanced gas-sensing property, *J Mater Sci* 50 (2015) 2229–2238. <https://doi.org/10.1007/s10853-014-8785-z>.
- [47] N. D. Khoang, D. D. Trung, N. V. Duy, N. D. Hoa, N. V. Hieu, Design of SnO<sub>2</sub>/ZnO hierarchical nanostructures for enhanced ethanol gas-sensing performance, *Sens. Actuators B: Chem.* 174 (2012) 594–601. <https://doi.org/10.1016/j.snb.2012.07.118>.

# CHAPTER 3.2

## Reduced graphene oxide (rGO) decorated NiO-SnO<sub>2</sub> nanocomposite sensor towards room temperature VOC sensing performance



*The sol-gel synthesized NiO-SnO<sub>2</sub> nanocomposites exhibited an enhancement of surface area after incorporation of rGO, and this substantial increment led to the gas sensing even at room temperature. The optimized sensor demonstrated an excellent sensing response ( $R_g/R_a \sim 7.8$ ) towards ~ 10 ppm acetone at room temperature ( $30 \pm 5^\circ\text{C}$ ) with response and recovery time of ~ 10 s and ~ 30 s respectively. It also detected ~ 10 ppm ethanol with response ~ 3.5 having response and recovery time ~ 10 s and ~ 25 s accordingly. Additionally, this sensor was able to differentiate healthy and diabetic breath in terms of trace concentration (~ 1 ppm) of acetone through exhaled human breath analysis. The sensor also displayed good stability and reproducible sensing performance. The sensing mechanism was explained using band structure model and electrical property was illustrated from impedance spectroscopy.*



**3.2.1. Introduction:**

In Chapter 3.1, the developed rGO decorated ZnO-SnO<sub>2</sub> ternary nanocomposite exhibited a good sensing performance towards VOCs (both acetone and ethanol) at a low operating temperature of ~ 150°C [1]. However, as discussed in the Chapter 1, the prime objective of this thesis work is to develop a sensor system for non-invasive breath biomarker detection which ought to be operated near room temperature. From this perspective, introduction of p-type NiO in n-type SnO<sub>2</sub> matrix generates a p-n heterojunction which can effectively attune charge carriers' concentration across heterojunction barrier and thereby elevate the sensing performance. Literature studies revealed that NiO-SnO<sub>2</sub> sensors can detect gases efficiently but operate at high working temperatures. However, high temperature operated sensors need more power consumption and consequent grain coalescence leads to a shortening of lifetime, which restrict them from commercial applications. Therefore, researchers are devoted to develop sensors operated at ambient temperature. Decoration of a binary MOS nanocomposite with rGO can effectively enlarge the surface area of sensing material and thereby reduce working temperature due to facile electron mobility. Some works [2-10] have also been reported on the development of rGO-based ternary nanocomposites operating at low temperatures. Inspired by these studies, in the present work, it was presumed to fabricate a novel rGO decorated NiO-SnO<sub>2</sub> (p-n type) heterojunction-based gas sensing material to exploit its VOC sensing properties at ambient condition.

**3.2.2. Experimental:**

Tin tetrachloride pentahydrate (SnCl<sub>4</sub>•5H<sub>2</sub>O) and nickel nitrate hexahydrate (Ni(NO<sub>3</sub>)<sub>2</sub>•6H<sub>2</sub>O) purchased from Sigma Aldrich were used as the precursor of SnO<sub>2</sub> and NiO respectively. Precursor solutions of pristine nickel oxide and tin oxide were prepared separately. For NiO-SnO<sub>2</sub> nanocomposites, the precursor chemicals with nickel and tin were mixed in such a way that mole ratio of their corresponding oxides be in 1:1, 1:2, 1:3, and 1:4. The resultant homogeneous sols were marked as NS1, NS2, NS3, and NS4 respectively. In a typical synthesis (Fig. 3.2.1), the gels were prepared following the detailed procedure described in Chapter 2 (Section 2.3.1). Finally, the gels were calcined at ~ 650°C (based on TG analysis) for ~ 2 hours to obtain corresponding pristine and nanocomposite powders.

For the synthesis of rGO decorated NiO-SnO<sub>2</sub> nanocomposites, different weight percent of rGO (1, 3, and 5 wt%) were added to an aqueous ethanol solution containing required amounts of NS3

powder and named as NS3R1, NS3R3, and NS3R5 respectively. The sols were converted to gels following the same process as mentioned above and cured at  $\sim 350^{\circ}\text{C}$  for  $\sim 2$  hours to acquire respective rGO decorated nanocomposite powders.

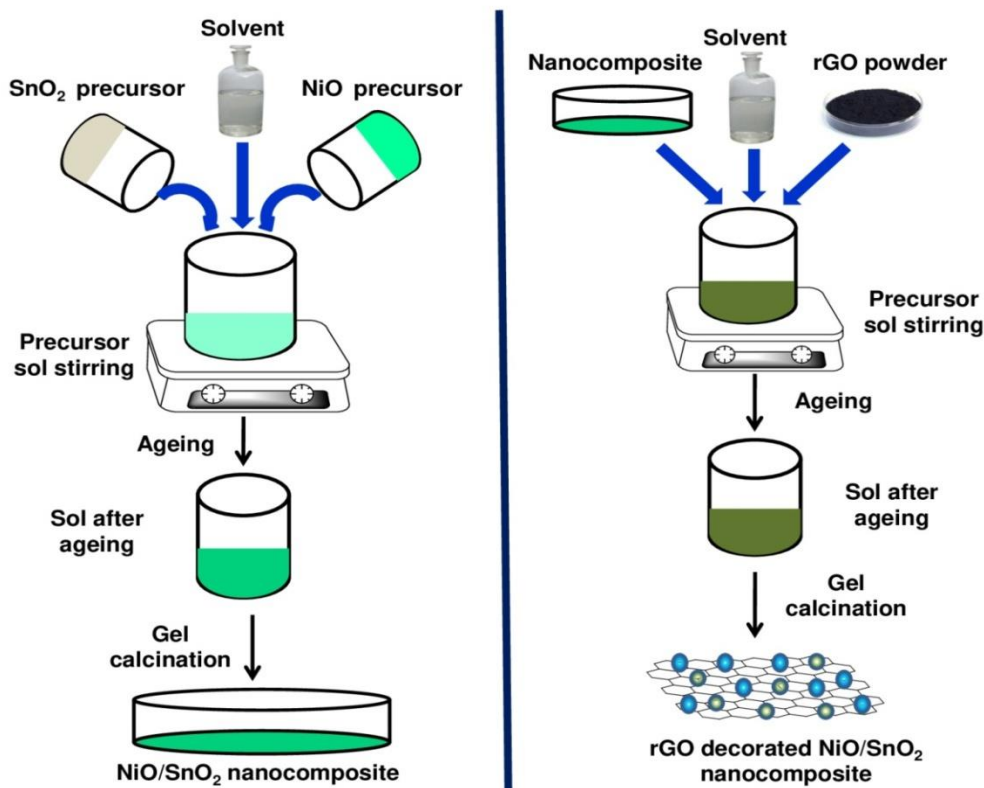


Figure-3.2.1: Schematic representation of nanocomposites synthesis

### 3.2.3. Results and discussions:

#### 3.2.3.1. Characterization of nanocomposites:

Thermogravimetric analyses of samples (Fig. 3.2.2) revealed three-step thermal degradation. The first step weight loss of  $\sim 10\%$  upto  $\sim 150^{\circ}\text{C}$  in pristine  $\text{SnO}_2$  was perhaps due to the removal of solvent molecules. Then,  $\sim 37\%$  weight loss at  $\sim 225^{\circ}\text{C}$  attributed to cross-linking between  $\text{Sn}(\text{OH})_4$  moieties. At the final stage,  $\sim 15\%$  mass loss near  $560^{\circ}\text{C}$  correlated conversion of hydroxide to oxide. In pristine  $\text{NiO}$ , initial mass loss was similar to tin oxide [11]. Afterwards, only  $\sim 10\%$  loss of weight  $\sim 400^{\circ}\text{C}$  was observed. Finally,  $\sim 15\%$  mass loss  $\sim 500^{\circ}\text{C}$  was due to the crystallization of  $\text{NiO}$  nanoparticles. In nanocomposite (NS3), the initial  $\sim 5\%$  mass loss till  $\sim 120^{\circ}\text{C}$  was also due to removal of water contents left behind during the synthesis process. It was

followed by a sharp weight loss of  $\sim 58\%$  upto  $\sim 200^\circ\text{C}$ , corresponding to loss of organic solvent and removal of decomposed binder molecules. Further,  $\sim 18\%$  loss in mass  $\sim 620^\circ\text{C}$  was noticed and beyond that no significant mass loss was observed [12]. Therefore, the calcination temperature of the nanocomposites was set to  $\sim 650^\circ\text{C}$ .

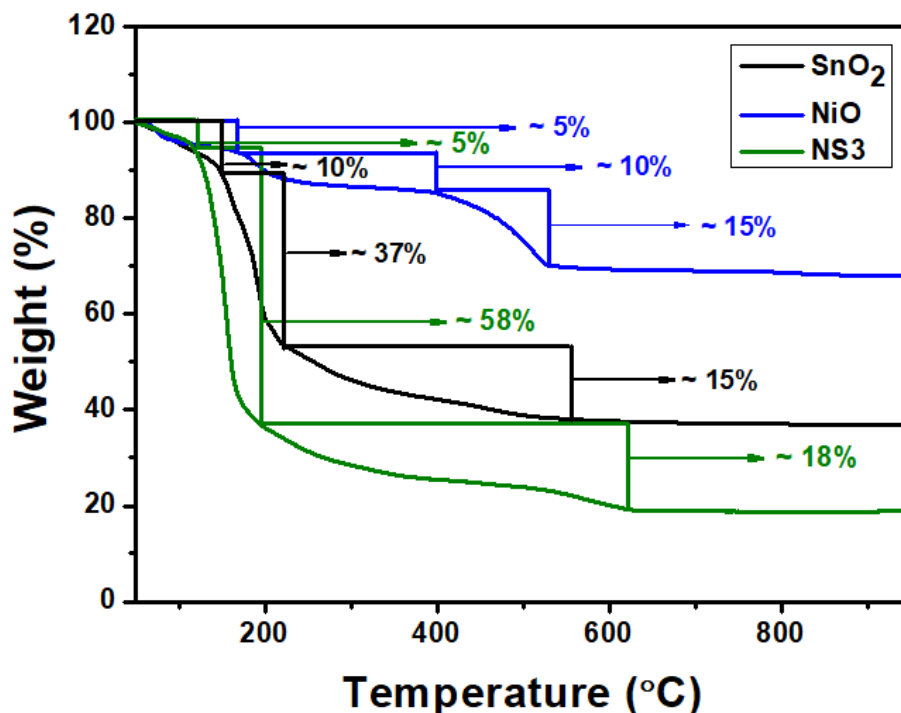


Figure-3.2.2: Thermogravimetric (TG) plot of pristine  $\text{SnO}_2$ ,  $\text{NiO}$  and  $\text{NS3}$

The XRD spectra exhibited diffraction planes that corresponded to tetragonal rutile structure (JCPDS: 41-1445) for pristine  $\text{SnO}_2$  [13, 14] and cubic crystal structure for  $\text{NiO}$  (JCPDS: 78-0423) [15, 16]. In  $\text{NiO-SnO}_2$  nanocomposites, the diffraction peaks corresponded to planes of tetragonal  $\text{SnO}_2$  and cubic  $\text{NiO}$ , as indexed in Fig. 3.2.3a. These coexisted diffraction peaks correlated to respective phases of corresponding metal oxides confirmed the formation of nanocomposites. The introduction of rGO in the NS3 matrix showed distinguishable broadening of diffraction peaks and dampening of peak intensities (Fig. 32.3b). Additionally, few peaks resembled orthorhombic  $\text{SnO}_2$  was also noticed. It has already been reported [17, 18] that orthorhombic  $\text{SnO}_2$  started to develop as a metastable phase at high temperature and pressure conditions. A similar trait of  $\text{SnO}_2$  was also observed in prepared nanocomposites.



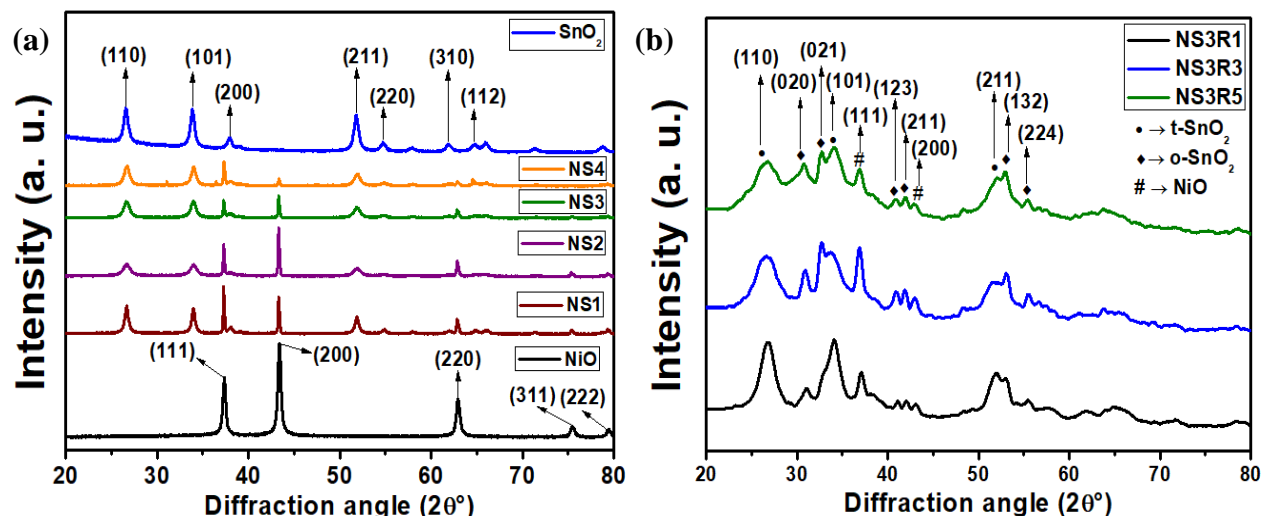


Figure-3.2.3: XRD spectra of (a) NiO-SnO<sub>2</sub> nanocomposites, (b) rGO decorated NS3 nanocomposites

FTIR study was performed to understand the presence of chemical bonds and functional groups in the nanocomposites. The stretching and bending signatures of -OH bonds were observed in NS3 and NS3R3 samples. The increased intensity of both the peaks of NS3R3 suggested the presence of rGO in the nanocomposites. Generally, the peaks correspond to metal oxide bonds obtained below 1000 cm<sup>-1</sup> [19, 20]. A similar result was observed in our sample (Fig. 3.2.4), and a simultaneous decrease in peak intensity in NS3R3 indicated the rGO incorporation in the NS3 nanocomposite.

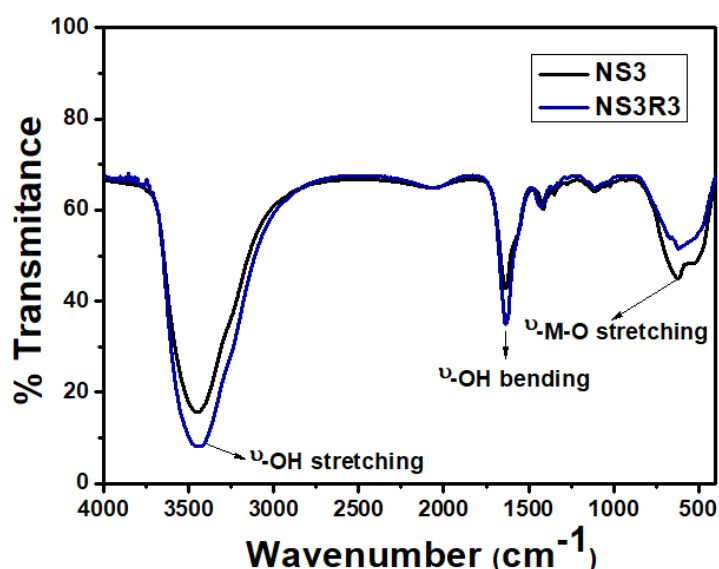
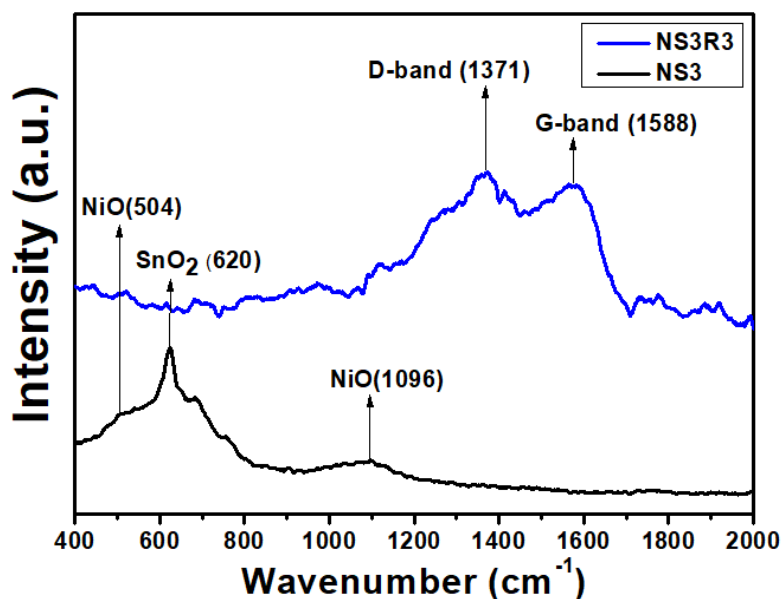


Figure-3.2.4: FTIR spectra of NS3 and NS3R3

Raman spectroscopic analysis of NS3 nanocomposite (Fig. 3.2.5) demonstrated a small peak of  $\sim 504 \text{ cm}^{-1}$  signified the longitudinal phonon mode of NiO, whereas the broad peak of  $\sim 1096 \text{ cm}^{-1}$  for the two-phonon mode of NiO. A sharp, high-intensity peak of  $\sim 620 \text{ cm}^{-1}$  was obtained for phonon mode vibration from surface layers of  $\text{SnO}_2$ . In NS3R3, the two peaks observed,  $\sim 1371 \text{ cm}^{-1}$  and  $\sim 1588 \text{ cm}^{-1}$ , were designated as D-band and G-band respectively [21, 22]. The D-band signifies the existence of defect sites in rGO, and the G-band originated from scattering of lattice C atoms. Their intensity ratio ( $I_D/I_G$ ) of  $\sim 1.1$  suggested the presence of more defect sites in the rGO structure. However, metal oxide vibration peaks were not well-distinguished, possibly due to high-intensity peaks originating from rGO. Thereby, the successful addition of rGO in NiO- $\text{SnO}_2$  nanocomposites was authenticated, and this defect-rich structural property of rGO proved beneficial in gas sensing applications.



*Figure-3.2.5: Raman spectra of NS3 and NS3R3 samples*

The  $\text{N}_2$  sorption isotherms (Fig. 3.2.6 a, b) and corresponding Barret-Joyner-Halenda (BJH) pore size distribution curves (Fig. 3.2.6 c, d) of NS3 and NS3R3 have been presented. The isotherms exhibited sharp capillary uptake at low  $P/P_0$ , suggesting the microporous nature of the samples. This was followed by a significant and steady increase in  $\text{N}_2$  uptake at a higher  $P/P_0$  region. Further, at high  $\text{N}_2$  partial pressure, there was a pronounced hysteresis. The isotherms for the samples NS3 and NS3R3 exhibited a type IV isotherm (according to the IUPAC convention) [23,

24]. Large desorption hysteresis, together with a steady increase in  $N_2$  uptake, could be attributed to the presence of a broad range of mesopores. The Brunauer-Emmett-Teller (BET) surface area of NS3  $\sim 17.08 \text{ m}^2/\text{g}$  and was increased to  $\sim 80 \text{ m}^2/\text{g}$  for NS3R3. It is evident that the incorporation of rGO in NiO-SnO<sub>2</sub> nanocomposites effectively enhanced the surface area of as-synthesized nanocomposites, which is expected to improve the gas sensing response.

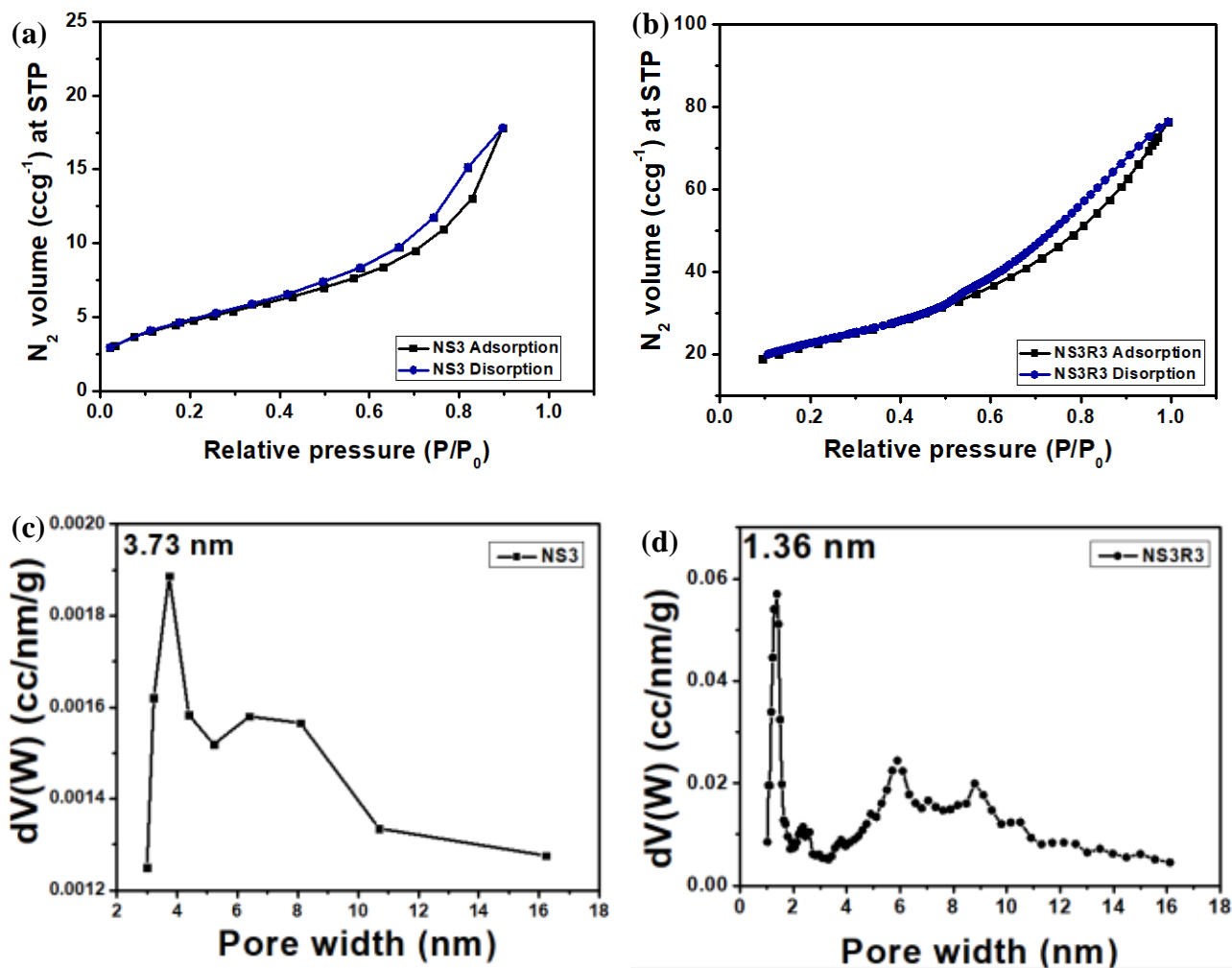
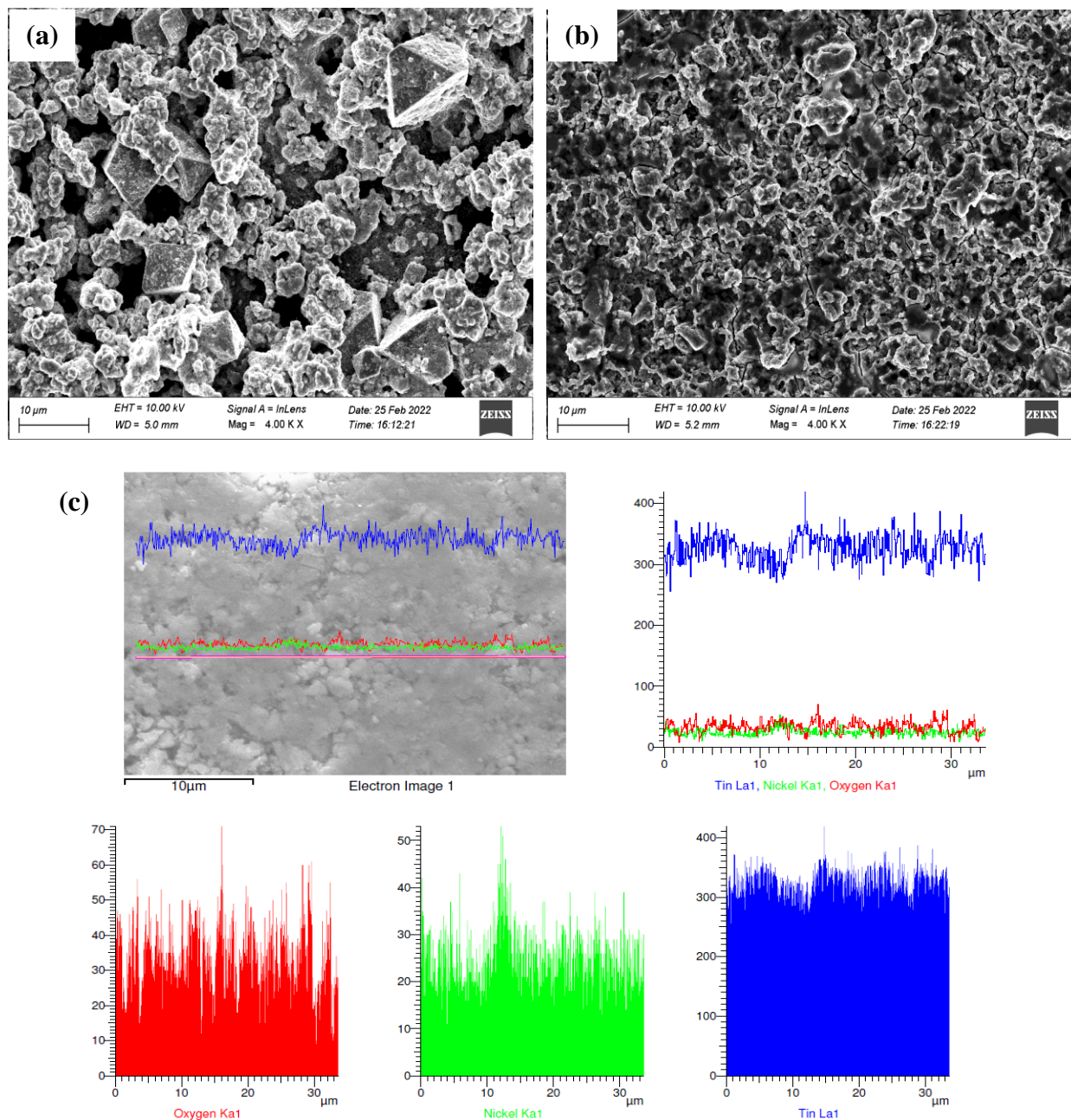


Figure-3.2.6: BET absorption-desorption isotherm (a) NS3 and (b) NS3R3, pore size distribution curve (c) NS3 and (d) NS3R3

Pore size distribution curves were obtained by the BJH method using a desorption set of  $N_2$  isotherm [25, 26]. The pore size distribution plot of NS3 showed pore size distribution in a wide range of  $\sim 3 \text{ nm}$  to  $\sim 16 \text{ nm}$ , with the peak centered at  $3.75 \text{ nm}$  and the measured pore volume was  $0.024 \text{ cc/g}$ . On the other hand, the NS3R3 sample showed microspores with peak maxima at

1.36 nm and a broad distribution of large mesopores of dimensions  $\sim 5.9$  nm and  $\sim 8.9$  nm, and the pore volume increased to 0.112 cc/g. Large mesopores with different pore dimensions could be attributed to the inter-particle void spaces and several defect sites in the nanocomposite.

The FESEM micrograph of NS3 (Fig. 3.2.7a) nanocomposite showed two different morphologies: agglomerated ovoid-shaped particles corresponding to  $\text{SnO}_2$  and some cuboid-shaped particles related to  $\text{NiO}$  [27, 28].



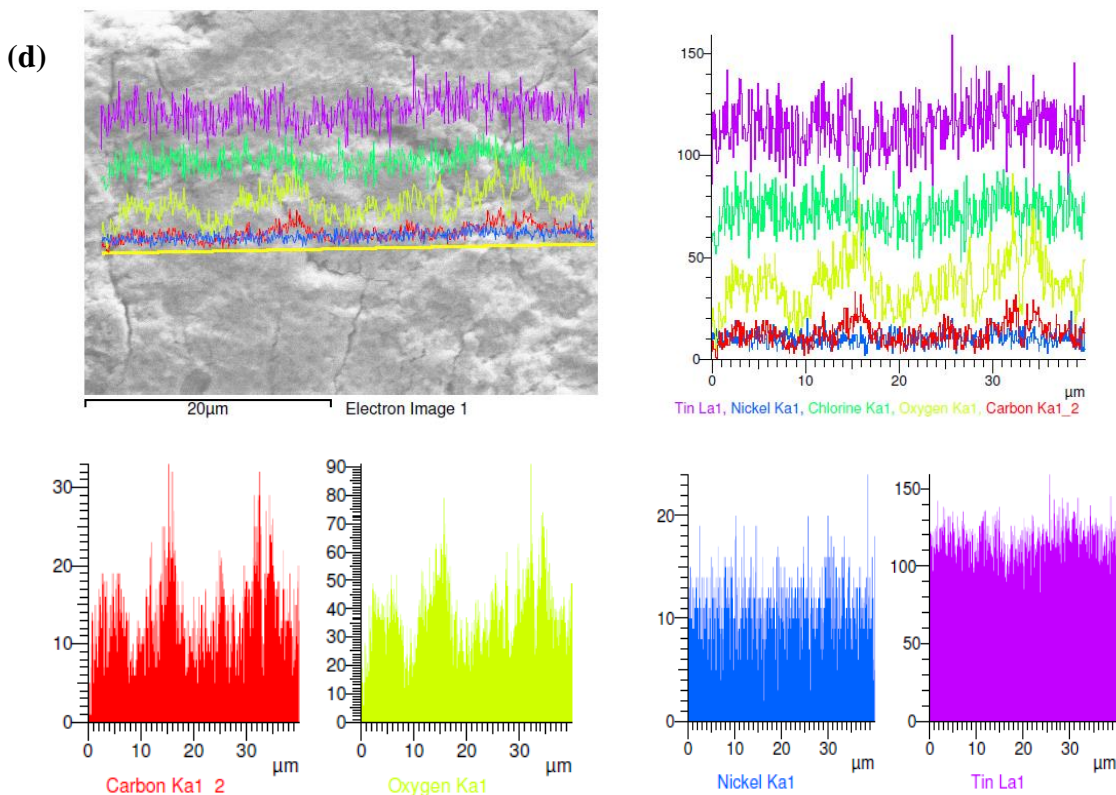


*Figure-3.2.7: FESEM micrograph of (a) NS3 and (b) NS3R3, line profile image and elemental distribution from FESEM micrograph of (c) NS3 and (d) NS3R3*

Besides these, the introduction of rGO in this NS3 matrix exhibited a walnut type of morphology with cracks across the grain boundaries (Fig. 3.2.7b) that induced some intrinsic strains and resulted in phase transition, as observed in XRD. Additionally, due to the porous, ultrathin 2D structure of rGO, the metal oxide particles were observed to be well dispersed on the rGO network. The EDX line profile scanning of NS3 revealed the uniform presence of Sn in the nanocomposite as a base material in which Ni and O were almost homogeneously dispersed (Fig. 3.2.7c). In the case of NS3R3, an additional presence of C was also detected in line profile imaging (Fig. 3.2.7d).

The bright field TEM (BFTEM) image of NS3 (Fig. 3.2.8a) exhibited the existence of two different types of morphologies [29, 30], as evidenced by the earlier FESEM micrographs. The HRTEM fringes of NS3 (Fig. 3.2.8b) correlated to (110) and (101) planes of  $\text{SnO}_2$ . The SAED pattern of NS3 (Fig. 3.2.8c) showed the diffraction from the (110), (101), and (211) planes of  $\text{SnO}_2$  and (200) plane of NiO. The BFTEM image of NS3R3 (Fig. 3.2.8d) showed a dispersed amorphous layer of rGO on which the metal oxide particles were dispersed.



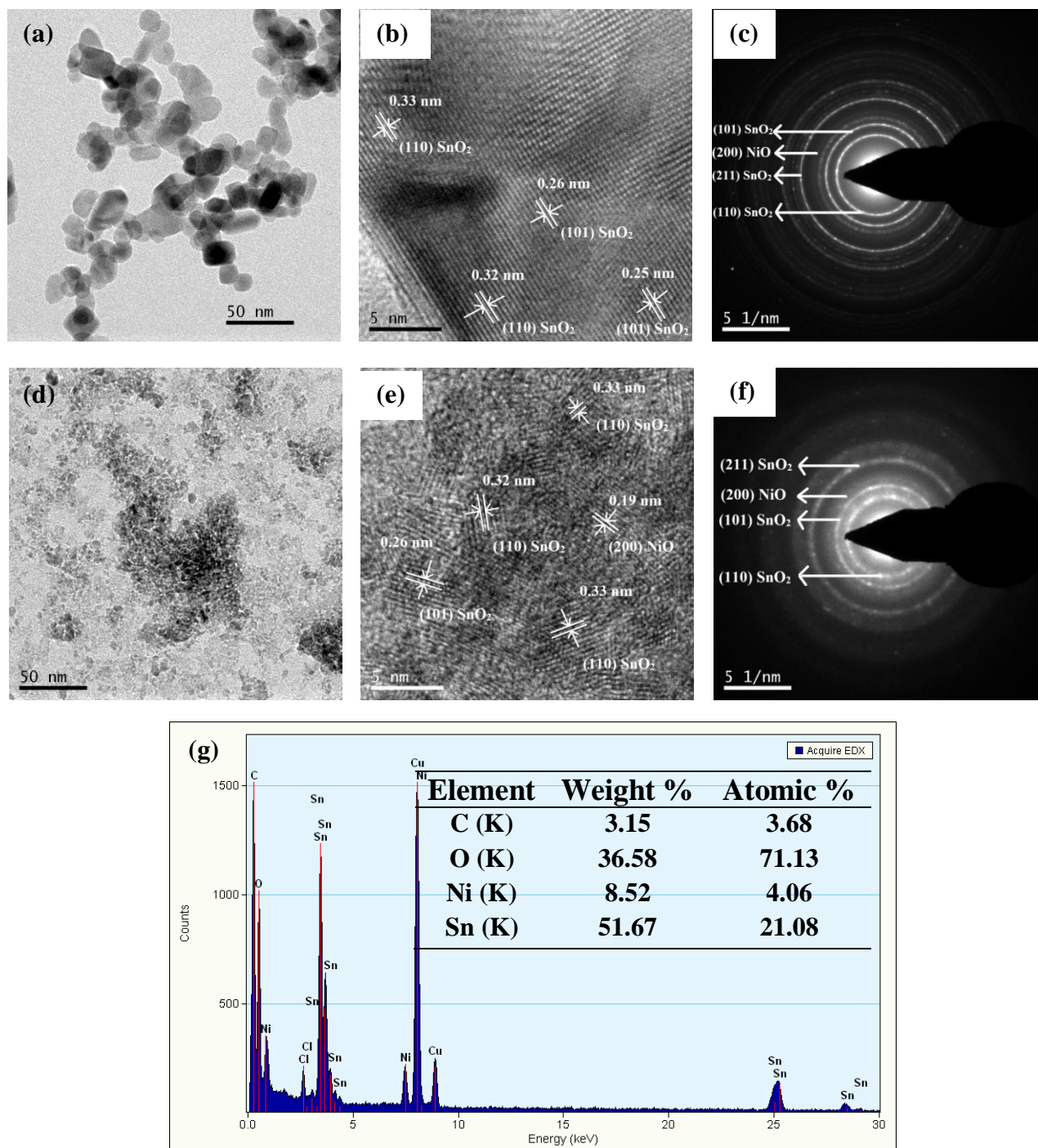


Figure -3.2.8: (a) BFTEM image, (b) HRTEM image, (c) SAED pattern of NS3; (d) BFTEM image, (e) HRTEM image, (f) SAED pattern, and (g) EDX spectrum of NS3R3

In the HRTEM image (Fig. 3.2.8e), the lattice fringes were similar to that of NS3. Additionally, a peak corresponding to the (200) plane of NiO was observed. The SAED pattern of NS3R3 (Fig. 3.2.8f) deduced similar properties as that of NS3. The EDX analysis of the NS3R3 sample (Fig.

8g) exhibited the presence of principle components as of Sn, Ni, O, and C (Cu from the mounting grid). The quantitative results obtained from the EDX analysis (inset of Fig. 3.2.8g) corresponded to the composition of the sample.

The chemical binding states of the components of NS3 (Fig. 3.2.9a) and NS3R3 (Fig. 3.2.9b) were determined by surface scan XPS analysis and deconvolution of the respective elemental peaks. The deconvoluted peak position of the respective elements (Sn, Ni, and O) showed a slight shift after rGO incorporation in the NS3 matrix (Fig. 3.2.9 c, e, and g).

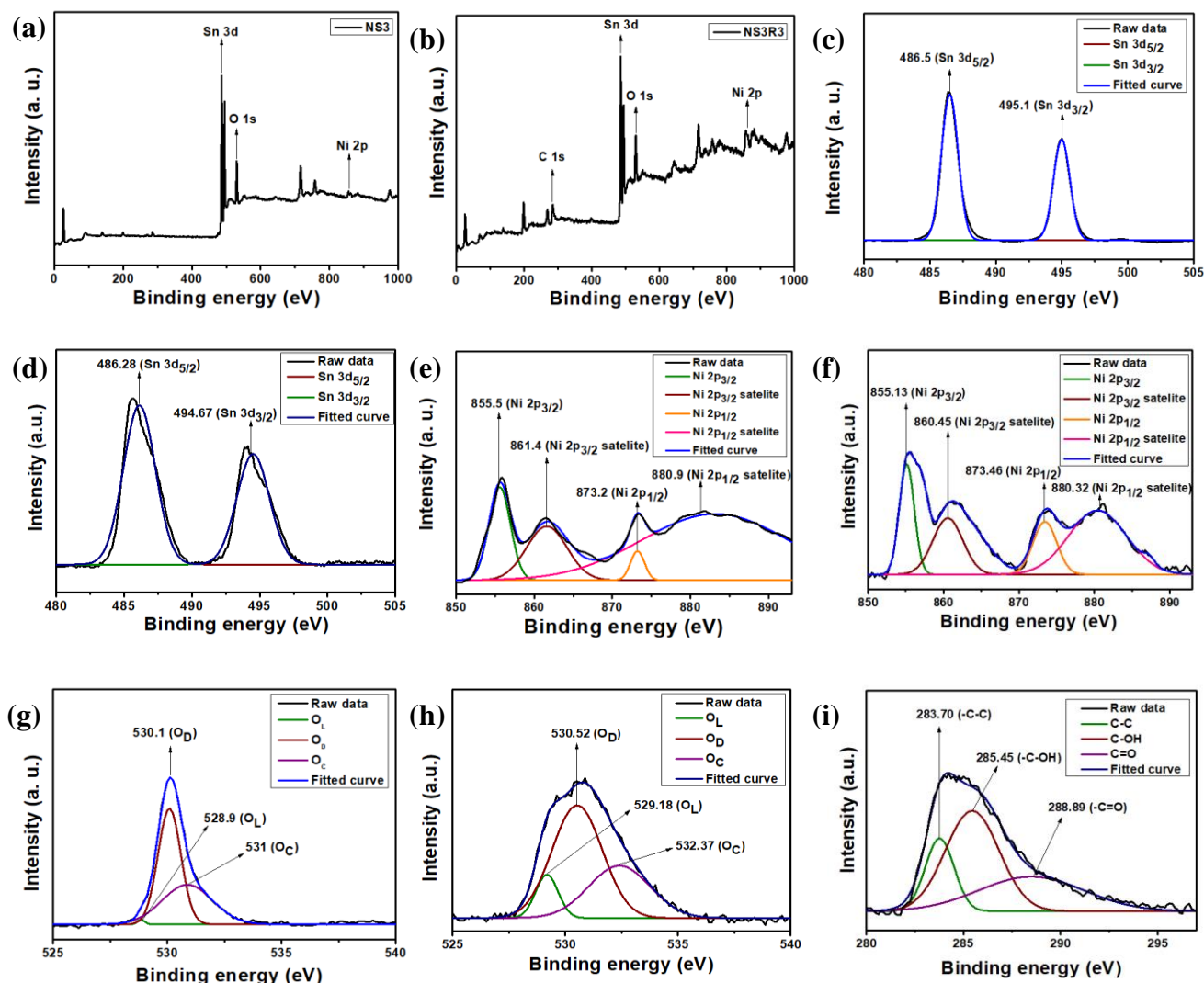


Figure-3.2.9: XPS full scan survey spectra (a) NS3 and (b) NS3R3, core level analysis: Sn 3d: (c) NS3 and (d) NS3R3, Ni 2p: (e) NS3 and (f) NS3R3, O 1s: (g) NS3 and (h) NS3R3, and C 1s: (i) NS3R3

The core level scan of Sn 3d (Fig. 3.2.9d) showed two peaks centered at 486.28 eV and 494.67 eV, corresponding to Sn 3d<sub>5/2</sub> and Sn 3d<sub>3/2</sub>, respectively [15]. The splitting of ~ 8.39 eV between two spin-states ensured that Sn was present in the +4 oxidation state. The core-level spectrum of Ni 2p (Fig. 3.2.9f) was deconvoluted into two prominent peaks and their corresponding satellite peaks. The two main peaks were observed at 855.13 eV for Ni 2p<sub>3/2</sub> and 873.46 eV for Ni 2p<sub>1/2</sub>, with their satellite peaks at 860.45 eV and 880.32 eV, respectively. No peak at ~ 853 eV confirmed the absence of Ni in the metallic state, i.e., Ni was oxidized entirely [31]. Moreover, the spin-orbit splitting of ~ 18.33 eV ensured the oxidation state of Ni was +2. The deconvoluted O 1s core-level spectrum (Fig. 3.2.9h) gave rise to three peaks [32] corresponding to different types of oxygen. The peak centered at 529.18 eV was for lattice O bonded with different metal ions, whereas the peak at 530.52 eV was generated from the oxygen defects/vacancies present in the nanocomposites. Another peak at 532.37 eV symbolized O<sup>x-</sup> ions originated from different chemisorbed oxygenated ions on the surface of the sensing material. Quantitative analysis of the area under the individual peaks in O 1s revealed that the NS3R3 nanocomposite consisted of ~ 9.91% lattice O atoms with ~ 57.55% contribution from different oxygen vacancies, ~ 32.53% chemisorbed O was present. Finally, deconvolution of the C 1s spectrum (Fig. 3.2.9i) yielded three peaks for different types of carbon [22]. The peaks at 283.70 eV for -C=C bonds, 285.45 eV for -C=O/-C-O-C- linkage, and 288.89 eV for -C=O bonds.

The optical characterizations of the nanocomposites were done by UV-visible absorption spectroscopy and photoluminescence spectroscopy. The absorption spectra were used to evaluate the band gap of the nanocomposites with the help of the Tauc equation. In UV-visible absorption spectra (Fig. 3.2.10a), pristine samples showed the presence of broad peaks; for SnO<sub>2</sub> it was at ~ 304.57 nm and for NiO at 333.11 nm. In NS3 nanocomposite the absorption peak was broadened at 286.91 nm [33, 34]. Further functionalization with rGO flattened the peak and it was blue-shifted to ~ 262.75 nm. The calculated band gap from the Tauc plot was ~ 2.61 eV for pristine SnO<sub>2</sub> (Fig. 3.2.10b) and ~ 2.57 eV for pristine NiO (Fig. 3.2.10c), which resembled the reported band gap value. The band gap energy of NS3 nanocomposite was calculated as ~ 3.74 eV (Fig. 3.2.10d), which was closely matched the pristine SnO<sub>2</sub> band gap. On the other hand, further decoration of NiO-SnO<sub>2</sub> nanocomposite (NS3) with rGO increased the band gap value of NS3R3 to ~ 3.83 eV (Fig. 3.2.10e). According to the quantum confinement effect, the increased dislocation density and microstrains of nanocomposites lead to the quantification of electronic



levels in the conduction band and consequent hole levels in the valence band. This resulted in the shifting of the band edge away from each other, which increased the optical band gap energy.

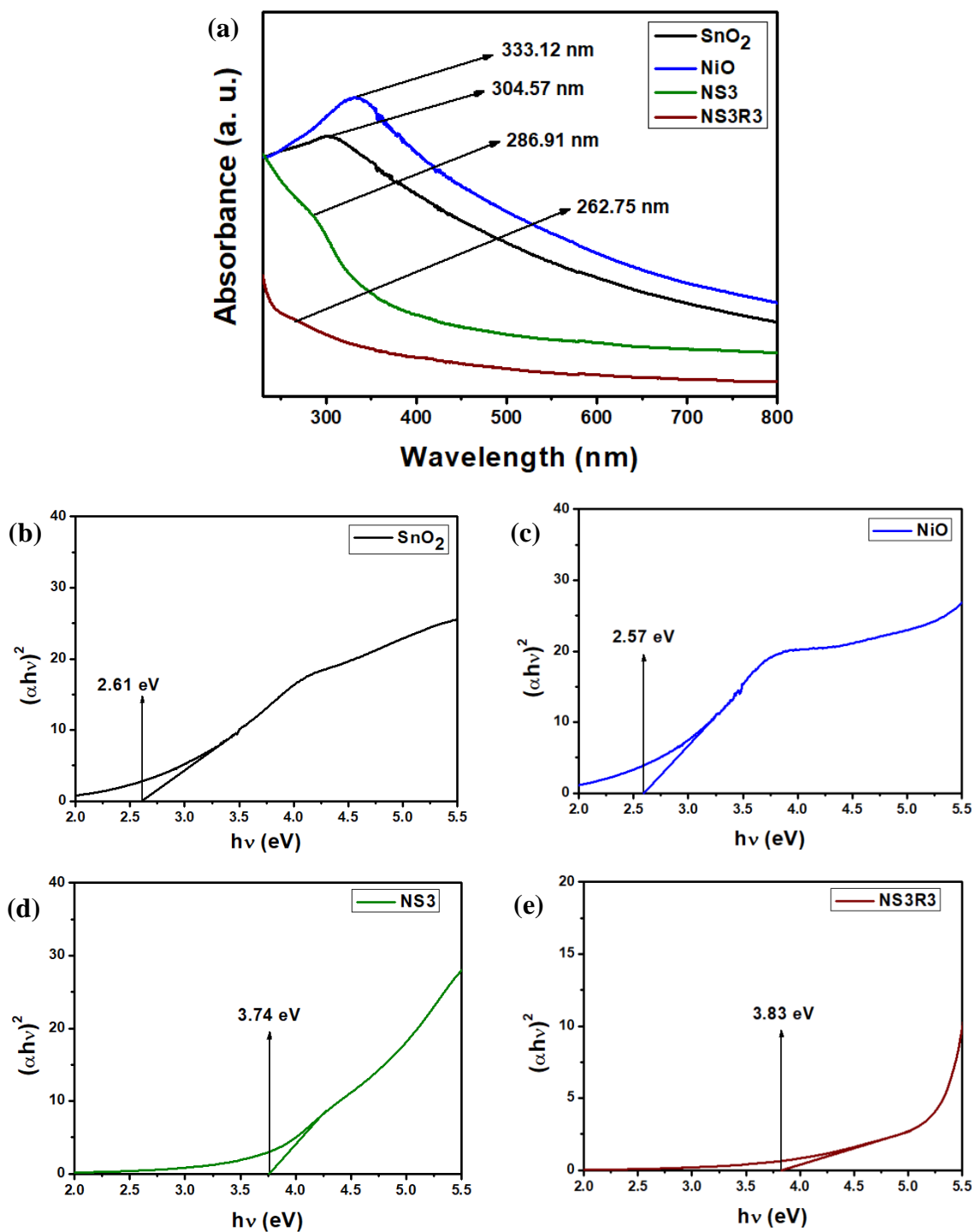


Figure-3.2.10: (a) UV-Visible spectra of pristine SnO<sub>2</sub>, NiO, NS3, and NS3R3, Tauc plot of (b) pristine SnO<sub>2</sub>, (c) pristine NiO, (d) NS3, and (e) NS3R3

The photoluminescence (PL) spectra (Fig. 3.2.11) for pristine  $\text{SnO}_2$ , NS3, and NS3R3 samples were recorded with an excitation wavelength of  $\sim 325$  nm at room temperature. All the samples showed similar spectral patterns with a gradual decrease in intensities.

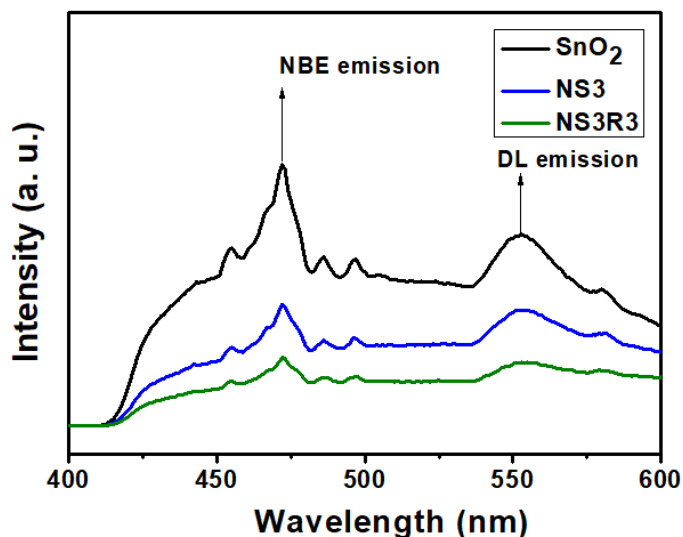


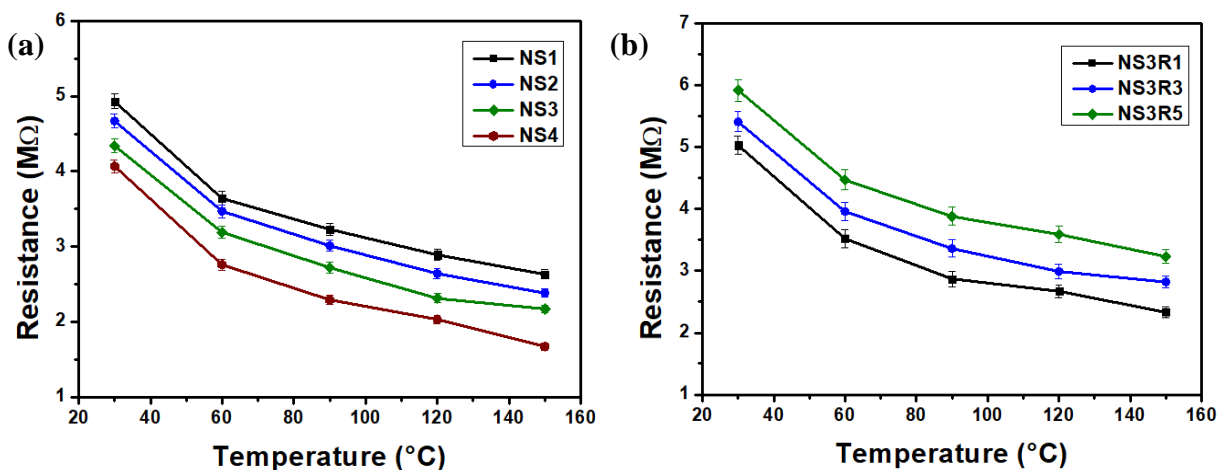
Figure-3.2.11: Photoluminescence spectra of pristine  $\text{SnO}_2$ , NS3, and NS3R3

In pristine nanocrystals, the recombination rate was maximum due to the proximity between the charge carriers (hole and electron), resulting in highly intense PL signatures. Upon rGO introduction in the matrix, the recombination rate subsided as the separation between the charge carriers increased, accounting for the dampening of emission intensities. The high intense peak centered at  $\sim 455$  nm might be aroused due to metal oxides' near band edge (NBE) emission [35, 36]. The electron-hole radiative recombination in nanocrystals gave rise to the NBE emission peak. Another emission peak at  $\sim 556$  nm corresponded to deep-level emission (DL), originating from the imperfections created in the pristine metal oxide matrix via functionalization.

### 3.2.3.2. Gas sensing performance study:

Optimization of the operating temperature of a sensor is an integral part of gas sensing measurement. Hence, initially, the base resistances (i.e., resistance in the air) of the sensors were recorded as a function of temperature. The sensor fabricated from the pristine oxides ( $\text{SnO}_2$  and  $\text{NiO}$ ) showed a very high resistance at ambient temperature as they required greater amount of activation energy as compared to nanocomposites. So, they were not included in this (Fig.

3.2.12a) graph. The NiO-SnO<sub>2</sub> nanocomposites revealed base resistance at ~ 5 MΩ at ambient temperatures. After rGO introduction the corresponding nanocomposites showed slightly increased base resistance. The sensors exhibited a gradual decrease of base resistances with an increase in temperature (Fig. 3.2.12 a, b), according to the semiconducting characteristic of metal oxide. Concurrently, the sensing responses of the sensors were also monitored in the presence of ~ 10 ppm acetone at these operating temperature ranges. All the sensors showed p-type response in the presence of experimental reducing gases with a bell-shaped profile of sensing response as a function of temperature. The sensing response of the NS3 sensor was highest compared to other NS-group of sensors (Fig. 3.2.12c), perhaps due to the formation of optimized solid-solution composite, beyond which segregation of metal oxides across the grain boundary deteriorated the sensing performances. It was also observed that the sensing response was amplified upon the incorporation of rGO in the NS3 nanocomposite (Fig. 3.2.12d). The rGO concentration was optimized to ~ 3 wt%, as per the sensing responses. A further increase in rGO concentration diminished the sensing responses as the agglomeration of rGO hindered the electronic transportation in nanocomposite [1]. Referring to the bell-shaped nature of the sensing response vs. temperature curve [37], the room temperature sensing response of the sensors was increased with an increase in temperature followed by a decrease after 100°C. However, the magnitude of enhancement of sensing response was too minimal to be highlighted; therefore, the detailed sensing performances of NS3 and NS3R3 sensors were measured at room temperature throughout.



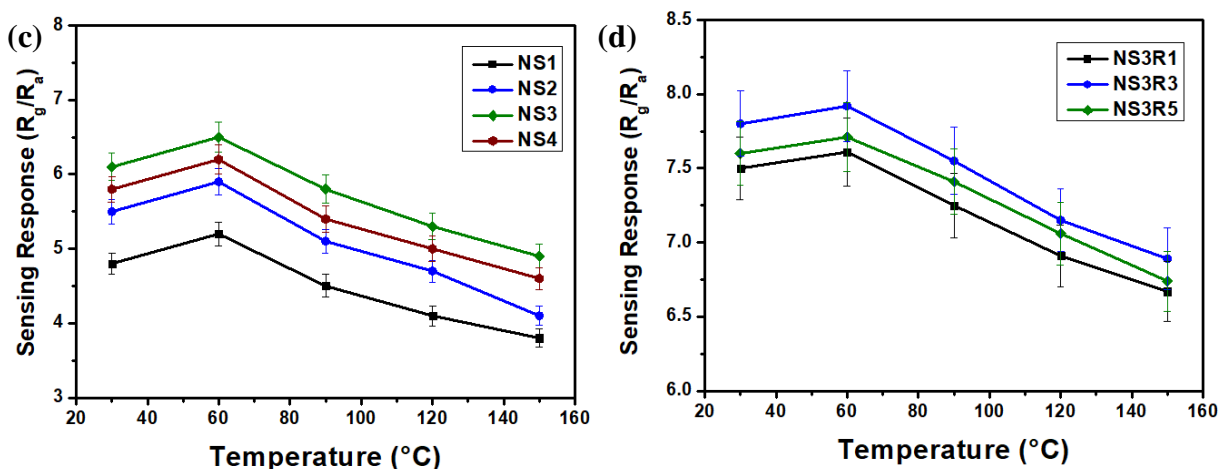


Figure-3.2.12: Change in resistance (a), (b) and change in sensing responses (c) (d) as a function of temperature for NiO-SnO<sub>2</sub> nanocomposite sensors and rGO decorated NS3 sensors respectively

The dynamic sensing response (Fig. 3.2.13) of the fabricated NS3 and NS3R3 sensors was measured at room temperature in various concentrations (1 to 10 ppm) of acetone. The NS3 sensor exhibited a sensing response of  $\sim 6.1$  in the presence of  $\sim 10$  ppm acetone, which was enhanced to  $\sim 7.8$  for the NS3R3 sensor at room temperature.

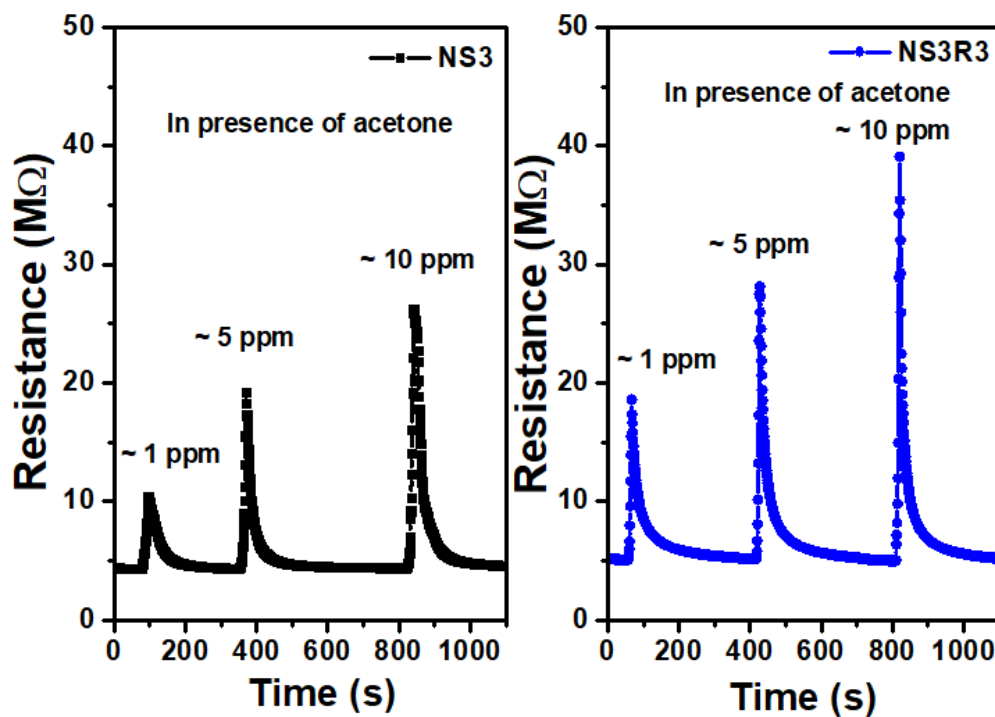
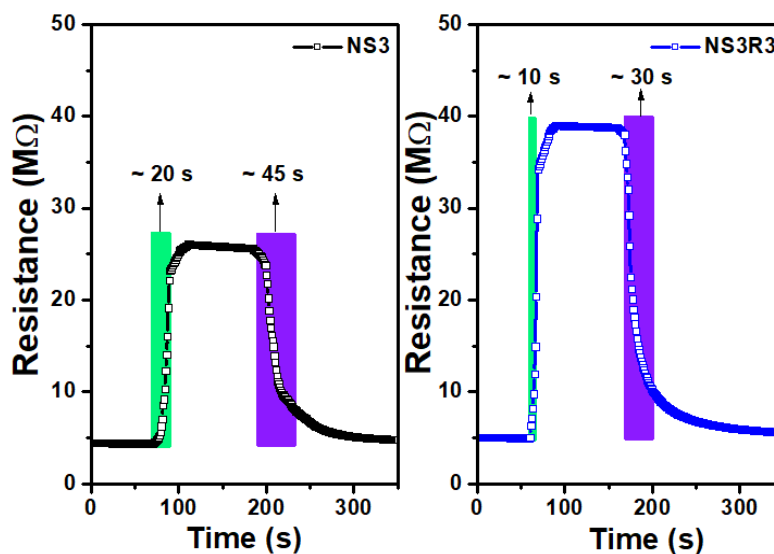


Figure-3.2.13: Dynamic sensing response in presence of acetone at operating temperature ( $30 \pm 5^\circ\text{C}$ )

Similarly, the sensing response in the presence of  $\sim 5$  ppm acetone was  $\sim 4.4$  for NS3 and  $\sim 5.4$  for NS3R3. These sensors could also detect as low as  $\sim 1$  ppm acetone under the same experimental conditions. The recorded sensing response in the presence of  $\sim 1$  ppm acetone for NS3R3 was  $\sim 3.6$  compared to  $\sim 2.4$  for NS3.

The response and recovery time of a sensor is defined as the time required attaining  $\sim 90\%$  of the steady-state resistance from baseline resistance and that of steady-state resistance to baseline resistance, respectively [38]. The saturated p-type sensing responses of the NS3 and NS3R3 sensors were obtained from acetone pulse of  $\sim 20$  s and  $\sim 10$  s respectively which were noted as response time and the consequential recovery times of the sensors were  $\sim 45$  s for NS3 and  $\sim 30$  s for NS3R3, without purging of any external gas (Fig. 3.2.14). The mesoporous defect-rich surface property, which facilitates adsorption/desorption of gases, might be responsible for such quick response/recovery time at ambient condition.



*Figure-3.2.14: Response and recovery time in presence of  $\sim 10$  ppm acetone*

The fabricated NS3 and NS3R3 sensors also exhibited considerable sensing responses in presence of different concentrations of ethanol at room temperature (Fig. 3.2.15). The sensing response of NS3 sensor in presence of  $\sim 10$  ppm ethanol was  $\sim 2.8$  which was increased to  $\sim 4.1$  for NS3R3 sensor, whereas, in presence of  $\sim 5$  ppm ethanol, sensing response was  $\sim 2.1$  of NS3 sensor which reached to  $\sim 2.8$  for NS3R3 sensor. Additionally, the sensors could sense  $\sim 1$  ppm of ethanol; for the NS3 sensor, the sensing response of  $\sim 1.3$  reached  $\sim 1.8$  for the NS3R3 sensor.

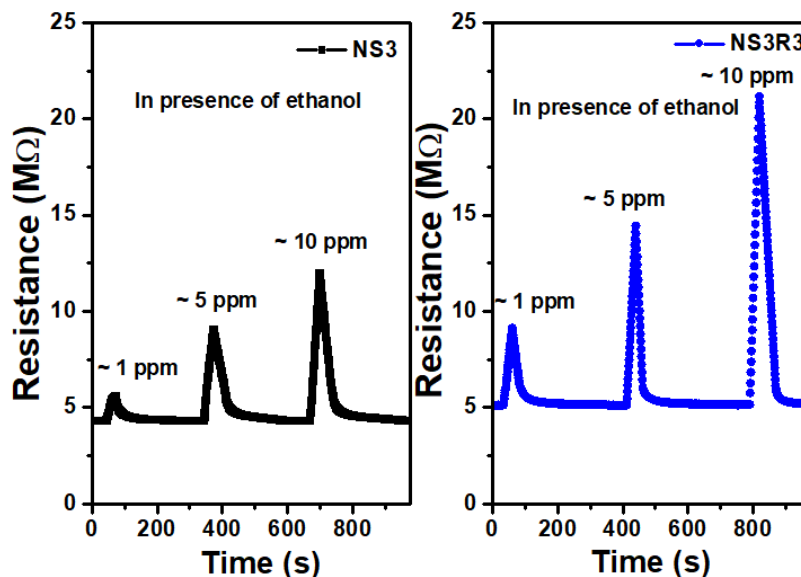


Figure-3.2.15: Dynamic sensing response towards ethanol at operating temperature ( $30 \pm 5^\circ\text{C}$ )

Similarly, the response/recovery time of the sensors for ethanol sensing was also calculated from the steady-state curves (Fig. 3.2.16). It was observed that the response time of the sensors ( $\sim 30$  s for NS3 sensor and  $\sim 25$  s for NS3R3 sensor) in presence of ethanol were little bit longer, perhaps due to greater bond dissociation energy of the ethanol ( $\sim 436 \text{ kJmol}^{-1}$ ) compared to acetone ( $\sim 393 \text{ kJmol}^{-1}$ ) [39], also might be accountable for the slowed recovery time of the sensors ( $\sim 65$  s for NS3 sensor and  $\sim 55$  s for NS3R3 sensor).

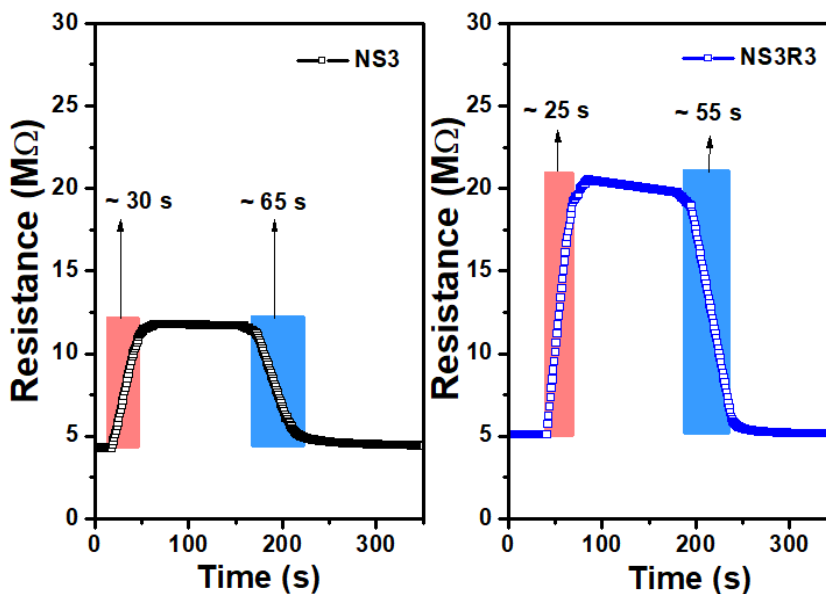
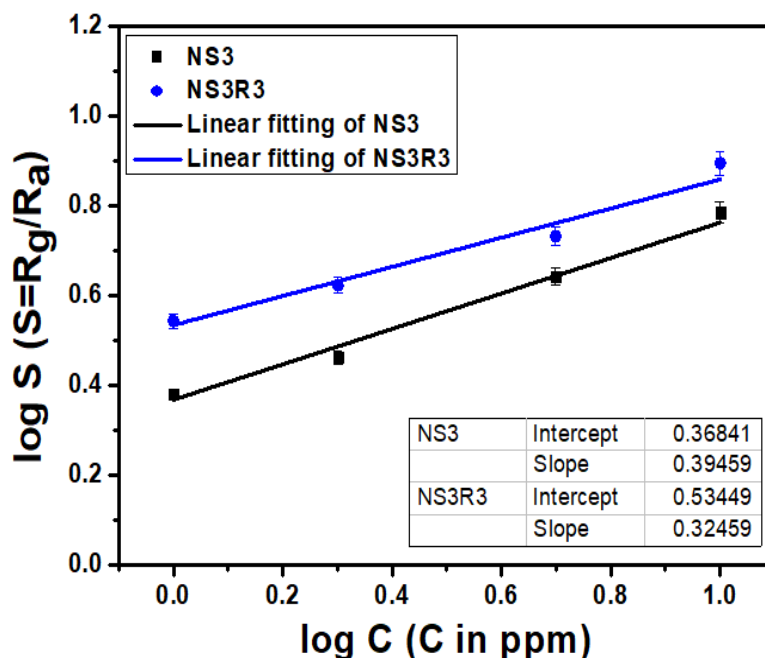


Figure-3.2.16: Response and recovery time in presence of  $\sim 10$  ppm ethanol

As stated earlier in Chapter 3.1 (Section 3.1.3.3), the interaction between sensing material and analyte gas could be determined from the  $\log S$  vs.  $\log C$  curve. From the slope ( $\beta$ ) of the linear fitting of the abovementioned plot the nature of adsorption would be perceived. According to literatures,  $\beta$  value is greater than 1 for chemisorption, and a value lesser than 1 indicates physisorption [40]. In this work, the value of  $\beta$  obtained from the slope of the linear fitting of the  $\log S$  vs.  $\log C$  graph (Fig. 3.2.17) was 0.7, and thereby, it could be inferred that here predominant physisorption prevailed.



*Figure-3.2.17:  $\log S$  vs.  $\log C$  plot of NS3 and NS3R3*

According to the Power Law of gas sensing [41] (equation – 3.2.1), the LOD value of the NS3R3 sensor was theoretically calculated.

$$C_L = (k \times S_b)/S \quad \dots\dots\dots (3.2.1)$$

$C_L$  is the lowest detection limit concentration of the sensor,  $S_b$  is the standard deviation of base resistances of the sensors at room temperature,  $S$  is the average sensing response, and  $k$  is the constant having a value of 3 recommended by IUPAC. The theoretically calculated value obtained for LOD was 0.065 ppm.

The optimized sensors were exposed to higher concentrations of acetone and it was observed that the sensing responses of the sensors gradually increased up to  $\sim 100$  ppm, and after that, the

sensing responses became almost invariant (Fig. 3.2.18). It is evident that the available active sites on the sensing materials surface were almost occupied by the analyte molecules at a high concentration of acetone (~ 100 ppm), and thereby sensing response reached almost saturation.

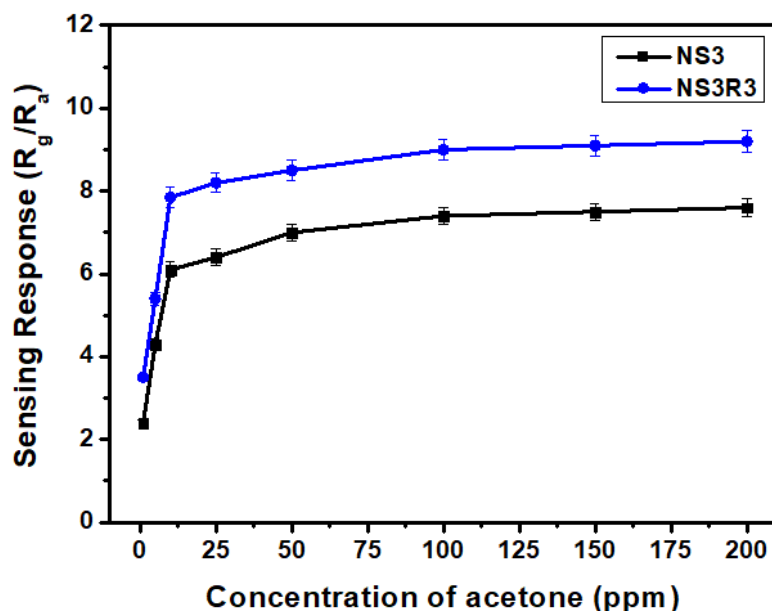


*Figure-3.2.18: Saturation curve of NS3 and NS3R3*

Generally, the base resistance of a sensor gradually decreases with an increase in relative humidity. Consequently, the sensing response also degrades due to hydroxyl groups' inhibition of active sites [42]. As the sensor is exposed to an ambient atmosphere with a plethora of water (vapour) molecules, the water molecules dissociate into  $H^+$  and  $OH^-$  ions. At lower humidity levels, the chemisorption (predominantly mono-layer adsorption) of hydroxyl groups leads to charge transportation. However, at a higher humidity condition, the excess water molecules undergo physisorption (multi-layer adsorption) over the chemisorbed hydroxyl layer and take part in ion hopping (Grotthus adsorption mechanism) [43]. Thus, significantly fewer oxygen ions could be adsorbed at an elevated humidity level due to the lack of vacant active sites on the sensing material surface. Thus, the decrease in the number of trapped electrons from the conduction band decreased base resistance and sensing response.



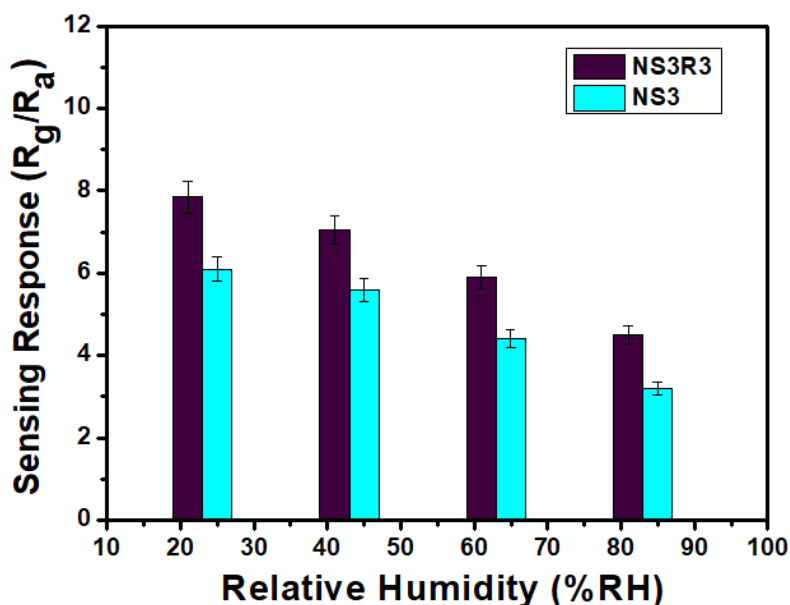


Figure-3.2.19: Change of sensing response of NS3 and NS3R3 as function of %RH

Nevertheless, at lower humidity conditions, the abundance of active sites enhanced the adsorption of atmospheric oxygen, and simultaneously, the sensing response improved. In this work, solutions of different % RH were prepared using saturated solutions of different inorganic salts mentioned elsewhere in the literature [44]. The fabricated sensors (NS3, NS3R3) were seasoned at respective % RH for ~ 12 hours and then used for sensing performance study at room temperature. From the recorded results presented in Fig. 3.2.19, it was perceptible that, in agreement with the previous discussion, our sensors also manifested a decrease in sensing response with the increase of % RH.

The NS3 and NS3R3 sensors showed minimal response towards ~ 10 ppm concentration of different gases like ammonia, methane,  $H_2S$ , formaldehyde, and CO (Fig. 3.2.20) compared to acetone and ethanol. The response of sensors towards acetone can be summarized by several factors [45, 46], mainly from the polarity of molecules and bond energy perspectives. Among the other molecules, acetone has the highest polarity (~ 2.91 D) and least bond dissociation energy (~ 393  $\text{kJmole}^{-1}$ , except ammonia ~ 391  $\text{kJmole}^{-1}$ ) as well as it has a maximum collision diameter (~ 0.616 nm) [47] which restricts the acetone molecules to permeate through the pores of nanocomposites.

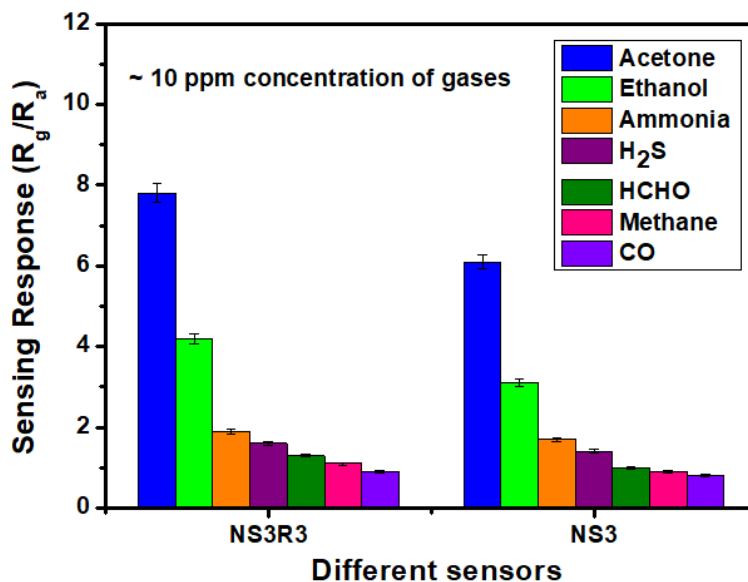


Figure-3.2.20: Selectivity curve for NS3 and NS3R3 sensors

In order to check the stability of the sensors, base resistance and sensing response of NS3 (Fig. 3.2.21a) and NS3R3 (Fig. 3.2.21b) sensors were recorded at room temperature in the presence of ~ 10 ppm acetone at an interval of 10 days for ~ 100 days span. There observed almost consistent sensing responses with minimal deviation ( $\pm 5\%$ ) that made it suitable for its real-time applications.

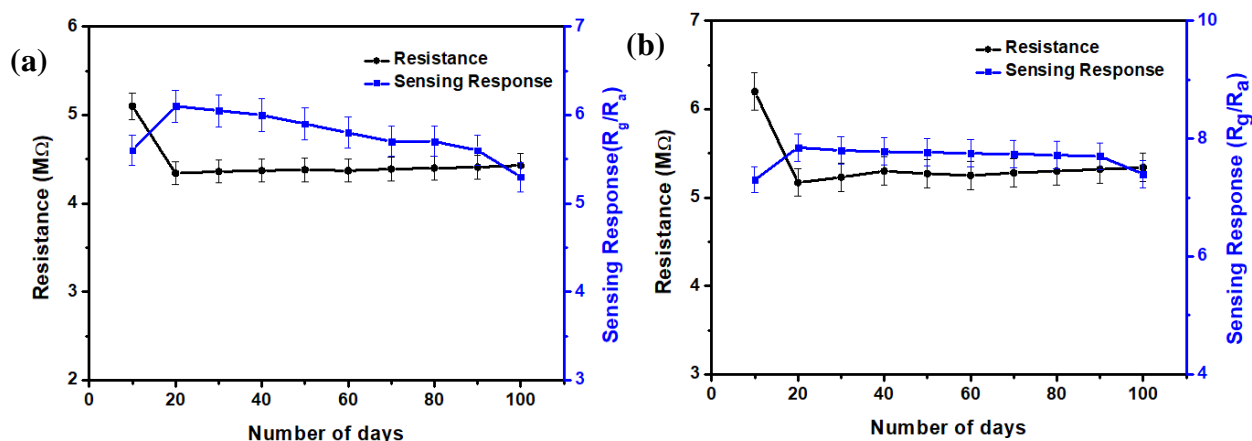
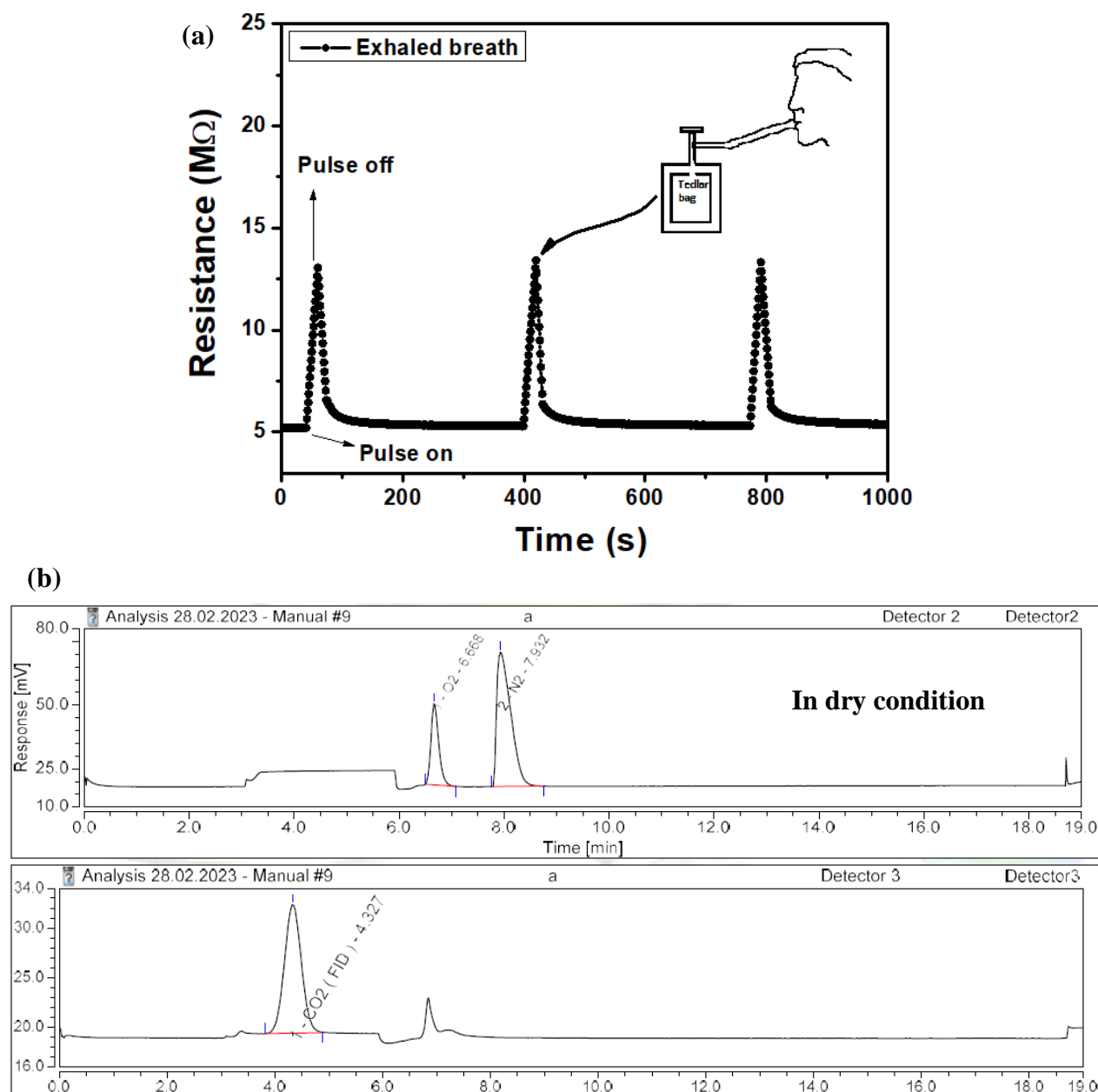


Figure-3.2.21: Stability curve of base resistance and sensing response of (a) NS3 and (b) NS3R3

The developed optimized sensor exhibited a reasonable sensing response ( $\sim 3.6$ ) in  $\sim 1$  ppm commercial acetone. Hence, it was used to detect breath acetone. Therefore, the exhaled human

breath of healthy person was collected in a ~ 1L Tedlar bag and fed to NS3R3 sensor. A p-type sensing response of ~ 2.5 was observed (Fig. 3.2.22a). This observed sensing response was relatively consistent with the previous result for ~ 1 ppm commercial acetone. However, the high moisture content in exhaled breath accounted for low response [48, 49]. This collected breath sample was also analyzed by an in-house GCMS system (Agilent 5977B GC/MSD) and the concentration obtained was < 1 ppm. Therefore it could be correlated (Fig. 3.2.22 b, c) that the NS3R3 sensor conceivably implemented for non-invasive detection of diabetes.



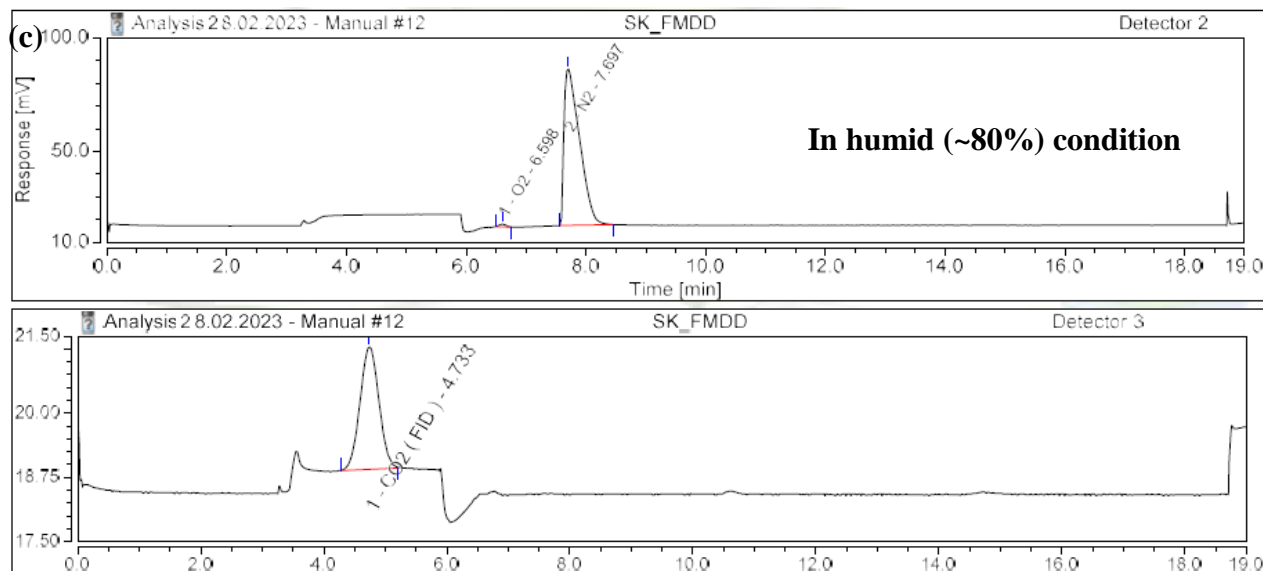


Figure-3.2.22: (a) Sensing response of NS3R3 in presence of human breath sample, Evidence of acetone oxidation on sensor surface from gas chromatography in (b) dry condition, (c) humid condition

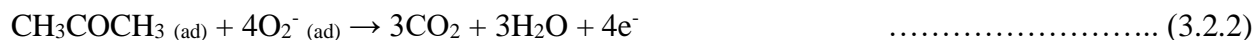
## 3.2.3.3. Gas sensing mechanism:

### 3.2.3.3.1. Electron depletion model:

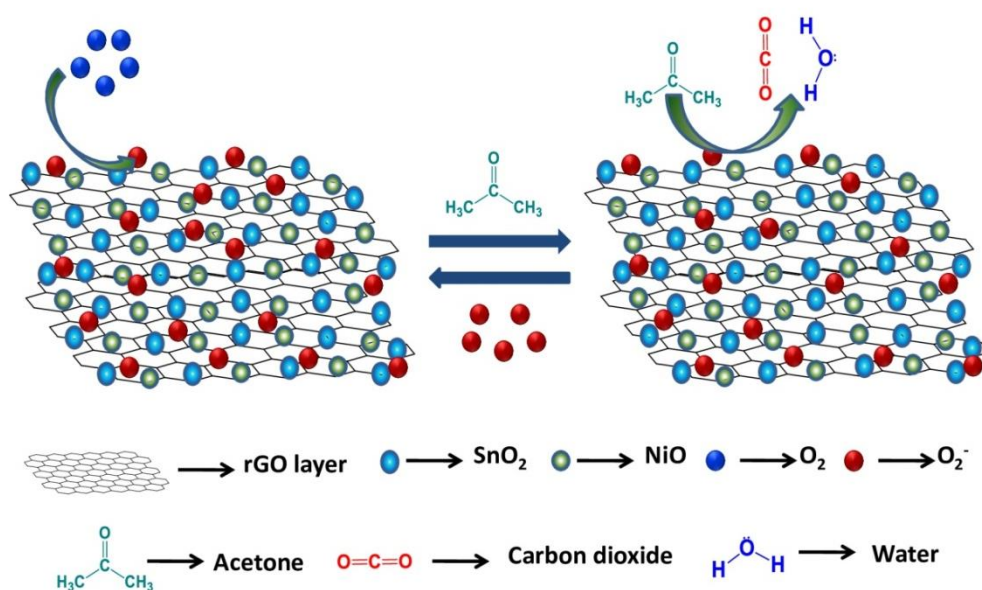
Conventionally, the charge carriers are negatively charged electrons for n-type semiconductors, whereas, for p-type semiconductors, they are positively charged holes [50]. Here, in NiO-SnO<sub>2</sub> nanocomposite across the p-n heterojunction domain, the charge carriers migrated according to their concentration gradient and attained Fermi-level equilibrium via hole-electron recombination. Incorporating rGO in this metal oxide matrix substantially improved the recombination rate by forming a p-p-n-type ternary system. In an ambient atmosphere, due to profusion of oxygen, they got adsorbed on the sensing material surface, and depending on the operating temperature of the sensor, they were converted to different oxygenated ions (O<sub>2</sub><sup>-</sup> primarily formed at room temperature) by scavenging electrons from the conduction band [51]. This developed depletion and accumulation layers across the n-type and p-type metal oxides, respectively. As a result, electron density at the sensing material surface was reduced, potential energy barrier height increased, and a high base resistance was recorded without any gas.

In the presence of reducing gas (viz., acetone, ethanol), there initiated a red-ox reaction between these chemisorbed oxygenated ions and analyte gas molecules (Fig. 3.2.23). Thereby, the gas molecules consumed the oxygen ions to oxidize themselves to CO<sub>2</sub> and water [15, 48].

Simultaneous removal of oxygen from the sensing material surface revert the trapped electrons to the conduction band. This, in turn, reduced the thickness of the depletion layer and accumulation layer, and hole-electron recombination resumed. Due to the scarcity of electrons in the conduction band, resistance increased, and a p-type sensing response was recorded.



As evidence of acetone oxidation on sensing material surface in dry and humid conditions (~ 80% humidity), the emitted gases after sensing experiments were collected in ~ 1-liter tedlar bags and injected in a Gas chromatographic instrument setup (Thermo Scientific Trace 1110 GC CO<sub>2</sub> detection was done using FID coupled with Methanizer). Both the test results confirmed the presence of CO<sub>2</sub> (Fig. 3.2.22 b, c), though the peak intensity of detected CO<sub>2</sub> in humid conditions is lower than the dry one. Due to large band-gap energies, room temperature sensing responses were hardly found in pristine metal oxides. Compositing between an n-type and a p-type metal oxide introduced impurity levels between the valence and conduction bands, accounting for room temperature sensing response. However, further addition of rGO in NiO-SnO<sub>2</sub> nanocomposite promoted the charge carrier mobility. Additionally, extended defect-rich surface properties of rGO also facilitated the adsorption of gas molecules onto the sensing material surface and these would lead to the improvement of sensing performance at room temperature.



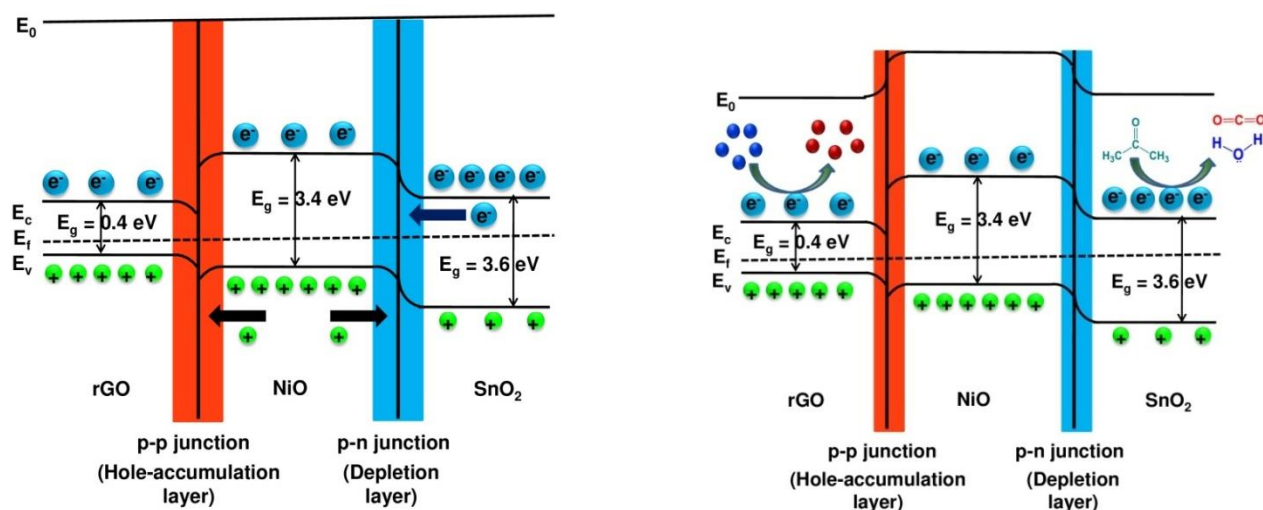


Figure-3.2.23: Illustration of acetone sensing mechanism of fabricated sensors

### 3.2.3.3.2. Impedance spectroscopy:

To comprehensively illustrate the electrical contributions of various electrical components (grain, grain boundary, and electrode interface) of a polycrystalline metal oxide semiconductor [51, 52],  $Z'$  and  $Z''$  data were collected at room temperature ( $\sim 30 \pm 5^\circ\text{C}$ ) over a broad frequency range (100 Hz to  $10^6$  Hz) for the NS3R3 sensor both in the absence and presence of  $\sim 10$  ppm acetone (Fig. 3.2.24a). It was observed from the Nyquist plot that there was only a complete single semicircle with a small tail appearing at the end of it. These suggested that most of the electrical contribution was from grains, with a minimal contribution coming from grain boundaries existing between the NiO and SnO<sub>2</sub> nanoparticles and no electrode interface contribution recorded. Furthermore, at room temperature, the impedance arcs were a part of large semicircles and slightly deformed from the real impedance axis. These traits of the Nyquist plot certified that the imperfections in semiconductor-based materials originated from the inhomogeneities and defect sites present in the nanocomposites.

The corresponding circuit diagram (inset of Fig. 3.2.24a) was modeled by using constant phase element (CPE), parallelly connected resistance, and Warburg element (open) in a series analogous to marginally deformed semicircles. This kind of semicircle resulted from a non-ideal Debye-type of relaxation caused by the presence of inhomogeneous surface phenomena [51]. Moreover, the existence of a small tail at the end of the first semicircle was explained with the Warburg

element, which was associated with the diffusion current in the charge transfer process. The tiny appearance of the diffusion component suggested minimal diffusion of charges between grain and grain boundary regions. The Nyquist plots at different experimental conditions (in the absence and presence of acetone) were fitted using ZView2 software.

Additionally, for spectroscopic plots,  $Z'$  and  $Z''$  were plotted separately against frequency in the absence and presence of acetone at room temperature. The variation of resistive component ( $Z'$ ) with frequency for NS3R3 (Fig. 3.2.24b) demonstrated that in the low-frequency region, the curves were almost constant and gradually decreased with an increase in frequency. At higher frequencies, the individual dispersed plots suddenly decreased and converged together.

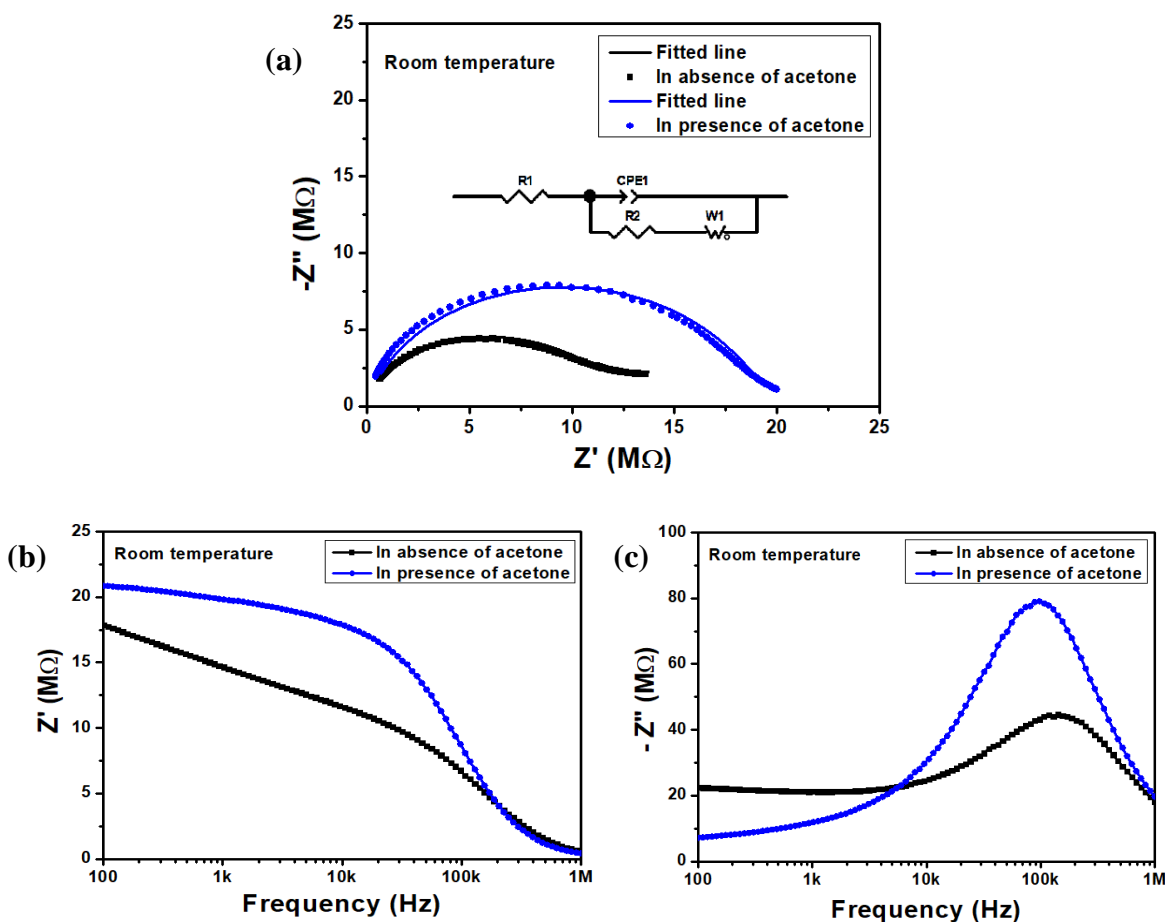


Figure-3.2.24: (a) Nyquist plot, (b) Variation of  $Z'$  with frequency, (c) Variation of  $(-Z'')$  with frequency of NS3R3 sensor in absence and presence of  $\sim 10$  ppm acetone

The plot of the reactive component of impedance ( $Z''$ ) with frequency (Fig. 3.2.24c) displayed maxima corresponding to relaxation frequency for the charge carriers' concentration alteration at

the grain region. It was evident that the maxima shifted to low frequency in the presence of acetone molecules, hinting that lesser activation energy was required for the gas-sensing process. It was worth mentioning that the conversion of atmospheric oxygen to oxygenated ions by scavenging electrons from the nanocomposite's conduction band was less facile than reverting electrons to the conduction band upon interaction with gas molecules. This might account for the excellent sensing response of the NS3R3-based sensor with rapid response/recovery time. The comparative sensing performance of some literature works with the developed rGO decorated NiO-SnO<sub>2</sub> nanocomposite sensor was tabulated here (Table 3.2.1).

Table – 3.2.1: Comparison of different VOC sensors based on NiO-SnO<sub>2</sub> nanocomposites:

Sensing material	Synthesis technique	Sensing gas	Working temp. (°C)	Detection conc. (ppm)	Response (R <sub>g</sub> /R <sub>a</sub> )	Ref.
GO/SnO <sub>2</sub> /NiO composite	Hydrothermal	Acetone	350	100	33.5	[2]
Graphene-loaded Ni-doped SnO <sub>2</sub> composite	Flame spray pyrolysis	Acetone	350	200	169.7	[3]
NiO/SnO <sub>2</sub> hierarchical structure	Hydrothermal	Acetone	300	50	20.18	[4]
NiO decorated SnO <sub>2</sub> composite	Hydrothermal	Ethanol	250	1000	123.7	[5]
NiO/SnO <sub>2</sub> heterostructure	Hydrothermal	Ethanol	160	100	23.87	[6]
NiO/SnO <sub>2</sub> heterojunction	Sputtering	Ethanol	250	100	7.9	[7]
NiO decorated SnO <sub>2</sub> /Zn <sub>2</sub> SnO <sub>4</sub> porous cubes	Precipitation	Ethanol	280	100	52.7	[8]
SnO <sub>2</sub> :NiO networks	Sputtering	Ethanol	300	50	9	[9]



Pd doped SnO <sub>2</sub> :NiO film	Sputtering	Ethanol	325	50	12	[10]
<b>rGO decorated NiO-SnO<sub>2</sub> nanocomposite</b>	<b>Sol-gel</b>	<b>Acetone</b>	<b>Room temp.</b>	<b>10</b>	<b>7.8</b>	<b>This work</b>
		<b>Ethanol</b>		<b>10</b>	<b>4.2</b>	

### 3.2.4. Conclusion:

In the present work, reduced graphene oxide (rGO) decorated (1, 3, and 5 wt%) NiO-SnO<sub>2</sub> nanocomposites with varying compositions (1:1, 1:2, 1:3, and 1:4 NiO and SnO<sub>2</sub> molar ratio) were synthesized by an environment-friendly sol-gel process and using the fabricated Taguchi-type sensors ppm-level VOC sensing performances were studied at room temperature. The optimized sensor (~ 3 wt% rGO decorated NiO-SnO<sub>2</sub>) demonstrated a repeatable and reproducible sensing response ( $R_g/R_a \sim 7.8$ ) in the presence of ~ 10 ppm acetone with fast response (~ 10 s) and recovery (~ 30 s) time. In the presence of ~ 10 ppm ethanol the sensing response was slightly dropped to ~ 4.2 and consequent response and recovery time of the sensor were comparatively delayed (~ 25 s response time and ~ 55 s recovery time). The developed sensor could also sense ~ 1 ppm VOCs with considerable sensing responses. This excellent sensing behavior was attributed to tailored defect sites, oxygen vacancies, and high specific surface area. Altogether, the demonstration of room temperature sensing response to ppm level VOC (acetone and ethanol) with rapid response/recovery time, good reproducibility, and stability made the sensor a futuristic candidate in different practical application areas, especially in non-invasive medical diagnosis and beverages industries.

### References:

- [1] S. Sen, S. Kundu, Reduced graphene oxide (rGO) decorated ZnO-SnO<sub>2</sub>: A ternary nanocomposite toward improved low concentration VOC sensing performance, *J. Alloys Compd.* 881 (2021) 160406. <http://doi.org/10.1016/j.jallcom.2021.160406>.
- [2] S. Singkammo, A. Wisitsoraat, C. Sriprachuabwong, A. Tuantranont, S. Phanichphant, C. Liewhiran, Electrolytically Exfoliated Graphene-Loaded Flame-Made Ni-Doped SnO<sub>2</sub> Composite Film for Acetone Sensing, *ACS Appl. Mater. Interfaces* 7 (2015) 3077-3092. <http://doi.org/10.1021/acsami.5b00161>.
- [3] J. Hu, J. Yang, W. Wang, Y. Xue, Y. Sun, P. Li, K. Lian, W. Zhang, L. Chen, J. Shi, Y. Chen, Synthesis and gas sensing properties of NiO/SnO<sub>2</sub> hierarchical structures toward ppb-level acetone detection, *Mater. Res. Bull.* 102 (2018) 294-303. <http://doi.org/10.1016/j.materresbull.2018.02.006>.
- [4] L. Zhang, J. He, W. Jiao, Synthesis and gas sensing performance of NiO decorated SnO<sub>2</sub> vertical-standing nanotubes composite thin films, *Sens. Actuators B: Chem.* 281 (2019) 326-334. <http://doi.org/10.1016/j.snb.2018.10.121>.
- [5] S. U. Din, M. Haq, M. Sajid, R. Khatoon, X. Chen, L. Li, M. Zhang, L. Zhu, Development of high-performance sensor based on NiO/SnO<sub>2</sub> heterostructures to study sensing properties towards various reducing gases, *Nanotechnology* 31 (2020) 395502. <http://doi.org/10.1088/1361-6528/ab98bb>.
- [6] Y. Wang, W. G. Tong, N. Han, Co-sputtered Pd/SnO<sub>2</sub>: NiO heterostructured sensing films for MEMS-based ethanol sensors, *Mater. Lett.* 273 (2020) 127924. <http://doi.org/10.1016/j.matlet.2020.127924>.
- [7] J. Fang, Y. Zhu, D. Wu, C. Zhang, S. Xu, D. Xiong, P. Yang, L. Wang, P. K. Chu, Gas sensing properties of NiO/SnO<sub>2</sub> heterojunction thin film, *Sens. Actuators B: Chem.* 252 (2017) 1163-1168. <http://doi.org/10.1016/j.snb.2017.07.013>.
- [8] S. Zhang, G. Sun, Y. Li, B. Zhang, L. Lin, Y. Wang, J. Cao, Continuously improved gas-sensing performance of SnO<sub>2</sub>/Zn<sub>2</sub>SnO<sub>4</sub> porous cubes by structure evolution and further NiO decoration, *Sens. Actuators B: Chem.* 255 (2018) 2936-2943. <http://doi.org/10.1016/j.snb.2017.09.114>.

- 
- [9] W. Tong, Y. Wang, Y. Bian, A. Wang, N. Han, Y. Chen, Sensitive Cross-Linked SnO<sub>2</sub>:NiO Networks for MEMS Compatible Ethanol Gas Sensors, *Nanoscale Res. Lett.* 15 (2020). <http://doi.org/10.1186/s11671-020-3269-3>.
- [10] Y. Wang, W. G. Tong, N. Han, Co-sputtered Pd/SnO<sub>2</sub>:NiO heterostructured sensing films for MEMS-based ethanol sensors, *Mater. Lett.* 273 (2020) 127924. <http://doi.org/10.1016/j.matlet.2020.127924>.
- [11] D. Wang, R. Xu, X. Wang, Y. Li, NiO nanorings and their unexpected catalytic property for CO oxidation, *Nanotechnology* 17 (2006) 979-983. <http://doi.org/10.1088/0957-4484/17/4/023>.
- [12] H. Ding, J. Zhu, J. Jiang, R. Ding, Y. Feng, G. Wei, X. Huang, Preparation and gas-sensing property of ultra-fine NiO/SnO<sub>2</sub> nano-particles, *RSC Adv.* 2 (2012) 10324-10329. <http://doi.org/10.1039/c2ra21121a>.
- [13] M. Taeño, D. Maestre, A. Cremades, Formation of NiO/SnO<sub>2</sub> p-n heterostructures grown by a single-step process based on a vapor-solid method, *Mater. Lett.* 271 (2020) 127801. <http://doi.org/10.1016/j.matlet.2020.127801>.
- [14] V. A. Agubra, L. Zuniga, D. Flores, H. Campos, J. Villarreal, M. Alcoutlabi, A comparative study on the performance of binary SnO<sub>2</sub>/NiO and Sn/C composite nanofibers as alternative anode materials for lithium ion batteries, *Electrochim. Acta* 224 (2017) 608-621. <http://doi.org/10.1016/j.electacta.2016.12.054>.
- [15] N. Jayababu, M. Poloju, J. Shruthi, M. V. R. Reddy, Semi shield driven p-n heterostructures and their role in enhancing the room temperature ethanol gas sensing performance of NiO/SnO<sub>2</sub> nanocomposites, *Ceram. Int.* 45 (2019) 15134-15142. <http://doi.org/10.1016/j.ceramint.2019.04.255>.
- [16] L. Liu, Y. Zhang, G. Wang, S. Li, L. Wang, Y. Han, X. Jiang, A. Wei, High toluene sensing properties of NiO-SnO<sub>2</sub> composite nanofiber sensors operating at 330°C, *Sens. Actuators B: Chem.* 160 (2011) 448-454. <http://doi.org/10.1016/j.snb.2011.08.007>.
- [17] C. D. Gu, H. Zheng, X. L. Wang, J. P. Tu, Superior ethanol-sensing behavior based on SnO<sub>2</sub> mesocrystals incorporating orthorhombic and tetragonal phases, *RSC Adv.* 5 (2015) 9143-9153. <http://doi.org/10.1039/c4ra13940b>.
- [18] B. J. Wang, S. Y. Ma, High response ethanol gas sensor based on orthorhombic and tetragonal SnO<sub>2</sub>, *Vacuum* 177 (2020) 109428. <http://doi.org/10.1016/j.vacuum.2020.109428>.

- [19] Y. Huang, X. Chen, K. Zhang, X. Feng, Preparation of graphene supported porous SnO<sub>2</sub>/NiO ternary composites as high capacity anode materials for Li-ion batteries, *Mater. Lett.* 161 (2015) 631-635. <http://doi.org/10.1016/j.matlet.2015.09.074>.
- [20] Y. Gu, P. Gao, Z. Yu, Y. Hu, Z. Xu, C. Zhang, J. Li, Y. An, Honeycomb-like Mesoporous NiO-SnO<sub>2</sub>/SO<sub>4</sub><sup>2-</sup> Solid Superacid for the Efficient Reaction of Methanol Oxidation, *Int. J. Electrochem. Sci.* 15 (2020) 2481-2498. <http://doi.org/10.20964/2020.03.41>.
- [21] Q. Yang, J. Zhao, T. Sun, J. Yu, Enhanced performance of SnO<sub>2</sub>-C composite fibers containing NiO as lithium-ion battery anodes, *Ceram. Int.* 41 (2015) 11213-11220. <http://doi.org/10.1016/j.ceramint.2015.05.071>.
- [22] J. Zhang, J. Wu, X. Wang, D. Zeng, C. Xie, Enhancing room-temperature NO<sub>2</sub> sensing properties via forming heterojunction for NiO-rGO composited with SnO<sub>2</sub> nanoplates, *Sens. Actuators B: Chem.* 243 (2017) 1010-1019. <http://doi.org/10.1016/j.snb.2016.12.062>.
- [23] S. Bai, Y. Tian, Y. Zhao, H. Fu, P. Tang, R. Luo, D. Li, A. Chen, C. C. Liu, Construction of NiO@ZnSnO<sub>3</sub> hierarchical microspheres decorated with NiO nanosheets for formaldehyde sensing, *Sens. Actuators B: Chem.* 259 (2018) 908-916. <http://doi.org/10.1016/j.snb.2017.10.176>.
- [24] D. Meng, D. Liu, G. Wang, Y. Shen, X. San, M. Li, F. Meng, Low-temperature formaldehyde gas sensors based on NiO-SnO<sub>2</sub> heterojunction microflowers assembled by thin porous nanosheets, *Sens. Actuators B: Chem.* 273 (2018) 418-428. <http://doi.org/10.1016/j.snb.2018.06.030>.
- [25] Z. Lin, N. Li, Z. Chen, P. Fu, The effect of Ni doping concentration on the gas sensing properties of Ni doped SnO<sub>2</sub>, *Sens. Actuators B: Chem.* 239 (2017) 501-510. <http://doi.org/10.1016/j.snb.2016.08.053>.
- [26] C. Gu, W. Guan, X. Liu, L. Gao, L. Wang, J. Shim, J. Huang, Controllable synthesis of porous Ni-doped SnO<sub>2</sub> microstructures and their enhanced gas sensing properties, *J. Alloys Compd.* 692 (2017) 855-864. <http://doi.org/10.1016/j.jallcom.2016.09.103>.
- [27] M. Wu, Y. Li, J. Du, C. Tao, Z. Liu, Oxygen-Evolution Activity of p-n Heterojunction NiO-SnO<sub>2</sub> Ceramic on Ti Substrate Fabricated Using a Simple Layer-by-Layer Method, *ACS Omega* 5 (2020) 22652-22660. <http://doi.org/10.1021/acsomega.0c03435>.

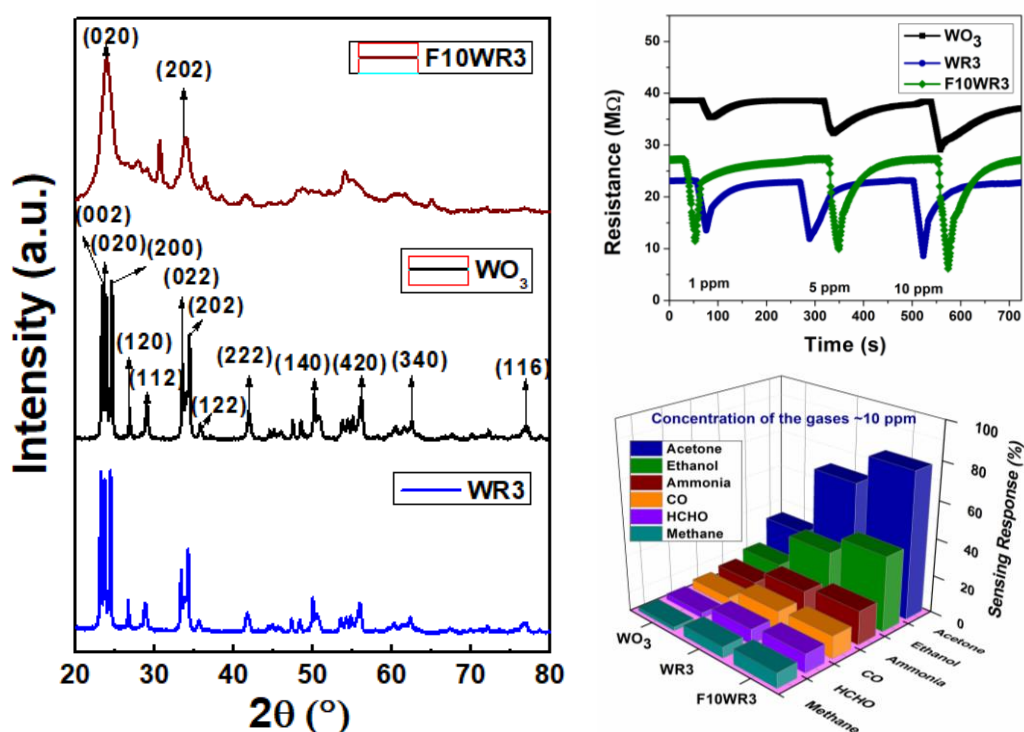
- [28] L. N. Moghadam, M. Salavati-Niasari, Facile synthesis and characterization of NiO-SnO<sub>2</sub> ceramic nanocomposite and its unique performance in organic pollutants degradation, *J. Mol. Struct.* 1146 (2017) 629-634. <http://doi.org/10.1016/j.molstruc.2017.06.038>.
- [29] V. S. Suvith, V. S. Devu, D. Philip, Facile synthesis of SnO<sub>2</sub>/NiO nano-composites: Structural, magnetic and catalytic properties, *Ceram. Int.* 46 (2020) 786-794. <http://doi.org/10.1016/j.ceramint.2019.09.033>.
- [30] L. Jiang, S. Tu, K. Xue, H. Yu, X. Hou, Preparation and gas-sensing performance of GO/SnO<sub>2</sub>/NiO gas-sensitive composite materials, *Ceram. Int.* 47 (2021) 7528-7538. <http://doi.org/10.1016/j.ceramint.2020.10.257>.
- [31] T. liu, Z. Yu, Y. Liu, J. Gao, X. Wang, H. Suo, X. Yang, C. Zhao, F. Liu, Gas sensor based on Ni Foam: SnO<sub>2</sub>-decorated NiO for Toluene detection, *Sens. Actuators B: Chem.* 318 (2020) 128167. <http://doi.org/10.1016/j.snb.2020.128167>.
- [32] S. Bai, J. Liu, J. Guo, R. Luo, D. Li, Y. Song, C. C. Liu, A. Chen, Facile preparation of SnO<sub>2</sub>/NiO composite and enhancement of sensing performance to NO<sub>2</sub>, *Sens. Actuators B: Chem.* 249 (2017) 22-29. <http://doi.org/10.1016/j.snb.2017.03.121>.
- [33] P. Tyagi, A. Sharma, M. Tomar, V. Gupta, SnO<sub>2</sub> thin film sensor having NiO catalyst for detection of SO<sub>2</sub> gas with improved response characteristics, *Sens. Actuators B: Chem.* 248 (2017) 998-1005. <http://doi.org/10.1016/j.snb.2017.02.168>.
- [34] R. M. Mohamed, E. S. Aazam, Photocatalytic Oxidation of Carbon Monoxide over NiO/SnO<sub>2</sub> Nanocomposites under UV Irradiation, *J. Nanotechnol.* 2012 (2011) 794874. <http://doi.org/10.1155/2012/794874>.
- [35] M. Taeño, D. Maestre, A. Cremades, Study of Sn doped NiO microwires with waveguiding behavior grown by a vapor-solid process, *J. Alloy Compd.* 881 (2021) 160654. <http://doi.org/10.1016/j.jallcom.2021.160654>.
- [36] P. Pascariu, A. Airinei, N. Olaru, I. Petrila, V. Nica, L. Sacarescu, F. Tudorache, Microstructure, electrical and humidity sensor properties of electrospun niO-SnO<sub>2</sub> nanofibers, *Sens. Actuators B: Chem.* 222 (2016) 1024-1031. <http://doi.org/10.1016/j.snb.2015.09.051>.
- [37] S. Zhang, G. Sun, Y. Li, B. Zhang, L. Lin, Y. Wang, J. Cao, Z. Zhang, Continuously improved gas-sensing performance of SnO<sub>2</sub>/Zn<sub>2</sub>SnO<sub>4</sub> porous cubes by structure evolution and further NiO decoration, *Sens. Actuators B: Chem.* 255 (2018) 2936-2943. <http://doi.org/10.1016/j.snb.2017.09.114>.

- 
- [38] J. Wang, K. T. Liao, W. J. Tseng, NiO/SnO<sub>2</sub> hybrid nanowires for enhanced NO<sub>2</sub> gas sensing, *Ceram. Int.* 43 (2017) S541-S546. <http://doi.org/10.1016/j.ceramint.2017.05.286>.
- [39] C. Zhang, J. Wang, R. Hu, Q. Qiao, X. Li, Synthesis and gas sensing properties of porous hierarchical SnO<sub>2</sub> by grapefruit exocarp biotemplate, *Sens. Actuators B: Chem.* 222 (2016) 1134-1143. <http://doi.org/10.1016/j.snb.2015.08.016>.
- [40] S. Bhattacharjee, S. Sen, S. Kundu, Development of La-impregnated TiO<sub>2</sub> based ethanol sensors for next generation automobile application, *J Mater. Sci.: Mater. Electron.* 33 (2022) 15296-15312. <http://doi.org/10.1007/s10854-022-08394-4>.
- [41] S. Kundu, A. Kumar, S. Sen, A. Nilabh, Bio-synthesis of SnO<sub>2</sub> and comparison its CO sensing performance with conventional processes, *J. Alloy Compd.* 818 (2020) 152841. <http://doi.org/10.1016/j.jallcom.2019.152841>.
- [42] S. W. Gumbi, P. S. Mkwae, I. Kortidis, R. E. Kroon, H. C. Swart, T. Moyo, S. S. Nkosi, Electronic and Simple Oscillatory Conduction in Ferrite Gas Sensors: Gas-sensing Mechanisms, Long-term Gas Monitoring, Heat Transfer, and Other Anomalies, *ACS Appl. Mater. Interfaces* 12 (2020) 443231-43249. <http://doi.org/10.1021/acsami.0c11208>.
- [43] P. Shankar, J. B. B. Rayappan, Room temperature ethanol sensing properties of ZnO nanorods prepared using an electrospinning technique, *J. Mater. Chem. C* 5 (2017) 10869. <http://doi.org/10.1039/c7tc03771f>.
- [44] L. Greenspan, Humidity Fixed Points of Binary Saturated Aqueous Solutions, *JOURNAL OF RESEARCH of the National Bureau of Standards- A. Physics and Chemistry*, 81A (1977) 89-96. <http://doi.org/10.6028/jres.081A.011>.
- [45] B. B. Rao, Zinc oxide ceramic semi-conductor gas sensor for ethanol vapour, *Mater. Chem. Phys.* 64 (2000) 62-65. [http://doi.org/10.1016/S0254-0584\(99\)00267-9](http://doi.org/10.1016/S0254-0584(99)00267-9).
- [46] A. Nilabh, S. Sen, M. Narjinary, S. Kundu, A novel ppm level ethanol sensor based on La loaded ITO impregnated with Pd and Sb additives, *Microchem. J.* 158 (2020) 105146. <http://doi.org/10.1016/j.microc.2020.105146>.
- [47] G. Jeevitha, R. Abhinayaa, D. Mangalaraj, N. Ponpandian, P. Meena, V. Mounasamy, S. Madanagurusamy, Porous reduced graphene oxide (rGO)/WO<sub>3</sub> nanocomposites for the enhanced detection of NH<sub>3</sub> at room temperature, *Nanoscale Adv.*, 1 (2019) 1799-1811. <http://doi.org/10.1039/c9na00048h>.

- [48] S. Sen, A. Nilabh, S. Kundu, Room temperature acetone sensing performance of Pt/Sb<sub>2</sub>O<sub>3</sub> impregnated Fe<sub>2</sub>O<sub>3</sub> thin film: Noninvasive diabetes detection, *Microchem. J.* 165 (2021) 106111. <http://doi.org/10.1016/j.microc.2021.106111>.
- [49] S. Das, M. Pal, Non-Invasive Monitoring of Human Health by Exhaled Breath Analysis: A Comprehensive Review, *J. Electrochem. Soc.* 167 (2020) 037562. <http://doi.org/10.1149/1945-7111/ab67a6>.
- [50] S. Bai, C. Liu, R. Luo, A. Chen, Metal organic frameworks-derived sensing material of SnO<sub>2</sub>/NiO composites for detection of triethylamine, *Appl. Surf. Sci.* 437 (2018) 304-313. <http://doi.org/10.1016/j.apsusc.2017.12.033>.
- [51] S. Sen, S. Maity, S. Kundu, Fabrication of Fe doped reduced graphene oxide (rGO) decorated WO<sub>3</sub> based low temperature ppm level acetone sensor: Unveiling sensing mechanism by impedance spectroscopy, *Sens. Actuators B: Chem.* 361 (2022) 131706. <http://doi.org/10.1016/j.snb.2022.131706>.
- [52] M. A. Ponce, P. R. Bueno, J. Varela, M. S. Castro, C. M. Aldao, Impedance spectroscopy analysis of SnO<sub>2</sub> thick-films gas sensors, *J. Mater. Sci.: Mater. Electron.* 19 (2008) 1169-1175. <http://doi.org/10.1007/s10854-007-9517-9>.

# CHAPTER 4.1

## Reduced graphene oxide (rGO) decorated Fe (III) doped WO<sub>3</sub> nanocomposite towards low temperature ppm level acetone detection



*Chemiresistive MOS-based acetone sensing device is a futuristic pathway for the non-invasive diagnosis of diabetes. This work demonstrated the synthesis of reduced graphene oxide (rGO) decorated Fe (III) doped WO<sub>3</sub> nanocomposites in a wet chemical sol-gel process. A maximum ~ 78% sensing response was obtained for the optimized composition of ~ 10 wt% Fe<sup>3+</sup> doped ~ 3 wt% rGO decorated WO<sub>3</sub>-based sensor towards ~ 10 ppm acetone gas. This sensing performance was observed at a comparatively low working temperature of ~ 130°C with fast response (~ 20 s) and recovery (~ 75 s) time. A further illustration of the versatility of the sensors revealed that the sensors could manifest a repeatable and reproducible sensing performance with prolonged stability and superior selectivity for acetone. The acetone sensing mechanism was illustrated with the help of an electron depletion model and impedance spectroscopy study.*





**4.1.1. Introduction:**

In previous chapters, the synthesis of rGO decorated binary n-n type (ZnO-SnO<sub>2</sub>) and p-n type (NiO-SnO<sub>2</sub>) MOS-based nanocomposites have been discussed. Taguchi-type sensors fabricated from the as-synthesized nanocomposites were used for VOC sensing performance study. In Chapter 3.1, the rGO decorated ZnO-SnO<sub>2</sub> nanocomposites demonstrated VOC (acetone and ethanol) sensing at ~ 150°C [1]. In Chapter 3.2, the operating temperature of the rGO decorated NiO-SnO<sub>2</sub> nanocomposites based sensors was reduced to room temperature (30 ± 5°C) [2]. However, the desired selectivity towards acetone (breath biomarker of diabetes) has not been achieved yet. Henceforth, in this chapter, the strategy was to explore the sensing performance of transition metal oxide. As a prolific candidate for VOC sensing material [3-6], WO<sub>3</sub>, a heavier transition metal oxide is highly appreciated. As well as, instead of binary composite formation, it was planned to dope metal ions in pristine MOS lattice followed by rGO decoration to improve the sensing performance. Although, there were several literatures [7-15] reported on WO<sub>3</sub>-based acetone sensor, however, they failed to showcase their potentiality to detect acetone at trace concentration and under ambient condition. Influenced by the above-reported works and to reduce the optimum operating temperature, Fe<sup>3+</sup> doped rGO-decorated WO<sub>3</sub> nanocomposite system has been developed.

**4.1.2. Experimental:**

In the preparation (Fig. 4.1.1), initially, a certain amount of sodium tungstate dihydrate (Na<sub>2</sub>WO<sub>4</sub>·2H<sub>2</sub>O, Sigma Aldrich) was refluxed with hydrogen peroxide (H<sub>2</sub>O<sub>2</sub>, Merck) and glacial acetic acid (CH<sub>3</sub>COOH, Merck) for several hours and then evaporated to prepare pristine WO<sub>3</sub>. For the synthesis of 1, 3, 5 wt% rGO decorated WO<sub>3</sub> nanocomposites, requisite amounts of rGO were added to the WO<sub>3</sub> solutions with necessary binder as discussed in Chapter 2 (section 2.3.4) and stirred to form homogeneous sols, and the sols were marked as WR1, WR3, and WR5 respectively. The sols were then aged and converted to gel. Finally, the gels were calcined at ~ 350°C for one hour. Fe<sup>3+</sup> doped rGO decorated WO<sub>3</sub> nanocomposites with different amounts (5, 10, and 15 wt%) of Fe<sup>3+</sup> were synthesized by using iron nitrate nonahydrate (Fe(NO<sub>3</sub>)<sub>3</sub>·9H<sub>2</sub>O, Sigma Aldrich) as a precursor of Fe<sup>3+</sup> and adding requisite amount of precursor Fe<sup>3+</sup> in WR3 sol and stirred to form homogeneous sols. The sols were named as F5WR3, F10WR3, and F15WR3

respectively. Finally, the gels were calcined at  $\sim 350^\circ\text{C}$  for one hour in air to get rGO decorated  $\text{Fe}^{3+}$ -doped  $\text{WO}_3$  nanocomposites.

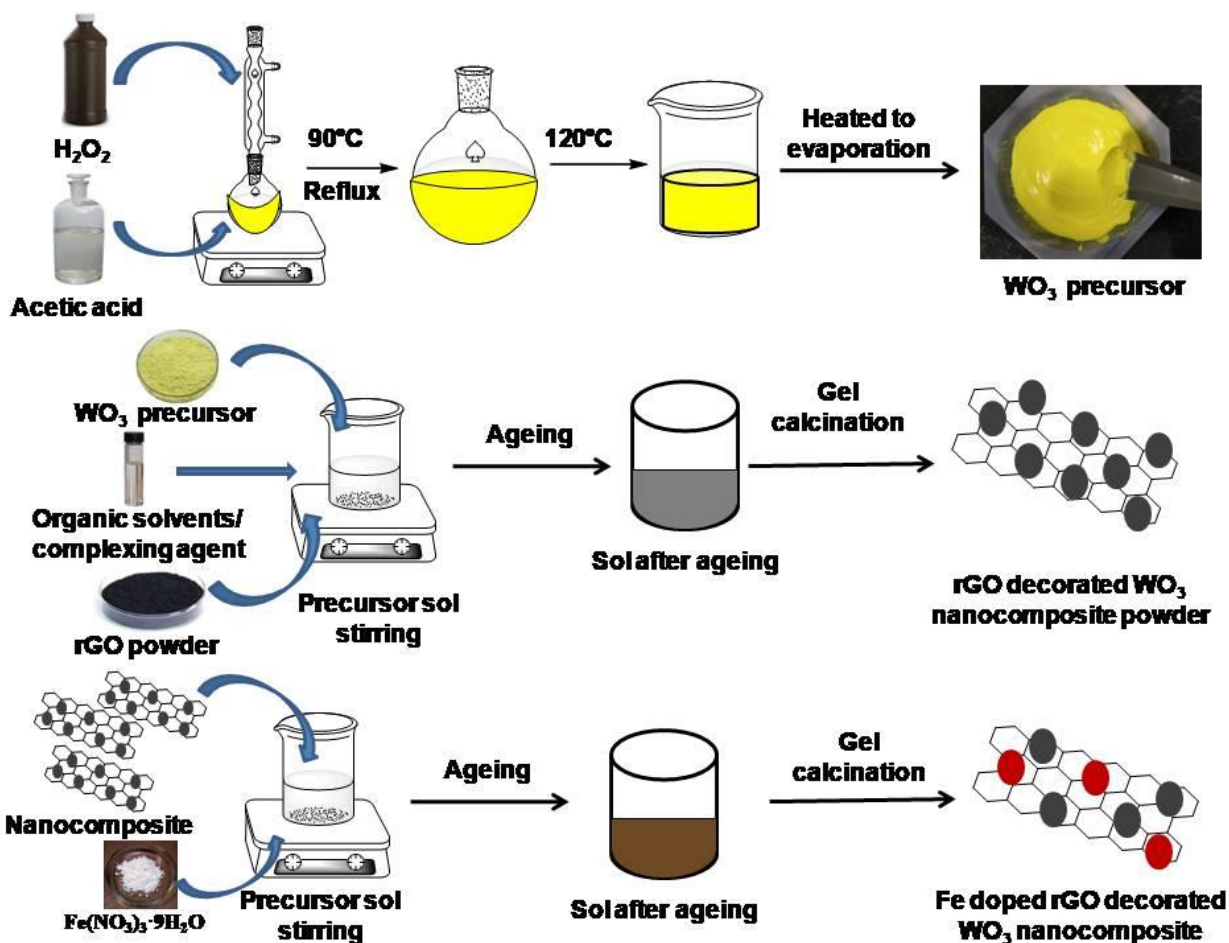


Figure-4.1.1: Schematic representation of nanocomposites synthesis

## 4.1.3. Results and discussions:

### 4.1.3.1. Characterization of nanocomposites:

Figure 4.1.2 exhibited the XRD patterns of pristine  $\text{WO}_3$  powder and its different synthesized nanocomposites. The XRD spectrum of the  $\text{WO}_3$  sample showed well-assigned characteristics peaks of monoclinic  $\text{WO}_3$  (JCPDS card no. : 83-0951) having primitive lattice structure. There was a high-intensity triplet at  $2\theta$  values 23.25, 23.74, and 24.50 for (002), (020), and (200) planes correspondingly [16, 17]. Other diffraction peaks at 26.74, 28.89, 33.42, 34.29, 35.67, 41.81, 50.07, 56.04, 62.41, and 76.80 assigned to (120), (112), (022), (202), (122), (222), (140),

(420), (340), and (116) planes respectively. The XRD patterns (Fig. 4.1.2) of rGO-decorated  $\text{WO}_3$  nanocomposites showed similar XRD pattern, and neither any additional peak nor significant peak broadening for rGO was observed due to its presence in low concentration and its exfoliation to nano-dimension. The crystalline phases of the samples also remained unchanged [18]. However, a certain peak shifting towards lower  $\theta$  values indicated the incorporation of rGO in  $\text{WO}_3$ .

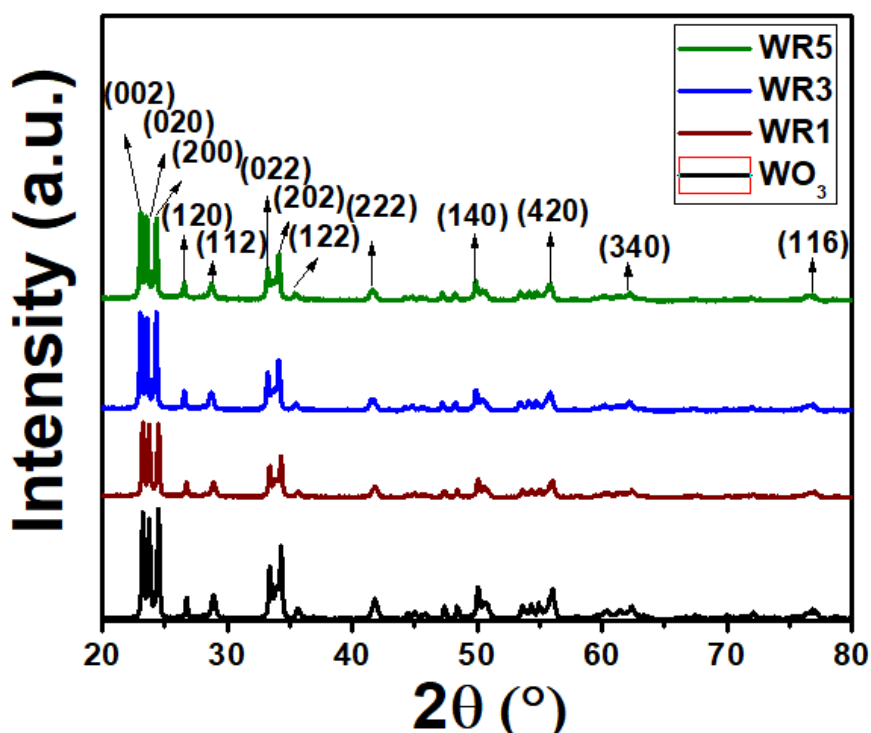


Figure-4.1.2: X-ray diffraction spectra of pristine  $\text{WO}_3$ , WR1, WR3, and WR5

Figure- 4.1.3a represented the XRD spectra of as-synthesized samples containing different amounts of  $\text{Fe}^{3+}$  in WR3. As a result of  $\text{Fe}^{3+}$  doping in the  $\text{WO}_3$  matrix, there were noticeable transmutations in XRD signatures in terms of peak broadening and damping of peak intensities (Fig. 4.1.2). Conventionally, the addition of dopant metal ions in the metal oxide semiconductor (MOS) matrix tailors its crystal structure, increasing the number of active sites to facilitate gas sensing. Similarly, in the pristine  $\text{WO}_3$  crystal,  $\text{W}^{6+}$  was coordinated with  $\text{O}^{2-}$  in an octahedral arrangement. As mentioned earlier,  $\text{Fe}^{3+}$  (0.64 nm) and  $\text{W}^{6+}$  (0.62nm) with almost similar ionic radii, and  $\text{Fe}^{3+}$  had more crystal field stabilization energy (CFSE) in the octahedral field than

$W^{6+}$ . The former readily substituted the later in some of its inherent lattice sites [19]. As expected, the characteristic change in peaks, in terms of peak broadening and damping of peak intensities observed in  $Fe^{3+}$ -doped samples as compared to pristine ones, might be attributed to  $Fe^{3+}$  doping in the  $WO_3$  matrix (Fig. 4.1.3b). As a result, this doping led to distortion of crystal alignment, generation of defect sites, and introduction of oxygen vacancies in the crystal lattice.

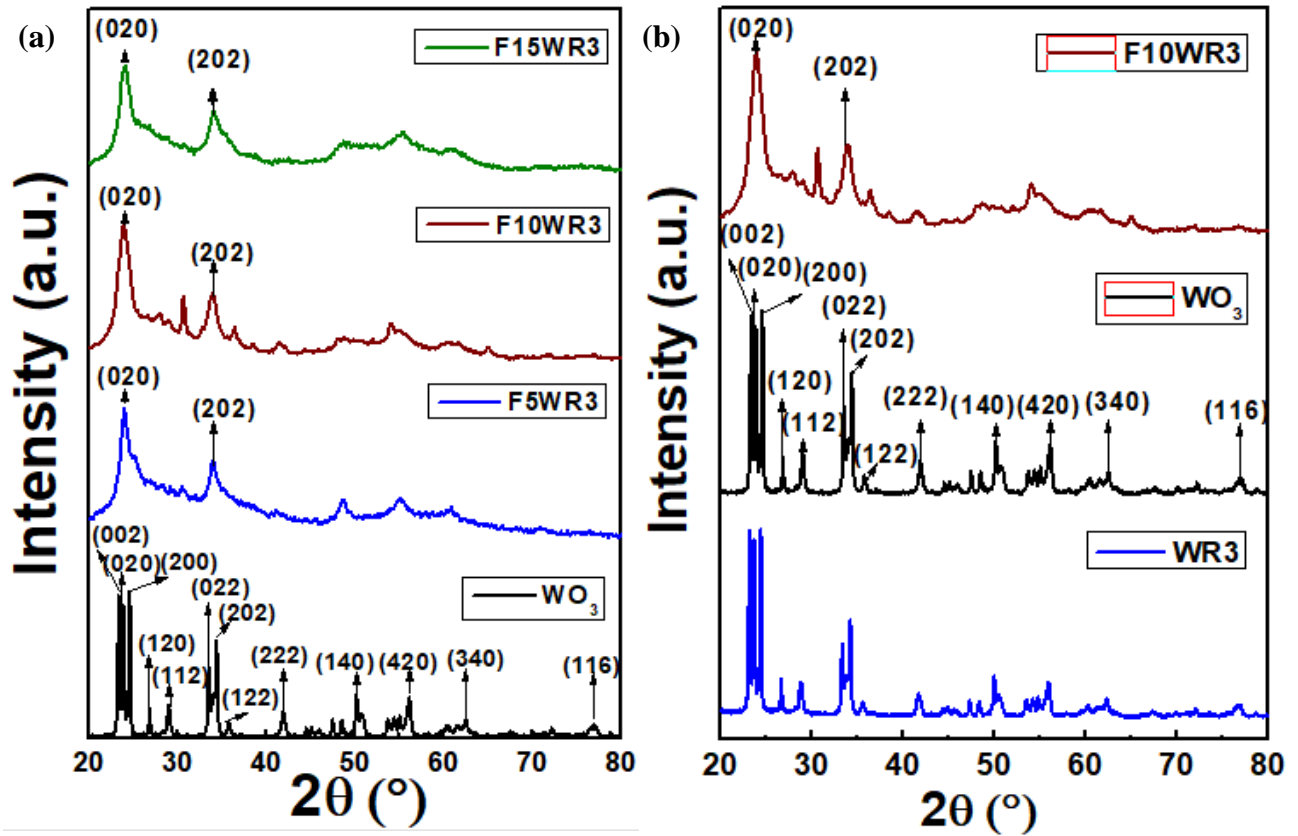


Figure-4.1.3: X-ray diffraction spectra of (a) pristine  $WO_3$ , F5WR3, F10WR3, and F15WR3, (b) pristine  $WO_3$ , WR3, and F10WR3

The crystalline properties of the nanocomposites were calculated using Debye-Scherrer's equation as follows:

$$Crystallitesize (D) = \frac{k\lambda}{\beta \cos \theta} \dots\dots\dots (4.1.1)$$

Where,  $\lambda$  is the wavelength of the X-ray radiations (1.54 Å),  $k$  is a constant valued 0.94,  $\beta$  is the FWHM (full width at half maxima) in radian unit, and  $\theta$  is the Bragg's angle. Other structural parameters such as dislocation density ( $\delta$ ), micro strain ( $\epsilon$ ), and stacking fault (SF) were also calculated by using following formulas:

$$\text{Dislocation density } (\delta) = \frac{1}{D^2} \dots\dots\dots (4.1.2)$$

$$\text{Micro strain } (\varepsilon) = \frac{\beta \cos \theta}{4} \dots\dots\dots (4.1.3)$$

$$\text{Stacking fault } (SF) = \left[ \frac{2\pi^2}{45(\tan \theta)^2} \right] \beta \dots\dots\dots (4.1.4)$$

It can be stated that if all the above-mentioned parameters were minimum, then the crystallinity of the as-prepared sample will be better. All the calculated results are summarized in Table 4.1.1.

Table – 4.1.1: Various structural parameters calculated from major peaks of the XRD patterns:

Sample name	Lattice plane	$d_{hkl}$ (nm)	Crystallite size (D) (nm)	Dislocation density $(\delta) \times 10^{-15} \text{ (m}^{-2}\text{)}$	Micro strain $(\varepsilon) \times 10^{-3}$	Stacking fault (SF) (degree)
WO <sub>3</sub>	(002)	0.382	44.47	0.505	0.813	0.183
	(020)	0.374	40.27	0.616	0.898	0.200
	(200)	0.362	47.03	0.452	0.769	0.169
WR1	(002)	0.382	46.94	0.452	0.771	0.174
	(020)	0.374	52.86	0.357	0.684	0.153
	(200)	0.363	49.80	0.403	0.726	0.159
WR3	(002)	0.385	46.94	0.453	0.771	0.174
	(020)	0.377	52.80	0.358	0.685	0.153
	(200)	0.365	49.80	0.403	0.726	0.160
WR5	(002)	0.384	49.70	0.404	0.728	0.164
	(020)	0.377	44.47	0.505	0.813	0.182
	(200)	0.365	47.03	0.452	0.769	0.170
F5WR3	(200)	0.372	3.95	64.06	9.16	2.04
F10WR3	(200)	0.373	4.30	54.06	8.41	1.87
F15WR3	(200)	0.370	3.88	66.43	9.32	2.07

This intrinsic lattice modification of the nanocomposites plays a vital role in sensing performance. Therefore, the synthesized nanocomposites' average particle size and lattice strain were calculated using the Williamson-Hall plot (Fig. 4.1.4 a-c). The total strain of a

nanocomposite system considering alteration in particle size as well as the lattice strain can be expressed as [20]:

$$\beta_{hkl} = \beta D + \beta_{\text{strain}} \quad (4.1.5)$$

$$\beta_{hkl} = (k \times \lambda) / (D \cos \theta) + 4 \epsilon \tan \theta \quad (4.1.6)$$

$$\beta_{hkl} \cos \theta = (k \times \lambda) / D + 4 \epsilon \sin \theta \quad (4.1.7)$$

Where  $D$  is the average particle size,  $k$  is constant,  $\lambda$  is the wavelength of incident x-ray,  $\beta$  is full width at half maxima (FWHM), and  $\theta$  is the diffracted angle.

This is a straight-line equation ( $y = mx + c$ ), and the plot of  $4 \epsilon \sin \theta$  against  $\beta_{hkl} \cos \theta$  is known as the Williamson-Hall plot. The slope of linearly fitted straight-line lattice strain is obtained, and the intercept is used to derive the average particle size (where  $k = 0.89$  and  $\lambda = 1.5406 \text{ \AA}$ ).

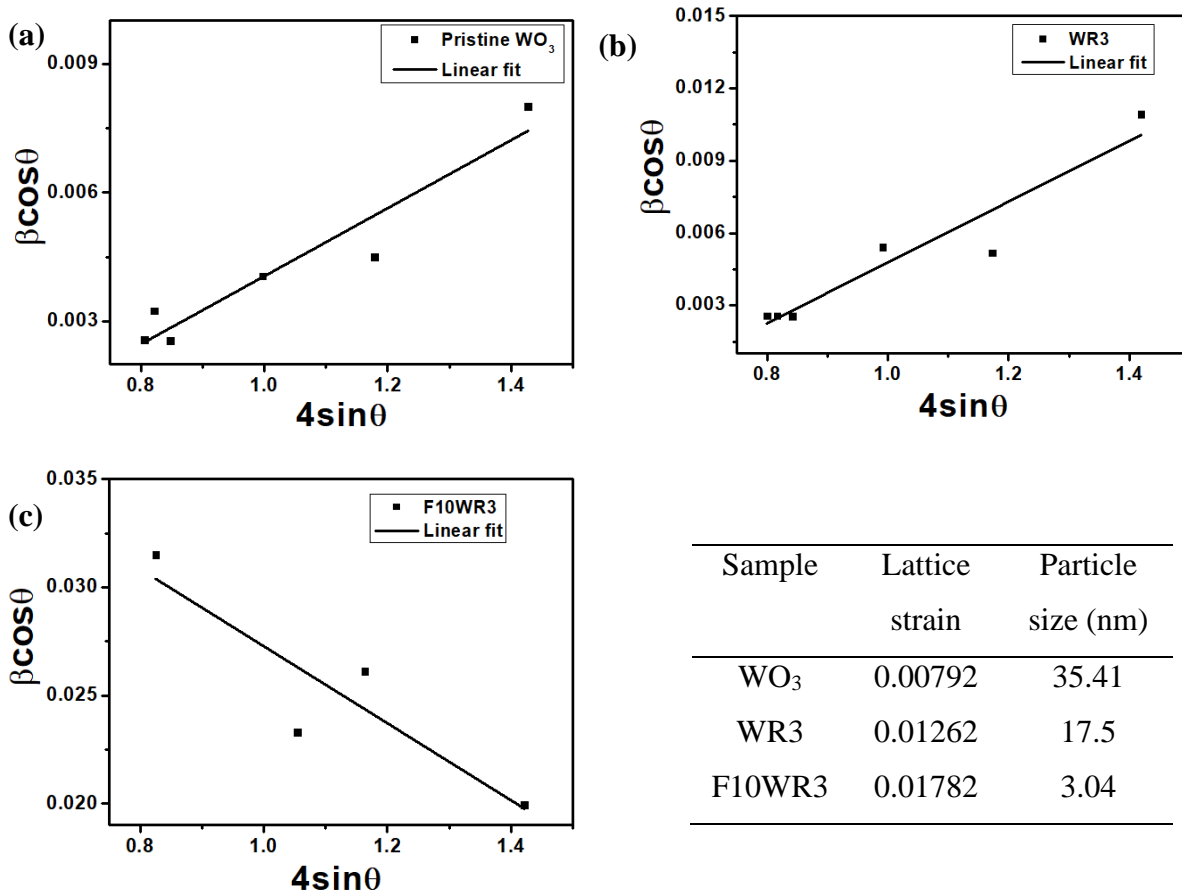


Figure-4.1.4: Williamson-Hall plot of (a) pristine WO<sub>3</sub>, (b) WR3, (c) F10WR3,  
Table – 4.1.2: Particle size and lattice strain of the as-synthesized nanocomposites using Williamson-Hall plot

The calculated values of strain and average particle size are tabulated in Table 4.1.2. The results suggested that the  $\text{Fe}^{3+}$  doping in the  $\text{WO}_3$  matrix reduced the particle size and increased the micro-strain by many folds, proving efficacious for the adsorption/desorption of gas during sensing.

All the FTIR spectra shown in Fig. 4.1.5 exhibited signature peaks at  $3125\text{ cm}^{-1}$  and  $1633\text{ cm}^{-1}$  attributed to  $-\text{O}-\text{H}$  and  $-\text{C}=\text{C}$  stretching vibration, respectively. A sharp, strong peak for  $-\text{OH}$  deformation vibration at  $1390\text{ cm}^{-1}$  was also observed. Except for rGO, the other three spectra displayed  $\text{WO}_3$  stretching vibrations below  $1000\text{ cm}^{-1}$ . The characteristic absorption for W-O-W stretching vibration was appeared as a doublet at  $815$  and  $770\text{ cm}^{-1}$  [21, 22]. It was noticeable that in the case of WR3 nanocomposite, the W-O-W vibration peaks shifted towards higher wave numbers, which confirmed the formation of the hybrid nanostructure. In the case of F10WR3, a doublet peak for W-O-W stretching was almost extinct due to the replacement of  $\text{W}^{6+}$  by  $\text{Fe}^{3+}$  from some of its lattice positions, assured successful  $\text{Fe}^{3+}$  doping in the  $\text{WO}_3$  matrix.

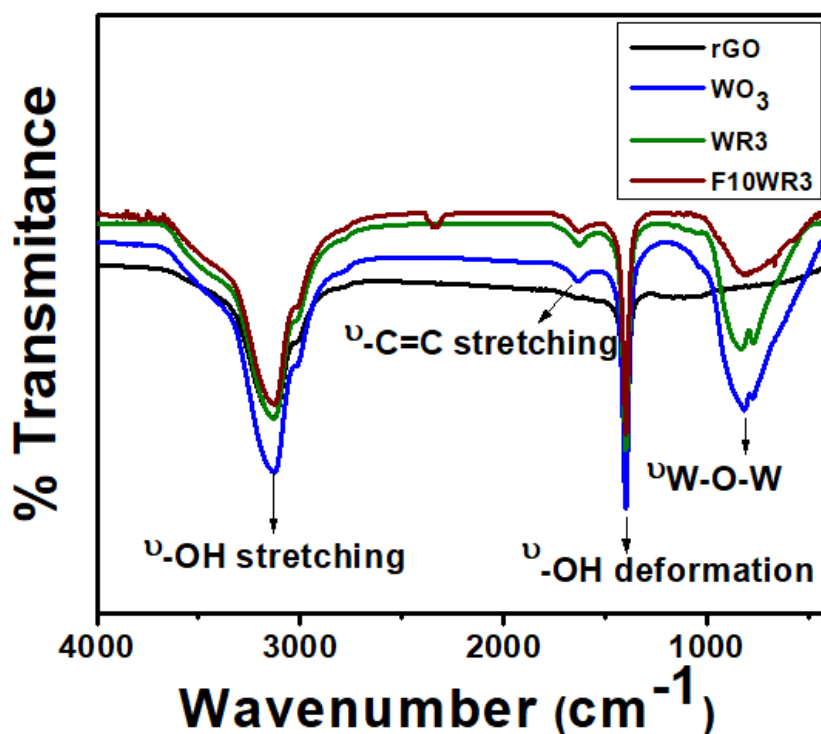


Figure-4.1.5: FTIR spectra of rGO, pristine  $\text{WO}_3$ , WR3, and F10WR3 nanocomposites



In case of pristine  $\text{WO}_3$ , two different Raman active modes were observed (Fig. 4.1.6). The peak at  $269\text{ cm}^{-1}$  was assigned to bending vibrations of O-W-O bond. One highly intense band at  $796\text{ cm}^{-1}$  corresponded to W-O-W stretching vibrations. A small and a broad shoulder at  $704\text{ cm}^{-1}$  and  $942\text{ cm}^{-1}$ , respectively, were also generated from W-O-W stretching vibration in the  $\text{WO}_3$  lattice [22]. In other two samples, these Raman active bands were also present. Generally, in Raman spectroscopy, rGO consistently exhibits two characteristic peaks, known as D and G-band. D-band arose due to the presence of  $\text{sp}^3\text{-C}$  atoms and crystal defects of rGO, and the G-band originated from the scattering of  $\text{sp}^2\text{-C}$  atoms in the rGO lattice. The intensity ratio ( $I_D/I_G$ ) of D-band to G-band gives an idea about the degree of defects and disorder in rGO crystal. Here also, it was expected that WR3 and F10WR3 should exhibit peaks for D and G-bands, and accordingly, in WR3, the observed D-band originated at  $1358\text{ cm}^{-1}$  and other peak at  $1603\text{ cm}^{-1}$  correlated to G-band [23]. For F10WR3, the D-band and G-band were found at the same wave numbers with a specific change in intensity ratios. The intensity ratio was  $\sim 0.97$  for WR3 and increased to  $\sim 1.08$  in the F10WR3 nanocomposite. This slight increase in intensity ratio was might be due to the coupling between the inherent lattice defect of rGO and lattice strain generated by  $\text{Fe}^{3+}$  doping in the  $\text{WO}_3$  lattice.

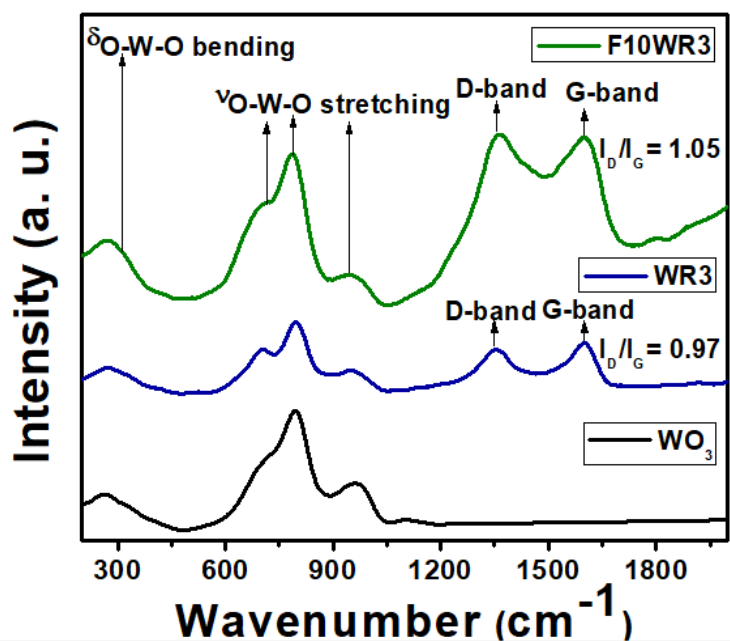
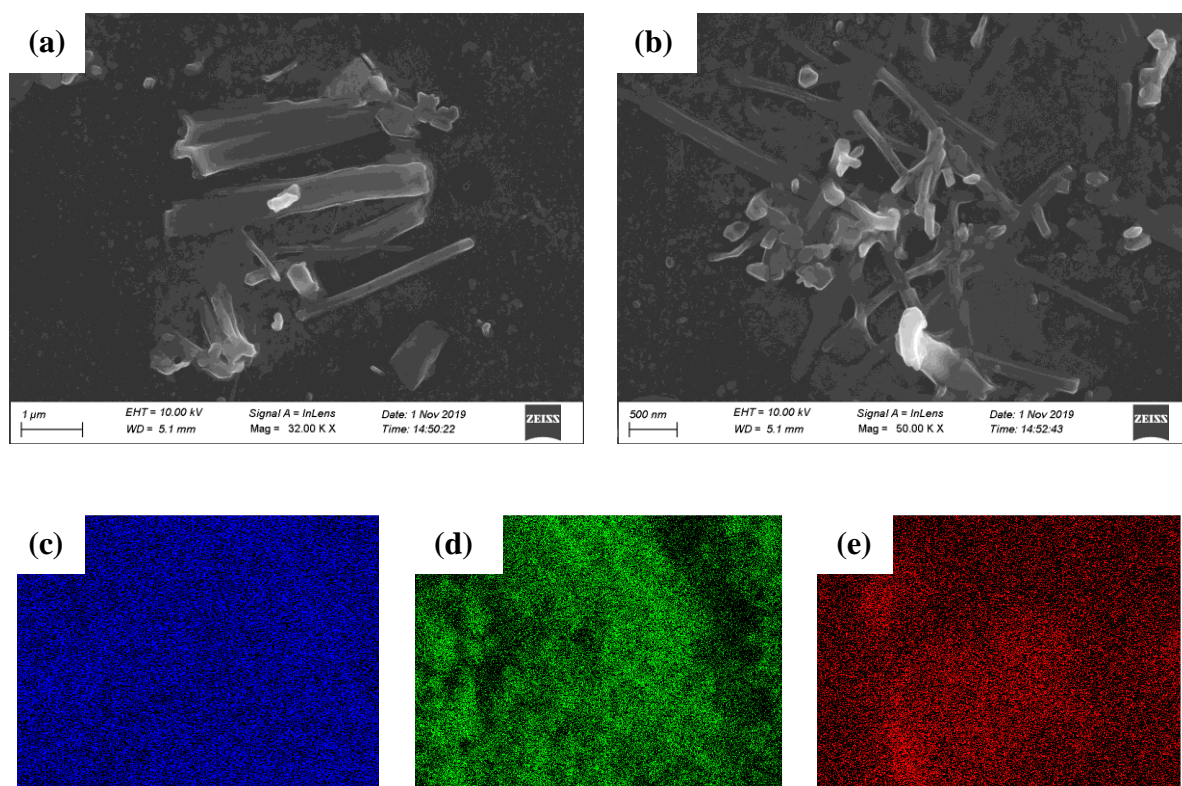


Figure-4.1.6: Raman spectra of pristine  $\text{WO}_3$ , WR3, and F10WR3 nanocomposites

The FESEM morphology revealed an agglomeration of irregularly shaped particles with some nanorods [24, 25] for WR3 and F10WR3 nanocomposites. Here, rGO provided an ultrathin support layer on which  $\text{WO}_3$  nanoparticles dispersed randomly with a mixed morphology (Fig. 4.1.7 a, b). The uniform distribution of W, O, and Fe in the nanocomposite was verified by elemental mapping and presented respectively in Fig. 4.1.7 c-e, which was in good agreement with the composition of the sample. To get more insight into the microstructure, TEM analysis was performed.



*Figure -4.1.7: FESEM images of (a) WR3, (b) F10WR3, elemental mapping of F10WR3 sample (c) W, (d) O, and (e) Fe*

The TEM and HRTEM micrographs of the as-synthesized samples were presented in Fig. 4.1.8 (a-f). The bright field TEM images of WR3 depicted in Fig. 4.1.8a that showed agglomerated  $\text{WO}_3$  embedded on the rGO network by a strong Van der Waal's interaction [21, 26]. For F10WR3, the bright field TEM image (Fig. 4.1.8d) exhibited the presence of dispersed  $\text{WO}_3$  nanorods on the rGO network with some particles. Different lattice planes were distinguished in

the typical HRTEM image (Fig.4.1.8b) of the WR3 sample, corresponding to (002), (222), and (140) planes of  $\text{WO}_3$ .

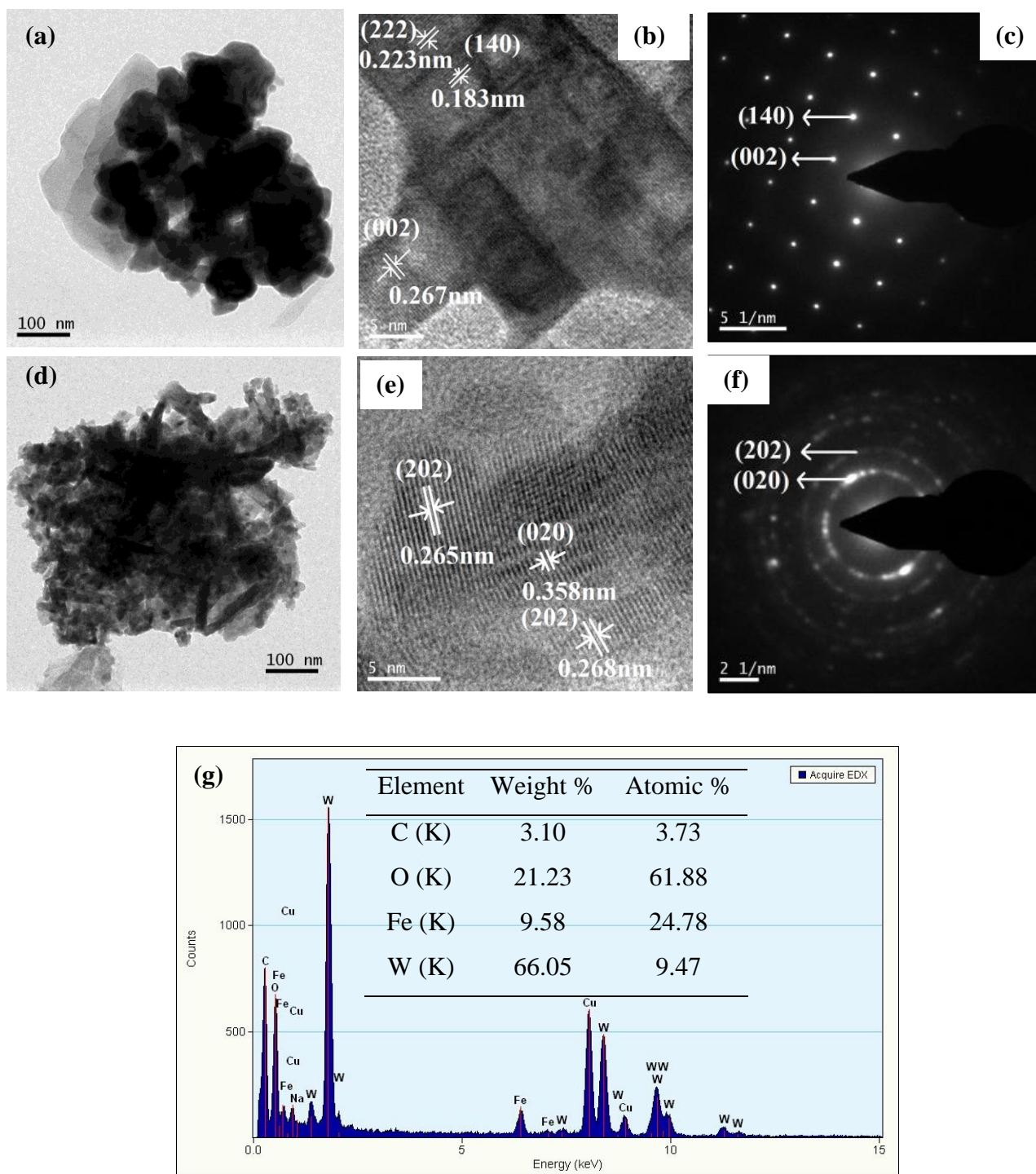


Figure -4.1.8: WR3: (a) Bright field TEM image, (b) HRTEM image, and (c) SAED pattern, F10WR3: (d) Bright field TEM image, (e) HRTEM image, and (f) SAED pattern, (g) EDX spectrum of F10WR3

The selected area energy diffraction (SAED) pattern (Fig. 4.1.8c) showed the existence of (002) and (140) planes of  $\text{WO}_3$ . HRTEM analysis (Fig. 4.1.8e) of F10WR3 showed lattice fringes for (020) and (202) planes, well-corresponded with the XRD peaks. The same result was established from the SAED pattern analysis (Fig. 4.1.8f) of the sample. Furthermore, to confirm the chemical composition and purity of the nanocomposite, EDX analysis of the sample was done. The spectrum (Fig. 4.1.8g) indicated that nanocomposite consisted of W, O, Fe, and C, and the quantitative analysis result presented in inset of Fig. 4.1.8g that was well coordinated with the composition of the sample used for nanocomposite synthesis. Impurity peaks of Cu, and small amount of C were generated from carbon-coated copper grid used for sample mounting.

The surface elemental compositions, stoichiometric, and chemical binding states were studied with the help of X-ray photoelectron spectroscopy (XPS). Full scan survey spectrum showed the presence of W, O, and C in WR3 (Fig. 4.1.9a) and F10WR3 (Fig. 4.1.9b), with additional Fe signal in F10WR3. The precise comparative analysis was done by deconvolution of core-level spectra of individual elements. In WR3 the high resolutions core-level spectra of W 4f (Fig. 4.1.9c) revealed two peaks at 33.95 eV and 36.06 eV related to W 4f<sub>7/2</sub> and W 4f<sub>5/2</sub> respectively with a spin-orbit separation of 2.11 eV, which was marginally shifted to higher binding energy in F10WR3 (Fig. 4.1.9d) to 34.05 eV and 36.20 eV accordingly, as well, the spin orbit splitting also increased to 2.15 eV [27]. The binding energies of the peaks indicated +6 oxidation state of W. However, the deconvoluted peaks of O 1s spectra of WR3 shifted to higher binding energy in comparison to F10WR3. For WR3 the peak was observed at 530.60 eV (Fig. 4.1.9e) whereas for F10WR3 it was at 528.82 eV (Fig. 4.1.9f) and the peak was attributed to the W=O bond present in the  $\text{WO}_3$  lattice, known as lattice oxygen [28]. Deconvolution of C 1s high-resolution spectrum revealed similar shifting of peaks. WR3 C 1s spectra showed peaks at 283.11 eV, 284.68 eV, and 286.02 eV (Fig. 4.1.9g) assigned for  $-\text{C}=\text{C}-$  bond,  $\text{sp}^3\text{-C}$  and lattice bonded C atoms respectively. The most substantial peak in F10WR3 (Fig. 4.1.9h) was at 283.28 eV was associated with  $\text{sp}^2\text{-C}$  atoms in  $-\text{C}=\text{C}$  bonds, and a moderately strong peak at 283.90 eV was ascribed to  $\text{sp}^3\text{-C}$  atoms [23]; both were expected to originate from rGO. Additionally, a broad and weak peak at 287.14 eV, associated with different oxygen-functionalized bonds, was brought about from W-O bonds and the rGO lattice. Deconvolution of Fe 2p spectra (Fig. 4.1.9i) gave rise to two peaks at 710.04 eV and 723.90 eV, assigned to Fe 2p<sub>3/2</sub> and Fe 2p<sub>1/2</sub> respectively [19]. Another peak was present at 715.15 eV, characterized as satellite peaks associated with  $\text{Fe}^{3+}$ .

Except these peaks, no peaks for any other oxidation state of Fe were obtained. The precise comparative investigation revealed shifting of peaks in the Fe<sup>3+</sup>-doped sample (F10WR3) compared to WR3. The same trait was also reported by Shen et al. [19]. Such alteration in peak positions ensured the introduction of Fe<sup>3+</sup> in the WO<sub>3</sub> matrix and consequent replacement of W<sup>6+</sup> from its lattice site by Fe<sup>3+</sup>.

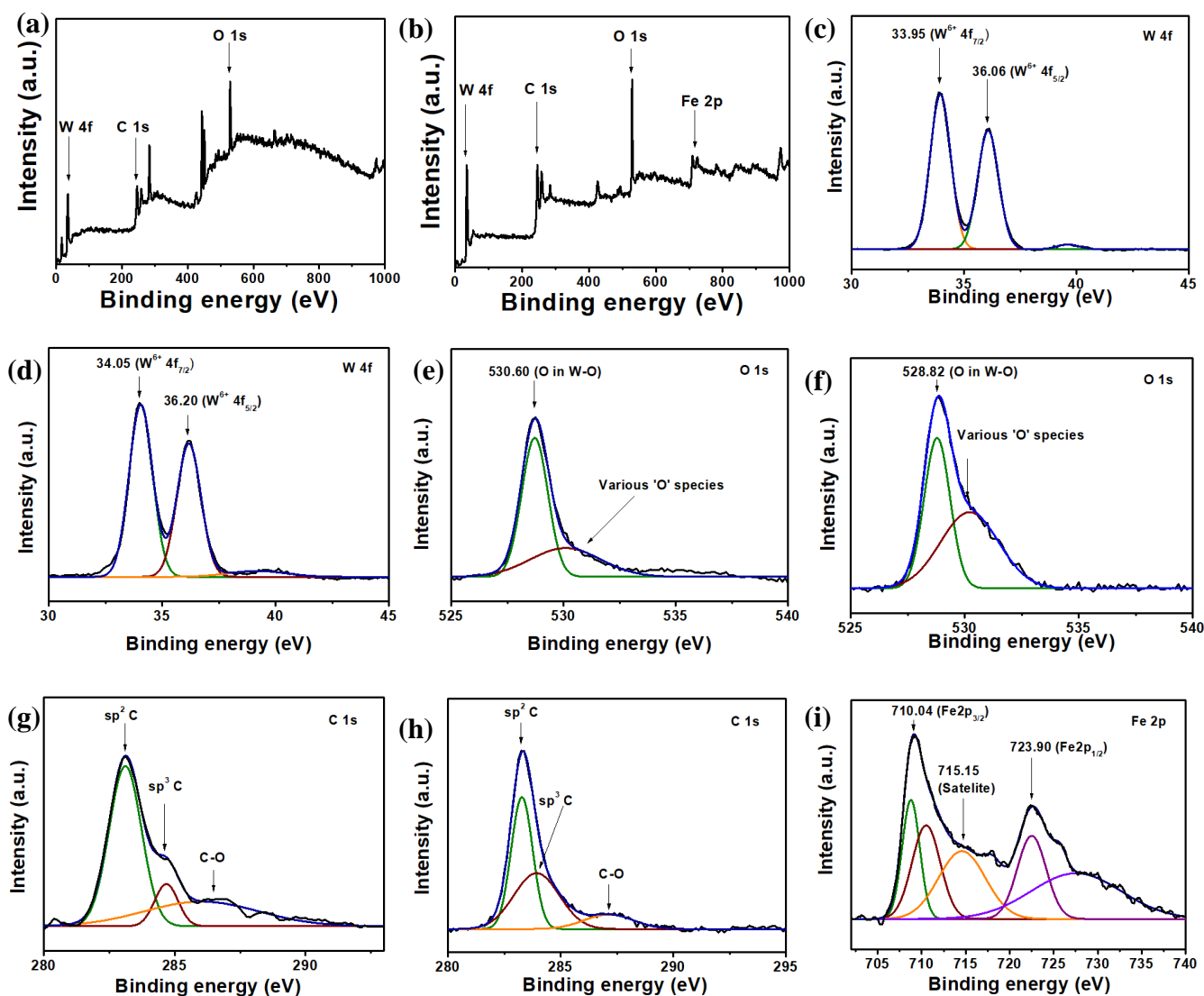


Figure 4.1.9: Full scan XPS survey spectra (a) WR3 and (b) F10WR3, core level analysis: W 4f (c) WR3 and (d) F10WR3, O 1s (e) WR3 and (f) F10WR3, C 1s (g) WR3 and (h) F10WR3, and Fe 2p (i) F10WR3

Analysis of its optical properties is of utmost necessity to ensure effective doping in a crystal lattice. So, in the present work, the alteration of optical characteristics of the as-synthesized



nanocomposites was monitored by using UV-Vis absorption spectra. Figure 4.1.10a demonstrated UV-Visible spectra of nanocomposites in the 275-800 nm range; corresponding Tauc plots were represented in Fig.4.1.10b. A broad absorbance peak at  $\sim 355$  nm was obtained for  $\text{WO}_3$  [29]. This peak was blue-shifted to  $\sim 343$  nm upon introducing rGO and further blue-shifted to  $\sim 329$  nm due to  $\text{Fe}^{3+}$  doping. The optical band gap energies of the corresponding peaks were estimated by Tauc plot. For pristine  $\text{WO}_3$ , the obtained value of band gap was 2.72 eV, which was increased to 2.81 eV due to rGO addition and further increased to 2.87 eV upon  $\text{Fe}^{3+}$  doping. This variation in band gap value could be explained from electronic transition and hybridization point of view. For pristine  $\text{WO}_3$ , the valence band was of O 2p character, and the conduction band was of W 5d character. On introducing the  $\text{sp}^2$  rGO lattice in  $\text{WO}_3$ , the change in electronic interactions increased the band gap. Again,  $\text{Fe}^{3+}$  doping in the  $\text{WO}_3$  lattice induced a Fe 3d level somewhere between valence band and conduction band; simultaneously, distortion of lattice alignment caused oxygen deficiency, accounted for increase in band gap energy.

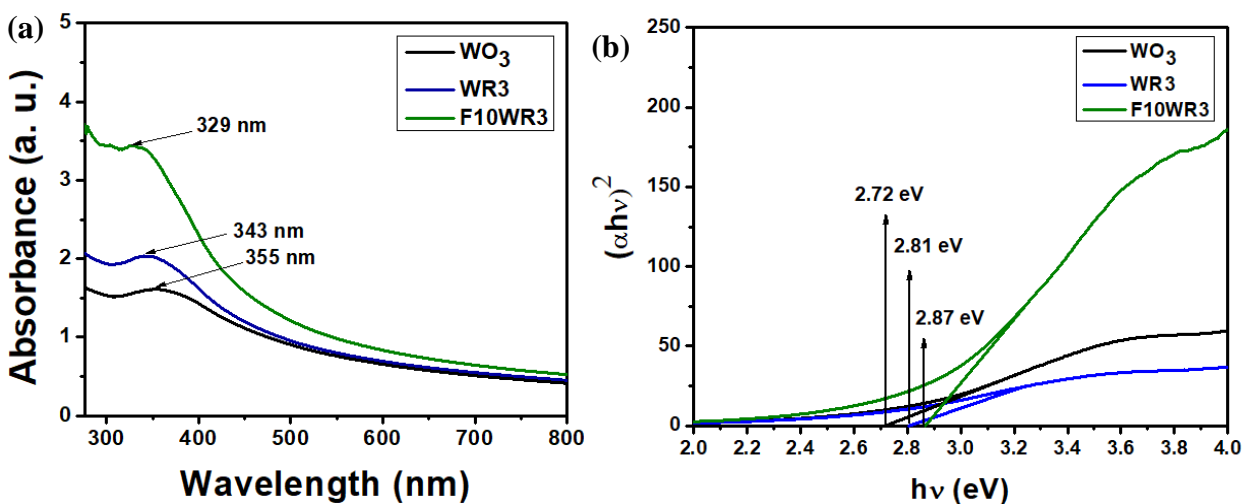


Figure-4.1.10: (a) UV-Vis spectra, (b) Tauc plots of pristine  $\text{WO}_3$ ,  $\text{WR3}$ , and  $\text{F10WR3}$

The PL emission spectra were recorded with an excitation wavelength of  $\sim 310$  nm in the 325–600 nm range at room temperature and depicted in Fig.4.1.11. Three intense peaks were observed for pristine  $\text{WO}_3$ . The peak at  $\sim 412$  nm was aroused due to the near-band-edge (NBE) transition, and the band at  $\sim 467$  nm corresponded to band-to-band transition of  $\text{WO}_3$ . Another broad peak at  $\sim 561$  nm was attributed to deep-level (DL) emission caused by various oxygen vacancies and defects. Upon rGO decoration, high-intensity peak for NBE transition shifted to a

higher wavelength and converted to a shoulder. In contrast, the peak due to band-to-band transition intensified [22, 23]. This might suggest that the presence of highly conducting rGO in contact with  $\text{WO}_3$  provided an additional pathway for the electronic transition from conduction band of  $\text{WO}_3$  (n-type) to valence band of rGO (p-type), which further delayed electron-hole recombination. Similar observations were reported for several graphene-metal oxides-based systems in the works of literature. On the other hand,  $\text{Fe}^{3+}$  doping in the  $\text{WO}_3$  lattice significantly quenched the peak intensities except the augmented peak at  $\sim 561$  nm. This indicated decreased electronic transitions by successful substitution of  $\text{W}^{6+}$  from its lattice sites by dopant  $\text{Fe}^{3+}$  ion.

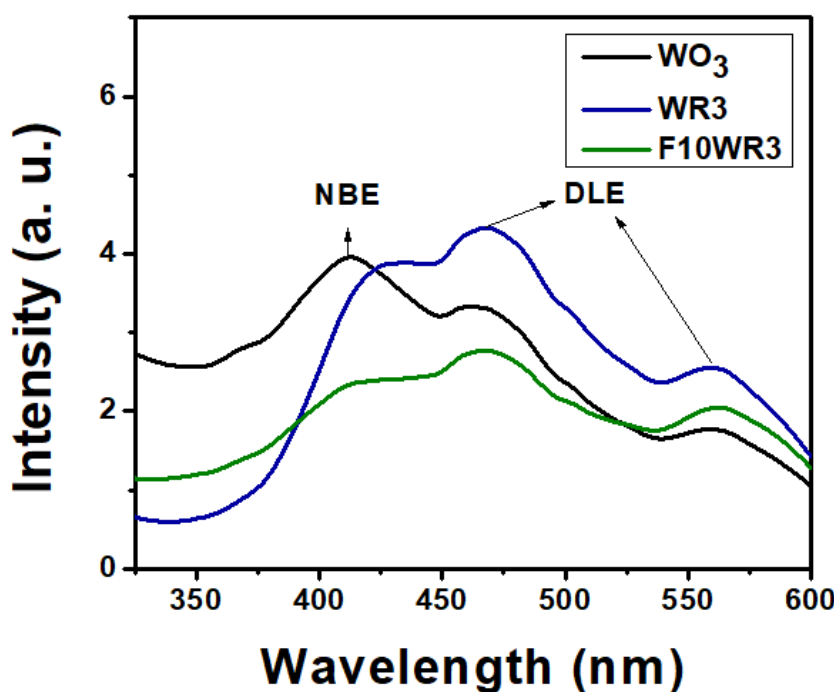


Figure-4.1.11: PL spectra of pristine  $\text{WO}_3$ , WR3, and F10WR3

## 4.1.3.2. Gas sensing performance study:

Optimization of the operating temperature of a sensor is an essential requirement as it is one of the primary characteristics. So, initially, the sensors' base resistance (i.e., resistance in presence of an open atmosphere) was recorded at different operating temperatures in the range  $100^\circ\text{C}$  to  $250^\circ\text{C}$ . Simultaneously, the sensing response of the sensors was also measured in the presence of  $\sim 10$  ppm acetone. It was observed that the resistance (Fig. 4.1.12a) of pristine  $\text{WO}_3$  and all the rGO decorated  $\text{WO}_3$ -based sensors was slowly decreased with an increase in temperature,

following the semiconducting behaviour of the sensing materials. Corresponding sensing graphs (Fig. 4.1.12b) revealed an increase of response upto  $\sim 205^{\circ}\text{C}$ , followed by a decrease beyond  $\sim 205^{\circ}\text{C}$ . This might be because the maximum gas absorption occurred at  $\sim 205^{\circ}\text{C}$ , and afterward, the desorption process predominated. So,  $\sim 205^{\circ}\text{C}$  was considered as the optimized operating temperature of these samples.

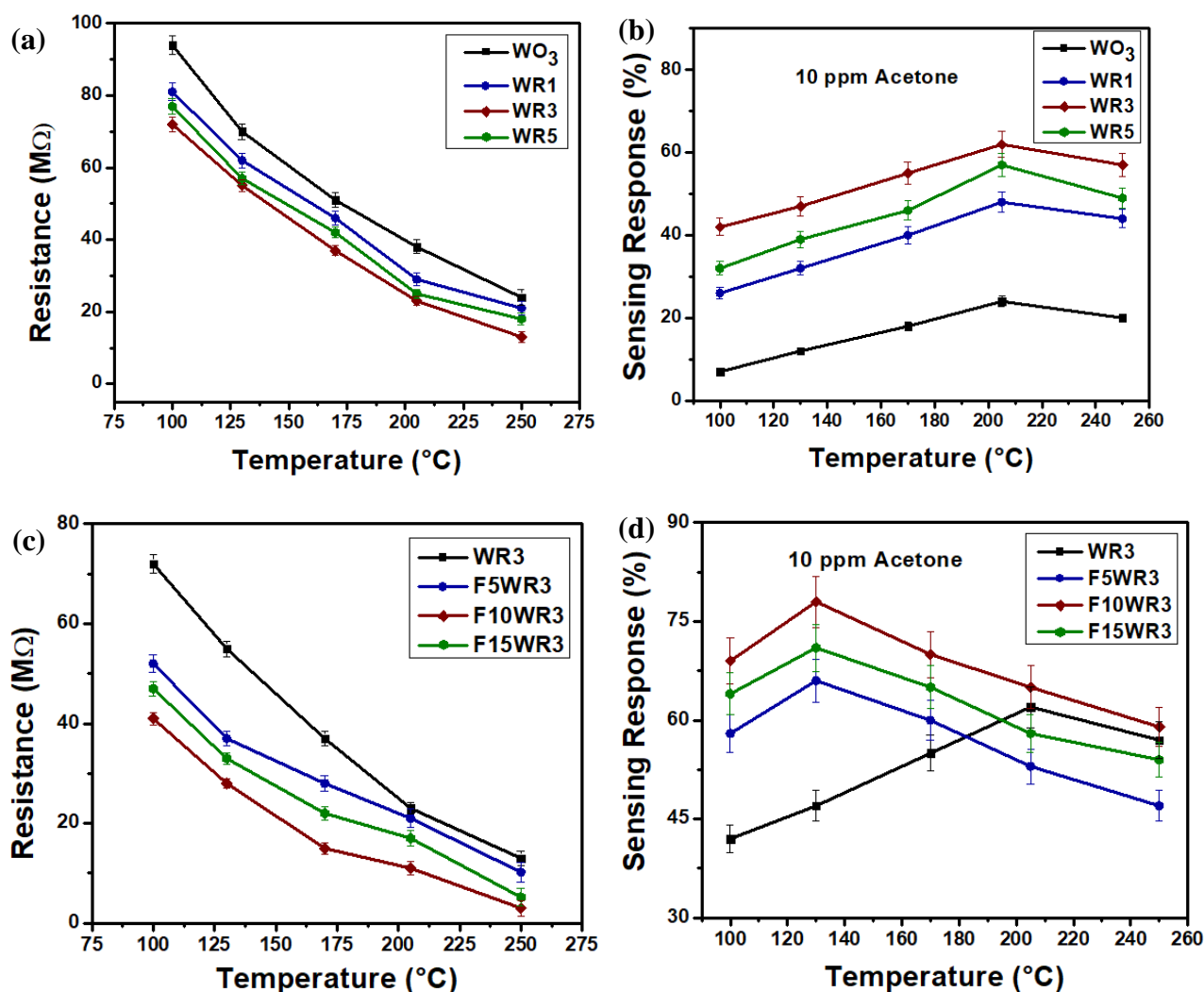


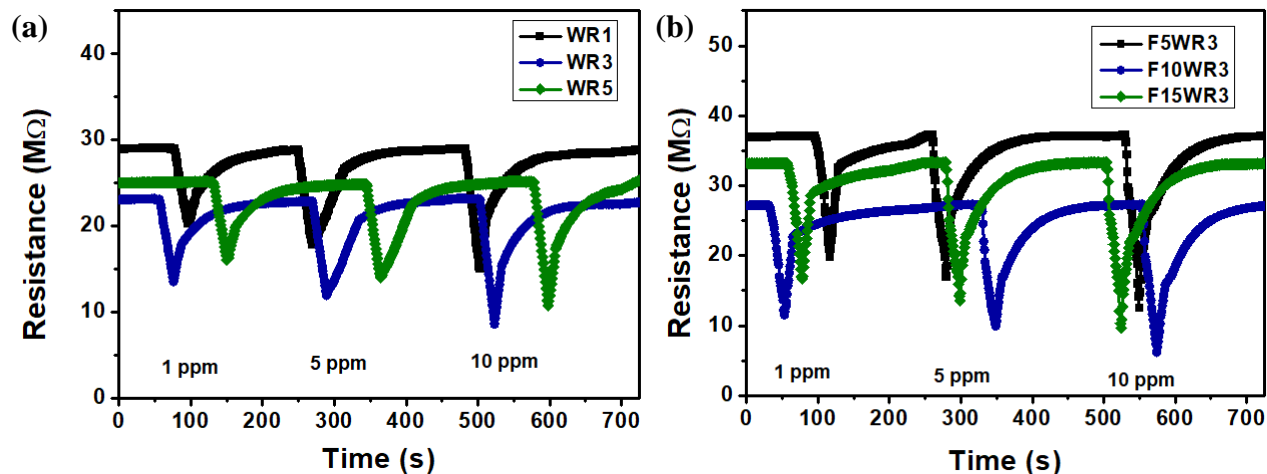
Figure-4.1.12: (a) Change in resistance, (b) change in sensing responses in presence of  $\sim 10$  ppm acetone, at different working temperatures of pristine WO<sub>3</sub>, WR1, WR3, and WR5. (c) Change in resistance, (d) change in sensing responses in presence of  $\sim 10$  ppm acetone, at different working temperatures of WR3, F5WR3, F10WR3, and F15WR3

Among all the WO<sub>3</sub> sensors with different wt% of rGO, the  $\sim 3$  wt% rGO decorated sample (WR3) revealed the maximum response ( $\sim 62\%$ ) at  $\sim 205^{\circ}\text{C}$ . Figure 4.1.12 (c, d) showed the effect of Fe<sup>3+</sup> doping on base resistance and sensing response respectively. The sensing graphs



exhibited similar trends as above. The introduction of  $\text{Fe}^{3+}$  enhanced the sensing response and reduced the optimum working temperature to  $\sim 130^\circ\text{C}$ .  $\sim 10$  wt%  $\text{Fe}^{3+}$  doped  $\text{WO}_3$  sample (F10WR3) demonstrated the maximum sensing response ( $\sim 78\%$ ) at  $\sim 130^\circ\text{C}$ . From the recorded sensing data, it was evident that rGO incorporation significantly decreased the base resistance of the sensors, and subsequently, the sensing response was increased. This is owing to the large surface area of rGO, which provided increased gas adsorption sites. Furthermore, introducing  $\text{Fe}^{3+}$  in this rGO-decorated  $\text{WO}_3$  lattice increased the oxygen vacancies, and the sensing response enormously increased.

Dynamic response curves ensured the reproducibility of the sensing materials and their reversible change in resistance with experimental gas pulses. The sensors were exposed to acetone gases of concentration  $\sim 1$  ppm,  $\sim 5$  ppm, and  $\sim 10$  ppm at their respective operating temperatures, and corresponding sensing responses (Table 4.1.3) were presented in Fig. 4.1.13 a-c. The WR3 sensor showed  $\sim 62\%$  response towards  $\sim 10$  ppm acetone compared to  $\sim 24\%$  response for the pristine  $\text{WO}_3$ -based sensor. This sensing response was enhanced to  $\sim 78\%$  for the F10WR3 sensor in the presence of  $\sim 10$  ppm acetone. Similarly, with the pulse of  $\sim 5$  ppm acetone, we also observed a gradual increase in sensing response from  $\sim 15\%$  for pristine  $\text{WO}_3$  to  $\sim 49\%$  for WR3 upto  $\sim 64\%$  for F10WR3. The as-prepared sensors also delineated appreciable sensing responses even at  $\sim 1$  ppm acetone. The sensing response was very low  $\sim 8\%$  for pristine  $\text{WO}_3$ , but, it was  $\sim 43\%$  for WR3 and it reached  $\sim 56\%$  for F10WR3.



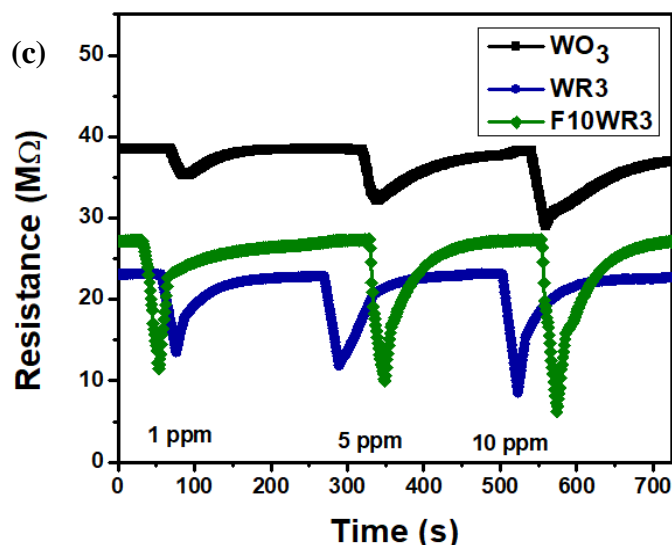


Figure –4.1.13: Dynamic sensing response of (a) WR1, WR3, and WR5, (b) F5WR3, F10WR3, and F15WR3, (c) pristine WO<sub>3</sub>, WR3, and F10WR3 sensors in presence of acetone at corresponding optimum operating temperature

Table 4.1.3: Sensing response of the sensors in presence of different acetone concentration:

Acetone concentration (ppm)	Sensing response (S%) $\pm$ 2%					
	WR1	WR3	WR5	F5WR3	F10WR3	F15WR3
1	30	43	36	47	56	50
5	37	49	44	54	64	59
10	48	62	57	66	78	71

These gas sensing performances indicated that the introduction of rGO and doping with Fe<sup>3+</sup> tailored the electronic properties of the materials in order to improve the sensing properties and also capable of detecting very low concentrations of acetone effectively. Besides superior sensing response, the effectiveness of a sensor was judged based on its fast response and recovery time. This quick response and recovery of a sensor depends on the adsorption interaction between the sensing material and experimental gas molecules. Over chemisorptions, physisorption requires less energy, providing a scope of fast response and recovery of the sensor.

Freundlich isotherm was used to determine the adsorption interaction in the gas sensing experiments, given by equation 4.1.8 [26]:

$$\log S = \log \alpha + \beta \log C \quad \dots\dots\dots (4.1.8)$$

Where  $S$  is the sensing response,  $\alpha$  is the proportionality constant,  $\beta$  is the exponential factor, and  $C$  is the gas concentration. The value of the exponential term below 1 is for physisorption, and for chemisorption, it is greater than 1. The slope of the linear fitting of the  $\log S$  vs.  $\log C$  curve determined the  $\beta$  value. In the present study, for the WR3 sensor, it was 0.1499, whereas for F10WR3, it was 0.1363 (Fig. 4.1.14a), i.e., in all the cases, the interaction between analyte gas molecules (acetone) and sensing material surface was physisorption, and hence short response and recovery times were anticipated.

The time required for a sensor to achieve  $\sim 90\%$  of its total response on exposure to the analyte gas is known as response time, and the time required regaining  $\sim 90\%$  of its base resistance after removal of the gas flow is recovery time [30]. All three sensors (pristine  $\text{WO}_3$ , WR3, and F10WR3) demonstrated (Fig.4.1.14b) a response time of  $\sim 20$  s. However, the pristine  $\text{WO}_3$  sensor showed the slowest recovery time of  $\sim 110$  s (recovery without purging of any gas), and that of F10WR3 was  $\sim 75$  s, which was the fastest one; the WR3 sensor exhibited a moderate recovery time of  $\sim 90$  s. This quick response and fast recovery time of sensors made them suitable for short-time multiple pulse detection.

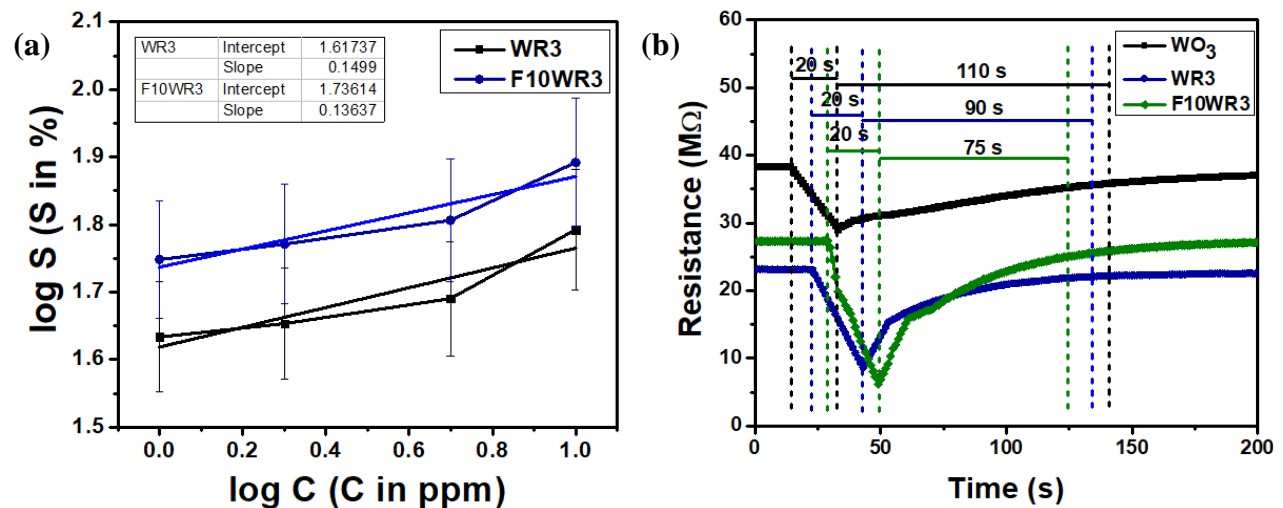


Figure-4.1.14: (a)  $\log S$  vs.  $\log C$  plot, (b) Response and recovery time of pristine  $\text{WO}_3$ , WR3 and F10WR3 sensor against  $\sim 10$  ppm of acetone vapour

It was already stated before that the efficiency of a sensor to detect a minute concentration of a gas is determined by its lowest limit of detection (LOD). Here, the lowest limit of detection of F10WR3 sensors was theoretically calculated by using the standard IUPAC equation [31] as follows:

$$C_L = (k \times S_b) / S \quad \dots\dots\dots (4.1.9)$$

The LOD value obtained by calculation was ~ 0.05 ppm for F10WR3 sensors.

The WR3 and F10WR3 sensors were also exposed to high concentrations of acetone to understand their saturation limit of detection. It was observed (Fig.4.1.15) that the sensing responses for both sensors were slightly increased upto ~ 50 ppm, and after that, the sensing responses became almost static. This near-saturation was achieved in the presence of a high concentration of analyte gas might be owing to limited active sites on the sensing material surface, and a further increase in gas concentration left the sensing material unperturbed.

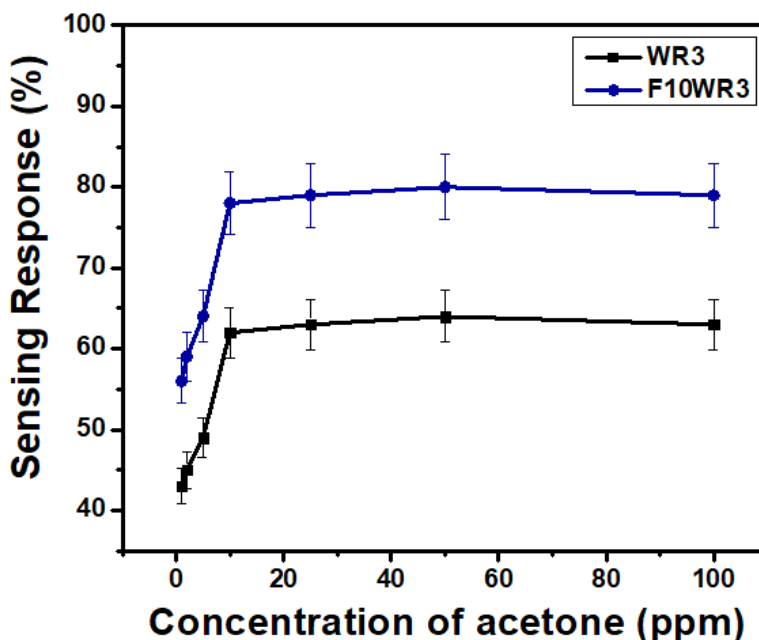


*Figure-4.1.15: Saturation of sensing response of WR3 and F10WR3 sensors*

Relative humidity (%RH) of the sensing environment could also influence the sensing response. Generally, with the increase in %RH, the sensing response decreases. Therefore, to study the effect of %RH on sensing, certain relative humid conditions were prepared using saturated solutions of some inorganic salts in closed vessels as per the literature [23, 29]. Then, the sensors

were exposed to these solutions for ~ 6 hours and the sensing performance in the presence of ~ 10 ppm acetone was recorded. It was observed (Fig. 4.1.16) that the sensing responses decreased with an increase in %RH. However, the deviations were almost negligible, which might be due to the presence of a few numbers of H<sub>2</sub>O molecules at operating temperatures higher than 100°C, where initially adsorbed H<sub>2</sub>O molecules were converted to vapour.

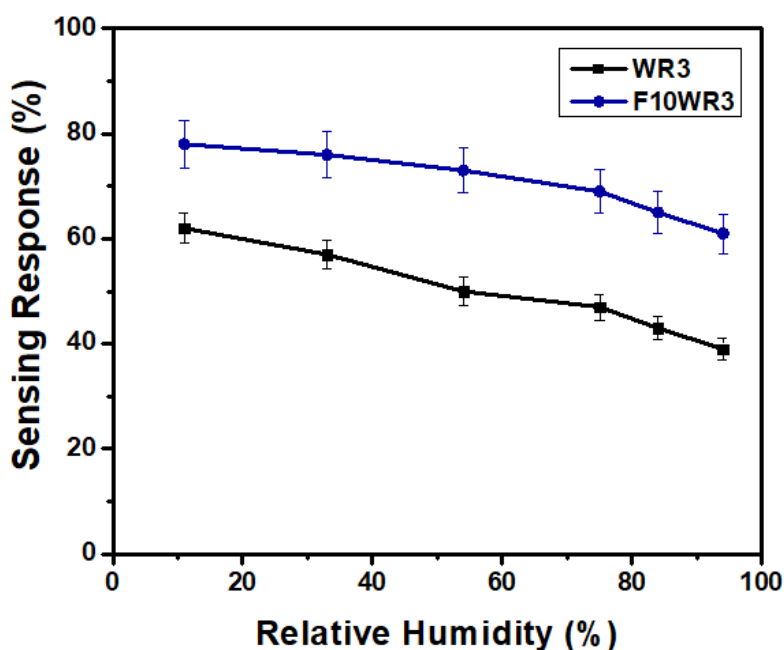


*Figure-4.1.16: Variation of sensing response with relative humidity for WR3 and F10WR3 sensors*

The cross-sensitivity of the sensors was studied to know their efficacy in selective detection of a gas in harsh environments. The selectivity of the fabricated sensors was measured at their corresponding operating temperature in the presence of ~ 10 ppm concentration of different interfering gases like ethanol, ammonia, formaldehyde, carbon monoxide, and methane. It was conveniently observed (Fig. 4.1.17) that all the sensors exhibited a superior response for acetone over other gases under identical experimental conditions. It was also found that the F10WR3 sensor detected acetone more efficiently. Generally, the selectivity of an MOS nanocomposite depends on several factors like doping, composite formation, surface morphology, operating temperature, target gas properties etc. In the present report, F10WR3 exhibited superior selectivity towards acetone in the presence of other interfering gases. Among the reported gases, acetone possesses the maximum dipole moment ( $\mu = 2.91$  D). Due to the high polarity of

acetone, a surface chemical reaction between analyte acetone and the prepared F10WR3 nanocomposite was primarily favorable. Besides this, the bond dissociation energy of acetone (~ 393 KJ/mole) might also facilitate its effective interaction with fabricated sensing material over other interfering gases. All these simultaneous and combined effects were presumably accountable for the high sensing response of the sensor towards acetone.

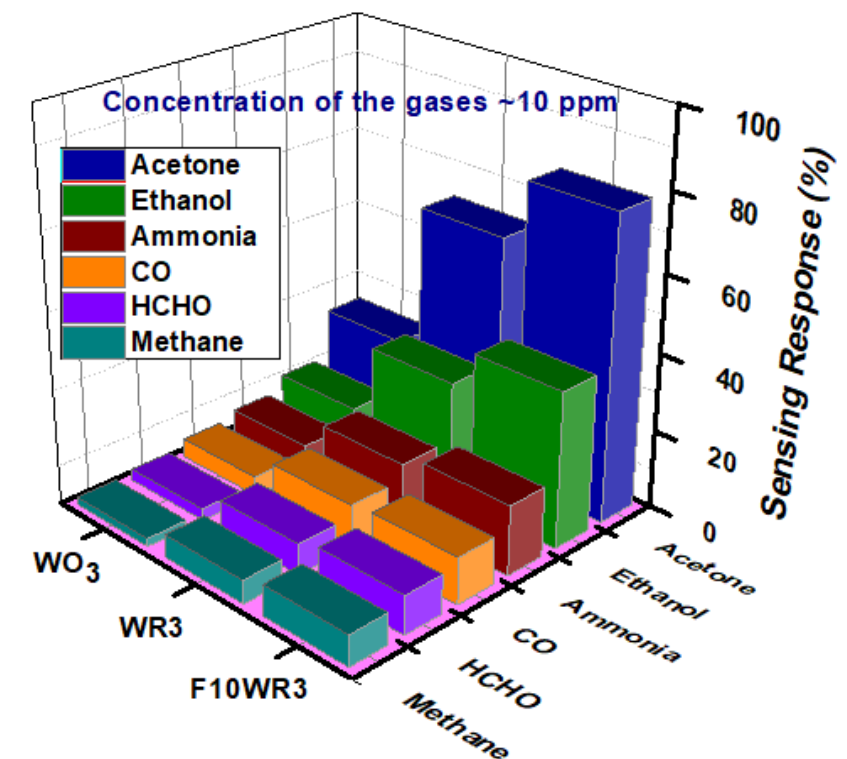


*Figure-4.1.17: Selectivity curve for pristine WO<sub>3</sub>, WR3, and F10WR3 sensors against ~ 10 ppm of different gases at corresponding operating temperatures*

Long-term durability and stable sensing response is other crucial factor that needs to be addressed from the commercial point of view. The base resistance and sensing response in the presence of ~ 10 ppm acetone for WR3 and F10WR3 sensors at their respective operating temperatures were recorded over 90 days at an interval of 10 days. Both the sensors showed (Fig. 4.1.18 a, b) almost negligible variation in base resistance with nearly constant sensing responses over 3 months. These results justified the prolonged stability of the as-prepared sensors.

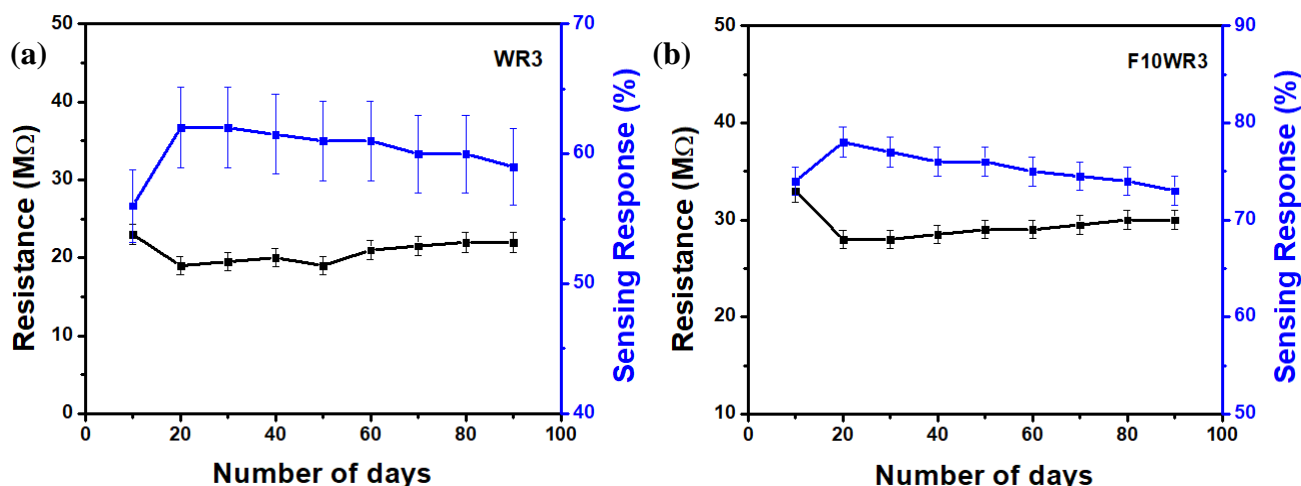


Figure-4.1.18: Stability graphs of (a) WR3 and (b) F10WR3 sensors

Since acetone in exhaled human breath has been regarded as a potential breath biomarker for non-invasive diabetes detection, its concentration in human breath beyond  $\sim 1$  ppm is considered diabetic. The previously described sensing performance study already revealed that the optimized F10WR3 sensor was demonstrated its efficacy in  $\sim 1$  ppm acetone detection. Now, to establish the developed sensor as a suitable candidate for diabetes detection, following experiments were done. Initially, the exhaled human breath of a healthy person was collected in a tedlar bag (Fig. 4.1.19a) and analyzed in an in-house GCMS system (Agilent 5977B GC/MSD). The concentration was obtained of  $< 1$  ppm ( $\sim 0.7$  ppm).

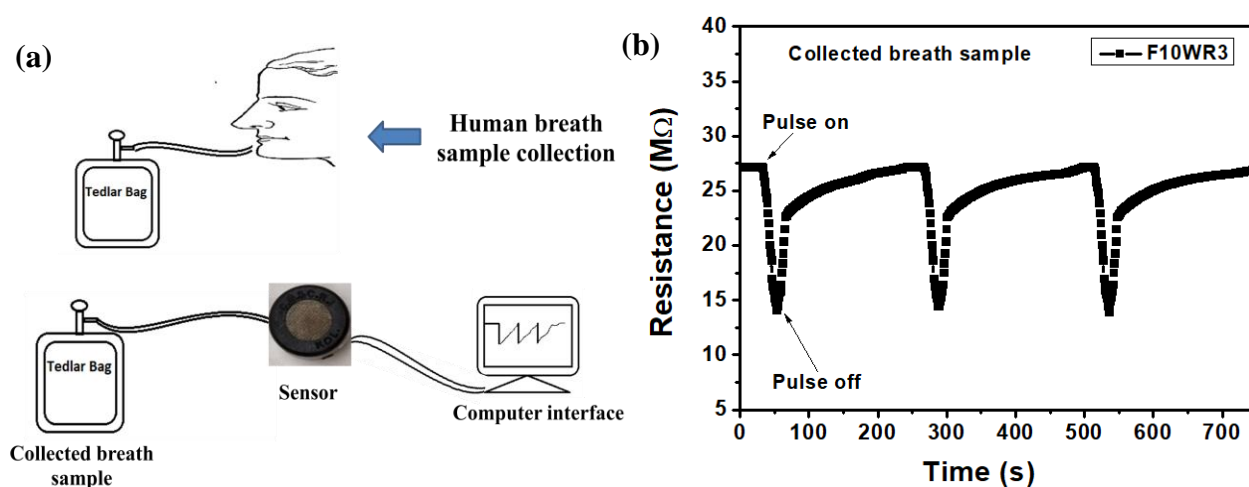


Figure-4.1.19: (a) Schematic diagram of a typical human breath sample collection, (b) Sensing response of F10WR3 in presence of human breath sample

This collected breath sample was then fed to the fabricated F10WR3 sensor through a silicon pipe stuffed with silica gel (used as moisture trap to adsorb moistures in the breath sample), and an n-type sensing response of ~ 45% (Fig. 4.1.19b) was observed. This sensing response was in good agreement with the ~ 56% sensing response obtained using the F10WR3 sensor in the presence of ~ 1 ppm commercially brought acetone. Therefore, it could be concluded that the F10WR3 sensor might be a potential candidate for non-invasive diabetes detection.

### 4.1.3.3. Gas sensing mechanism:

#### 4.1.3.3.1. Electron depletion model:

The outstanding sensing performance of the fabricated sensors could be rationalized with the help of the electron depletion model (Fig. 4.1.20 a, b) and consequent band bending concept [32, 33]. Since, the band gap energies of pristine WO<sub>3</sub> and its functionalized nanocomposites were in the range of 2.7 – 2.9 eV, some electrons from the valence band jumped to the conduction band at respective working temperatures and exhibited good conductivity. In an open atmosphere, they got adsorbed on the sensing material surface due to the presence of plenty of oxygen. The oxygen molecules converted themselves to different oxygenated species, depending on the operating temperature, by extracting electrons from the conduction band, as follows [29]:



These ionized oxygen molecules served as surface receptor groups in the presence of analyte gas. The scavenging of electrons from the conduction band by the oxygen molecules created an electron depletion layer on the sensing material surface. As a result of this reduction in electron density, the potential energy barrier increased and resulted in increased resistance of the sensors. This steady-state resistance is generally termed as base resistance.

In the presence of an experimental acetone gas pulse, a redox-type reaction was initiated between acetone gas molecules and surface-adsorbed oxygenated ions. This surface chemical reaction oxidized acetone to CO<sub>2</sub> and H<sub>2</sub>O and simultaneously concentration of oxygenated ions reduced which revert the trapped electrons to the conduction band, as per equation 4.1.14 [29].





With the return of electrons, the accumulation and depletion layers became thinner, and the potential energy barrier decreased. In the presence of large number of electrons, the conductivity increased, resulting in a decrease of resistance and n-type sensing response observed.

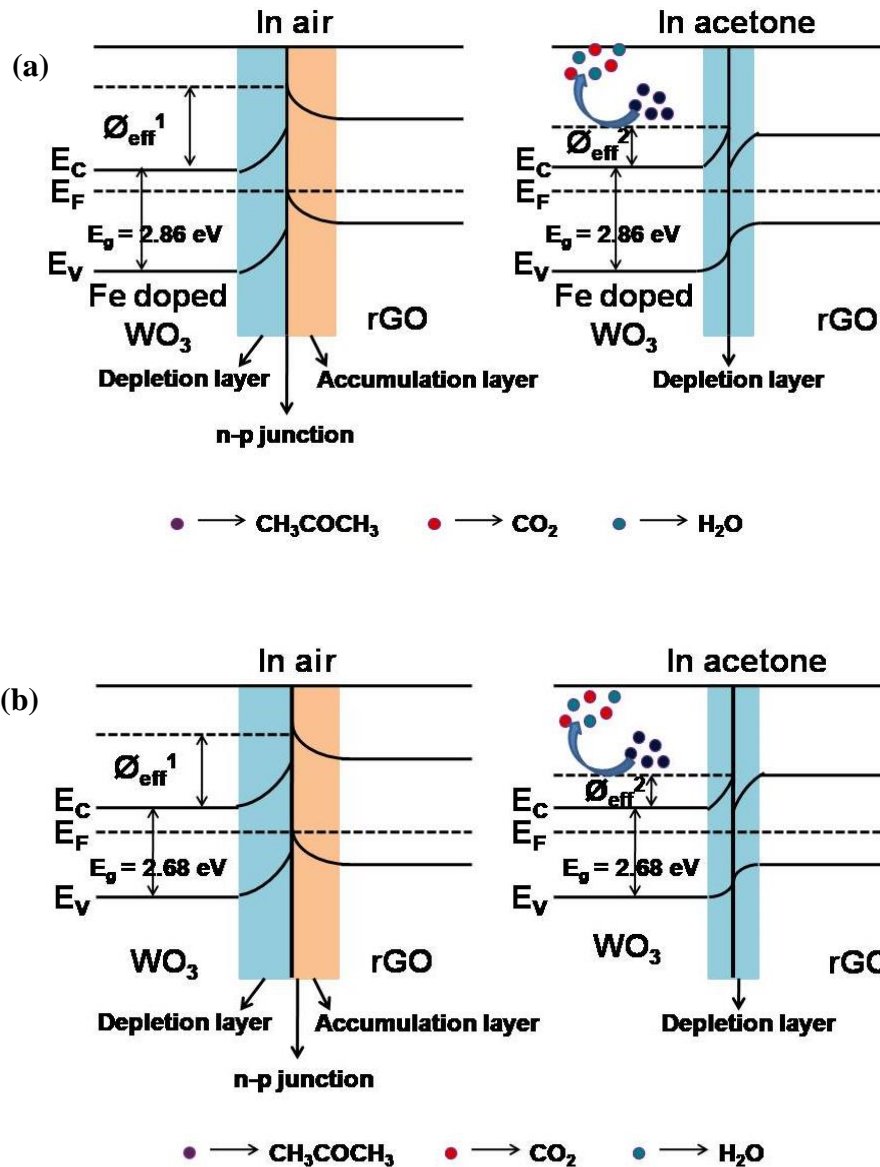


Figure-4.1.20: Schematic representation of acetone sensing mechanism of fabricated sensors using electron depletion model (a) rGO decorated  $WO_3$ ; (b)  $Fe^{3+}$  doped rGO decorated  $WO_3$

Pristine  $WO_3$ , having shallow defect density and a low active gas adsorption site, could transfer few electrons to the conduction band. Therefore, very few oxygenated ions formed that could react with analyte gas, and a poor sensing response by the pristine  $WO_3$ -based sensor was

observed. Upon rGO introduction, a p-n heterojunction was created. Decoration of pristine  $\text{WO}_3$  with rGO increased the defect densities, active surface area, and band gap energy, which could tailor the electronic properties of the nanocomposite. Now, more oxygenated ions developed a depletion layer across the n-type material and created an accumulation layer around the p-type material, accounting for lower base resistance and consequently improving the sensing response. However, further on  $\text{Fe}^{3+}$  doping, as earlier mentioned, some  $\text{Fe}^{3+}$  replaced  $\text{W}^{6+}$  from their inherent lattice sites, and such incorporation of  $\text{Fe}^{3+}$  increased lattice defects and generated oxygen vacancies. It was evidenced by the deconvoluted O 1s XPS spectra comparison of WR3 (Fig. 9f) and F10WR3 (Fig. 9g), which revealed that the oxygen vacancy increased to  $\sim 53\%$  in F10WR3 compared to  $\sim 35\%$  of WR3. This perturbation of lattice proved to be beneficial for the enhancement of sensing response. Thus, as we moved from pristine  $\text{WO}_3$  to WR3 to F10WR3, the number of active gas adsorption sites increased as more oxygenated ions formed, resulting in interaction with an enhanced number of experimental gas molecules and accounting for amplified gas sensing performance.

#### **4.1.3.3.2. Impedance spectroscopy:**

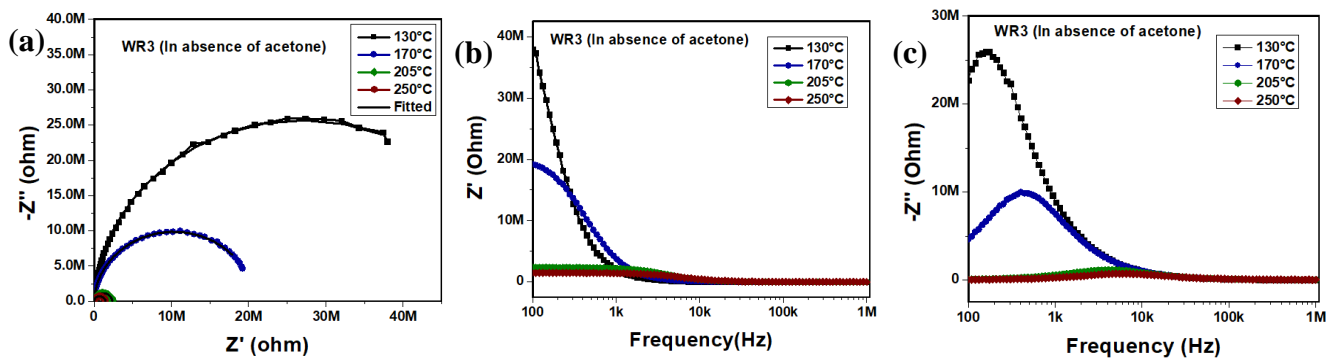
In order to get better perspectives regarding the electrical properties of the as-synthesized metal oxide semiconducting materials, impedance measurement was carried out. Generally, impedance spectroscopy reveals the electrical behavior of different components (grain, grain boundary, and electrode interface) of a polycrystalline sensing material, effectively differentiating their contribution towards overall electrical properties [34, 35]. Comprehensive analysis of the real and imaginary components of complex impedance ( $Z$ ) at varying frequencies and temperatures gives an idea about an electrical characteristic of the material. Nyquist plot, a plot of resistive component ( $Z'$ ) against reactive component ( $Z''$ ) of impedance, clarifies the contributions of different electrical components depending on the number of semicircles produced. A single semicircle indicates the grain contribution, whereas the grain boundary contribution describes by the second semicircle and the presence of a third semicircle specifies the contribution from the electrode interface.

To illustrate these contributions, for WR3 and F10WR3 samples,  $Z'$  and  $Z''$  data were collected over a broad frequency range (100 Hz to  $10^6$  Hz) and temperature range ( $130^\circ\text{C}$  to  $250^\circ\text{C}$ ), both in the absence and presence of  $\sim 10$  ppm acetone. The Nyquist plots of WR3 (Fig. 4.1.21 a, d)

and F10WR3 (Fig. 4.1.21 g, j) at different temperatures were presented. It was observed that there existed only one single semicircle, which represented a complete electrical contribution from grain with no grain boundary or electrode interface contribution. Furthermore, at a lower temperature range, the impedance arcs were a part of large semicircles, and with an increase in temperature, the curvatures of the impedance arcs gradually depressed. The appearance of this kind of semicircle completely justified the nature of fabricated nanocomposite thin film where the majority of charge carriers were residing at grain sites and charge carriers' concentration at grain boundary was negligible [36].

The corresponding circuit diagram was modeled using a resistance and parallelly connected constant phase element (CPE), which was analogous to marginally deformed semicircles, with the center of the arc below the  $Z'$  axis. This kind of semicircle resulted from a non-ideal Debye type of relaxation caused by inhomogeneous surface phenomena of the materials. The Nyquist plots at different temperatures were fitted using ZView2 software. Another noticeable fact was that there was a gradual decrease in resistance of the sensors in the presence of experimental gas and with a temperature rise. The decrease in resistance in the presence of acetone ensured the n-type characteristic of the sensing material. However, the change in resistance with temperature certified the typical semiconducting nature.

Additionally,  $Z'$  and  $Z''$  were separately plotted against frequency at the experimental temperature range. The variation of  $Z'$  with frequency for WR3 (Fig. 4.1.21 b, e) and F10WR3 (Fig. 4.1.21 h, k) demonstrated that at the low-frequency region, the curves at different temperatures exhibited a dispersed nature accompanying a decrease in resistive impedance ( $Z'$ ) with temperature. This accounted for the negative temperature coefficient of resistance (NTCR), a characteristic of semiconductor. Nonetheless, the individually dispersed plots converged to a single line at the high-frequency zone.



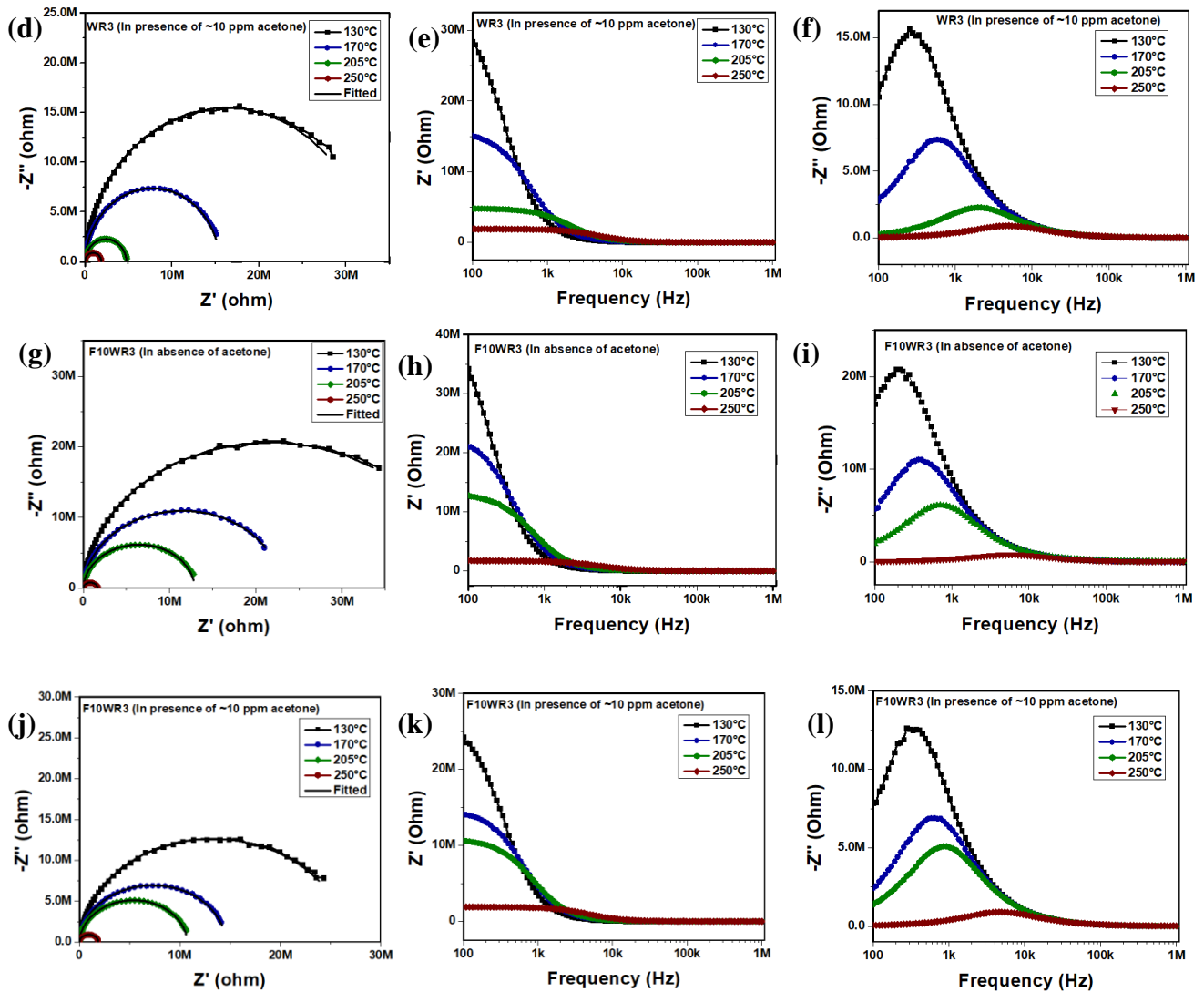


Figure-4.1.21: At variable frequency, in absence of acetone for WR3 (a) Nyquist plot, (b) variation of real part of impedance ( $Z'$ ), (c) variation of imaginary part of impedance ( $Z''$ ), in presence of  $\sim 10$  ppm acetone for WR3 sensor (d) Nyquist plot, (e) variation of real part of impedance ( $Z'$ ), (f) variation of imaginary part of impedance ( $Z''$ ), in absence of acetone for F10WR3 (g) Nyquist plot, (h) variation of real part of impedance ( $Z'$ ), (i) variation of imaginary part of impedance ( $Z''$ ), in presence of  $\sim 10$  ppm acetone for WR3 sensor (j) Nyquist plot, (k) variation of real part of impedance ( $Z'$ ), (l) variation of imaginary part of impedance ( $Z''$ )

The plot of the reactive component of impedance ( $Z''$ ) with frequency displayed maxima corresponding to different temperatures, known as relaxation frequency ( $f_{\max}$ ). It was evident that with an increase in temperature, the maxima shifted toward high frequency for WR3 (Fig. 4.1.21 c, f) and F10WR3 (Fig. 4.1.21 i, l), accounting for the temperature-dependent relaxation process.

The activation energy of this relaxation process could be calculated by using the Arrhenius type relation:

$$f_{\max} = f_0 e^{(-E_{\text{rel}}/kT)} \quad \dots\dots\dots (4.1.15)$$

Where,  $E_{\text{rel}}$  is the activation energy of the relaxation process. The plot of  $\ln f_{\max}$  with  $(1000/T)$ , followed by a linear fitting, produced the activation energy values (Fig. 4.1.22). The results furnished that the F10WR3 sensor required less activation energy than the WR3 sensor, as per the lower optimum operating temperature for the F10WR3 sensor. It is well known that most conducting species are charged oxygenated ions in a semiconductor lattice. The hopping of these ions modulates the oxygen vacancies in the sensing material. In the absence and presence of analyte gas molecules, a potential energy barrier developed via the variation of charge carrier concentration. As reported in some literature, the activation energy close to 1 eV indicates doubly ionized oxygen vacancies and singly ionized oxygen vacancies are  $\sim 0.3 - 0.5$  eV. The calculated value of activation energy of the F10WR3 sample was  $\sim 0.52$  eV, which pointed out that the oxygenated ions produced here during gas sensing were singly charged oxygen ions.

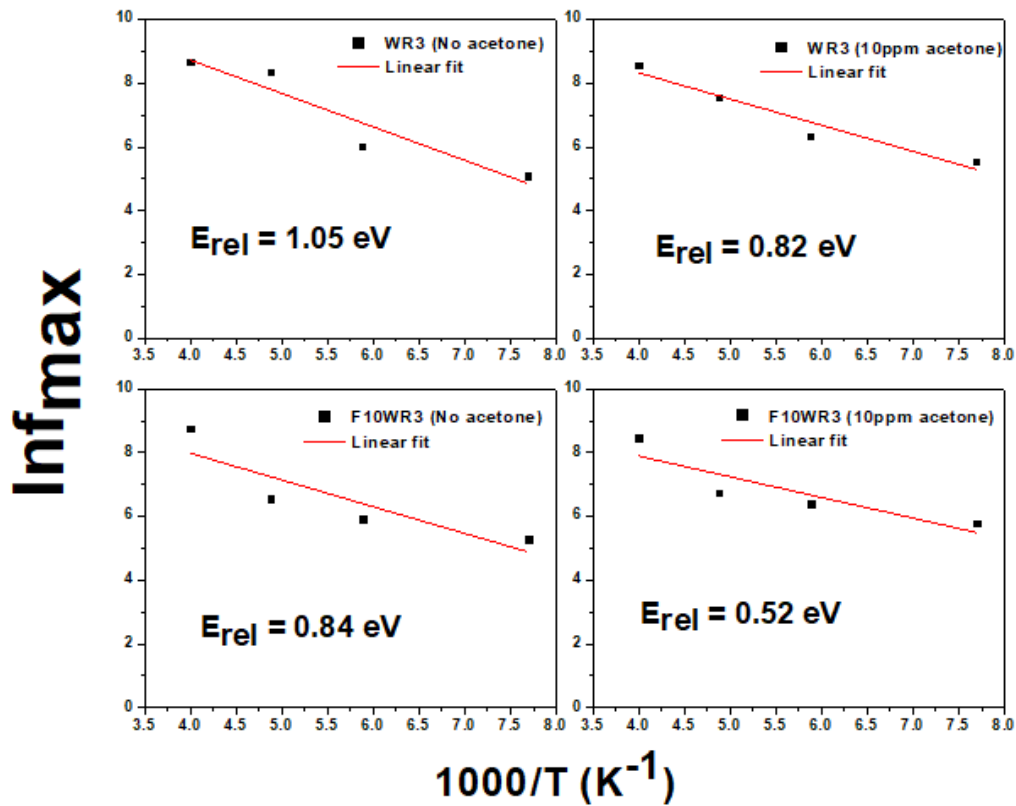


Figure-4.1.22: Activation energy from  $\ln f_{\max}$  vs.  $(1000/T)$  graph for relaxation processes

The comparative sensing performance of some literature works with the developed rGO decorated Fe<sup>3+</sup> doped WO<sub>3</sub> nanocomposite sensor was tabulated here (Table 4.1.4).

Table – 4.1.4: Comparative study of acetone sensors based on WO<sub>3</sub> nanocomposite:

Sensing material	Synthesis technique	Working temp. (°C)	Detection conc. (ppm)	Response (R <sub>a</sub> /R <sub>g</sub> )	Res./ Rec. time (s)	Ref.
Graphene oxide-WO <sub>3</sub> composite nanofibers	Electrospinning	375	100	35.9	4/10	[7]
Ultrathin WO <sub>3</sub> modified by g-C <sub>3</sub> N <sub>4</sub>	Hydrothermal	340	100	35	9/3.8	[8]
WO <sub>3</sub> -SnO <sub>2</sub> nano sphere composite	Hydrothermal	210	1000	16	15/11	[9]
WO <sub>3</sub> nanorods/thin SnO <sub>2</sub> coverage	Hydrothermal	300	100	6	3/28	[10]
WO <sub>3</sub> nanomaterials	Hydrothermal	260	50	36.7	5/7	[11]
3D ordered WO <sub>3</sub> /Au nanocomposites	Template assisted synthesis	410	1.5	7.6	7/8	[12]
Bimetallic AuPd alloy nanoparticles decorated macroporous WO <sub>3</sub>	Template assisted synthesis	300	10	12	8/5	[13]
Sn-doped WO <sub>3</sub> thin films	Sputtering	300	1.5	30%	180/240	[14]
Gd doped WO <sub>3</sub> /rGO nanocomposite	Precipitation	200	50	54	-/-	[15]

---

<b>Fe<sup>3+</sup> doped rGO decorated WO<sub>3</sub> nanocomposite</b>	<b>Sol-gel</b>	<b>130</b>	<b>10</b>	<b>4.6</b>	<b>20/75</b>	<b>This work</b>
---------------------------------------------------------------------------------	----------------	------------	-----------	------------	--------------	----------------------

---

### 4.1.4. Conclusion:

In this work, reduced graphene oxide (rGO) (1, 3, and 5 wt%) decorated WO<sub>3</sub> and Fe<sup>3+</sup>-doped (5, 10, and 15 wt%) rGO decorated WO<sub>3</sub> were synthesized in a facile sol-gel process. The fabricated sensors produced repeatable and reproducible ppm-level selective acetone sensing performance at a comparatively low temperature. The optimized ~ 3 wt% rGO decorated ~ 10 wt% Fe<sup>3+</sup>-doped WO<sub>3</sub> (F10WR3) sensor revealed an enhancement of acetone sensing response (~ 78%) in the presence of ~ 10 ppm acetone even at a lower temperature (~ 130°C) compared to that of the pristine WO<sub>3</sub> (~ 205°C), with fast response (~ 20 s) and recovery (~ 75 s) time. The developed sensor could detect as low as ~ 1 ppm acetone with considerable sensing response. This significant sensing performance with long-term stability was attributed to modulated defect density by virtue of doping with Fe<sup>3+</sup> in pristine WO<sub>3</sub> and its decoration with rGO. The selective acetone sensing of the optimized sensor could be cumulatively presented as an effect of multiple parameters, such as bond dissociation energy, polarity of the analyte molecule, collision diameter, nature of the sensing material, etc. This enhanced sensing performance towards acetone was well established using different characterization studies and electrical properties investigation through impedance spectroscopy. Overall, the manifestation of a prolific sensing response to low ppm acetone gas with adequate selectivity, good reproducibility, and stability made the sensor a promising member in the actual time application domain, especially in breath acetone detection for non-invasive diagnosis of diabetes.

**References:**

- [1] S. Sen, S. Kundu, Reduced graphene oxide (rGO) decorated ZnO-SnO<sub>2</sub>: A ternary nanocomposite toward improved low concentration VOC sensing performance, *J. Alloys Compd.* 881 (2021) 160406. <http://doi.org/10.1016/j.jallcom.2021.160406>.
- [2] S. Sen, S. Maity, S. Kundu, Reduced graphene oxide (rGO) decorated NiO-SnO<sub>2</sub> nanocomposite based sensor towards room temperature diabetic biomarker detection, *J. Alloys Compd.* 966 (2023) 171533. <http://doi.org/10.1016/j.jallcom.2023.171533>.
- [3] A. Staerz, U. Weimar, N. Barsan, Understanding the potential of WO<sub>3</sub> based sensors for breath analysis, *Sensors* 16 (2016) 1815. <http://doi.org/10.3390/s16111815>.
- [4] H. Long, W. Zeng, H. Zhang, Synthesis of WO<sub>3</sub> and its gas sensing: a review, *J. Mater. Sci.: Mater. Electron* 26 (2015) 4698-4707. <http://doi.org/10.1007/s10854-015-2896-4>.
- [5] C. Dong, R. Zhao, L. Yao, Y. Ran, X. Zhang, Y. Wang, A review on WO<sub>3</sub> based gas sensors: Morphology control and enhanced sensing properties, *J. Alloy Compd.* (2019) 153194. <http://doi.org/10.1016/j.jallcom.2019.153194>.
- [6] V. Hariharan, B. Gnanavel, R. Sathiyapriya, V. Aroulmoji, A review on tungsten oxide (WO<sub>3</sub>) and their derivatives for sensor applications, *Int. J. Adv. Sci. Eng.* 5 (2019) 1163-1168. <http://doi.org/10.29294/IJASE.5.4.2019.1163-1168>.
- [7] J. Zhang, H. Lu, C. Yan, Z. Yang, G. Zhu, J. Gao, F. Yin, C. Wang, Fabrication of conductive graphene oxide-WO<sub>3</sub> composite nanofibers by electrospinning and their enhanced acetone gas sensing properties, *Sens. Actuators B Chem.* 264 (2018) 128-138. <http://doi.org/10.1016/j.snb.2018.02.026>.
- [8] X. Zhang, B. Dong, W. Liu, X. Zhou, M. Liu, X. Sun, J. Lv, L. Zhang, W. Xu, X. Bai, L. Xu, S. Mintova, H. Song, Highly sensitive and selective acetone sensor based on three-dimensional ordered WO<sub>3</sub>/Au nanocomposite with enhanced performance, *Sens. Actuators B Chem.* 320 (2020) 128405. <https://doi.org/10.1016/j.snb.2020.128405>.
- [9] F. Zheng, L. Zhang, Y. Li, Q. Liu, Z. Li, H. Yao, Bimetallic AuPd alloy nanoparticles decorated on macroporous WO<sub>3</sub> supports for selective detection of acetone, *ACS Appl. Nano Mater.* 4 (2021) 2713-2720. <https://doi.org/10.1021/acsanm.0c03345>.
- [10] S. Sachdeva, A. Agarwal, R. Agarwal, A comparative study of gas sensing properties of tungsten oxide, tin oxide and tin-doped tungsten oxide thin films for acetone gas detection, *J. Electronic Mater.* (2019). <http://doi.org/10.1007/s11664-018-06881-1>.



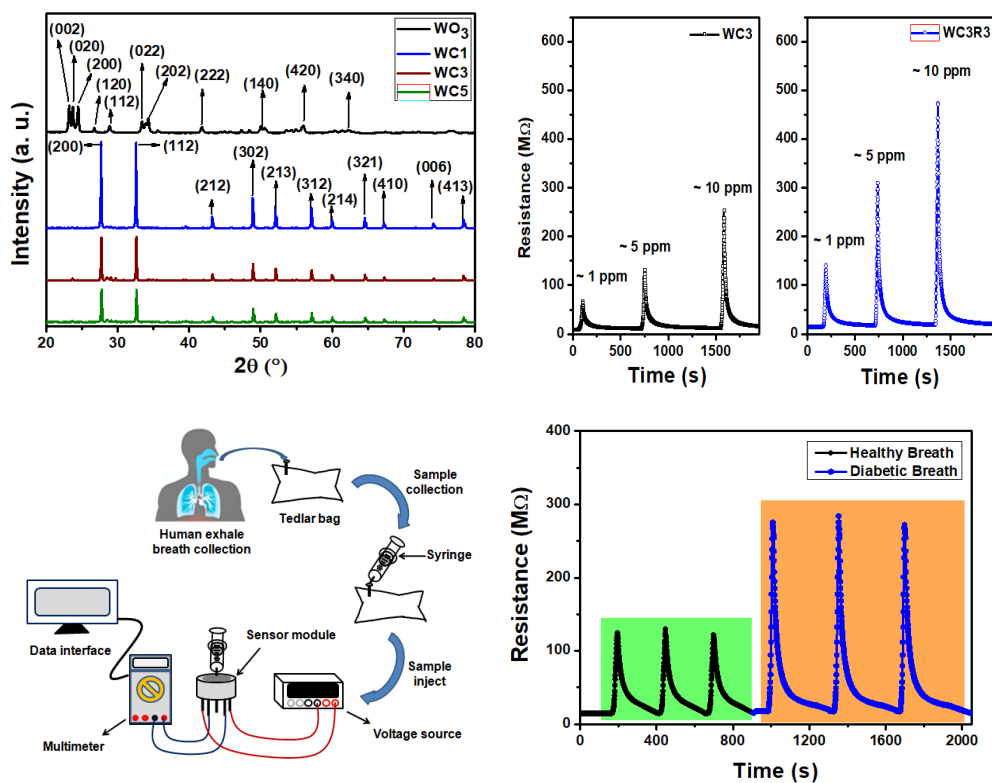
- [11] J. Kaur, K. Anand, A. Kaur, R. C. Singh, Sensitive and selective acetone sensor based on Gd doped WO<sub>3</sub>/reduced graphene oxide nanocomposite, *Sens. Actuators B Chem.* 258 (2018) 1022-1035. <https://doi.org/10.1016/j.snb.2017.11.159>.
- [12] D. Wang, S. Huang, H. Li, A. Chen, P. Wang, J. Yang, X. Wang, J. Yang, Ultrathin WO<sub>3</sub> nanosheets modified by g-C<sub>3</sub>N<sub>4</sub> for highly efficient acetone vapour detection, *Sens. Actuators B Chem.* 282 (2019) 961-971. <http://doi.org/10.1016/j.snb.2018.11.138>.
- [13] Y. Zhu, H. Wang, J. Liu, M. Yin, L. Yu, J. Zhou, Y. Liu, F. Qiao, High-performance gas sensor based on WO<sub>3</sub>-SnO<sub>2</sub> nanosphere composites, *J. Alloy Compd.* 782 (2019) 789-795. <http://doi.org/10.1016/j.jallcom.2018.12.178>.
- [14] Y. Liang, Y. Chao, Enhancement of acetone gas sensing responses of tapered WO<sub>3</sub> nanorods through sputtering coating with a thin SnO<sub>2</sub> coverage layer, *Nanomaterials* 9 (2019) 864-874. <http://doi.org/10.3390/nano9060864>.
- [15] S. Wei, S. Li, R. Wei, S. Liu, W. Du, Different morphologies of WO<sub>3</sub> and their exposed facets-dependent acetone sensing properties, (2020). *Sens. Actuators B Chem.* 329 (2021) 129188. <http://doi.org/10.1016/j.snb.2020.129188>.
- [16] C. Dong, X. Liu, H. Guan, G. Chen, X. Xiao, I. Djerdj, Y. Wang, Combustion synthesized hierarchically porous WO<sub>3</sub> for selective acetone sensing, *Mater. Chem. Phys.* 184 (2016) 155-161. <https://doi.org/10.1016/j.matchemphys.2016.09.036>.
- [17] Y. S. Haiduk, A. A. Khort, N. M. Lapchuk, A. A. Savitsky, Study of WO<sub>3</sub>-In<sub>2</sub>O<sub>3</sub> nanocomposites for highly sensitive CO and NO<sub>2</sub> gas sensors, *J. Solid State Chem.* 273 (2019) 25-31. <https://doi.org/10.1016/j.jssc.2019.02.023>.
- [18] W. Zhu, F. Sun, R. Goei, Y. Zhou, Facile fabrication of RGO-WO<sub>3</sub> composites for effective visible light photocatalytic degradation of sulfamethoxazole, *Appl. Catal. B: Environ.* 207 (2017) 93-102. <https://doi.org/10.1016/j.apcatb.2017.02.012>.
- [19] J. Shen, M. Wang, Y. Wang, J. Hu, Y. Zhu, Y. Zhang, Z. Li, H. Yao, Iron and carbon codoped WO<sub>3</sub> with hierarchical walnut-like microstructure for highly sensitive and selective acetone sensor, *Sens. Actuators B Chem.* 256 (2018) 27-37. <https://doi.org/10.1016/j.snb.2017.10.073>.

- [20] D. Nath, F. Singh, R. Das, X-ray diffraction analysis by Williamson-Hall, Halder-Wagner and size-strain plot methods of CdSe nanoparticles- a comparative study, *Mater. Chem. Phys.* 239 (2020) 122021. <https://doi.org/10.1016/j.matchemphys.2019.122021>.
- [21] C. M. Hung, D. Q. Dat, N. V. Duy, V. V. Quang, N. V. Toan, N. V. Hieu, N. D. Hoa, Facile synthesis of ultrafine rGO/WO<sub>3</sub> nanowire nanocomposites for highly sensitive toxic NH<sub>3</sub> gas sensors, *Mater. Res. Bull.* 125 (2020) 110810. <https://doi.org/10.1016/j.materresbull.2020.110810>.
- [22] J. Kaur, K. Anand, N. Kohli, A. Kaur, R. C. Singh, Temperature dependent selective detection of hydrogen and acetone using Pd doped WO<sub>3</sub>/reduced graphene oxide nanocomposite, *Chem. Phys. Lett.* 701 (2018) 115-125. <https://doi.org/10.1016/j.cplett.2018.04.049>.
- [23] G. Jeevitha, R. Abhinayaa, D. Mangalaraj, N. Ponpandian, P. Meena, V. Mounasamy, S. Madanagurusamy, Porous reduced graphene oxide (rGO)/WO<sub>3</sub> nanocomposites for the enhanced detection of NH<sub>3</sub> at room temperature, *Nanoscale Adv.* 1 (2019) 1799-1811. <https://doi.org/10.1039/c9na00048h>.
- [24] C. Wang, X. Li, Y. Yuan, B. Wang, J. Huang, F. Xia, H. Zhang, J. Xiao, Effects of sintering temperature on sensing properties of V<sub>2</sub>O<sub>5</sub>-WO<sub>3</sub>-TiO<sub>2</sub> electrode for potentiometric ammonia sensor, *Sens. Actuators B Chem.* 241 (2017) 268-275. <https://doi.org/10.1016/j.snb.2016.09.117>.
- [25] S. B. Kulkarni, Y. H. Navale, S. T. Navale, F. J. Stadler, N. S. Ramgir, V. S. Patil, Hybrid polyaniline-WO<sub>3</sub> flexible sensor: A room temperature competence towards NH<sub>3</sub> gas, *Sens. Actuators B Chem.* 288 (2019) 279-288. <https://doi.org/10.1016/j.snb.2019.02.094>.
- [26] X. Chang, S. Xu, S. Liu, N. Wang, S. Sun, X. Zhu, J. Li, O. Ola, Y. Zhu, Highly sensitive acetone sensor based on WO<sub>3</sub> nanosheets derived from WS<sub>2</sub> nanoparticles with inorganic fullerene-like structure, *Sens. Actuators B Chem.* 343 (2021) 130135. <https://doi.org/10.1016/j.snb.2021.130135>.
- [27] S. Shao, X. Chen, Y. Chen, M. Lai, L. Che, Ultrasensitive and highly selective detection of acetone based on Au@WO<sub>3</sub>-SnO<sub>2</sub> corrugated nanofibers, *Appl. Surf. Sci.* 473 (2019) 902-911. <https://doi.org/10.1016/j.apsusc.2018.12.208>.

- [28] M. Imran, S. S. A. A. H. Rashid, Y. Sabri, N. Motta, T. Tesfamichael, P. Sonar, M. Shafiei, Template based sintering of  $\text{WO}_3$  nanoparticles into porous tungsten oxide nanofibers for acetone sensing applications, *J. Mater. Chem. C* 7 (2019) 2961-2970. <https://doi.org/10.1039/c8tc05982a>.
- [29] L. Chen, L. Huang, Y. Lin, L. Sai, Q. Chang, W. Shi, Q. Chen, Fully gravure-printed  $\text{WO}_3/\text{Pt}$ -decorated rGO nanosheets composite film for detection of acetone, *Sens. Actuators B Chem.* 255 (2018) 1482-1490. <https://doi.org/10.1016/j.snb.2017.08.158>.
- [30] T. Kida, T. Kuroiwa, M. Yuasa, K. Shimanoe, N. Yamazoe, Study on the response and recovery properties of semiconductor gas sensors using a high-speed gas-switching system, *Sens. Actuators B Chem.* 134 (2008) 928-933. <http://doi.org/10.1016/j.snb.2008.06.044>.
- [31] Analytical Methods Committee, Recommendations for the definition, estimation and use of the detection limit, *Analyst* 112 (1987) 199-204. <http://doi.org/10.1039/AN9871200199>.
- [32] J. Shi, Z. Cheng, L. Gao, Y. Zhang, J. Xu, H. Zhao, Facile synthesis of reduced graphene oxide/hexagonal  $\text{WO}_3$  nanosheets composites with enhanced  $\text{H}_2\text{S}$  sensing properties, *Sens. Actuators B Chem.* 230 (2016) 736-745. <http://doi.org/10.1016/j.snb.2016.02.134>.
- [33] Q. Wang, H. Wu, Y. Wang, J. Li, Y. Yang, X. Cheng, Y. Luo, B. An, X. Pan, E. Xie, Ex-situ XPS analysis of yolk-shell  $\text{Sb}_2\text{O}_3/\text{WO}_3$  for ultra-fast acetone resistive sensor, *J. Hazardous Mater.* 412 (2021) 125175. <http://doi.org/10.1016/j.jhazmat.2021.125175>.
- [34] P. Gupta, P. K. Mahapatra, R. N. P Choudhary, Investigation on structural and electrical properties of Co and W modified  $\text{BaTiO}_3$ , *Ceram. Int.* 45 (2019) 22862-22871. <http://doi.org/10.1016/j.ceramint.2019.07.329>.
- [35] M. A. Ponce, R. Parra, R. Savu, E. Joanni, P. R. Bueno, M. Cilense, J. A. Varela, M. S. Castro, Impedance spectroscopy analysis of  $\text{TiO}_2$  thin film gas sensors obtained from water-based anatase colloids, *Sens. Actuators B Chem.* 139 (2009) 447-452. <http://doi.org/10.1016/j.snb.2009.03.066>.
- [36] S. Maity, A. Sasmal, S. Sen, Comprehensive characterization of  $\text{Ba}_{1-x}\text{Sr}_x\text{TiO}_3$ : Correlation between structural and multifunctional properties, *J. Alloy. Compd.* 884 (2021) 161072. <http://doi.org/10.1016/j.jallcom.2021.161072>.

# CHAPTER 4.2

## Reduced graphene oxide (rGO)-Cr (III) doped hexagonal WO<sub>3</sub> nanocomposite towards room temperature ppm-level acetone detection



Low ppm acetone detection from exhaled human breath is a promising technique for non-invasive early-stage diagnosis and monitoring of diabetes. To develop room temperature operated diabetic biomarker (acetone) detector sensor, in this work, reduced graphene oxide (rGO) decorated Cr<sup>3+</sup> doped WO<sub>3</sub> nanocomposites were synthesized by sol-gel method and Taguchi-type sensors were fabricated. The optimized sensor exhibited sensing response ( $R_g/R_a$ ) ~ 24.1 against ~ 10 ppm and ~ 9.12 towards ~ 1 ppm acetone at room temperature (30±5°C). The kinetic analysis of the dynamic response curve revealed a fast response and recovery time of ~ 10 s and ~ 30 s respectively. The sensor delineated selectivity towards acetone and sustainable stability for ~ 120 days. The optimized sensor was able to distinguish between healthy and diabetic breath by exhibiting different sensing responses under identical experimental conditions.



**4.2.1. Introduction:**

In the previous chapter,  $\text{Fe}^{3+}$  doped rGO decorated  $\text{WO}_3$  nanocomposite sensor exhibited selective acetone sensing performance at operating temperature  $\sim 130^\circ\text{C}$  [1]. Although, in comparison to Chapter 3.1 and 3.2, the selectivity towards diabetic breath biomarker (acetone) was achieved and the optimum operating temperature of the sensor decreased a little bit, but, yet there was a scope to reduce the working temperature of the sensor furthermore near to the room temperature. Therefore, in this work, instead of n-type dopant ( $\text{Fe}^{3+}$ ), it was planned to introduce a p-type dopant ion in the pristine  $\text{WO}_3$  matrix, followed by the incorporation of rGO in it. Some works already published involving p-type dopant for improved sensing performance of  $\text{WO}_3$  based sensors [2-5], as it could induce hole-electron combination pathway for fluent electronic transportation. According to a comprehensive literature study [6-14], among different p-type dopants,  $\text{Cr}^{3+}$  was considered as efficient one.

**4.2.2. Experimental:**

Pristine  $\text{WO}_3$  was synthesized accordingly as mentioned in Chapter 4.1 (Section: 4.1.2). The requisite amount of  $\text{WO}_3$  precursor was dissolved in aqueous ethanol to obtain pristine  $\text{WO}_3$  sol and marked as WC0. Thereafter, to prepare  $\text{Cr}^{3+}$  doped  $\text{WO}_3$  nanomaterials (Fig. 4.2.1), chromium nitrate ( $\text{Cr}(\text{NO}_3)_3 \cdot 9\text{H}_2\text{O}$ , Sigma Aldrich) was taken as precursor and the dopant ( $\text{Cr}^{3+}$ ) concentration was varied as 1, 3, and 5 wt% in  $\text{WO}_3$  precursor sols separately and designated as WC1, WC3, and WC5 accordingly. The homogeneous sols were magnetically stirred for  $\sim 4$  hours and kept  $\sim 72$  hours for ageing. Afterwards, the desired nanocomposite powders were obtained by gel-calcination process at a  $\sim 600^\circ\text{C}$  for  $\sim 2$  hours in an air atmosphere according to the temperature profile obtained from the TGA curve (Fig. 4.2.2).

To synthesis rGO decorated  $\text{Cr}^{3+}$  doped  $\text{WO}_3$  nanocomposite (Fig. 4.2.1), varying concentrations of rGO (1, 3, and 5 wt %) were separately added in aqueous ethanol solution of WC3 nanopowder and labeled as WC3R1, WC3R3, and WC3R5 respectively. Similarly, the sols were aged for  $\sim 3$  days and then converted to gel by following the same procedure as above. The corresponding nanocomposite powders were obtained by gel-calcination at  $\sim 350^\circ\text{C}$  for  $\sim 2$  hours in an air atmosphere.

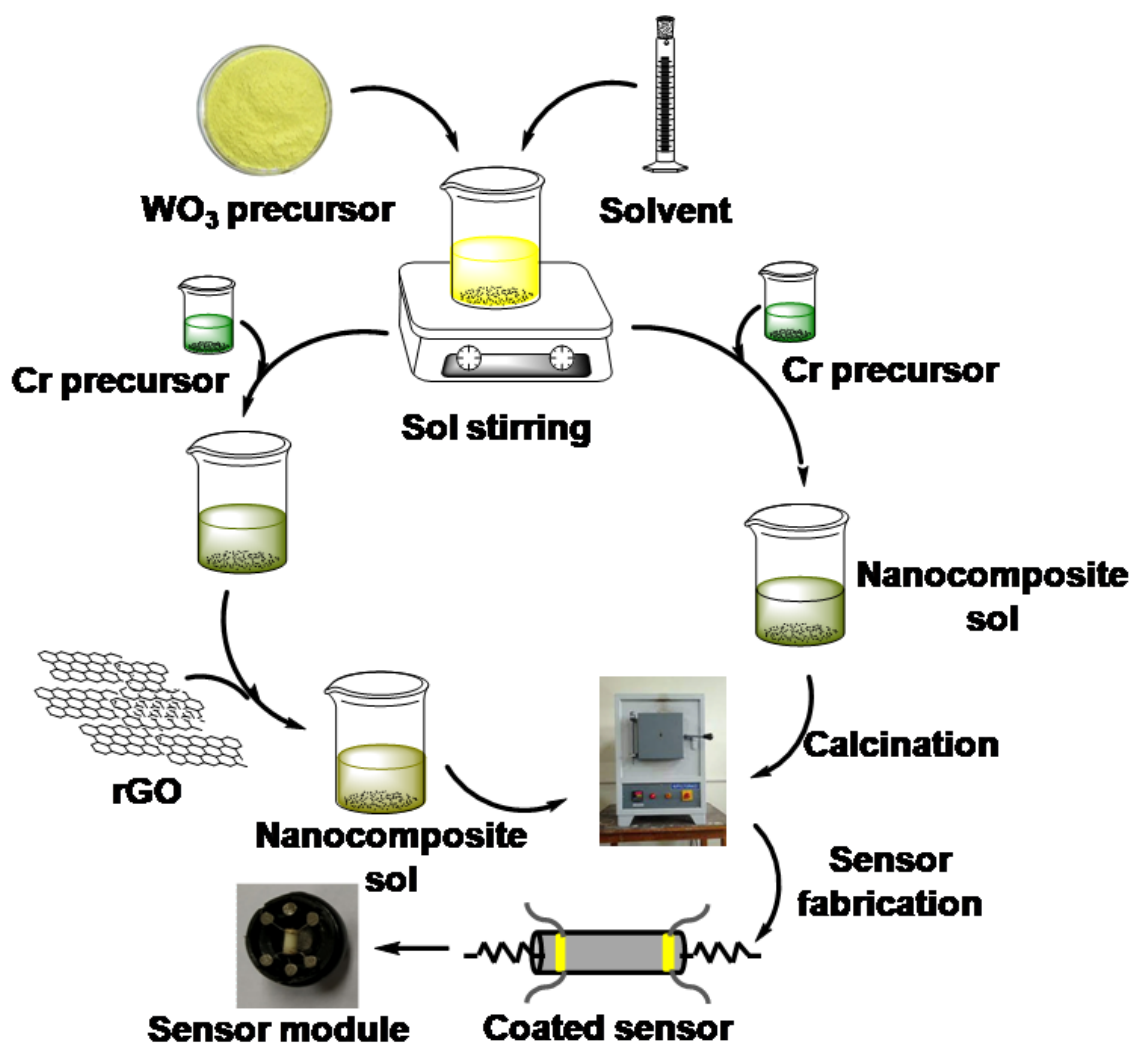


Figure-4.2.1: Schematic presentation of nanocomposites synthesis

### 4.2.3. Results and discussions:

#### 4.2.3.1. Characterization of nanocomposites:

Thermogravimetric analysis (TGA) of pristine WO<sub>3</sub> showed one step mass loss of ~ 11.1 wt% upto 390°C, corresponded to removal of water, acid molecules, and other chelating agents (Fig. 4.2.2). On the other hand, Cr<sup>3+</sup> doped WO<sub>3</sub> showed a three step mass loss [15, 16]. At the first step, ~ 6.7% mass loss ~ 115°C was due to elimination of adsorbed water. In the next step, ~ 3.5% mass loss till ~ 375°C correlated to binder molecules removal. The final mass loss of ~ 1.5% at a temperature ~ 510°C corresponded to formation of doped nanomaterial.

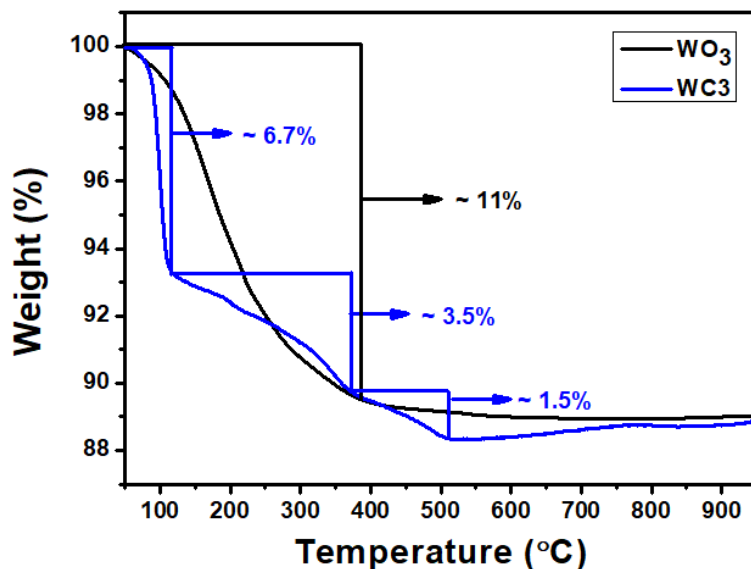
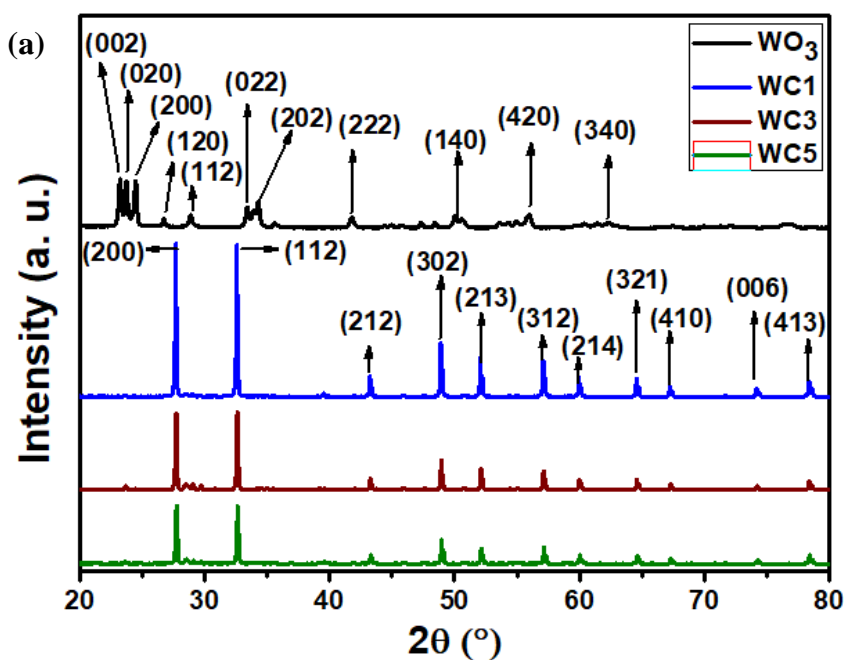


Figure-4.2.2.: TGA plot of pristine WO<sub>3</sub> and WC<sub>3</sub>

The X-Ray diffraction pattern of pristine WO<sub>3</sub> (Fig. 4.2.3a) revealed the peaks of monoclinic primitive lattices [17, 18] with space group P2<sub>1</sub>/n (JCPDS no.: 83-0951). However, introduction of dopant Cr<sup>3+</sup> resulted in phase change of pristine WO<sub>3</sub> from monoclinic to hexagonal lattice [19, 20] having a space group P6<sub>3</sub>/mcm (JCPDS no.: 85-2459).





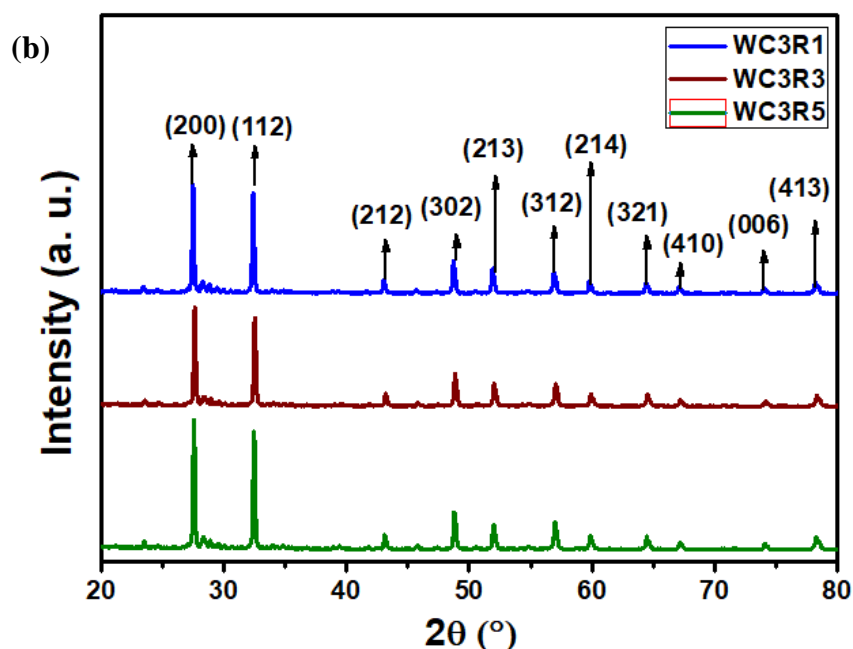


Figure-4.2.3: XRD spectra of (a)  $\text{Cr}^{3+}$  doped  $\text{WO}_3$  nanocomposites, (b) rGO decorated WC3 nanocomposites

The dopant  $\text{Cr}^{3+}$  replaced some of the  $\text{W}^{6+}$  ions from their native lattice sites, owing to the comparable ionic radii of  $\text{Cr}^{3+}$  (0.61 Å) and  $\text{W}^{6+}$  (0.65 Å) and to maintain the charge neutrality some oxygen vacancies were also generated [21]. Such distortion in pristine lattice orientation induced a modulation in periodic corner-sharing octahedral arrangement between  $\text{W}^{6+}$  and  $\text{O}^{2-}$  which instigated phase change from monoclinic to hexagonal lattice with an increase in symmetry and shrinkage of unit cell volume. This mutation of lattice structure developed defect-rich nanocomposite which was proved to be favorable for gas sensing applications. Further, rGO incorporation hardly exhibited signature of any peak corresponded to rGO (Fig. 4.2.3b), except the shifting of hexagonal  $\text{WO}_3$  peaks towards lower diffraction angle. This accounted for an increase in lattice spacing (d) between the diffraction planes which facilitated the swift electronic movements during gas sensing experiments.

The metal oxide stretching peaks were observed in  $1000\text{ cm}^{-1}$  to  $500\text{ cm}^{-1}$  range in the FTIR spectra of both WC3 and WC3R3 (Fig. 4.2.4). The peak intensities of different metal oxide bonds (W=O, O-W-O, and W-O-W) were slightly increased in WC3R3 compared to WC3. As observed in most of the cases [20, 22], here also a broad peak at higher wavenumber correlated to –OH stretching vibration and consequent bending vibration around  $1640\text{ cm}^{-1}$  were observed.

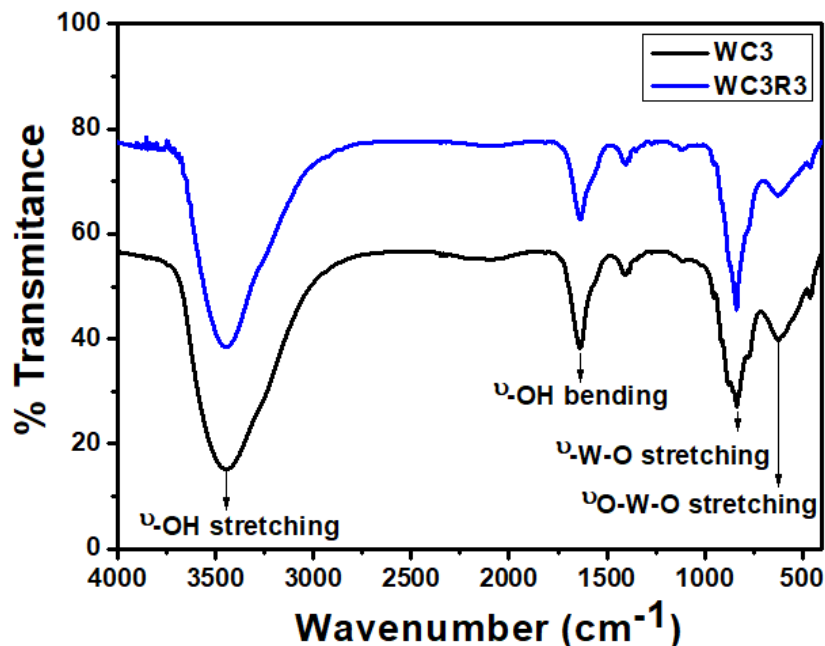


Figure-4.2.4: FTIR graph of WC3 and WC3R3

The Raman spectra of both WC3 and WC3R3 (Fig. 4.2.5) exhibited a signature peak at  $\sim 215 \text{ cm}^{-1}$  for lattice bond vibrations of crystalline  $\text{WO}_3$ . Besides this, two peaks at  $\sim 274 \text{ cm}^{-1}$  and  $\sim 388 \text{ cm}^{-1}$  were aroused due to bending vibrations of O-W-O bridging, and another peak at  $\sim 590 \text{ cm}^{-1}$ , was assigned to bending mode oscillation of W-O-W linkages [22, 23].

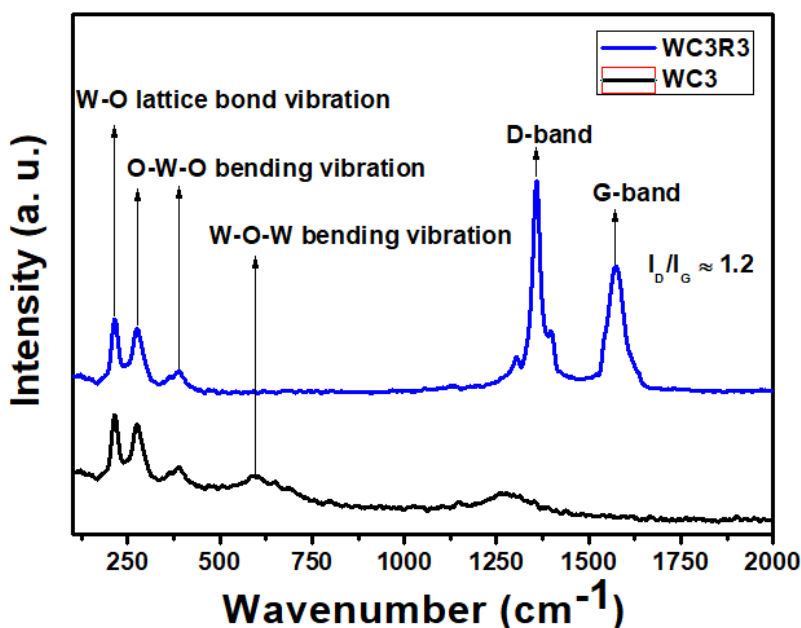
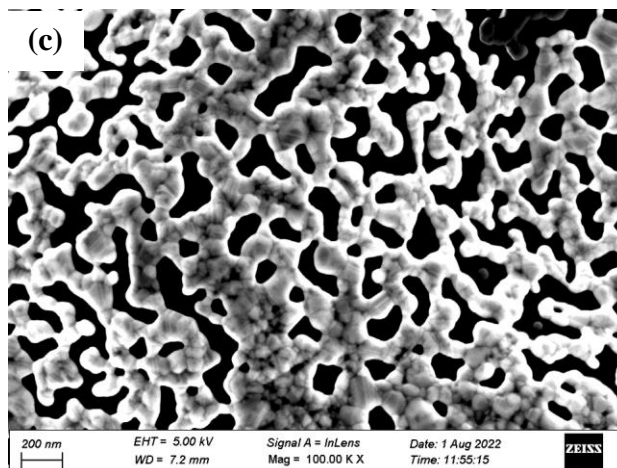
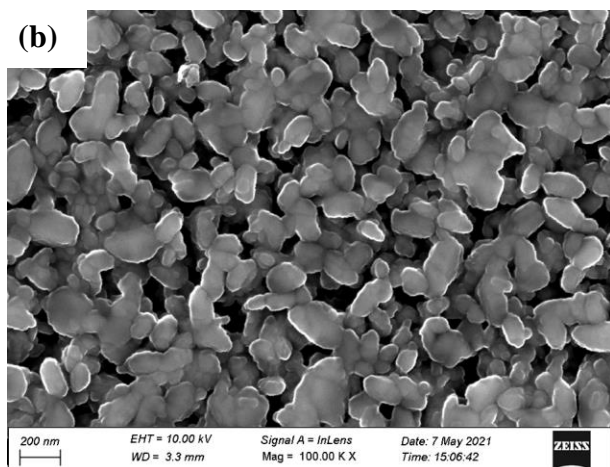
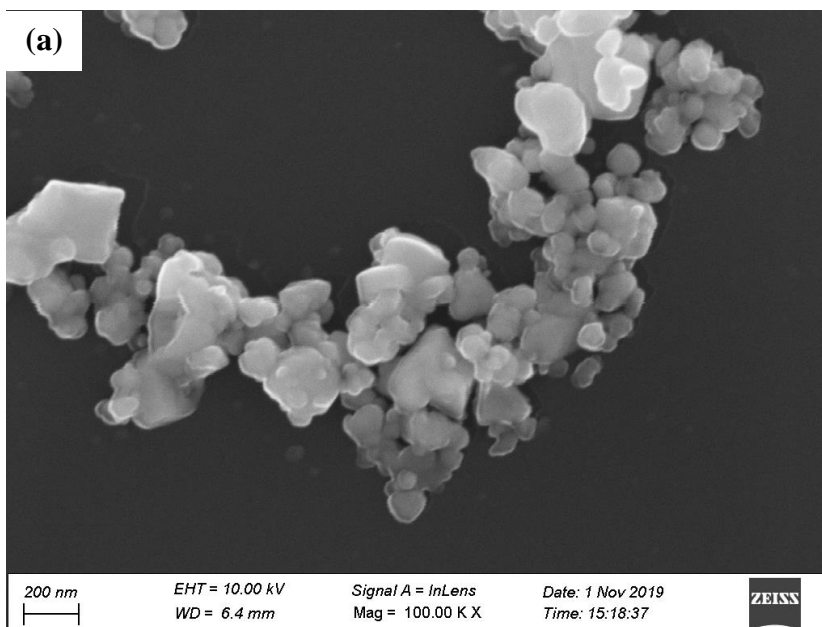


Figure-4.2.5: Raman spectra of WC3 and WC3R3

In WC3R3, additionally two new high-intensity peaks at higher wavenumber were present. The peak  $\sim 1359\text{ cm}^{-1}$  was characterized as D-band generated due to oscillation of  $\text{sp}^3\text{-C}$  atoms and defect sites of the rGO lattice [24]. Another peak  $\sim 1586\text{ cm}^{-1}$  marked as G-band signified the presence of  $\text{sp}^2\text{-C}$  atoms in the rGO matrix [25]. The intensity ratio of these peaks ( $I_D/I_G$ ) was  $\sim 1.15$ , which ensured the successful conversion of GO to rGO [1].

FESEM study was carried out to analyze the surface morphological properties of the synthesized nanoparticles. Pristine  $\text{WO}_3$  nanoparticles exhibited the presence of agglomerated ovoid-shaped particles (Fig. 4.2.7a). However, doping with  $\text{Cr}^{3+}$  in  $\text{WO}_3$  matrix changed the shape of the particles with an almost uniform distribution (Fig. 4.2.7b).



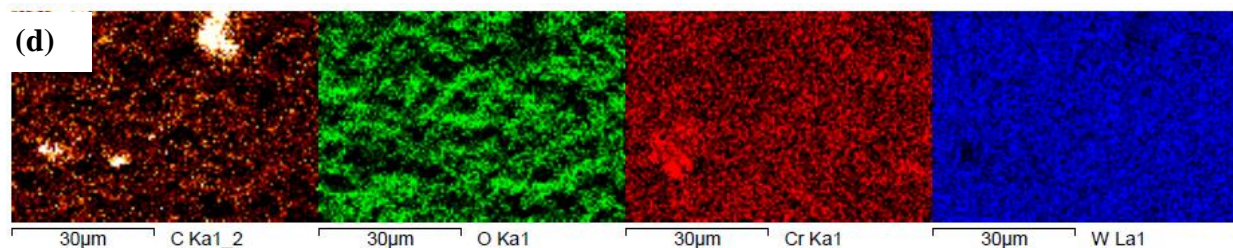
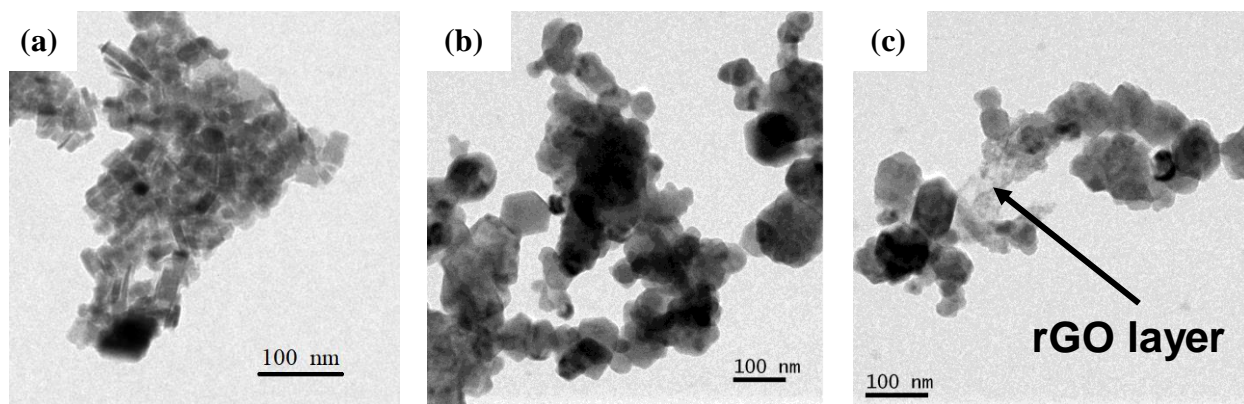


Figure-4.2.7: FESEM micrographs of (a) pristine  $WO_3$ , (b)  $WC_3$ , (c)  $WC_3R_3$ , and (d) Elemental mapping of  $WC_3R_3$

Further, rGO decoration showed a network-like matrix formation where the nanoparticles were distributed on the porous rGO layer (Fig. 4.2.7c). The homogeneous distribution of elements was verified from elemental mapping of  $WC_3R_3$  sample (Fig. 4.2.7d).

To obtain a better insight into the microstructures, TEM was performed. The bright-field TEM (BFTEM) image of pristine  $WO_3$  showed the presence of inhomogeneous shaped particles (Fig. 4.2.8a), whereas in  $WC_3$  agglomerated hexagonal shaped particles were observed (Fig. 4.2.8b). On the other hand, the incorporation of rGO in  $WC_3$  resulted in a distribution of nanoparticles on the rGO matrix (Fig. 4.2.8c). The HRTEM images of pristine  $WO_3$  showed the existence of lattice planes (002) and (222) of monoclinic lattice (Fig. 4.2.8d). The HRTEM images of  $WC_3$  (Fig. 4.2.8e) and  $WC_3R_3$  (Fig. 4.2.8f), both revealed lattice fringes corresponded to (200) and (112) planes according to the XRD pattern of hexagonal lattice. The EDX spectrum of  $WC_3R_3$  (Fig. 4.2.8g) confirmed the presence of W, Cr, O, and C in the sample (quantitative analysis showed in inset of Fig. 4.2.8g) whereas the Cu signal came from the sample-mounted grid and Na peak was from the residual ion of  $WO_3$  precursor.





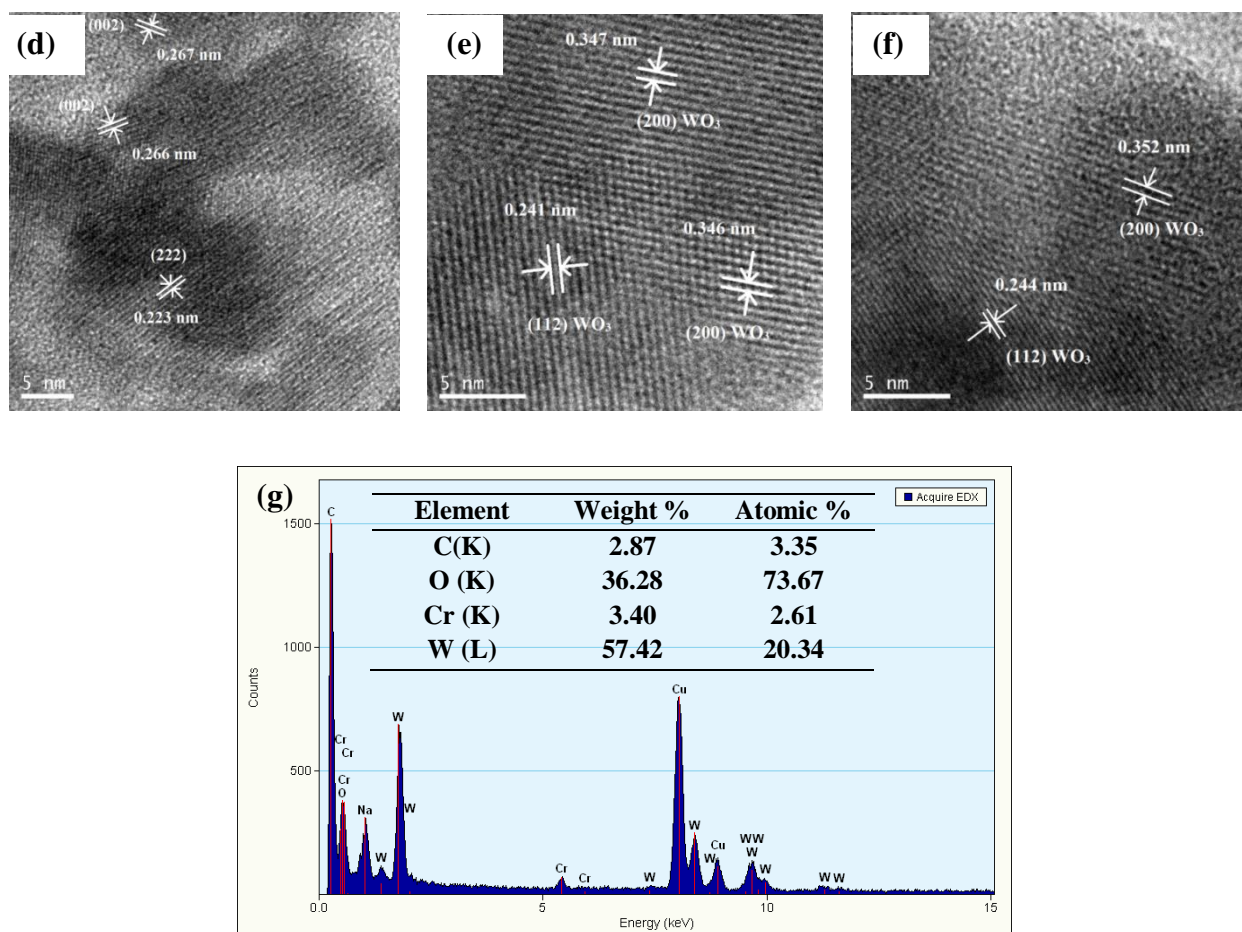
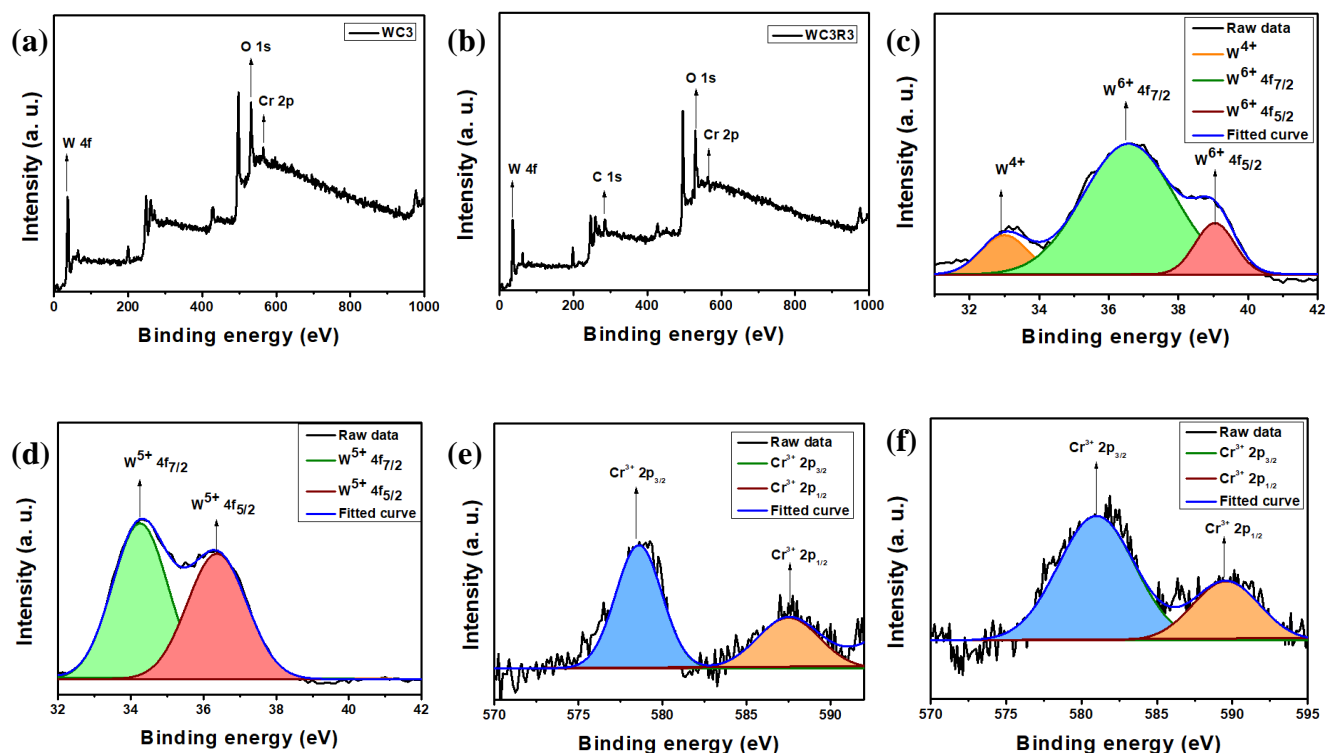


Figure-4.2.8: BFTEM images of (a) pristine  $\text{WO}_3$ , (b)  $\text{WC}_3$ , and (c)  $\text{WC}_3\text{R}_3$ , HRTEM images of (d) pristine  $\text{WO}_3$ , (e)  $\text{WC}_3$ , and (f)  $\text{WC}_3\text{R}_3$ , and (g) EDX of  $\text{WC}_3\text{R}_3$  (inset quantitative analysis)

The chemical components and oxidation state of corresponding elements of the nanocomposites were determined from the XPS study. The surface scanning spectrum revealed the presence of W, O, and Cr in both the samples ( $\text{WC}_3$  and  $\text{WC}_3\text{R}_3$ ) and a peak corresponded to C was obtained only in  $\text{WC}_3\text{R}_3$  sample. Notably, compared to  $\text{WC}_3$  (Fig. 4.2.9a) the photoemission peaks of the respective elements were shifted towards lower binding energies in  $\text{WC}_3\text{R}_3$  sample (Fig. 4.2.9b). Again, the signal obtained from Cr was quite noisy perhaps due to the low doping concentration. Core level analysis of W 4f from the  $\text{WC}_3$  sample (Fig. 4.2.9c) showed a doublet peak at 36.58 eV and 39.04 eV for  $4f_{7/2}$  and  $4f_{5/2}$  respectively, which corresponded to  $\text{W}^{6+}$  [9, 21]. Besides these peaks, one low binding energy peak was deconvoluted at 32.98 eV indicted to the presence of some reduced  $\text{W}^{4+}$ . On the other hand, for  $\text{WC}_3\text{R}_3$ , the W 4f peak (Fig. 4.2.9d) showed a spin-orbit doublet at 34.25 eV and 36.37 eV for  $4f_{7/2}$  and  $4f_{5/2}$  correspondingly,

signified the presence of  $W^{5+}$  in the sample [27, 28]. To rationalize this variation in oxidation state of W, it could be interpreted that, the incorporation of rGO in WC3 induced some reduction effect on tungsten. The deconvoluted Cr 2p signal demonstrated two peaks at 580.97 and 589.59 for WC3 (Fig. 4.2.9e), and at 578.60 eV and 587.50 eV for WC3R3 (Fig. 4.2.9f). The peaks were corresponded to two different spin states of +3 oxidation state of Cr:  $2p_{3/2}$  and  $2p_{1/2}$  respectively [6, 11]. The O 1s peak deconvolution yielded a peak at 531.73 eV in WC3 (Fig. 4.2.9g) and at 529.78 eV in WC3R3 (Fig. 4.2.9h) for lattice oxides. As well as, both the samples showed absorbed oxygen peaks at 536.17 eV and 534.23 eV for WC3 and WC3R3 respectively [29, 30]. Further investigation of the absorbed oxygen peaks (area under the curve analysis) revealed that the amount of absorbed oxygen ( $\sim 24.83\%$ ) in the WC3 sample enhanced ( $\sim 30.71\%$ ) upon rGO incorporation in WC3R3. The increased absorbed oxygen in WC3R3 would be beneficial for gas sensing. The C1s peak from WC3R3 (Fig. 4.2.9i) showed two peaks, one at 284.20 eV corresponding to  $-C=C-$  bonds originating from skeletal carbons of rGO, and the other peak at 286.35 eV indicating the presence of  $-C-O-C-$  which ensured the functionalization of pristine graphene structure [1, 24].



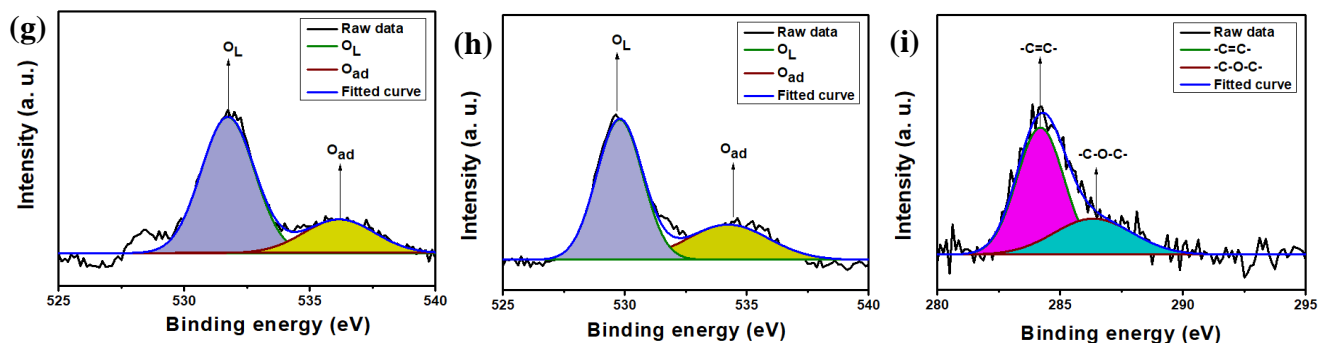


Figure-4.2.9: XPS full scan spectrum (a) WC3, (b) WC3R3, core level analysis: W 4f (c) WC3, (d) WC3R3, Cr 2p (e) WC3, (f) WC3R3, O 1s (g) WC3, (h) WC3R3, and (i) C 1s of WC3R3

Optical characterization of the samples was primarily carried out with the help of UV-visible spectroscopy (Fig. 4.2.10a). Pristine WO<sub>3</sub> exhibited a broad peak at ~ 240 nm, which was red shifted after Cr<sup>3+</sup> doping in it, WC3 nanocomposite showed the broad peak at ~ 283 nm and this absorption peak further red-shifted to ~ 291 nm after rGO incorporation in WC3R3 [17, 22]. Along with these peaks, for Cr<sup>3+</sup> doped samples one absorption peak was noticed; for WC3 it was at ~ 395 nm and for WC3R3 it was at ~ 406 nm. These absorption spectra were further used to calculate the band gap energy of the nanocomposites according to the Tauc equation [17, 31]. The calculated band gap energy for pristine WO<sub>3</sub> was ~ 2.91 eV that was decreased in WC3 sample to ~ 2.80 eV, which was further decreased to ~ 2.70 eV upon rGO introduction (Fig. 4.2.10b). The modulation of pristine WO<sub>3</sub> lattice either by Cr<sup>3+</sup> doping or via rGO incorporation, provided a low-energy consuming facile route of electronic transportation between the nanocomposite's valance band and conduction band. It thereby resulted in the shrinkage of band gap energy and also facilitated the electronic transition by consuming lesser activation energy.

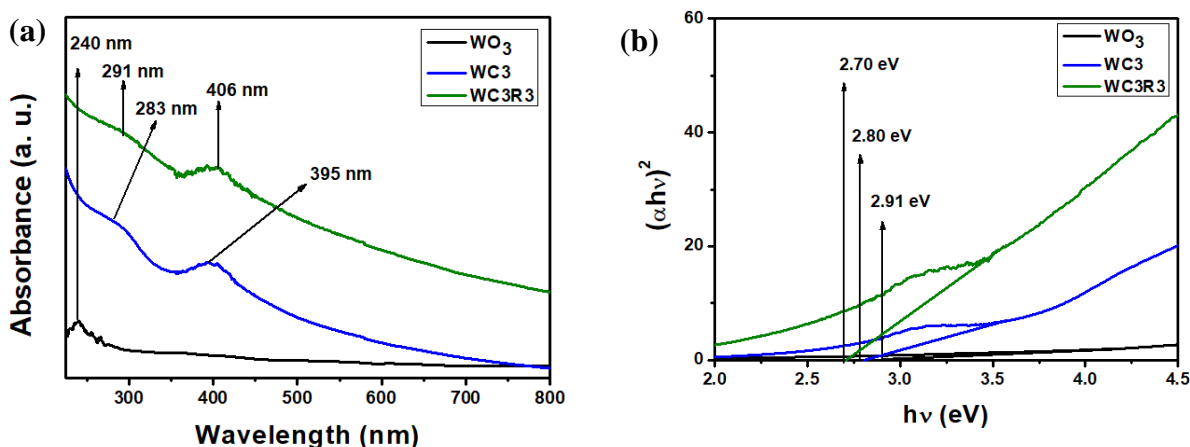


Figure -4.2.10: (a) UV-visible spectra, (b) Tauc plot pristine WO<sub>3</sub>, WC3 and WC3R3

Besides absorption spectroscopy, emission spectroscopy in the form of photoluminescence was also used to characterize the presence of defects and oxygen vacancies in the as-synthesized nanomaterials [10, 32]. The nanomaterials showed near-band-edge (NBE) emission due to different defect sites in the range of  $\sim 450$  nm to  $\sim 500$  nm (Fig. S4c).

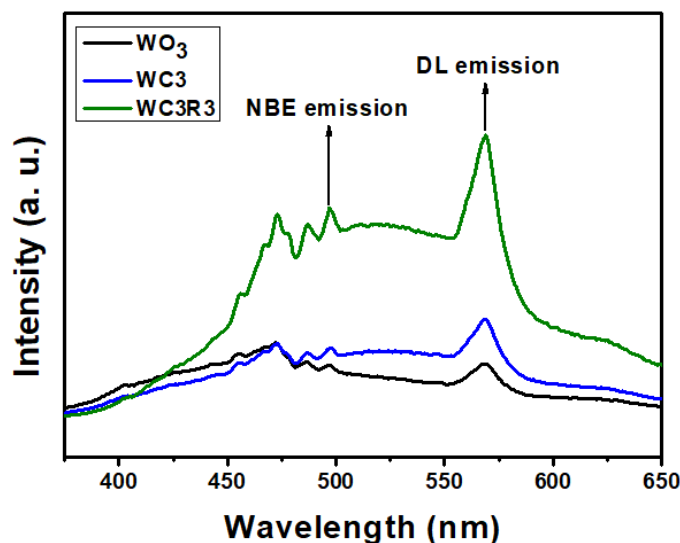


Figure -4.2.11: PL spectra of pristine  $WO_3$ ,  $WC_3$  and  $WC_3R_3$

The intensity of the peaks in the  $WC_3$  sample was almost similar to that of pristine  $WO_3$ ; however, those were too minimal compared to the  $WC_3R_3$  nanocomposite. It indicated towards the generation of more defect-rich nature when rGO incorporated in  $WC_3$ . On the other hand, another peak was observed at  $\sim 570$  nm, marked as a deep-level (DL) emission peak, signifying the oxygen vacancies of the nanocomposites. These peaks in the PL spectra assured the presence of high oxygen vacancies and defect-rich surface properties of the nanomaterials.

### 4.2.3.2. Gas sensing performance study:

At first, the resistances vs. temperature profile (Fig. 4.2.12 a, b) of all the fabricated sensors were studied in the temperature range  $30^\circ\text{C}$  to  $150^\circ\text{C}$ . At the same time the response of all these sensors were also recorded (Fig. 4.2.12 c, d) in presence of  $\sim 10$  ppm acetone. It was noteworthy that, the sensor fabricated from pristine  $WO_3$  did not show any measurable resistance (within multimeter limit  $\sim 500$  M $\Omega$ ) below  $250^\circ\text{C}$ , hence, it was not possible to study the sensing performance of this sensor. The obtained sensing responses revealed that the functionalized  $WO_3$



based sensors showed maximum sensing response at  $\sim 60^\circ\text{C}$ ; beyond which the sensing response decreased perhaps due to predominant desorption of gas over adsorption at higher temperature ranges [21, 26]. However, the enhancement of sensing response compared to room temperature ( $\sim 30 \pm 5^\circ\text{C}$ ) sensing response was trivial. Henceforth, the detailed sensing performance study was carried out at room temperature. It was observed that, among  $\text{Cr}^{3+}$  doped  $\text{WO}_3$  sensors;  $\sim 3$  wt%  $\text{Cr}^{3+}$  doped  $\text{WO}_3$  (WC3) sensors exhibited the best sensing response ( $\sim 19.9$ ) at room temperature. Additionally, it was observed that, after rGO addition in WC3 nanomaterials enhanced the sensing response and here also the  $\sim 3$  wt% rGO incorporated WC3 sensor (WC3R3) showed maximum sensing response ( $\sim 24.1$ ) at identical experimental condition.

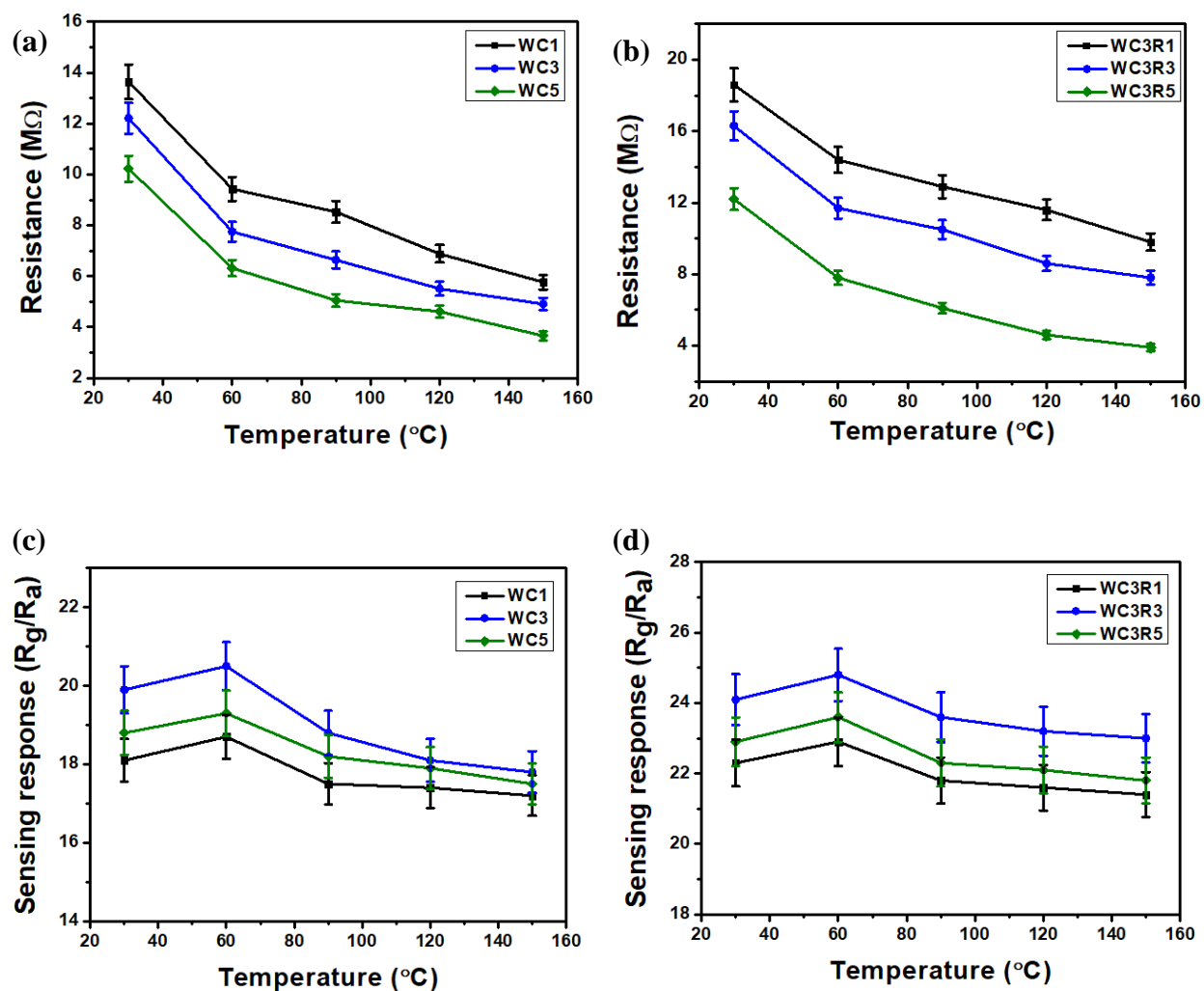
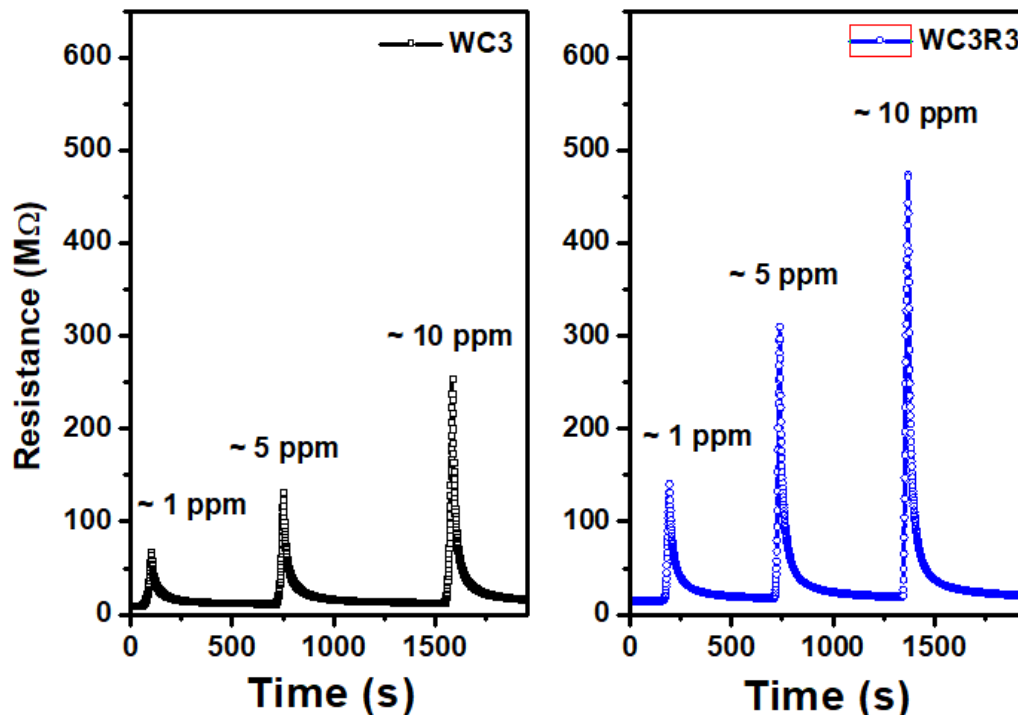


Figure-4.2.12: Change in resistance (a) WC3, (b) WC3R3 and change in sensing response (in presence of  $\sim 10$  ppm acetone) (c) WC3, (d) WC3R3, as a function of temperatures

After determining the operating temperature, the dynamic responses of the optimized sensors (WC3 and WC3R3) were measured in the presence of different acetone concentrations (Fig. 4.2.13).



*Figure-4.2.13: Dynamic sensing response in presence of different concentrations of acetone at operating temperature ( $30 \pm 5^\circ\text{C}$ )*

In the fabricated  $\text{Cr}^{3+}$  doped  $\text{WO}_3$  sensors though the base material ( $\text{WO}_3$ ) is n-type semiconductor, but the sensor exhibited p-type sensing response perhaps due to formation of an ‘inversion space-charge layer’ near the surface of the sensing material. It could be explained in such a way that, for functionalized  $\text{WO}_3$  based sensors due to alteration in pristine  $\text{WO}_3$  lattice, there developed several oxygen vacancies [33, 34].



Here,  $\text{O}_\text{O}$  is the labile oxygen ions and  $\text{V}_{\text{O}\bullet\bullet}$  denotes oxygen vacancies. Atmospheric oxygen molecules would be attracted by these vacant sites and thereby capturing electrons from the conduction band and converted to different oxygenated ions. Now, as the surface is populated with the negatively charged ions the electrostatic potential would be reduced in the space-charge layer as compared to holes. Thus ‘inversion space-charge layer’ created and holes became the principle charge carrier which might be accounted for observed p-type sensing response [35, 36].

Table: 4.2.1: Dynamic sensing response of fabricated sensors at room temperature:

Concentration of acetone	Sensing response ( $R_g/R_a$ )	
	WC3	WC3R3
~ 1 ppm	6.91	9.12
~ 5 ppm	11.02	16.95
~ 10 ppm	19.9	24.1
~ 25 ppm	20.1	24.6
~ 50 ppm	20.5	24.8
~ 100 ppm	20.6	24.9

The sensing responses of both the sensors (WC3 and WC3R3) were recorded (Table 4.2.1) in a wide concentration range of acetone (~ 1 ppm to ~ 100 ppm) at room temperature. The obtained results showed that the sensing response was ~ 6.91 (WC3) and ~ 9.12 (WC3R3) in presence of ~ 1 ppm acetone and it was gradually increased upto ~ 25 ppm; beyond that, sensing responses were nearly invariable with an increase in acetone concentration (Fig. 4.2.14). Henceforth, it can be inferred that the sensing response towards acetone was saturated at ~ 25 ppm.

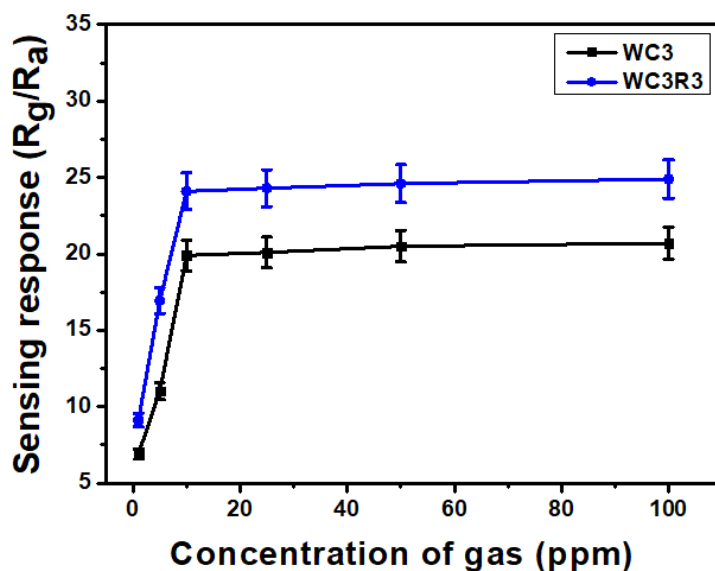
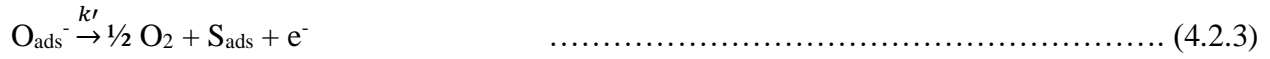
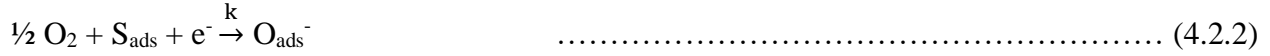


*Figure-4.2.14: Saturation curves of WC3 and WC3R3*

During gas sensing, pre-adsorbed oxygenated ions ( $O_{ads}^-$ ) on the sensing material surface react with experimental gas molecules. Consequently, the change in electron concentration resulted in alteration in resistance. Applying Eley-Rideal theoretical model [37, 38], this process can be represented as follows:



Where,  $S_{ads}$  represents adsorption site on the sensor surface,  $k$  is the adsorption rate constant,  $k'$  is desorption rate constant, and  $k''$  is the rate constant for interaction between oxygenated ions and gas molecules.

The sensing response of a sensor is primarily the function of number of adsorbed oxygenated ions and the extent of reaction between the oxygenated ions and gaseous molecules. If the number of available adsorption site on the sensing material surface was  $N_0$  and in a stipulated time ( $t$ ) the number of occupied sites was  $N_t$ , then the rate of the reaction expressed as:

$$[d(N_t)/dt] = k(N_0 - N_t)C_0 - k''N_tC_g - k'N_t \quad \dots\dots\dots (4.2.5)$$

Here,  $C_0$  and  $C_g$  represented the conductance in absence and presence of analyte gas respectively.

Now, dividing both sides by  $N_0$ , equation: 4.2.5 could be rewrite as:

$$[d(N_t/N_0)/dt] = k(1 - N_t/N_0)C_0 - k''(N_t/N_0)C_g - k'(N_t/N_0) \quad \dots\dots\dots (4.2.6)$$

Now, considering the fraction of occupied adsorption site ( $\phi$ ) as  $(N_t/N_0)$ , the equation: 4.2.6 could be written as:

$$(d\phi/dt) = k(1-\phi)C_0 - k''\phi C_g - k'\phi \quad \dots\dots\dots (4.2.7)$$

$$[d\phi/k(1-\phi)C_0 - k''\phi C_g - k'\phi] = dt \quad \dots\dots\dots (4.2.8)$$

Integrating both sides, the obtained expression for  $\phi$  would be:

$$\phi = [kC_0/(kC_0 + k' + k''C_g)] \times [1 - \exp \{-(kC_0 + k' + k''C_g)t\}] \quad \dots\dots\dots (4.2.9)$$

As mentioned earlier, there would a linear dependency of change in conductance on the fraction of surface coverage; the transient gas sensing response could be represented as [39, 40]:

$$G(t_{res}) = G_0 + G[1 - \exp(-t/\tau_{res})] \quad \dots\dots\dots (4.2.10)$$

Comparing equations (9) and (10):

$$\tau_{res} = [1/(kC_0 + k' + k''C_g)] \quad \dots\dots\dots (4.2.11)$$

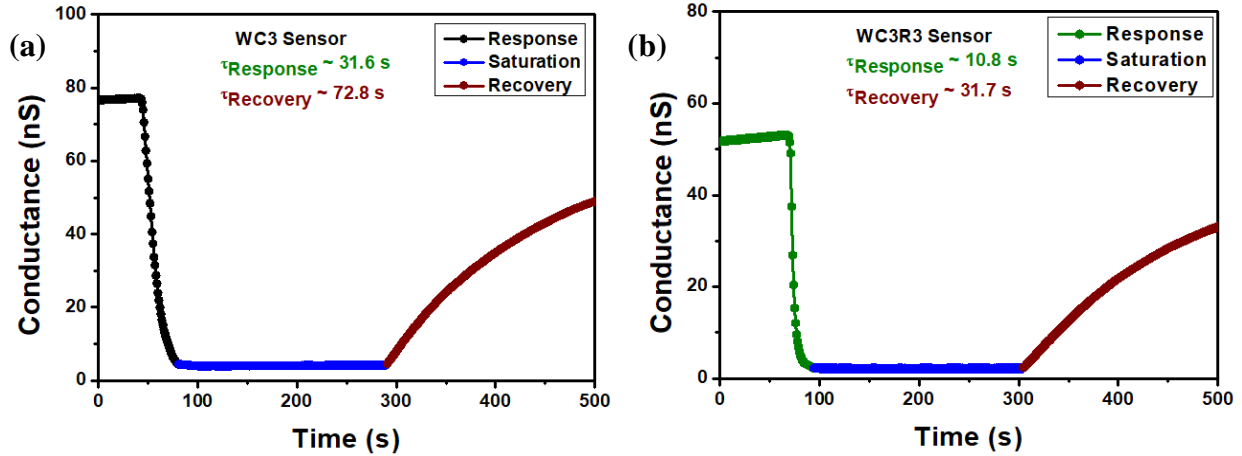


Figure-4.2.15: Transient conductance graphs (a) WC3 and (b) WC3R3

Similarly, the recovery time could be represented as:

$$G(t_{\text{rec}}) = G_0 + G [1 - \exp(-t/\tau_{\text{rec}})] \quad \dots\dots\dots (4.2.12)$$

Comparing equations (9) and (12), and considering  $C_g$  as zero (since, during recovery process the flow of gas was removed):

$$\tau_{\text{rec}} = [1/(kC_0 + k')] \quad \dots\dots\dots (4.2.13)$$

Where,  $G_0$  is the baseline conductance of the sensor at time  $t = 0$ ,  $G$  is a constant,  $\tau_{\text{res}}$  is the response time, and  $\tau_{\text{rec}}$  is recovery time.

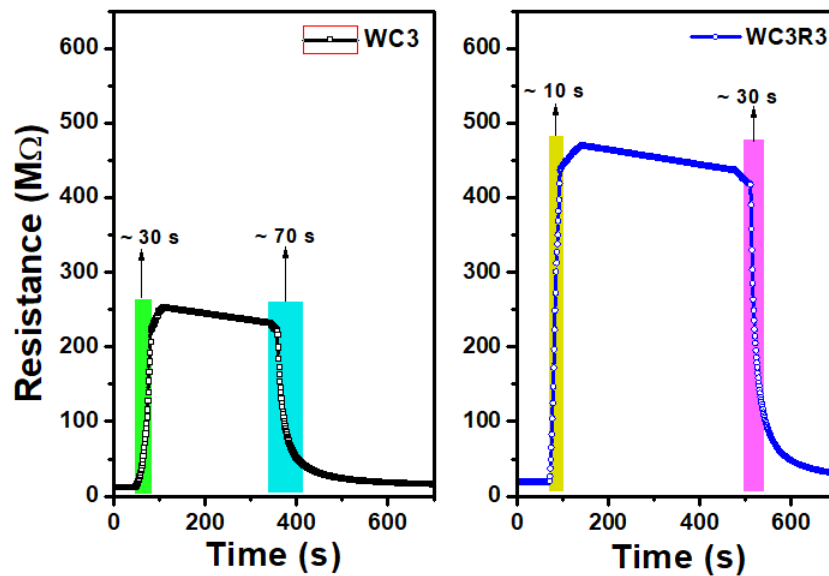


Figure-4.2.16: Response and recovery time in presence of  $\sim 10 \text{ ppm}$  acetone at operating temperature  $(30 \pm 5^\circ\text{C})$

Now, the response and recovery time for WC3 (~ 31.6 s and ~ 72.8 s) and WC3R3 (~ 10.8 s and ~ 31.7 s) were calculated, using equations (4.2.11) and (4.2.13) from the transient conductance curves (Fig. 4.2.15 a, b) fitting. Again, response and recovery times were also determined from the dynamic response curves in the presence of ~ 10 ppm acetone (Fig. 4.2.16). A faster response and recovery time, subsequently ~ 10 s and ~ 30 s, were obtained for the WC3R3 sensor. However, the response and recovery time (~ 30 s and ~ 70 s respectively) were a bit longer for the WC3 sensor and both the results were justified each other.

MOS-based nanomaterials' gas sensing depends on the adsorption-desorption phenomena of gas molecules on the surface of the sensing material. In order to get a rapid response and recovery time, there ought to be predominantly physisorption type of interaction. To understand this, we could apply the concept of Freundlich isotherm [41], and from the consequent log S vs. log C curve (Fig. 4.2.17), the nature of the interaction can be determined. The equation can be presented as follows:

$$S = \alpha C^\beta \quad \dots\dots\dots (4.2.14)$$

$$\log S = \log \alpha + \beta \log C \quad \dots\dots\dots (4.2.15)$$

The sensing response S corresponded to a constant concentration of gas C,  $\alpha$  and  $\beta$  are proportionality constant and exponential terms respectively. The linear fitting of the log S vs. log C graph gave the  $\beta$  value from the slope, indicating adsorption's nature ( $\beta > 1$  for chemisorption and  $\beta < 1$  imply physisorption). In this work, the  $\beta$  value was ~ 0.41, which ensured physisorption between the gas molecules and sensing materials.

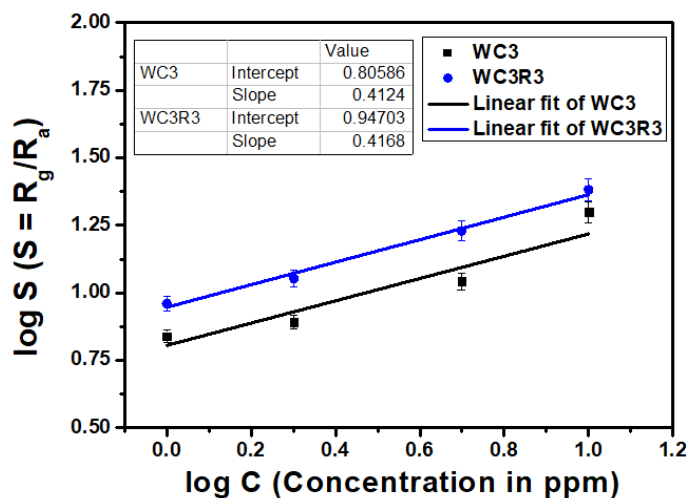


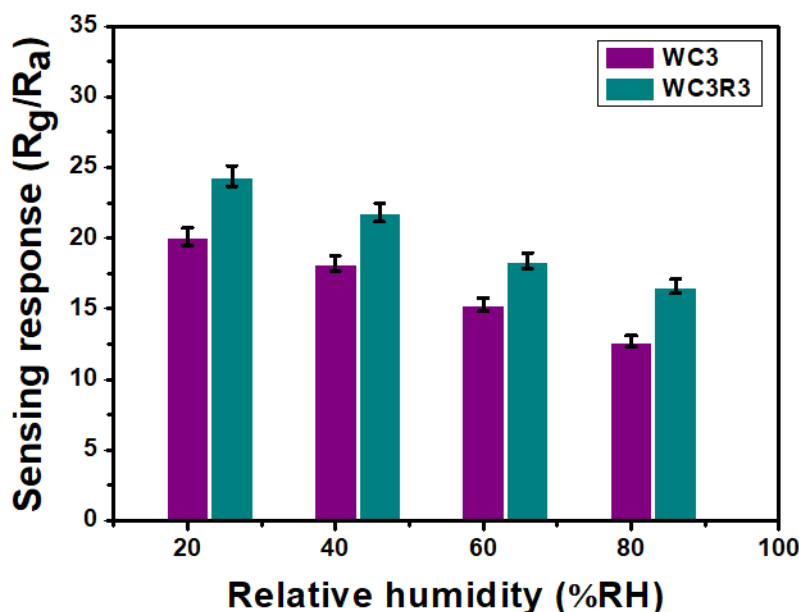
Figure-4.2.17: log S vs. log C plot of WC3 and WC3R3

The efficacy of a sensor for the detection of low concentrations of gas could be deduced from the information of its lowest limit of detection (LOD) value. Now, the theoretical LOD of a sensor could be calculated by applying the ‘theory of power law’ and adopting the IUPAC recommendations, using the following equation [42]:

$$C_L = (k \times S_b) / S \quad \dots\dots\dots (4.2.16)$$

The detectable lowest concentration of gas is  $C_L$ , the standard deviation of base resistance is  $S_b$ ,  $S$  is the sensing response and  $k$  is the constant valued 3 (IUPAC recommendation). Here, the calculated LOD value for WC3R3 sensor was obtained  $\sim 0.053$  ppm.

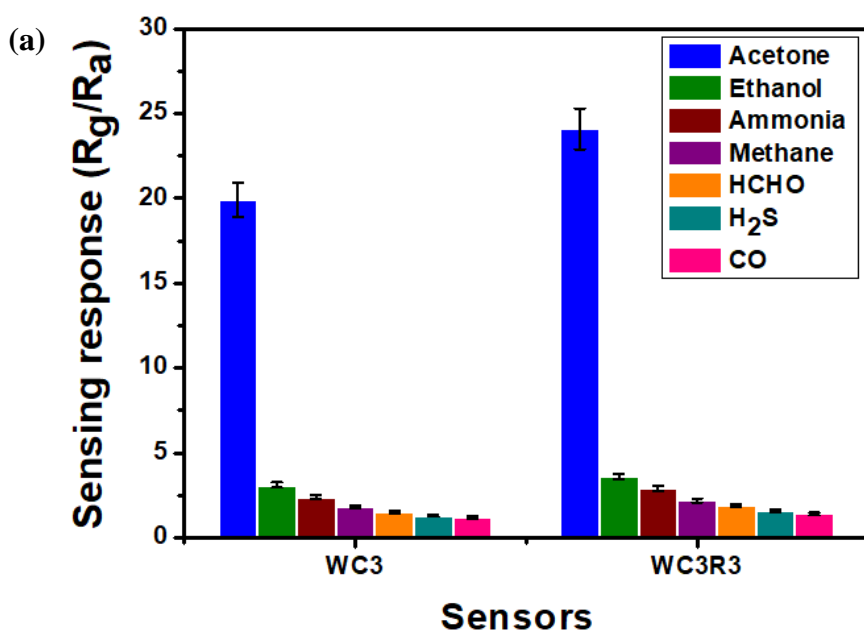
As the study of the effect of relative humidity (%RH) on room temperature sensing performance was imperative and it had already depicted for other room temperature operated sensors that the sensing response inversely related to relative humidity. In this work, the sensing experiments were carried out at a %RH of  $30 \pm 2\%$ . However, the detailed study on humidity effect (sensors were seasoned in the respective humidity conditions of  $\sim 20\%$  to  $\sim 85\%$  for  $\sim 12$  hours, and afterward, they were exposed to  $\sim 10$  ppm acetone) revealed the similar trend of a gradual decrease of sensing response with an increase in %RH (Fig. 4.2.18). In an ambient atmosphere, abundant water molecules (in the form of moisture) chemisorbed (monolayer) on the sensing material surface, thereby obstructing some active sites from oxygenated ions adsorption.



*Figure-4.2.18: Change of sensing response as a function of %RH*

However, at an elevated %RH, due to the profusion of water molecules, they undergo multilayer physisorption on the chemisorbed single layer. Under these circumstances, the water molecules dissociated to ions ( $H^+$  and  $OH^-$ ), and most of the active sites become pre-occupied prior to gas molecules' adsorption due to the hopping of the ions in the physisorbed layer (Grotthus mechanism) [43, 44]. Therefore, in our study, at a lower %RH ( $\sim 20 \pm 2\%$ ), the sensing response increased marginally compared to room temperature experimental humidity (%RH of  $30 \pm 2\%$ ). In contrast, at high humidity (%RH  $> 50\%$ ), the sensing response gradually decreased.

The selectivity of a gas sensor towards a specific target gas needs to be specified in presence of several other interfering gases in surroundings. Therefore, the response of the sensors (Fig. 4.2.19a) was measured in the presence of  $\sim 10$  ppm concentration of different gases and cross-sensitivity of WC3 (Fig. 4.2.19b) and WC3R3 (Fig. 4.2.19c) sensors with respect to acetone were calculated from the selectivity factors ( $S_{\text{acetone}}/S_{\text{interfering VOCs}}$ ) [45]. It was observed that, the optimized sensors demonstrated a profound selectivity towards acetone with an almost insubstantial response toward other gases under identical experimental conditions. Such selectivity of the WC3R3-based sensor could be rationalized as a cumulative effect of various parameters like bond dissociation energy, kinetic diameter, polarity of the analyte gas molecules, etc. Moreover, the interaction energy between the adsorbed oxygenated ions and the analyte gas molecules' closely matched compared to the other interfering gases that promoted the rapid redox reaction between these species.





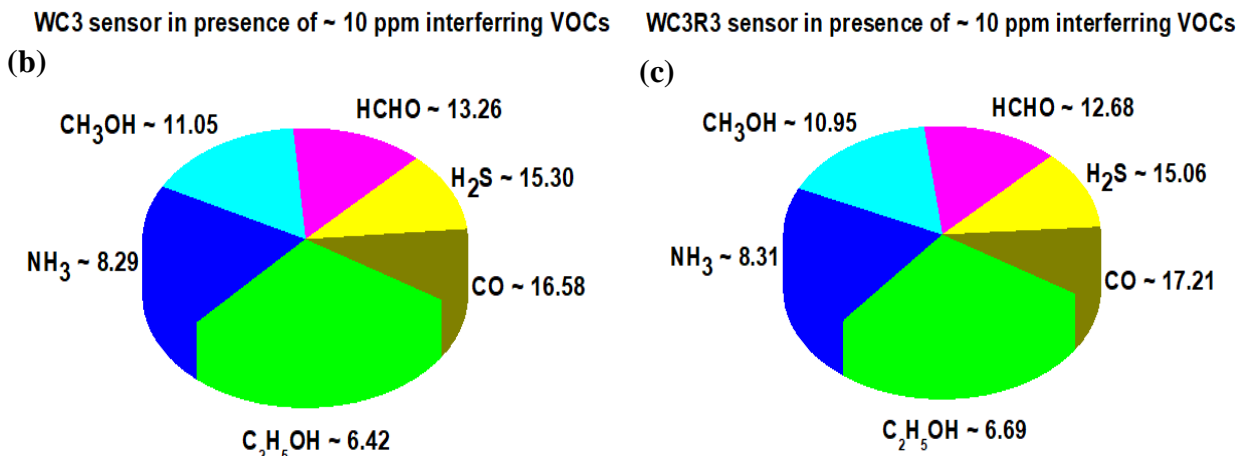


Figure-4.2.19: (a) Selectivity curve for WC3 and WC3R3 sensors; Selectivity factor of (b) WC3 and (c) WC3R3 for ~ 10 ppm of different interfering VOCs with respect to acetone

From the commercial point of view, a sensor's prolonged stability is very essential. The base resistances and sensing responses of WC3 (Fig. 4.2.20a) and WC3R3 (Fig. 4.2.20b) sensors were noted at specific intervals of days for ~ 120 days. The results depicted almost consistent sensing performances for both the optimized sensors, without any major alteration in sensing conditions.

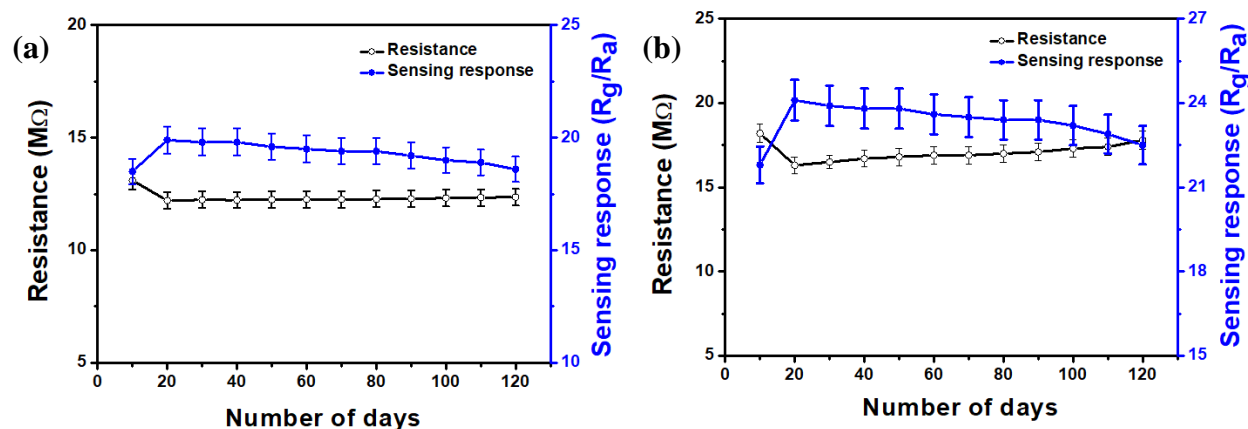


Figure-4.2.20: Stability curve (a) WC3 and (b) WC3R3

The fabricated optimized sensor WC3R3 was also exploited to evaluate its efficiency as a non-invasive diabetic breath biomarker (acetone) detector. Exhaled breath of a healthy person and a diabetic person were separately collected in ~ 1 L Tedlar bag (initially vacuum dried to avoid any air interference in the breath sample) and used as stock sample for breath acetone detection (Fig. 4.2.21a).

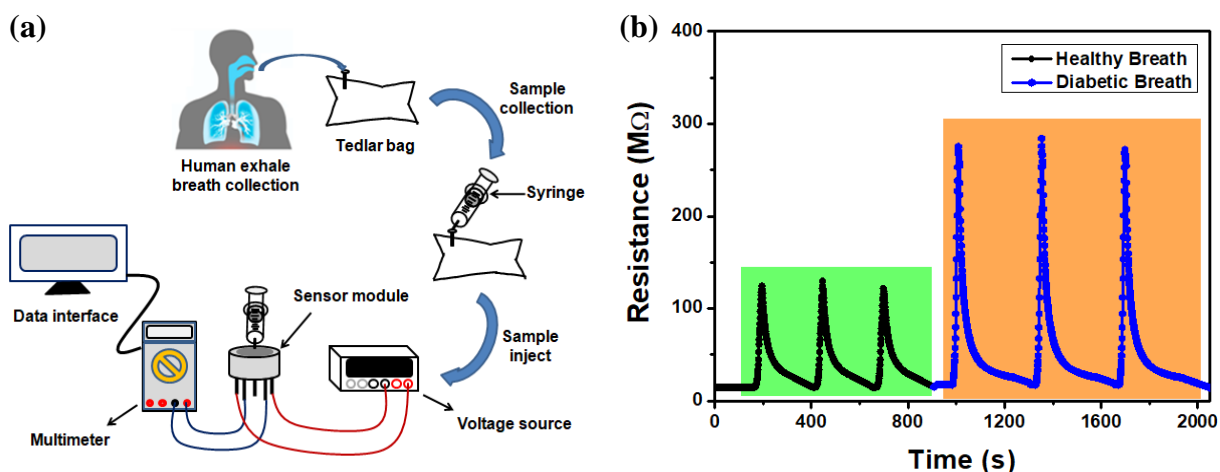


Figure-4.2.21: (a) Schematics of human exhaled breath sample collection and sensing measurement, (b) Sensing response to healthy and diabetic breath sample by WC3R3 sensor

At first, the WC3R3 sensor was exposed to the pulses of exhaled healthy human breath and it demonstrated a sensing response of  $\sim 7.4$  in the presence of  $\sim 10$  s pulses at ambient conditions (Fig. 4.2.21b). After that, the WC3R3 sensor exhibited a sensing response  $\sim 12.8$  towards  $\sim 10$  s pulses of collected diabetic exhaled breath under similar experimental conditions. The response revealed that, the breath acetone concentration was  $< 1$  ppm in healthy breath and that was enhanced in diabetic person. The results also corroborated with the analyzed results obtained from the GCMS system (Agilent 5977B GC/MSD). Therefore, the fabricated sensor could be implemented for non-invasive diabetic biomarker detection in human exhaled breath samples.

### 4.2.3.3. Gas sensing mechanism:

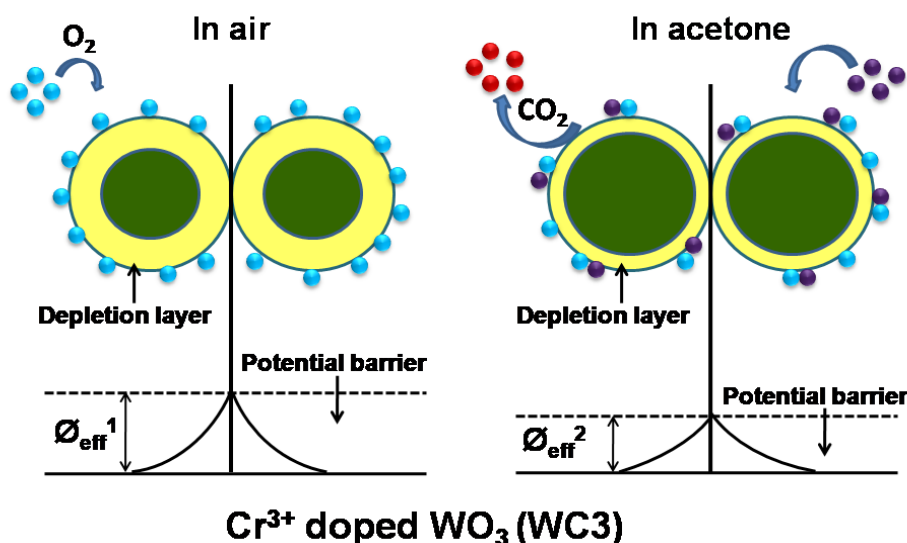
#### 4.2.3.3.1. Electron depletion model:

The gas sensing properties of a sensor is a cumulative effect of several parameters. It mainly depends on the nature of nanocomposite sensing material and its surface properties. Here in the present work, owing to the comparable ionic radii of  $\text{Cr}^{3+}$  and  $\text{W}^{6+}$ , doping of  $\text{Cr}^{3+}$  in pristine  $\text{WO}_3$  matrix attributed to adequate substitution of  $\text{W}^{6+}$  from their inherent lattice sites and simultaneously for charge neutralization created oxygen vacancies. Due to the electropositive nature of these oxygen vacancies, they attracted electrons from the conduction band and allowed the adsorption of oxygenated ions [6, 9, 11].



Where,  $\text{Cr}'''_{\text{W}}$  represented the substituted dopant  $\text{Cr}^{3+}$  ion in the  $\text{W}^{6+}$  site and  $\text{h}^{\bullet}$  denoted holes. This dopant ion introduced an acceptor level somewhere in between the forbidden energy gap of pristine  $\text{WO}_3$  [34] and this regulated the concentration of electrons and holes which led to the alteration of resistance of the sensors (Fig. 4.2.22).

On the other hand, introduction of rGO in the WC3 nanocomposite enhanced the surface area, providing ample adsorption sites for the attachments of atmospheric oxygen. Depending on the optimized operating temperature of the sensor, oxygen molecules were converted to different oxygenated species (generally  $\text{O}_2^-$  formed for sensor operated at room temperature) [46] by capturing labile electrons from the conduction band of the sensing material. This resulted in the thickening of the electron-depletion layer and increased height of the potential energy barrier. Moreover, the introduction of rGO in nanocomposite resulted in a decrease in the energy band-gap of the nanocomposite (Tauc plot) due to the incorporation of a foreign impurity layer in the forbidden gap between the valence band and conduction band. The newly introduced shallow energy level facilitated electronic transportation across the forbidden gap and thus reduced the requirement of activation energy for sensing. Now, in the presence of an acetone pulse, there initiated a chemical reaction on the sensor surface between pre-adsorbed oxygenated ions and the experimental gas molecules [1, 47].



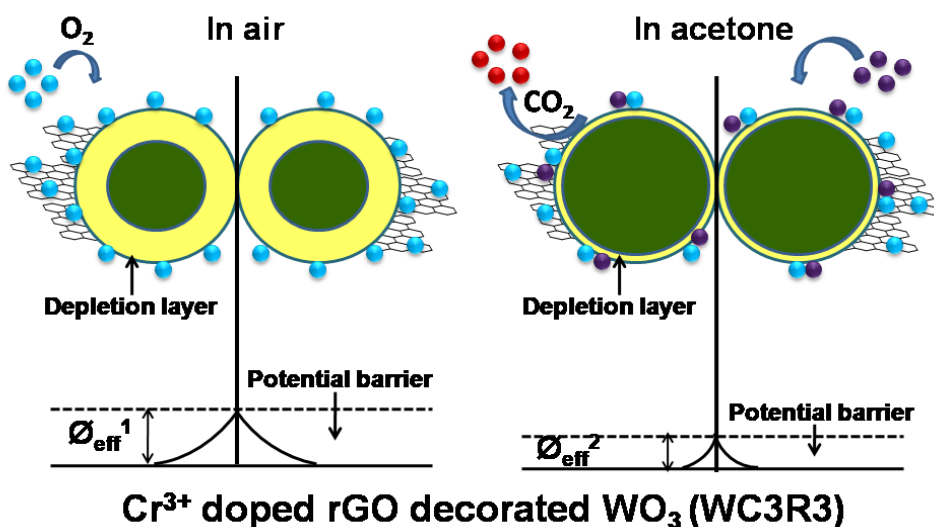


Figure-4.2.22: Illustration of acetone sensing mechanism of fabricated sensors using electron depletion model



Consequently, the trapped electrons were released to the conduction band, which accounted for the decrease in electron depletion layer thickness, and the height of the potential energy barrier was also shortened. As these reverted electrons triggered the hole-electron recombination in the conducting channel of the sensing material, there observed a sudden surge of resistance; which was recorded as a p-type sensing response.

#### 4.2.3.3.2. Impedance spectroscopy:

The cumulative electrical contribution of a polycrystalline MOS-based sensor's components (grain, grain boundary, and electrode) can be rationalized from impedance spectroscopy. The nature of the Nyquist plot, a plot of the real part of impedance ( $Z'$ ) against the imaginary part ( $Z''$ ), provides a wholesome perspective regarding the electrical contribution of the individual components [48-51]. In this work, the impedance data were recorded for WC3 and WC3R3 sensors at room temperature over a frequency domain 1 kHz to 1 MHz, both in the absence and presence of acetone. The stimulation of the recorded data and its fitting to the equivalent circuit model was done using Zview2 software (Table 4.2.2). The plot (Fig. 4.2.23 a, b) of the resistive

part ( $Z'$ ) against the reactive part ( $Z''$ ) demonstrated a single semicircle along with a prominent extension at the end of it.

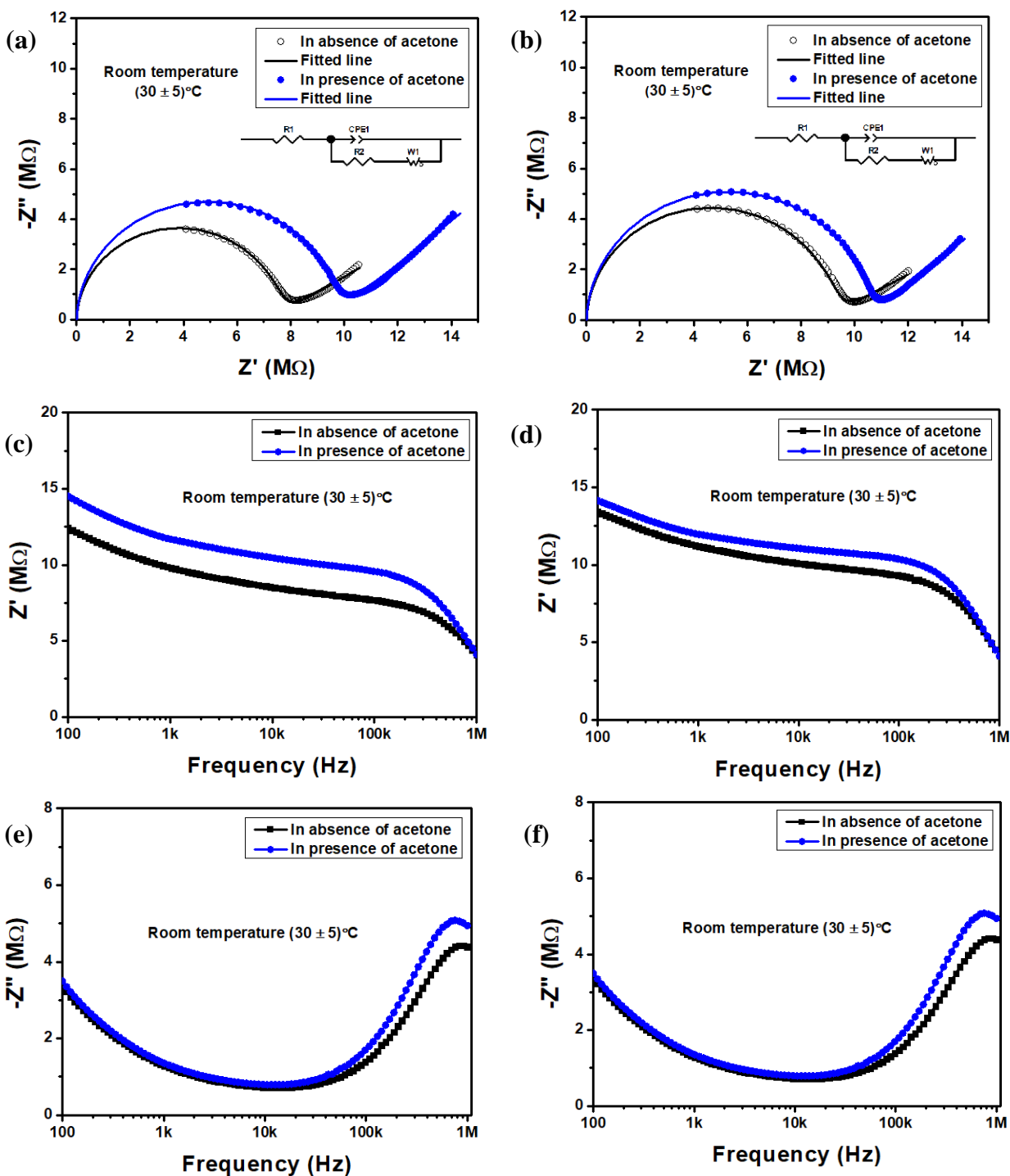


Figure-4.2.23: Nyquist plots (a) WC3 and (b) WC3R3, Variation of  $Z'$  with frequency (c) WC3 and (d) WC3R3, Variation of  $-Z''$  with frequency (e) WC3 and (f) WC3R3, in absence and presence of  $\sim 10$  ppm acetone

The single semicircle signified the electrical contributions from grain regions. Notably, at room temperature the semicircles were part of large impedance arc marginally deformed in the real impedance axis and were extrapolated to obtain the corresponding grain resistances. This nature of the Nyquist plot suggested the non-ideal Debye-type interactions in inhomogeneous, defect-rich synthesized nanocomposites. In the presence of experimental gas (acetone), the grain resistances were increased, according to the p-type response of the sensors. On the other hand, the extension at the end of the semicircle was fitted by the Warburg element (open) in the equivalent circuit model, representing the presence of reflective boundaries at the grains, reflected back the charge carriers by reducing the tunneling of charges across the grains. The fitting parameters corresponded to the Warburg element accompanied by a small Warburg resistance (W-R) of a slightly deformed nature ( $W-P < 0.5$ , as 0.5 signifies a perfect Warburg element with  $45^\circ$  phase angle). Moreover, the diffusion time (W-T) of the charge carriers in the grains was very fast ( $< 1$  s), which ensured fluent electronic mobility in the nanocomposites.

Table - 4.2.2: Fitting parameters of Nyquist plot for WC3 and WC3R3 sensors:

	WC3		WC3R3	
	In absence of acetone	In presence of acetone	In absence of acetone	In presence of acetone
R1 ( $\Omega$ )	10	10	10	10
CPE-T ( $\mu F$ )	10	10	10	10
CPE-P	0.98	0.98	0.98	0.98
R2 ( $M\Omega$ )	7.2	9.4	8.7	10.2
W-R ( $M\Omega$ )	0.40	0.45	0.55	0.5
W-T (s)	0.3	0.5	0.7	0.99
W-P	0.18	0.23	0.17	0.225

In Fig. 4.2.23 c, d, the variation of the real part of impedance ( $Z'$ ) with respect to  $\log f$  showed almost consistent change in the lower frequencies and suddenly decreased at a higher frequency. The individual plots for the sensors (WC3 and WC3R3), both in the absence and presence of acetone, converged at a higher frequency range, accounting for the mobilization of the trapped

charge carriers after interaction between oxygenated species and experimental gas (acetone) molecules. The change of the imaginary part of impedance ( $Z''$ ) with  $\log f$  (Fig. 4.2.23 e, f) displayed the hopping nature of the charge carriers along with maxima at the high frequency (near  $\sim 1$  MHz). In the presence of acetone, the maxima slightly shifted to the lower frequency, which indicated towards facile movement (required lesser energy) of electrons after the interaction of gas molecules and sensing materials.

The comparative sensing performance of some literature works with the developed rGO decorated  $\text{Cr}^{3+}$  doped  $\text{WO}_3$  nanocomposite sensor was tabulated here (Table 4.2.3).

Table –4.2.3: Present state-of-art of  $\text{Cr}^{3+}$  doped  $\text{WO}_3$  nanomaterial-based gas sensors:

Sensing material	Synthesis technique	Sensing gas	Working temp. ( $^{\circ}\text{C}$ )	Detection conc. (ppm)	Response ( $R_g/R_a$ )	Ref.
Cr doped $\text{WO}_3$ nanofibers	Electrospinning	Xylene	255	100	35.04	[6]
Pt- $\text{Cr}_2\text{O}_3$ - $\text{WO}_3$ composite	Hydrothermal	Xylene	325	10	74.3	[7]
$\text{Cr}_2\text{O}_3$ functionalized $\text{WO}_3$ nanorods	CVD	Ethanol	300	200	5.58	[8]
Hierarchical Cr-doped $\text{WO}_3$	Hydrothermal	$\text{H}_2\text{S}$	80	100	153	[9]
Cr-doped $\text{WO}_3$ nanosheets	Precipitation	HCHO	200	50	82%	[10]
Cr- $\text{WO}_3$ powders	Sol-gel	$\text{NH}_3$	250	500	-	[11]
Hierarchical nanostructured Co-doped $\text{WO}_3/\text{C}$	Sol-gel	Acetone	50	2	2.67	[12]
Iron and carbon codoped $\text{WO}_3$	Precipitation	Acetone	300	2	10.3	[13]

WO <sub>3</sub> /Pt-decorated rGO nanosheets	Hydrothermal	Acetone	200	10	12.2	[14]
<b>Cr<sup>3+</sup> doped rGO decorated WO<sub>3</sub> nanocomposite</b>	<b>Sol-gel</b>	<b>Acetone</b>	<b>Room temperature (30 ± 5°C)</b>	<b>10</b>	<b>24.1</b>	<b>This work</b>

#### 4.2.4. Conclusion:

In the present work, Cr<sup>3+</sup> doping (1, 3, and 5 wt%) in the pristine WO<sub>3</sub> matrix induced a mutation from monoclinic to hexagonal phase. This structural change led to the enrichment of oxygen vacancies and the fabricated Taguchi-type sensors exhibited an excellent p-type acetone sensing response at room temperature. The sensing response ( $R_g/R_a$ ) towards ~ 10 ppm acetone of ~ 3 wt% Cr<sup>3+</sup> doped WO<sub>3</sub> nanomaterial (WC3) was maximum ~ 19.9, which was further improved after ~ 3 wt% rGO incorporation and the response increased to ~ 24.1. The generation of ‘inversion space-charge layer’ on the sensing material surface accounted for obtaining a p-type sensing response using an n-type MOS (WO<sub>3</sub>). Eley-Rideal theoretical model was adopted to delineate the kinetic aspects of sensing which revealed a fast response/recovery time (~ 10 s/~ 30 s) of the sensor. The prime selectivity of the optimized sensor towards acetone amidst of other interfering VOCs was ensured from the high selectivity factor. The sensors also demonstrated prolonged stability of ~ 120 days in terms of base resistance and sensing response. The optimized sensor was exposed to stimulate human exhaled breath and it was effectively able to identify between healthy and diabetic breath. The chemiresistive sensing mechanism illustrated using a band-diagram modeling and impedance spectroscopy was utilized to elucidate the electrical charge carriers’ properties of the sensors. All the results and mechanism analysis proved that; this sensor could be considered as a futuristic contender for real-life non-invasive diabetic breath biomarker detection in ambient condition.



### References:

- [1] S. Sen, S. Maity, S. Kundu, Fabrication of Fe doped reduced graphene oxide (rGO) decorated WO<sub>3</sub> based low temperature ppm level acetone sensor: Unveiling sensing mechanism by impedance spectroscopy, *Sens. Actuators B: Chem.* 361 (2022) 131706. <https://doi.org/10.1016/j.snb.2022.131706>.
- [2] V. K. Tomer, K. Singh, H. Kaur, M. Shorie, P. Sabherwal, Rapid acetone detection using indium loaded WO<sub>3</sub>/SnO<sub>2</sub> nanohybrid sensor, *Sens. Actuators B: Chem.* 253 (2017) 703-713. <https://doi.org/10.1016/j.snb.2017.06.179>.
- [3] Y. Gui, L. Yang, K. Tian, H. Zhang, S. Fang, P-type Co<sub>3</sub>O<sub>4</sub> nanoarrays decorated on the surface of n-type flower-like WO<sub>3</sub> nanosheets for high performance gas sensing, *Sens. Actuators B: Chem.* 288 (2019) 104-112. <https://doi.org/10.1016/j.snb.2019.02.101>.
- [4] Z. Liu, B. Liu, W. Xie, H. Li, R. Zhou, Q. Li, T. Wang, Enhanced selective acetone sensing characteristics based on Co-doped WO<sub>3</sub> hierarchical flower-like nanostructures assembled with nanoplates, *Sens. Actuators B: Chem.* 235 (2016) 614-621. <https://doi.org/10.1016/j.snb.2016.05.140>.
- [5] H. Zhou, D. Xu, H. Zuo, W. Liu, S. Lin, Preparation of Flower-Like Cu-WO<sub>3</sub> Nanostructures and Their Acetone Gas Sensing Performance, *J. Chem.* (2015) 382087. <https://doi.org/10.1155/2015/382087>.
- [6] F. Li, S. Ruan, N. Zhang, Y. Yin, S. Guo, Y. Chen, H. Zhang, C. Li, Synthesis and characterization of Cr-doped WO<sub>3</sub> nanofibers for conductometric sensors with high xylene sensitivity, *Sens. Actuators B: Chem.* 265 (2018) 355-364. <https://doi.org/10.1016/j.snb.2018.03.054>.
- [7] C. Feng, Z. Jiang, J. Wu, B. Chen, G. Lu, C. Huang, Pt-Cr<sub>2</sub>O<sub>3</sub>-WO<sub>3</sub> composite nanofibers as gas sensors for ultra-high sensitive and selective xylene detection, *Sens. Actuators B: Chem.* 300 (2019) 127008. <https://doi.org/10.1016/j.snb.2019.127008>.
- [8] S. Choi, M. Bonyani, G. Sun, J. K. Lee, S. K. Hyun, C. Lee, Cr<sub>2</sub>O<sub>3</sub> nanoparticle-functionalized WO<sub>3</sub> nanorods for ethanol gas sensors, *Appl. Surf. Sci.* 432 (2018) 241-249. <https://doi.org/10.1016/j.apsusc.2017.01.245>.

- [9] Y. Wang, B. Liu, S. Xiao, X. Wang, L. Sun, H. Li, W. Xie, Q. Li, Q. Zhang, T. Wang, Low-Temperature H<sub>2</sub>S Detection with Hierarchical Cr-doped WO<sub>3</sub> Microspheres, *ACS Appl. Mater. Interfaces* 8 (2016) 9674-9683. <https://doi.org/10.1021/acsami.5b12857>.
- [10] S. B. Upadhyay, R. K. Mishra, P. P. Sahay, Cr-doped WO<sub>3</sub> nanosheets: Structural, optical and formaldehyde sensing properties, *Ceram. Int.* 42 (2016) 15301-15310. <https://doi.org/10.1016/j.ceramint.2016.06.170>.
- [11] M. Epifani, N. Garcia-Castello, J. D. Prades, A. Cirera, T. Andreu, J. Arbiol, P. Siciliano, J. R. Morante, Suppression of the NO<sub>2</sub> interference by chromium addition in WO<sub>3</sub>-based ammonia sensors. Investigation of the structural properties and of the related sensing pathways, *Sens. Actuators B: Chem.* 187 (2013) 308-312. <https://doi.org/10.1016/j.snb.2012.11.072>.
- [12] V. Saasa, T. Malwela, Y. Lemmer, M. Beukes, B. Mwakikunga, The hierarchical nanostructured Co-doped WO<sub>3</sub>/carbon and their improved acetone sensing performance, *Mater. Sci. Semicond.* 117 (2020) 105157. <https://doi.org/10.1016/j.mssp.2020.105157>.
- [13] J. Shen, M. Wang, Y. Wang, J. Hu, Y. Zhu, Y. Zhang, Z. Li, H. Yao, Iron and carbon codoped WO<sub>3</sub> with hierarchical walnut-like microstructure for highly sensitive and selective acetone sensor, *Sens. Actuators B: Chem.* 256 (2018) 27-37. <https://doi.org/10.1016/j.snb.2017.10.073>.
- [14] L. Chen, L. Huang, Y. Lin, L. Sai, Q. Chang, W. Shi, Q. Chen, Fully gravure-printed WO<sub>3</sub>/Pt-decorated rGO nanosheets composite film for detection of acetone, *Sens. Actuators B: Chem.* 255 (2018) 1482-1490. <https://doi.org/10.1016/j.snb.2017.08.158>.
- [15] S. Xue, S. Cao, Z. Huang, D. Yang, G. Zhang, Improving Gas-Sensing Performance Based on MOS Nanomaterials: A Review, *Materials* 14 (2021) 4263. <https://doi.org/10.3390/ma14154263>.
- [16] D. Y. Nadargi, A. Umar, J. D. Nadargi, S. A. Lokare, S. Akbar, I. S. Mulla, S. S. Suryavanshi, N. L. Bhandari, M. G. Chaskar, Gas sensors and factors influencing sensing mechanism with a special focus on MOS sensors, *J. Mater. Sci.* 58 (2023) 559-582. <https://doi.org/10.1007/s10853-022-08072-0>.
- [17] V. Luxmi, A. Kumar, Enhanced photocatalytic performance of m-WO<sub>3</sub> and m-Fe-doped WO<sub>3</sub> cuboids synthesized via sol-gel approach using egg albumen as a solvent, *Mater. Sci. Semicond.* 104 (2019) 104690. <https://doi.org/10.1016/j.mssp.2019.104690>.

- [18] E. M. Ngigi, P. N. Nomngongo, J. C. Ngila, Synthesis and Application of Fe-Doped  $\text{WO}_3$  Nanoparticles for Photocatalytic Degradation of Methylparaben Using Visible-Light Radiation and  $\text{H}_2\text{O}_2$ , *Catal. Lett.* 149 (2019) 49-60. <https://doi.org/10.1007/s10562-018-2594-y>.
- [19] Y. Li, Q. Zhou, S. Ding, Z. Wu, Research Progress of Gas Sensing Performance of 2D Hexagonal  $\text{WO}_3$ , *Front. Chem.* 9 (2021) 786607. <https://doi.org/10.3389/fchem.2021.786607>.
- [20] R. A. Capeli, C. J. Dalmaschio, s. R. Teixeira, V. R. Mastelaro, A. J. Chiquito, E. Longo, F. M. Pontes, One-step controllable synthesis of three-dimensional  $\text{WO}_3$  hierarchical architectures with different morphologies decorated with silver nanoparticles: enhancing the photocatalytic activity, *RSC Adv.* 10 (2020) 6625. <https://doi.org/10.1039/c9ra10173j>.
- [21] Z. Zhu, L. Zheng, S. Zheng, J. Chen, M. Liang, Y. Tian, D. Yang, Cr doped  $\text{WO}_3$  nanofibers enriched with surface oxygen vacancies for highly sensitive detection of the 3-hydroxy-2-butanone biomarker, *J. Mater. Chem. A* 6 (2018) 21419. <https://doi.org/10.1039/c8ta08670b>.
- [22] C. M. Hung, D. Q. Dat, N. V. Duy, V. V. Quang, N. V. Toan, N. V. Hieu, N. D. Hoa, Facile synthesis of ultrafine rGO/ $\text{WO}_3$  nanowire nanocomposites for highly sensitive toxic  $\text{NH}_3$  gas sensors, *Mater. Res. Bull.* 125 (2020) 110810. <https://doi.org/10.1016/j.materresbull.2020.110810>.
- [23] E. Rossinyol, A. Prim, E. Pellicer, J. Arbiol, F. H. Ramírez, F. Peiró, A. Cornet, J. R. Morante, L. A. Solovyov, B. Tian, T. Bo, D. Zhao, Synthesis and Characterization of Chromium-Doped Mesoporous Tungsten Oxide for Gas-Sensing Applications, *Adv. Funct. Mater.* 17 (2007) 1801-1806. <https://doi.org/10.1002/adfm.200600722>.
- [24] G. Jeevitha, R. Abhinayaa, D. Mangalaraj, N. Ponpandian, P. Meena, V. Mounasamy, S. Madanagurusamy, Porous reduced garphene oxide (rGO)/ $\text{WO}_3$  nanocomposites for the enhanced detection of  $\text{NH}_3$  at room temperature, *Nanoscale Adv.* 1 (2019) 1799. <https://doi.org/10.1039/c9na00048h>.
- [25] J. Kaur, K. Anand, A. Kaur, R. C. Singh, Sensitive and selective acetone sensor based on Gd doped  $\text{WO}_3$ /reduced graphene oxide nanocomposite, *Sens. Actuators B: Chem.* 258 (2018) 1022-1035. <https://doi.org/10.1016/j.snb.2017.11.159>.

- [26] M. D'Arienzo, M. Crippa, P. Gentile, C. M. Mari, S. Polizzi, R. Ruffo, R. Scotti, L. Wahba, F. Morazzoni, Sol-gel derived mesoporous Pt and Cr-doped WO<sub>3</sub> thin films: the role played by mesoporosity and metal doping in enhancing the gas sensing properties, *J. Sol-Gel Sci. Technol.* 60 (2011) 378-387. <https://doi.org/10.1007/s10971-011-2568-7>.
- [27] J. Shen, L. Zhang, J. Ren, J. Wang, H. Yao, Z. Li, Highly enhanced acetone sensing performance of porous C-doped WO<sub>3</sub> hollow spheres by carbon spheres as templates, *Sens. Actuators B: Chem.* 239 (2017) 597-607. <https://doi.org/10.1016/j.snb.2016.08.069>.
- [28] Q. Ding, Y. Wang, P. Guo, J. Li, C. Chen, T. Wng, K. Sun, D. He, Cr-Doped Urchin-Like WO<sub>3</sub> Hollow Spheres: The Cooperative Modulation of Crystal Growth and Energy-band Structure for High-Sensitive Acetone Detection, *Sensors* 20 (2020) 3473. <https://doi.org/10.3390/s20123473>.
- [29] Q. Hao, T. Liu, J. Liu, Q. Liu, X. Jing, H. Zhang, G. Huang, J. Wang, Controllable synthesis and enhanced gas sensing properties of a single-crystalline WO<sub>3</sub>-rGO porous nanocomposite, *RSC Adv.* 7 (2017) 14192. <https://doi.org/10.1039/c6ra28379a>.
- [30] S. F. Shaikh, B. G. Ghule, P. V. Shinde, S. D. Raut, S. K. Gore, M. Ubaidullah, R. S. Mane, A. M. Al-Enizi, Continuous hydrothermal flow-inspired synthesis and ultra-fast ammonia and humidity room-temperature sensor activities of WO<sub>3</sub>nanobricks, *Mater. Res. Express* 7 (2020) 015076. <https://doi.org/10.1088/2053-1591/ab67fc>.
- [31] A. Renitta, K. Vijayalakshmi, A novel room temperature ethanol sensor based on catalytic Fe activated porous WO<sub>3</sub> microspheres, *Catal. Commun.* 73 (2016) 58-62. <https://doi.org/10.1016/j.catcom.2015.10.014>.
- [32] D. Wang, J. Sun, X. Cao, Y. Zhu, Q. Wang, G. Wang, Y. Han, G. Lu, G. Pang, S. Feng, High-performance gas sensing achieved by mesoporous tungsten oxide mesocrystals with increased oxygen vacancies, *J. Mater. Chem. A*, 1 (2013) 8653. <https://doi.org/10.1039/c3ta11506b>.
- [33] H. Kim, J. Yoon, K. Choi, H. W. Jang, A. Umar, J. Lee, Ultraselective and sensitive detection of xylene and toluene for monitoring indoor air pollution using Cr-

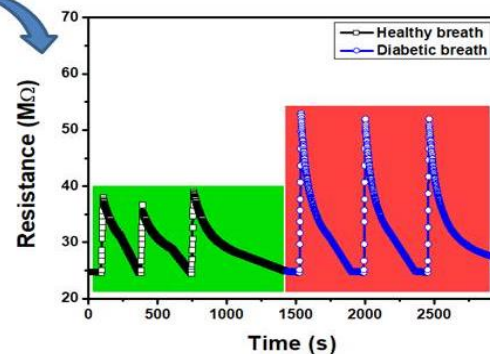
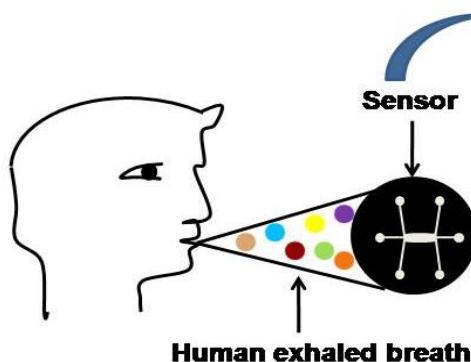
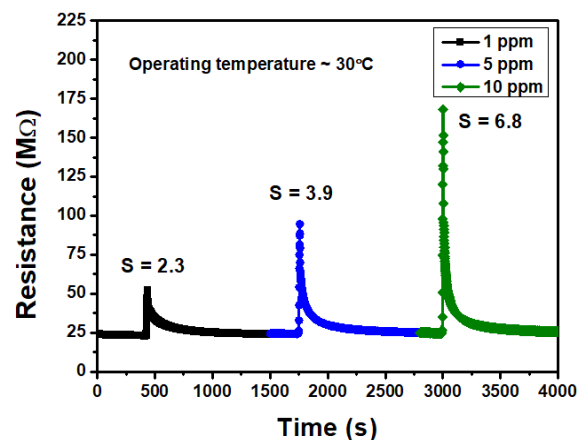
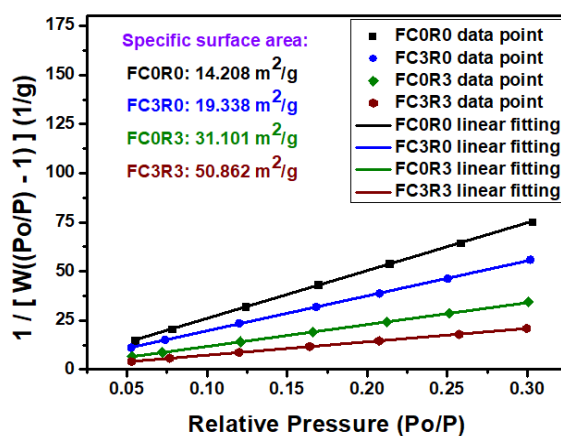
- doped NiO hierarchical nanostructures, *Nanoscale* 5 (2013) 7066. <https://doi.org/10.1039/c3nr01281f>.
- [34] B. Lyson-Sypien, A. Czapla, M. Lubecka, P. Gwizdz, K. Schneider, K. Zakrzewska, K. Michallow, T. Graule, A. Reszka, M. Rekas, A. Lacz, M. Radecka, Nanopowders of chromium doped TiO<sub>2</sub> for gas sensors, *Sens. Actuators B: Chem.* 175 (2012) 163-172. <https://doi.org/10.1016/j.snb.2012.02.051>.
- [35] Y. Qin, X. Sun, X. Li, M. HuRoom temperature NO<sub>2</sub>-sensing properties of Ti-added nonstoichiometric tungsten oxide nanowires, *Sens. Actuators B: Chem.* 162 (2012) 244-250. <https://doi.org/10.1016/j.snb.2011.12.074>.
- [36] W. Y. Qiao, H. Ming, W. Xiao-Ying, A study of transition from n- to p-type based on hexagonal WO<sub>3</sub> nanorods sensor, *Chin. Phys. B* 23 (2014) 040704. <https://doi.org/10.1088/1674-1056/23/4/040704>.
- [37] D. R. Jones, T. G. G. Maffei, Analysis of the kinetics of surface reactions on a zinc oxide nanosheets-based carbon monoxide sensor using an Eley-Rideal model, *Sens. Actuators B: Chem.* 218 (2015) 16-24. <https://doi.org/10.1016/j.snb.2015.04.072>.
- [38] N. M. Vuong, D. Kim, H. Kim, Surface gas sensing kinetics of a WO<sub>3</sub> nanowire sensor: Part 2-Reducing gases, *Sens. Actuators B: Chem.* 224 (2016) 425-433. <https://doi.org/10.1016/j.snb.2015.10.070>.
- [39] V. B. Kamble, A. M. Umarji, Effect of Pt doping on Gas Sensing properties of porous Chromium Oxide films through Kinetic Response Analysis Approach, *RSC Adv.* 5 (2015) 27509-27516. <https://doi.org/10.1039/C5RA02186C>.
- [40] N. M. Vuong, N.D. Chinh, B. T. Huy, Y. Lee, CuO-Decorated ZnO Hierarchical Nanostructures as Efficient and Established Sensing Materials for H<sub>2</sub>S Gas Sensors, *Sci. Rep.* 6 (2016) 26736. <https://doi.org/10.1038/srep26736>.
- [41] S. Sen, S. Kundu, Reduced graphene oxide (rGO) decorated ZnO-SnO<sub>2</sub>: A ternary nanocomposite towards improved low concentration VOC sensing performance, *J. Alloys Compd.* 881 (2021) 160406. <https://doi.org/10.1016/j.jallcom.2021.160406>.
- [42] S. Kundu, A. Kumar, S. Sen, A. Nilabh, Bio-synthesis of SnO<sub>2</sub> and comparison its CO sensing performance with conventional processes, *J. Alloys Compd.* 818 (2020) 152841. <https://doi.org/10.1016/j.jallcom.2019.152841>.

- [43] S. Sen, S. Maity, S. Kundu, Reduced graphene oxide (rGO) decorated NiO-SnO<sub>2</sub> nanocomposite based sensor towards room temperature diabetic biomarker detection, *J. Alloys Compd.* 966 (2023) 171553. <https://doi.org/10.1016/j.jallcom.2023.171553>.
- [44] Q. Li, Q. Yin Y. Zheng, Z. Sui, X. Zhou, D. Chen, Y. Zhu, Insights into Hydrogen Transport behavior on Perovskite Surfaces: Transition from the Grotthuss Mechanism to the Vehicle Mechanism, *Langmuir* 35 (2019) 9962-9969. <https://doi.org/10.1021/acs.langmuir.8b04138>.
- [45] D. R. Patil, L. A. Patil, D. P. Amalnerkar, Ethanol gas sensing properties of Al<sub>2</sub>O<sub>3</sub>-doped ZnO thick film resistors, *Bull. Mater. Sci.* 30 (2007) 553-559. <https://doi.org/10.1007/s12034-007-0086-6>.
- [46] S. Bhattacharjee, S. Sen, S. Kundu, Development of La-impregnated TiO<sub>2</sub> based ethanol sensors for next generation automobile application, *J. Mater. Sci.: Mater. Electron.* 33 (2022) 15296-15312. <https://doi.org/10.1007/s10854-022-08394-4>.
- [47] S. Sen, A. Nilabh, S. Kundu, Room temperature acetone sensing performance of Pt/Sb<sub>2</sub>O<sub>3</sub> impregnated Fe<sub>2</sub>O<sub>3</sub> thin film: Noninvasive diabetes detection, *Microchem. J.* 165 (2021) 106111. <https://doi.org/10.1016/j.microc.2021.106111>.
- [48] M. Parthibavarman, M. Karthik, P. Sathishkumar, R. Poonguzhali, Rapid synthesis of novel Cr-doped WO<sub>3</sub> nanorods: an efficient electrochemical and photocatalytic performance, *J. Iranian Chem. Soc.* 15 (2018) 1419-1430. <https://doi.org/10.1007/s13738-018-1342-y>.
- [49] N. Al-Hardan, M. J. Abdullah, A. A. Aziz, Impedance spectroscopy of undoped and Cr-doped ZnO gas sensors under different oxygen concentrations, *Appl. Surf. Sci.* 257 (2011) 8993-8997. <https://doi.org/10.1016/j.apsusc.2011.05.078>.
- [50] Y. Gönüllü, K. Kelm, S. Mathur, B. Saruhan, Equivalent Circuit Models for Determination of the Relation between the Sensing Behavior and Properties of Undoped/Cr Doped TiO<sub>2</sub> NTs, *Chemosensors* 2 (2014) 69-84. <https://doi.org/10.3390/chemosensors2010069>.
- [51] C. Wang, X. Zhang, Q. Rong, N. Hou, H. Yu, Ammonia sensing by closely packed WO<sub>3</sub> microspheres with oxygen vacancies, *Chemosphere* 204 (2018) 202-209. <https://doi.org/10.1016/j.chemosphere.2018.04.050>.



# CHAPTER 5

## Reduced graphene oxide (rGO)-Cr (III) doped $\alpha$ -Fe<sub>2</sub>O<sub>3</sub> nanocomposite towards room temperature ppm-level acetone detection



In this work, rGO decorated Cr<sup>3+</sup> doped Fe<sub>2</sub>O<sub>3</sub> nanocomposites were synthesized and its ppm level acetone sensing properties was explored. At low temperature sensors revealed p-type sensing response and n-type sensing response at a higher operating temperature. The optimized sensor showed a p-type sensing response of ~ 6.8 towards ~ 10 ppm acetone at room temperature. Moreover, the sensor exhibited a rapid response (~ 10 s) and recovery time (~ 10 s) suitable for multiple pulse detection in short time. It showed stable and reproducible sensing performance over a long period of time. Furthermore, this sensor was also distinguished between healthy and diabetic breath in terms of acetone concentration analysis in exhaled human breath.





### 5.1. Introduction:

In Chapter 4.1 and 4.2, low temperature selective acetone sensing performance of rGO decorated transition metal ion ( $\text{Fe}^{3+}$  and  $\text{Cr}^{3+}$ ) doped  $\text{WO}_3$  based sensors was described. At first, Chapter 4.1 explained acetone sensing at  $\sim 130^\circ\text{C}$  using sensors fabricated from rGO decorated  $\text{Fe}^{3+}$  doped  $\text{WO}_3$  [1]. In the next chapter (Chapter 4.2),  $\text{WO}_3$  lattice was modulated by changing the dopant ion ( $\text{Cr}^{3+}$ ) followed by further incorporation of rGO in it and room temperature ( $30 \pm 5^\circ\text{C}$ ) selective acetone sensing performance was studied. Thus, the previous chapters established the supremacy of higher transition metal oxide as a low temperature operated effective acetone sensor, however,  $\text{WO}_3$  itself synthesized from costly precursors. Henceforth, in this chapter, the main goal was to explore the low concentration acetone sensing behavior of suitable, low cost, lower transition metal oxide and manifest its capability as a diabetic breath biomarker detector by differentiating acetone concentration in exhaled human breath of healthy and diabetic persons. Among several lower transition metal oxides, iron oxide is highly abundant, cost-effective, and proclaimed VOC detector [2-5]. However, as discussed earlier (Chapter 1), in pristine state, the  $\text{Fe}_2\text{O}_3$  based sensors also suffer from low response and require high operating temperature for sensing. To overcome such drawbacks, doping of metal ions in MOS lattice could prove to be influential, as dopants could impart their catalytic activities as well as introduce some defect sites and oxygen vacancies. As well as, rGO incorporation enhances the specific surface area of the nanocomposite which could result into amplification of sensing response and reduction of operating temperature of the sensors. Several reports already published over the years [6-14], although, they seldom fail to demonstrate their efficacy as low concentration acetone sensor operated at low temperature. Therefore, in this work, pristine  $\text{Fe}_2\text{O}_3$  was doped with  $\text{Cr}^{3+}$  and further decorated with rGO and Taguchi-type sensors were fabricated to study their ppm-level acetone sensing performance at low working temperature. The optimized sensor was also employed to distinguish the change in acetone (diabetic breath biomarker) concentration in exhaled breath of healthy and diabetic person at ambient condition.

### 5.2. Experimental:

Pristine  $\text{Fe}_2\text{O}_3$ ,  $\text{Cr}^{3+}$  doped  $\text{Fe}_2\text{O}_3$  nanomaterials, and their composites with rGO were synthesized (Fig. 5.1) using sol-gel process (details discussed in Chapter 2, Section 2.3.1). As a

precursor of  $\text{Fe}_2\text{O}_3$  and  $\text{Cr}^{3+}$  ion, iron nitrate nonahydrate ( $\text{Fe}(\text{NO}_3)_3 \cdot 9\text{H}_2\text{O}$ , Sigma Aldrich) and chromium nitrate nonahydrate ( $\text{Cr}(\text{NO}_3)_3 \cdot 9\text{H}_2\text{O}$ , Sigma Aldrich) were used respectively. The pristine  $\text{Fe}_2\text{O}_3$  was marked as FC0R0. The dopant concentration was varied as  $\sim 1$ ,  $\sim 3$ , and  $\sim 5$  wt%, and labeled them as FC1R0, FC3R0, and FC5R0 accordingly. The nanomaterial powders were obtained by gel calcination at  $\sim 550^\circ\text{C}$  (as per TGA analysis) as discussed in Chapter 2, Section 2.3.1. The rGO decorated  $\text{Fe}_2\text{O}_3$  nanocomposites were synthesized with different concentration of rGO ( $\sim 1$ ,  $\sim 3$ , and  $\sim 5$  wt%) added to an aqueous ethanol solution containing required amounts of pristine  $\text{Fe}_2\text{O}_3$  nanomaterials and named as FC0R1, FC0R3, and FC0R5 respectively. Simultaneously, the  $\text{Cr}^{3+}$  doped rGO decorated  $\text{Fe}_2\text{O}_3$  nanocomposites were also prepared similarly by varying rGO concentration ( $\sim 1$  wt%,  $\sim 3$  wt%, and  $\sim 5$  wt%) in FC3 and named as FC3R1, FC3R3 and FC3R5 respectively. The sols were converted to gels and cured at  $\sim 350^\circ\text{C}$  for  $\sim 2$  hours to obtain respective rGO-decorated nanocomposite powders.

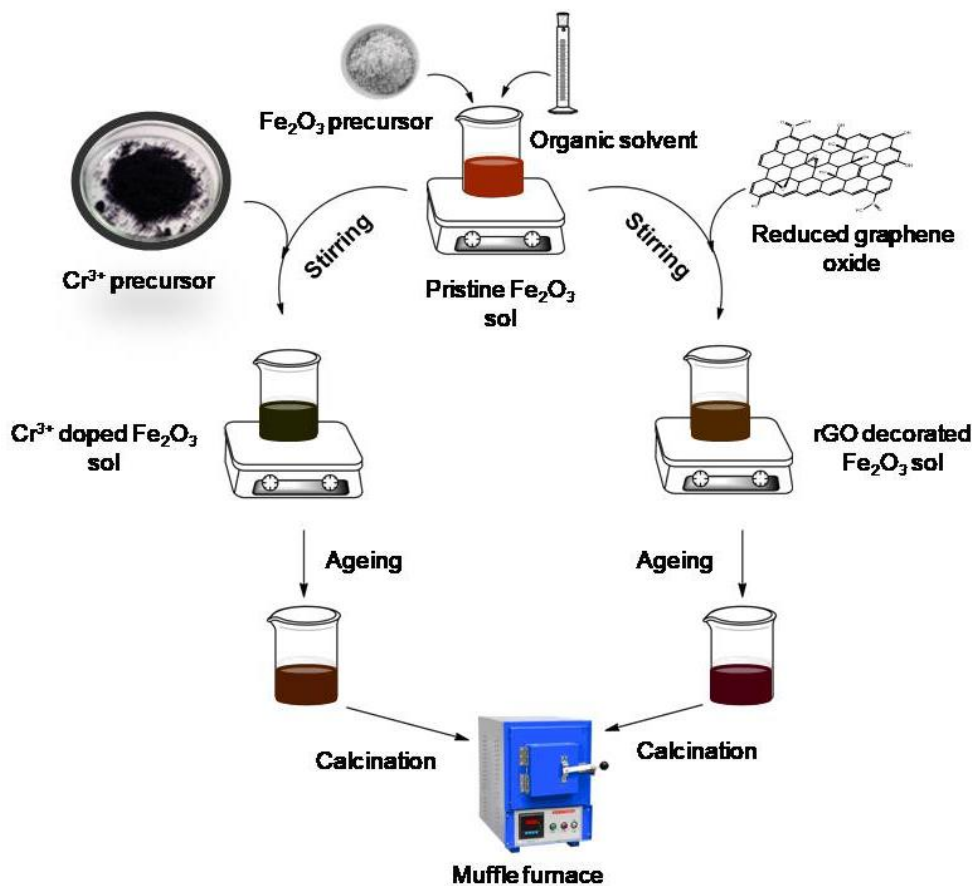


Figure-5.1: Schematic presentation of nanocomposites synthesis

### 5.3. Results and discussions:

#### 5.3.1. Characterization of nanocomposites:

Both pristine and  $\text{Cr}^{3+}$  doped iron oxide samples revealed three step mass loss patterns [15] in the temperature range  $50^\circ\text{C}$  to  $950^\circ\text{C}$  (Fig. 5.2). The initial mass loss of  $\sim 6.5\%$  upto  $\sim 155^\circ\text{C}$  in pristine sample was due to removal of solvent molecules and water contents present there, whereas, for  $\text{Cr}^{3+}$  doped sample it was  $\sim 9\%$  upto  $\sim 210^\circ\text{C}$ .

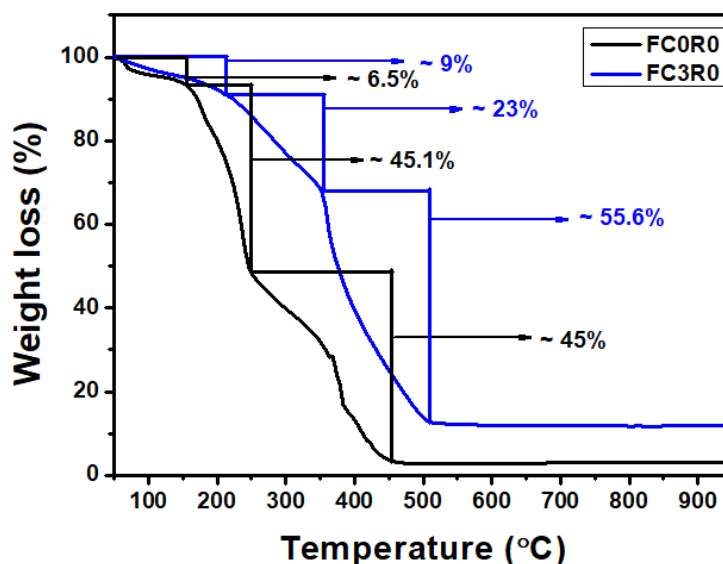


Figure-5.2.: TGA plot of pristine  $\text{Fe}_2\text{O}_3$  (FC0R0) and  $\text{Cr}^{3+}$  doped  $\text{Fe}_2\text{O}_3$  (FC3R0) samples

In the next step the pristine sample showed a sharp mass loss  $\sim 45.1\%$  in the temperature range  $155^\circ\text{C}$  to  $250^\circ\text{C}$ , attributed to the removal of binder molecules used during synthesis process. In  $\text{Cr}^{3+}$  doped sample the second step mass loss of  $\sim 23\%$  at a temperature  $210^\circ\text{C}$  to  $350^\circ\text{C}$  for the similar reason. At the final stage, the pristine sample exhibited a mass loss of  $\sim 45\%$  at  $250^\circ\text{C}$  to  $450^\circ\text{C}$ , and here  $\text{Cr}^{3+}$  doped sample showed a sharp mass loss of  $\sim 55\%$  in the temperature range  $350^\circ\text{C}$  to  $500^\circ\text{C}$  might be correlated to the nanocomposite formation. Henceforth, the calcination temperature of the samples was determined  $\sim 550^\circ\text{C}$  to ensure complete metal oxide formation.

The XRD pattern of pristine  $\text{Fe}_2\text{O}_3$  nanoparticles resembled to the hexagonal lattice structure with R3c space group (JCPDS card no.: 33-0664). The diffraction peaks were indexed accordingly in Fig. 5.3a [16, 17]. The relatively higher intensity of (104) plane indicated predominant crystal growth along that plane. The high intensity peaks indicated the high

crystallinity of the as-synthesized nanomaterials. The introduction of dopant  $\text{Cr}^{3+}$  ion in pristine  $\text{Fe}_2\text{O}_3$  lattice showed hardly any significant alteration in the XRD pattern, perhaps due to small addition concentration (Fig. 5.3a). However, a minor broadening of the diffraction peaks was observed and the extent of broadening was increased with the dopant concentration (Fig. 5.3d). Actually, the ionic radii of  $\text{Fe}^{3+}$  (0.64 Å) and  $\text{Cr}^{3+}$  (0.62 Å) ions are almost similar and therefore substitution of  $\text{Fe}^{3+}$  by  $\text{Cr}^{3+}$  from some the inherent lattice sites imparted marginal effect in the lattice orientation, which was clearly evident from the XRD patterns.

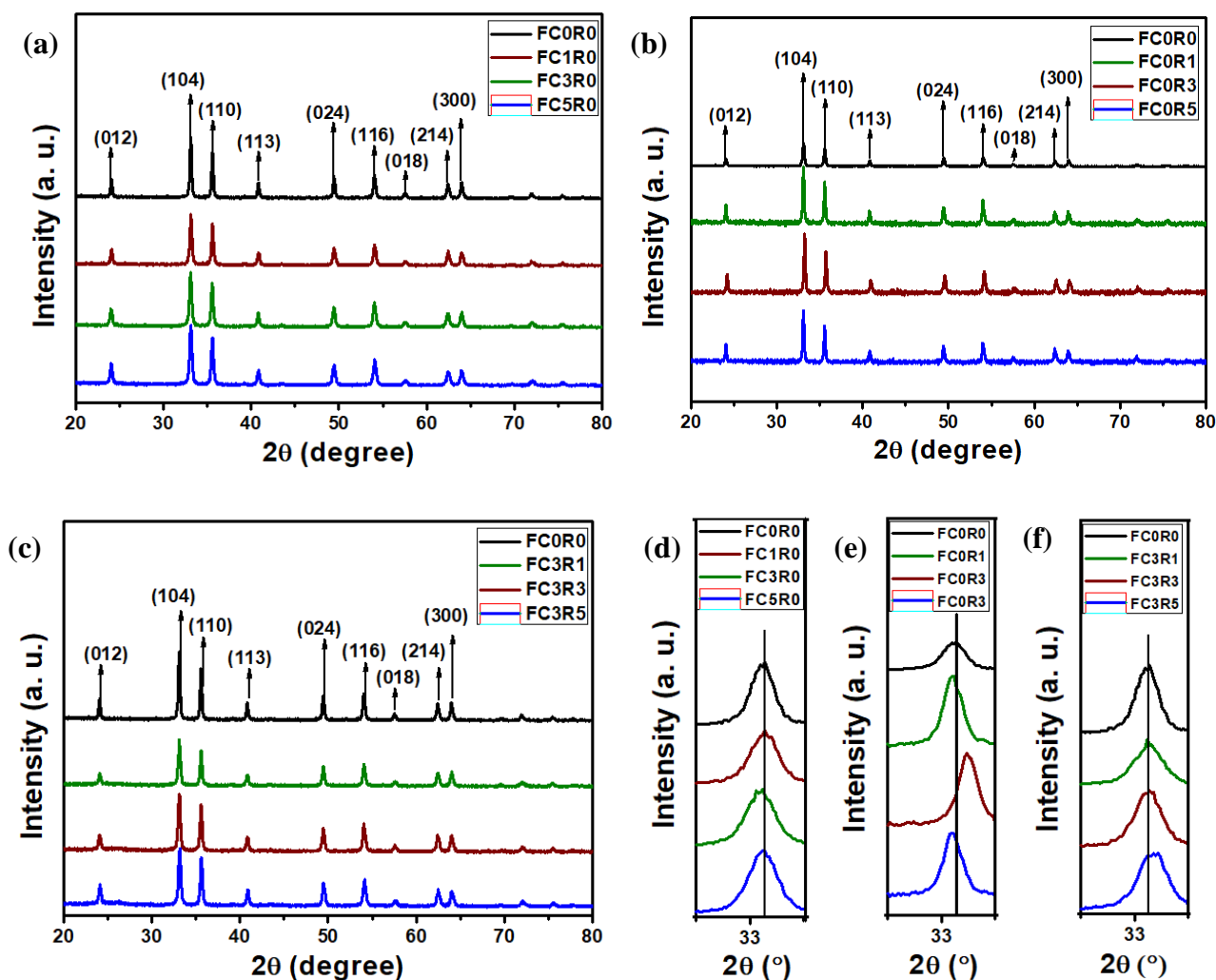


Figure-5.3: XRD spectra of (a)  $\text{Cr}^{3+}$  doped  $\text{Fe}_2\text{O}_3$  nanomaterials, (b) rGO decorated  $\text{Fe}_2\text{O}_3$  nanocomposites, and (c) rGO decorated FC3 nanocomposites, magnified (104) peak of (d)  $\text{Cr}^{3+}$  doped  $\text{Fe}_2\text{O}_3$  nanomaterials, (e) rGO decorated  $\text{Fe}_2\text{O}_3$  nanocomposites, (f) rGO decorated FC3 nanocomposites

On the other hand, addition of rGO revealed a marginal shifting of the diffraction peaks (Fig. 5.3e); only the  $\sim 3$  wt% rGO containing sample (FC0R3) showed the shifting of the peak towards higher  $2\theta$  values, whereas other two samples (FC0R1 and FC0R5) exhibited the shifting of the peak to lower  $2\theta$  angles (Fig. 5.3b). It was observed that in presence of a certain concentration of rGO, there would be effective interaction between metal oxide nanoparticles and rGO, beyond which the excess rGO started to segregate in the nanocomposite, also, at a very low addition concentration there would be hardly any significant interaction. Shifting of peaks towards higher diffraction angle associated with decrease in d-spacing and vice-versa. In  $\text{Cr}^{3+}$  doped  $\text{Fe}_2\text{O}_3$ -rGO nanocomposites (Fig. 5.3c, e), the XRD peaks did not show any shifting of peaks except decrease in peak intensity. After rGO addition in FC3R0 nanomaterial, the crystallinity of the peaks decreased.

The FTIR spectra (Fig. 5.4) revealed the presence of a broad peak beyond  $3000\text{ cm}^{-1}$  attributed to stretching vibration of hydroxyl group and a sharp peak at  $1405\text{ cm}^{-1}$  for  $-\text{OH}$  group bending vibration, due to abundant moistures in environment [18]. The peak at  $1631\text{ cm}^{-1}$  ascribed to the  $-\text{C}=\text{C}-$  stretching vibration. Another two peaks at  $540\text{ cm}^{-1}$  and  $463\text{ cm}^{-1}$  corresponded to Fe-O stretching vibration of metal oxide [19]. The intensity of metal oxide stretching peaks were decreased after  $\text{Cr}^{3+}$  doping might be due to successful substitution of some  $\text{Fe}^{3+}$  ions from their lattice sites.

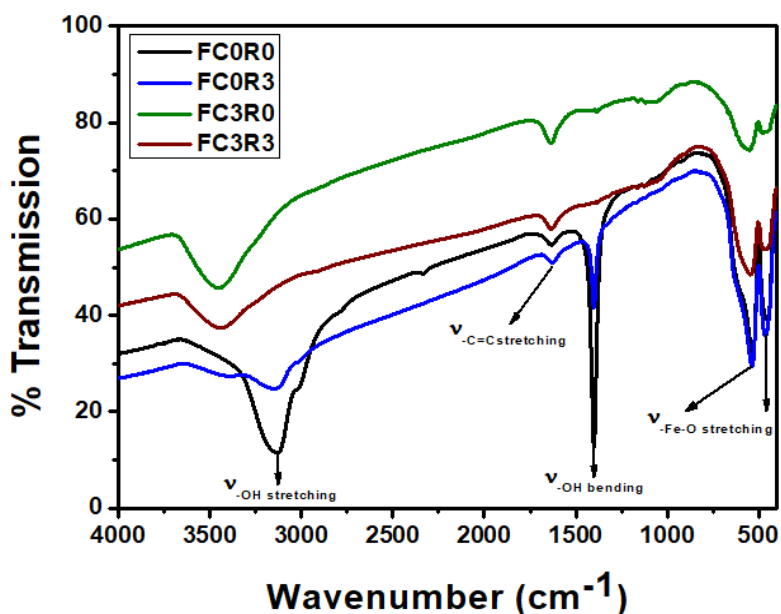


Figure-5.4: FTIR graph of FC0R0, FC3R0, FC0R3, and FC3R3

In the Raman spectra (Fig. 5.5) the peak at  $221\text{ cm}^{-1}$  corresponded to  $A_{1g}$  vibration mode and the other two peaks at  $287\text{ cm}^{-1}$  and  $401\text{ cm}^{-1}$  denoted vibrational  $E_g$  mode of Fe-O bonds [20]. In rGO decorated samples, along with these metal oxide stretching peaks, two characteristic peaks observed at  $1335\text{ cm}^{-1}$  and  $1595\text{ cm}^{-1}$ , designated as D-band and G-band respectively [21]. The D-band originated from  $sp^3$ -C atoms which signified oxidation of graphene moiety and the presence of defect and disorder in the lattice, whereas the G-band symbolized the existence of  $sp^2$ -C atoms. Their intensity ratio ( $I_D/I_G$ ) was  $\sim 1.47$  for FC0R3, which was decreased in FC3R3 to  $\sim 1.07$ . Intensity ratio greater than 1 indicated the presence of defect-rich rGO moieties in the nanocomposites.

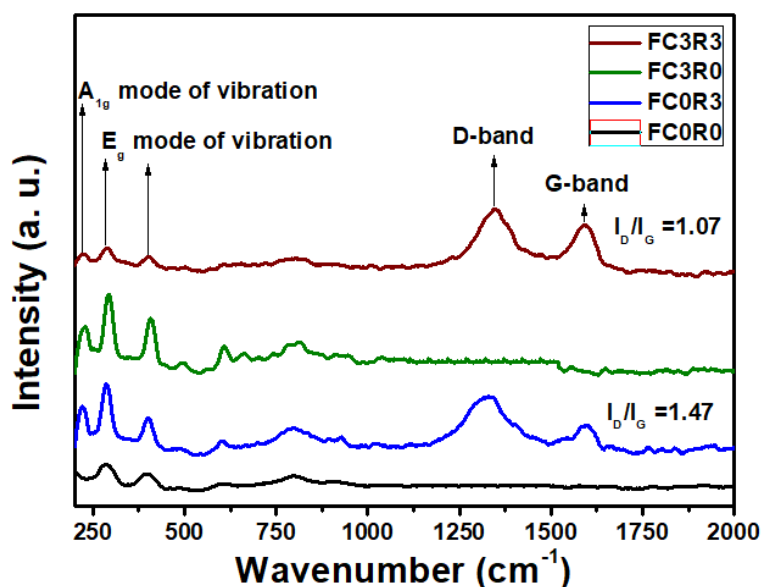


Figure-5.5: Raman spectra of FC0R0, FC3R0, FC0R3, and FC3R3

The Brunauer-Emmett-Teller (BET) surface area of synthesized nanomaterials was calculated from the acquired multi-point BET plot (Fig. 5.6a) using the equations mentioned in Chapter 2 (Section 2.4.5). The calculated specific surface area of pristine  $Fe_2O_3$  was  $\sim 14.208\text{ m}^2/\text{g}$ , which was enhanced to  $\sim 19.338\text{ m}^2/\text{g}$  after  $Cr^{3+}$  doping as obtained from FC3R0 sample. Interestingly, after incorporation of rGO in both pristine and  $Cr^{3+}$  doped  $Fe_2O_3$ , the surface area was significantly increased by virtue of the 2D planar architecture of rGO. The surface area of FC0R3 sample was  $\sim 31.101\text{ m}^2/\text{g}$  and for FC3R3 sample it was increased to  $\sim 50.862\text{ m}^2/\text{g}$ . It was evident that the enhancement of surface area after addition of rGO expected to improve the

gas sensing response [22, 23]. Additionally, for rGO containing samples  $N_2$  adsorption-desorption curves were obtained (Fig. 5.6b). Both the sorption isotherms presented a sharp capillary uptake at low  $P/P_0$ , followed by a steady increase in  $N_2$  uptake at a higher  $P/P_0$  region. At higher partial pressure, presence of pronounced hysteresis (type IV isotherm) suggested the microporous nature of samples [24]. The prominent hysteresis property of  $N_2$  sorption curve of FC3R3 sample compared to FC0R3 sample justified the increased surface area of former sample.

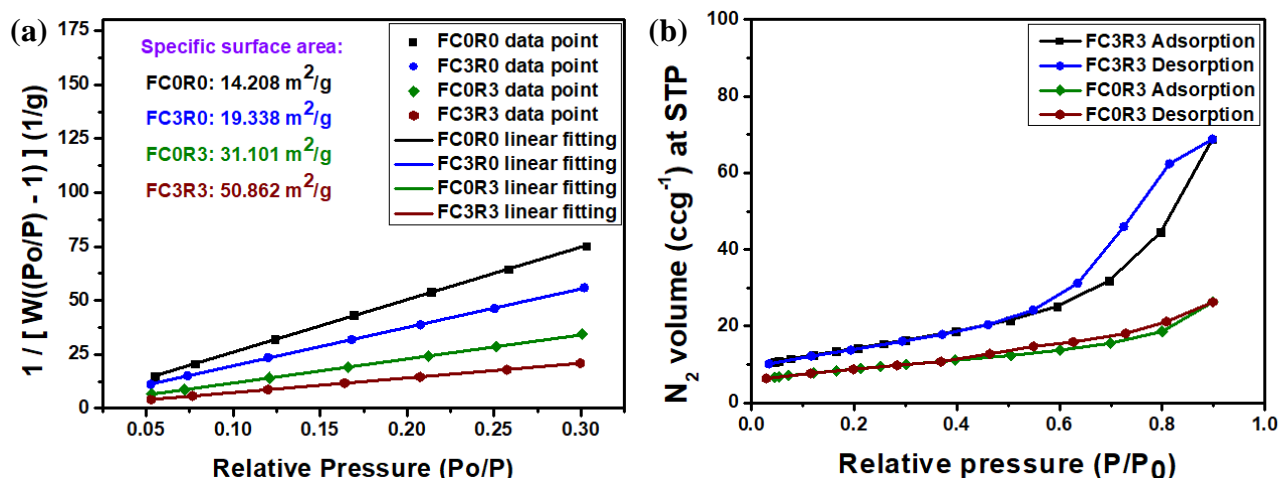
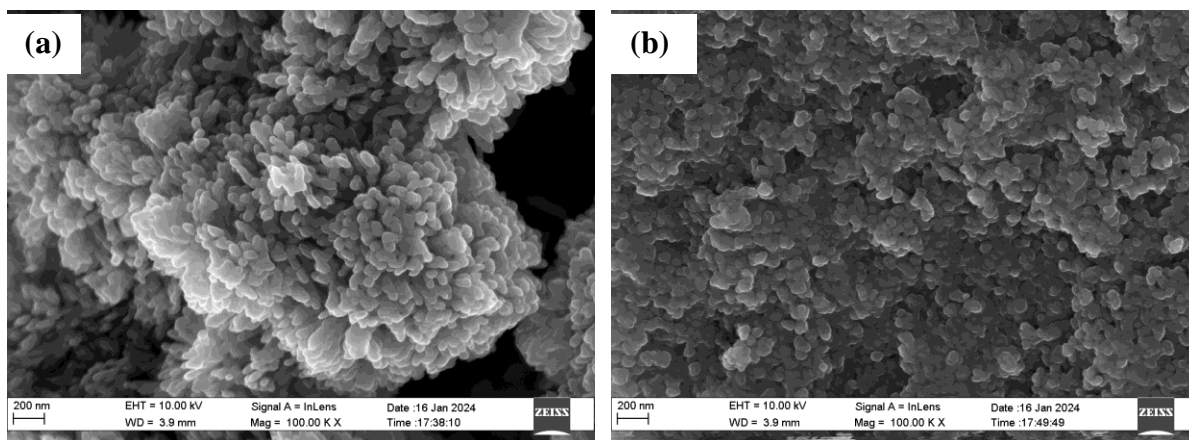


Figure-5.6: (a) Multi-point BET plots, (b) BET  $N_2$  sorption isotherm of FC0R3 and FC3R3

The morphological ideas about the as-synthesized nanomaterials were collected from FESEM images. The FC0R0 showed closely packed assembly of small elongated type of particles (Fig. 5.7a). After  $Cr^{3+}$  doping, in FC3R0 sample (Fig. 5.7b) there observed a prominent change of particle morphology; the elongated particles converted to ovoid shaped particles.





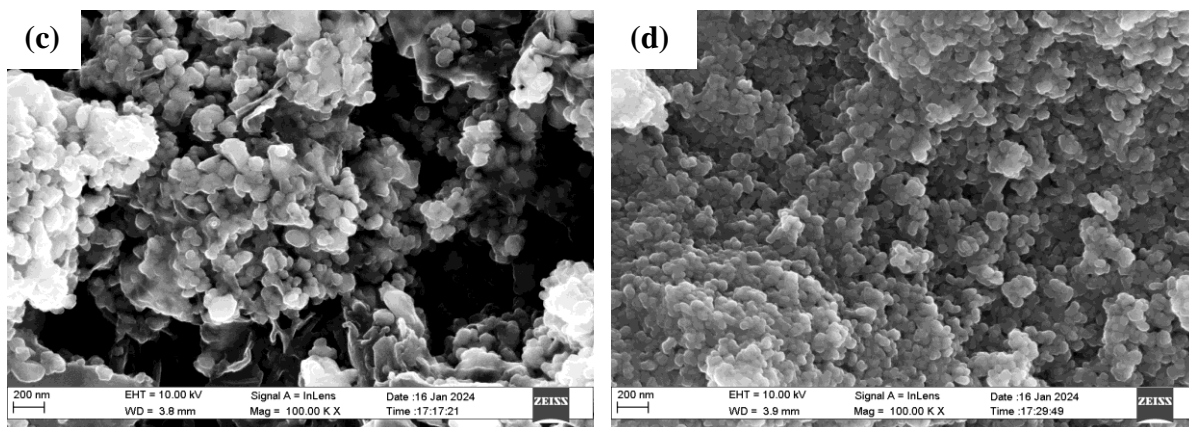
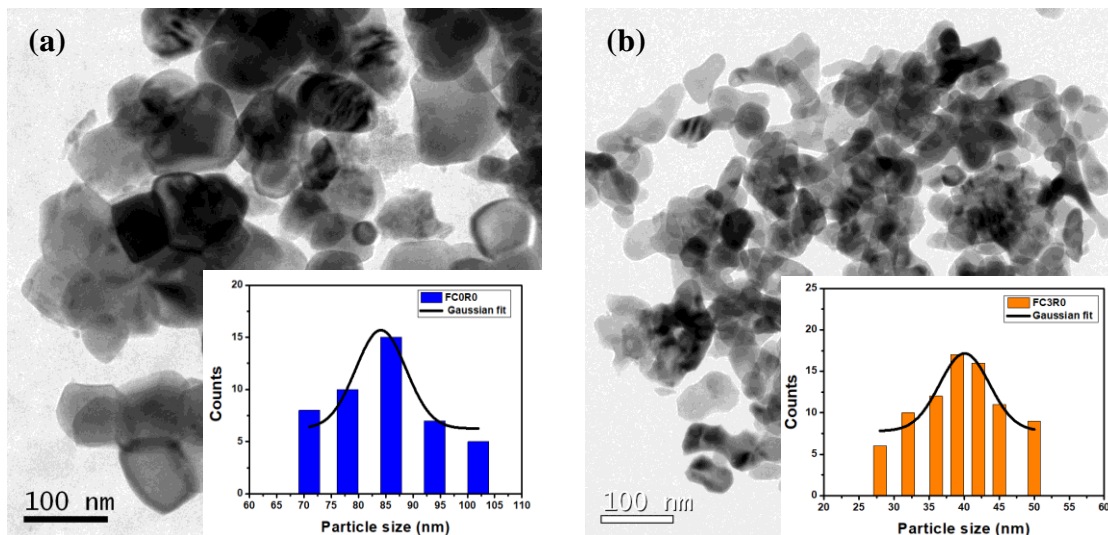


Figure-5.7: FESEM micrographs (a) FC0R0, (b) FC3R0, (c) FC0R3 and (d) FC3R3

The particles were agglomerated due to existing Van der Waals force of attraction between them. On the other hand, rGO incorporated FC0R3 exhibited (Fig. 5.7c) distributed  $\text{Fe}_2\text{O}_3$  nanoparticles over ultrafine rGO layers and that somehow reduced the agglomeration between the nanoparticles. Addition of rGO in FC3R0 nanomaterial (FC3R3) revealed hardly any distinguishable change in particles morphology (Fig. 5.7d).

The bright field TEM image of pristine  $\text{Fe}_2\text{O}_3$  (Fig. 5.8a) showed spherical particle-like morphology present in the agglomerated form due to Van der Waal's force of attraction [25, 26]. Functionalization of pristine  $\text{Fe}_2\text{O}_3$  lattice, either by  $\text{Cr}^{3+}$  doping (Fig. 5.8b) or addition of rGO (Fig. 5.8 c, d) resulted into a more dispersed particles distribution. In rGO decorated samples the nanoparticles were distributed on the thin rGO layer.



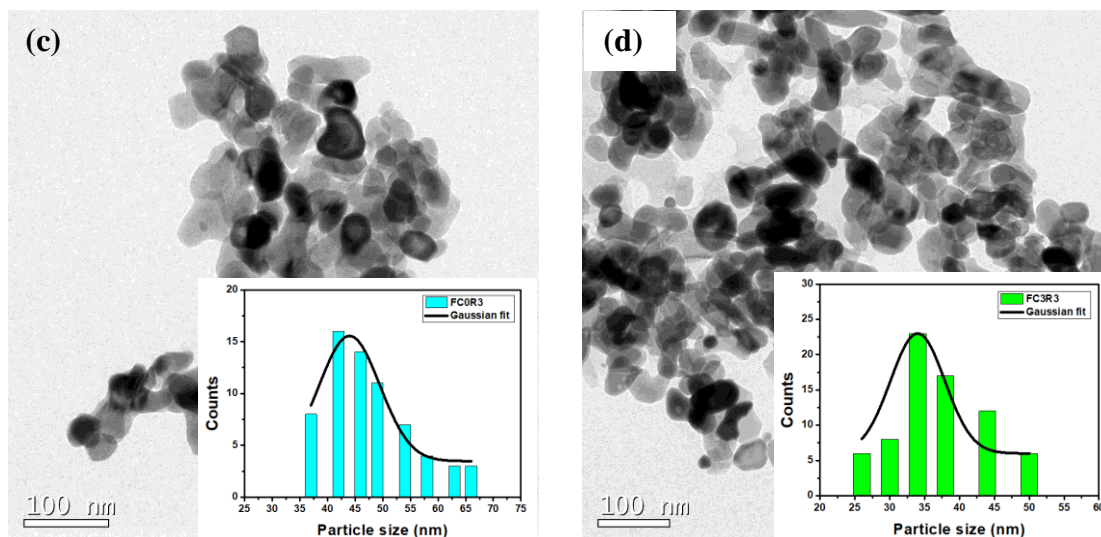
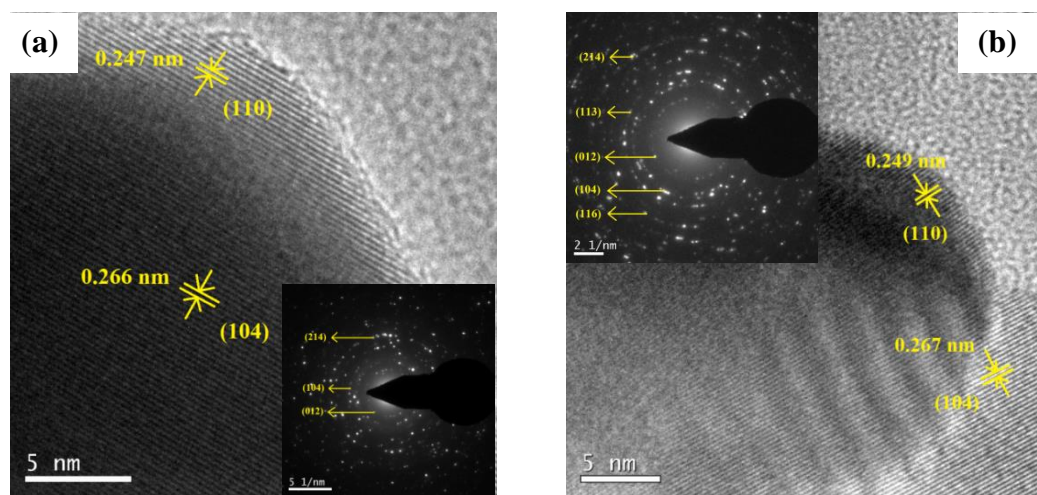


Figure-5.8: BFTEM images (corresponding particle size distribution in inset) of (a) FC0R0, (b) FC3R0, (c) FC0R3, and (d) FC3R3

Average particle size distribution revealed that pristine  $\text{Fe}_2\text{O}_3$  has a larger particle size ( $\sim 85$  nm) which was reduced upon functionalization. The FC3R0 ( $\sim 39$  nm), FC0R3 ( $\sim 42$  nm), and FC3R3 ( $\sim 34$  nm) samples showed almost similar average particle size distribution. The HRTEM images of all the synthesized nanomaterials exhibited the presence of predominant lattice fringes corresponded to (104) and (110) lattice planes of  $\text{Fe}_2\text{O}_3$  (Fig. 5.9 a-d), no other fringes corresponded to  $\text{Cr}^{3+}$  or rGO was found due to relatively low concentration. Similarly the SAED pattern (in the inset of corresponding HRTEM images) showed the diffraction plane (012), (104), (113), (116), and (214) of  $\text{Fe}_2\text{O}_3$  in all the nanomaterials.



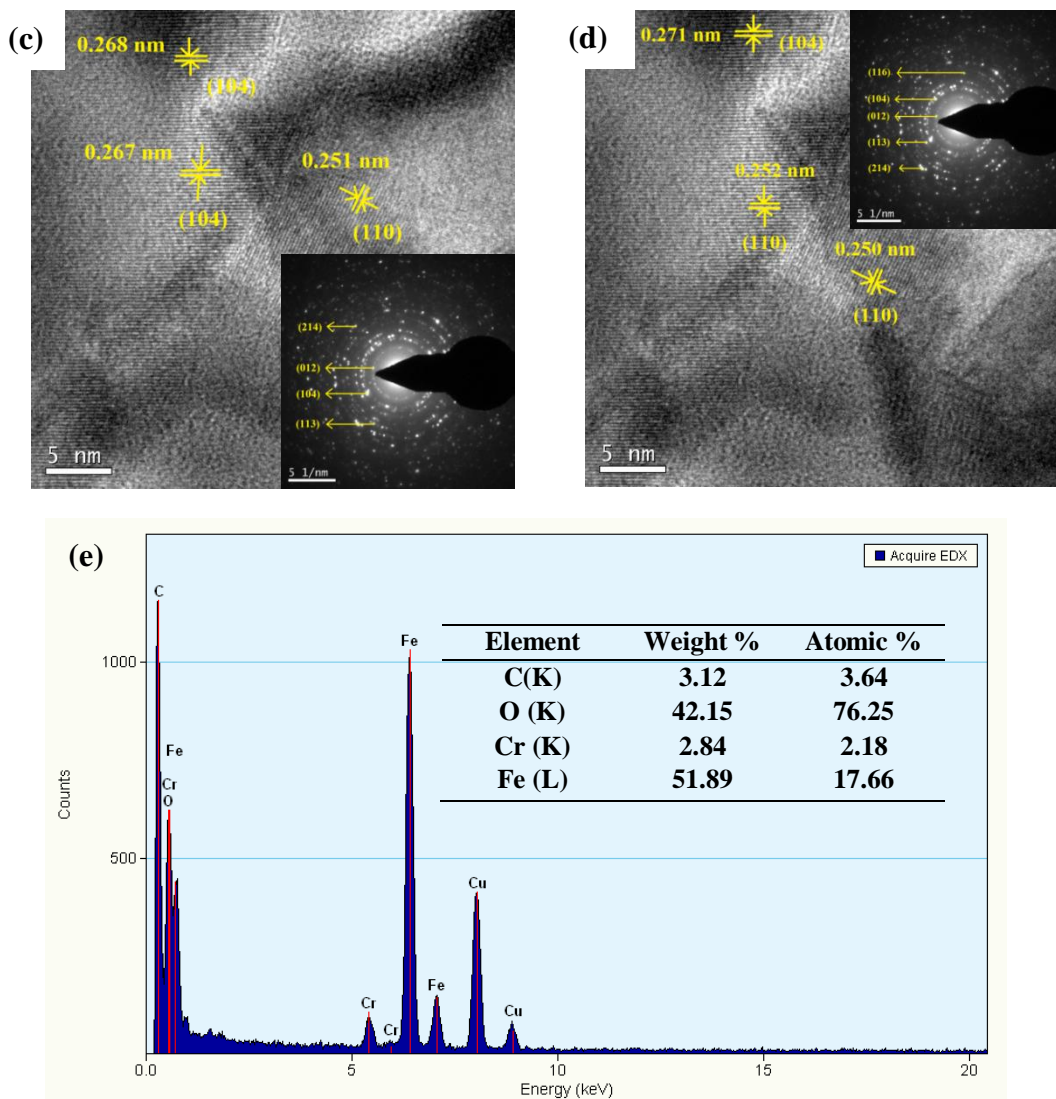


Figure-5.9: HRTEM images (SAED pattern in inset) of (a) FC0R0, (b) FC3R0, (c) FC0R3, and (d) FC3R3, (e) EDX of FC3R3 (inset quantitative analysis)

The EDS spectrum of FC0R3 (Fig. 5.9e) revealed the presence of Fe, O, and C in the sample, whereas additional Cr signal was obtained for FC3R3 sample, impurity peak of Cu originated from the sample mounted grid.

The surface chemical composition and the chemical binding state of the corresponding elements were determined by XPS analysis. The full scan survey analysis of pristine Fe<sub>2</sub>O<sub>3</sub> (FC0R0, Fig. 5.10a) revealed the presence of Fe and O only, whereas along with those two peaks, additional Cr peak was detected in Cr<sup>3+</sup> doped Fe<sub>2</sub>O<sub>3</sub> (FC3R0, Fig. 5.10b), C peak detected in rGO

decorated  $\text{Fe}_2\text{O}_3$  (FC0R3, Fig. 5.10c), and both Cr and C peaks were obtained in rGO decorated  $\text{Cr}^{3+}$  doped  $\text{Fe}_2\text{O}_3$  (FC3R3, Fig. 5.10d).

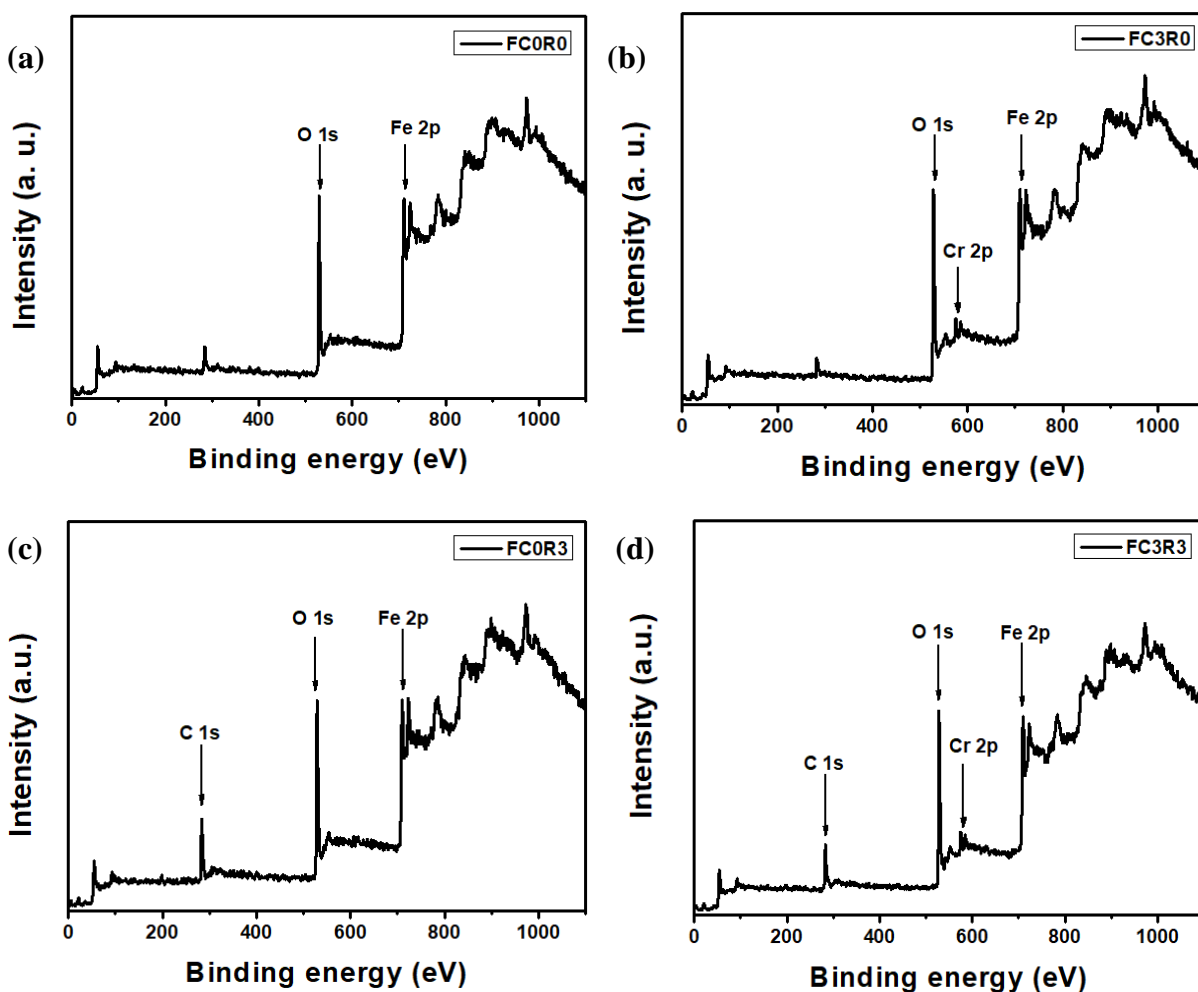


Figure-5.10: XPS full scan spectrum (a) FC0R0, (b) FC3R0, (c) FC0R3, and (d) FC3R3

In FC0R0 sample, the Fe 2p peak deconvolution showed a doublet at 709.71 eV and 723.39 eV for Fe  $2p_{3/2}$  and Fe  $2p_{1/2}$  [27, 28] respectively (Fig. 5.11a). The corresponding satellite peak of Fe  $2p_{3/2}$  was observed at 714.59 eV. These peak positions indicated the +3 oxidation state of Fe. Afterwards, it was observed that, on functionalization of pristine  $\text{Fe}_2\text{O}_3$  (FC0R0), the binding energies of the peaks were shifted to lower binding energies due to generation of distortion in ordered pristine lattice. In  $\text{Cr}^{3+}$ -doped sample (FC3R0) showed the shifting of Fe 2p doublet to 708.82 eV and 722.24 eV marked as Fe  $2p_{3/2}$  and Fe  $2p_{1/2}$  accordingly, whereas the satellite peak



moved to the higher binding energy at 716.93 eV (Fig. 5.11b). On the other hand, after rGO incorporation in  $\text{Fe}_2\text{O}_3$  (FC0R3) the XPS peaks were less shifted towards lower binding than  $\text{Cr}^{3+}$  doped sample as the Van der Waal's type of interaction between  $\text{Fe}_2\text{O}_3$  and rGO created comparatively lesser perturbation in the pristine lattice. The deconvolution revealed Fe  $2p_{3/2}$  peak at 708.93 eV with the satellite peak at 714.63 eV and the Fe  $2p_{1/2}$  peak at 722.55 eV (Fig. 5.11c). The FC3R3 sample showed maximum shifting of peaks towards lower binding energy. The peaks corresponded to two spin states of Fe 2p located at 708.67 eV (Fe  $2p_{3/2}$ ) and 722.14 eV ( $2p_{1/2}$ ) with the satellite peak at 714.40 eV (Fig. 5.11d).

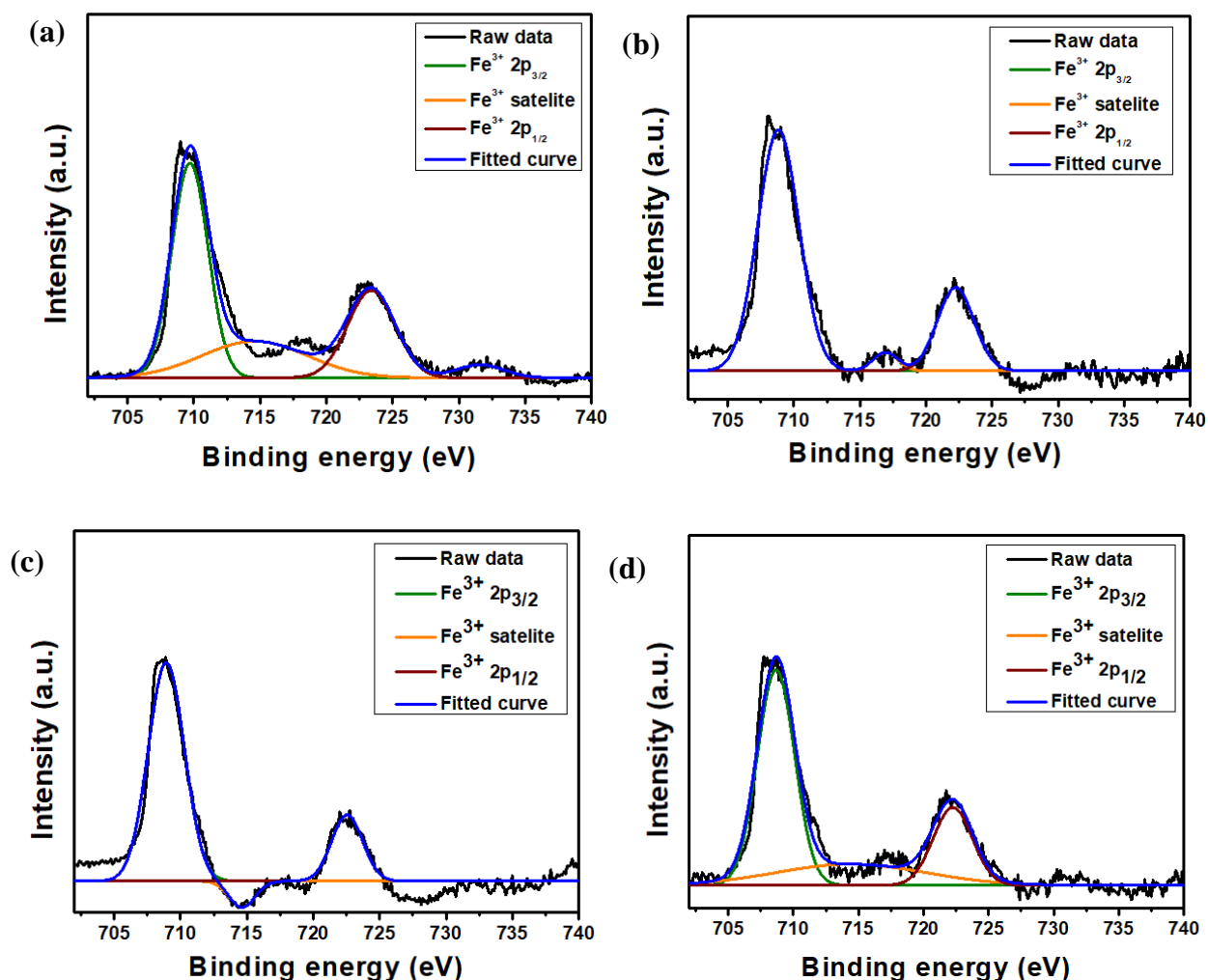
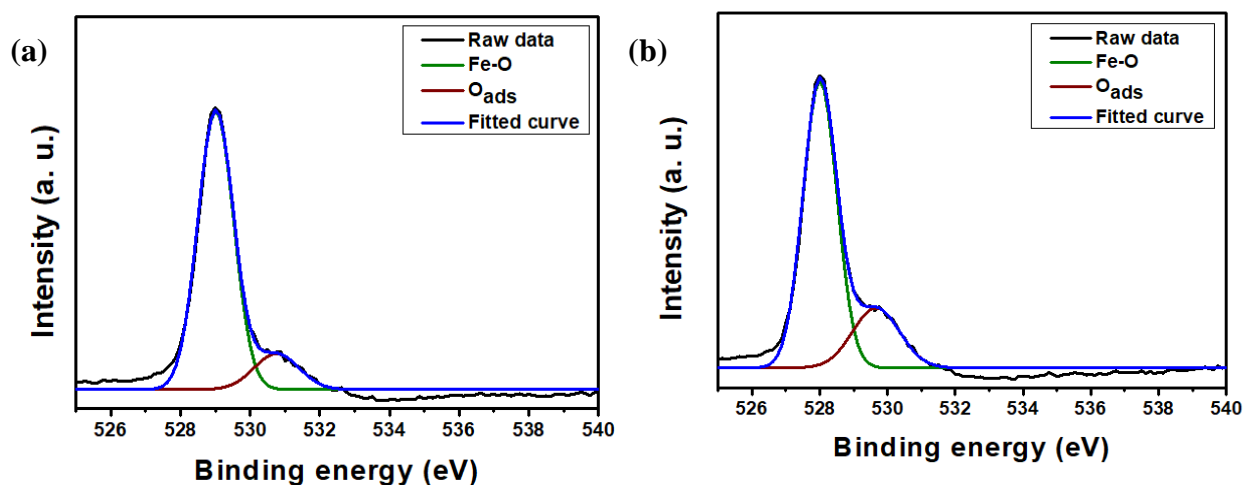


Figure-5.11: Core level analysis of Fe 2p (a) FC0R0, (b) FC3R0, (c) FC0R3, and (d) FC3R3

The O 1s peak of pristine Fe<sub>2</sub>O<sub>3</sub> (FC0R0) sample was split into two peaks (Fig. 5.12a); one at 529.01 eV corresponded to lattice oxygen bonded to the Fe<sup>3+</sup> ions and the other peak at 530.77 eV signified the chemisorbed oxygenated ions [29, 30]. In Cr<sup>3+</sup> doped sample (FC3R0), the O 1s core level spectra showed a doublet; one peak at 528 eV for Fe-O bond and other peak for chemisorbed oxygen at 529.66 eV (Fig. 5.12b). From O 1s spectrum of rGO incorporated Fe<sub>2</sub>O<sub>3</sub> (FC0R3), one peak for metal-oxygen bond was at 528.24 eV and the peak at 529.41 eV assigned as adsorbed oxygen (Fig. 5.12c). For Cr<sup>3+</sup> doped rGO incorporated Fe<sub>2</sub>O<sub>3</sub> (FC3R3), the O1s signal for lattice oxygen was obtained at 527.83 eV and that of surface bonded oxygen ions was at 529.40 eV (Fig. 5.12d). The area under the curve of O 1s peaks of different samples was analyzed to rationalize the effect of pristine lattice functionalization on gas sensing (Table 5.1). It was evident that, in FC0R0 sample highest percentage of lattice oxygen observed as compared to least amount of chemisorbed oxygen as small amount of oxygen adsorbed on the ordered lattice structure due to limited active sites on the surface.

Table-5.1: Analysis of area under the curve of XPS O 1s spectra:

Sample	O 1s peak deconvolution	
	Lattice oxygen	Chemisorbed oxygen
FC0R0	86.16%	13.83%
FC3R0	77.59%	22.40%
FC0R3	38.93%	61.06%
FC3R3	70.32%	29.67%



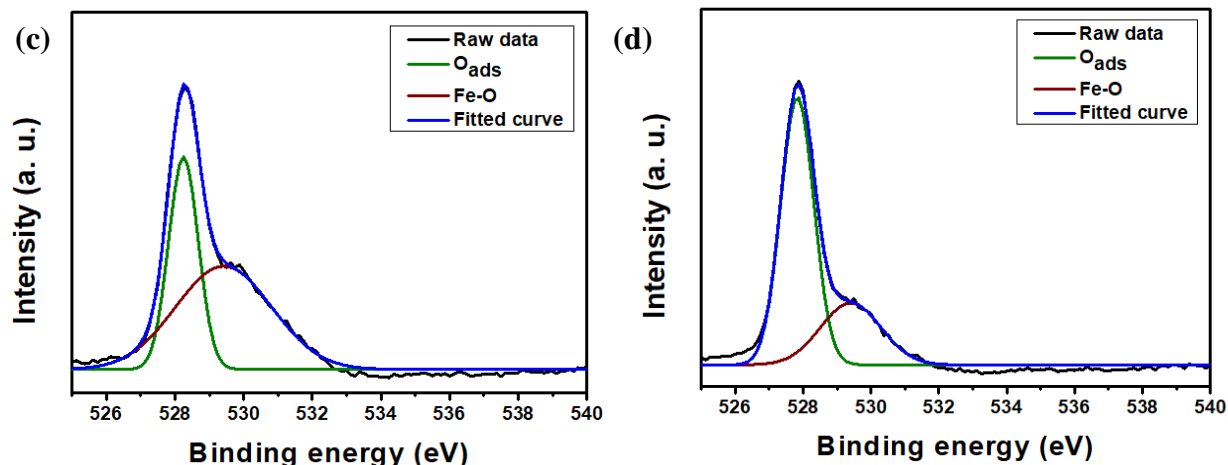
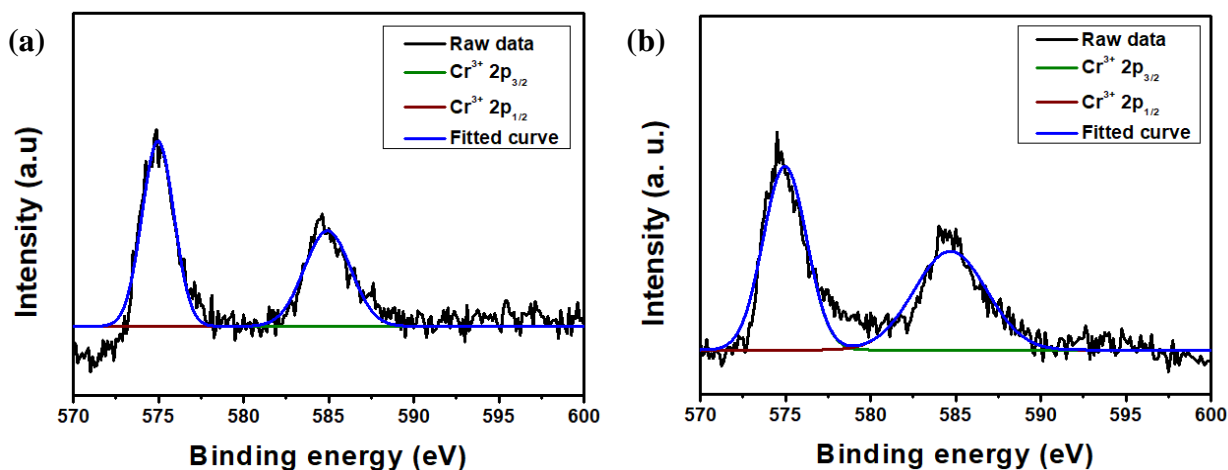


Figure-5.12: Core level analysis of O 1s (a) FC0R0, (b) FC3R0, (c) FC0R3, and (d) FC3R3

Upon functionalization of pristine  $\text{Fe}_2\text{O}_3$  with  $\text{Cr}^{3+}$  and rGO, the lattice oxygen decreased with an increase in chemisorbed oxygen percentage. The presence of maximum chemisorbed oxygen was observed in the FC0R3 sample by virtue of profuse amount of available active sites on rGO surface. Thus, it would be inferred that increase in chemisorbed oxygen was primarily responsible for improved sensing performance. The Cr 2p peak deconvolution of FC3R0 exhibited two peaks: at 574.98 eV for Cr  $2p_{3/2}$  and 584.92 eV for Cr  $2p_{1/2}$  (Fig. 5.13a). The spin-orbit splitting energy of  $\sim 9.94$  eV indicated +3 oxidation state of Cr dopant ion [31]. On the other hand, Cr 2p peaks in FC3R3 was observed at 574.96 eV and 584.68 eV designated as Cr  $2p_{3/2}$  and Cr  $2p_{1/2}$  respectively (Fig. 5.13b), also the spin orbit splitting was slightly decreased to 9.72 eV.



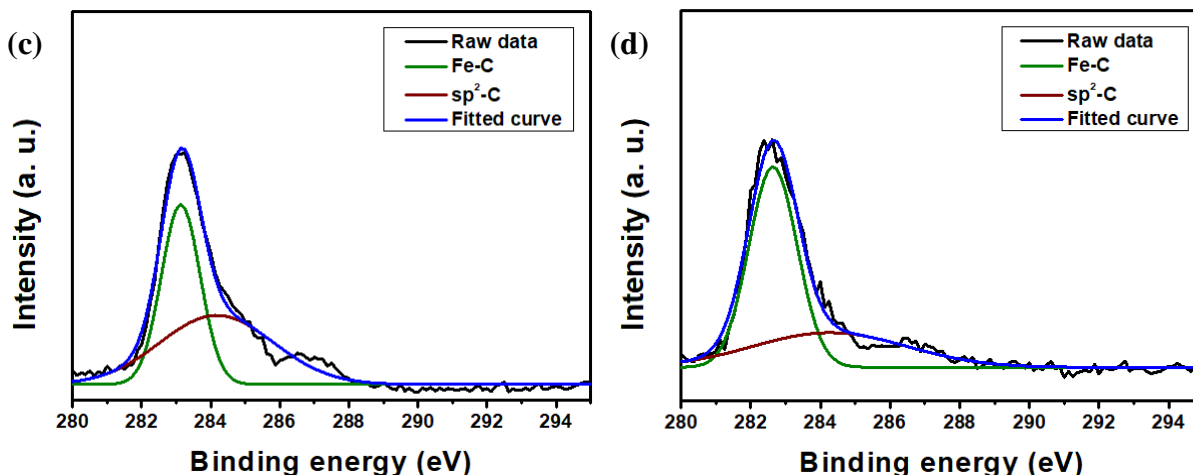


Figure-5.13: Core level analysis Cr 2p (a) FC3R0, (b) FC3R3, and C 1s of (c) FC0R3, (d) FC3R3

The marginal decrease in spin-orbit coupling value was might be due to different atomic environment around the dopant  $\text{Cr}^{3+}$  ion for the presence of rGO in FC3R3. The C 1s peak in FC0R3 obtained from rGO deconvoluted to two peaks corresponded to two different carbon atoms; the metal-carbon binding peak at 283.13 eV and the peak for  $\text{sp}^2$ -C bond (graphitic-type carbon) was observed at 284.1 eV (Fig. 5.13c) [32]. In FC3R3, the C 1s peak for Fe-C positioned at 282.64 eV and the graphitic-type  $\text{sp}^2$ -C peak was at 284.26 eV (Fig. 5.13d).

UV-visible spectroscopy was performed to analyze the optical properties of the nanomaterials. The absorption peak (Fig. 5.14a) of the pristine  $\text{Fe}_2\text{O}_3$  was obtained at 261.1 nm which was red shifted to 262.7 nm after  $\text{Cr}^{3+}$  doping in FC3R0 and to 263.3 nm after decoration with rGO in FC0R3. Significantly, in FC3R3 the absorption peak was red shifted to 267.1 nm as compared to pristine sample. From this absorbance curves the optical band gap of the samples was determined using the Tauc equation [33]. The terms were having usual meaning as mentioned earlier in the works of literature. The order of transition  $n$  for  $\text{Fe}_2\text{O}_3$  is 2, due to direct allowed transition. The calculated band gap value for pristine sample (FC0R0) was  $\sim 4.61$  eV (Fig. 5.14b) and it was decreased to  $\sim 4.60$  eV in FC3R0 (Fig. 5.14c) and to  $\sim 4.59$  eV in FC0R3 (Fig. 5.14d). The least band gap was obtained in FC3R3 sample to  $\sim 4.50$  eV (Fig. 5.14e). This reduction in band gap actually imparted a quantum confinement effect by introducing a new impurity level in between valence and conduction band of pristine sample. This in turn facilitated the mobilization of electrons through the grains during gas sensing.



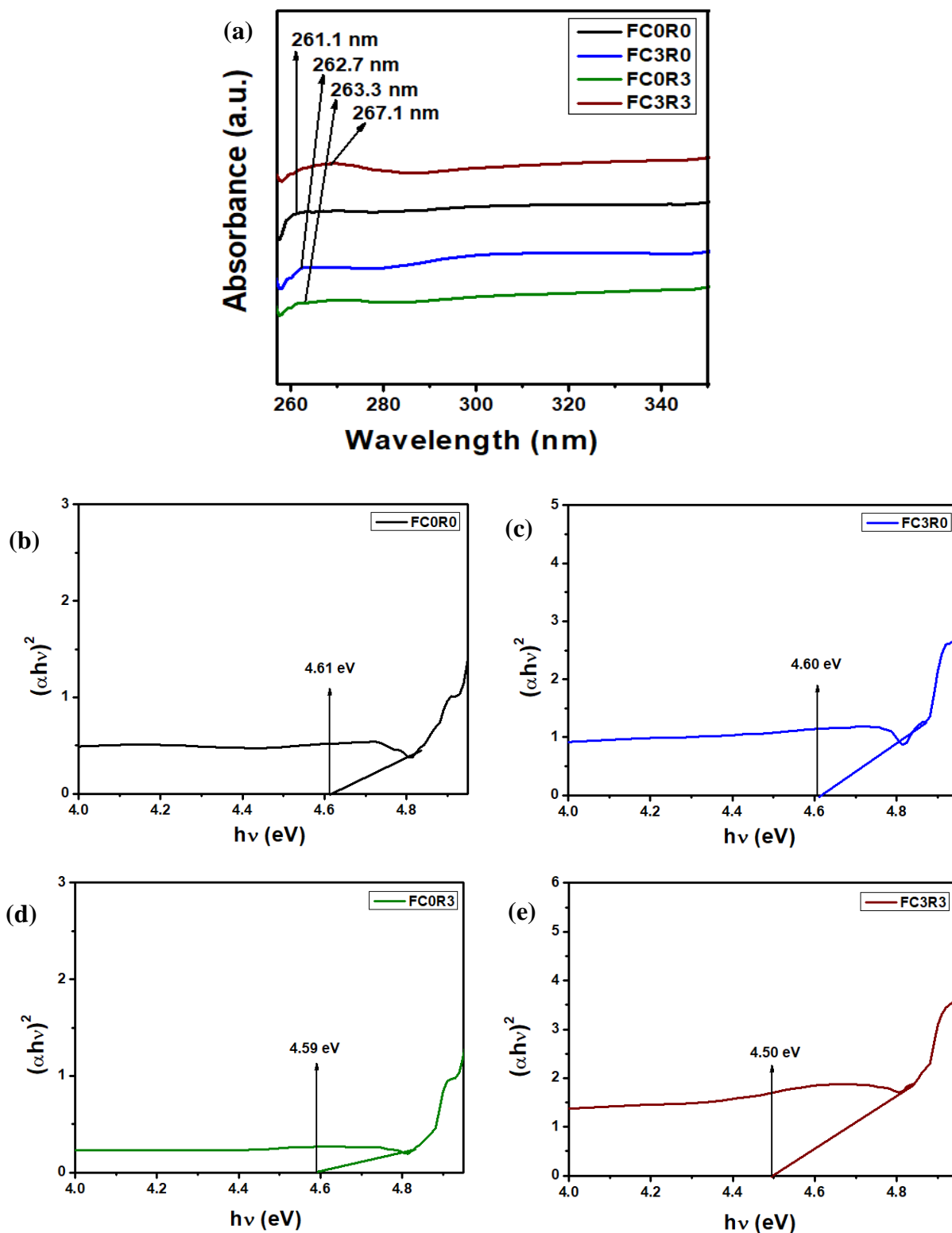


Figure-5.14: (a) UV-Vis spectra of FC0R0, FC3R0, FC0R3, and FC3R3, Tauc plots of (b) FC0R0, (c) FC3R0, (d) FC0R3, and (e) FC3R3

Pristine  $\text{Fe}_2\text{O}_3$  (FC0R0),  $\text{Cr}^{3+}$  doped  $\text{Fe}_2\text{O}_3$  nanomaterial (FC3R0), rGO decorated  $\text{Fe}_2\text{O}_3$  nanocomposite (FC0R3) and  $\text{Cr}^{3+}$  doped rGO decorated  $\text{Fe}_2\text{O}_3$  nanocomposite (FC3R3), all the samples exhibited almost similar spectral pattern on excitation at a wavelength  $\sim 256$  nm. Two significant peaks were observed (Fig. 5.15); near band emission (NBE) peak after 450 nm and deep level emission (DL) peak after 550 nm. The NBE peaks signify the oxygen vacancies whereas DL emission peaks arise from defect sites in the sample. Notably, the intensity of the peaks in rGO incorporated nanocomposites justified the existence of more oxygen vacancies and defect rich nature of the samples. After  $\text{Cr}^{3+}$  doping in  $\text{Fe}_2\text{O}_3$  lattice a slight shifting of DL emission peak towards lower wavelength was observed which might be due to perturbation created in pristine lattice by metal ion doping. The PL peak intensity of the rGO decorated nanocomposites were greater as compared to other nanomaterials, as well as, the DL emission peak of rGO incorporated samples was shifted to a higher wavelength, ensured the presence of defect-rich rGO in the nanocomposites.

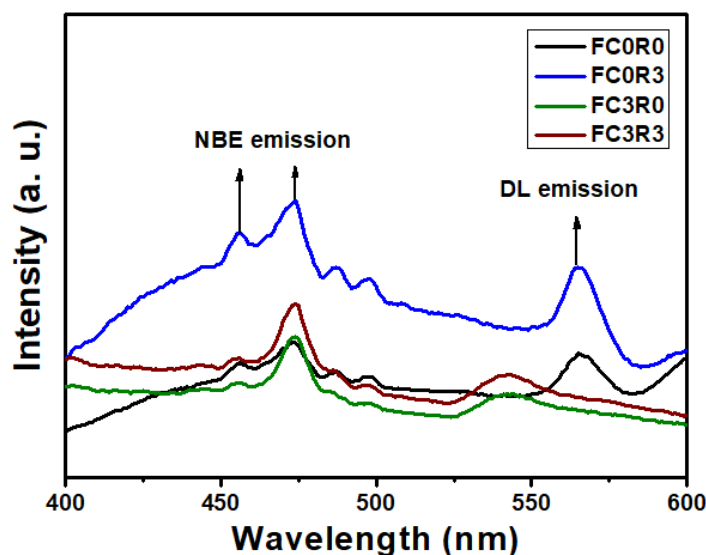


Figure -5.15: PL spectra of pristine FC0R0, FC3R0, FC0R3, and FC3R3

## 5.3.2. Gas sensing performance study:

Taguchi-type sensors were fabricated from the as-synthesized nanomaterials and their operating temperatures were optimized from the measurements of base resistance and sensing response ( $\sim 10$  ppm acetone) in the temperature range  $30^\circ\text{C}$  to  $240^\circ\text{C}$ . Pristine  $\text{Fe}_2\text{O}_3$  based sensor (FC0R0)

showed no measureable resistance till the temperature reached  $\sim 90^\circ\text{C}$  (Fig. 5.16a). After  $\text{Cr}^{3+}$  doping measurable resistance was recorded from  $\sim 60^\circ\text{C}$  (Fig. 5.16b). It was noticed that the resistance of the sensors were gradually decreased with increase in temperature, following the characteristic of semiconductor materials [7]. However, introduction of rGO in the nanomaterials further reduced the operating temperature to the room temperature (Fig. 5.16 c). The obtained sensing responses revealed that for FC0R0 sensor maximum sensing response was obtained at  $\sim 180^\circ\text{C}$  (Fig. 5.16d) whereas for  $\text{Cr}^{3+}$  doped  $\text{Fe}_2\text{O}_3$  based sensors the optimized operating temperature reduced to  $\sim 120^\circ\text{C}$  (Fig. 5.16e) at which maximum sensing response obtained from  $\sim 3$  wt%  $\text{Cr}^{3+}$  doped  $\text{Fe}_2\text{O}_3$  sensor (FC3R0) and at room temperature maximum sensing responses were recorded for FC0R3 and FC3R3 sensors (Fig. 5.16f). All the sensors represented a bell-shape profile of sensing response at varying temperature ranges [31].

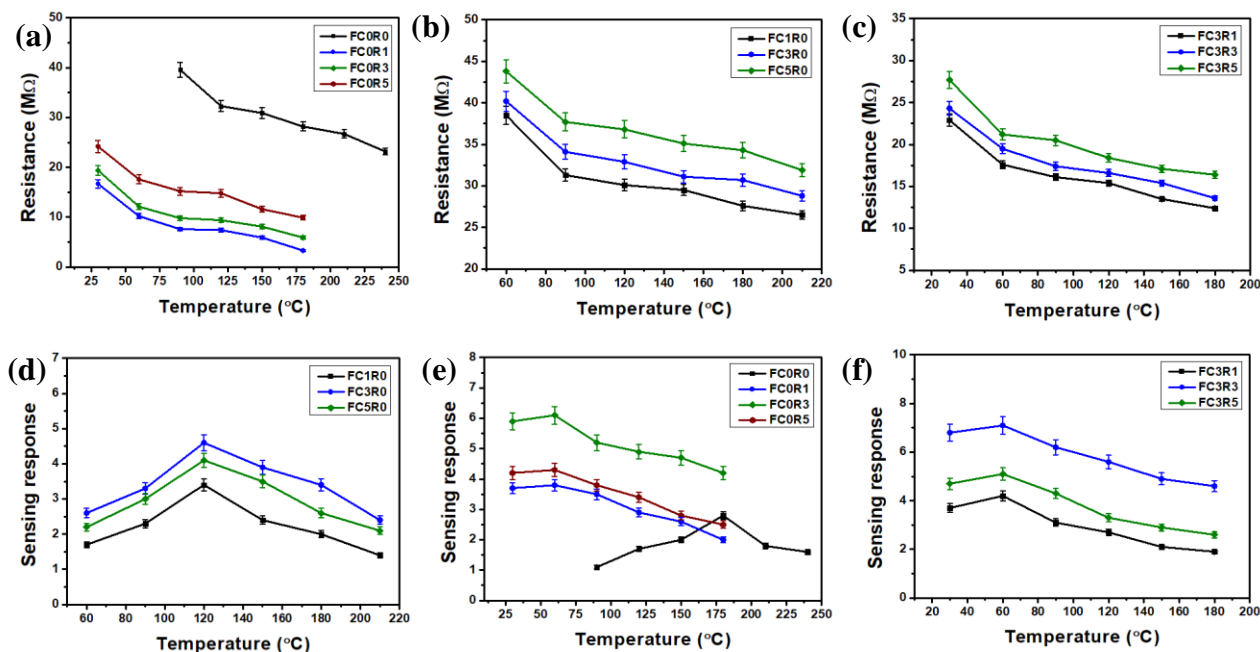
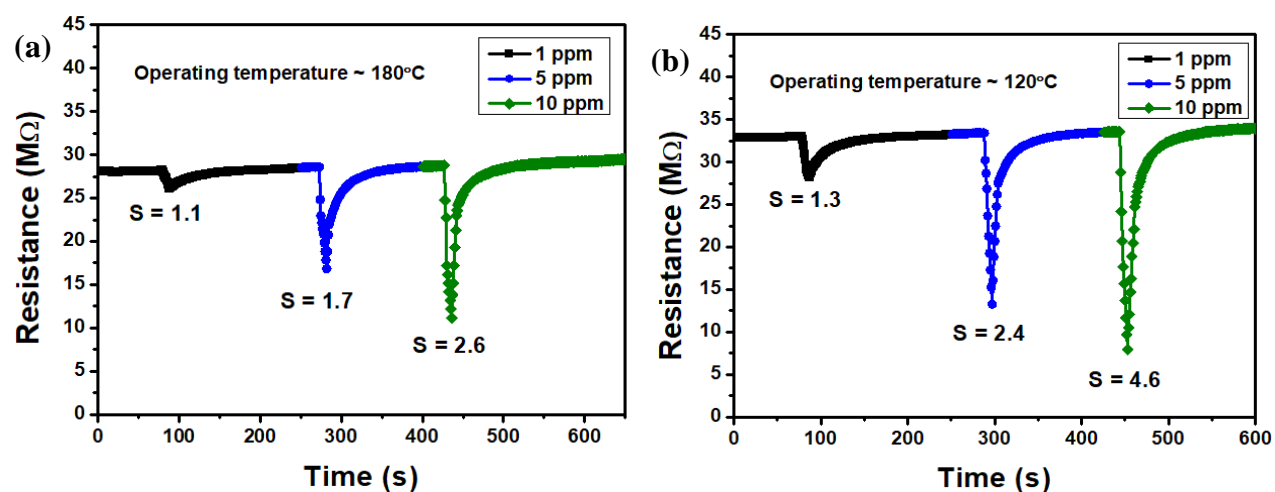


Figure-5.16: Change in resistance (a) Pristine  $\text{Fe}_2\text{O}_3$  and rGO decorated  $\text{Fe}_2\text{O}_3$ , (b)  $\text{Cr}^{3+}$  doped  $\text{Fe}_2\text{O}_3$ , and (c) rGO decorated FC3 sensors, change in sensing response (in presence of  $\sim 10$  ppm acetone) (d) Pristine  $\text{Fe}_2\text{O}_3$  and rGO decorated  $\text{Fe}_2\text{O}_3$ , (e)  $\text{Cr}^{3+}$  doped  $\text{Fe}_2\text{O}_3$ , and (f) rGO decorated FC3 sensors, as a function of temperatures

Increase in rGO concentration beyond this threshold limit perhaps provided an alternative channel for electronic mobilization and thereby the numbers of available charge carriers

decreased. Simultaneously, higher concentration of rGO might hinder the active gas adsorption sites and also resist the interaction between analyte gas and oxygenated ions which eventually reduced the sensing response. Interestingly, the fabricated sensors demonstrated n-type sensing response at an operating temperature greater than  $\sim 60^\circ\text{C}$  (Fig. 5.18 a, b) but at lower temperature a p-type sensing response (Fig. 5.18 c, d) observed. It is well known that, the nature of sensing response primarily depends on the charge carriers' property. Here, at lower temperature, atmospheric oxygen molecules extracted electrons from the conduction band to form oxygenated ions ( $\text{O}_2^-$ ) [34, 35] and due to this, the electrostatic potential of the 'space-charge layer' reduced and holes became the primary charge carrier. At a relatively higher temperature the increased amount of thermal energy generated more number of free electrons and therefore, instead of holes the electrons became the charge carrier. Hence, due to formation of inversion charge layer switching of sensing response from p-type to n-type was observed with increase in temperature. At the respective optimized operating temperature the dynamic sensing response of the sensors were measured by exposing them to different concentrations of acetone ( $\sim 1$ ,  $\sim 5$ , and  $\sim 10$  ppm). The sensing responses were observed to be increased as a function of acetone concentration. The FC0R0 sensor showed maximum response of  $\sim 2.6$  towards  $\sim 10$  ppm acetone at  $\sim 180^\circ\text{C}$  (Fig. 5.17a), which was enhanced to  $\sim 4.6$  to the same concentration of acetone, for FC3R0 sensor at a lower operating temperature of  $\sim 120^\circ\text{C}$  (Fig. 5.17b). The rGO incorporated sensors FC0R3 and FC3R3 showed sensing responses of  $\sim 5.9$  (Fig. 5.17c) and  $\sim 6.8$  respectively, in presence of  $\sim 10$  ppm acetone (Fig. 5.17d), at room temperature.



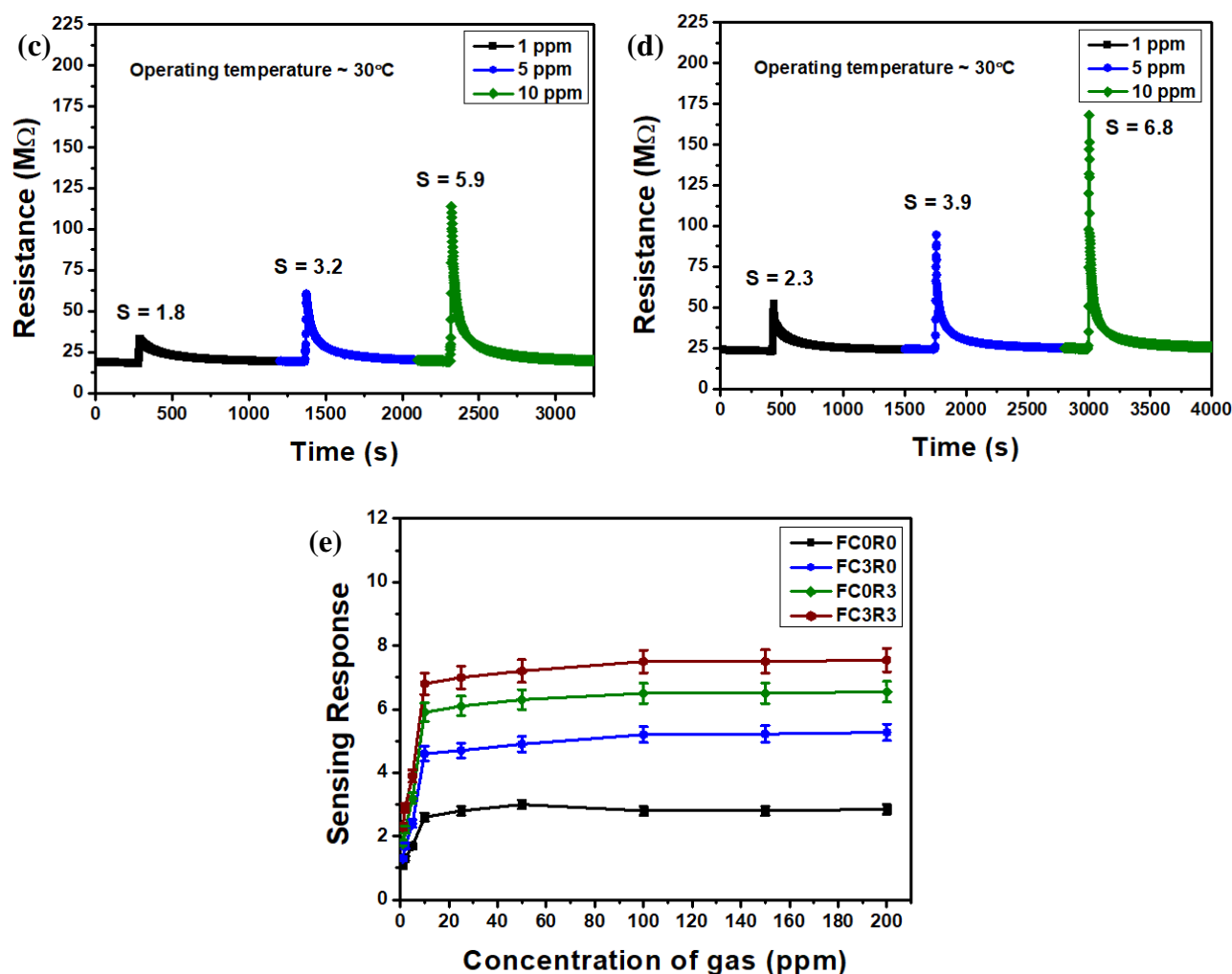


Figure-5.17: Dynamic sensing response in presence of different concentrations of acetone at operating temperature ( $30 \pm 5^\circ\text{C}$ ) (a) FC0R0, (b) FC3R0, (c) FC0R3, and (d) FC3R3, (e) Saturation curve

Table: 5.2: Dynamic sensing response of sensors at their optimized operating temperature:

Concentration of acetone	Sensing response ( $R_g/R_a$ )			
	FC0R0	FC3R0	FC0R3	FC3R3
$\sim 1$ ppm	1.1	1.3	1.8	2.3
$\sim 2$ ppm	1.3	1.7	2.2	2.9
$\sim 5$ ppm	1.7	2.4	3.2	3.9
$\sim 10$ ppm	2.6	4.6	5.9	6.8
$\sim 25$ ppm	2.8	4.7	6.1	7.0
$\sim 50$ ppm	3.0	4.9	6.3	7.2
$\sim 100$ ppm	2.8	5.2	6.5	7.5

The sensing response of the sensors towards other low concentration of acetone at their respective operating temperatures was presented in a tabulated form (Table 5.2). The sensing response was gradually increased upto acetone concentration  $\sim 100$  ppm, beyond that there was no significant enhancement of sensing response, perhaps due to attainment of almost complete occupancy of available active sites, i.e., the sensing response saturated near the acetone concentration  $\sim 100$  ppm (Fig. 5.17e).

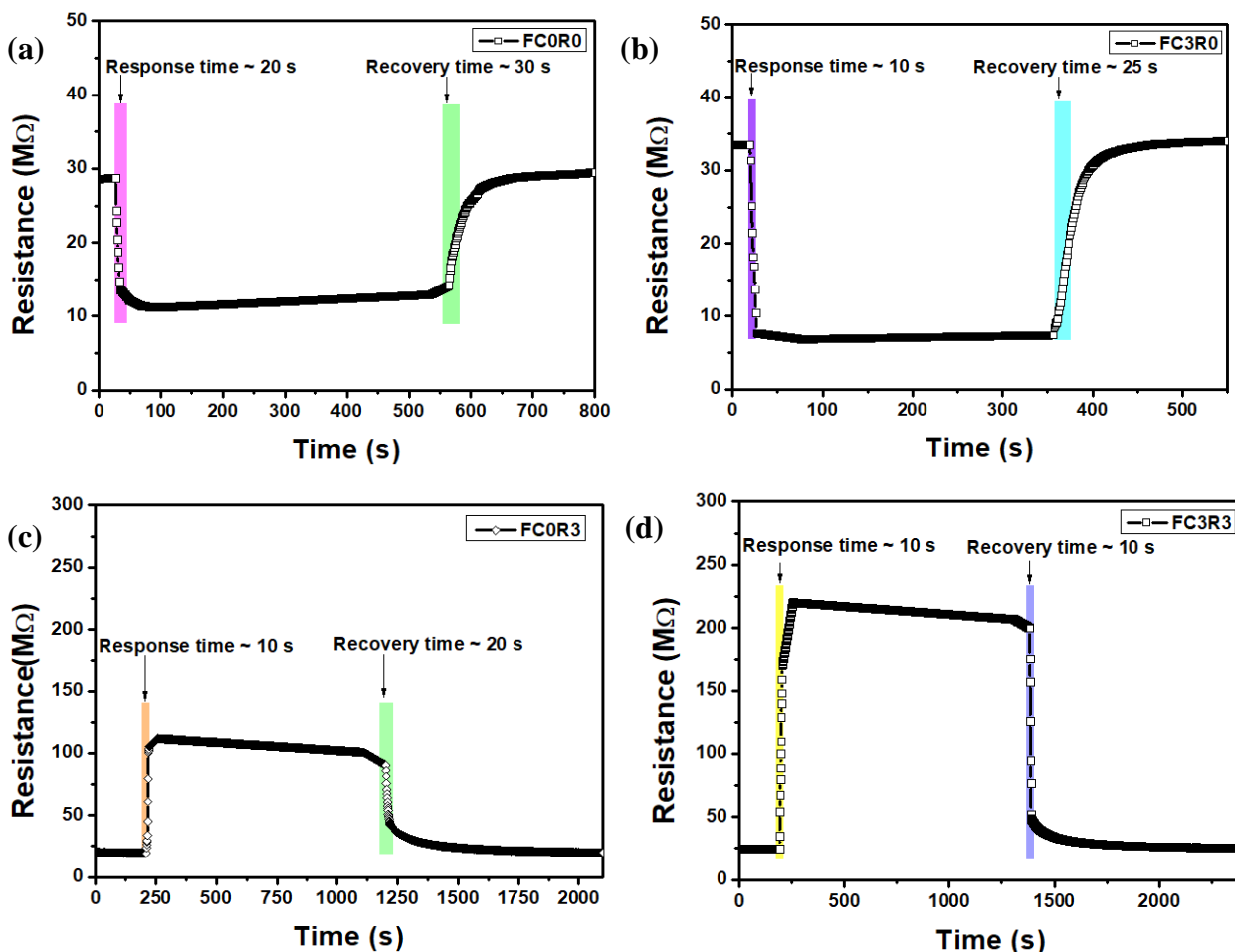


Figure-5.18: Response and recovery time in presence of  $\sim 10$  ppm acetone at operating temperature ( $30 \pm 5^\circ\text{C}$ ) (a) FC0R0, (b) FC3R0, (c) FC0R3, and (d) FC3R3

The response and recovery time of the respective sensors were calculated from their transient response curves considering the dynamic response of the sensors in presence of  $\sim 10$  ppm acetone. The FC0R0 sensor showed maximum response time ( $\sim 20$  s) and recovery time ( $\sim 30$  s) (Fig. 5.18a), due to slow adsorption kinetics. Although the other three sensors revealed a faster

response time of  $\sim 10$  s, the recovery time of the FC3R0 sensor was  $\sim 25$  s (Fig. 5.18b) which became slightly faster in FC0R3 sensor of  $\sim 20$  s (Fig. 5.18c) and fastest recovery time of  $\sim 10$  s was recorded for FC3R3 sensor (Fig. 5.18d). Fast response-recovery of FC3R3 sensor attributed to facile sorption and fast reaction kinetics of gas molecules on sensing material surface.

As the quick response/ recovery time is the key to the potential utility of a sensor for short time multiple pulse detection purpose, the desired interaction between the analyte gas and sensing material surface should be physisorption. Theoretical analysis of Freundlich isotherm in terms of linear fitted  $\log S$  vs.  $\log C$  curve for individual sensors [31], (the slope value  $> 1$  for chemisorption and  $< 1$  for physisorption) could be correlated to the prevailing adsorption process. From the Fig. 5.19 the obtained slope value was in the range of 0.29 to 0.44 and this implied the physisorption interaction during gas sensing process.

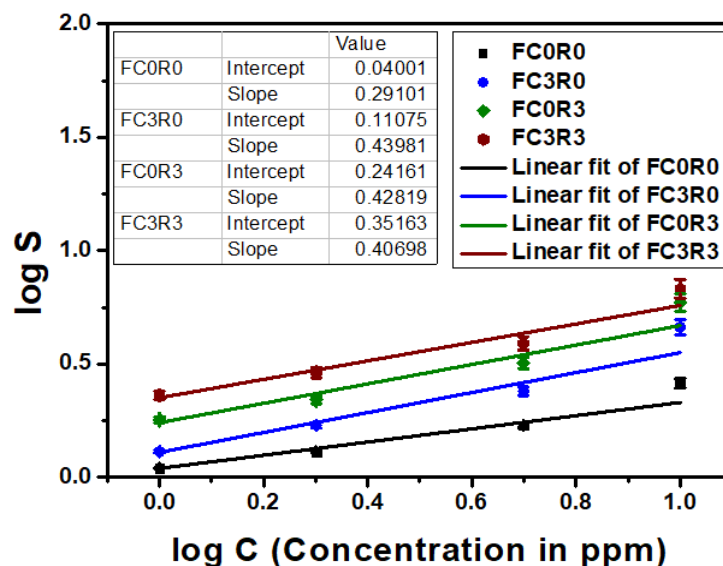


Figure-5.19:  $\log S$  vs.  $\log C$  plot of the fabricated sensors

The effect of relative humidity on the sensing response was studied for room temperature operated sensors (FC0R3 and FC3R3) only, as at higher working temperature ( $> 100^\circ\text{C}$ ) due to faster desorption of water molecules humidity barely affected the sensing response. Now, for FC0R3 and FC3R3 sensors the sensing responses were observed to be decreased at higher humidity conditions (Fig. 5.20). According to Grotthuss mechanism [6, 36], due to hopping of  $\text{H}^+$  and  $\text{OH}^-$  ions, with increase in %RH of the sensing environment, majority of active sites on the

sensing material surface remained preoccupied. Therefore, available sites left for gas molecules interaction were very less, resulted into a decrease in sensing response.

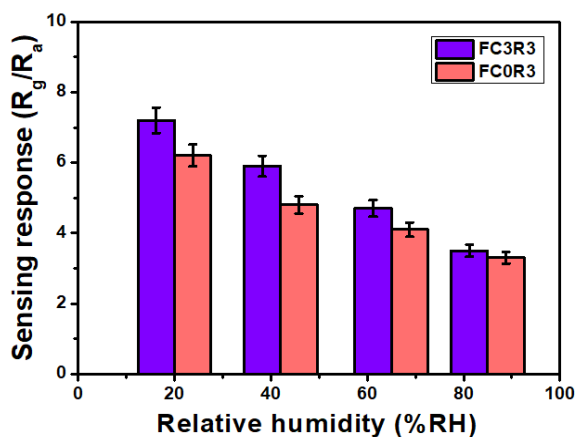


Figure-5.20: Change of sensing response as a function of %RH

The fabricated sensors established their promising selectivity towards acetone in presence of other interfering VOCs (~ 10 ppm concentration of each) at their respective operating temperatures (Fig. 5.21). Such selectivity towards acetone could be summarized as a cumulative effect of multiple factors; such as bond dissociation energy, collision diameter, polarity of the analyte gas molecule, etc [14]. Acetone having least bond dissociation energy (~ 366 kJ/mole), and also its LUMO energy was almost comparable to the developed optimized composition and hence it was easily detected by the sensing materials compared to the other VOCs.

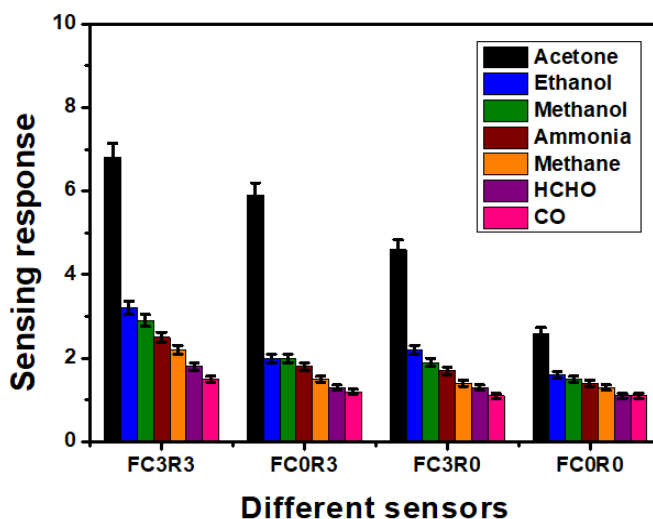


Figure-5.21: Selectivity graph of the sensors



From the durability perspectives, the reproducibility and stability of the sensors in terms of base resistance and sensing response is essential. FC0R0 (Fig. 5.22a) and FC3R0 (Fig. 5.22b) sensors exhibited stability for  $\sim 90$  days, after which the sensing properties were started to degrade, whereas, FC0R3 (Fig. 5.22c) and FC3R3 (Fig. 5.22d) sensors hardly showed any sign of such degradation in sensing performance till  $\sim 150$  days. This increased stability of the sensors might be attributed to the elimination of heating element for room temperature operation.

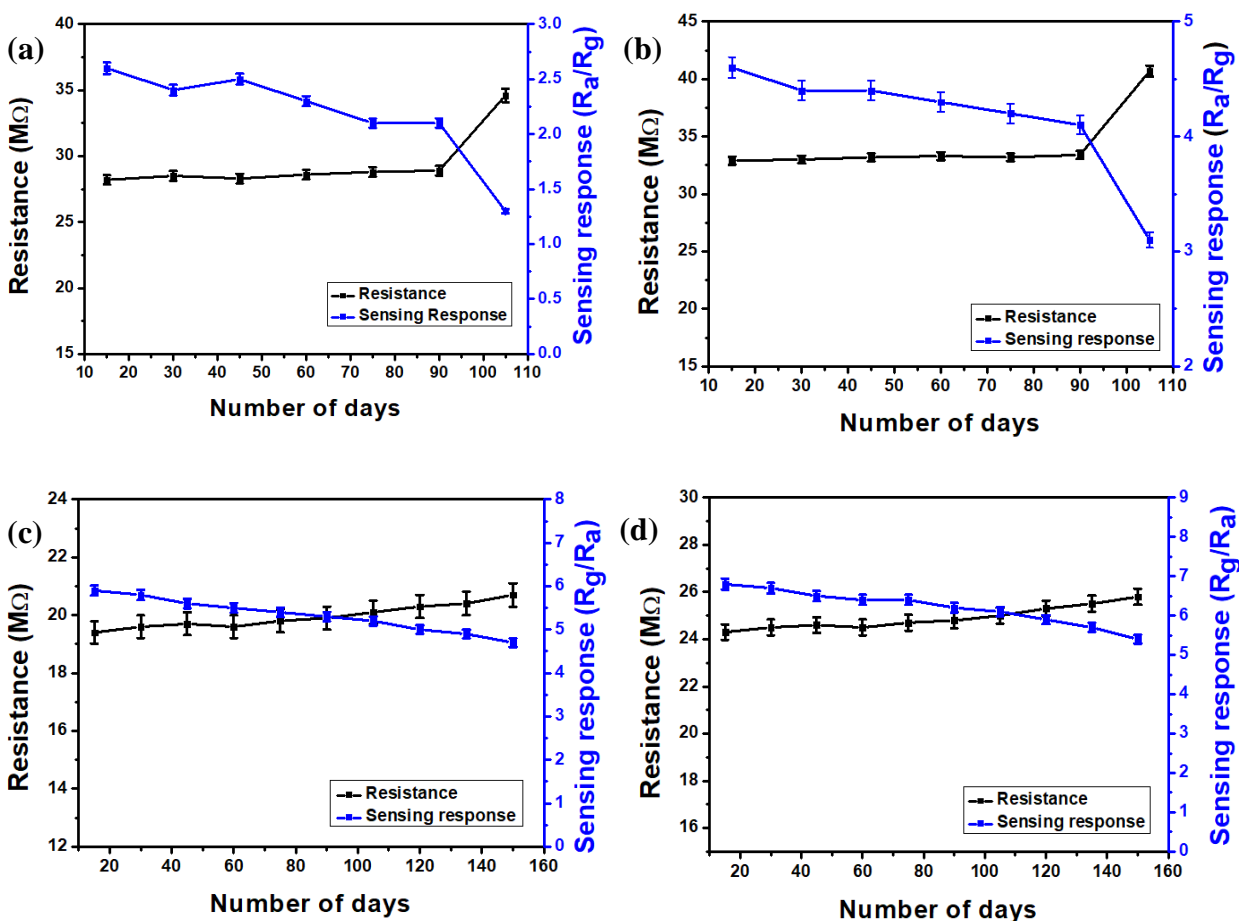


Figure-5.22: Stability curves (a) FC0R0, (b) FC3R0, (c) FC0R3, and (d) FC3R3

The optimized FC3R3 sensor was utilized to understand its efficacy as diabetic breath biomarker (acetone) detector. Although human exhaled breath contains plethora of gas molecules, but under certain pathological condition without any major disease, the acetone concentration for a healthy person is below 1 ppm which goes beyond 1 ppm (specifically  $\sim 1.8$  ppm) for diabetic-prone

person. Exhaled breath of a healthy person as well as of a diabetic patient was collected separately in an ~ 1 L Tedlar bag and used as the stock sample for further sensing measurement.

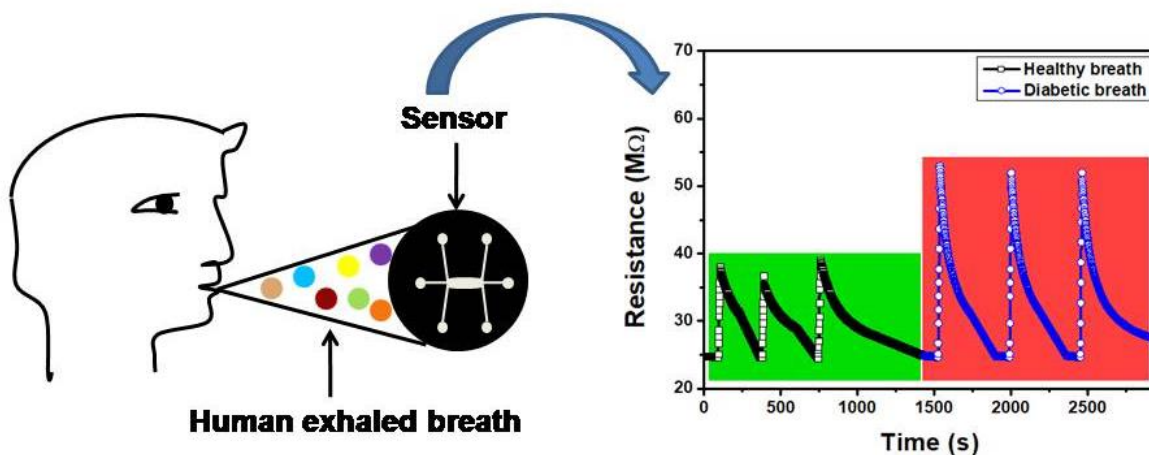


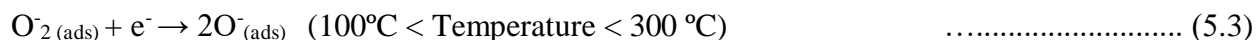
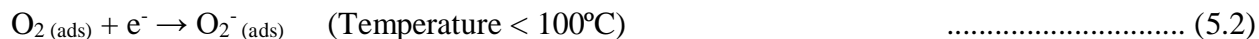
Figure-5.23: Schematics of human exhaled breath sample sensing and sensing response to healthy and diabetic breath sample by FC3R3 sensor

At ambient condition the sensor was exposed to ~ 10 s pulse of healthy breath which showed a sensing response ( $R_g/R_a$ ) ~ 1.6, which was increased to ~ 2.2 in presence of the pulse of diabetic patient's breath (Fig. 5.23). Thus, the sensor was able to distinguish between healthy and diabetic breath by differentiating them in terms of difference in sensing responses according to the acetone concentration in it. High moisture content (~ 90%RH) in human exhaled breath sample was responsible for low response value compared to the sensing response towards commercial acetone ( $N_2$  balance).

### 5.3.3. Gas sensing mechanism:

Chemiresistive gas sensing of MOS-based sensors is primarily a surface phenomena which is monitored by adsorption-desorption of gas molecules on the sensing material surface and consequent change in sensor's resistance expressed as sensing response. As the sensor exposed to air, the atmospheric oxygen molecules adsorbed on the sensor surface and extracted labile

electrons from the conduction band to convert themselves to different oxygenated ions, according to the operating temperature of sensor [31, 34], as follows:



As a result of this, the carrier concentration of  $\text{Fe}_2\text{O}_3$  decreased which developed a depletion layer at the grain boundary and the potential barrier height increased. In presence of analyte gas (acetone) pulse, the reaction with pre-adsorbed oxygen ions reverted the trapped electrons, accounted for decrease in potential barrier height which caused shrinkage of depletion layer [37].

The alteration in resistance expressed in terms of sensing response [7, 11].

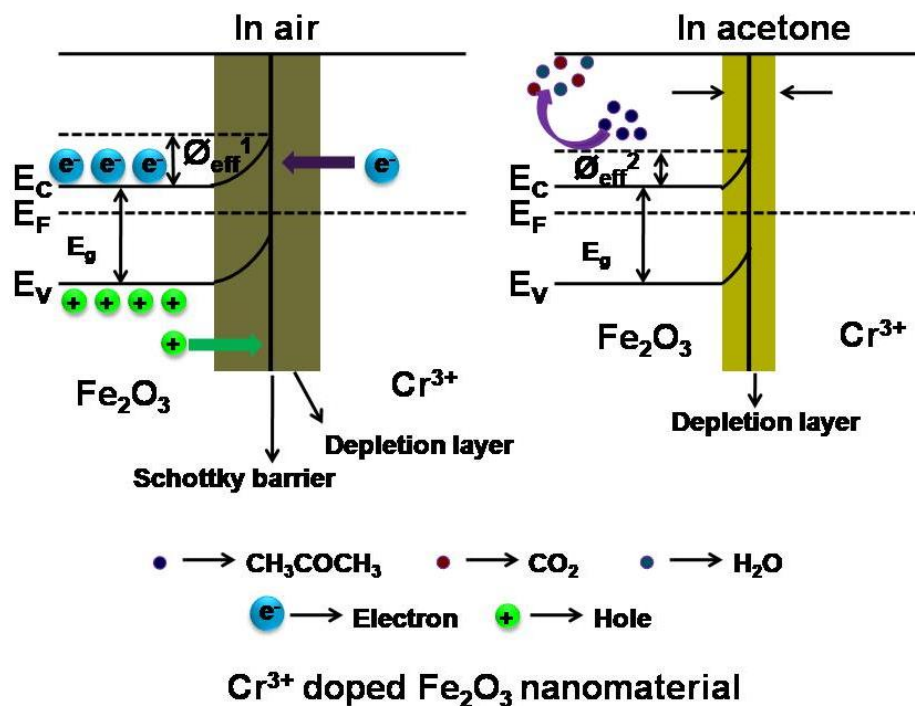
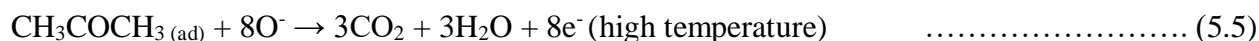


Figure-5.24: Electron depletion model of acetone sensing mechanism of FC3R0 sensor

In  $\text{Cr}^{3+}$  doped  $\text{Fe}_2\text{O}_3$  nanomaterial, due to formation of schottky junction, electrons flow from  $\text{Cr}^{3+}$  to  $\text{Fe}_2\text{O}_3$  until the Fermi-level equilibrium was achieved, which increased the charge carriers

concentration in  $\text{Fe}_2\text{O}_3$  (Fig. 5.24). As well, as a catalyst,  $\text{Cr}^{3+}$  ions also facilitated the oxygenated ion formation and thus, more number of oxygenated ions adsorbed on the sensing material surface caused thickening of the depletion layer. Thereby, the electronic and chemical sensitization (spillover effect) cumulatively reduced the activation energy of interplay between oxygen ions and acetone and the sensing response of the sensor improved [38].

On the other hand, the introduction of p-type rGO in n-type  $\text{Fe}_2\text{O}_3$  induced the electron transportation from  $\text{Fe}_2\text{O}_3$  to rGO across the p-n junction and resulted into hole-electron recombination. Thereby, the charge carriers' concentration decreased at the junction boundary and there developed an accumulation layer and depletion layer towards rGO and  $\text{Fe}_2\text{O}_3$  respectively (Fig. 5.25). Moreover, rGO also provided a large number of active sites on its surface which promoted the adsorption of large number of oxygen molecules. Thus, the activation energy required for the chemical interaction was very less and the operating temperature of the sensor reduced to the room temperature. Furthermore, in presence of acetone the carrier concentration modulation resulted into an enhanced sensing response.

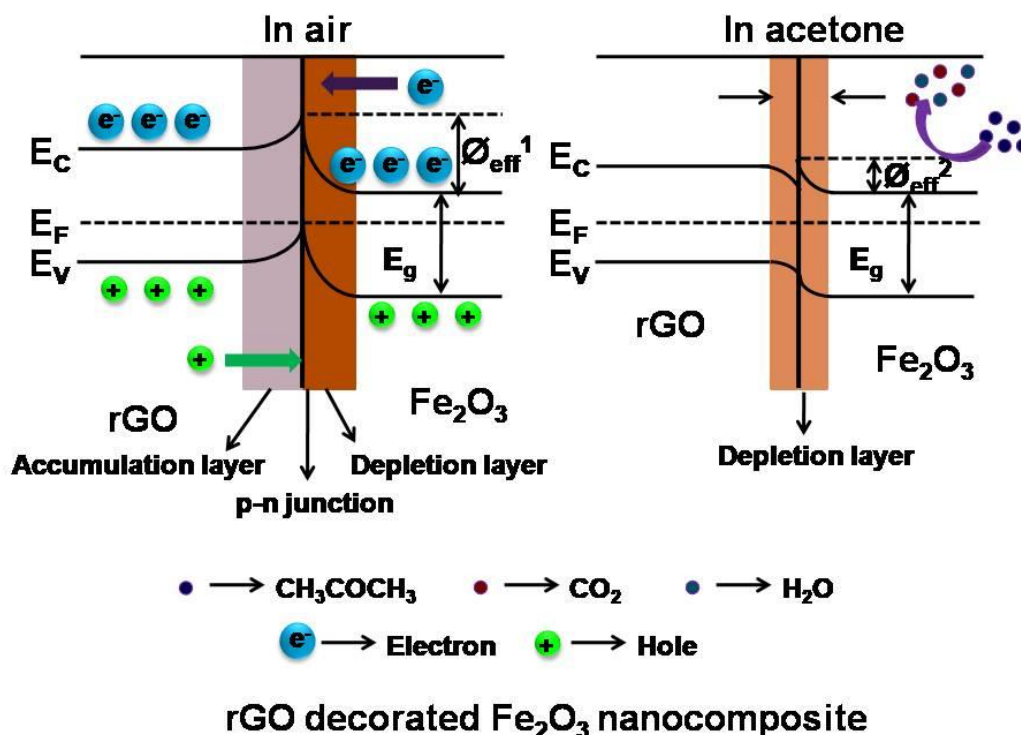


Figure-5.25: Electron depletion model of acetone sensing mechanism of FCOR3 sensor

In  $\text{Cr}^{3+}$  doped rGO decorated  $\text{Fe}_2\text{O}_3$  nanocomposite, the enhancement of sensing response was rationalized in terms of combined outcome of two factors; one was the developed p-n heterojunction between rGO and  $\text{Fe}_2\text{O}_3$  and the other was the synergistic effect of  $\text{Cr}^{3+}$  dopant and  $\text{Fe}_2\text{O}_3$ . Earlier, the impact of these two aspects was individually illustrated. Now, as a combined effect of these two, a myriad of oxygenated ions were adsorbed to the active sites on the sensing material which triggered the thickening of depletion layer to a greater extent (Fig. 5.26). As the sensor was exposed to acetone gas pulse, a large number of acetone molecules involved in redox reaction with oxygen ions and due to returning of trapped electrons back to conduction band, the depletion layer became thinner. Therefore, the sensor exhibited an enhanced sensing response at ambient condition.

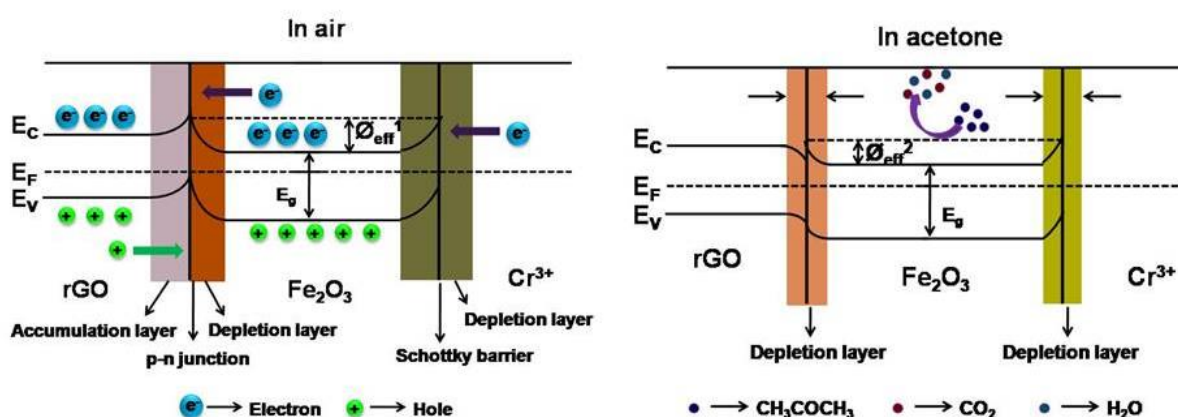


Figure-5.26: Electron depletion model of acetone sensing mechanism of FC3R3 sensor

The comparative sensing performance of some literature works with the developed rGO decorated  $\text{Cr}^{3+}$  doped  $\alpha\text{-Fe}_2\text{O}_3$  nanocomposite sensor was tabulated here (Table 4.2.3).

Table-5.1: Literature works on  $\text{Fe}_2\text{O}_3$  based acetone sensors:

Sensing material	Synthesis technique	Working temperature ( $^{\circ}\text{C}$ )	Detection conc. (ppm)	Response ( $R_a/R_g$ )	Res./ Rec. time (s)	Ref.
$\alpha\text{-Fe}_2\text{O}_3$ ameliorated rGO sheets	Hydrothermal	225	100	13.9	2/20	[6]

rGO/ $\alpha$ -Fe <sub>2</sub> O <sub>3</sub> composite nanofibers	Electro-spinning	375	100	8.9	3/9	[7]
PrFeO <sub>3</sub> hollow nanofibers	Electro-spinning	180	500	234.4	5/5	[8]
Fe <sub>3</sub> O <sub>4</sub> /carbon flake-like nanocomposite	Solvothermal	370	100	-	6/13	[9]
Pt-loaded Fe <sub>2</sub> O <sub>3</sub> nanocubes	Precipitation	139	100	25.7	3/22	[10]
Au nanoparticle modified $\alpha$ -Fe <sub>2</sub> O <sub>3</sub> nanodisk	Hydrothermal	275	100	19.5	4/7	[11]
ZnSnO <sub>3</sub> / $\alpha$ -Fe <sub>2</sub> O <sub>3</sub> hierarchical microspheres	Hydrothermal	200	50	14.24	3/7	[12]
$\alpha$ -Fe <sub>2</sub> O <sub>3</sub> nanoparticles	Template assisted synthesis	183	100	27	1/80	[13]
TiO <sub>2</sub> / $\alpha$ -Fe <sub>2</sub> O <sub>3</sub> heterojunction	Seed assisted synthesis	225	100	21.9	13/10	[14]
<b>Cr<sup>3+</sup> doped rGO decorated <math>\alpha</math>-Fe<sub>2</sub>O<sub>3</sub></b>	<b>Sol-gel</b>	<b>30 <math>\pm</math> 5</b>	<b>10</b>	<b>6.8</b>	<b>10/10</b>	<b>This work</b>

#### 5.4. Conclusion:

In short,  $\text{Cr}^{3+}$  doping in the pristine  $\text{Fe}_2\text{O}_3$  matrix induced oxygen vacancies and the fabricated Taguchi-type sensors exhibited an excellent p-type acetone sensing response at room temperature which was inversed to n-type sensing at high temperature operation. The generation of ‘inversion space-charge layer’ on the sensing material surface accounted for obtaining a p-type sensing response using an n-type MOS ( $\text{Fe}_2\text{O}_3$ ). The sensing response ( $R_g/R_a$ ) of  $\sim 3$  wt%  $\text{Cr}^{3+}$  doped and  $\sim 3$  wt% rGO decorated  $\text{Fe}_2\text{O}_3$  nanomaterial (FC3R3) was maximum  $\sim 6.8$  towards  $\sim 10$  ppm acetone at room temperature. Analysis of transient response curve of the sensors revealed a fast response/recovery time ( $\sim 10$  s/ $\sim 10$  s) of FC3R3 sensor. The optimized sensors revealed good selectivity, reproducible sensing performances and prolonged stability of  $\sim 150$  days without much deterioration in base resistance and sensing response. The optimized sensor was also exposed to collected human exhaled breath and it was effectively able to identify between healthy and diabetic breath by exhibiting different sensing response. The chemiresistive sensing mechanism was illustrated using an electron band-diagram modeling. Altogether, this sensor might be considered for futuristic real-life non-invasive diabetic breath biomarker detection in ambient condition.

## References:

- [1] S. Sen, S. Maity, S. Kundu, Fabrication of Fe doped reduced graphene oxide (rGO) decorated WO<sub>3</sub> based low temperature ppm level acetone sensor: Unveiling sensing mechanism by impedance spectroscopy, *Sens. Actuators B: Chem.* 361 (2022) 131706. <https://doi.org/10.1016/j.snb.2022.131706>.
- [2] N. T. A. Thu, N. D. Cuong, L. C. Nguyen, D. Q. Khieu, P. C. Nam, N. V. Toan, C. M. Hung, N. V. Hieu, Fe<sub>2</sub>O<sub>3</sub> nanoporous network fabricated from Fe<sub>3</sub>O<sub>4</sub>/reduced graphene oxide for high-performance ethanol sensor, *Sens. Actuators B: Chem.* 255 (2018) 3275-3283. <https://doi.org/10.1016/j.snb.2017.09.154>.
- [3] Y. Teng, X. Zhang, T. Xu, Z. Deng, Y. Xu, L. Huo, S. Gao, A spendable gas sensor with high sensitivity and lowest detection limit towards H<sub>2</sub>S: Porous  $\alpha$ -Fe<sub>2</sub>O<sub>3</sub> hierarchical tubule derived from poplar branch, *Chem. Eng. J.* 392 (2020) 123679. <https://doi.org/10.1016/j.cej.2019.123679>.
- [4] D. D. Vuong, L. H. Phuoc, V. X. Hien, N. D. Chien, Hydrothermal synthesis and ethanol-sensing properties of  $\alpha$ -Fe<sub>2</sub>O<sub>3</sub> hollow nanospindles, *Mater. Sci. Semicond. Process* 107 (2020) 104861. <https://doi.org/10.1016/j.mssp.2019.104861>.
- [5] Y. Wu, B. Song, X. Zhang, Z. Deng, L. Huo, S. Gao, Microtubular  $\alpha$ -Fe<sub>2</sub>O<sub>3</sub>/Fe<sub>2</sub>(MoO<sub>4</sub>)<sub>3</sub> heterostructure derived from absorbent cotton for enhanced ppb-level H<sub>2</sub>S gas-sensing performance, *J. Alloys Compd.* 867 (2021) 158994. <https://doi.org/10.1016/j.jallcom.2021.158994>.
- [6] B. Zhang, J. Liu, X. Cui, Y. Wang, Y. Gao, P. Sun, F. Liu, K. Shimanoe, N. Yamazoe, G. Lu, Enhanced gas sensing properties to acetone vapor achieved by  $\alpha$ -Fe<sub>2</sub>O<sub>3</sub> particles ameliorated with reduced graphene oxide sheets, *Sens. Actuators B: Chem.* 241 (2017) 904-914. <https://doi.org/10.1016/j.snb.2016.11.023>.
- [7] L. Guo, X. Kou, M. Ding, C. Wang, L. Dong, H. Zhang, C. Feng, Y. Sun, Y. Gao, P. Sun, G. Lu, Reduced graphene oxide/ $\alpha$ -Fe<sub>2</sub>O<sub>3</sub> composite nanofibers for application in gas sensors, *Sens. Actuators B: Chem.* 244 (2017) 233-242. <https://doi.org/10.1016/j.snb.2016.12.137>.



- [8] L. Ma, S. Y. Ma, X. F. Shen, T. T. Wang, X. H. Jiang, Q. Chen, Z. Qiang, H. M. Yang, H. Chen, PrFeO<sub>3</sub> hollow nanofibers as a highly efficient gas sensor for acetone detection, *Sens. Actuators B: Chem.* 255 (2018) 2546-2554. <https://doi.org/10.1016/j.snb.2017.09.060>.
- [9] X. Liang, Y. Qin, W. Xie, Z. Deng, C. Yang, X. Su, Facile synthesis of high-stable and monodisperse Fe<sub>3</sub>O<sub>4</sub>/carbon flake-like nanocomposites and their excellent gas sensing properties, *J. Alloys Compd.* 818 (2020) 152898. <https://doi.org/10.1016/j.jallcom.2019.152898>.
- [10] S. Zhang, M. Yang, K. Liang, A. Turak, B. Zhang, D. Meng, C. Wang, F. Qu, W. Cheng, M. Yang, An acetone gas sensor based on nanosized Pt-loaded Fe<sub>2</sub>O<sub>3</sub> nanocubes, *Sens. Actuators B: Chem.* 290 (2019) 59-67. <https://doi.org/10.1016/j.snb.2019.03.082>.
- [11] H. Yang, R. Zhou, Y. Sun, P. Li, W. Zhang, Z. Zhao, J. Shi, J. Hu, Y. Chen, Optimization and gas sensing properties of Au nanoparticle modified  $\alpha$ -Fe<sub>2</sub>O<sub>3</sub> nanodisk structures for highly sensitive acetone detection, *New J. Chem.* 44 (2020) 16174, <https://doi.org/10.1039/d0nj03111a>.
- [12] J. Zhang, X. Jia, D. Lian, J. Yang, H. Song, Controlled synthesis of urchin-like ZnSnO<sub>3</sub>/ $\alpha$ -Fe<sub>2</sub>O<sub>3</sub> hierarchical hollow microspheres with enhanced acetone gas sensing properties, *J. Mater. Sci. Mater. Electron.* 31 (2020) 15446-15455. <https://doi.org/10.1007/s10854-020-0107-x>.
- [13] Z. Cao, Z. Jiang, L. Cao, Y. Wang, C. Feng, C. Huang, Y. Li, Lattice expansion and oxygen vacancy of  $\alpha$ -Fe<sub>2</sub>O<sub>3</sub> during gas sensing, *Talanta* 221 (2021) 121616. <https://doi.org/10.1016/j.talanta.2020.121616>.
- [14] C Wang, Y. Wang, P. Cheng, L. Xu, F. Dang, T. Wang, Z. Lei, In-situ generated TiO<sub>2</sub>/ $\alpha$ -Fe<sub>2</sub>O<sub>3</sub> heterojunction arrays for batch manufacturing of conductometric acetone gas sensors, *Sens. Actuators B: Chem.* 340 (2021) 129926. <https://doi.org/10.1016/j.snb.2021.129926>.
- [15] A. P. Singh, M. Mishra, P. Sambyal, B. K. Gupta, B. P. Singh, A. Chandra, S. K. Dhawan, Encapsulation of  $\gamma$ -Fe<sub>2</sub>O<sub>3</sub> decorated reduced graphene oxide in polyaniline core-shell tubes as an exceptional tracker for electromagnetic environmental pollution, *J. Mater. Chem. A* 2 (2014) 3581. <https://doi.org/10.1039/c3ta14212d>.

- [16] P. Sun, C. Wang, X. Zhou, P. Cheng, K. Shimanoe, G. Lu, N. Yamazoe, Cu-doped  $\alpha$ -Fe<sub>2</sub>O<sub>3</sub> hierarchical microcubes: Synthesis and gas sensing properties, *Sens. Actuators B: Chem.* 193 (2014) 616-622. <https://doi.org/10.1016/j.snb.2013.12.015>.
- [17] A. K. Basu, P. S. Chauhan, M. Awasthi, S. Bhattacharya,  $\alpha$ -Fe<sub>2</sub>O<sub>3</sub> loaded rGO nanosheets based fast response/recovery CO gas sensor at room temperature, *Appl. Surf. Sci.* 465 (2019) 56-66. <https://doi.org/10.1016/j.apsusc.2018.09.123>.
- [18] A. K. Basu, A. N. Sah, M. M. Dubey, P. K. Dwivedi, A. Pradhan, S. Bhattacharya, MWCNT and  $\alpha$ -Fe<sub>2</sub>O<sub>3</sub> embedded rGO-nanosheets based hybrid structure for room temperature chloroform detection using fast response/recovery cantilever based sensors, *Sens. Actuators B: Chem.* 305 (2020) 127457. <https://doi.org/10.1016/j.snb.2019.127457>.
- [19] T. V. Nguyen, N. A. Luong, V. T. Nguyen, A. T. Pham, A. T. Le, T. L. To, V. Q. Nguyen, Effect of the phase composition of iron oxide nanorods on SO<sub>2</sub> gas sensing performance, *Mater. Res. Bull.* 134 (2021) 111087. <https://doi.org/10.1016/j.materresbull.2020.111087>.
- [20] H. Mei, S. Zhou, M. Lu, Y. Zhao, L. Cheng, Construction of pine-branch-like  $\alpha$ -Fe<sub>2</sub>O<sub>3</sub>/TiO<sub>2</sub> hierarchical heterostructure for gas sensing, *Ceram. Int.* 46 (2020) 18675-18682. <https://doi.org/10.1016/j.ceramint.2020.04.181>.
- [21] M. Wang, T. Shen, M. Wang, D. Zhang, Z. Tong, J. Chen, One-pot synthesis of  $\alpha$ -Fe<sub>2</sub>O<sub>3</sub> nanoparticles-decorated reduced graphene oxide for efficient nonenzymatic H<sub>2</sub>O<sub>2</sub> biosensor, *Sens. Actuators B: Chem.* 190 (2014) 645-650. <https://doi.org/10.1016/j.snb.2013.08.091>.
- [22] A. Prakash, S. Chandra, D. Bahadur, Structural, magnetic, and textural properties of iron oxide-reduced graphene oxide hybrids and their use for the electrochemical detection of chromium, *Carbon* 50 (2012) 4209-4219. <https://doi.org/10.1016/j.carbon.2012.05.002>.
- [23] G. Bharath, R. Madhu, S. Chen, V. Veeramani, D. Mangalaraj, N. Ponpandian, Solvent Free Mechanochemical Synthesis of Graphene Oxide and Fe<sub>3</sub>O<sub>4</sub>/Reduced Graphene Oxide Nanocomposites for Sensitive Detection of Nitrite, *J. Mater. Chem. A* 00 (2013) 1-3. <https://doi.org/10.1039/C5TA03179F>.

- [24] M. Dutt, A. Ratan, M. Tomar, V. Gupta, V. Singh, Mesoporous metal oxide- $\alpha$ - $\text{Fe}_2\text{O}_3$  nanocomposites for sensing formaldehyde and ethanol at room temperature, *J. Phys. Chem. Solids* 145 (2020) 109536. <https://doi.org/10.1016/j.jpcs.2020.109536>.
- [25] I. Tiwari, M. Singh, C. M. Pandey, G. Sumana, Electrochemical genosensor based on graphene oxide modified iron oxide-chitosan hybrid nanocomposite for pathogen detection, *Sens. Actuators B: Chem.* 206 (2015) 276-283. <https://doi.org/10.1016/j.snb.2014.09.056>.
- [26] S. Liang, J. Zhu, C. Wang, S. Yu, H. Bi, X. Liu, X. Wang, Fabrication of  $\alpha$ - $\text{Fe}_2\text{O}_3$ @graphene nanostructures for enhanced gas-sensing property to ethanol, *Appl. Surf. Sci.* 292 (2014) 278-284. <https://doi.org/10.1016/j.apsusc.2013.11.130>.
- [27] J. Ouyang, J. Pei, Q. Kuang, Z. Xie, L. Zheng, Supersaturation-Controlled Shape Evolution of  $\alpha$ - $\text{Fe}_2\text{O}_3$  Nanocrystals and Their Facet-Dependent Catalytic and Sensing Properties, *ACS Appl. Mater. Interfaces* 15 (2014) 12505-12514. <https://doi.org/10.1021/am502358g>.
- [28] P. Clement, I. Hafaiedh, E. J. Parra, A. Thamri, J. Guillot, A. Abdelghani, E. Llobet, Iron oxide and oxygen plasma functionalized multi-walled carbon nanotubes for the discrimination of volatile organic compounds, *Carbon* 78 (2014) 510-520. <https://doi.org/10.1016/j.carbon.2014.07.032>.
- [29] V. Haridas, A. Sukhananazerin, J. M. Sneha, B. Pullithadathil, B. Narayanan,  $\alpha$ - $\text{Fe}_2\text{O}_3$  loaded less-defective graphene sheets as chemiresistive gas sensor for selective sensing of  $\text{NH}_3$ , *Appl. Surf. Sci.* 517 (2020) 146158. <https://doi.org/10.1016/j.apsusc.2020.146158>.
- [30] P. Hao, G. Qu, P. Song, Z. Yang, Q. Wang, Synthesis of Ba-doped porous  $\text{LaFeO}_3$  microspheres with perovskite structure for rapid detection of ethanol gas, *Rare Met.* 40 (2021) 1651-1661. <https://doi.org/10.1007/s12598-020-01672-2>.
- [31] D. Xue, R. Zhou, X. Lin, X. Duan, Q. Li, T. Wang, A highly selective and sensitive  $\text{H}_2\text{S}$  sensor at low temperatures based on Cr-doped  $\alpha$ - $\text{Fe}_2\text{O}_3$  nanoparticles, *RSC Adv.* 9 (2019) 4150. <https://doi.org/10.1039/c8ra07365a>.
- [32] B. Zhang, G. Liu, M. Cheng, Y. Gao, L. Zhao, S. Li, F. Liu, X. Yan, T. Zhang, P. Sun, G. Lu, The preparation of reduced graphene oxide-encapsulated  $\alpha$ - $\text{Fe}_2\text{O}_3$  hybrid and

- its outstanding NO<sub>2</sub> gas sensing properties at room temperature, *Sens. Actuators B: Chem.* 261 (2018) 252-263. <https://doi.org/10.1016/j.snb.2018.01.143>.
- [33] L. Wang, B. Hong, H. D. Chen, J. C. Xu, Y. B. Han, H. X. Jin, D. F. Jin, X. L. Peng, H. L. Ge, X. Q. Wang, The highly improved gas-sensing performance of  $\alpha$ -Fe<sub>2</sub>O<sub>3</sub>-decorated NiO nanowires and the interfacial effect of p-n heterojunctions, *J. Mater. Chem. C* 8 (2020) 3855. <https://doi.org/10.1039/c9tc06614d>.
- [34] X. Jia, D. Lian, B. Shi, R. Dai, C. Li, X. Wu, Facile synthesis of  $\alpha$ -Fe<sub>2</sub>O<sub>3</sub>@graphene oxide nanocomposites for enhanced gas-sensing performance to ethanol, *J. Mater. Sci. Mater. Electron.* 28 (2017) 12070-12079. <https://doi.org/10.1007/s10854-017-7019-y>.
- [35] B. G. Ghule, S. F. Shaikh, N. M. Shinde, S. S. Sangale, P. V. Shinde, R. S. Mane, Promoted room-temperature LPG gas sensor activities of graphene oxide@Fe<sub>2</sub>O<sub>3</sub> composite sensor over individuals, *Mater. Res. Express* 5 (2018) 125001. <https://doi.org/10.1088/2053-1591/aaddcc>.
- [36] A. K. Zak, H. Shirmahd, S. Mohammadi, S. M. Banihashemian, Solvothermal synthesis of porous Fe<sub>3</sub>O<sub>4</sub> nanoparticles for humidity sensor application, *Mater. Res. Express* 7 (2020) 025001. <https://doi.org/10.1088/2053-1591/ab6e3c>.
- [37] Z. Lou, F. Li, J. Deng, L. Wang, T. Zhang, Branch-like Hierarchical Heterostructure ( $\alpha$ -Fe<sub>2</sub>O<sub>3</sub>/TiO<sub>2</sub>): A Novel Sensing Material for Trimethylamine Gas Sensor, *ACS Appl. Mater. Interfaces* 5 (2013) 12310-12316. <https://doi.org/10.1021/am402532v>.
- [38] M. Liu, P. Song, X. Zhong, Z. Yang, Q. Wang, Facile synthesis of Au-decorated  $\alpha$ -Fe<sub>2</sub>O<sub>3</sub>/rGO ternary hybrid structure nanocomposites for enhanced triethylamine gas-sensing properties, *J. Mater. Sci. Mater. Electron.* 31 (2020) 22713-22726. <https://doi.org/10.1007/s10854-020-04796-4>.



# CHAPTER 6

## Summary and Future Scope

Chapter 1

Chapter 2

Chapter 3.1

Chapter 4.1

Chapter 3.2

Chapter 4.2

Chapter 5

Chapter 6



*The significant outcomes of this dissertation works have been summarized in this chapter. Different pristine metal oxide nanomaterials, binary nanocomposites, doped nanomaterials and their composites with rGO have been synthesized. After detailed material characterization corresponding Taguchi-type sensors have been fabricated and their sensing performances studied. The salient features and fundamental outcomes related to every work have been highlighted. Finally, the key prospects and future scopes of the ongoing work have been pointed out.*



### **6.1. Summary and conclusions:**

Development of low temperature operated selective VOC sensor was the prime objective of the dissertation work. Selective VOC sensors are promising for non-invasive diagnosis of diseases through breath analysis and here, low temperature operation could be energy saving and increase the life-time of the sensors. After understanding the importance of MOS-based sensors in the field of gas sensing and their existing drawbacks, in this Ph. D. dissertation work, different metal oxide semiconductors (pristine/binary heterojunction/doped) and their functionalized nanocomposites with rGO were synthesized by environment friendly wet chemical (sol-gel) method. Taguchi-type sensors were fabricated using these as-synthesized nanomaterials with the aim of achieving low temperature ppm-level VOC sensing performance. Finally, some of these developed sensors were exposed to stimulated human exhaled breath sample in order to rationalize their efficacy in diabetes breath biomarker identification.

Chapter 1 described the background history, brief general introduction and versatile application fields of sensor in our everyday's life. An elaborated discussion was presented on general overview of sensors with a focused emphasis on MOS-based gas sensors. With a special attention, the state-of-art of Taguchi-type sensors and their gas sensing mechanisms were vividly described. On the course of the work, several opportunities and obstacles related to MOS-based sensors and various factors to influence the sensing performance were pointed out. From the application perspectives, non-invasive breath biomarker analysis for disease diagnosis by MOS-based sensors and its potential futuristic applicability has been portrayed. In this purpose, the usefulness of low temperature operated sensor and the importance of graphene material to attain the same has also been delineated. Conclusively, the motivations, scope of the work with specific objectives, and the methodical work toward a targeted dissertation have been outlined.

Chapter 2 explained the nanomaterials synthesis, their characterization, Taguchi-type sensor fabrication and finally sensing measurement strategies. Initially, laboratory scale nanomaterial synthesis procedure, primarily adopting sol-gel methodology, has been described. The details procedure and mechanisms of materials characterization techniques have been discussed. After that, in sensor fabrication part the substrate preparation with miniaturized electrodes and heating elements, sensing layer casting on sensing substrate and their packaging in customized sensing module have been precisely described. Finally, the details of gas sensing measurement in an in-



house customized set-up, data acquisition, and sensing response calculation from the recorded result have been emphasized.

In Chapter 3.1, n-n heterojunction based binary nanocomposites were prepared having different composition (wt %) of ZnO and SnO<sub>2</sub>. The sensor fabricated from the optimized nanocomposite showed n-type sensing response of ~ 60% in presence of ~ 10 ppm acetone at ~ 300°C with a response and recovery time of ~ 20 s and ~ 135 s respectively. After rGO addition, the optimum operating temperature of the sensor reduced to ~ 150°C and the sensing response was enhanced to ~ 91% with faster response/recovery time of ~ 10 s/~ 100 s. These fabricated sensors also exhibited a good sensing response towards ethanol; for optimized ZnO-SnO<sub>2</sub> nanocomposite it was ~ 44% and after rGO incorporation it was increased to ~ 65% at their respective optimized working temperatures. The fabricated sensors showed a good repeatability and stability of ~ 90 days in terms of their base resistance and sensing responses with marginal deviation.

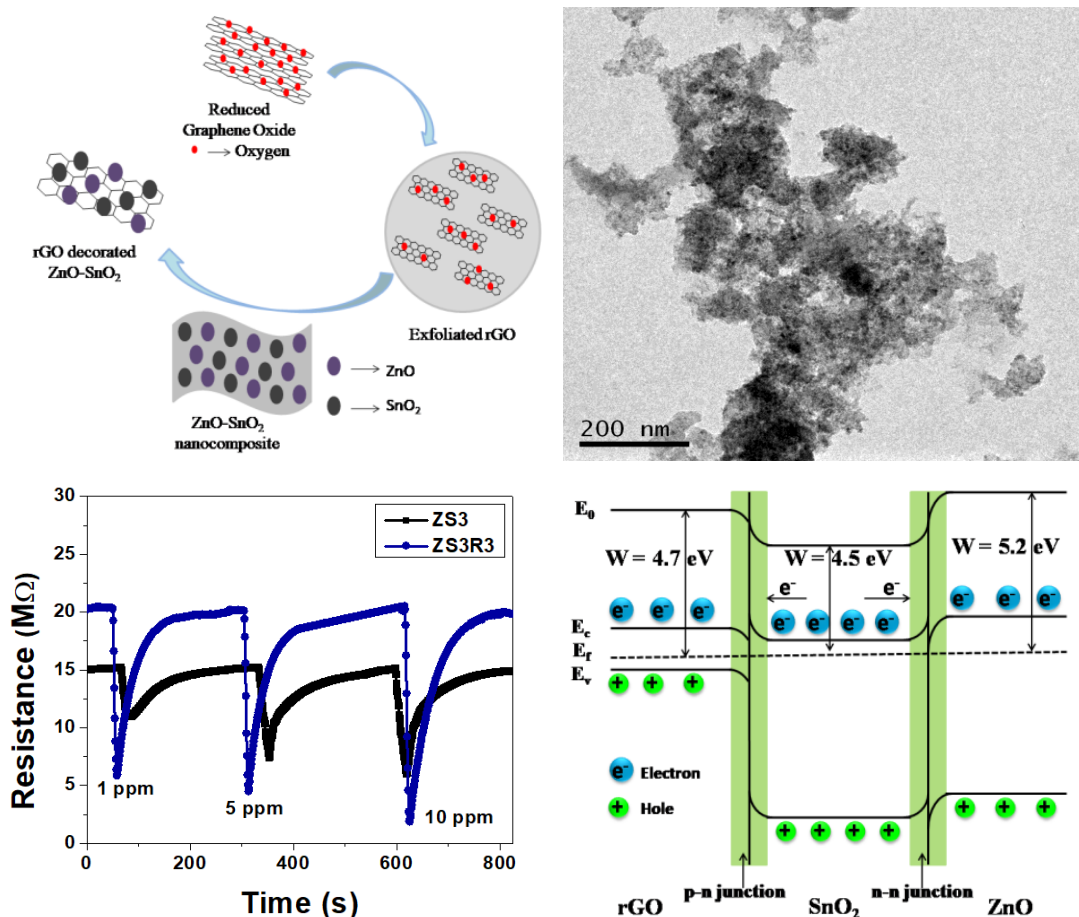


Figure-6.1: Graphical abstract of Chapter 3.1

In Chapter 3.2, n-type ZnO was replaced by p-type NiO to develop a p-n type heterojunction in NiO-SnO<sub>2</sub> nanocomposite which was further composited with rGO. The fabricated sensors showed p-type sensing response at room temperature ( $30 \pm 5^\circ\text{C}$ ). The sensing response of optimized binary NiO-SnO<sub>2</sub> nanocomposite was  $\sim 6.1$  towards  $\sim 10$  ppm acetone which was further enhanced to  $\sim 7.8$  after rGO incorporation. Besides these, the optimized NiO-SnO<sub>2</sub> sensor was also detected ethanol ( $\sim 10$  ppm) with sensing response  $\sim 2.8$  and that was  $\sim 4.1$  in rGO incorporated sensor. Moreover, the optimized rGO decorated NiO-SnO<sub>2</sub> based sensor was used to distinguish between healthy and diabetic patients by the difference in sensing response towards acetone concentration in exhaled breath samples. These sensors exhibited a prolong stability of  $\sim 120$  days with marginal deviation in their sensing responses. The room temperature sensing mechanisms of the sensors were elucidated with the help of schematic band diagram.

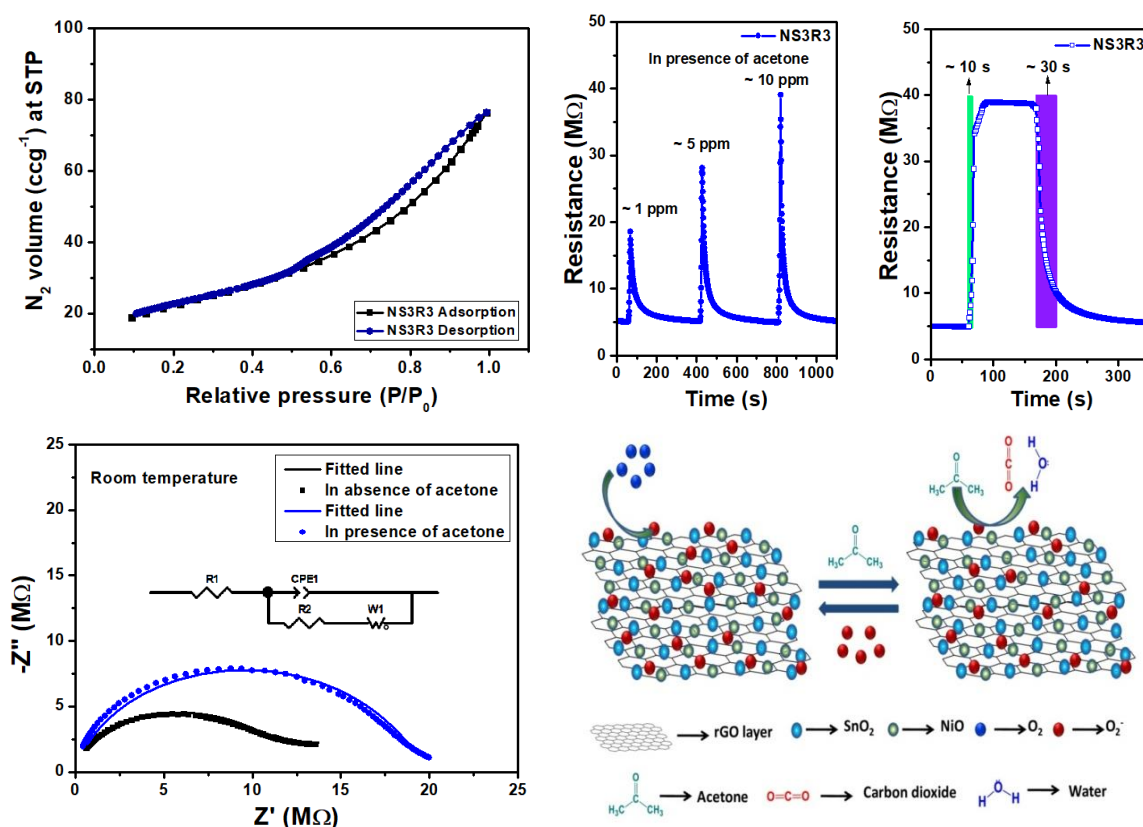


Figure-6.2: Graphical abstract of Chapter 3.2

In Chapter 4.1, Fe<sup>3+</sup> ion doped WO<sub>3</sub> nanomaterial and their nanocomposites with rGO were prepared using sol-gel process. The optimized Fe<sup>3+</sup> doped WO<sub>3</sub> sensor showed selective ppm-

level acetone sensing responses of at optimized temperature of  $\sim 205^{\circ}\text{C}$ , which was reduced to  $\sim 130^{\circ}\text{C}$  after rGO addition. As well as, the sensing response of the former one of  $\sim 62\%$  was enhanced to  $\sim 78\%$  in presence of  $\sim 10$  ppm acetone. The response/recovery time of  $\sim 20$  s/ $\sim 90$  s also became faster of  $\sim 20$  s/ $\sim 75$  s after rGO incorporation. The fabricated optimized sensor was also capable to detect less than 1 ppm acetone present in exhaled human breath.

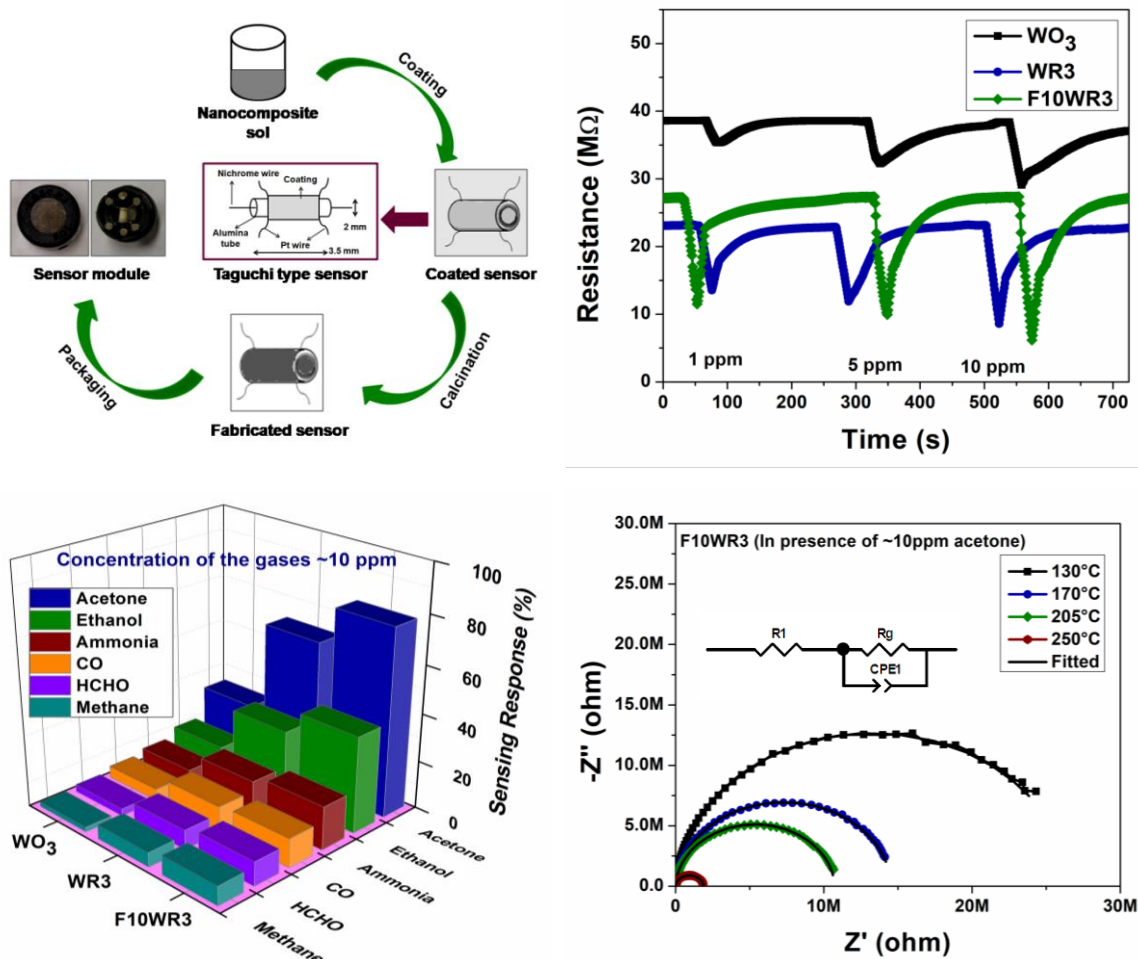


Figure-6.3: Graphical abstract of Chapter 4.1

In Chapter 4.2,  $\text{Cr}^{3+}$  doping in pristine  $\text{WO}_3$  lattice resulted into phase change from monoclinic to hexagonal and this modulation in lattice structure facilitated the sensing performance by reducing the operating temperature to room temperature. The fabricated optimized sensor showed p-type sensing responses of  $\sim 19.9$  towards  $\sim 10$  ppm acetone, which was enhanced to  $\sim 24.1$  in rGO incorporated sensor. The response/recovery time of  $\sim 30$  s/ $\sim 70$  s also shortened to  $\sim$

10 s/~ 30 s after rGO addition. The optimized sensor effectively distinguished the difference in acetone concentration in exhaled breath of healthy person and diabetic patient.

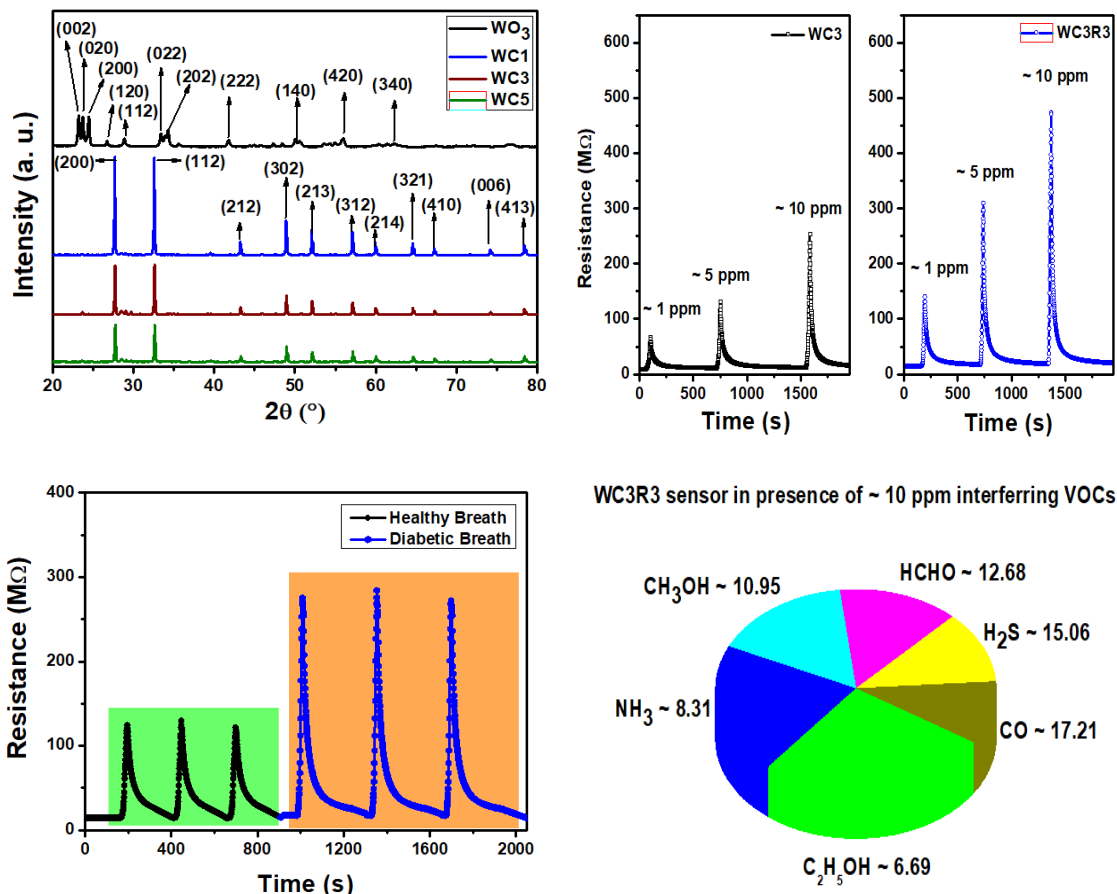


Figure-6.4: Graphical abstract of Chapter 4.2

Chapter 5 explored the selective acetone sensing performance of lower transition metal oxide. Pristine Fe<sub>2</sub>O<sub>3</sub> was functionalized by Cr<sup>3+</sup> doping and further modified by rGO decoration. The sensor fabricated from pristine Fe<sub>2</sub>O<sub>3</sub> showed n-type sensing response (~ 2.6) at ~ 180°C and this operating temperature was reduced to ~ 120°C after Cr<sup>3+</sup> doping with an enhancement of sensing response to ~ 4.6 in presence of ~ 10 ppm acetone. As a result of rGO incorporation, the optimum operating temperature was reduced to room temperature and simultaneously the nature of the sensing response towards acetones inversed from n-type to p-type. After rGO addition in pristine Fe<sub>2</sub>O<sub>3</sub> the sensing response increased to ~ 5.9 and maximum sensing response of ~ 6.8 was obtained from rGO decorated Cr<sup>3+</sup> doped Fe<sub>2</sub>O<sub>3</sub> based sensor. The optimized sensor also

showed fastest response ( $\sim 10$  s) and recovery ( $\sim 10$  s) time. The sensors demonstrated repeatable and reproducible sensing performances under identical experimental conditions. The optimized sensor was efficiently detected healthy and diabetic breath through differences in sensing responses towards different concentrations of acetone was present in it.

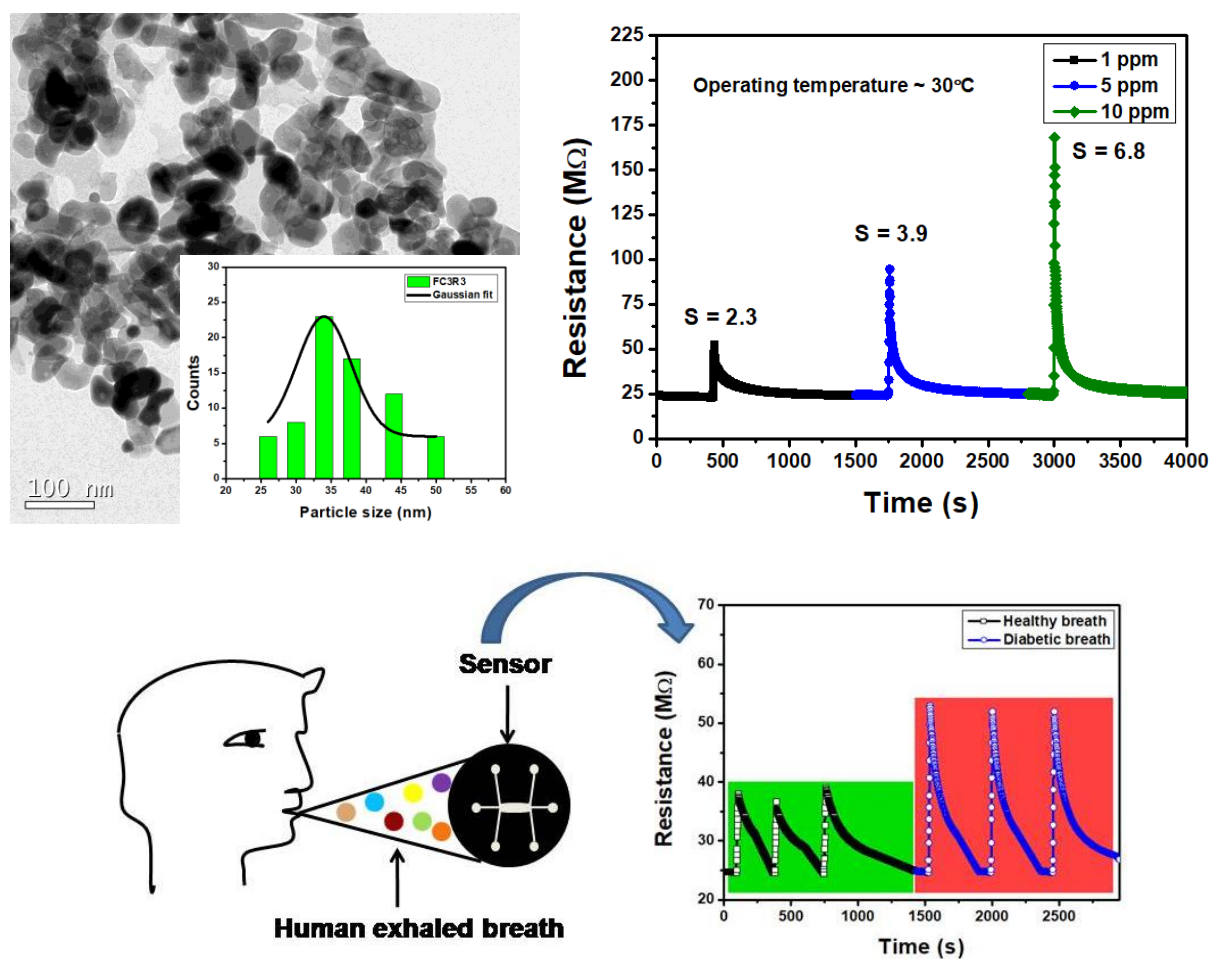


Figure-6.5: Graphical abstract of Chapter 5

In the final chapter, Chapter 6, overall summarization of this dissertation work was presented. Although, there would be enough scope of improvements, as well as, in spite of maximum effort it was not possible to achieve superior results from every perspectives of sensing parameters. It was obvious that improvements of one parameter marginally worsen the other. Nonetheless, some of the reported systems have sufficient potential to emerge as a futuristic candidate for selective non-invasive breath biomarker detector for the diagnosis of diabetes.

## **6.2. Future perspectives:**

The comprehensive study of different rGO-metal oxide nanocomposites were significantly emphasized on optimizing the VOC sensing performance at ambient conditions. Some fabricated Taguchi-type sensors also presented their potential utility as non-invasive diabetic breath biomarker detector by analyzing the acetone concentration in exhaled human breath. Nevertheless, several crucial aspects of this research work needed additional efforts to shed light on its advancement and give it a new dimension.

- The processing parameters should be engineered in such a way that the adopted synthesis procedure could be used for facile and scalable synthesis of rGO-MOS nanocomposites.
- Although the fabricated sensors exhibited a selective, reproducible sensing response over a certain period of time, the base resistances were still in the higher ranges. To overcome this, there is a scope for further research to reduce the base resistance of the sensors to simplify the device fabrication.
- Some of the developed sensors have already demonstrated selective acetone sensing performance at room temperature conditions and established their potential in the field of point-of-care detection of diabetes through human exhaled breath analysis. However, it's worth mentioning that there are several stages of every disease and the concentration of a certain VOC in exhaled breath related to a specific disease depends on the stage of illness, medication schedule, and also on patient's food habits. Thus, a profile chart should be prepared based on these parameters by recording data from a good number of volunteers to improve the versatility of the developed sensor.
- The developed sensor module should be assembled with miniaturized electronics design in the form of hand-held futuristic device, so that it could be useful for non-invasive exhaled breath analysis. Therefore, designing of the sensing device is of high priority in the purpose of real-time practical applications
- The device can be improvised in the form of a sensor array by combining selective acetone sensor with some other selective VOC ( $\text{NH}_3$ ,  $\text{H}_2\text{S}$ ,  $\text{HCHO}$ , ethanol, etc.) sensors for the detection of multiple diseases at a time from a single breath pulse.



**SYMBOLS**

$R_S$	Resistance of sensor
$R_g$	Resistance of sensor in presence of gas
$R_a$	Resistance of sensor in presence of air
$R_L$	Load resistance
$\Omega$	Ohm
$V_H$	Source voltage
$V_S$	Voltage drop against the load
$S$	Sensing response
$S_b$	Standard deviation of base resistances
$N_A$	Avogadro number
$C$	Concentration
$C_L$	Concentration of lowest limit of detection
$T$	Temperature
$^{\circ}C$	Degree centigrade
$k$	Boltzmann constant
$E_b$	Activation energy
$E_g$	Band gap energy
$L$	Depletion layer thickness
$D$	Crystallite size
$d$	Spacing between diffraction planes
$\text{\AA}$	Angstrom
$\lambda$	Wavelength of X-ray beam
$\theta$	Diffraction angle
$n$	Order of diffraction
$\delta$	Dislocation density
$\beta$	Full width at half maxima
$\mu$	Dipole moment
$h$	Planck's constant
$\nu$	Frequency



$\Delta\nu$	Raman shift
$\lambda_0$	Incident wavelength
$\lambda_1$	Spectral wavelength
$\Delta E$	Energy difference
$I_D$	Intensity of D-band
$I_G$	Intensity of G-band
$A$	Absorbance
$I_0$	Intensity of incident light
$I$	Intensity of emitted light
$l$	Optical path length
$\alpha$	Absorption coefficient
$\varepsilon$	Molar extinction coefficient
$W$	Weight of adsorbed gas
$W_m$	Weight of adsorbate
$P/P_0$	Relative pressure
$S_{BET}$	Specific surface area
$Z$	Electrical impedance
$ Z $	Modulus of electrical impedance
$Z'$	Resistive part of impedance
$Z''$	Reactive part of impedance
$f_0$	Initial frequency
$f_{max}$	Relaxation frequency
$h\bullet$	Hole
$O^{x-}$	Oxygenated ions
$O_o$	Lattice oxygen
$V_{o\bullet}$	Oxygen vacancy
$\tau_{res}$	Transient response time
$\tau_{rec}$	Transient recovery time
$g$	Gas

**ABBREVIATIONS**

MOS	Metal Oxide Semiconductor
GO	Graphene Oxide
rGO	Reduced Graphene Oxide
VOC	Volatile Organic Compound
TGS	Taguchi Gas Sensor
LOD	Lowest Limit of Detection
ppm	parts per million
ppb	parts per billion
ads	Adsorbed
m	Meter
cm	Centimeter
mm	Millimeter
nm	Nanometer
ml	Milliliter
eV	Electron Volt
keV	Kilo Electron Volt
Hz	Hertz
kHz	Kilo Hertz
MHz	Mega Hertz
kJ/mol	Kilo Joule per Mole
%RH	Percentage of Relative Humidity
wt%	Weight percentage
0D	Zero Dimensional
1D	One Dimensional
2D	Two Dimensional
3D	Three Dimensional
CTAB	Cetyl Trimethyl Ammonium Bromide
LPG	Liquefied Petroleum Gas
CNG	Compressed Natural Gas

CVD	Chemical Vapour Deposition
PVD	Physical Vapour Deposition
RF	Radio Frequency
AC	Alternating Current
DC	Direct Current
GC	Gas Chromatography
MS	Mass Spectrometry
FID	Flame Ionization Detector
MFC	Mass Flow Controller
sscm	Standard Cubic Centimeter per Minute
GUI	Graphical User Interface
MRI	Magnetic Resonance Imaging
ECG	Electrocardiogram
CT	Computed Tomography
TGA	Thermogravimetric analysis
XRD	X-Ray Diffraction
FWHM	Full Width at Half Maxima
CFSE	Crystal Field Stabilization Energy
SF	Stacking Fault
UV	Ultraviolet
IR	Infrared
FTIR	Fourier Transform Infra Red
BET	Brunauer-Emmett-Teller
BJH	Barrett-Joyner-Halenda
XPS	X-ray Photoelectron Spectroscopy
KE	Kinetic Energy
BE	Binding Energy
FESEM	Field Emission Scanning Electron Spectroscopy
TEM	Transmission Electron Microscopy
BFTEM	Bright Field Transmission Electron Microscopy
HRTEM	High Resolution Transmission Electron Microscopy

EDS	Energy Dispersive Spectroscopy
SAED	Selected Area Electron Diffraction
EDAX	Energy Dispersive X-ray Analysis
CCD	Charge Coupled Device
PL	Photoluminescence
NBE	Near Band Edge
DL	Deep Level
HOMO	Highest Occupied Molecular Orbital
LUMO	Lowest Unoccupied Molecular Orbital
CPE	Constant Phase Element
NTCR	Negative Temperature Coefficient of Resistance
R&D	Research and Development
WHO	World Health Organization
JCPDS	Joint Committee on Powder Diffraction Standards
IUPAC	International Union of Pure and Applied Chemistry
FPG-PP	Fasting Plasma Glucose Post Prandial
OGTT	Oral Glucose Tolerance Test



**LIST OF PUBLICATIONS**

1. Reduced graphene oxide (rGO) decorated ZnO-SnO<sub>2</sub>: A ternary nanocomposite towards improved low concentration VOC sensing performance, **Sovandeb Sen**, Susmita Kundu\*, Journal of Alloys and Compounds, 881 (2021) 160406. **DOI no.:** **10.1016/j.jallcom.2021.160406. I.F. :6.2.**
2. Fabrication of Fe doped reduced graphene oxide (rGO) decorated WO<sub>3</sub> based low temperature ppm level acetone sensor: Unveiling sensing mechanism by impedance spectroscopy, **Sovandeb Sen**, Sourav Maity and Susmita Kundu\*, Sensors and Actuators B: Chemical, 361 (2022) 131706. **DOI no.:** **10.1016/j.snb.2022.131706. I.F. : 9.221.**
3. Reduced graphene oxide (rGO) decorated NiO-SnO<sub>2</sub> nanocomposite based sensor towards room temperature diabetic biomarker detection, **Sovandeb Sen**, Sourav Maity, Susmita Kundu\*, Journal of Alloys and Compounds, 966 (2023) 171553. **DOI no.:** **10.1016/j.jallcom.2023.171553. I.F. :6.2.**
4. Room temperature acetone sensing performance of Pt/Sb<sub>2</sub>O<sub>3</sub> impregnated Fe<sub>2</sub>O<sub>3</sub> thin film: Noninvasive diabetes detection, **Sovandeb Sen**, Amit Nilabh, and Susmita Kundu\*, Microchemical Journal, 165 (2021) 106111. **DOI no.:** **10.1016/j.microc.2021.106111. I.F. : 5.304.**
5. Bio-synthesis of SnO<sub>2</sub> and comparison its CO sensing performance with conventional process, Susmita Kundu\*, Amit Kumar, **Sovandeb Sen**, Amit Nilabh, Journal of Alloys and Compounds, 818 (2020) 152841. **DOI no.:** **10.1016/j.jallcom.2019.152841. I.F. :6.2.**
6. A novel ppm level ethanol sensor based on La loaded ITO impregnated with Pd and Sb additives, Amit Nilabh, **Sovandeb Sen**, Mousumi Narjinary, Susmita Kundu\*, Microchemical Journal, 158 (2020) 105146. **DOI no.:** **10.1016/j.microc.2020.105146. I.F. :5.304.**

7. Development of La-impregnated TiO<sub>2</sub> based ethanol sensors for next generation automobile application, Saheli Bhattacharjee, **Sovandeb Sen**, Susmita Kundu\*, Journal of Materials Science: Materials in Electronics, 33 (2022) 15296-15312. **DOI no.: 10.1007/s10854-022-08394-4. I.F.: 2.478.**
8. Study the role of rGO in enhancing the electrochromic performance of WO<sub>3</sub> film, Saheli Bhattacharjee, **Sovandeb Sen**, Soumya Samanta, Susmita Kundu\*, Electrochimica Acta, 427 (2022) 140820. **DOI no.: 10.1016/j.electacta.2022.140820. I. F.: 7.336.**

### LIST OF CONFERENCES, SEMINARS, AND WORKSHOPS ATTENDED

1. Synthesis and characterization of gel calcined ZnO/SnO<sub>2</sub> nanocomposite for formaldehyde sensing application – **Sovandeb Sen**, Susmita Kundu\*, 12<sup>th</sup> Asia Pacific Microscopy Conference (APMC), held at HICC, Hyderabad, February 3-7, 2020.
2. Fabrication of sol-gel prepared WO<sub>3</sub>-rGO thin film based room temperature operated acetone sensor – **Sovandeb Sen**, Susmita Kundu\*, 2<sup>nd</sup> Indian Materials Conclave and 31<sup>st</sup> AGM at Kolkata, organized by Materials Research Society of India (MRSI), CSIR-CGCRI, Kolkata, February 11-14, 2020.
3. Fabrication of rGO decorated Fe doped WO<sub>3</sub> sensors for low temperature acetone sensing application – **Sovandeb Sen**, Susmita Kundu\*, School of Applied and Interdisciplinary Sciences Symposium 2020, held at Indian Association for the Cultivation of Science, Kolkata, December 4-5, 2020.
4. Fabrication of rGO decorated ZnO-SnO<sub>2</sub> sensors for acetone sensing application – **Sovandeb Sen**, Susmita Kundu\*, InCerS Conference 2020, Kolkata, December 10-12, 2020.
5. Room temperature gas sensing properties of reduced graphene oxide (rGO) decorated NiO-SnO<sub>2</sub> nanocomposite – **Sovandeb Sen**, Susmita Kundu\*, International Symposium on Materials of the Millennium: Emerging Trends and Future Prospects (MMETFP 2021), held at School of Technology, Pandit Deendayal Energy University, Gujarat, November 19-21, 2021.
6. Workshop on Wet chemical synthesis: gold and silver nanoparticles – **Sovandeb Sen**, CSIR – Indian Institute of Toxicology Research, December 15, 2021.
7. Reduced graphene oxide (rGO) decorated La-doped TiO<sub>2</sub> nanocomposite and its gas sensing properties – **Sovandeb Sen**, Susmita Kundu\*, International Conference on Chemical And Environmental Sciences (ICCAES 2021), Institute of Engineering and Management, Kolkata, December 17-19, 2021.



8. Fe doped reduced graphene oxide (rGO) decorated  $\text{WO}_3$  based low temperature ppm level acetone sensing – **Sovandeb Sen**, Susmita Kundu\*, 58<sup>th</sup> Annual Convention of Chemists, 2021 & International Conference on Recent Trends in Chemical Science (RTCS 2021), organized by the Indian Chemical Society, Kolkata, December 21-24, 2021.
9. Low temperature acetone sensing performance by Fe doped reduced graphene oxide (rGO) decorated  $\text{WO}_3$  nanocomposite - **Sovandeb Sen**, Susmita Kundu\*, Glamics Fiesta 2022, held at CSIR-CGCRI, Kolkata, June 9-10, 2022.
10. Room temperature VOC sensing properties of reduced graphene oxide decorated  $\text{NiO-SnO}_2$  nanocomposite - **Sovandeb Sen**, Susmita Kundu\*, Young Scientists' Colloquium 2022, organized by Materials Research Society of India, Kolkata, held at CSIR-CGCRI, Kolkata, December 16, 2022.
11. Low temperature non-invasive detection of diabetes by functionalized  $\text{WO}_3$  nanocomposite - **Sovandeb Sen**, Susmita Kundu\*, One Day National Workshop on Bioactive Glass, Ceramics and Composites in Healthcare: Current Technological Trends, 2022 (BIOCOM 2022), Kolkata, held at CSIR-CGCRI, Kolkata, December 16, 2022.
12. Online Five Days Short Term Training Programme (STTP) on Emerging Multidisciplinary Research (EMR) – **Sovandeb Sen**, held at School of Energy Technology, Pandit Deendayal Energy University, Gujarat, January 9-13, 2023.
13. Room temperature carbon monoxide sensing by perovskite  $\text{BaSnO}_3$  nanocomposite - **Sovandeb Sen**, Susmita Kundu\*, International Conference on Nano Composites for Aerospace Applications (ICNCAS 2023) organized by Department of Basic Science and Electronics & Communication Engineering held at Cambridge Institute of Technology, Bangalore, February 2-4, 2023.
14. Room temperature acetone sensing properties of Cr (III) doped reduced graphene oxide (rGO) decorated  $\text{WO}_3$  nanocomposite - **Sovandeb Sen**, Susmita Kundu\*, Young Scientists' Colloquium 2023, organized by Materials Research Society of India, Kolkata, held at Jadavpur University, Kolkata, December 01, 2023.

*“Equipped with his five senses, man explores  
the universe around him and calls the  
adventure Science”*

*——— Edwin Powell Hubble*





# Reduced graphene oxide (rGO) decorated ZnO-SnO<sub>2</sub>: A ternary nanocomposite towards improved low concentration VOC sensing performance

Sovandeb Sen, Susmita Kundu\*

Functional Materials and Devices Division, CSIR, Central Glass & Ceramic Research, Institute, Kolkata 700032, India

## ARTICLE INFO

### Article history:

Received 2 March 2021

Received in revised form 24 April 2021

Accepted 12 May 2021

Available online 18 May 2021

### Keywords:

Sol-gel synthesis

rGO decorated ZnO-SnO<sub>2</sub> nanocomposite

Taguchi type sensors

VOC sensing

Low ppm sensing

## ABSTRACT

A ternary p-n-n heterojunction has been prepared by introducing reduced graphene oxide (rGO) in ZnO-SnO<sub>2</sub> nanocomposite and its ppm level volatile organic compounds (VOCs) sensing properties have been exploited. Using a simple, facile sol-gel process, initially, ZnO-SnO<sub>2</sub> nanocomposites containing different concentrations of ZnO and SnO<sub>2</sub> were prepared and subsequently this was followed by rGO incorporation. The as-synthesized powders were well characterized through XRD, FTIR, Raman spectroscopy, FESEM, TEM, and XPS analyses. The sensing study revealed that, the ternary nanocomposite sensor delineated ~91% n-type sensing response towards ~10 ppm acetone gas at an optimum working temperature of 150 °C. Even it could sense ~1 ppm acetone with appreciable sensing response of ~71%. Additionally, the sensor displayed fast response (~10 s) and recovery time (~100 s) suitable for detection of multiple pulses in short time duration. It also exhibited a considerable ~65% sensing response towards ~10 ppm ethanol at 150 °C. These superior sensing performances of rGO decorated ZnO-SnO<sub>2</sub> nanocomposite illustrated with band structure modification. Our results indicated that, the fabricated rGO decorated ZnO-SnO<sub>2</sub> sensor, with remarkable high sensing response, minimum interference from other toxic, inflammable gases and profound long term stability, could be considered as a prolific candidate for real time detection of low concentration VOCs in versatile commercial applications.

© 2021 Elsevier B.V. All rights reserved.

## 1. Introduction

In past few decades, the study of gas sensors have been evaluated as most discussed topic due to their growing impact in versatile applications starting from air pollution monitoring to detection of toxic, flammable and explosive gas leakages in combustible gas plants [1–4] for health and safety purpose etc. Recently gas/ volatile organic compounds (VOCs) detection in low concentration level also get extra importance as some of them have been recognized as breath biomarkers for non-invasive detection of different diseases [5–7]. Therefore, intense research efforts are devoted throughout the world for the generation of high performance real time gas sensors with good sensing response, selectivity as well as with low detection limit. In this context, chemiresistive metal oxide semiconductor (MOS) based sensors [8–11] attract the attention of the researchers by virtue of their simplicity in scale-up production, cost efficiency, excellent sensing performance, good electrical conductivity and

environment friendliness. But, MOS sensing materials still suffer from several disadvantages like very high operating temperature, low selectivity and poor long term stability. These drawbacks can be overcome by effectively improving the physicochemical properties of MOSs, through tailoring crystal orientation and morphologies, decreasing crystal size and increasing defect densities [12,13].

Among all the MOSs, SnO<sub>2</sub> is a typical n-type material having large band gap energy (3.6 eV) at 300 K [14,15] and extensively used in numerous applications, viz. Li-ion batteries, sensitized solar cell, gas sensors etc. But, its practical applications as efficient gas sensor are limited due to poor selectivity, long response/recovery time and low sensing response. On the other hand, ZnO is another well known n-type semiconductor with wide band gap (3.4 eV) and large exciton binding energy (60 meV) at room temperature [16,17]. It is considered as an exciting sensing material for its non-toxicity, high electrochemical stability, good response to several oxidizing and reducing gases and suitability of doping. In spite of these inherent superiorities, ZnO-based sensors have several unsolved drawbacks like limited physical and chemical properties of the material and short lifetime which restrict their potential applications. As we

\* Corresponding author.

E-mail addresses: [ksusmita@cgcri.res.in](mailto:ksusmita@cgcri.res.in), [ksusmita4@gmail.com](mailto:ksusmita4@gmail.com) (S. Kundu).





# Fabrication of Fe doped reduced graphene oxide (rGO) decorated WO<sub>3</sub> based low temperature ppm level acetone sensor: Unveiling sensing mechanism by impedance spectroscopy

Sovandeb Sen, Sourav Maity, Susmita Kundu \*

Functional Materials and Devices Division, CSIR-Central Glass & Ceramic Research Institute, Kolkata 700032, India

## ARTICLE INFO

### Keywords:

Sol-gel synthesis  
Fe doped rGO decorated WO<sub>3</sub>  
Thin film sensors  
ppm level acetone sensing  
Low operating temperature  
Impedance spectroscopy

## ABSTRACT

Chemiresistive MOS-based acetone sensing device is a futuristic pathway for non-invasive diagnosis of diabetes. Although their potential deployment is restricted till now due to lack of selective, low temperature operated ppm-level sensors. In this work, we demonstrated synthesis of iron doped reduced graphene oxide (rGO) decorated WO<sub>3</sub> nanocomposites in a facile, environment friendly wet chemical sol-gel process. The as-synthesized nanocomposites were comprehensively characterized by using different characterization techniques. A maximum ~78% sensing response was obtained for the optimized composition of ~10 wt% Fe doped 3 wt% rGO decorated WO<sub>3</sub> based thin film (thickness ~700 nm) sensor towards ~10 ppm acetone gas. This sensing performance was observed at comparatively low working temperature of ~130 °C with fast response (~20 s) and recovery (~75 s) time. The efficacy of the fabricated sensors was established by their capabilities to sense a very low concentration of ~1 ppm acetone under similar working environment. Further illustration of versatility of the sensors revealed that, the sensors could be able to manifest a repeatable and reproducible sensing performance with prolong stability and superior selectivity for acetone over other interfering gases. The acetone sensing mechanism was illustrated with the help of electron depletion model and impedance spectroscopy study. Impedance spectroscopy quantifies different electrical properties and enlightens the smooth electronic transition mechanism between analyte and sensing material.

## 1. Introduction

At present, several toxic gases and volatile organic compounds (VOCs) evolved from our different habitual style of living; impart an adverse effect on environment and raise a great concern for human health [1–4]. On the other hand, some of them are generated in human body due to different metabolic processes and recently identified as potential biomarker [5–8] for early stage non-invasive detection of diseases. It has been observed that under certain pathological conditions, in ppm level concentration, acetone is breath biomarker for diabetes [9,10], ammonia for kidney disorder [11,12], hydrogen sulfide for asthma [13,14] etc. In this respect, real time monitoring of these gaseous species in minute concentration is utmost necessity. Generally, analytical technologies involving spectroscopy and chromatography are in use for their detection. Although, they are significantly accurate but seemed to be complicated, non-portable and tedious. In order to avail cost effective and hand-held user-friendly device with good accuracy,

reproducibility and fast response/recovery time, several research works are in progress. Worldwide researchers are interested in metal oxide semiconductors (MOSSs) based chemiresistive sensors [15–20] because of their excellent reproducibility, non-toxicity and ease of production. However, their practical applications are challenging due to poor selectivity and high temperature of operation. At elevated operating temperature range the sensors consume high power and leads to complication in device fabrication. The temperatures also degrade the sensing behavior through grain coalescence and thus shorten their life-time. Hence, recent research studies are devoted almost entirely in fabrication of low temperature sensors.

From this viewpoint, WO<sub>3</sub>, an n-type metal oxide semiconductor, is considered as one of the significant candidate for gas sensing [21–24]. The superiority of WO<sub>3</sub> prevails due to its different crystalline nano-structures with high oxygen vacancies and excellent electrical conductivity. In spite of that, WO<sub>3</sub> based sensors suffer from drawbacks like poor sensitivity and high working temperature. With this viewpoint,

\* Corresponding author.

E-mail addresses: [ksusmita4@gmail.com](mailto:ksusmita4@gmail.com), [ksusmita@cgcri.res.in](mailto:ksusmita@cgcri.res.in) (S. Kundu).

<https://doi.org/10.1016/j.snb.2022.131706>

Received 12 November 2021; Received in revised form 1 March 2022; Accepted 10 March 2022

Available online 24 March 2022

0925-4005/© 2022 Elsevier B.V. All rights reserved.





# Reduced graphene oxide (rGO) decorated NiO-SnO<sub>2</sub> nanocomposite based sensor towards room temperature diabetic biomarker detection

Sovandeb Sen, Sourav Maity, Susmita Kundu<sup>\*</sup>

Functional Materials and Devices Division, CSIR, Central Glass & Ceramic Research Institute, Kolkata 700032, India

## ARTICLE INFO

### Keywords:

Sol-gel synthesis  
Taguchi type sensors  
Room temperature sensing  
Non-invasive diabetic biomarker  
Impedance spectroscopy

## ABSTRACT

In the present work, reduced graphene oxide (rGO) decorated NiO-SnO<sub>2</sub> nanocomposites were synthesized by using a facile sol-gel process and their structural (XRD, FTIR, Raman), morphological (BET, FESEM, TEM), and optical (UV-Vis, PL) characterizations were carried out. The as-synthesized NiO-SnO<sub>2</sub> nanocomposite exhibited an enhancement of surface area after the incorporation of rGO and this substantial increment was expected to be beneficial for gas sensing at room temperature. Therefore, Taguchi-type sensors were fabricated and deployed for the detection of VOCs. The optimized sensor containing ~ 3 wt% rGO in NiO-SnO<sub>2</sub> nanocomposite demonstrated an excellent sensing response ( $R_g/R_a \sim 7.8$ ) towards ~ 10 ppm acetone at room temperature ( $30 \pm 5^\circ\text{C}$ ) with response and recovery time of ~ 10 s and ~ 30 s respectively. It also exhibited good reproducibility and stability over ~ 3 months. Additionally, this sensor selectively detected trace concentration ( $< 1$  ppm) of acetone in exhaled human breath (ethanol present in a healthy person's exhaled breath is insignificant), which is a non-invasive biomarker of diabetes. The sensing performance was analyzed from an electronic transportation point-of-view and consequent band structure modulation. The electrical property of the sensing material was illustrated using impedance spectroscopy to support the sensing mechanism.

## 1. Introduction

In the twentieth century, fast-track advancements in science and technology have adversely affected human health due to releasing of several toxic gasses and volatile organic compounds (VOCs) [1–8]. However, some VOCs (present in ppb/ppm level in exhaled breath) have recently been considered biomarkers for early-stage non-invasive detection of different diseases. Under certain pathological conditions, detecting a specific exhaled VOC can identify a particular disease [9–12]. The gas sensors are very promising to identify these VOCs, but the real challenge is their trace concentration. Acetone in exhaled breath has been recognized as a biomarker for the non-invasive detection of diabetes [13–16] at a concentration  $> 1$  ppm. Therefore, developing a selective acetone sensor with good sensing response at low concentrations and fast response/recovery time is imperative.

Among various types of metal oxide semiconductors (MOSs) based chemiresistive gas sensors [17,18], SnO<sub>2</sub> is used extensively owing to its chemical stability and good sensitivity [19–22]. Nevertheless, its commercialization has constraints due to high operating temperature, lack of selectivity, low precision, and sluggish response/recovery time.

To solve these problems, worldwide researchers are employing different strategies like microstructure modification, functionalization with noble metals [23–25], heterojunction formations [26–28] etc. Combining two semiconductor materials to form a binary heterojunction might be a fruitful successor as it can provide fluent electronic transportation via hole-electron recombination pathways. From this perspective, the introduction of p-type NiO in n-type SnO<sub>2</sub> matrix develops a p-n heterojunction which can effectively attune charge carriers' concentration across heterojunction barrier and thereby elevate sensing performance [29,30], e.g., Zhang et al. [31] demonstrated 500 ppm methane sensing at  $330^\circ\text{C}$  by porous NiO nanosheets decorated with SnO<sub>2</sub>, Wei et al. [32] showed NO<sub>2</sub> sensing performance of hydrothermally synthesized SnO<sub>2</sub> nanoneedle-anchored NiO microsphere at  $230^\circ\text{C}$ . These literature studies reveal that NiO-SnO<sub>2</sub> sensors can detect gases efficiently but operate at high working temperatures. However, high temperature operated sensors need more power consumption and grain coalescence leads to a shortening of lifetime, restricting them from commercial applications. Henceforth, researchers are devoted to fabricate sensors operated at ambient temperature [33,34].

It is worth mentioning that enhancement of the surface area of

<sup>\*</sup> Corresponding author.

E-mail addresses: [ksusmita4@gmail.com](mailto:ksusmita4@gmail.com), [ksusmita@cgcri.res.in](mailto:ksusmita@cgcri.res.in) (S. Kundu).

<https://doi.org/10.1016/j.jalcom.2023.171553>

Received 15 June 2023; Received in revised form 25 July 2023; Accepted 26 July 2023

Available online 28 July 2023

0925-8388/© 2023 Elsevier B.V. All rights reserved.







# Room temperature acetone sensing performance of Pt/Sb<sub>2</sub>O<sub>3</sub> impregnated Fe<sub>2</sub>O<sub>3</sub> thin film: Noninvasive diabetes detection

Sovandeb Sen, Amit Nilabh, Susmita Kundu\*

Functional Materials and Devices Division, CSIR-Central Glass & Ceramic Research Institute, Kolkata 32, India

## ARTICLE INFO

### Keywords:

Room temperature  
Acetone sensing  
Sub-ppm level  
Thin film  
Noninvasive breath measurement  
Diabetes detection

## ABSTRACT

In the present report, an enhanced sub-ppm level acetone sensing performance of a novel Pt and Sb<sub>2</sub>O<sub>3</sub> impregnated nanocrystalline Fe<sub>2</sub>O<sub>3</sub> thin film operating at room temperature has been explored. Starting from organic precursor sols, thin films of thickness ~ 6 μm were drop-casted on planar alumina substrates pre-attached with the platinum electrodes and cured at ~ 350°C. The characterizations of the materials have been carried out using X-ray Diffraction, FTIR, Raman Spectroscopy, micro structural study through FESEM and TEM as well as XPS analyses. The sensing characteristics including sensing response, lowest detection limit, recovery time etc. of these chemiresistive thin films were studied on exposing them to various concentrations (0.25 to 1 ppm) of acetone at room temperature. The sensing response of ~2.4 with ~ 95 s recovery time was observed on exposure to 1 ppm acetone for 10 s. Even at 0.25 ppm acetone, the response observed ~ 1.4. Selectivity study on different alcohols and other interfering gases of breath has also been tested. Additionally, a real time breath acetone measurement was carried out and acetone sensing mechanism has been elucidated.

## 1. Introduction

Recently analysis of volatile organic components (VOC) in exhaled breath has been established as a promising and non-invasive technique for early stage diagnosis of different diseases [1]. Worldwide research studies identified exhaled ammonia for kidney related diseases, [2] combinations of NO<sub>x</sub>, CO for lung cancer [3] etc. Similarly, presence of acetone in human breath has linked with ketosis and hence considered as biomarker [4] for preliminary detection of diabetes. Considering other pathological conditions under control, breath acetone concentration ~ 1 ppm indicates presence of diabetes [5]. Hence, exhaled breath acetone analysis can be an excellent method for non-invasive diabetes detection. However, breath analysis in a cost effective, patient friendly mode needs a highly sophisticated sensing platform, for selective and precise detection of sub-ppm acetone [6-9] in presence of other VOCs and moisture in breath.

From the last few years, different research groups are working on the development of selective acetone sensing materials. Among different types of sensors, metal oxide semiconductor (MOS) based sensors play an important role due to high sensitivity, low cost, robustness and portability. Now, most of the available metal oxide-based sensing device can only function at elevated operating temperatures (higher

than 100°C) [10-14]. At such high temperature, the oxygen molecules adsorb on the surface and interact with target gas molecules, leading to high responses. Furthermore, high operating temperature allows fast response and recovery times. However, working at high operating temperature increases the power consumption and in some cases, may lead to a change in the sensing behavior of the metal oxide-based sensors. Therefore, gas sensing research, now a day mainly devoted to the fabrication of sensors working at room temperature. Room temperature sensor system can simplify device design by eliminating the heater component, save electrical power and can assemble on flexible polymer substrates. It also slows down the degradation of the sensing materials such as grain coalescence or grain-boundary alteration, which improves the lifetime of the sensor.

Now, it has been observed that it is very difficult to fabricate low power consumption sensing devices with thick film sensing layers. In this context, new techniques may become fruitful in future which aim at deposition of thin films of sensing material. Surface oxygenated functional groups and defective sites in the thin films can boost the sensing performance. Due to their high surface to volume ratio, they perform as active gas adsorption sites for facile binding of gas molecules.

There are several techniques which are generally used for thin film deposition like sputtering [15], hydrothermal [16], solvothermal [17],

\* Corresponding author.

E-mail address: [ksusmita@cgcri.res.in](mailto:ksusmita@cgcri.res.in) (S. Kundu).

<https://doi.org/10.1016/j.microc.2021.106111>

Received 19 November 2020; Received in revised form 18 February 2021; Accepted 19 February 2021

Available online 23 February 2021

0026-265X/© 2021 Elsevier B.V. All rights reserved.





# Bio-synthesis of SnO<sub>2</sub> and comparison its CO sensing performance with conventional processes



Susmita Kundu\*, Amit Kumar, Sovandeb Sen, Amit Nilabh

Functional Materials and Devices Division, CSIR-Central Glass and Ceramic Research Institute, Kolkata, India

## ARTICLE INFO

### Article history:

Received 30 July 2019

Received in revised form

21 October 2019

Accepted 27 October 2019

Available online 28 October 2019

### Keywords:

Biosynthesis

Nanostructured tin oxide

CO sensing

## ABSTRACT

The present paper reports on a unique eco-friendly bio-synthesis process of tin oxide using water extract of soaked kabuli chickpea seeds as natural binder. The structural, microstructural and CO sensing properties of the newly synthesized tin oxide were compared with those of conventional sol-gel and sonochemical processes. XRD results of the bio-synthesized material revealed the formation of single tetragonal phase of SnO<sub>2</sub> similar to sol-gel and sonochemical processes. The bio approach led to the formation of finer nanoparticles with a higher specific surface area ~ 60 m<sup>2</sup>/gm compared to the others. The average sizes of tin oxide nanoparticles as observed from TEM images were about 35 nm, 15 and 6 nm for the sonochemical, sol-gel and biosynthesis respectively. These tin oxide powders were used to fabricate Taguchi based sensors and their CO sensing performance were evaluated. The biosynthesized tin oxide sensor showed ~53% sensing performance for 30 ppm CO which was better than sol-gel (~44%) or sonochemical (~42%) tin oxides operating at similar condition. The reported results suggest that the biosynthesis is a promising cost effective method to prepare nanocrystalline SnO<sub>2</sub> for sensing application.

© 2019 Elsevier B.V. All rights reserved.

## 1. Introduction

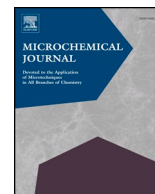
Recently, the whole world is showing an increasing interest in the use of natural polymers as they are non toxic, less expensive and freely available. One of the most emphasised researches going on nowadays is the synthesis of nanomaterials using different procedure for different applications like gas sensing [1–7], Li-ion batteries [8–11] etc. Now if natural elements can be used for the processing of nanomaterials, it will lead to great advantages in synthesis area. Therefore, efforts are continuing worldwide towards the synthesis of several nanoparticles [11–14] using natural resources. Tin oxide (SnO<sub>2</sub>) is a *n*-type wide band gap ( $E_g = 3.6$  eV) semiconducting material and offers wide range of potential technological applications in gas sensing, transparent conducting electrodes, electrochemical devices and dye based solar cells [15] etc. due to its unique optical, electrical and electrochemical properties. Thus, the synthesis of SnO<sub>2</sub> nanocrystallites of high crystallinity and well-defined particle morphologies with narrow-size distribution is of great technological and scientific interest. Various

methods, including molten-salt synthesis [1] hydrothermal method [2], sol-gel [3], microwave technique [4], carbothermal reduction [5] and sonochemical [6,7] have been developed to synthesize SnO<sub>2</sub> nanostructures. But most of the methods require sophisticated instruments or costly chemicals. In the present effort, remnant water (ideally kitchen waste) collected from soaked Kabuli chickpea (*Cicer arietinum* L.) seed has been used for the synthesis of tin oxide nanoparticles. According to our knowledgebase, recently some discrete works have been reported on synthesis of doped tin oxides from natural resources [16,17]. K. P. Gattu et al. reported on bio green synthesis of gold doped tin oxide and its NO<sub>2</sub> sensing property was evaluated. But their synthesis procedure was through precipitation followed by centrifuging which led to particle size ~25 nm, comparable to the conventionally used methods and overall no improvement in properties of tin oxide was found. Here, we selected gel calcination method for bio-synthesis and the structural, microstructural properties of the biosynthesized powder were compared systematically with the tin oxide prepared through sol-gel and sonochemical processes. Nanocrystalline tin oxide is widely used for different gas sensing purpose. In the present work, one of the most common toxic carbon monoxide was chosen as target gas. This is an effort to explore and establish a cost effective, green and amenably reproducible process for scaling up

\* Corresponding author.

E-mail address: [ksusmita@cgcri.res.in](mailto:ksusmita@cgcri.res.in) (S. Kundu).





# A novel ppm level ethanol sensor based on La loaded ITO impregnated with Pd and Sb additives

Amit Nilabh, **Sovandeb Sen**, Mousumi Narjinary, Susmita Kundu\*

Functional Materials and Devices Division, CSIR-Central Glass & Ceramic Research Institute, Kolkata 32, India

## ARTICLE INFO

### Keywords:

La loaded indium tin oxide  
Taguchi type sensor  
Ethanol sensing  
ppm level  
Effect of Pd and Sb additives

## ABSTRACT

The present work reports on a novel resistive ppm level ethanol sensor, prepared from nanocrystalline lanthanum loaded indium tin oxide (ITO) impregnated with palladium and antimony additives. A simple unique gel calcination process was adapted to synthesize the nanocomposite powders from their water based precursor salts. This was followed by detailed material characterizations through X-ray diffractometer, FESEM, TEM, EDX and XPS analyses. Fabricated Taguchi type sensor with an optimum concentration of Pd exhibited an excellent sensing performance towards a wide concentration range of (1–100 ppm) ethanol vapour. The sensor showed ~87% sensing response for 10 ppm ethanol vapour at an operating temperature of 300 °C. Even at 1 ppm concentration, ~53% response was observed with fast response and recovery time. The sensing action has been elucidated as the catalytic oxidation of ethanol to carbon di oxide over the La loaded ITO surface layer that resulted in electron transfer to the indium tin oxide site. In addition, synergistic effect of palladium and antimony enhanced the sensing performance as well as reduced the base resistance of the sensor by chemical/electronic sensitization and increasing carrier ion concentration respectively. Comparatively low resistance, negligible cross sensitivity, quick response/recovery time and good long term stability makes the sensor suitable for deployment in practical applications.

## 1. Introduction

In recent years, indium tin oxide (ITO) has been emerged as the most efficient transparent conducting oxide material in different optoelectronic devices [1–5] for its good optical transparency ( $T > 85\%$  at 550 nm) and high electrical conductivity ( $\rho \sim 10^{-4} \Omega\text{-cm}$ ). It is also an excellent stable material with respect to time and temperature. Now, the gas sensing performance of a metal oxide depends on the surface feature and usually studied by measuring the change of the sensor resistance on exposure to the target gas. Therefore, it is desirable from electronic point of view that the resistance of the sensor should be low enough so that it could monitor a minor change of resistance and thereby be able to determine the small concentration difference of gas. Additionally, the sensor could also be easily integrated with electronic circuits. ITO is basically a  $\text{SnO}_2$  doped  $\text{In}_2\text{O}_3$  where Sn atoms replace In atoms of  $\text{In}_2\text{O}_3$  lattice and give rise to nonstoichiometric oxygen defects which could enhance the sensing performance. Besides, the smooth morphology and high electrical conductivity of ITO would also be the great advantages of using this as a promising TCO based sensing material compared to other metal oxides used for gas sensing [6–8]. Literature survey reveals that there are several reports on sensing

behaviour of indium tin oxide [9–12] but it is towards different gases like ammonia, ethanol, formaldehyde etc. In addition most of them are lacking in their supremacy with respect to sensitivity and selectivity as well as response and recovery time.

Ethanol is one of the most commonly and widely used chemical compound and applied in many fields such as chemical industry, medicine, and food/ beverage industries. Furthermore, ethanol fuel is also a clean, efficient, and promising candidate for a renewable energy source that will overcome current challenges such as air pollution and the global energy crisis. In this growing ethanol fuel economy, safety challenges involving ethanol production, transportation, and storage require precise quantitative detection of ethanol vapour at ppm level [13]. Most of the ethanol sensors available in the market are sensitive to the concentration range of 100 ppm and above and they are mainly used by the traffic police for detection of alcohol consumption of drunken drivers. Hence, recently many research groups have paid attention to prepare the ppm level sensors accordingly. S. Mariani et al. reported [14] optical sensors using nanostructured porous silicon interferometers. Tse-Hsien Ou et al. [15] published a paper for detection of low concentration methanol, ethanol using electrolyte-free nanogap electrochemical cells. These processes are either expensive or

\* Corresponding author.

E-mail address: [ksusmita@cgcric.res.in](mailto:ksusmita@cgcric.res.in) (S. Kundu).

<https://doi.org/10.1016/j.microc.2020.105146>

Received 18 February 2020; Received in revised form 7 May 2020; Accepted 8 June 2020

Available online 11 June 2020

0026-265X/ © 2020 Elsevier B.V. All rights reserved.





# Development of La-impregnated TiO<sub>2</sub> based ethanol sensors for next generation automobile application

Saheli Bhattacharjee<sup>1</sup>, Sovandeb Sen<sup>1</sup>, and Susmita Kundu<sup>1,\*</sup>

<sup>1</sup> Functional Materials and Devices Division, CSIR- Central Glass & Ceramic Research Institute, Kolkata 700032, India

Received: 3 March 2022

Accepted: 7 May 2022

Published online:

11 June 2022

© The Author(s), under exclusive licence to Springer Science+Business Media, LLC, part of Springer Nature 2022

## ABSTRACT

Bio-fuel, a blend of ethanol (~ 10 to 85%) and gasoline with various compositions, is one of the promising next generation energy sources in automobile industries, especially in flex-fuel vehicles. Here, the detection of ethanol content is essential for adjusting different fuel combustion parameters. But till date no dedicated sensor is available in the market for this purpose. With this perspective, in the present work, we have developed a selective ethanol sensor based on La<sup>3+</sup> impregnated TiO<sub>2</sub>, which would be capable to detect and differentiate different high concentration of ethanol in gasoline quite precisely. We have used a facile sol-gel procedure to synthesize the pristine and La-impregnated (~ 2 to 6 at.%) titania nanopowders. The phase transformation, structural, and morphological analyses were carried out using thermogravimetric analysis (TGA), X-ray diffraction (XRD), transmission electron microscope (TEM), energy dispersive X-ray (EDX), UV-Visible and photoluminescence (PL) measurements. Taguchi type sensors were fabricated from the as-prepared powders and their ethanol sensing performances were studied. ~ 4 at.% of La concentration was found to be most efficient to stabilize the sensing favorable anatase phase of TiO<sub>2</sub>, as well as gave the best sensing response, ~ 82% in 10% ethanol at operating temperature of ~ 350 °C. This sensing response increased to 96% for pure ethanol. The selectivity of the sensor toward the ethanol with respect to other gases in bio-fuel was quite high. A model bio-fuel composition (E10) was also prepared and performance was evaluated.

## 1 Introduction

Ethanol (C<sub>2</sub>H<sub>5</sub>OH) is an important chemical in various domains, including healthcare, cosmetics, food and beverage industries [1]. Not only that, recently the use of ethanol has also expanded its horizon even to the automobile industries in making bio-fuel.

Being obtained from a biomass feedstock, ethanol is used as a renewable energy source. In case of bio-fuels, it is blended with gasoline and diesel in a required percentage as per the demand of the atmospheric environment. Blending of ethanol not only reduces the consumption of fossil fuels but also helps in enhancing the octane number of the fuel element

Address correspondence to E-mail: ksusmita@cgcri.res.in; ksusmita4@gmail.com







# Study on the role of rGO in enhancing the electrochromic performance of WO<sub>3</sub> film

Saheli Bhattacharjee<sup>a</sup>, Sovandeb Sen<sup>a</sup>, Soumya Samanta<sup>b</sup>, Susmita Kundu<sup>a,\*</sup>

<sup>a</sup> Functional Materials and Devices Division, CSIR- Central Glass and Ceramic Research Institute, Kolkata 700032, India

<sup>b</sup> School of Chemical Sciences, Indian Association for the Cultivation of Science, India

## ARTICLE INFO

### Keywords:

rGO incorporated WO<sub>3</sub>  
Dip-Coating  
Fast switching response  
Coloration efficiency  
Cyclic stability

## ABSTRACT

In the present work, an improved electrochromic thin film has been developed with faster color switching time on incorporation of rGO in WO<sub>3</sub> film. Here, pristine WO<sub>3</sub> and rGO-WO<sub>3</sub> (rGO concentration varying from 1–7wt %) based nanocomposite electrochromic films were fabricated on ITO coated glass substrate, by utilizing a facile sol-gel dip-coating technique. Detailed structural and morphological analyses of the films were carried out using XRD, FESEM, TEM and Raman Spectroscopy. Assimilating the electrochromic properties of all the films showed that, 5wt% rGO incorporated WO<sub>3</sub> film gave a maximized electrochemical performance with minimum degradation in optical transmittance. The film also exhibited an optical modulation of ~ 50% and a better switching response having coloration time ( $t_c$ ) ~ 5.3 s and bleaching time ( $t_b$ ) ~ 6.2 s as compared to the pristine film ( $t_c$  ~ 9.6 s,  $t_b$  ~ 10.4 s). Incorporation of rGO also resulted in an enhancement of coloration efficiency from ~ 81 to ~ 386 cm<sup>2</sup>/C. The Electrochemical Impedance Spectroscopy (EIS) analysis of pristine and rGO loaded film clearly revealed better charge transfer on incorporation of rGO. The cyclic stability study exhibited ~ 25% deterioration in optical transparency of the bare WO<sub>3</sub> film which was < 10% for the rGO impregnated film. An *ex-situ* XRD analysis demonstrated that a crystal dislocation occurring in pristine WO<sub>3</sub> sample was responsible for the same.

## 1. Introduction

The phenomena of electrochromism i.e. the change of color of a material with the application of a small amount of voltage, has gained a huge amount of attention since the past five decades. The applied electrical voltage leads to double intercalation and de-intercalation of electrons and ions ( $H^+$ ,  $Li^+$ ,  $Na^+$ ) and makes the electrochromic (EC) material undergo a redox reaction. Now the EC materials having different optical properties such as reflectance and transmittance in different oxidation states, exhibit reversible change of color on the change of external voltage [1–4]. The EC materials have encompassed the field of electronics from almost every other aspects including smart windows [5–7], display applications [8,9], sunglasses [10], rear view mirrors in cars [11] to electronic skins [12–14], soft robotics [15,16], even up to biological monitoring [17], artificial intelligence [18] and many more. In general the EC materials are classified as inorganic and organic materials. The organics include organic dyes and conducting polymers [19], while inorganic EC films composed mainly of transition metal oxides [WO<sub>3</sub>, TiO<sub>2</sub>, V<sub>2</sub>O<sub>5</sub>, Nb<sub>2</sub>O<sub>5</sub> etc.] and metal coordination complexes [(CoFe(CN)<sub>6</sub>, prussian blue etc.]. Amid which, the transition

metal oxides are most commonly used as the electrochromic thin film layer [20–22] and among them tungsten trioxide due to its remarkable switching response, enormously high cyclic stability and high amount of coloration efficiency [23–25] is more frequently taken into account [26–29]. Till date, massive advancement has been taken place in the domain of WO<sub>3</sub> based EC devices. In the bleached state, WO<sub>3</sub> exhibits +6 oxidation state with a pale yellow hue, on charge insertion tungsten oxides tend to show color changing phenomena as a result of an optical intervalence charge transfer (IVCT) occurring between the metal center in its lattice structure. According to the IVCT model, during electrochromism, the electron first get localized on a  $W^{6+}$  ion and form  $W^{5+}$  leading to a negatively charged species. In the next step, the electron transfers to the adjacent  $W^{6+}$  ion from  $W^{5+}$  [30]. In this way, the intervalence charge insertion or extraction process promotes reduction or oxidation of the metal centers and facilitates the change of color. Upon electrochemical reduction, owing to the electron intercalation from Transparent Conducting Electrode (TCE) to the lattice of WO<sub>3</sub>, the oxidation state changes to a lower one, thereby forming  $W_x^{5+}W_{(1-x)}^{6+}O_3$ . Now in order to neutralize this negative charge, the positively charged cations such as  $Li^+$  or  $H^+$  present in the electrolyte solution combines

\* Corresponding author.

E-mail address: [ksusmita@cgcrici.res.in](mailto:ksusmita@cgcrici.res.in) (S. Kundu).

<https://doi.org/10.1016/j.electacta.2022.140820>

Received 18 April 2022; Received in revised form 7 June 2022; Accepted 5 July 2022

Available online 7 July 2022

0013-4686/© 2022 Elsevier Ltd. All rights reserved.

